

Annual Research Briefs – 2000

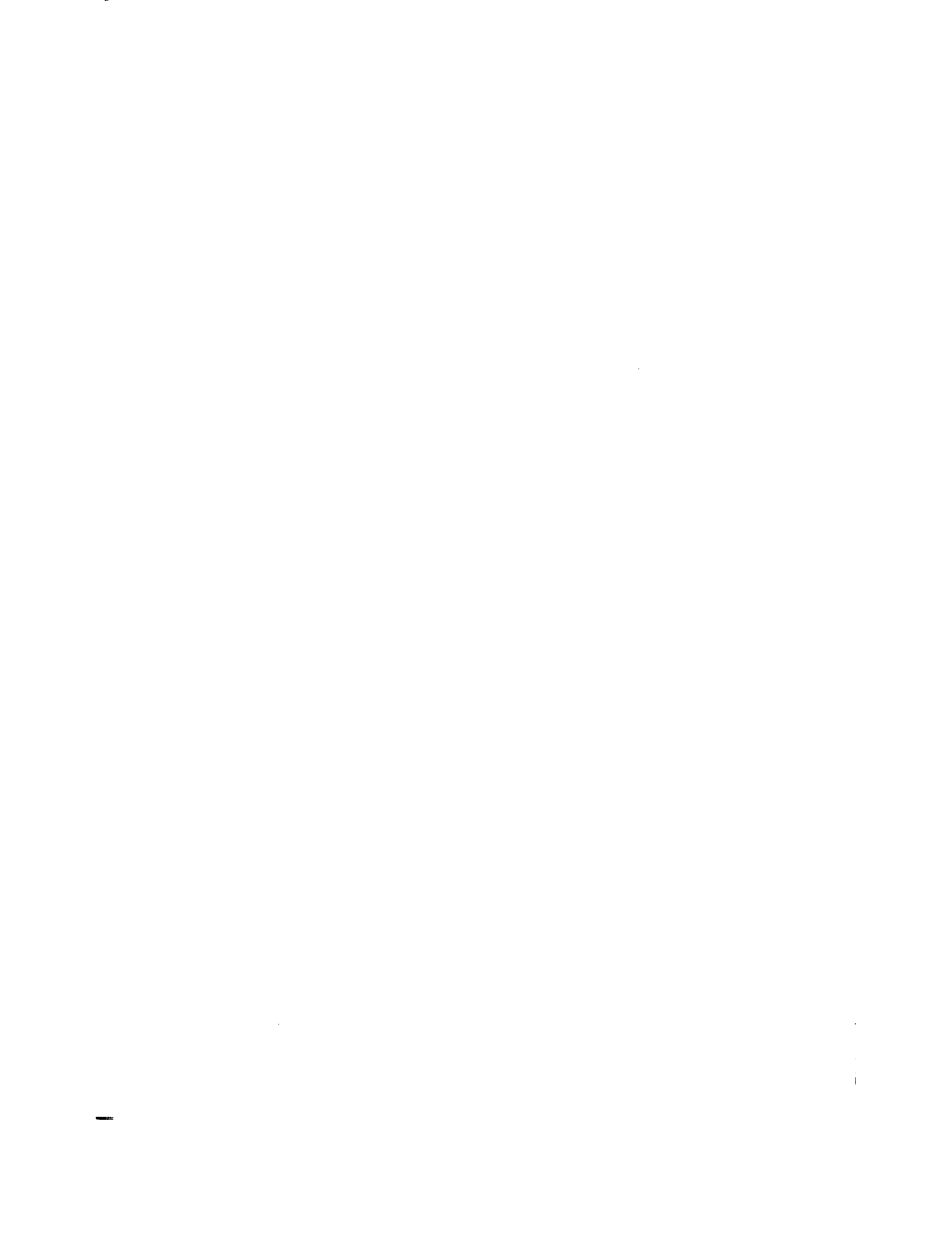
Center for Turbulence Research

December 2000

Dedicated to the memory of

*Richard A Seebass
(1936 - 2000)*





CONTENTS

Preface	1
Calculating free energies using scaled-force molecular dynamics algorithm. E. DARVE, M. W. WILSON and A. POHORILLE	3
In pursuit of structures in protoplanetary disks. O. M. UMURHAN	17
Evolutionary optimization for flow experiments. I. F. SBALZARINI, L. K. SU and P. KOUMOUTSAKOS	31
Control and optimization of turbulent jet mixing. A. HILGERS	45
High-frequency excitation of a plane wake. A. B. CAIN and M. M. ROGERS	55
Low-dimensional dynamics of near-wall turbulence. J. JIMÉNEZ and M. SIMENS	67
Experimental results on the stabilization of lifted jet diffusion flames. L. K. SU, D. HAN and M. G. MUNGAL	79
Stochastic modeling of scalar dissipation rate fluctuations in non-premixed turbulent combustion. H. PITSCH and S. FEDOTOV	91
A level-set approach to large eddy simulation of premixed turbulent combustion. L. DUCHAMP DE LAGENESTE and H. PITSCH	105
Local extinction-reignition in turbulent nonpremixed combustion. P. SRIPAKAGORN, G. KOSÁLY and H. PITSCH	117
Doubly-conditional moment closure modeling of turbulent nonpremixed combustion. C. M. CHA, G. KOSÁLY, and H. PITSCH	129
Mapping closure approximation to conditional dissipation rate for turbulent scalar mixing. G. HE and R. RUBINSTEIN	141
Extended flamelet model for LES of non-premixed combustion. H. PITSCH	149
A high-order approximate-mass spline collocation scheme for incompressible flow simulations. O. BOTELLA	159
Construction of commutative filters for LES on unstructured meshes. L. MARSDEN, O. VASILYEV and P. MOIN	179
Shock-capturing in LES of high-speed flows. M. P. MARTIN	193
A new method for accurate treatment of flow equations in cylindrical coordinates using series expansions. G. S. CONSTANTINESCU and S. K. LELE	199

An evaluation of a conservative fourth order DNS code in turbulent channel flow. J. GULLBRAND	211
Large-eddy simulation of gas turbine combustors. K. MAHESH, G. CONSTANTINESCU and P. MOIN	219
Towards LES models of jets and plumes. A. T. WEBB and N. N. MANSOUR	229
Dynamic wall modeling for LES of complex turbulent flows. M. WANG	241
Flow in an impeller stirred tank using an immersed boundary method. R. VERZICCO, G. IACCARINO, M. FATICA and P. ORLANDI	251
Unsteady 3D RANS simulations using the v^2 - f model. G. IACCARINO & P. DURBIN	263
Prediction of the turbulent flow in a diffuser with commercial CFD codes. G. IACCARINO	271
Computation of turbulent flow in a rotating pipe using the structure-based model. S. V. POROSEVA, S. C. KASSINOS, C. A. LANGER and W. C. REYNOLDS	279
Towards a robust and efficient v^2 - f implementation with application to transonic bump flow. G. KALITZIN	291
Appendix: Center for Turbulence Research 2000 Roster	301

Preface

This report contains the 2000 annual progress reports of the postdoctoral Fellows and visiting scholars of the Center for Turbulence Research. It summarizes the research efforts undertaken under the core CTR program. Last year, CTR sponsored sixteen resident Postdoctoral Fellows, nine Research Associates, and two Senior Research Fellows, hosted seven short term visitors, and supported four doctoral students. The Research Associates are supported by the Departments of Defense and Energy.

In addition to supporting the work reported in this volume, CTR sponsored its eighth summer program, its largest ever, with forty participants. A separate report documenting the findings of this summer program was published earlier this year. CTR publications including this one and the Summer Proceedings are available at CTR's site on the world wide web (<http://ctr.stanford.edu>). The combustion program has continued to benefit from increased collaborations with NASA-Glenn Research Center through the Ultra Efficient Engine Technology Program and the Department of Energy's ASCI program at Stanford. Through additional planned appointments, we expect combustion physics and simulation to remain a major focus of CTR in the future. In addition, CTR's new efforts in computational biology and protoplanetary disks will increase moderately. Here our approach has been to appoint fellows interested in applying their experience in turbulence analysis and diverse areas of flow physics to research in these areas.

The reports in this volume are divided into five groups. The first group largely consists of the new areas of interest at CTR. It includes efficient algorithms for molecular dynamics, stability in protoplanetary disks, and experimental and numerical applications of evolutionary optimization algorithms for jet flow control. The next group of reports is in experimental, theoretical, and numerical modeling efforts in turbulent combustion. As more challenging computations are attempted, the need for additional theoretical and experimental studies in combustion has emerged. A pacing item for computation of non-premixed combustion is the prediction of extinction and re-ignition phenomena, which is currently being addressed at CTR. The third group of reports is in the development of accurate and efficient numerical methods, which has always been an important part of CTR's work. This is the tool development part of the program which supports our high fidelity numerical simulations in such areas as turbulence in complex geometries, hypersonics, and acoustics. The final two groups of reports are concerned with LES and RANS prediction methods. There has been significant progress in wall modeling for LES of high Reynolds number turbulence and in validation of the $v^2 - f$ model for industrial applications.

At the time of this writing, we became aware of the death of Richard Seebass, current Chairman of the CTR Advisory Committee. Professor Seebass was a renowned aerodynamicist, a great advisor for NASA, and a champion of fundamental engineering research in the United States. He served both as member and chairman of the CTR Advisory Committee. We dedicate this volume to his enormous contributions.

As usual, we are indebted to Debra Spinks, the Center's long-term administrative associate, for the day-to-day management of CTR and for compilation of this report. This was the last year for Debra at CTR. She has been a tremendous asset to the Center, and her contributions will be missed. We will strive to maintain her high standards in the preparation of these reports.

Parviz Moin
William C. Reynolds
Nagi N. Mansour

Calculating free energies using scaled-force molecular dynamics algorithm

By Eric Darve, Michael A. Wilson† AND Andrew Pohorille†

1. Motivation and objectives

One common objective of molecular simulations in chemistry and biology is to calculate the free energy difference between different states of the system of interest. Examples of problems that have such an objective are calculations of receptor-ligand or protein-drug interactions, associations of molecules in response to hydrophobic, and electrostatic interactions or partition of molecules between immiscible liquids. Another common objective is to describe evolution of the system towards a low energy (possibly the global minimum energy), “native” state. Perhaps the best example of such a problem is folding of proteins or short RNA molecules.

Both types of problems share the same difficulty. Often, different states of the system are separated by high energy barriers, which implies that transitions between these states are rare events. This, in turn, can greatly impede exploration of phase space. In some instances this can lead to “quasi non-ergodicity”, whereby a part of phase space is inaccessible on timescales of the simulation.

A host of strategies has been developed to improve efficiency of sampling the phase space. For example, some Monte Carlo techniques involve large steps which move the system between low-energy regions in phase space without the need for sampling the configurations corresponding to energy barriers (J-walking). Most strategies, however, rely on modifying probabilities of sampling low and high-energy regions in phase space such that transitions between states of interest are encouraged. Perhaps the simplest implementation of this strategy is to increase the temperature of the system. This approach was successfully used to identify denaturation pathways in several proteins, but it is clearly not applicable to protein folding. It is also not a successful method for determining free energy differences. Finally, the approach is likely to fail for systems with co-existing phases, such as water-membrane systems, because it may lead to spontaneous mixing. A similar difficulty may be encountered in any method relying on global modifications of phase space.

A new, promising technique is the multicanonical Monte Carlo method. In this algorithm, sampling of energy proportional to the Boltzmann factor is substituted by sampling from the uniform energy probability distribution. This means that multicanonical simulation corresponds to a random walk in one-dimensional energy space and, therefore, the system does not experience energy barriers. Since multicanonical weights are not known initially, they have to be estimated in the first step of the simulations. The multicanonical Monte Carlo method appears to be particularly suitable to study helix-coil transition in proteins because a single simulation can provide information about both the low-temperature, helical state and the high-temperature, disordered state.

Many problems of chemical or biological interest can be formulated in terms of evo-

† NASA Ames & UCSF

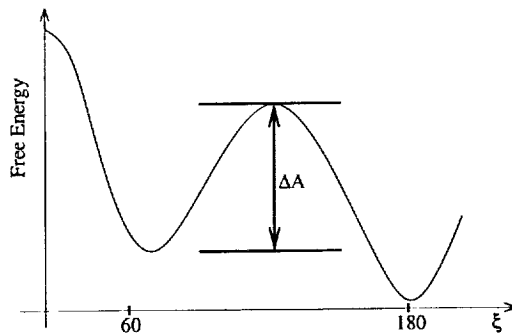
lution of a system along a small number of slow degrees of freedom in the potential of mean force exerted by the remaining coordinates. Then an effective strategy is to add to the Hamiltonian a biasing potential chosen such that free energy barriers in this reduced representation decrease. Sometimes identifying the slow degrees of freedom is not easy, especially if a formally defined reaction coordinate is sought. In many instances, however, our intuitive understanding of the problem can guide us successfully in this process. For example, transport of ions and small molecules across membranes can be well described by calculating the potential of mean force associated with moving the center of mass of the solute in the direction perpendicular to the membrane. In another example, folding of peptides or small, single-domain proteins can be studied by selecting ϕ , ψ (angles in the peptide backbone) and, possibly, some χ angles (angle of rotation of side chains) as slow degrees of freedom.

The method of biasing potentials has several important advantages. First, using a reduced representation is very helpful in planning the simulations and analyzing their results. In fact, it can be argued that, precisely for this reason, it is extremely useful to identify the slow degrees of freedom from the very beginning. Second, if motion along only a few, selected slow degrees of freedom is modified, the chances for the correct identification of pathways along which the system evolves improve markedly. The approach also has a serious disadvantage. To design a useful biasing potential, a good, initial guess about the shape of the potential of mean force is required. If, however, no such guess is available, the approach may turn into a very frustrating experience. Unfortunately, correct estimation of the potential of mean force is often quite difficult because it depends on several contributions of different origin, such as solute-solvent interactions, solvent reorganization, and interactions between solute atoms separated by many bonds but close in space.

In this paper, we present a new approach to the problem of efficient sampling of phase space, based on the molecular dynamics (MD) algorithm in the canonical ensemble. As in the methods of biasing potential, it requires the initial identification of slow degrees of freedom. It does not, however, suffer from the main disadvantage of these methods; no prior assumptions about the shape of the potential of mean force are needed. Even without this assumption, the free energy differences between states in the reduced phase space can be calculated efficiently, perhaps even optimally.

We prove that the derivative of the free energy along a selected generalized degree of freedom can be expressed by an average force, which is a function of this coordinate, and its derivatives with respect to time and positions of the particles. Thus, it can be easily calculated numerically. If this force is scaled by $0 \leq \alpha \leq 1$ or completely eliminated and substituted by another, suitably chosen force, sampling of the generalized coordinate improves markedly. To underscore this feature we call our approach the Scaled Force Algorithm (SFA). Even though the new force acting on the selected coordinate is not, in general, derived from a Hamiltonian, it is still possible, under appropriate conditions, to calculate the free energy change along the selected coordinate in the unmodified system.

In the next section, we present the main idea and the implementation of the method. As the test case, we selected conformational transition of 1,2-dichloroethane in water. The main body of the paper closes with the summary and the outline of future work.

FIGURE 1. Free energy $A(\xi)$ for DCE - schematic

2. Thermodynamics force

We consider a system of N particles. This system can be characterized by the position of the particles $\mathbf{x}_1, \dots, \mathbf{x}_N$ and their momenta $\mathbf{p}_{\mathbf{x}_1}, \dots, \mathbf{p}_{\mathbf{x}_N}$.

Very often we may be only interested in a much more limited number of degrees of freedom. Typically these degrees of freedom can be torsion angles, distances between centers of mass of molecules, distance between center of mass of a molecule and a membrane, etc. From a more abstract point of view, these can simply be viewed as functions of the position and momenta of the particles.

For simplicity we consider the case of 1,2-dichloroethane (DCE) for which we are interested in only one degree of freedom, the torsion angle ξ for the Cl-C-C-Cl bonds. It is well-known that for this case there are three stable configurations: gauche (60 deg), trans (180 deg), gauche-prime (300 deg).

The relative stability of these configurations can be obtained from the free energy $A(\xi)$. It can be defined as:

$$A(\xi) \stackrel{def}{=} -\kappa T \log P(\xi) + A_0 \quad (2.1)$$

where $P(\xi)$ is the probability density function of the torsion angle ξ . A_0 is an arbitrary constant. See Fig. 1 for an illustration. When the theory of transition state approximation is valid, the probability to go from one configuration, say gauche, to another configuration, say trans, is equal to:

$$P(\text{gauche} \rightarrow \text{trans}) = \frac{1}{\mathcal{N}} \exp(-\beta \Delta A)$$

where ΔA is the energy barrier separating 60 deg from 180 deg (see Fig. 1). \mathcal{N} is a normalization factor and $\beta \stackrel{def}{=} 1/(\kappa T)$.

One of the usual methods to compute the free energy uses Eq. (2.1) and explicitly computes $P(\xi)$. Another approach consists in considering the derivative of the free energy $dA/d\xi$. This quantity has dimension of a force and can be viewed as the average force acting on ξ .

More precisely, the following equations can be derived. The probability density for a system at temperature T to be in state $\mathbf{x}_1, \dots, \mathbf{x}_N$ and $\mathbf{p}_{\mathbf{x}_1}, \dots, \mathbf{p}_{\mathbf{x}_N}$ is given by:

$$P(\mathbf{x}, \mathbf{p}) = \frac{1}{\mathcal{N}} \exp -\beta H$$

where H is the Hamiltonian of the system. Equation (2.1) becomes:

$$A(\xi) = -\kappa T \log \int_{S_\xi} \exp -\beta H + \kappa T \log \mathcal{N} + A_0$$

where S_ξ is the set of all \mathbf{x} and \mathbf{p} such that $\xi(\mathbf{x}) = \xi$.

The derivative of A can now be explicitly evaluated:

$$\frac{\partial A}{\partial \xi} = \frac{\int_{S_\xi} \frac{\partial H}{\partial \xi} \exp -\beta H}{\int_{S_\xi} \exp -\beta H} = \left\langle \frac{\partial H}{\partial \xi} \right\rangle_{S_\xi} \quad (2.2)$$

where $\langle \rangle_{S_\xi}$ denotes the statistical average. Thus $\frac{\partial A}{\partial \xi}$ is equal to the statistical average of the force $-\frac{\partial H}{\partial \xi}$ acting on ξ .

To properly define the partial derivative with respect to ξ , it is necessary to introduce generalized coordinates. We define the set of functions q_1, \dots, q_{3N-1} :

$$\begin{aligned} q_1 &= q_1(\mathbf{x}_1, \dots, \mathbf{x}_N) \\ q_{3N-1} &= q_{3N-1}(\mathbf{x}_1, \dots, \mathbf{x}_N) \end{aligned}$$

such that $(\xi, q_1, \dots, q_{3N-1})$ forms a basis equivalent to $\mathbf{x}_1, \dots, \mathbf{x}_N$. We mean that for each set of values $\mathbf{x}_1, \dots, \mathbf{x}_N$ there is a unique set of values $(\xi, q_1, \dots, q_{3N-1})$ such that:

$$\begin{aligned} \mathbf{x}_1 &= \mathbf{x}_1(\xi, q_1, \dots, q_{3N-1}) \\ \mathbf{x}_N &= \mathbf{x}_N(\xi, q_1, \dots, q_{3N-1}) \end{aligned}$$

The derivative with respect to ξ can now be defined as the derivative computed with q_1, \dots, q_{3N-1} constant:

$$\frac{\partial}{\partial \xi} = \left(\frac{\partial}{\partial \xi} \right)_{q_1, \dots, q_{3N-1}}$$

To give a more precise expression for Eq. (2.2), we need to introduce some notations. We can define the Jacobian of this transformation, denoted J :

$$J \stackrel{def}{=} \begin{pmatrix} \frac{\partial \xi}{\partial \mathbf{x}_1} & \frac{\partial \xi}{\partial \mathbf{x}_2} & \dots & \frac{\partial \xi}{\partial \mathbf{x}_N} \\ \frac{\partial q_1}{\partial \mathbf{x}_1} & \frac{\partial q_1}{\partial \mathbf{x}_2} & \dots & \frac{\partial q_1}{\partial \mathbf{x}_N} \\ \dots & \dots & \dots & \dots \\ \frac{\partial q_{3N-1}}{\partial \mathbf{x}_1} & \frac{\partial q_{3N-1}}{\partial \mathbf{x}_2} & \dots & \frac{\partial q_{3N-1}}{\partial \mathbf{x}_N} \end{pmatrix} \quad (2.3)$$

and its inverse J^{-1} . We denote Z the following matrix:

$$Z \stackrel{def}{=} JM^{-1}J^t$$

where J^t is the transpose of J and M is the mass matrix

$$M = \begin{pmatrix} m_1 & 0 & \dots & 0 \\ 0 & m_2 & \dots & 0 \\ \dots & \dots & \dots & \dots \\ \dots & \dots & \dots & m_N \end{pmatrix}$$

We make the assumption for simplicity that the matrix Z can be written:

$$Z = \begin{pmatrix} Z_\xi & 0 \\ 0 & Z_q \end{pmatrix} \quad (2.4)$$

$$Z_\xi \stackrel{def}{=} \sum_{k=1}^N \frac{1}{m_k} \left(\frac{\partial \xi}{\partial x_k} \right)^2 \quad (2.5)$$

where Z_q is a $3N - 1 \times 3N - 1$ matrix.

It is well-known that if the Hamiltonian H of the system is:

$$H(\mathbf{x}, \mathbf{p}_x) = \frac{1}{2} \sum_i \frac{\mathbf{p}_{x_i}^2}{m_i} + \Phi(\mathbf{x})$$

it is possible to define an Hamiltonian for $\xi, q_1, \dots, q_{3N-1}$:

$$H(\xi, q, p_\xi, p_q) = \frac{1}{2} Z_\xi p_\xi^2 + \frac{1}{2} p_q^t Z_q p_q + \Phi(\xi, q) \quad (2.6)$$

We are now in position to give a more precise expression for Eq. (2.2), using Eq. (2.6):

$$\frac{\partial A}{\partial \xi} = \left\langle \frac{1}{2} \frac{\partial Z_\xi}{\partial \xi} p_\xi^2 + \frac{1}{2} p_q^t \frac{\partial Z_q}{\partial \xi} p_q + \frac{\partial \Phi(\xi, q)}{\partial \xi} \right\rangle_{S_\xi} \quad (2.7)$$

Obviously, such a formula is not very useful since we need to explicitly define the functions q_1, \dots, q_{3N-1} to compute $\frac{\partial A}{\partial \xi}$. The purpose of Section 2.1 is to give an equivalent form of (2.7) in which no reference is explicitly made to q and p_q .

The two following sections, Sections 2.2 and 2.3, will explain how this expression can be adapted to the case where ξ is decoupled from the other degrees of freedom and is varying in a quasi-static fashion.

2.1. Unconstrained simulation

In the following sections we will use the following notations:

$$\mathbf{x}'_i \stackrel{def}{=} \sqrt{m_i} \mathbf{x}_i \quad \mathbf{p}'_{\mathbf{x}_i} \stackrel{def}{=} \frac{\mathbf{p}_i}{\sqrt{m_i}} \quad (2.8)$$

$$\mathcal{H} \stackrel{def}{=} \left(\frac{\partial^2 \xi}{\partial \mathbf{x}'_i \partial \mathbf{x}'_j} \right) = \left(\frac{1}{\sqrt{m_i m_j}} \frac{\partial^2 \xi}{\partial \mathbf{x}_i \partial \mathbf{x}_j} \right) \quad (2.9)$$

Recall that

$$\frac{\partial H}{\partial \xi} = -\frac{dp_\xi}{dt} \quad (2.10)$$

$$p_\xi \stackrel{def}{=} \frac{\dot{\xi}}{Z_\xi} \quad (2.11)$$

Thus the derivative of H is equal to:

$$\frac{\partial H}{\partial \xi} = -\frac{\ddot{\xi}}{Z_\xi} + \frac{\dot{\xi}}{Z_\xi^2} \frac{dZ_\xi}{dt} \quad (2.12)$$

We now denote \cdot a dot product or a matrix-vector product. From the rules of derivation:

$$\frac{dZ_\xi}{dt} = \sum_i \frac{\partial Z_\xi}{\partial \mathbf{x}_i} \frac{d\mathbf{x}_i}{dt} = \frac{\partial Z_\xi}{\partial \mathbf{x}'} \cdot \mathbf{p}'_x \quad (2.13)$$

Using Eq. (2.12) & (2.13) and Definition (2.11):

$$\frac{\partial H}{\partial \xi} = -\frac{\ddot{\xi}}{Z_\xi} + \frac{p_\xi}{Z_\xi} \frac{\partial Z_\xi}{\partial \mathbf{x}'} \cdot \mathbf{p}'_{\mathbf{x}} \quad (2.14)$$

Since

$$\mathbf{p}_{\mathbf{x}} = J^t \begin{pmatrix} p_\xi \\ p_q \end{pmatrix} \quad (2.15)$$

we have:

$$\int e^{-\beta H} \frac{p_\xi}{Z_\xi} \frac{\partial Z_\xi}{\partial \mathbf{x}'} \cdot \mathbf{p}'_{\mathbf{x}} dp_q = \int e^{-\beta H} \frac{p_\xi}{Z_\xi} \frac{\partial Z_\xi}{\partial \mathbf{x}'} \cdot (J')^t \begin{pmatrix} p_\xi \\ p_q \end{pmatrix} dp_q$$

As we integrate over p_q the only non-zero contribution is:

$$\int e^{-\beta H} \frac{p_\xi}{Z_\xi} \frac{\partial Z_\xi}{\partial \mathbf{x}'} \cdot (J')^t \begin{pmatrix} p_\xi \\ p_q \end{pmatrix} dp_q = \int e^{-\beta H} \frac{p_\xi^2}{Z_\xi} \frac{\partial Z_\xi}{\partial \mathbf{x}'} \cdot \frac{\partial \xi}{\partial \mathbf{x}'} dp_q$$

using Definition (2.3) of J .

Finally using Definition (2.5) of Z_ξ and Definition (2.9) of \mathcal{H} :

$$\int e^{-\beta H} \frac{p_\xi}{Z_\xi} \frac{\partial Z_\xi}{\partial \mathbf{x}'} \cdot \mathbf{p}'_{\mathbf{x}} dp_q = 2 \int e^{-\beta H} \frac{p_\xi^2}{Z_\xi} \frac{\partial \xi}{\partial \mathbf{x}'} \cdot \mathcal{H} \cdot \frac{\partial \xi}{\partial \mathbf{x}'} dp_q \quad (2.16)$$

We can compute the integral over p_ξ now and obtain, using Eq. (2.6):

$$\int p_\xi^2 \exp\left(-\frac{\beta}{2} Z_\xi p_\xi^2\right) dp_\xi = \frac{1}{\beta Z_\xi} \int \exp\left(-\frac{\beta}{2} Z_\xi p_\xi^2\right) dp_\xi \quad (2.17)$$

Gathering Eqs. (2.14), (2.16), and (2.17), we have proved that

$$\frac{\partial A}{\partial \xi} = \left\langle \frac{\partial H}{\partial \xi} \right\rangle_{q, p_q, p_\xi} = \left\langle -\frac{\ddot{\xi}}{Z_\xi} + \frac{2}{\beta Z_\xi^2} \frac{\partial \xi}{\partial \mathbf{x}'} \cdot \mathcal{H} \cdot \frac{\partial \xi}{\partial \mathbf{x}'} \right\rangle_{q, p_q, p_\xi} \quad (2.18)$$

$$\ddot{\xi} = -\frac{\partial \Phi}{\partial \mathbf{x}'} \cdot \frac{\partial \xi}{\partial \mathbf{x}'} + \mathbf{p}'_{\mathbf{x}} \cdot \mathcal{H} \cdot \mathbf{p}'_{\mathbf{x}} \quad (2.19)$$

where $\langle \rangle_{q, p_q, p_\xi}$ denotes an average with respect to q , p_q , and p_ξ . We call thermodynamics force F_ξ the force defined by:

$$F_\xi \stackrel{def}{=} \frac{1}{Z_\xi} \ddot{\xi} - \frac{2}{\beta Z_\xi^2} \frac{\partial \xi}{\partial \mathbf{x}'} \cdot \mathcal{H} \cdot \frac{\partial \xi}{\partial \mathbf{x}'} \quad (2.20)$$

Equation (2.18) is very convenient from a numerical point of view since it involves only quantities which can be readily computed: ξ and its derivatives with respect to time and position.

2.2. Arbitrary motion along ξ

In SFA the motion along ξ is decoupled from the rest of the system. Then, ξ is advanced in some manner that ensures uniform sampling of ξ , for example by using Langevin equation of motion. In this new system the free energy along ξ is no longer properly defined and Equation (2.18) no longer applies. However, it is possible to compute the free energy of the original (unmodified) system, provided that the motion of ξ is quasistatic. This requires transforming Equation (2.18). Deriving the appropriate formula for $\frac{\partial A}{\partial \xi}$ is the objective of this section.

Suppose that we run a MD simulation at fixed $\xi = \xi_0$. In the case of a Hamiltonian system, the probability density for (q, p_q, p_ξ) at $\xi = \xi_0$ is equal to $\exp(-\beta H_{\xi_0})$ where

$$H_{\xi_0}(q, p_q, p_\xi) = \frac{1}{2} Z_{\xi_0} p_\xi^2 + \frac{1}{2} p_q^t Z_q p_q + \Phi_{\xi_0}(q)$$

However, when ξ is decoupled from other degrees of freedom and advanced quasistatically using an independent equation, we sample with a probability equal to $\exp(-\beta H_{\xi_0}^*)$, where

$$H_{\xi_0}^*(q, p_q, p_\xi) = K^{ext}(p_\xi) + \frac{1}{2} p_q^t Z_q p_q + \Phi_{\xi_0}(q)$$

The function K^{ext} depends on the equation of motion for ξ . If this is a diffusion equation (Langevin)

$$K^{ext}(p_\xi) = \frac{1}{2} \frac{T}{T_\xi} p_\xi^2$$

where T_ξ is the temperature used in the Langevin equation (see Section 3). Because we sample from a different probability distribution function it is not possible to use Equation (2.18) directly. This difficulty can be solved by calculating analytically the integral over p_ξ in Equation (2.18). To do so we first identify the terms which depend on p_ξ : the acceleration $\dot{\xi}$ and the probability density. More specifically considering Equation (2.18) and (2.19), we need to calculate:

$$\int f_\xi p'_x \cdot \mathcal{H} \cdot p'_x dp_\xi$$

where $f_\xi = \exp(-\frac{\beta}{2} Z_\xi p_\xi^2)$.

Denoting $f_{p_q} = \exp(\frac{-\beta}{2} p_q^t Z_q p_q)$ we have:

$$\int f_{p_q} p'_x \cdot \mathcal{H} \cdot p'_x dp_q = \int f_{p_q} \begin{pmatrix} p_\xi \\ p_q \end{pmatrix} \cdot J' \mathcal{H} (J')^t \cdot \begin{pmatrix} p_\xi \\ p_q \end{pmatrix} dp_q \quad (2.21)$$

$$= p_\xi^2 \frac{\partial \xi}{\partial x'} \cdot \mathcal{H} \cdot \frac{\partial \xi}{\partial x'} \int f_{p_q} dp_q + \int f_{p_q} p_q \cdot J'_q \mathcal{H} (J'_q)^t \cdot p_q dp_q \quad (2.22)$$

using Equation (2.15), and the fact that integration is performed over p_q .

Next we consider the integral over p_ξ and use Equation (2.17):

$$\int f_\xi p_\xi^2 \frac{\partial \xi}{\partial x'} \cdot \mathcal{H} \cdot \frac{\partial \xi}{\partial x'} dp_\xi = \frac{1}{\beta Z_\xi} \frac{\partial \xi}{\partial x'} \cdot \mathcal{H} \cdot \frac{\partial \xi}{\partial x'} \int f_\xi dp_\xi \quad (2.23)$$

Using this equation, we observe that the following transformation is possible on statistical averages:

$$\left\langle p'_x \cdot \mathcal{H} \cdot p'_x + \left(\frac{1}{\beta Z_\xi} - \frac{\dot{\xi}^2}{Z_\xi^2} \right) \frac{\partial \xi}{\partial x'} \cdot \mathcal{H} \cdot \frac{\partial \xi}{\partial x'} \right\rangle_{q, p_q, p_\xi} = \langle p'_x \cdot \mathcal{H} \cdot p'_x \rangle_{q, p_q, p_\xi}$$

Further, using Equation (2.22) and (2.23)

$$\begin{aligned} \left\langle p'_x \cdot \mathcal{H} \cdot p'_x + \left(\frac{1}{\beta Z_\xi} - \frac{\dot{\xi}^2}{Z_\xi^2} \right) \frac{\partial \xi}{\partial x'} \cdot \mathcal{H} \cdot \frac{\partial \xi}{\partial x'} \right\rangle_{q, p_q, p_\xi} = \\ \left\langle \frac{1}{\beta Z_\xi} \frac{\partial \xi}{\partial x'} \cdot \mathcal{H} \cdot \frac{\partial \xi}{\partial x'} + p_q \cdot J'_q \mathcal{H} (J'_q)^t \cdot p_q \right\rangle_{q, p_q, p_\xi} \end{aligned}$$

We have proven the following result:

$$\int \exp(-\beta H_{\xi_0}) F_{\xi} = \int \exp(-\beta H_{\xi_0}) F_{\xi}^{(2)}$$

with
$$F_{\xi}^{(2)} = \frac{1}{Z_{\xi}} \ddot{\xi} - \left(\frac{1}{\beta} + \frac{\dot{\xi}^2}{Z_{\xi}} \right) \frac{1}{Z_{\xi}^2} \frac{\partial \xi}{\partial \mathbf{x}'} \cdot \mathcal{H} \cdot \frac{\partial \xi}{\partial \mathbf{x}'}$$

(see Equation (2.20) for the definition of F_{ξ}). Moreover $\int f_{p_q} F_{\xi}^{(2)} dp_q$ is independent of p_{ξ} . Thus, we have removed the dependence of the average force on p_{ξ} . This is a desirable result because the dependence on p_{ξ} changes with implementation of quasistatic process. Thus we can conclude:

$$\int dp_{\xi} f_{\xi} \int dp_q f_{p_q} F_{\xi}^{(2)} = \int dp_q f_{p_q} F_{\xi}^{(2)} \times \int dp_{\xi} \exp\left(-\frac{\beta}{2} Z_{\xi} p_{\xi}^2\right) \propto \frac{1}{\sqrt{Z_{\xi}}} \int dp_q f_{p_q} F_{\xi}^{(2)}$$

We proved that when ξ is decoupled and moves quasistatically, the following equation applies:

$$\frac{\partial A}{\partial \xi} = \frac{\left\langle \frac{1}{\sqrt{Z_{\xi}}} F_{\xi}^{(2)} \right\rangle_{q, p_q}}{\left\langle \frac{1}{\sqrt{Z_{\xi}}} \right\rangle_{q, p_q}} = \frac{\left\langle \frac{-1}{Z_{\xi}^{3/2}} \ddot{\xi} + \left(\frac{1}{\beta} + \frac{\dot{\xi}^2}{Z_{\xi}} \right) \frac{1}{Z_{\xi}^{5/2}} \frac{\partial \xi}{\partial \mathbf{x}'} \cdot \mathcal{H} \cdot \frac{\partial \xi}{\partial \mathbf{x}'} \right\rangle_{q, p_q}}{\left\langle \frac{1}{\sqrt{Z_{\xi}}} \right\rangle_{q, p_q}} \quad (2.24)$$

where A is the free energy of the original system.

2.3. Constrained simulation

The case of the constrained simulation is a corollary of the previous result. It is a particular case of a “quasi-static” motion where the velocity of ξ is zero.

In this case $F_{\xi}^{(2)}$ is simply equal to:

$$F_{\xi}^{(2)} = \frac{-1}{Z_{\xi}} \ddot{\xi} + \frac{1}{\beta} \frac{1}{Z_{\xi}^2} \frac{\partial \xi}{\partial \mathbf{x}'} \cdot \mathcal{H} \cdot \frac{\partial \xi}{\partial \mathbf{x}'}$$

Thus the complete expression for $\frac{\partial A}{\partial \xi}$ is

$$\frac{\partial A}{\partial \xi} = \frac{\left\langle \frac{-1}{Z_{\xi}^{3/2}} \ddot{\xi} + \frac{1}{\beta} \frac{1}{Z_{\xi}^{5/2}} \frac{\partial \xi}{\partial \mathbf{x}'} \cdot \mathcal{H} \cdot \frac{\partial \xi}{\partial \mathbf{x}'} \right\rangle_{q, p_q}}{\left\langle \frac{1}{\sqrt{Z_{\xi}}} \right\rangle_{q, p_q}} \quad (2.25)$$

This expression is identical to Otter and Briels (1998).

3. Description of the algorithm

At each timestep we need to calculate the force along ξ , which is of the form $\lambda(t) \frac{\partial \xi}{\partial \mathbf{x}}$. This is the centerpiece of SFA. The force must be such that:

$$Z_{\xi} \lambda(t) - \frac{\partial \Phi}{\partial \mathbf{x}'} \cdot \frac{\partial \xi}{\partial \mathbf{x}'} + \mathbf{p}'_{\mathbf{x}} \cdot \mathcal{H} \cdot \mathbf{p}'_{\mathbf{x}} = 0$$

To compute the value of $\lambda(t)$ we use a modified version of RATTLE, for which the “constraints” are updated at each timestep.

Consider the traditional RATTLE algorithm and suppose that we have a constraint $\sigma(\mathbf{x}) = \sigma_0$, which has to be satisfied at each timestep. The algorithm consists of two steps. After advancing the position from time t to $t + dt$, RATTLE is used to compute the force $\mu^r \nabla \sigma$, such that $\sigma(\mathbf{x}(t + dt)) = \sigma_0$. After advancing the velocity from time $t + dt/2$ to $t + dt$, RATTLE is used to compute the force $\mu^v \nabla \sigma$, such that $v \cdot \nabla \sigma = 0$.

In contrast, in SFA we need to add a force which exactly compensates the acceleration of ξ due to the interatomic forces. Since the constraint has to be changed at each timestep the algorithm is slightly different. After advancing the position from time t to $t + dt$, RATTLE is used to compute the force $\lambda^r \nabla \xi$, such that $\xi(t + dt) = \xi(t) + dt \dot{\xi}(t)$, where $\dot{\xi}(t)$ is the velocity before the forces are applied at time t . After advancing the velocity from time $t + dt/2$ to $t + dt$, RATTLE is used to compute the force $\lambda^v \nabla \xi$, such that $v \cdot \nabla \xi(t + dt) = \xi(t + dt) = \xi(t)$, where $\dot{\xi}(t)$ is the velocity before the forces are applied at time t .

Once ξ is decoupled from the other degrees of freedom, we apply a Langevin force to ξ so that we obtain a diffusive motion along ξ . We define $\mu(t)$ with:

$$\mu(t) = -\zeta \dot{\xi} + R(t)$$

and

$$\langle R(t)R(t') \rangle = 2\zeta kT_\xi \delta(t - t')$$

where ζ is friction coefficient, $R(t)$ is normally distributed random force, whose ensemble average is zero, and T_ξ is the temperature. Note that ζ is related to the diffusion constant, D , by the Einstein relation:

$$D = kT/\zeta$$

The total external force applied to the system is equal to the RATTLE force plus the Langevin force:

$$\left(\lambda(t) + \frac{\mu(t)}{Z_\xi} \right) \frac{\partial \xi}{\partial \mathbf{x}}$$

3.1. RATTLE Lagrange multipliers

In this section the equations for λ^r and λ^v the position and velocity Lagrange multiplier for RATTLE are given. We will show that λ^r can be used to compute the value of $\dot{\xi}$.

Let us consider the position RATTLE. The position is advanced using:

$$r(t + dt) = r(t) + v(t + dt/2)dt \quad (3.1)$$

while the velocity is advanced using:

$$v(t + dt/2) = v(t) + \frac{dt}{2} \frac{F(t)}{m} \quad (3.2)$$

After position RATTLE is applied we want ξ to be equal to:

$$\xi^R(t + dt) = \xi(t) + dt \dot{\xi}(t) \quad (3.3)$$

Using a Taylor-Lagrange approximation, we obtain the equation for λ^r :

$$\lambda^r(t) = \frac{-dt}{2Z_\xi(t)} \left(\frac{F(t)}{m} \nabla \xi + v(t) \cdot \mathcal{H} \cdot v(t) \right) = \frac{dt}{2} \frac{-\ddot{\xi}(t)}{Z_\xi} \quad (3.4)$$

See Eq. (2.19). This equation means that λ^r can be used to compute the value of $\ddot{\xi}$ at each time-step.

For velocity RATTLE we have a similar equation. For the velocity:

$$v(t+dt) = v(t) + \frac{dt}{2} \frac{F(t)}{m} + \lambda^r \frac{\nabla \xi(t)}{m} + \frac{dt}{2} \frac{F(t+dt)}{m} \quad (3.5)$$

$$v^R(t+dt) = v(t+dt) + \lambda^v \frac{\nabla \xi(t+dt)}{m} \quad (3.6)$$

As the constraint on $v^R(t+dt)$ is $v^R(t+dt) = v(t)$ we obtain:

$$\lambda^v = \frac{-dt}{2Z_\xi(t+dt)} \left(\frac{F(t)}{m} \nabla \xi + \frac{2}{dt} \lambda^r \frac{\nabla \xi(t) \cdot \nabla \xi(t+dt)}{m} + \frac{F(t+dt)}{m} \nabla \xi \right)$$

At first order using Eq. (3.4):

$$\begin{aligned} \lambda^v(t) &= \frac{-dt}{2Z_\xi(t+dt)} \left(\frac{F(t)}{m} \nabla \xi + \frac{2Z_\xi(t)}{dt} \lambda^r + \frac{F(t+dt)}{m} \nabla \xi \right) \\ &= \frac{-dt}{2Z_\xi(t+dt)} \left(\frac{F(t+dt)}{m} \nabla \xi - v(t) \cdot \mathcal{H} \cdot v(t) \right) \end{aligned}$$

Note that only λ^r is equal to $-\frac{dt}{2} \frac{\ddot{\xi}(t)}{Z_\xi}$. For λ^v the sign in front of $v(t) \cdot \mathcal{H} \cdot v(t)$ is opposite.

4. Application - isomerization of 1,2-dichloroethane in water

To test the performance of the SFA, we studied the rotation around the C-C bond in 1,2-dichloroethane (DCE) dissolved in water. Specifically, we calculated the free energy $A(\xi)$ as a function of the Cl-C-C-Cl torsional angle ξ . The same quantity was previously calculated for DCE in several different environments, including the gas phase, bulk water, bulk Hexane, and water-Hexane interface, using conventional methods (Benjamin and Pohorille (1993), Pohorille and Wilson (1993)). See Fig. 2. In all environments, $A(\xi)$ exhibits local minima corresponding to the trans and gauche arrangements of the chlorine atoms. However, the relative stabilities of these two conformations and the free energy barrier that separates them change with environment. The trans conformation was found to be favored by 1.1 kcal/mol in the gas phase, whereas gauche conformations were slightly favored in water (by 0.3 kcal/mol) (Benjamin and Pohorille (1993), Pohorille and Wilson (1993)). The shift of 1.4 kcal/mol stabilizing the gauche conformations in aqueous solutions can be attributed to strong, favorable interactions between these polar conformations and water. Note that the symmetrical, trans conformation has no permanent dipole moment. Also, the free energy barrier between the gauche and trans states increased from 3.5 kcal/mol in the gas phase to 4.4 kcal/mol in aqueous solution. This indicates that the solvent provides a considerable contribution to the potential of mean force around ξ .

The system studied consisted of one DCE molecule and 343 water molecules placed in a cubic box whose edge length was 21.73 Å. This corresponds to a water density of approximately 1 g/cm³. Periodic boundary conditions were applied in the three spatial directions. The water-water interactions were described by the TIP4P potential model (Jorgensen (1983)). For DCE, an all-atom, fully flexible model was used. This model was described in detail previously (Benjamin and Pohorille (1993)). All intermolecular

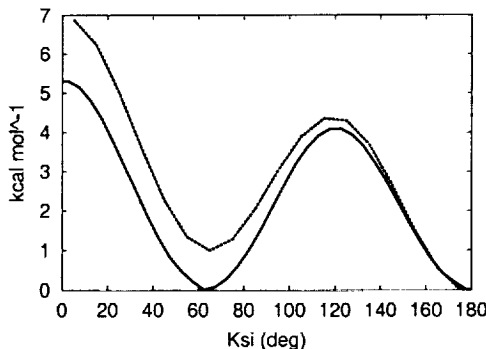


FIGURE 2. DCE in different environments: gas phase (.....) and in bulk water (—). These free energies were computed with a traditional window method.

interactions were truncated smoothly with a cubic spline function between 8.0 and 8.5 Å.

The MD equations of motion were integrated using the velocity Verlet algorithm with a time step of 1 fs. The temperature of the system was 300 K. The bond and angular constraints were resolved using RATTLE (Andersen (1983)). The same algorithm was also used to calculate the force of constraint acting on ξ whenever necessary. To generate configurations from the canonical ensemble, the Martyna *et al.* implementation (Martyna (1992)) of the Nose-Hoover algorithm was used.

Initially, we performed simulations of the system without scaling ($\alpha=1$) in both microcanonical and canonical ensembles. $A(\xi)$ was obtained from a series of calculations in which ξ was constrained by a harmonic potential in 2 overlapping windows. The MD trajectory for each window was 1.0 ns long. From this trajectory the probability distribution, $P(\xi)$, of finding DCE in a conformation defined by ξ was obtained and used to calculate $A(\xi)$ from Equation (2.1).

The free energy profile in the full range of ξ was generated by matching $A(\xi)$ in the overlapping regions of consecutive windows. This was required to ensure that $A(\xi)$ was a continuous function of ξ . Matching was done using the Weighted Histograms Method (Kumar (1992)).

The free energy profiles in the microcanonical and canonical ensembles were nearly identical and were quite similar to those calculated previously using the same potential functions (Benjamin and Pohorille (1993), Pohorille and Wilson (1993)). Gauche and trans conformations were found to have nearly the same free energy and were separated by a barrier 4.2 kcal/mol high. The profiles, shown in Fig. 3, served as the reference to determine accuracy of the SFA. Their statistical precision was further confirmed by fitting a Fourier series to $A(\xi)$ and repeating the calculations using the series as the biasing potential. As expected, the free energy profile so generated was flat. The same calculations were also used to estimate the rotational diffusion constant, D , needed for the Langevin term in SFA. This was done by calculating the velocity autocorrelation function and employing the formula:

$$D = \frac{1}{2} \int_0^{\infty} \langle v(0)v(t) \rangle dt,$$

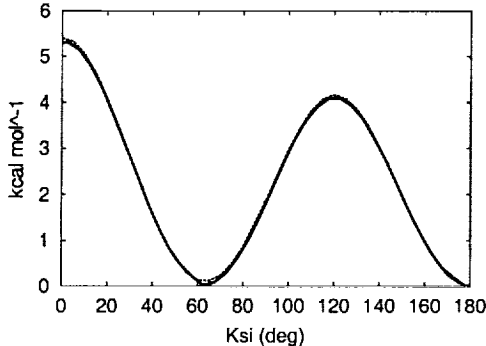


FIGURE 3. DCE in bulk water. This figure shows the reference result, computed with a traditional window method (—), and SFA with a biasing potential (·····).

where $v(t)$ is the velocity of the torsional angle and $\langle \dots \rangle$ denotes a statistical average. The diffusion coefficient was computed to be $0.53 \text{ rad}^2/\text{ps}$.

In the next step, we compute the free energy using Eq. (2.18) and not the probability density (Eq. (2.1)). In this simulation (Fig. 3), we use the original interaction forces and add a biasing potential to the system to obtain a uniform sampling. At every MD step, the values of the constraint force (i.e. obtained using RATTLE) are binned in small intervals of ξ , and at the end of the simulation, the average value of the force of constraint in each bin is calculated. Next, these values are corrected for the geometrical factor according to Eq. (2.18), yielding the thermodynamic force as a function of ξ . This force is then integrated numerically to provide $A(\xi)$.

The important point is that we are still in a Hamiltonian framework which guarantees a convergence to the exact solution as the simulation time goes to $+\infty$.

The simulation was run for 1 ns and the resulting free energy profile is shown in Fig. 3 and compared with the profile obtained from the previous calculations and Eq. (2.1). As can be seen, the agreement between the two profiles is excellent.

Then, simulations of the same system are performed using SFA with $\alpha = 1$. This means that the angle ξ is fully decoupled from the rest of the system. To advance this angle the Langevin equation of motion is integrated. We choose different diffusion coefficients. In this table we summarize the run times and number of windows used:

Diffusion Coefficient	Number of windows	Simulation time
$0.53 \text{ rad}^2/\text{ps}$	1	1ns
$0.53 \times 10^{-1} \text{ rad}^2/\text{ps}$	1	1ns
$0.53 \times 10^{-2} \text{ rad}^2/\text{ps}$	2	1ns
$0.13 \times 10^{-2} \text{ rad}^2/\text{ps}$	3	2ns

The simulation time is per window. The number of windows and simulation time have to be increased because as the diffusion constant goes to zero it takes more and more time to cover the complete range from 50 deg to 190 deg.

For this simulation we use Eq. (2.24) to compute the free energy. This is the equation

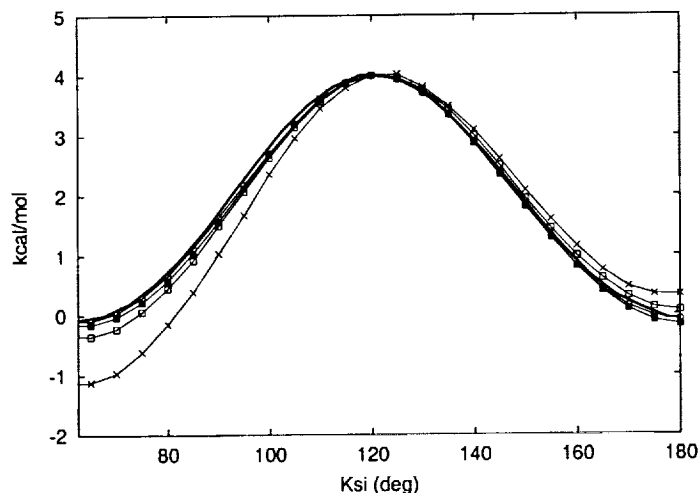


FIGURE 4. DCE in bulk water. These are the results obtained with SFA using a Langevin force with different diffusion constants: 0.53 ($-x-$), 0.53×10^{-1} ($-\square-$), 0.53×10^{-2} ($-■-$) and 0.13×10^{-2} rad^2/ps ($-o-$). The reference curve ($-$) is shown with a thick line. Only the range $[60-180]$ degrees was computed. Note that since the free energy is defined up to a constant, we decided to align all the curves at the point $\xi = 120$ deg. The fact that the difference with the reference curve is more significant at 60 deg than 180 deg reflects the fact that the precise shape of the free energy around 60 deg depends on precise interactions with the water and correct equilibration at these configurations.

that we need to use when ξ is decoupled from the other degrees of freedom and advanced in a quasi-static manner.

For these simulations we no longer have a Hamiltonian system. The free energy profile converges to the exact solution only when ξ is a sufficiently “slow” degree of freedom. This means that ξ has to change in a quasi-static way to get a correct convergence. If it changes sufficiently fast that the rest of the rest of the system cannot relax in response to its movements, the system is in a non-equilibrium state and the free energy converges to the wrong value.

We progressively lower the diffusion coefficient and observe that the free energy converges to the exact solution as the motion of ξ becomes quasi-static. The results are shown in Fig. 4.

5. Conclusion and future work

We developed a new method called Scaled Force Algorithm to compute free energies. It is based on decoupling the reaction coordinates from the other degrees of freedom. The free energy of the original system can then be computed using Eq. (2.24). The advantage of the method is that the sampling is guaranteed to be homogeneous, which is the best possible sampling to minimize CPU time.

We made two kinds of computations. In the first we applied a biasing potential and the system was Hamiltonian. In this case, the general theory of Hamiltonian system applies and the computed free energy (with Eq. (2.18)) converges to the exact free energy when the simulation time goes to $+\infty$. In the second we applied a Langevin force and the system was not Hamiltonian. In this case we need to satisfy a quasi-static hypothesis to converge towards the exact free energy (Eq. (2.24)).

We are currently developing a new method, the Adaptive Biasing Force, which has two main advantages:

- The system converges towards a Hamiltonian system. We are thus guaranteed to converge towards the exact free energy regardless of the quasi-static hypothesis. This is an advantage over the Langevin force variant.
- The Adaptive Biasing Force is computed as the simulation goes and thus no a priori guess is needed. This is an advantage over the biasing potential variant.

Early tests confirm that the new method will yield even better results than the ones presented in this report (biasing potential and Langevin force).

We are also planning to study two-dimensional or multi-dimensional cases where the number of slow degrees of freedom is two or more.

A very important application of the method is the problem of protein folding. The solution of these problems has so far been limited because the computational time is extremely large. A full computation requires on the order of 10^9 time-steps to reach the micro-second time-scale. Such a large number of time-steps results from the fact that the system has to cross energy barriers between intermediate steps of the folding. SFA will allow to lower these energy barriers and thus reduce the computational time of the solution.

REFERENCES

- ANDERSEN, H. C. 1983 Rattle: a 'velocity' version of the shake algorithm for molecular dynamics calculations. *J. Comput. Phys.* **52**, 24-34.
- BENJAMIN, I. & POHORILLE, A. 1993 Isomerization reaction dynamics and equilibrium at the liquid-vapor interface of water — a molecular dynamics study. *J. Chem. Phys.* **98**, 236-242.
- DEN OTTER, W. K. & BRIELS, W. J. 1998 The calculation of free-energy differences by constrained molecular-dynamics simulation. *J. Chem. Phys.* **109**(11), 4139-4146.
- JORGENSEN, W. L., CHANDRASEKHAR, J., MADURA, J. D., IMPEY, R. W. & KLEIN, M. L. 1983 Comparison of simple potential functions for simulating liquid water. *J. Chem. Phys.* **79**, 926-935.
- KUMAR, S., BOUZIDA, D., SWENDSEN, R. H., KOLLMAN, P. A. & ROSENBERG, J. M. 1992 The weighted histogram analysis method for free-energy calculations on biomolecules 1: The method. *J. Comput. Chem.* **13**, 1011-1021.
- MARTYNA, G. J., KLEIN, M. L. & TUCKERMAN, M. 1992 Nose-Hoover chains — the canonical ensemble via continuous dynamics. *J. Chem. Phys.* **97**, 2635-2643.
- POHORILLE, A. & WILSON, M. A. 1993 Isomerization reactions at aqueous interfaces. In Jortner, J., Levine, R. D. & Pullman, B. editors, *Reaction Dynamics in Clusters and Condensed Phases — The Jerusalem Symposia on Quantum Chemistry and Biochemistry*, **26**, 207, Kluwer, Dordrecht.

In pursuit of structures in protoplanetary disks

By O. M. Umurhan

1. Motivation and objectives

This brief summarizes work devoted to studying the linear stability of baroclinic protoplanetary Keplerian disks. This work largely builds on the foundation and fundamental results obtained by Barranco, Marcus & Umurhan (2000) (hereafter BMU) which presented a model to describe structures in weakly baroclinic Keplerian disks.

Interest in protoplanetary disks has grown since the discovery of the first of what are now dozens of extrasolar planets around F and G type stars (Marcy 1996, Perryman 2000). The apparent ubiquity of planets suggests that the nebular disks (or *protoplanetary disks*), out of which these stars are born, must be susceptible to the development of structures. However, theoretical work (see references in BMU) argues that purely pressure-supported gaseous barotropic Keplerian disks do not undergo any known type of hydrodynamic instabilities. The basis for this claim is that the strong rotation in Keplerian shear flows manages to suppress any of the usual instabilities seen in laboratory shear flows such as the Taylor-Couette and Kelvin-Helmholtz instabilities (Drazin & Reid, 1982). Some investigators (*e.g.* Shu *et al.*, 1993) have gone so far as to claim that protoplanetary disks are featureless objects totally bereft of vortical structures or long-lasting stable patterns.

To counter this assertion, some investigators have suggested that the protoplanetary disk is sufficiently magnetized to undergo a magneto-rotational instability as first explored by Chandrasekhar (1956) using linear analysis and later demonstrated numerically by Balbus, Hawley & Stone (1996) for fully nonlinear flows. However, Desch (2000) has indicated that disks suspected to be around solar type stars will be too cool and weakly ionized such that local dust particles in short time will sweep up the ionization in the gas, leaving the fluid nearly neutral. What little ionization is left in the disk is too little to allow strong coupling to an external magnetic field. Thus this mechanism is unlikely to play an important role in the formation of planets at the radii where the large gas giants are observed to reside.

The point of view taken by BMU is that a weakly baroclinic Keplerian disk will produce the type of shear flow that will promote hydrodynamical instabilities. The assumption was that the added component of vertical shear driven by baroclinic effects generates coherent structures in an otherwise featureless protoplanetary disk. To isolate this effect they derived a number of asymptotic reductions of the 3D Euler equations in cylindrical geometry with a central mass source. The work here outlines the linear theory of these reduced equations in order to:

- Study and determine the conditions for which waves in these baroclinic disks are unstable in order to develop a physical intuition of the instability process.
- Provide analytical results to test the numerical techniques to be used in simulating the fully three dimensional Euler equations on a section of the protoplanetary disk.

Ongoing collaborative work with P. Marcus and J. Barranco is exploring the proposition that disk baroclinicity may be sufficient to generate structures. This work is being

done mainly through the development and implementation of fully three-dimensional simulations of the reduced 3D Euler equations derived in BMU.

The second half of this brief is concerned with work done with N. J. Balmforth and C. Picollo at the University of California, Santa Cruz, concerning the problem of characterizing the development of vortical structures in two-dimensional shearing flows in a planetary-scale vorticity field.

2. Physical considerations, the reduced equations, and linear theory

A baroclinic disk is an equilibrated pressure-supported gaseous disk with a central gravitational source in which the pressure and density iso-lines do not align. The physical cause for such a misalignment is most likely the uneven penetration, absorption, and heating of the gas by radiation coming from the central star. For a cylindrical geometry, *barotropic* pressure-supported Keplerian disks have azimuthal velocities that, though they are sheared strongly in the radial direction, have no variation of their speeds in the disk vertical direction. However, with only the most conservative assumptions for the baroclinic heating of the steady disk, it was shown in BMU that there will be a slight vertical shear of the azimuthal velocity. This result establishes the setting for what follows.

The asymptotic reduction of the full three-dimensional Euler equations have a number of physical assumptions built into them. First, that the disk is so cold that its vertical scale height is much smaller than its radial extent. Second, that dynamical structures (if they exist) appear in the baroclinic disk as small amplitude departures atop an otherwise featureless medium. Third, that coherent vortex structures of interest should be subsonic in the reference frame moving with respect to the vortex center. This last requirement provides additional constraints on the length and time scales to be explored within the 3D Euler equations. Since the rotation and shear in Keplerian disks are of comparable strengths, to hunt for vortex structures that are both subsonic and coherent means one must explore length scales that are small in the disk radial direction compared to the azimuthal and vertical directions. The picture is not of shallow structures in a thin disk, but rather of deep radially thin structures instead.

We investigate only two of the three sets of reduced asymptotics in BMU. The equations presented below are in non-dimensional form using the scalings assumed in BMU. In short, the velocities were scaled according to the local Mach number (ϵ). The sound speed is defined by

$$c_s^2 = \bar{P}(R_0, 0) / \bar{\rho}(R_0, 0), \quad (2.1)$$

where $\bar{P}(R_0, 0)$ and $\bar{\rho}(R_0, 0)$ are the pressure and density values at the disk midplane at a reference radial position R_0 . The velocity is given by

$$v_{scale} = \Omega L_r \quad \Omega = \sqrt{GM/R_0}, \quad \epsilon = v_{scale}/c_s$$

where Ω is the local Keplerian rotation frequency at R_0 given by the mass of the central object, M . L_r is the radial length scale assumed of the vortical structure. Time is scaled to reflect the advective times for the disturbances. L_r is chosen so that the difference of the radial Keplerian speed across that length is the same order of magnitude as the velocity disturbances themselves. For notational convenience the equations are expressed in terms of momentum density, or $u = \bar{\rho}v$, where $\bar{\rho}$ is the steady-state disk density evaluated at the radial position R_0 . The reduction procedure involves the *local* Cartesianization of the

cylindrical disk: in the resulting units x represents the disk azimuthal direction, y is the radial direction and, z denotes the vertical.

In the limit where the radial, azimuthal, and vertical disturbance scales are of equal magnitude but much smaller (as measured by the Mach number ϵ) than the scale of variations of the vertical component of the disk shear or the vertical disk gravity, we find the following equations,

$$\frac{\partial u_x}{\partial t} = -\nabla \cdot \left(\frac{\mathbf{u}u_x}{\bar{\rho}(R_0, z)} \right) + 2u_y - \frac{\partial \bar{P}}{\partial x} \quad (2.2)$$

$$\frac{\partial u_y}{\partial t} = -\nabla \cdot \left(\frac{\mathbf{u}u_y}{\bar{\rho}(R_0, z)} \right) - 2 \left((u_x - \bar{\rho}(R_0, z)(3y/2 + \epsilon^2 \beta z^2)) \right) - \frac{\partial \bar{P}}{\partial y} \quad (2.3)$$

$$\frac{\partial u_z}{\partial t} = -\nabla \cdot \left(\frac{\mathbf{u}u_z}{\bar{\rho}(R_0, z)} \right) - \frac{\partial \bar{P}}{\partial z} - \epsilon^2 \bar{\rho} z \quad (2.4)$$

$$0 = \nabla \cdot \mathbf{u}. \quad (2.5)$$

In BMU this reduced set was referred to as the *Round Vortices* equations. These reduced equations are anelastic owing to the assumed dominance of advection, thus sound waves are not present. Density and pressure, $\bar{\rho}$ and \bar{P} respectively, represent their fluctuations from the steady disk state. The explicit appearance of z on the right-hand side of Eq. (2.4) represents the variable gravitational force as one moves vertically in the disk. The steady-state baroclinic Keplerian shear appears as a forcing term on the right-hand side of Eq. (2.3) because the reduction procedure that results in these equations involves subtracting the featureless disk from the full 3D Euler equations. On the length scales considered, the radial component of the Keplerian shear appears as a linear term in y while the baroclinic contribution appears as a term quadratic in z . The degree of baroclinicity is measured by the parameter β . We refer the reader for further details to BMU, § 3.

The other set of reduced equations we study assumes that the azimuthal and vertical extent of structures are of equal magnitude to the variations of the vertical shear and gravity but are much larger than the radial scale of the structures. These assumptions result in what is referred to in BMU as *Elongated Dynamics*:

$$\frac{\partial u_x}{\partial t} = -\nabla \cdot \left(\frac{\mathbf{u}u_x}{\bar{\rho}(R_0, z)} \right) + 2u_y - \frac{\partial \bar{P}}{\partial x} \quad (2.6)$$

$$0 = -2 \left(u_x - \bar{\rho}(R_0, z)(3y/2 + \beta z^2) \right) - \frac{\partial \bar{P}}{\partial y} \quad (2.7)$$

$$\frac{\partial u_z}{\partial t} = -\nabla \cdot \left(\frac{\mathbf{u}u_z}{\bar{\rho}(R_0, z)} \right) - \frac{\partial \bar{P}}{\partial z} - \bar{\rho} z \quad (2.8)$$

$$\nabla \cdot \mathbf{u} = 0. \quad (2.9)$$

A notable difference between these equations and the ones presented before is that motion in the radial direction is entirely geostrophic, meaning that there is a constant balance between the Coriolis and pressure terms at all times during the flow.

In the following two subsections we explore the linear stability of these above two sets of equations. We do this using (a) standard channel flow boundary conditions and (b) periodic conditions in the “sliding box” coordinate system (Rogallo 1981).

2.1. Round vortex linear theory

We linearly perturb Eqs. (2.2)–(2.5) about the steady Keplerian state and write,

$$u_x = \bar{u}_x + u'_x \quad u_z = 0 + u'_z \quad u_y = 0 + u'_y \quad \bar{P} = \bar{P}'. \quad (2.10)$$

For notational convenience we define $\bar{v}_x \equiv \bar{u}_x/\bar{\rho}(R_0, \epsilon z)$ so that in the unit scalings appropriate for Eqs. (2.2)–(2.5), the steady velocity shear appears as,

$$\bar{v}_x = 3y/2 + \beta\epsilon^2 z^2. \quad (2.11)$$

We assume that the disturbances are isothermal so that $\bar{P}' = \bar{T}(R_0, \epsilon z)\bar{\rho}'$ where $\bar{T}(R_0, \epsilon z)$ is the steady-state temperature profile evaluated at R_0 , the radial position of the perturbation in cylindrical coordinates. We use the simplest form for \bar{T} : a constant plus local variations that are quadratic in ϵz . Linearizing Eqs. (2.2)–(2.5) gives,

$$\left(\frac{\partial}{\partial t} + \bar{v}_x \frac{\partial}{\partial x}\right) u'_x = -\frac{\partial \bar{P}'}{\partial x} + \frac{1}{2}u'_y - 2\beta\epsilon^2 z u'_z \quad (2.12)$$

$$\left(\frac{\partial}{\partial t} + \bar{v}_x \frac{\partial}{\partial x}\right) u'_y = -\frac{\partial \bar{P}'}{\partial y} - 2u'_x \quad (2.13)$$

$$\left(\frac{\partial}{\partial t} + \bar{v}_x \frac{\partial}{\partial x}\right) u'_z = -\frac{\partial \bar{P}'}{\partial z} - \epsilon^2 z \bar{P}' \quad (2.14)$$

$$\frac{\partial u'_x}{\partial x} + \frac{\partial u'_y}{\partial y} + \frac{\partial u'_z}{\partial z} = 0. \quad (2.15)$$

In the following we present results for the different boundary conditions of interest.

2.1.1. Channel geometry

In this section we look for solutions of the form $\exp i(\omega t + k_x x)$. For the boundary conditions at both the \hat{z} and \hat{y} boundaries we use,

$$(i) u'_z = 0 \text{ at } z = \pm\zeta \quad \text{and} \quad (ii) u'_y = 0 \text{ at } y = \pm 1, \quad (2.16)$$

which means no vertical flow at the top and bottom boundaries and no radial flow perturbations at the radial boundaries, $y = \pm 1$. For flexibility, we consider the the z boundary conditions at $\pm\zeta$ with ζ now a tunable parameter. We assume that β is an order 1 quantity and we write all quantities and solutions to Eqs. (2.12)–(2.15), including the frequency ω , as a perturbation series in powers of ϵ^2 ,

$$\bar{P}' = \bar{P}'_0 + \epsilon^2 \bar{P}'_2 + \dots, \quad u'_x = u'_{x0} + \epsilon^2 u'_{x2} + \dots, \quad \omega = \omega_0 + \epsilon^2 \omega_2 + \dots, \quad (2.17)$$

and similarly for u'_y and u'_z . We insert the expansion Eq. (2.17) into Eqs. (2.12)–(2.15) and collect like powers of ϵ . At lowest order we combine equations and find,

$$(1 - \psi^2) \left(k_x^2 - \frac{\partial^2}{\partial z^2}\right) u'_{y0} - \left(\psi^2 \frac{\partial^2}{\partial y^2} - k_x^2\right) u'_{y0} = 0, \quad (2.18)$$

with $\psi = \omega_0 + \frac{3}{2}y$. Equation (2.18) is separable so we assume solutions of the form,

$$u'_{y0} = \Psi_\ell(y) Z_m(z). \quad (2.19)$$

Upon enforcing the no vertical flow boundary condition at $z = \pm\zeta$, we find that the vertical eigenfunctions $Z_m(z)$ are given by

$$Z_m(z) = \cos \pi n s \text{frac} z \zeta, \quad (2.20)$$

in which $m = (2n + 1)/2$ where n is any integer. The solutions to Eq. (2.18) show that the $\Psi_\ell(y)$'s are a discrete infinite set of eigenfunctions (ordered by integer ℓ) composed of linear combinations of Bessel functions of the first and second kinds. The specific linear combinations are determined by imposing the boundary conditions at $y = \pm 1$. The lowest order frequencies are real and have been confirmed by numerical computations of the eigenvalue problem. Furthermore, the following orderings for ω_0 hold: $|\omega_0(\ell_1, k_x)| > |\omega_0(\ell_2, k_x)|$ for $|\ell_1| < |\ell_2|$.

In the long wave limit, $k_x \rightarrow 0$, the frequency reduces to,

$$\omega_0^2 = 4m^2 / (\ell^2 \zeta^2 + 4m^2), \quad (2.21)$$

while for short waves it is,

$$\lim_{k_x \rightarrow \pm\infty} \omega_0 = \text{sgn}(k_x) \left| \frac{3}{2} k_x \right|, \quad (2.22)$$

Equation (2.22) implies that the mode frequencies for all ℓ cluster together around $\frac{3}{2} k_x$ for $|k_x| \gg 1$.

The effect of disk baroclinicity, which appears in the vertical shear term, shows up at the next expansion order. Carrying out the perturbation expansion to order ϵ^2 and demanding that the boundary conditions be satisfied reveals that the resulting frequency corrections are real, and this has been validated by numerical computations. Thus, the no-radial/no-vertical boundary conditions explored here shows no destabilizing tendency due to disk baroclinicity to this order in ϵ .

2.1.2. Sliding box coordinates

We consider here Eqs. (2.12)–(2.15) in a reference frame that moves with the x -direction mean motion. The following coordinate transformation achieves this aim,

$$x' = x + \frac{3}{2} y t \quad t' = t \quad y' = y \quad z' = z, \quad (2.23)$$

where the primes in Eq. (2.23) represent the transformed coordinate. These “sliding box” coordinates have previously been used in studies of plane Couette and other shearing flows (Marcus & Press 1977, Rogallo 1981 and Korycansky 1992). Inserting the coordinate transformation Eq. (2.23) into Eqs. (2.12)–(2.15) and assuming periodic solutions in the x' and y' directions, *i.e.* $\sim \exp i(k'_y y' + k'_x x')$, results in,

$$\frac{\partial u'_x}{\partial t} = -i k_x \tilde{P}' + \frac{1}{2} u'_y - i k_x \beta \epsilon^2 z^2 u'_x - 2 \beta \epsilon^2 u'_z \quad (2.24)$$

$$\frac{\partial u'_y}{\partial t} = -2 u'_y - i (k_y - \frac{3}{2} k_x t) \tilde{P}' - i k_x \beta \epsilon^2 z^2 u'_y \quad (2.25)$$

$$\frac{\partial u'_z}{\partial t} = -\mathcal{L} \tilde{P}' - i k_x \beta \epsilon^2 z^2 u'_z \quad (2.26)$$

$$0 = \left(k_x^2 + (k_y - \frac{3}{2} k_x t)^2 - \frac{\partial}{\partial z} \mathcal{L} \right) \tilde{P}' - i k_x u'_y - 2i (k_y - \frac{3}{2} k_x t) u'_x - 4i k_x \beta \epsilon^2 z^2 u'_z, \quad (2.27)$$

with $\mathcal{L} \equiv \partial/\partial z + \epsilon^2 z$. For notational ease we have dropped primes from the coordinates. We solve the resulting partial differential equations (now in t and z) subject to the boundary conditions that there be no vertical flow at $z = \pm \zeta$.

Series solutions for Eqs. (2.24)–(2.27) are sought in powers of ϵ^2 , *i.e.*

$$u'_x = u'_{x0} + \epsilon^2 u'_{x2} + \dots, \quad (2.28)$$

and similarly for the other fluid quantities. We insert these expansions into Eqs. (2.24)–(2.27) and collect like powers of ϵ . The resulting lowest order equations admit separable solutions of the form,

$$\begin{aligned} u'_{x0} &= \hat{u}_{x0}(t)Z_m(z) & u'_{y0} &= \hat{u}_{y0}(t)Z_m(z) \\ \tilde{P}'_0 &= \hat{P}_0(t)Z_m(z) & u'_{z0} &= \hat{u}_{z0}(t)(\partial Z_m(z)/\partial z). \end{aligned} \quad (2.29)$$

The vertical eigenfunction $Z_m(z)$ is the same one that appears in Eq. (2.20). After inserting Eq. (2.29) into the lowest order set of equations we find that we are faced with having to solve the result numerically. However, by a dominant balance argument (Bender & Orszag, 1999) we find the (numerically verified) long time behavior of the solutions to be,

$$\hat{u}_{x0} \sim a_0 \left| \frac{3}{2}k_x t - k_y \right|^{X^+} + b_0 \left| \frac{3}{2}k_x t - k_y \right|^{X^-} \quad \text{for } |t| \gg \frac{2k_y}{3k_x}, \quad (2.30)$$

where a_0 and b_0 depend on the choice of initial conditions, and where,

$$\chi_{\pm} = -(1 \pm \nu)/2, \quad \nu = (1 - 16m^2/9k_x^2)^{\frac{1}{2}}. \quad (2.31)$$

We note that \hat{u}_{z0} has the same long time behavior as \hat{u}_{x0} (*i.e.* $\hat{u}_{z0} \sim \mathcal{O}(\hat{u}_{x0})$), while the long time behavior of the radial momentum term is $\hat{u}_{y0} \sim \mathcal{O}(\hat{u}_{x0}/t)$. We can see from the solution of Eq. (2.30) that all modes decay algebraically since $0 \leq \text{Re}(\nu) < 1$ for all values of m and k_x . Thus we conclude that the lowest order solution which describes disturbances of a barotropic disk show no linear instability.

By carrying the perturbation analysis out to order ϵ^2 introduces disk baroclinicity. By demanding that the next order perturbation quantities satisfy the requisite boundary condition at $z = \pm\zeta$, the following long time behavior (numerically verified) is,

$$u'_{x2}/Z(z) \sim \beta a_2 \left| \frac{3}{2}k_x t - k_y \right|^{1+X^+} + \beta b_2 \left| \frac{3}{2}k_x t - k_y \right|^{1+X^-} + \mathcal{O}(t^{X^+}, t^{X^-}), \quad (2.32)$$

where a_2, b_2 are constants that depend on the initial conditions. The long time trend for u'_{x2} has the same temporal form as Eq. (2.32). However, u'_{y2} is down by a power of t , *viz.* $u'_{y2} \sim \mathcal{O}(u'_{x2}/t)$.

Introducing disk baroclinicity predicts that modes should exhibit $t^{1/2}$ (for ν imaginary) and $t^{1/2 \pm \nu/2}$ (for ν real) amplitude growth for $t \gg |2k_y/3k_x|$, showing that a baroclinic disk is indeed unstable. Strictly speaking, the perturbation analysis breaks down when $\beta\epsilon^2 t = \mathcal{O}(1)$ since the correction term (*e.g.* u'_{x2}) breaks its ordering and competes with the lowest order term u'_{x0} . This signifies that linear theory is no longer valid at that late time and that disk baroclinicity has introduced a dynamically active feature. It is interesting to note that since u'_{y2} is down by one power of t , the radial momentum correction term exhibits algebraic decay in the long time limit despite the other terms (*e.g.* u'_{x2}, u'_{z2}) exhibiting algebraic growth.

2.2. Elongated theory

We now linearly perturb Eqs. (2.6)–(2.9) about the steady Keplerian state just as in Eqs. (2.10). We wish to demonstrate some of the peculiarities of these “elongated” asymptotic equations by adopting a couple of simplifications: disk baroclinicity is turned off ($\beta = 0$), and we assume no density fluctuations $\tilde{\rho} = 0$. In this limit the steady velocity

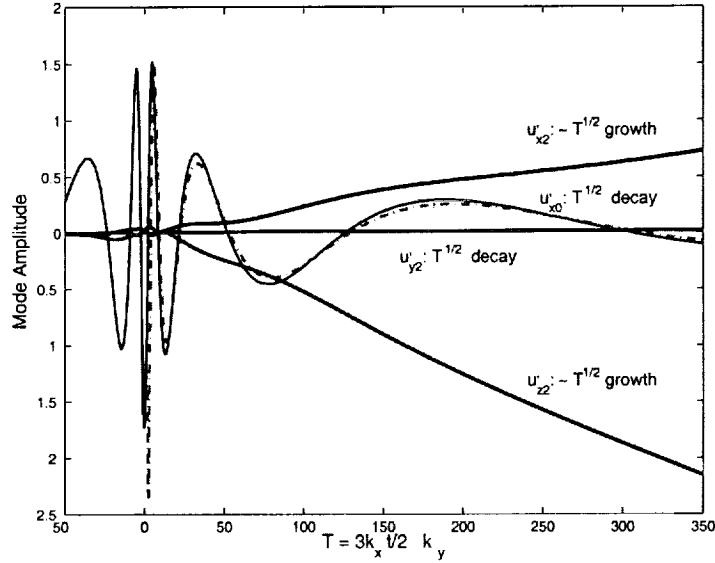


FIGURE 1. Mode evolution for the Round Vortices asymptotics in the sliding box coordinate frame. Shown here is the numerical evolution of a representative mode: $k_x = 1$ $k_y = 30$. The baroclinic effect, introduced here as a correction term in the analysis, predicts $t^{1/2}$ growth for the u'_x and u'_z velocity components corrections. The u'_y correction exhibits $t^{-1/2}$ decay. Also shown is the lowest order u'_x velocity together with the dominant balance result (— · —).

appears as $\bar{v}_x = 3y/2$. The linearized equations become,

$$\left(\frac{\partial}{\partial t} + \bar{v}_x \frac{\partial}{\partial x} \right) u'_x = -\frac{\partial \bar{P}'}{\partial x} + \frac{1}{2} u'_y \quad (2.33)$$

$$0 = -\frac{\partial \bar{P}'}{\partial y} - 2u'_x \quad (2.34)$$

$$\left(\frac{\partial}{\partial t} + \bar{v}_x \frac{\partial}{\partial z} \right) u'_z = -\frac{\partial \bar{P}'}{\partial z} \quad (2.35)$$

$$0 = \frac{\partial u'_x}{\partial x} + \frac{\partial u'_y}{\partial y} + \frac{\partial u'_z}{\partial z}. \quad (2.36)$$

2.2.1. Channel geometry

We adopt the same periodic solutions and channel flow boundary conditions as in §2.1.1. Equations (2.33)–(2.36) may be combined into a single equation for the perturbation pressure,

$$-(\omega + \frac{3}{2}k_x y)^2 \frac{\partial^2 \bar{P}'}{\partial y^2} + \frac{\partial^2 \bar{P}'}{\partial z^2} = 0. \quad (2.37)$$

The following relationships hold between the pressure perturbation and the other fluid quantities,

$$u'_x = \frac{1}{2} \frac{\partial \bar{P}'}{\partial y}, \quad u'_y = -i(\omega + \frac{3}{2}k_x y) \frac{\partial \bar{P}'}{\partial y} + 2ik_x \bar{P}'. \quad (2.38)$$

Since Eq. (2.37) is in separable form, we adopt the following ansatz,

$$\tilde{P}' = \Psi_{m\ell}(y)Z_m(z). \quad (2.39)$$

Enforcing the no vertical flow boundary condition reveals that the vertical structure function $Z_m(z)$ is the same one appearing in Eq. (2.20). The solution for $\Psi_{m\ell}$ is given by

$$\Psi_{m\ell} = \left(\frac{\omega_{m\ell} + \frac{3}{2}k_x y}{\omega_{m\ell} - \frac{3}{2}k_x} \right)^{\frac{1}{2} + i\frac{1}{2}\Delta} + \left(\frac{5 + 3i\Delta}{5 - 3i\Delta} \right) \left(\frac{\omega_{m\ell} + \frac{3}{2}k_x y}{\omega_{m\ell} - \frac{3}{2}k_x} \right)^{\frac{1}{2} - i\frac{1}{2}\Delta}, \quad (2.40)$$

$$\Delta = \left(\frac{16\pi^2 m^2}{9\zeta^2 k_x^2} - 1 \right)^{\frac{1}{2}} \quad (2.41)$$

where ℓ is any non-zero integer.

Stability of the eigenvalues $\omega_{m\ell}$ depend on the sign of the expression appearing under the square root in Eq. (2.41),

$$\omega_{m\ell} = \frac{3}{2}k_x \coth\left(\frac{\ell\pi}{\delta}\right), \quad \text{for } 16\pi^2 m^2 - 9\zeta^2 k_x^2 > 0 \quad (2.42)$$

$$\omega_{m\ell} = -i\frac{3}{2}k_x \cot\left(\frac{\ell\pi}{\delta}\right), \quad \text{for } 16\pi^2 m^2 - 9\zeta^2 k_x^2 < 0, \quad (2.43)$$

where $\delta = i\Delta$. Clearly, the situation in which $16\pi^2 m^2 - 9\zeta^2 k_x^2 < 0$ corresponds to waves that exhibit exponential growth. Thus, modes are unstable when both $|m| < 3\zeta|k_x|/4\pi$ and

$$\begin{aligned} 0 < \text{mod}_\pi(\ell\pi/\delta) < \pi/2 & \quad \text{for } k_x > 0 \\ \pi/2 < \text{mod}_\pi(\ell\pi/\delta) < \pi & \quad \text{for } k_x < 0. \end{aligned} \quad (2.44)$$

2.2.2. Sliding box coordinates

We adopt the same coordinate transformations of Eq. (2.23) and the same solution form and flow boundary-initial conditions as was done in §2.1.2. Inserting the transformations into Eqs. (2.33)–(2.36) results in the following linear equations of motion,

$$\frac{\partial u'_x}{\partial t} = -ik_x P + \frac{1}{2}u'_y \quad (2.45)$$

$$0 = -2u'_x - i(k_y - \frac{3}{2}k_x t)\tilde{P}' \quad (2.46)$$

$$\frac{\partial u'_x}{\partial t} = -\frac{\partial}{\partial z}\tilde{P}' \quad (2.47)$$

$$0 = ik_x u'_x + i(k_y - \frac{3}{2}k_x t)u'_y + \frac{\partial}{\partial z}u'_z. \quad (2.48)$$

Since Eqs. (2.45)–(2.48) are autonomous in z , their solutions may be written in separable form (in t and z),

$$u'_x = \hat{u}_x(t)Z_m(z) \quad u'_y = \hat{u}_y(t)Z_m(z) \quad \tilde{P}' = \hat{P}(t)Z_m(z) \quad u'_z = \hat{u}_z(t)(\partial Z_m(z)/\partial z), \quad (2.49)$$

and the vertical eigenfunctions $Z_m(z)$ are the same ones that appear in Eq. (2.20).

Inserting Eq. (2.49) into Eqs. (2.45)–(2.48) and subsequent simplification results in,

$$\frac{3}{4}k_x^2 \frac{\partial}{\partial T} \left(2T + T^2 \frac{\partial}{\partial T} \right) \hat{P} + \frac{4\pi^2 m^2}{\zeta^2} \hat{P} = 0, \quad T \equiv \frac{3}{2}k_x t - k_y. \quad (2.50)$$

Exact solutions to Eq. (2.50) are,

$$\hat{P} = a\left(\frac{3}{2}k_x t - k_y\right)^{\chi_+} + b\left(\frac{3}{2}k_x t - k_y\right)^{\chi_-} \quad \chi_{\pm} = -\frac{3 \pm \nu}{2}, \quad \nu = \left(1 - \frac{16m^2\pi^2}{9\zeta^2 k_x^2}\right)^{\frac{1}{2}}. \quad (2.51)$$

where a and b in Eq. (2.51) depend on the initial condition for that mode. The solution predicts that all perturbations in which $k_y k_x > 0$ will experience an algebraic singularity at $t_{\text{sing}} = 2k_y/3k_x$ while those modes in which $k_y k_x < 0$ exhibit algebraic decay as $t \rightarrow \infty$. This means that adopting sliding box coordinates to describe the stability of these elongated dynamics predicts some rather curious stability properties. This suggests that our analysis of the reduced equations is highly sensitive to the boundary conditions that we adopt. Consequently, future work must answer the question as to which or what are the most physically appropriate boundary conditions to use in protoplanetary disk simulations.

Additionally, the algebraic singularity in the sliding box coordinates suggests that the elongated dynamics equations may have only limited applicability. The singularity at t_{sing} is not physical since, in the vicinity of t_{sing} , the temporal scalings that led to Eqs. (2.6)–(2.9) break down as the perturbation time scale becomes very short,

$$\frac{\partial}{\partial t} \sim \mathcal{O}\left(\frac{1}{\Delta t}\right), \quad \text{as } t \rightarrow t_{\text{sing}}, \quad (2.52)$$

in which, $\Delta t = t_{\text{sing}} - t$. In other words, in this regime the time scales are no longer the advective ones that we assumed in deriving the asymptotic equations. Thus, the total time derivative term that is missing from Eq. (2.7) will become the same order of magnitude as the other terms in that equation when $\Delta t \sim \mathcal{O}(\epsilon)$, and ignoring this will lead to erroneous conclusions. Further analysis of this matter is needed.

2.3. Discussion

The asymptotic equations for each qualitative regime (*i.e.* round vortices or elongated dynamics) predict instabilities of some type. The elongated dynamics analysis predicts that there will be rather violent instabilities if one considers disturbances from the vantage point of the sliding box coordinate frame. As was discussed before, we do not expect the instability to be as violent as the results predict, primarily because the asymptotic equations begin to lose their validity in the immediate vicinity of the algebraic instability. However, the results strongly suggest that a 3D disk simulation will experience a significant dynamical response that, in all likelihood, will manifest itself as a finite amplitude phenomenon.

Because the equations describing Round Vortices are better posed (they retain all three time derivatives), their results are more indicative of the relative strength of the baroclinic instability. We saw that when the baroclinic effect was turned off (*i.e.* the lowest order linear solution) there was no linear instability, while when it was on there was a growth rate proportional to $t^{1/2}$. On the other hand, Rogers (1991) shows that sheared homogeneous flow (no rotation) in a sliding box frame is predicted to be linearly unstable with a growth rate that scales as $t \log t$ in the long time limit, much stronger than the instability predicted here. We view the relative weakness of the baroclinic instability to mean that instead of widespread turbulence the disk may support coherent structures in a way that is similar to organized large scale convection cells in atmospheres that only marginally exceed their critical Rayleigh numbers.

3. Dynamical structures of 2d jets in planetary vorticity fields

The following is a summary of work done in collaboration with N. J. Balmforth and C. Piccolo at the University of California, Santa Cruz, as presented in Balmforth, Piccolo & Umurhan, 2000 (BPU for short). We studied the stability and developed a reduced asymptotic model (a variant of the classical “single-wave model”) for the 2D incompressible Bickley jet in a rotating planetary vorticity field (the β -plane). The Bickley jet profile in a planetary vorticity field has often been employed as a model to describe planetary scale jets like the Gulf Stream in the North Atlantic. The mathematical structure of the Bickley jet makes it relatively easy to develop asymptotically valid descriptions of the onset of coherent vortices, their shedding, and the generation of planetary scale jet meander. These asymptotic models also provide deeper insights into the dynamical differences between purely inviscid and nearly inviscid flows.

Sheehan *et al.* (1999) have proposed that protoplanetary disks may support jet flows that are similar to the jets observed on the outer cloud layers of Jupiter. If such strongly counterflowing jets do exist in the protoplanetary disk (and this would be borne out through numerical simulations), then it would not be a surprise if they also undergo a similar type of dynamical instability that are experienced by jets. A description of such disk jet instabilities by a reduced asymptotic model would be useful because it would provide a framework to study flow mixing and the cascade of the flow into increasingly complex structures. The work presented here for a simpler flow serves as a template for future endeavors in the context of exploring jet instabilities in protoplanetary disks.

Work in protoplanetary disks generally assumes inviscid flow since the viscosities appropriate for hydrogen and helium under typical disk temperatures predict Reynolds numbers on the order of 10^{12-14} (see BMU for details). Even if numerical simulations are attempted to reflect this nearly inviscid situation, as a practical matter some sort of artificial dissipation must be introduced in order to stabilize the schemes. However, the presence of viscosity may change the physical behavior of the flow from that of nearly or perfectly inviscid circumstances. Thus, it should be clearly understood what the differences are for nearly inviscid as opposed to totally inviscid flows since one assumption might predict dynamics different from the other.

3.1. Problem formulation and linear theory

We consider incompressible jet flow on a two-dimensional (x, y) plane. The plane is located in a rotating reference frame whose Coriolis parameter varies as a linear function of its planetary latitude (the β -plane), which is the y coordinate. In the following, all quantities have been non-dimensionalized by their appropriate length and time scale units. The equations governing the evolving portion of the fluid flow are,

$$\omega_t + U\omega_x + J(\psi, \omega) = \nu \nabla^2 \omega + (U_{yy} - \beta)\omega_x \quad (3.1)$$

$$\psi_{xx} + \psi_{yy} = \omega, \quad (3.2)$$

where $\psi(x, y, t)$ and $\omega(x, y, t)$ denote the streamfunction and vorticity respectively. The quantity ν is the non-dimensionalized viscosity parameter, which is the inverse of the Reynolds number. The Bickley jet profile is given as $U(y) = \text{sech}^2(y)$. Subscript y 's and x 's denote differentiation with respect to the y and x coordinate respectively. The nonlinear term J is $\psi_x \omega_y - \psi_y \omega_x$. The strength of the gradient of the planetary Coriolis parameter is given by β . For boundary conditions we choose periodic flow in x , and we find that the stability and evolution is insensitive to the boundary conditions in the y direction. For numerical purposes we require that the stream function be zero at some

suitably large value of $\pm y_0$, and for analytical purposes we require that the streamfunction be bounded as $y \rightarrow \pm\infty$.

Linear theory of Eqs. (3.1)–(3.2), which has been covered at least in part by others (*e.g.* Maslowe 1991 and Balmforth & Piccolo 2000), shows a number of interesting features. After assuming an $\exp i(kx - ct)$ solution form where k is the horizontal wavenumber and where c is the temporal eigenvalue, we find that the linear stability can be characterized by two parameters k and β . We refer the reader to Balmforth & Piccolo (2000) and BPU for details. Only some relevant highlights are discussed below.

The linear stability is qualitatively characterized by three regimes in the β - k^2 parameter plane: one in which Rossby waves propagate, one in which there exists a complex conjugate pair of modes (of which one is unstable) and one in which there is a continuous spectrum of eigenmodes. † The continuous spectrum occurs whenever the horizontal wavenumber is real and matches the flow speed, defining *the critical level*. The β - k^2 boundary for the continuous spectrum is where the critical level and the inflection point of the total flow (*i.e.* where $U_{yy} - \beta = 0$) coincide.

The parameter value pair $(\beta, k^2) = (-2, 6)$ is special because it represents the spot where all three dynamical regimes meet: much like a triple point in gaseous phase transitions. Physically, this parameter value represents the coincidence of the inflection point/critical-level at the jet tip. This special value of the parameter pair is where we develop an asymptotic description of the instability. It results in a variant of the *single-wave model* appearing often in plasma physics (Balmforth & Piccolo, 2000 and references therein).

3.2. Results

One of the challenges in deriving a weakly nonlinear description of the dynamics near the critical point $(\beta, k^2) = (-2, 6)$ is that the unstable mode that appears emerges out of the continuous spectrum. Standard center manifold type reductions of dynamical systems are successful because they exploit the fact that marginally unstable modes are isolated from other modes of the system. In this case, the emerging unstable mode comes from a continuum of modes, which in practice means that this continuum will also be excited as the system becomes unstable. In our analysis we take this effect into account (for details see BPU). The analysis considers small departures from the critical parameter value in powers of the small parameter ϵ ,

$$\frac{\partial}{\partial t} \rightarrow -1 + \epsilon^2 \frac{\partial}{\partial T}, \quad k^2 \rightarrow 6 + \epsilon\mu \quad \beta \rightarrow -2 + \epsilon^2\beta_2, \quad \nu \rightarrow \epsilon^4\nu_4, \quad (3.3)$$

and the streamfunction and vorticity have amplitudes scaled by ϵ^3 . The analysis requires a number of matched asymptotic expansions relating the flow field away from the jet tip to the dynamics occurring in the tip region. The resulting nonlinear reduced model is expressed in terms of the scaled streamfunction and vorticity, Φ and Ω ,

$$\Omega_T + Y^2\Omega_x + \Phi_x\Omega_Y = \lambda\Omega_{YY} - \kappa\Phi_T - \gamma\Phi_x \quad (3.4)$$

$$A \equiv \frac{1}{2\pi} \int_{-\pi}^{\pi} dx \int_{-\infty}^{\infty} dY e^{-ix}\Omega \quad \text{and} \quad \Phi = Ae^{ix} + c.c. \quad (3.5)$$

† By continuous spectrum we mean a collection of eigenmodes that have eigenfrequencies that are dense on a segment of the real axis.

where the coordinate x has been scaled by the the critical wavenumber $k_c = \sqrt{6}$. The departure parameters are,

$$\lambda = \nu_4/k_c, \quad \kappa = 6/\mu, \quad \gamma = 3\beta_2/4\mu. \quad (3.6)$$

Balmforth conducted numerical simulations of Eq. (3.1)-(3.2) to compare to the results of the reduced model Eq. (3.4)-(3.5) for values of the (unscaled) viscosity $\nu = 10^{-6}$. The agreement was exceptionally good, and the results were reported on at length in BPU. The reduced model predicted the onset and development of vortex structures at the tip of the jet in accordance with the numerical simulations.

Constructing a linear theory of the reduced set (assuming $\exp -i(cT + x)$ solutions) reveals subtle differences between the predictions of the nearly inviscid versus exactly inviscid flow. The first of these is that the predictions for the types of modes that propagate differs between the $\nu = 0$ and $\nu \rightarrow 0$ cases. The results are summarized in Fig. 2(a) and Fig. 3.

The $\nu = 0$ theory predicts that waves that are outside of the unstable regime (as depicted in Fig. 2) are neutrally stable. On the other hand, the $\nu > 0$ theory predicts that the eigenvalue c of at least one mode is approximately,

$$c \approx \frac{\lambda^{1/4} e^{-i\pi/8}}{\kappa}. \quad (3.7)$$

This predicts that those waves that are neutrally stable in the $\nu \rightarrow 0$ limit become viscously unstable if $k^2 < 6$ ($\mu < 0$) (see Fig. 4) and remain stable for $k^2 > 6$ ($\mu > 0$).

Another curious result of the inviscid versus nearly inviscid theory is that the inviscid theory predicts that there are either zero, one, or two modes of the system. In the nearly inviscid theory, in addition to the modes of the inviscid theory, there are a countably infinite number of viscous modes given by

$$c \approx (2n + 3/4)\sqrt{\lambda}e^{-i\pi/4}, \quad (3.8)$$

where n are the positive integers. For the problem at hand these modes are decaying and do not dynamically play an active role. However, in other problems they may possess different stability characteristics and one must be aware of their existence.

In summary, we have reduced the complicated dynamics of critical-layer/inflexion-point instabilities of a jet in a planetary vorticity field to a manageable set of asymptotic equations. The asymptotic validity of the equations was demonstrated, and we found that the reduced set offers a transparent view into some of the differences between assuming viscous versus inviscid flow. The methodology developed can be used in studying and dissecting the dynamics of other jet flows that might be manifest in protoplanetary disks.

4. Current directions

Current work with Barranco and Marcus is focused on developing a fully parallel three-dimensional spectral simulation of the Euler equations on an annular section of a Keplerian protoplanetary disk. We are preparing the simulation to be run on the SP2 Blue Horizon machine at the San Diego supercomputing center. The linear theory developed in § 2 will be used to provide checks for the code as it is developed. In addition, we have a number of analytical tasks that must be performed in support of the numerical simulations. These include the following:

- No analogous asymptotic expression for the energy content of the fluid has yet been developed. We must perform a similar analysis to the one performed in BMU in order to

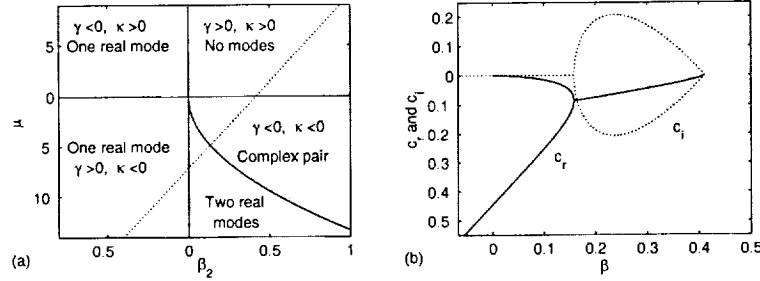


FIGURE 2. The types of propagating modes for the $\nu = 0$ theory. For $\beta_2 < 0$, all modes are neutral and they represent Rossby waves. In panel (b) we see the frequency and growth rates for the modes as a function along the dotted-line cut shown in panel (a). Note how the transition to instability occurs when the two real (Rossby) waves merge. c_r and c_i represent the real and imaginary parts of the eigenvalue. This

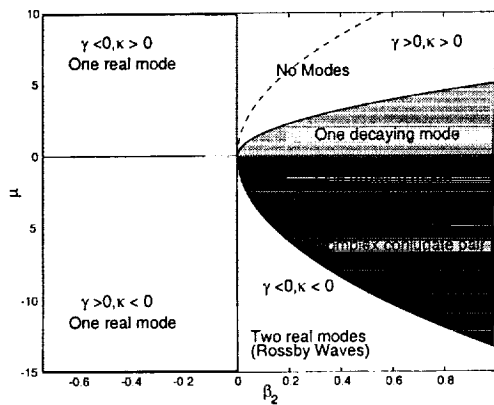


FIGURE 3. The $\nu \rightarrow 0$ limit of the viscous linear theory. The predictions should be compared to the $\nu = 0$ theory in Fig. 2. The types of modes that propagate as a function of parameter values are different between the two theories.

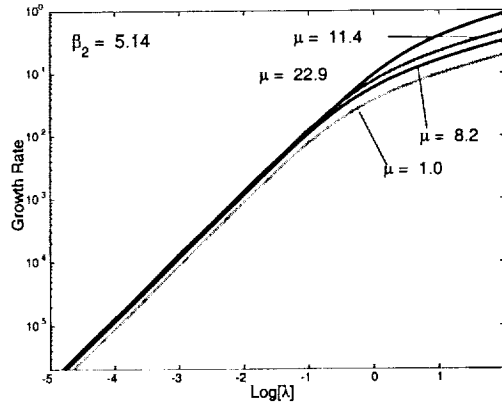


FIGURE 4. $\nu > 0$ tendency for $\beta_2 = -5.16$ for assorted values of μ . Whereas in the $\nu \rightarrow 0$ limit, the Rossby wave for this parameter regime is neutrally stable, the waves become viscously unstable when the viscosity is non-zero.

determine an asymptotically valid expression for a heat equation for the fluid. Analysis and judgments need to be made as to the relative time scales involved between the heating and cooling of the baroclinic disk against the time scales involved with the advected fluid fluctuations. Two extreme limits of the thermal time will yield an equation of state that is either isothermal or adiabatic.

- As seen throughout § 2, though baroclinicity induces some sort of instability in most cases, boundary conditions play a role in the onset criteria for instability of disturbances. Therefore, a detailed understanding of the implications of the various boundary conditions is required to judge whether or not the numerical simulations predict physically realizable phenomena. At the very least, interpretation of an instability will require an understanding of how the prescribed boundary conditions physically effect the flow and contribute to the instability.

Acknowledgment

I would like to thank Alan Wray for reading this manuscript and offering many scientific suggestions and numerical advice throughout the course of this and ongoing work.

REFERENCES

- BARRANCO, J. & MARCUS, P. S. & UMURHAN, O. M. 2000 Scalings and Asymptotics of Coherent Vortices in Protoplanetary Disks. *Summer Program Proceedings*, Center For Turbulence Research, NASA Ames/Stanford Univ. 85-95.
- BALBUS, S. A. & HAWLEY, J. F. & STONE, J. M. 1996 Nonlinear stability, hydrodynamic turbulence, and transport in disks, *Astrophys. J.* **467**, 76-86.
- BALMFORTH, N. & PICCOLO, C. 2000 Onset of meandering in a barotropic jet. *J. Fluid Mech.* *in submission*.
- BALMFORTH, N. & PICCOLO, C. & UMURHAN, O. 2000 Critical layer dynamics at the tip of a jet. *J. Fluid Mech.* *in submission*.
- BENDER, C. M. & ORSZAG, S. A. 1999 Advanced mathematical methods for scientists and engineers. Springer Verlag.
- CHANDRESEKHAR, S. 1954 The instability of a layer of fluid heated below and subject to the simultaneous action of a magnetic field and rotation. I. *Astrophys. J.* **237**, 173-184.
- DESCH, S. 2000 Private communication.
- DRAZIN, P. G. & REID, W. H. 1982 Hydrodynamic Stability. Cambridge University Press.
- KNOBLOCH, E. & SPRUIT, H. C. 1986 Baroclinic waves in a vertically stratified thin disk. *Astron. Astrophys.* **166**, 359-367.
- MARCUS, P. S. 1984 Simulation of Taylor-Couette flow. II. Numerical results for wavy-vortex flow with one traveling wave. *J. Fluid Mech.* **146**, 65-113.
- MARCUS, P. S. 1993 Jupiter's Great Red Spot and other vortices. *ARAA* **31**, 523-573.
- MARCUS, P. S. & PRESS, W. H. 1977 Green's Functions for Small Disturbances of Plane Couette Flow. *J. Fluid Mech.* **79**, 525-534.
- MARCUS, P. S. & TUCKERMAN, L. S. 1987 Simulation of flow between concentric rotating spheres - Part II - Transitions, *J. Fluid Mech.* **185**, 31-66.
- MARCY, G. W. & BUTLER, R. P. 1996 A planetary companion to 70 Virginis. *Astrophys. J.* **464**, L147-L151.
- MASLOWE, S.A. 1991 Barotropic instability of the Bickley jet. *J. Fluid Mech.* **266**, 417-426.
- PERRYMAN, MAC 2000 Extra-solar planets. *Reports on Progress in Physics.* **63**, 1209-1272.
- ROGALLO, R. S. 1981 Numerical experiments in homogeneous turbulence. *NASA Tech. Mem.* **81315**, 1-91.
- ROGERS, M. M. 1991 The structure of a passive scalar field with a uniform mean gradient in rapidly sheared homogeneous turbulent flow. *Phys. Fluids A.* **3**, 144-154.
- SHEEHAN, D. P. & DAVIS, S. S. & CUZZI, J. N. & ESTBERG, G. N. 1999 Rossby wave propagation and generation in the protoplanetary nebula. *Icarus.* **142**, 238-248.
- SHU, F. A. & JOHNSTONE, D. & HOLLENBACH, D. 1993 Photoevaporation of the solar nebula and the formation of the giant planets. *Icarus.* **106**, 92-101.

Evolutionary optimization for flow experiments

By Ivo F. Sbalzarini[†], Lester K. Su AND Petros Koumoutsakos^{†‡}

1. Motivation and objective

Despite the ever increasing power of digital computers and numerical algorithms, experiments are still the ultimate test for physical reality. However, in a design cycle they are usually conducted in later stages in order to test the configurations that have been selected by theoretical or computational studies. The reasons are usually the expense associated with experiments as well as the lack of automation. For parameter optimization, the latter drawback can be alleviated by implementing evolution strategies for the optimization cycle.

Evolution Strategies (ES) were initially developed for experiments four decades ago (see e.g. Box (1957) or Schwefel (1977)). In the absence of computers, they were implemented by hand using paper, pencil, and the throwing of a dice to simulate random numbers. Early studies have shown that ES cover the whole search space, and that is what makes them better suited for experimental purposes than grid search methods (Box & Wilson (1951)). Today's ES are based on random mutations rather than the pattern based variations of their ancestors (Schwefel (1977), Rechenberg (1994)). This makes them more efficient, and they have proven to be a very powerful tool in computational optimum seeking. Moreover, they are highly portable since every optimization problem that can be formulated as a vector of parameters being sought in order to maximize (or minimize) one or several quantities (called *cost function* or *fitness function*) can be addressed by Evolution Strategies. Due to the fact that many experiments belong to this class of problems, it has been the objective of this work to implement and develop suitable evolutionary algorithms for the automation of optimization in experiments.

Inexpensive general purpose digital computers, hardware interfaces such as A/D converters, and suitable control software have made it possible for a computer to take the place of the experimenter for routine tasks and repeating measurement cycles. Evolution Strategies communicate the methodical selection of parameters to the control software of the experimental device using an interface and they could ultimately control the course of the experiment on a higher level, just as a human experimenter would do.

This paper is organized as follows: Section 2 of this paper gives a short introduction to Evolution Strategies in general as well as to the specific Evolution Strategy used for this work. Section 3 describes the basic set-up of an automatic experiment and gives detailed information about the communication interface that has been developed. Section 4 discusses some of the main problems and issues of using evolution to control optimization in experiments and introduces variance analysis. Section 5 shows how this methodology has been applied to the problem of finding optimal parameters to control high Reynolds number round air jets, and Section 6 presents results obtained from the experiments.

[†] Swiss Federal Institute of Technology (ETH), 8092 Zürich, Switzerland

[‡] Also at CTR Stanford/NASA Ames

ivo,petros@eniac.ethz.ch, lsu@stanford.edu

2. Evolution strategies

The fundamental concept of ES is the imitation of the natural process of biological evolution. The problem to be solved is described using a certain number of *parameters* (design variables). One then creates a group of $\lambda (> 0)$ different parameter vectors and considers it as a *population of individuals*. The quantity λ is called the *population size*. The quality of a certain vector of parameters (i.e. an *individual* in the population) is expressed in terms of a scalar valued *fitness function* (objective function). Depending on whether one wants to minimize or maximize the objective function, individuals (i.e. parameter vectors) with lower or greater fitness are considered better, respectively. The algorithm then proceeds to choose the μ , ($\mu < \lambda$) best individuals out of the population to become the parents of the next generation (natural *selection*, survival of the fittest). Therefore, μ denotes the *number of parents*. The smaller μ that is chosen compared to λ , the higher the *selection pressure* will be. Out of the μ individuals chosen to be parents for the next generation, one then creates a new population of λ offspring \mathbf{x}_i^{g+1} by applying *mutation* (c.f. Fogel (1997)) on the parents \mathbf{x}_j^g as follows:

$$\mathbf{x}_i^{g+1} = \mathbf{x}_j^g + \mathcal{N}(0, \Sigma) \quad , i = 1, \dots, \lambda \quad , j \in \{1, \dots, \mu\} \quad (2.1)$$

where $\mathcal{N}(0, \Sigma)$ denotes a vector of jointly distributed Gaussian random numbers with zero mean and covariance matrix Σ . The standard deviations (i.e. the square roots of the diagonal elements σ_i^2 of Σ) of the additive random numbers determine “how far away from its parent a child will be on the average” and are called *step sizes* of the mutation. Now, the first iteration is completed and the algorithm loops back to the evaluation of the fitness function for the new individuals. Several different techniques for adaptation and control of the mutation step size have been developed (see e.g. Bäck (1997a), Bäck (1997b), Bäck (1993), Hansen & Ostermeier (1996) or Hansen & Ostermeier (1997)).

2.1. The (1+1)-ES

For this work, one of the simplest and yet powerful evolution strategies has been employed: the “one plus one evolution strategy”, denoted by (1+1)-ES. In this strategy, both the number of parents and the population size (i.e. number of offspring) are set to one: $\mu = \lambda = 1$. Mutation is accomplished by adding a vector of uncorrelated Gaussian random numbers, i.e. $\Sigma = \text{diag}(\sigma_i^2)$. Step size adaptation has been performed according to Rechenberg’s 1/5-rule: if less than 20% of the past generations are successful (i.e. offspring better than parent), then decrease the step size for the next generation; if more than 20% are successful, then increase the step size in order to accelerate convergence. This adaptation is done every $N \cdot L_R$ generations where N is the number of parameters (i.e. dimension of search space) and L_R is a constant, usually equal to one. Selection is done out of the set union of parent and offspring, i.e. the better one of the two is chosen to become the parent of the next generation.

3. Subsystems of an automatic experiment

Our automated optimization experiment as driven by evolution consists of the following functional blocks: the experimental hardware set-up, hardware computer interfaces such as D/A and A/D converters, a general purpose digital computer, a data acquisition and control software, an evolution strategy code, and a communication interface between the ES code and the acquisition/control software. We will not discuss experimental hardware,

File	Format	Usage/Meaning
evo.in	NF16.9 \n F16.9	actual parameters, fitness value
evo.out	N[F16.9 \n]	parameter values to be tested
flag	I1.1	measurement status
Nstart	I3.3	index shift for restart
abort	I1.1	global execution control

TABLE 1. Interface ASCII files.

digital computers, or hardware interfaces in this paper, but will focus on the software needed.

3.1. Data acquisition and control software

This piece of software provides the only connection of the ES code to the real, physical world. It can be viewed as a replacement for the eyes and hands of the experimenter. For this work, National Instrument's LabView 5.1† running on a Microsoft Windows 98 PC has been used. It was set up to control the whole experiment in its sequential course and collect all the measurement data needed.

3.2. Evolution Strategy code

The evolution algorithm may be viewed as a simple replacement for the strategy of the experimenter. It looks at measurement readings and decides where to go next in order to eventually achieve the optimum it is looking for. For this work, a restartable (1+1)-ES has been implemented in Fortran with a communication subroutine connecting it to LabView.

3.3. Communication interface

The evolution code and LabView are assumed to be running on the same computer in a multitasking mode that allows them to be executed concurrently. To ensure portability across computing platforms, a simple file interface has been chosen to handle all communication. Both LabView and the ES code write and read shared files to exchange information or monitor flag files for the sake of synchronization. The interface consists of the files shown in table 1. The format column indicates the numeric format of each ASCII file in Fortran notation where N is the number of parameters, $\backslash n$ means a newline character, and $N[F16.9 \backslash n]$ indicates N numbers separated by newline characters.

The control flow proceeds as follows:

1. ES code starts, initializes its parameters or reads a restart file, writes a zero in the files "flag" and "abort", writes the current generation number to "Nstart", and creates the first (or next if a restart) parameter vector to be tested.
2. LabView starts, initializes and reads "Nstart" to determine the current generation number. For all output of LabView, Nstart will be added to the value of its loop counter to get the correct generation number.
3. LabView monitors the file "flag" every t seconds. It sits idle as long as the file contains a zero.

† <http://www.ni.com/labview/>

4. ES deletes the old "evo.in" file.
5. ES writes the current parameter vector to be evaluated in "evo.out".
6. ES writes a one in "flag" to tell LabView to start.
7. ES test for the existence of "evo.in" in fixed time intervals.
8. LabView starts the experiment using actual values as close to the parameter values as possible (i.e. next discrete digital level).
9. When the measurement is completed, LabView calculates the fitness value and writes the actual parameters as well as the fitness value to "evo.in". It also checks the file "abort" and terminates if it contains a nonzero value. Otherwise, LabView loops back to step 3.
10. ES detects existence of "evo.in".
11. ES writes a zero in "flag" to set LabView on hold.
12. ES starts reading "evo.in". If an error occurs because LabView has not yet finished writing the file, the ES code will step back and try again later. It reads the actual parameters (overwriting its internal representation of the parameter vector) and the fitness value for this population member.
13. ES checks "abort" file. If it contains a nonzero value, execution is terminated. If the next generation is the last one, ES writes a one in "abort" to halt LabView and itself after the next evaluation.
14. ES writes the current information to a restart file, performs selection based on the latest fitness values, and creates a new population before looping back to step 4.

Since LabView will not overwrite any files without prompting the user for permission, the ES code has to make sure that all files are deleted before LabView overwrites them. Otherwise, LabView will display a message box and wait for user action, which is in contradiction to the goal of having automated experiments. A second point to consider is that LabView is very strict regarding file formats and separator characters. That is why all file I/O in Fortran has to be done using explicit, fixed format specifiers instead of list directed output. The same format specifiers have to be used in LabView. Moreover, numbers that are passed to LabView need to be separated by a well defined delimiting character. This ultimately means that they need to be on separate lines using the newline character as a delimiter because Fortran will pad and number to the right length using spaces. If the numbers were on the same line, there would be an unknown amount of spaces between each of them and, therefore, no well defined delimiter, since LabView is sensitive to the number of spaces.

4. Main problems and issues

Applying evolution to experiments means coping with additional effects that are usually not present in computation. They can roughly be divided into effects caused by measurement uncertainties (or errors), digital signal quantification, and uncontrollable environmental influences. The following subsections discuss each of these causes in turn and proposes some solutions.

4.1. Measurement uncertainties

During selection, the ES code determines the population member with the highest (or lowest) fitness value, and it assumes that the differences in fitness between different individuals are entirely caused by the differences in their parameters, i.e. a better fitness value corresponds to better parameters. However, if the fitness is determined in measurements and the difference between two fitness values is less or equal to the measurement

uncertainty, it could possibly be that the “better” individual only has a better fitness value due to measurement errors and not due to its parameter set, which could actually be worse than others. This can mislead the ES since it relies on information that is no more than an artifact of the experimental procedure. To avoid this problem, mutation step sizes must always be larger than any uncertainty in order to get changes in the objective function that are larger than the general measurement noise. This poses a lower limit to the convergence of the Evolution Strategy and an additional constraint to the method of step size adaptation to ensure that step sizes are always significant. ES using recombination (Booker, Fogel, Whitley & Angeline (1997)) are more robust against distorted selection and should, therefore, be favored for experimental purposes. Other strategies to cope with this problem could include a cutoff coefficient, which forces the ES to select variances larger than this cutoff. If the distance between two individuals in objective space is less than the cutoff value, the ES should not take the “better” of them as a parent for the next generation but rather the mean of them.

4.2. Digital quantification

Digital hardware is capable of producing or measuring signals only in discrete steps. For certain hardware such as on-board waveform generators, these steps can be as large as 0.5%, depending on the buffer size of the device. For a wave form generator, this could mean that frequencies around 1000Hz can only be varied in steps of 5Hz. This means that parameter vectors differing less than one such discrete step will cause the same physical output to be produced and are, therefore, actually identical. Besides adding another lower limit for the mutation step size of the ES, this quantification also calls for some feedback mechanism to “tell” the ES what values have actually been produced instead of the parameter vector it requested. The ES should then take these physical values to replace its internal representation of the parameter vector in order to be consistent with the fitness value that has been caused by the physical values. This calls for a certain robustness of the ES against unpredictable changes in the parameter vectors. Problems can occur in ES that have some sort of “memory” to keep track of the evolution path in order to improve their convergence (e.g. the CMA-ES by Hansen & Ostermeier (1996)).

4.3. Uncontrollable environmental factors

Every experiment is affected by various uncontrollable external factors, such as ambient temperature or pressure, electro-magnetic fields, sunlight, etc. Since these factors can not be controlled by the ES, one has to make sure that they do not affect the fitness function. In other words, the same parameter vector should (within experimental accuracy) always produce the same fitness value regardless of changes in any environmental quantity. The easiest way to achieve this is to determine the most important environmental factors (impact analysis) and normalize the fitness function accordingly.

5. Application to jet control

We consider the application of an evolutionary optimization procedure to the problem of control of high Reynolds number jet flows. These flows have been the subject of several experimental works, and they have been chosen because it is a quite well known, old (Leconte (1958)) issue where lots of reference works in conventional experiments (e.g. Lepicovski, Ahuja & Salikuddin (1984), Lepicovski & Ahuja (1985), Lee & Reynolds (1985), Parekh, Reynolds & Mungal (1987), Lepicovski, Ahuja, Brown, Salikuddin & Morris (1988), Parekh, Leonard & Reynolds (1988) and Juvet & Reynolds (1993)) as

well as computational studies (e.g. Urbin, Brun & Metais (1997) and Freund & Moin (1998)) have been done. Evolution Strategies have been successfully applied to numerical simulations at lower Reynolds numbers (Koumoutsakos, Freund & Parekh (1998), Müller, Milano & Koumoutsakos (1999) and Koumoutsakos, Freund & Parekh (2001)), involving methods with step size adaptation developed by Hansen & Ostermeier (1997).

5.1. Basic experimental set-up

The experimental set-up consists of a vertical jet of warm (about 35°C) air exiting from a straight nozzle (inner diameter $D = 20\text{mm}$). The surrounding air was air-conditioned to about 20°C. Temperature profiles were measured on a straight path from the center of the jet outward using a type K thermocouple connected to a Fluke thermocouple adaptor. The thermocouple was moved across the jet $d = 122.2\text{mm}$ ($d/D = 6.11$) above the nozzle exit. The jet was acoustically excited using 5 loudspeakers. 4 of them were used to create a helical excitation of certain frequency, amplitude, and phase, and one was used to create an axial excitation. Detailed descriptions of the set-up and the hardware can be found in Parekh, Reynolds & Mungal (1987), Parekh, Leonard & Reynolds (1988) and Juvet & Reynolds (1993). The inputs of the amplifiers driving the speakers were connected to the outputs of D/A converters (National Instruments BNC-2090 DAQ board for the two helical channels and Data Translation 2D16A board for the axial channel), which in turn were connected to a computer. The temperature sensor was mounted on an arm and moved across the jet by a step motor controlled by the computer. Temperature readings at each point were digitized using the National Instruments BNC-2090 DAC and fed to the computer. Temperatures were measured at certain distances from the center of the jet, collecting 3000 samples per point at a sampling rate of 500Hz.

5.2. Excitation

The jet was acoustically excited using two different modes: helical and axial. The helical excitation was done by four speakers, regularly arranged around the centerline of the jet at angles of 90°. Their sound was fed into the jet right before the exit nozzle using wave guides. The excitation signal was sinusoidal, and the phase corresponded to the geometrical set-up, i.e. one speaker was fed a sine wave, the one to its right a cosine wave, the one opposite of it a negative sine wave, and the one to its left a negative cosine wave. Therefore, the phase between adjacent speakers was 90° in normal operation mode. However, this phase could be shifted by adding some value. Opposite speakers were always 180° out of phase regardless of the phase shift between adjacent ones. The two pairs of opposite speakers (i.e. the ones fed with a sine wave and the ones fed with a cosine wave) were connected to two different channels of the same power amplifier (Kenwood Stereo Power Amplifier Basic M2A). Phase reversal for opposite speakers was done by simply changing the polarity of the wires. The amplifier was adjusted to a gain of 60, which corresponds to a maximal output amplitude of $16V_{RMS}$.

The axial excitation was done by a single loudspeaker sitting in the bottom of the jet column. It was connected to the output of a second power amplifier (Kenwood Stereo Power Amplifier Basic M1 and Kenwood C1 preamplifier) and fed with a simple sine wave of specific frequency. The amplifier was adjusted to a gain of 30, which also corresponds to a maximal output amplitude of $16V_{RMS}$.

All 5 speakers were 120 Watt compression drivers of type JBL 2485J. Their frequency range is 300Hz to 3000Hz, and they are designed to be used in large systems such as those found in stadiums. The amplitudes and frequencies for both modes as well as the phase shift of the helical excitation were controlled by the computer.

5.3. Parameters

The parameters to be optimized were:

- frequency of helical excitation (f_h) in Hertz
- frequency of axial excitation (f_a) in Hertz
- amplitude of helical excitation (A_h) in Volts
- amplitude of axial excitation (A_a) in Volts
- phase shift of helical excitation (φ) in radians

The parameters were subject to the following constraints defining the boundaries of the search space: both frequencies have to be between 300Hz and 3000Hz (band limit of the speakers), both amplitudes have to be between $0V_{RMS}$ and $16V_{RMS}$ (amplifier power limitation), and the phase shift is between 0 and π (periodicity).

5.4. Fitness function

Since the goal was to maximize the spreading of the jet, the fitness function was chosen to be proportional to the discrete variance of the normalized temperature profile, normalized to the number of measurement points, i.e.:

$$F = \frac{100}{N} \sum_{i=1}^N \left(\frac{T_i}{T_{max}} - \mu_T \right)^2 \quad (5.1)$$

where T_i is the physical temperature at the i -th measurement point, N is the number of measurement points per profile, T_{max} is the peak value of the profile:

$$T_{max} = \max_i T_i \quad (5.2)$$

and μ_T is the mean of the normalized temperature profile:

$$\mu_T = \frac{1}{N} \sum_{i=1}^N \frac{T_i}{T_{max}} \quad (5.3)$$

5.5. Variance analysis

As mentioned in Section 4.1, the changes in fitness due to parameter changes have to be significantly larger than the ones due to measurement noise. To see whether a certain experiment can be treated by evolution using a given fitness function, a small variance analysis should be performed. One simply measures the fitness values at certain fixed points in parameter space several times to get an estimate of mean and variance at these points. If the error bars for two parameter sets do not overlap, evolution strategies will be able to distinguish between them and use this information to converge towards the better point. Variance analysis for the jet has been done for the parameter sets listed in table 2. For all sets, the phase of the helical excitation has been fixed at 0 and the amplitudes have been fixed to their maximal values of $16V_{RMS}$. 5 temperature profiles have been taken for each set under varying environmental conditions (i.e. ambient temperature and jet temperature) on different days, and the fitness values for all profiles have been calculated according to Section 5.4. Each profile consisted of 8 measurement points at 0, 5, 10, 15, 20, 30, 40, and 50mm distance from the center of the jet. All runs were performed at $Re_D = 10^5$, which corresponds to an exit velocity of about $77 \frac{m}{s}$. The “strong blooming condition” was found by Juvet & Reynolds (1993) as a condition

Set nr.	Meaning of point	Helical [Hz]	Axial [Hz]
1	Natural jet, no excitation	0	0
2	Lower boundary of search domain	300	300
3	"Strong blooming condition"	896	2060
4	Random starting point for ES	1000	1800
5	Best point of ES run 1	777	1773
6	Upper boundary of search domain	3000	3000

TABLE 2. Parameter sets for variance analysis.

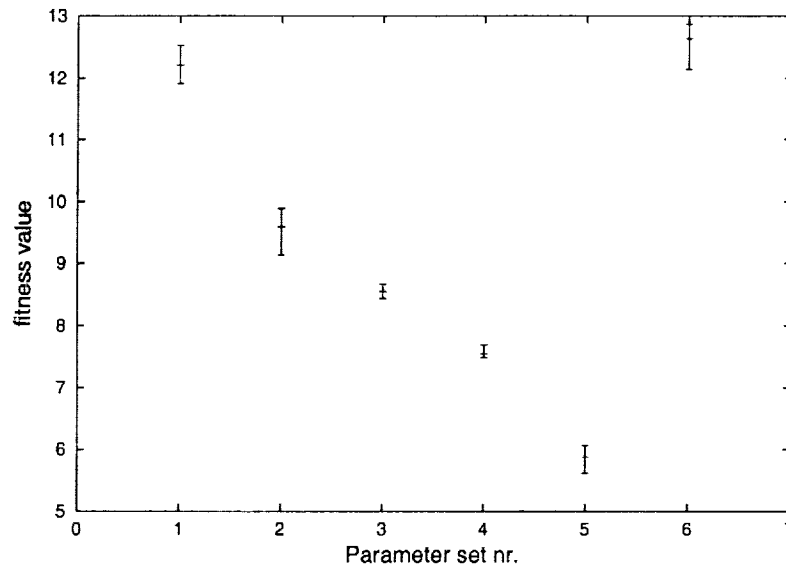


FIGURE 1. Variance analysis for the jet. See table 2 for parameter values.

which gives very high spreading. The best point of the ES run was taken from the (1+1) optimization of both frequencies (see Section 6.1).

The bar plot in Fig. 1 shows mean and span for all measurements of each parameter set. It can be seen that the bars generally do not overlap except for the natural jet and the upper domain boundary. Moreover, the variation due to measurement uncertainties seems to be small enough to allow evolution with an accuracy of at least one unit in fitness value. This implies that if the difference in fitness of two parameter vectors is more than one, it can be considered a significant difference, and one parameter set is clearly better than the other. It can also be seen that there must exist a (at least local) minimum in the search space chosen since there are points between the domain boundaries that have lower fitness values than the boundaries themselves.

6. Results for the jet

Several runs under different conditions were performed for the jet. The amplitudes have been fixed to their maximal value for all runs since higher amplitudes always cause higher

spreading and, therefore, they should simply be as high as possible (Müller, Milano & Koumoutsakos (1999)). In the first run presented here, both frequencies have been varied independently; the phase shift was fixed at 0 and the evolution started from a random point. In the second run, the frequency ratio has been optimized starting from the “strong blooming condition” found by Juvet & Reynolds (1993). Finally, in the third run, both frequencies and the phase have been varied independently, starting from the same point as the first run. The results are presented in the following subsections.

6.1. Run 1: Two frequencies at $Re = 102000$

Both frequencies were optimized using a (1+1)-ES as described in Section 2.1, while the amplitudes were fixed at their maximum of $A_a = 16V_{RMS}$ and $A_h = 16V_{RMS}$. The phase shift has been fixed at 0, which means that adjacent speakers were 90° out of phase (c.f. Section 5.2). The initial step sizes for the ES were 50Hz for both frequencies, and step size adaptation was done every 20 generations. The temperature was measured at 8 points at distances of 0, 5, 10, 15, 20, 30, 40, and 50mm from the center of the jet (i.e. at $l/D = 0, 0.25, 0.5, 0.75, 1, 1.5, 2, 2.5$). We collected 3000 samples at each point at a sampling rate of 500Hz, which corresponds to a sampling time of 6 seconds. Statistical analysis showed that this sampling time is sufficient to get a stable mean within 1%. The stagnation pressure in the jet right before the exit was fixed at 15 inches of water over ambient pressure, which translates into an exit velocity of about $78 \frac{m}{s}$ (by isentropic calculation). The Reynolds number based on the inner diameter of the exit nozzle was $Re_D = 102000$ for this run. The starting values for the parameters were: helical frequency $f_h = 1000\text{Hz}$ and axial frequency $f_a = 1800\text{Hz}$, which corresponds to Strouhal numbers (based on the inner diameter of the exit nozzle) of $St_h = 0.26$ and $St_a = 0.46$, respectively. The initial fitness value at this point was 6.8. The ambient temperature was between 21°C and 22°C during the whole period of measurement, and the temperature of the jet was between 35°C and 38°C at the exit nozzle. The ES was run for 100 generations.

Figure 2 shows the fitness values of all the individuals that have been created by the ES. The best parameter vector has been found at generation 48 as $f_h = 777\text{Hz}$ ($St_h = 0.20$), $f_a = 1773\text{Hz}$ ($St_a = 0.45$) and had a fitness value of 3.4, which is half of the fitness value at the starting point. Since the change in fitness was clearly larger than one, it can be considered a *significant* (c.f. Section 5.5) improvement. Figure 3 shows the temperature profiles (normalized to the peak temperature) for initial and best parameters as well as for the natural jet without any excitation. The profiles got clearly flatter, which implies a higher spreading of the jet. The results found by the ES are supported by computational results of Freund & Moin (1998) that strong flapping of the jet appears for $St_h = 0.2$. The same has been observed in experiments by Parekh, Kibens, Glezer, Wiltse & Smith (1996). Moreover, a large amplification of signals was observed by Parekh, Kibens, Glezer, Wiltse & Smith (1996) and Parekh, Leonard & Reynolds (1988) for $St_a \approx 0.4$. The same Strouhal numbers have also been found in the first attempt to find optimal actuation parameters for compressible jets with numerical simulations and ES by Koumoutsakos, Freund & Parekh (1998). This suggests that ES work well on experiments and that they have found reasonable parameters in this case.

6.2. Run 2: Frequency ratio at $Re = 95000$

In this run, the frequency ration was optimized while the frequency of the axial excitation has been fixed at 2060Hz ($St_a = 0.56$). Both amplitudes were fixed at their maximal values of $16V_{RMS}$ each. and the phase shift was again fixed at 0. The helical frequency was varied by the (1+1)-ES starting from 896Hz ($St_h = 0.24$) with an initial step size of

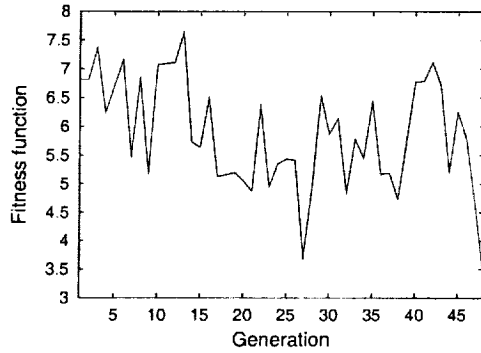


FIGURE 2. Path of (1+1)-ES

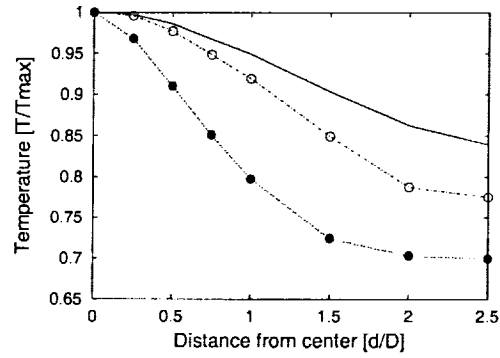


FIGURE 3. Normalized temperature profiles of natural jet (—●—), initial condition for ES (—○—) and best result of ES (—).

50Hz. Step size adaptation was performed every 10 generations. The temperature profiles were measured in exactly the same way and at exactly the same positions as in the first run. The stagnation pressure in the jet right before the exit was fixed at 13.2 inches of water over ambient pressure, which corresponds to an exit velocity of about $73.6 \frac{m}{s}$ (isentropic calculation) and a Reynolds number of $Re = 95000$. The starting values for this run correspond to a frequency ratio of 2.3, which is clearly within the range for blooming (Lee & Reynolds (1985)). They are identical to the parameters of the “strong blooming condition” that have been found by Juvet & Reynolds (1993) as a condition of very high spreading. They also fixed the axial frequency to 2060Hz and run at the same Reynolds number. The only differences between their measurements and the present work are that they used a shrouded jet (which should not have any influence on the position of the optimum, however) and hot-wire velocity measurements instead of temperature measurements. The initial fitness value for the strong blooming point was found to be 8.3. The ambient temperature fluctuated between 21°C and 25°C ; the temperature of the jet was between 35°C and 38°C at the exit nozzle. The ES was run for 100 generations.

Figure 4 shows the fitness values of all the individuals that have been created by the ES. The best parameter vector has been found at generation 25 as $f_h = 791\text{Hz}$ ($St_h = 0.21$), which corresponds to a frequency ratio of 2.6 and a fitness value of 4.5. Compared to the initial fitness value of 8.3, this is again a significant improvement. Figure 5 shows the temperature profiles (normalized to the peak temperature) for initial (strong blooming) and best parameters as well as for the natural jet without any excitation. Even compared to the “strong blooming condition”, the evolution has achieved a significant improvement.

6.3. Run 3: Two frequencies and phase at $Re = 102000$

In a third run, both frequencies plus the phase shift between adjacent speakers of the helical excitation have been varied independently. Again, the amplitudes were fixed at their maximal value of $16V_{RMS}$ each. Frequencies and phase were varied by the (1+1)-ES starting at the same point as in the first run, i.e. $f_h = 1000\text{Hz}$ ($St_h = 0.26$), $f_a = 1800\text{Hz}$ ($St_a = 0.46$), and $\varphi = 0$, with an initial step size of 50Hz for both frequencies and 0.1rad for the phase shift. Step size adaptation was done every 30 generations. The temperature profiles were measured in exactly the same way and at exactly the same positions as in the previous two runs. The jet exit velocity was the same as in run 1, i.e. this run was done at $Re = 102000$ as well. The initial fitness value was 6.9, which is (within

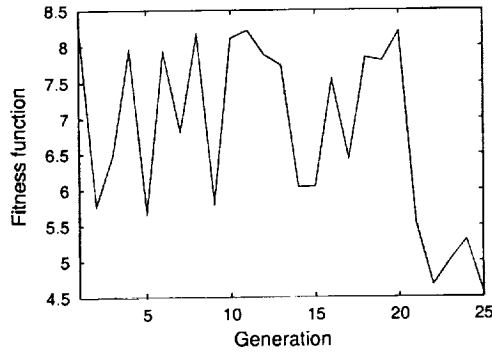


FIGURE 4. Path of (1+1)-ES

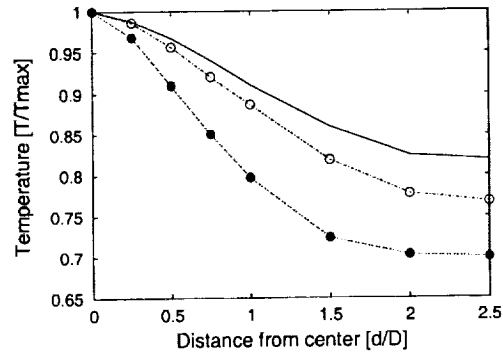


FIGURE 5. Normalized temperature profiles of natural jet (—●—), strong blooming condition (—○—) and best result of ES (—).

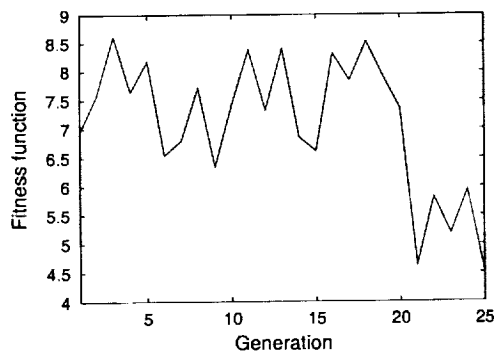


FIGURE 6. Path of (1+1)-ES

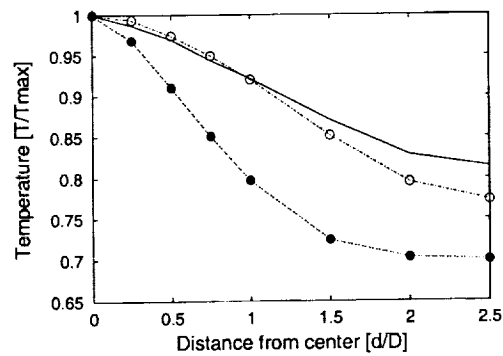


FIGURE 7. Normalized temperature profiles of natural jet (—●—), initial condition for ES (—○—) and best result of ES (—).

given experimental accuracy) the same as in run 1. The ambient temperature fluctuated between 21°C and 23°C; the temperature of the jet was between 35°C and 38°C at the exit nozzle. The ES was run for 100 generations.

Figure 6 shows the fitness values of all the individuals that have been created by the ES. The best parameter vector has been found at generation 25 as $f_h = 952\text{Hz}$ ($St_h = 0.24$), $f_a = 1645\text{Hz}$ ($St_a = 0.42$), $\varphi = -0.488\text{rad}$ (28°), which corresponds to a fitness value of 4.5. Figure 7 shows the temperature profiles (normalized to the peak temperature) for initial and best parameters as well as for the natural jet without any excitation.

7. Conclusions and future work

We have shown that Evolution Strategies can successfully be applied to the optimization of control parameters in experimental set-ups. The results found by these strategies demonstrate that they can successfully complement human expertise. Some key issues of the implementation of evolution algorithms in an experimental set-up have been identified and addressed. However, further work is needed in this area in order to improve certain properties of ES for experiments. Such work should include the application of different ES in order to compare their performance. Above all, ES with recombination, time

averaging, or self-adaptation of step sizes should be tested for better robustness against measurement errors and parameter changes. As far as the jet experiment is concerned, different fitness functions and their influence on the optimum found should be investigated. Runs at different Reynolds numbers and with different numbers of measurement points per profile should be performed in order to test whether the fitness function and the location of the optimum are independent of them or not. In summary, we believe that, with today's hardware and software technologies, evolutionary algorithms offer a strong candidate for the automation of optimization and design cycles in realistic set-ups.

Acknowledgments

The authors thank Prof. Bill Reynolds and Prof. Parviz Moin for their many useful suggestions and discussions and particularly for hosting us at CTR's jet laboratory for the experiments described in this paper.

REFERENCES

- BÄCK, T. 1993 Optimal mutation rates in genetic search. In Forrest, S., editor, *Proceedings of the 5th International Conference on Genetic Algorithms, Urbana-Champaign, IL, July 1993*, Morgan Kaufmann, San Mateo, CA. 2-8.
- BÄCK, T. 1997a Self-adaptation. In Bäck, T., Fogel, D. B. and Michalewicz, Z., editors, *Handbook of Evolutionary Computation*. 97/1, C7.1, IOP Publishing Ltd. and Oxford University Press.
- BÄCK, T. 1997b Mutation parameters. In Bäck, T., Fogel, D. B. and Michalewicz, Z., editors, *Handbook of Evolutionary Computation*. 97/1, E1.2, IOP Publishing Ltd. and Oxford University Press.
- BOOKER, L. B., FOGEL, D. B., WHITLEY, D. & ANGELINE, P. J. 1997 Recombination. In Bäck, T., Fogel, D. B. and Michalewicz, Z., editors, *Handbook of Evolutionary Computation*. 97/1, C3.3, IOP Publishing Ltd. and Oxford University Press.
- BOX, G. E. P. & WILSON, K. B. 1951 On the Experimental Attainment of Optimum Conditions. *Journal of the Royal Statistical Society, Series B (Methodological)*. Vol. XIII, No. 1, 1-45.
- BOX, G. E. P. Jun. 1957 Evolutionary Operation: A Method for increasing industrial Productivity. *Applied Statistics*. 6(2), 81-101.
- FOGEL, D. B. 1997 Mutation, Real-valued vectors. In Bäck, T., Fogel, D. B. and Michalewicz, Z., editors, *Handbook of Evolutionary Computation*, 97/1, C3.2.2, IOP Publishing Ltd. and Oxford University Press.
- FREUND, J. B. & MOIN, P. 1998 Mixing enhancement in jet exhaust using fluidic actuators: direct numerical simulations. *ASME: FEDSM98-5235*.
- HANSEN, N. & OSTERMEIER, A. 1996 Adapting Arbitrary Normal Mutation Distributions in Evolution Strategies: The Covariance Matrix Adaptation. *Proceedings of the 1996 IEEE International Conference on Evolutionary Computation (ICEC '96)*. 312-317.
- HANSEN, N. & OSTERMEIER, A. 1997 Convergence Properties of Evolution Strategies with the Derandomized Covariance Matrix Adaptation: The $(\mu/\mu_I, \lambda)$ -CMA-ES. *Proceedings of the 5th European Conference on Intelligent Techniques and Soft Computing (EUFIT '97)*. 650-654.
- JUVET, P. J. D. & REYNOLDS, W. C. Sept. 1993 Control of high Reynolds number

- round jets, *Report No. TF-59*, Thermosciences Division, Dept. of Mechanical Engineering, Stanford University.
- KOUMOUTSAKOS, P., FREUND, J. B. & PAREKH, D. 1998 Evolution Strategies for Parameter Optimization in Jet Flow Control. *Proceedings of the Summer Program*, Center for Turbulence Research, NASA Ames/Stanford Univ. 121-132.
- KOUMOUTSAKOS, P., FREUND, J. B. & PAREKH, D. 2001 Evolution Strategies for Automatic Optimization of Jet Mixing. *AIAA J.*, to appear.
- LECONTE, J. 1958 On the influence of musical sounds on the flame of a jet of coal-gas. *Phil. Mag.* **15**, 235-239.
- LEE, M. & REYNOLDS, W. C. 1985 Bifurcating and Blooming jets, *Report No. TF-22*, Thermosciences Division, Dept. of Mechanical Engineering, Stanford University.
- LEPICOVSKI, J., AHUJA, K. K. & SALIKUDDIN, M. 1984 An experimental study of tone excited heated jets. *AIAA paper 84-2341*. AIAA 9th Aeroacoustics Conference, Williamsburg, Virginia.
- LEPICOVSKI, J. & AHUJA, K. K. 1985 Acoustic control of free jet mixing. *AIAA paper 85-0569*. AIAA Shear Flow Control Conference, Boulder, Colorado.
- LEPICOVSKI, J., AHUJA, K. K., BROWN, W. H., SALIKUDDIN, M. & MORRIS, P. J. 1988 Acoustically Excited Heated Jets. *NASA Report CR 4129*.
- MÜLLER, S. D., MILANO, M. & KOUMOUTSAKOS, P. 1999 Application of machine learning algorithms to flow modeling and optimization. *Annual Research Briefs*, Center for Turbulence Research, NASA Ames/Stanford Univ. 169-178.
- PAREKH, D. E., REYNOLDS, W. C. & MUNGAL, M. G. 1987 Bifurcation of round air jets by dual-mode acoustic excitation. *AIAA Paper 87-0164*. AIAA 25th Aerospace Sciences Meeting, Reno, Nevada.
- PAREKH, D., LEONARD, A. & REYNOLDS, W. C. 1988 Bifurcating jets at high Reynolds numbers. *Report No. TF-35*, Thermosciences Division, Dept. of Mechanical Engineering, Stanford University.
- PAREKH, D., KIBENS, V., GLEZER, A., WILTSE, J. M. & SMITH, D. M. 1996 Innovative Jet Flow Control: Mixing Enhancement Experiments. *AIAA paper 96-0308*. AIAA 34th Aerospace Science Meeting, Reno.
- RECHENBERG, I. 1994 Evolutionsstrategie - Optimierung technischer Systeme nach Prinzipien der biologischen Evolution. Fromann-Holzboog, Stuttgart.
- SCHWEFEL, H. P. 1977 Numerische Optimierung von Computer-Modellen mittels der Evolutionsstrategie. *Interdisciplinary Systems Research 26*, Basel, Birkhäuser, Basel, Switzerland.
- URBIN, G., BRUN, C. & METAIS, O. 1997 Large Eddy Simulation of three-dimensional spatially evolving round jets. In *11th Symposium on Turbulent Shear Flows*, Grenoble.

Control and optimization of turbulent jet mixing

By Angela Hilgers

1. Motivation and objective

The control of turbulent jet flows has applications in various fields such as combustion, aerodynamic noise, and jet propulsion. Control of mixing can be achieved by manipulation of the large-scale, global instabilities of the flow. In combustors it is important to enhance turbulent mixing of the chemical species in order to achieve high combustion efficiency and to reduce the emission of pollutants. In jet engines, aerodynamic noise can be reduced by controlling flow unsteadiness that produces noise. One aim of enhanced mixing in jet propulsion applications is to decrease the plume temperature and suppress infrared radiation.

The mixing rate of a turbulent jet can be significantly altered by applying a suitable excitation at the jet orifice. Since the external forcing interacts with the natural modes of the jet in a nonlinear way, it is not possible to predict which kind of actuation is optimal to increase mixing. Various experiments have been carried out that study the reaction of jets to the nozzle geometry and to external forcing (Lee & Reynolds (1985), Parekh (1987), Parekh (1988)). Different types of actuators such as piezoelectric devices and synthetic jets have been tested (Wiltse (1993), Parekh (1996)). It has been shown that a large spreading of the jet can be achieved with a small mass flow actuation if suitable frequencies are chosen (Parekh (1996)). Numerical simulations of compressible and incompressible jet flows have been carried out that confirm many observations made in experiments with periodically forced jets (Freund (1998), Freund (1999), Danaila (1998), Urbin (1997)). So far it is difficult to carry out a systematic search for the optimal forcing because the simulations are very computationally intensive. Koumoutsakos *et al.* (1998) showed that evolution strategies are capable of finding suitable actuations for a vortex model and direct numerical simulations of compressible jets.

In this paper we describe a systematic search for combined axial and helical forcing of a round jet that maximize mixing. While stochastic search strategies and direct numerical simulation (DNS) of a jet have been combined before (Hilgers (1999), Hilgers (2000)), this work concentrates on the optimization of jets at higher Reynolds numbers using large eddy simulation (LES). Different search strategies are introduced and their performance for the optimization of jet mixing is compared. The strategies are used to search for an actuation that maximizes mixing in jets at Reynolds numbers $Re = 6000$ and $Re = 100000$.

2. Accomplishments

2.1. Numerical method

For a free round jet issuing from a circular orifice in a solid wall, the incompressible Navier-Stokes equations and the transport equation for a passive scalar are solved in a spherical coordinate system. Spatial derivatives are calculated on a staggered grid. The time integration is carried out with a second order Adams-Bashforth method. The

computational domain is bounded in the radial direction by the surfaces $r = 5D$ and $r = 15D$ and the cone starting from the center of the sphere with an opening angle of 36° . This geometry is able to cover the streamwise spreading of the jet and allow a well-balanced resolution of the flow field with a reasonable number of grid points.

For the control of jets at higher Reynolds numbers, we included a subgrid scale model in our simulation to keep the computational cost affordable. The idea of LES is to resolve only the large scales of the flow while modeling the contribution of the small (subgrid) scales. The LES equations are obtained by applying a spatial filter to the momentum equations. In order to account for the subgrid-scale contribution to the flux of momentum, the molecular viscosity is augmented by an eddy viscosity $\nu_t = C\Delta^2|\mathbf{S}|$, where \mathbf{S} is the subgrid strain tensor and C the Smagorinsky constant. We have used an LES based on the dynamic procedure by Germano (1990), which determines the constant C as a function of space and time. The dynamic procedure does not contain any model constants.

At the inflow section, the following mean streamwise velocity profile is imposed

$$V_{z0}(r_c) = \frac{V_0}{2} \left(1 + \tanh \left[0.25D/\Theta_0(D/(4r_c) - 4r_c/D) \right] \right), \quad (2.1)$$

where D is the jet diameter, V_0 the centerline velocity, and r_c the radius in a cylindrical system (z, r_c, ϕ) . The initial momentum thickness was $\Theta_0 = D/60$ in our simulations.

At the lateral boundary, the total normal stress is set to zero, which allows fluid exchange across the boundary. This condition properly simulates the entrainment of ambient fluid in the spreading jet flow. A so-called convective boundary condition (Orlanski (1976)) is used to evacuate the vortex structures through the downstream boundary. Details of the numerical scheme can be found in Boersma (1998).

For the LES of a jet with Reynolds number $Re = 6000$ based on orifice velocity V_0 and diameter D , the spherical grid consists of $192 \times 128 \times 64$ points in the radial, tangential, and azimuthal directions respectively. Typical CPU times for the calculation of a fully developed jet are 1800 node hours on an Origin 2000, using the Message Passing Interface (MPI). The optimization requires the simulation of up to 100 jets for different actuation parameters. It is therefore necessary to reduce the CPU time during the optimization process.

In unforced jets, large coherent structures are observed that are related to the instability modes of the jet. The dominant modes are the axisymmetric or varicose mode and helical modes. The axisymmetric mode causes the shear layer to roll up into vortex rings. By applying axial forcing to the shear layer, the frequency of vortex ring generation and the pairing of the vortex rings may be altered. The initial shear layer is able to amplify a large range of frequencies. The frequency f which leads to the maximum amplification of the initial shear layer is called the natural frequency. It can be obtained by linear spatial instability analysis (Michalke (1984), Ho (1984)). For an axisymmetric jet with the initial velocity profile given in Eq. (2.1), it is $St_{\Theta_0} = f\Theta_0/V_0 = 0.018$. The frequency f_p of the axial perturbation that produces the largest total amplification is called the preferred mode of the jet. It corresponds to the frequency of vortices at the end of the potential core. This frequency has been determined by Crow and Champagne to be $St_p \approx 0.3$ (Crow (1971)). However, other studies have found the preferred Strouhal number to vary between 0.25 and 0.5 (Hussain (1981), Mankbadi (1985)). Mankbadi (1985) observed for a round jet under axisymmetric forcing that mixing is enhanced if the forcing Strouhal number is equal to about twice the jet's preferred mode.

Mixing can be increased significantly if axial and helical forcing are combined (Lee

& Reynolds (1985), Parekh (1987), Parekh (1996)). In the following we will denote the Strouhal numbers of axial and helical forcing with St_a and St_h . Large spreading angles (up to 80°) have been observed for certain ratios $\beta = St_a/St_h$ of the Strouhal numbers. In particular, the jet splits into two branches for $\beta = 2$ (bifurcating jet). It has been discussed by Parekh (1988) that these flow patterns appear for both low and high Reynolds numbers.

In our simulation the actuation of the shear layer was achieved by imposing periodic disturbances on the initial velocity profile. The actuation we used is a superposition of axial and helical modes

$$V_z(r_c, \phi, t) = V_{z0}(r) \left[1 + A_a \sin \left(2\pi St_a \frac{V_0}{D} t \right) + A_h \sin \left(2\pi St_h \frac{V_0}{D} t + \alpha \right) \cos(\phi) \frac{2r_c}{D} \right]. \quad (2.2)$$

Here A_a and A_h are the amplitudes of the axial and helical mode and St_a, St_h are the respective Strouhal numbers. We have chosen the helical part of the actuation to be phase locked in the plane $\phi = 0$. The angle α determines the plane of spreading. The actuation Eq. (2.2) with $\beta = 2$ has been used before to model bifurcating jets (Boersma (1998)). In the following sections we will investigate which parameter vector $\mathbf{x} = (St_a, St_h, A_a, A_h)$ maximizes the spreading of the jet.

2.2. Optimization strategies

The optimization problem is described by a vector of parameters that are varied during the procedure and an objective function that evaluates the performance of the parameters. In the following, we will call the sequence of parameter vectors that are evaluated during the optimization procedure a search trajectory. The objective function measures the spreading of the jet by performing an LES of the jet flow. The surface that describes the objective function value as a function of the parameters is referred to as the fitness landscape. The dynamic behavior of the jet is determined by the nonlinear interaction of different modes. This is likely to cause a complicated dependence of the jet development on the actuation parameters. We therefore expect the objective function to be multimodal, which suggests that stochastic procedures are the method of choice for optimization of jet mixing since they are able to avoid premature convergence to a local optimum. Our approach of optimizing jet mixing implies that for each search step an LES of the jet flow has to be performed, which is very expensive. Even when various approximations to reduce the CPU time and parallel processing of the jet code are used, the total number of jet flow calculations that can be achieved is of the order 100.

We have compared the following optimization procedures: a simulated annealing algorithm, implemented by Goffe (1994), a single-membered and a multi-membered evolution strategy with Covariance Matrix Adaption of the steplength (Hansen (1996)), implemented by Koumoutsakos *et al.* (1998) and adapted to the problem of jet optimization by Hilgers (1999).

Simulated annealing (Kirkpatrick (1983)), also known as Monte Carlo annealing, is a serial procedure which is very efficient and straightforward. It is based on the analogy between the annealing of solids, i.e. the way in which a solid cools and freezes into a crystalline structure with minimal energy, and the problem of solving large optimization problems. The algorithm, first proposed by Kirkpatrick (1983) is easy to implement and very efficient. It employs a random search which does not only accept changes that improve the objective function f , such that $\Delta f = f(\mathbf{x}_{n+1}) - f(\mathbf{x}_n) < 0$ in a minimization

problem, it also accepts an increase $\Delta f > 0$ with probability

$$p = \exp\left(-\frac{\Delta f}{T}\right). \quad (2.3)$$

Here T is the ‘system temperature’ which is high in the beginning of the annealing process and approaches zero towards its end. Eq. (2.3), known as the Metropolis criterion, determines the amount of uphill movement that is allowed. The optimization procedure consists of a sequence of ‘temperatures’ T . At each T , a random search with a fixed number of search steps (a Markov chain of certain length) is generated, where new parameter vectors are obtained by random variation. In our optimization, a step that leads to a value outside the allowed range is considered unsuccessful and is repeated until allowed values are obtained. If several repetitions of the random step fail, the parameters are defined randomly within the given limits. If no better solution has been found at the end of the chain, the start parameters of the search are kept as initial points for the search at the next T . The parameter T ensures that at the beginning of the search steps are possible that lead to a worse objective function value, which enables the trajectory to leave a local optimum. At the end of the search, when the vicinity of the global optimum is reached, the probability of accepting a worse solution is very low to ensure rapid convergence to the optimum. As the rule for decrementing the temperature, the so-called annealing schedule, we have chosen an exponential cooling scheme (Kirkpatrick (1983)). The initial temperature was set such that the average probability for accepting a worse parameter vector is about 0.7 (Kirkpatrick (1983)). The steplength is adjusted according to the successful number of trials.

Evolution strategies make use of the principles of evolution – reproduction, mutation, and selection – to find an optimal solution (Rechenberg (1971)). They are easy to implement, efficient, and inherently parallel. Examples for the application of evolution strategies to problems in fluid mechanics and first results for the optimization of jet mixing have been presented in Koumoutsakos *et al.* (2000). Evolution strategies operate on populations of individuals which represent possible solutions of the given problem. Each individual consists of a vector \mathbf{x} containing n parameters and an associated vector \mathbf{s} containing n mutation steplength. The number of parents in each generation is μ ; the number of offspring is λ , with $\lambda \geq \mu$. If $\mu > 1$, multiple trajectories are evaluated in parallel. Starting from an initial generation of μ parents, the offspring are generated by mutation

$$\mathbf{x}_o^{i+1} = \mathbf{x}_p^i + \mathbf{s}_p^i N(0, 1). \quad (2.4)$$

Here, the indices p and o denote parent and offspring and i is the number of the generation. $N(0, 1)$ is a normal distributions with zero average and unit variance.

After λ offspring have been generated, their fitness values are determined and the best μ individuals are selected. The steplengths of the mutation are decreased if the offspring are better than the parents; otherwise, they are increased. The μ best individuals, i.e. the vectors of the best parameters, and the corresponding mutation steplengths are used as parents for the next generation. The best individuals are chosen among the $\mu + \lambda$ parents and offspring ($(\mu + \lambda)$ strategy).

The μ best individuals, i.e. the vectors of the best parameters, may also inherit their associated mutation steplength. A speed-up of the procedure is achieved by the Covariance Matrix Adaption scheme by Hansen (1996). The search is terminated if either the improvement made during the search gets smaller than a certain value or if a maximum number of function evaluations is reached.

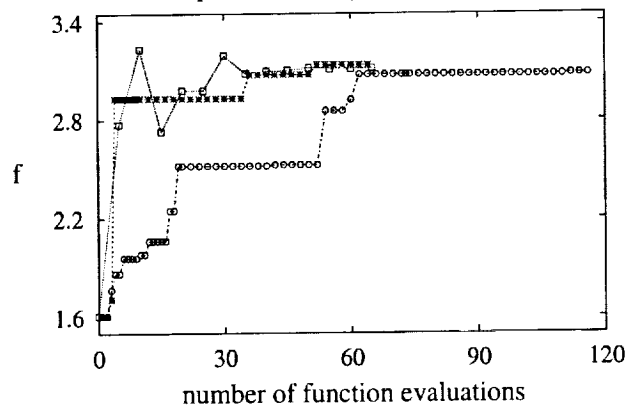


FIGURE 1. Convergence of the evolution strategies ((1+1) circles, (2+5) squares) and simulated annealing (crosses) for the parameter vector $\mathbf{x} = (St_a, St_h)$, $\mathbf{x}_0 = (0.45, 0.14)$, and $A_a = 0.025$, $A_h = 0.075$ fixed.

2.3. Jet optimization

The actuation of the jet is described by the parameter vector \mathbf{x} , which consists of two Strouhal numbers and two amplitudes $\mathbf{x} = (St_a, St_h, A_a, A_h)$. The limits of the parameters have been chosen as follows. In laboratory experiments by Parekh (1988) and numerical simulations by Freund (1999), flapping jets have been found for Strouhal numbers $St_h \in [0.2, 0.4]$, bifurcating jets for $St_a \in [0.4, 0.65]$. We have varied the Strouhal numbers in a somewhat wider range $0.2 < St_a < 1.0$ and $0.1 < St_h < 0.7$.

Large spreading corresponds to efficient mixing of a passive scalar, transported by the flow, with the surrounding air. We have therefore maximized the integral of the radial velocity (in the cylindrical system)

$$f(\mathbf{x}, t_0) = \int_V v_{r_c}^2(r, \theta, \varphi, t_0) dV' \quad (2.5)$$

where V is the computational domain. The integral of $v_{r_c}^2$ is time dependent. A suitable time t_0 must be chosen in the jet simulation for the evaluation of the objective function. Other choices for the objective function are described in Hilgers (2000).

Our computations have shown that the optimization strategy tends to choose at least one of the amplitudes to be as large as possible within the given limits. Since an actuation with very large amplitudes is not desirable, we have kept the axial amplitude constant at $A_a = 0.025$ and varied the helical amplitude $0.025 < A_h < 0.075$. In order to reduce the CPU time, we have used a coarse grid in the optimization procedure. The overall behavior of the jet, in particular at early stages of the simulation, is captured by simulations on this coarser grid. We note that under-resolved simulations can only be used for a rough estimate of the jet dynamics, but since the jet flow is controlled by large scale structures, the overall dynamic is preserved by this approximation. Details about the comparison of different grids and the choice of the time for the evaluation of the fitness function are given in Hilgers (2000).

For a simple test case, a jet at low Reynolds number $Re = 1500$, we repeated the optimization procedure with the following search algorithms: the simulated annealing algorithm, an evolution strategy using only one search path ((1 + 1) strategy), and an evolution strategy using a population of two parents and five offspring in each generation ((2 + 5) strategy), which corresponds to the simultaneous evaluation of two search paths.

In order to test and compare the different search strategies for the maximization of the objective function (2.5), we have started the optimization at different points in phase space. On average, simulated annealing and the (2, 5) evolution strategy with covariance matrix adaption of the steplength were able to find the global optimum using a comparable number of function evaluations, the number being slightly lower for simulated annealing. A typical example is shown in Fig. 1. For the (2 + 5) strategy, the resulting curve is not monotonic because the offspring are obtained by random mutation of the average parent vectors and, therefore, may have lower fitness values. For simulated annealing and the (1 + 1) ES on the other hand, the best solution is kept until it is replaced by a better one. The fact that the number of function evaluations for the (2, 5) evolution strategy is not lower than that for simulated annealing indicates that the number of search steps that can be achieved for this computationally expensive problem is too small to allow efficient use of the information gathered on the search path. We have therefore used this method mainly for the less expensive optimization at low Reynolds numbers and simulated annealing for the optimization at higher Re , which will be presented in the next section. Repeating our tests for different values of A_a and A_h , we found that the location of the extrema does not depend significantly on the amplitudes. We conclude that the shape of the fitness landscape is mainly determined by the two Strouhal numbers.

2.4. Results of the optimization

For the optimization of jets at low Reynolds number, $Re = 1500$, a pronounced global maximum was found at $(St_a, St_h) \approx (0.66, 0.31)$. In addition, local maxima were identified at $(St_a, St_h) \approx (0.9, 0.32)$ and $(St_a, St_h) \approx (1.1, 0.32)$. In fact, mixing is enhanced for a range of values of A_a when $St_h \approx 0.31$.

We will now discuss the results of the optimization of jet mixing at higher Reynolds numbers using LES. We confined the search to the space of the Strouhal numbers, assuming that they are the relevant parameters for control of jet mixing, and kept the amplitudes constant at $A_a = 0.025$ and $A_h = 0.075$. The optimization was performed with the simulated annealing algorithm, which on average needed the lowest number of objective function evaluations for the test case.

First, we compared simulations on grids with different resolution. For $Re = 6000$, we found that a grid with $160 \times 120 \times 32$ points in the radial, tangential, and azimuthal direction respectively is small enough to allow repeated calculation of the objective function while being sufficiently large to give a reliable estimate of the jet dynamics. Comparing the objective function (2.5) as a function of time for different parameter values, we have chosen the time for the evaluation of the function as $t_0 = 1.8$. The CPU time for one evaluation of the objective function was 32 node hours, as compared to 1800 node hours for the full LES on a $192 \times 128 \times 64$ grid. At $Re = 100000$, a grid with $384 \times 200 \times 96$ was used for the full LES. The LES of the optimization was done on a coarser grid with $252 \times 150 \times 64$ points. The CPU time for one evaluation of the objective function on this grid was approximately 120 node hours.

For the case $Re = 6000$, the search was started at $\mathbf{x}_0 = (St_a, St_h) = (0.66, 0.31)$. The best value was reached after 52 evaluations of the objective function at $(St_a, St_h) = (0.79, 0.36)$. Comparing the absolute fitness values, we found that the maximum value reached at this Reynolds number is approximately 1.5 times higher than that for $Re = 1500$, suggesting that the spreading of the jet is larger for the $Re = 6000$ jet. Apart from the global maximum, we found parameters with comparably high value at $\mathbf{x} = (0.90, 0.45)$ and at $\mathbf{x} = (0.58, 0.22)$. For $Re = 100000$, the search was started at $(St_a, St_h) =$

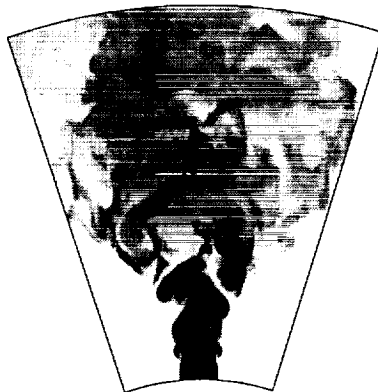


FIGURE 2. Snapshot of the scalar concentration at time $t = 8$ for a jet at $Re = 6000$, $St_a = 0.79$, $St_h = 0.36$, $A_a = 0.025$ and $A_h = 0.075$.

(0.8, 0.36). The best value was reached at $(St_a, St_h) = (0.6, 0.33)$ after 48 evaluations of the fitness function. Another high value of the objective function was reached at $\mathbf{x} = (0.74, 0.38)$.

Apparently, the structure of the fitness landscape at high Reynolds numbers is different from that found for $Re = 1500$. In particular, high fitness values do not only appear at $St_h \approx 0.33$. Since we were only able to determine a small number of points on the fitness landscape, a guess of its structure is difficult. Like in most optimization problems, there is no certainty about whether the global optimum has been reached. However, we have found a good solution within reasonable time.

2.5. Discussion of the results

For the best actuation parameters found by the evolution strategies, we have repeated the LES of the jet on a fine grid as described above. Fig. 2 shows a snapshot of the passive scalar concentration obtained for the jet at $Re = 6000$ actuated with (2.5) and the optimal Strouhal numbers $St_a = 0.79$ and $St_h = 0.36$. The figure shows the jet in the plane of the actuation, $\varphi = 0$. Different shades of grey denote different concentration C of the scalar. The concentration is approximately one in the inner (dark) region and zero far outside (white region). The jet spreads rapidly in the plane of the actuation and contracts in the orthogonal plane. Despite the small amplitudes of the actuation, the dual-frequency actuation leads to an impressive spreading of the jet, visualized by the large area to which the tracer is transported. The center of the jet shows a strong flapping motion which is due to the large amplitude of the helical forcing. The jet column is completely dispersed near the end of the computational domain.

In Fig. 3 a snapshot of the scalar concentration is plotted for a jet at $Re = 100000$ which was obtained using the best actuation $St_a = 0.60$ and $St_h = 0.33$ found for this Reynolds number. For this simulation a grid with $384 \times 200 \times 96$ points was used. The calculation was terminated at time $t = 5.5$ due to the high computational cost of the LES. Although the jet is not fully developed at this stage, a strong flapping motion of the jet column is clearly visible. Apart from the large spreading of the jet, it can be seen

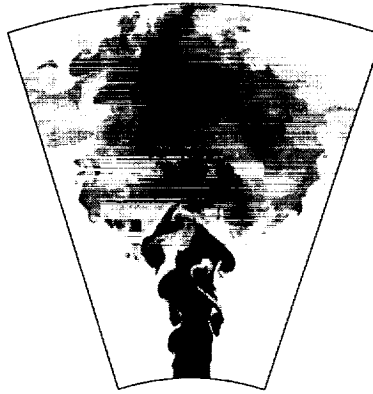


FIGURE 3. Snapshot of the scalar concentration at time $t = 8$ for a jet at $Re = 100000$, $St_a = 0.60$, $St_h = 0.33$, $A_a = 0.025$ and $A_h = 0.075$.

	St_a	St_h
$Re = 1500$	0.66	0.31
$Re = 6000$	0.79	0.36
$Re = 100000$	0.60	0.33

TABLE 1. Best actuation parameters found by the optimization strategies; $A_a = 0.025$, $A_h = 0.075$

that the jet column disintegrates soon after the initial pairing. Further downstream the scalar concentration is low, indicating good mixing in the jet.

The main results of our optimization are summarized in table 1. In all cases, the spreading of the jet is most pronounced at helical Strouhal numbers $St \approx 0.3 \dots 0.36$. It differs from the natural Strouhal number, for which linear instability analysis predicts the largest amplification of signals (Michalke (1984)), but is in agreement with the preferred frequency of the jet found by Mankbadi (1985). The optimal axial Strouhal number found by the optimization procedure is approximately twice as large as the preferred frequency, as predicted by Mankbadi (1985). The Strouhal numbers found are in very good agreement with experimental results by Lee & Reynolds (1985).

3. Summary

In this paper we have combined stochastic search programs and numerical simulation of a jet to search for actuation parameters that enhance mixing in the jet. Since jet flows are governed by the dynamics of the large eddies, we have used a coarse grid for

the LES in the optimization procedure. We have found that the spreading of the jet and hence the amount of mixing depends mainly on the actuation Strouhal numbers and that it grows with the amplitudes. The spreading is most pronounced for helical and axial Strouhal numbers $St_h \approx 0.31 \dots 0.36$ and $St_a \approx 2 \cdot St_h$, which correspond approximately to the preferred Strouhal number of the jet and twice its value. These optimal Strouhal numbers were found for all Strouhal numbers investigated here: $Re = 1500$, $Re = 6000$, and $Re = 100000$. The spreading of the jet as measured by our objective function is larger at higher Reynolds numbers.

Comparing different optimization methods, we have found that multi-membered evolution strategies and in particular simulated annealing are well suited for this problem. Due to the high computational cost of the LES at high Reynolds numbers, it is not possible to search the phase space of Strouhal numbers in a systematic way. Nevertheless, we were able to find actuation parameters that induce a pronounced spreading of the jet for Reynolds numbers as high as $Re = 100000$. In a real experiment the perturbation is not described by a simple mathematical function like in our simulation, and, therefore, a one-to-one comparison between simulation and experiment is difficult. However, we expect that the frequency range found to be best in our simulations is similar to that for experiments under comparable conditions.

4. Acknowledgments

The author is grateful to B. Boersma for providing the DNS and LES codes and for valuable discussions throught this work, and to H. Steiner for his help with the implementation of the LES model. The evolution strategies have been made available by S. Müller and P. Koumoutsakos. Support from the US Air Force Office of Scientific Research and the Boeing Company is gratefully acknowledged.

REFERENCES

- BOERSMA B. J., BRETHOUWER G., AND NIEUWSTADT F. T. M 1998 A numerical investigation on the effect of the inflow conditions on a self-similar region of a round jet. *Phys. Fluids*. **10**, 899-909 (1998).
- CROW S. C. & CHAMPAGNE F. H. 1971 Orderly structures in jet turbulence. *J. Fluid Mech.* **48**, 547-591.
- DANAILA I. & BOERSMA B. J. 1998 Mode interaction in a forced homogeneous jet at low Reynolds numbers. *Proceedings of the 1998 Summer Program*, Center for Turbulence Research, NASA Ames/Stanford Univ. 141-158.
- FREUND J. B. & MOIN P. 1998 Mixing enhancement in jet exhaust using fluidic actuators: direct numerical simulations. *ASME FEDSM98-5235*.
- FREUND J. B. & MOIN P. 1998 Jet mixing enhancement by high amplitude fluidic actuation. In preparation.
- GERMANO M., PIOMELLI U., MOIN P., & CABOT W. 1990 Dynamic subgrid-scale eddy viscosity model. *Proceedings of the 1990 Summer Program*, Center for Turbulence Research, NASA/Stanford Univ., 5-17.
- GOFFE B., FERRIER M., & ROGERS N. 1994 Global optimization of statistical functions with Simulated Annealing. *J. Econometrics*. **60**, 65-100.
- HANSEN N. & OSTERMEIER A. 1996 Adapting arbitrary normal mutation distributions

- in evolution strategies: the covariance matrix adaptation. Proceedings of the IEEE International Conference on Evolutionary Computation (ICEC'96), 312-317.
- HILGERS A. & BOERSMA B. J. 2000 Optimization of Turbulent Jet Mixing. In preparation.
- HILGERS A. 1999 Parameter optimization in jet flow control. *Annual Research Briefs*, Center for Turbulence Research, NASA Ames/Stanford Univ. 179-193.
- HO C. M. & HUERRE P. 1984 Perturbed Free Shear Layers. *Ann. Rev. Fluid Mech.* **16**, 365-424.
- HUERRE P., & MONKEWITZ P. 1990 Local and global instabilities in spatially developing flows. *Ann. Rev. Fluid Mech.* **22**, 473-537.
- HUSSAIN A. K. M. Z. & ZAMAN K. B. M. Q. 1981 The 'preferred mode' of the axisymmetric jet. *J. Fluid Mech.* **110** 39-71.
- KIRKPATRICK S., GERLATT C. D., & VECCHI M. P. 1983 Optimization by Simulated Annealing. *Science*. **220**, 671-680.
- KOUMOUTSAKOS P., FREUND J. B. AND PAREKH D. 1998 Evolution strategies for parameter optimization in jet flow control. *Proceedings of the 1998 Summer Program*, Center for Turbulence Research, NASA Ames/Stanford Univ. 121-132.
- KOUMOUTSAKOS P., MÜLLER S., HILGERS A., FREUND J. B., & PAREKH D. 2000 Evolution strategies for jet mixing optimization. *IEEE Transactions on Evolutionary Computation*.
- LEE M. & REYNOLDS W. C. 1985 Bifurcating and blooming jets. *Report No. TF-22*, Department of Mechanical Engineering, Stanford University.
- MANKBADI R. R. 1985 The mechanism of mixing enhancement and suppression in a circular jet under excitation conditions. *Phys. Fluids*. **28**, 2062-2075.
- MICHALKE A. 1984 Survey on jet instability theory. *Prog. Aerospace Sci.* **21**, 159-199.
- ORLANSKI I. 1976 A simple boundary condition for unbounded hyperbolic flows. *J. Comp. Phys.* **21**, 251-269.
- PAREKH D., LEONARD A., REYNOLDS W. C., & MUNGAL M. G. 1987 Bifurcating of round air jets by dual-mode acoustic excitation. *AIAA Paper*. 87-0164.
- PAREKH D., LEONARD A., & REYNOLDS W. C. Bifurcating jets at high Reynolds numbers. *Report Nr. TF-35* Department of Mechanical Engineering, Stanford University.
- PAREKH D., KIBENS V., GLEZER A., WILTSE J. M., & SMITH D. M. 1996 Innovative jet flow control: mixing enhancement experiments. 34th Aerospace Science Meeting, Reno, *AIAA Paper* 96-0308.
- RECHENBERG I. 1971 *Evolutionsstrategie - Optimierung technischer Systeme nach Prinzipien der biologischen Evolution*. Fromann-Holzboog, Stuttgart; Rechenberg I. 1994 *Evolutionsstrategie '94*. Fromann-Holzboog, Stuttgart.
- URBIN G, BRUN C. & MÉTAIS O. 1997 Large eddy simulation of three-dimensional spatially evolving round jets. In *11th Symposium on Turbulent Shear Flows* Grenoble.
- WILTSE J. M. & GLEZER A. 1993 Manipulation of free shear layers using piezoelectric actuators. *J. Fluid Mech.* **249** 261-283.

High-frequency excitation of a plane wake

By Alan B. Cain† AND Michael M. Rogers‡

1. Motivation and objectives

In the early 1990's, Glezer and his co-workers at Georgia Tech made a startling discovery. They found that forcing at frequencies too high to directly affect the production scales led to a dramatic alteration in the development of a turbulent shear layer. An experimental study of this phenomenon is presented in Wiltse & Glezer (1998). They used piezoelectric actuators located near the jet exit plane to force the shear layers of a square low-speed jet. The actuators were driven at a high frequency in the Kolmogorov inertial subrange, much higher than the frequencies associated with the large-scale motion (where the turbulent energy is produced and located) but much lower than those associated with the Kolmogorov scale (where the turbulent energy is dissipated). Measurements of the shear-layer turbulence showed that direct excitation of small-scale motion by high-frequency forcing led to an increase in the turbulent dissipation of more than an order of magnitude in the initial region of the shear layer! The turbulent dissipation gradually decreased with downstream distance but remained above the corresponding level for the unforced flow at all locations examined. The high-frequency forcing increased the turbulent kinetic energy in the initial region near the actuators, but the kinetic energy decreased quite rapidly with downstream distance, dropping to levels that were a small fraction of the level for the unforced case. Perhaps most importantly from the present standpoint, the high-frequency forcing significantly decreased the energy in the large-scale motion, increasingly so with downstream distance. Wiltse and Glezer interpreted this behavior as an enhanced transfer of energy from the large scales to the small scales.

The initial work by Wiltse & Glezer (1998) has expanded into other applications. To explore the potential of high-frequency forcing for active acoustic suppression, in 1998 the first author proposed a set of experiments involving an edge tone shear layer and an open cavity flow. This work was funded by the US Air Force Research Laboratory, and the experiments were developed and executed at Boeing by Raman and Kibens (Raman, Kibens, Cain & Lepicovsky 2000). These experiments involved high-frequency forcing applied to low-speed flows using wedge piezo actuators and powered resonance tubes. The system is simple, open loop, compact, potentially requires little power, and is easily integrated. Dramatic results, such as reductions of 20 dB in spectral peaks and 5-8 dB in overall levels across the entire acoustic spectrum, were obtained in some cases. Sample results are presented in Fig. 1. Following this success in low-speed flows, an international cooperative program continuing this work involved transonic experiments in a mid-size facility in the United Kingdom. Similar reductions in noise level were obtained in these transonic experiments. Discussion of this work is given in Raman *et al.* and Stanek, Raman, Kibens, & Ross (2000). Other experiments at Georgia Tech have shown significant potential of high-frequency forcing in controlling reaction rates in chemically reacting flows (Davis 2000).

† Innovative Technology Applications Company, Chesterfield, MO 63006

‡ NASA Ames Research Center, Moffett Field, CA 94035

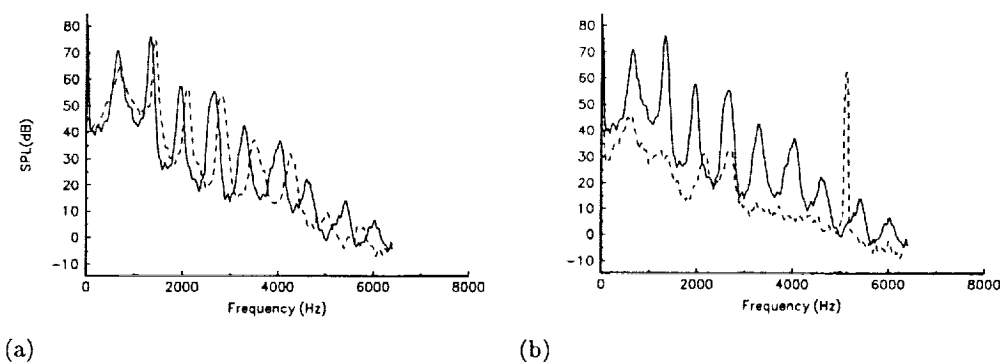


FIGURE 1. Effect of high-frequency excitation on an edgetone spectrum. Mach number $M=0.07$. Primary edgetone at 672 Hz. Excitation amplitudes (actuator displacement) (a) 0.2mm and (b) 6.0mm. — : (a) & (b) Run 23a; - - - : (a) Run 25a, (b) Run 32a. Figure taken from Raman, Kibens, Cain and Lepicovsky (2000).

This recent work at Georgia Tech and Boeing is in sharp contrast to earlier ideas on how control of free shear flows should be approached. The review by Ho & Huerre (1984) characterizes the perspectives of the 1970's and 1980's, demonstrating the link between large-scale structures and linear stability theory. Drazin & Reid (1981) identify approaches to linear stability theory that determine the scale of exponentially growing disturbances. The work by Ho & Huerre extends the earlier stability theory/large-scale structure ideas by discussing vortex pairing and the more general merging of many large-scale structures. Ho and Huerre provide convincing experimental demonstrations of flow control by excitation frequencies that produce exponentially growing disturbances according to linear stability theory. Cain & Thompson (1986) provide another example of the merits of linear stability analysis. They show that the growth rates predicted by linear theory are able to predict the evolution of finite amplitude disturbances to a saturated state as given by a full nonlinear simulation. These are a few examples of many studies that characterize the control possibilities of free shear flows using "low-frequency", stability-theory-guided frequency selections. The Georgia Tech/Boeing studies constitute a major departure from earlier work. These recent studies do not dispute the results of the earlier work, only the assumption that turbulence theory and linear stability theory preclude interesting effects in the "high-frequency" excitation regime. The new "high-frequency" regime is currently without a theoretical basis, and the present study is aimed at adding detailed quantitative insight into this phenomenon.

There is a need to understand the basic mechanism behind effective high-frequency forcing so that scaling laws can be developed to facilitate reliable large-scale system design. The Boeing experiments sometimes produce dramatic results, but other high-frequency control systems don't show the same improvement. An understanding of the physics is required to ensure reliable application of the technology.

2. Results

Here we use direct numerical simulations of free shear layers to investigate the impact of high-frequency forcing on various aspects of shear layer evolution. To ensure that

the results found are representative of what would be observed in flows of practical interest, it is necessary to have the ability to simulate realistic high-Reynolds number turbulent shear flows. For this purpose, the pseudospectral free shear layer code used by Rogers and Moser (1994) and Moser, Rogers, and Ewing (1998) has been chosen (the version of the code used to generate the simulations described here actually uses a different numerical representation of the flow variables in the inhomogeneous direction, as described in Rogers (2001)). This code is designed to simulate incompressible temporally evolving plane free shear layers. By simulating a temporally evolving flow, much higher turbulence Reynolds numbers can be achieved and cleaner boundary conditions can be implemented. Although the temporally evolving flow possesses symmetries not present in spatially developing flows, the dynamics of the large-scale structures are similar between these two flows, and the results obtained here should be relevant to spatially developing flows as well. Thus the incompressible flows simulated here should be comparable to the experimental flows of Wiltse & Glezer (1998).

The turbulent plane wake flow was selected as the first flow of investigation, with the new simulations being compared to the baseline cases presented in Moser *et al.* (1998). These previously simulated baseline cases include three different plane wake flows, an “unforced” case, a (weakly) “forced” case, and a “strongly forced” case, the two forced cases having additional energy added to the two-dimensional modes of the computation at the initiation of the wake. The “strongly forced” case does not achieve self-similarity and is, therefore, a poor choice for a baseline flow. Both the “unforced” and “forced” cases evolve self-similarly once developed and exhibit statistical properties similar to experimental wakes. The “unforced” case spreads relatively slowly compared to the “forced” case and to most experiments, and it has little large-scale organization. One of the goals of this work is to determine whether high-frequency forcing can reduce the spreading rate of a free shear layer (and perhaps the associated level of large-scale organization) and this may not be possible for a baseline flow that is already spreading at a minimal rate. For this reason, the “forced” case (termed “FWAK”) was chosen as a baseline flow for the investigation described here; although spreading at a rate typical of experimental flows, it is possible for the flow spreading rate to be reduced.

As described in Moser *et al.* (1998), the wake flows are generated by placing two different realizations from a turbulent boundary layer simulation (Spalart 1988) together as if they were forming on either side of an infinitely thin plate. At time $t = 0$ the plate is removed and the boundary layer turbulence evolves into free shear flow turbulence. For the forced case considered here, additional turbulent kinetic energy is added to all of the two-dimensional Fourier modes of the computation at $t = 0$ as well. As noted in Moser *et al.*, statistics from the forced wake case indicate self-similar evolution for non-dimensional times $\tau = tU_d^2/\bar{m}$ greater than about 65 (where U_d is the initial free-stream velocity of the turbulent boundary layers relative to “the plate” and \bar{m} is the conserved mass flux deficit of the wake). After about $\tau = 120$, the observed self-similarity begins to break down as a result of the limited computational domain size of the simulation. The Reynolds number based on the wake half velocity width and velocity deficit is about 2,000 during the self-similar period.

In order to document a sustained impact of high-frequency forcing on the wake, we hope to observe a change in the self-similar state achieved by the wake. Thus the high-frequency forcing should be applied prior to the start of the self-similar period at $\tau = 65$. On the other hand, the turbulence at $\tau = 0$ is still “boundary-layer” turbulence with significant viscous diffusion and a cusp-shaped mean velocity profile. In most experiments

Case	$ k_x b^0 $	$ k_x L_x /(2\pi)$	$ k_z b^0 $	$ k_z L_z /(2\pi)$	a_0	f	α	l/b^0
TURB1	[22.49,23.83]	[84,89]	0	0	0	20	0.0	0
TURB2	[22.49,23.83]	[84,89]	[27.85,29.99]	[26,28]	0	20	0.0	0
TURB3	[34.54,37.22]	[129,139]	[40.70,42.85]	[38,40]	1.0	250	0.5	1.64
TURB4	[34.54,37.22]	[129,139]	[0,1.07]	[0,1]	1.0	250	0.5	0.94
FTRANS	[34.54,37.22]	[129,139]	[0,1.07]	[0,1]	1.0	2500	0.5	0.94
HTRANS	[34.54,37.22]	[129,139]	[0,1.07]	[0,1]	0	25	0.5	0.94

TABLE 1. Parameters of the high-frequency forcing for each forced case. The first four columns indicate the (k_x, k_z) wavenumber range over which the forcing is applied and the last four columns characterize the y -profile of the forcing, given by $a_0 + f \exp\{-\alpha(|y-l|^2/b^0)\}$. The ‘‘TURB’’ cases are begun from the ‘‘FWAK’’ baseline case at $\tau = 12.17$. The ‘‘FTRANS’’ and ‘‘HTRANS’’ cases are begun from the ‘‘TRANS’’ case at $\tau = 12.17$ and $\tau = 89.43$, respectively.

the high-frequency forcing is applied somewhat downstream of the initiation of the free shear layer, and this choice has also been made in the computations, with the high-frequency forcing typically being applied at $\tau = \tau_f = 12.17$.

2.1. Description of cases simulated

Two classes of high-frequency forced simulations have been generated. The first consists of turbulent cases in which energy has been added to various high-frequency modes of the baseline FWAK computation at $\tau_f = 12.17$. The second consists of transitional flows in which energy has been added to high-frequency modes of a modified baseline flow, this modified flow being generated by reducing the amplitude of all the turbulent fluctuations of FWAK by a factor of ten at $\tau_f = 12.17$ (while leaving the mean profile unaltered). This modified base flow, labeled ‘‘TRANS’’ here, has thus been ‘‘relaminarized’’ to a large extent but still contains broad band three-dimensional disturbances. Flow visualization confirms that the flow is dominated by large-scale vortices that form an irregular Karman vortex street and have small-scale motions superimposed on them.

The baseline flows without high-frequency forcing are thus here referred to as FWAK and TRANS. The parameters for the cases with high-frequency forcing are listed in Table 1 and described below. Four simulations with high-frequency forcing were begun from the FWAK flow at $\tau_f = 12.17$. These cases differ in the amount of high-frequency forcing, the k_x (streamwise) and k_z (spanwise) wavenumbers into which energy has been added, and the y (cross-stream) profile of the forcing. The high-frequency forcing in the ‘‘TURB1’’ flow has been applied to two-dimensional modes ($k_z = 0$) over six streamwise wavenumbers $22.49 < |k_x b^0| < 23.83$ across the entire wake (i.e. for all y). The existing amplitudes of these Fourier modes have been increased by a factor of 20, corresponding to an initial increase in turbulent kinetic energy of 3.7%. Case ‘‘TURB2’’ uses the same multiplicative factor of 20 for the same k_x wavenumber range but for $27.85 < |k_z b^0| < 29.99$ rather than $k_z = 0$. The increase in turbulent kinetic energy for this flow is 5.0%. For the ‘‘TURB3’’ case, the forcing has been limited to narrow layers in the cross-stream (y) direction according to the profile $1 + 250 \exp\{-0.5(|y-l|^2/b^0)\}$, where l is chosen to be $1.64b^0$. This forcing is applied only for wavenumbers $34.54 < |k_x b^0| < 37.22$ and

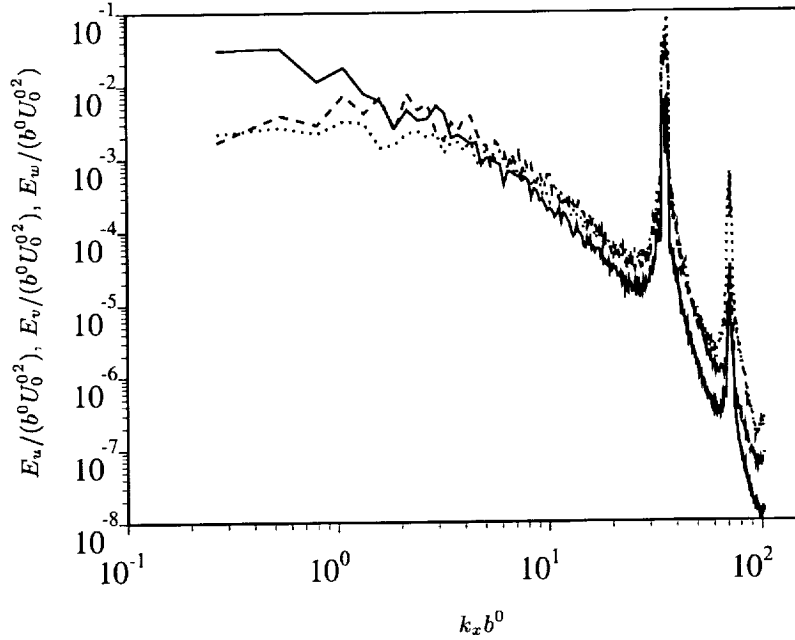


FIGURE 2. Energy spectra of the three velocity components for case TURB4 at $\tau = 12.30$, shortly after the high-frequency forcing is applied.

$40.70 < |k_z b^0| < 42.85$. The multiplicative factor of up to 251 by which the existing amplitudes have been amplified is only active over a limited range in y ; despite this large value, the overall increase in the y -integrated turbulent kinetic energy is only 0.9%. The high-frequency forcing in case “TURB4” is applied to the same k_x wavenumbers as in TURB3 but for only the lowest three k_z wavenumbers of the computation, 0 and $\pm 1.07/b^0$. The forcing has also been applied closer to the layer centerline, with $l = 0.94b^0$. The initial increase in y -integrated turbulent kinetic energy is substantially larger for this case, being 49%.

Two other simulations with high-frequency forcing were run from the TRANS baseline case. In both, the high-frequency forcing was applied to the same k_x and k_z wavenumbers as in the TURB4 flow. In the “FTRANS” flow, the high-frequency forcing was applied at $\tau_f = 12.17$ in narrow layers located at $l = 0.94b^0$. The y -profile of the forcing is as given above except that the multiplicative factor has been increased to 2500 from 250. The “HTRANS” flow is the result of high-frequency forcing applied at a later time, $\tau_h = 89.43$, when the flow is more developed. At this point in the transition, the y -integrated production of turbulent kinetic energy is near its maximum. The forcing profile is given by $25 \exp\{-0.5(|y| - l)^2/b^2\}$, with l again equal to $0.94b^0$. The multiplicative factor is reduced because the growing disturbances at the later time τ_h are larger in amplitude. The increase in the initial y -integrated turbulent kinetic energy caused by the forcing was 4784% and 35% for the FTRANS and HTRANS cases, respectively.

In order to verify that the forcing used in the computations is qualitatively similar to that found in the experiments, energy spectra from the forced flows have been examined. The streamwise k_x wavenumber spectra for $\overline{u'^2}$, $\overline{v'^2}$, and $\overline{w'^2}$ at $\tau = 12.30$ (shortly after the forcing has been initiated) in the TURB4 flow are shown in Fig. 2. The spectra are similar to those observed by Wiltse & Glezer (1998), with the energy associated with the

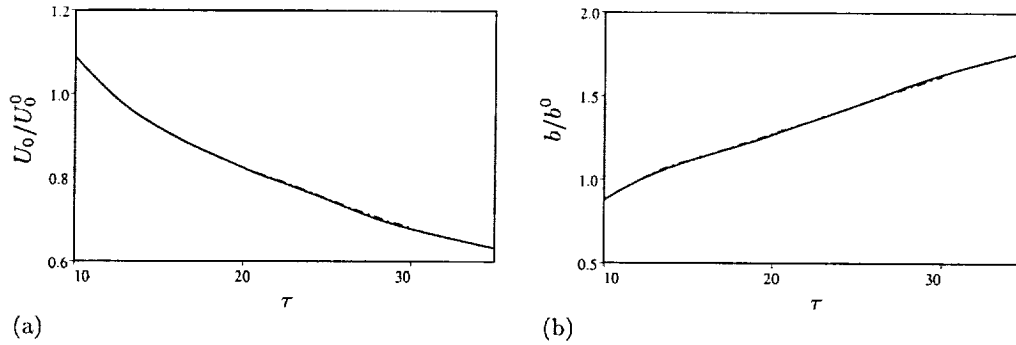


FIGURE 3. Time evolution of (a) the wake peak mean velocity deficit U_0 and (b) the wake width b . — FWAK, - - - TURB1, TURB2, - · - · - TURB3, and — — — TURB4.

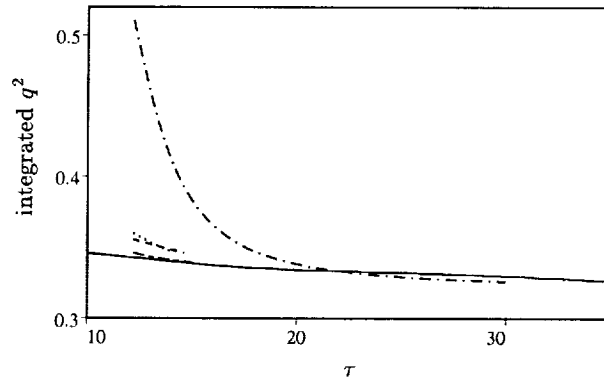


FIGURE 4. Time evolution of the cross-stream integrated turbulent kinetic energy. — FWAK, - - - TURB1, TURB2, - · - · - TURB3, and — — — TURB4.

forcing being at about the same relative wavenumber, of similar relative width, and of similar amplitude compared to the energetic large scales of the turbulence.

2.2. Forcing of a fully turbulent wake

In this section the impact of high-frequency forcing on a fully turbulent plane wake is investigated. The figures presented here contain results from the four “TURB” simulations as well as for the unforced baseline case “FWAK”. As noted above, the forcing is applied at $\tau_f = 12.17$. The forced runs are terminated at $\tau \approx 15$ for TURB1, TURB2, and TURB3, and at $\tau = 30$ for TURB4.

The evolution of the scale parameters describing the wake mean velocity profile, the magnitude of the peak mean velocity deficit U_0 , and the full width of the wake at the half-deficit points b are shown in Fig. 3. These parameters have been non-dimensionalized by their values at $\tau = 12.17$, denoted by U_0^0 and b^0 . The mean profile evolution for all four forced flows is virtually identical to the baseline case, with only barely perceptible differences in U_0 and b .

The evolution of the turbulence is impacted to a greater degree than the mean velocity profile. The evolution of twice the cross-stream (y) integrated turbulent kinetic energy is shown in Fig. 4. Relatively little turbulent kinetic energy has been added to the TURB1, TURB2, and TURB3 cases by the forcing, and what has been added starts decaying fairly rapidly. In contrast, the integrated kinetic energy has been greatly (by 49%) augmented

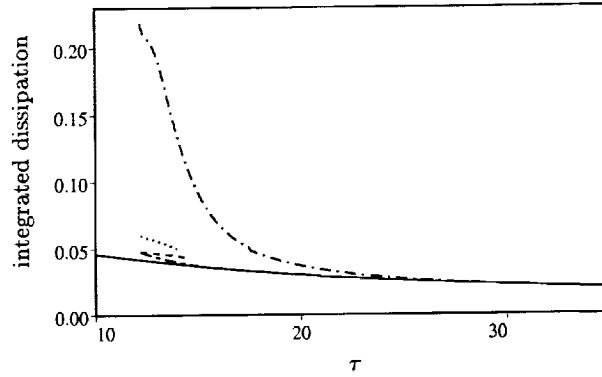


FIGURE 5. Time evolution of the cross-stream integrated turbulent kinetic energy dissipation. — FWAK, --- TURB1, TURB2, -.- TURB3, and - - - TURB4.

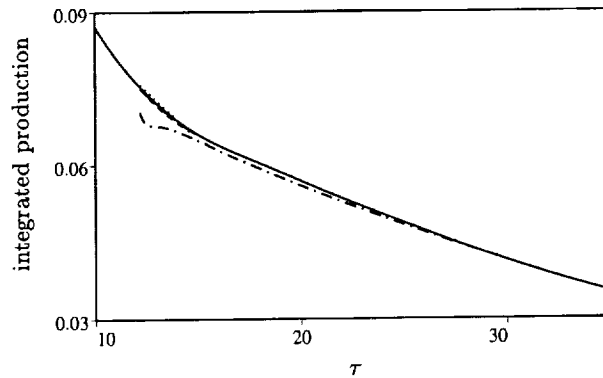


FIGURE 6. Time evolution of the cross-stream integrated turbulent kinetic energy production. — FWAK, --- TURB1, TURB2, -.- TURB3, and - - - TURB4.

by the forcing in TURB4. In this case too, however, the energy decays rapidly, assuming a value slightly (1.2%) below that of the baseline unforced case by $\tau = 30$. Although this reduction in turbulent kinetic energy once the flow is developed is qualitatively similar to the experimental observations of Wiltse & Glezer (1998), the magnitude of the effect is much weaker.

The impact of the forcing on the turbulent kinetic energy dissipation rate is even more pronounced, as expected since the dissipation is associated with strong velocity gradients at small scales. The evolution of the cross-stream integrated turbulent kinetic energy dissipation rate is shown in Fig. 5. The relative increase in dissipation rate is thus higher than that of the kinetic energy, reaching 425% initially at τ_f for case TURB4. This increase also decays rapidly, with the TURB4 dissipation level at $\tau = 30$ being indistinguishable from the baseline case, indicating that the high-frequency forcing has not resulted in a sustained increase in dissipation level.

The impact of the forcing on the production of turbulent kinetic energy is much less pronounced, as expected since production is not strongly impacted by the small-scale motions. The evolution of the cross-stream integrated turbulent kinetic energy production rate is shown in Fig. 6. The TURB1, TURB2, and TURB3 flows depart only negligibly from the baseline case. The high-frequency forcing results in a 6.7% reduction in the

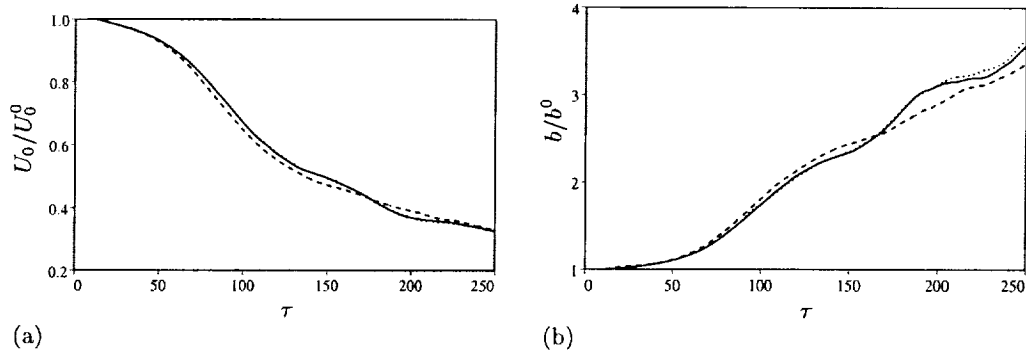


FIGURE 7. Time evolution of (a) the wake peak mean velocity deficit U_0 and (b) the wake width b . — TRANS, ---- FTRANS, and HTRANS.

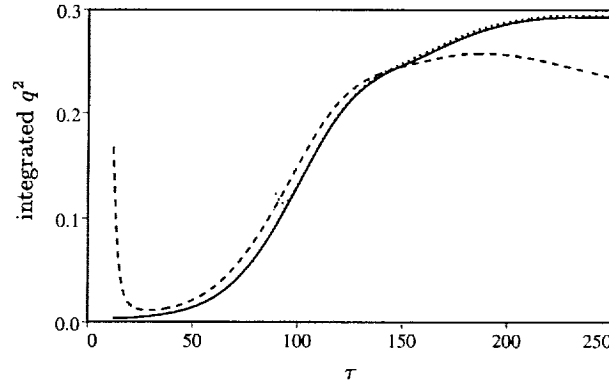


FIGURE 8. Time evolution of the cross-stream integrated turbulent kinetic energy. — TRANS, ---- FTRANS, and HTRANS.

production for case TURB4, but after initially further decreasing relative to the baseline case, the evolution becomes identical to that of FWAK by $\tau = 30$.

2.3. Forcing of a transitional wake

The effects of high-frequency forcing in the simulations of fully turbulent wakes die out quickly and have no lasting impact. In order to determine whether transitional wakes are more sensitive to high-frequency forcing, three additional simulations were made as outlined in section 2.1.

The impact of the high-frequency forcing when applied early in the transition process (FTRANS) is more significant than when applied later (HTRANS) or when applied to the fully turbulent wake examined in section 2.2. Additionally, it appears that some of the effects may be sustained, persisting even once the wake is developed.

The time evolutions of the peak mean velocity deficit and the wake width are shown in Fig. 7. The evolution of both quantities in the HTRANS flow is very similar to the corresponding evolution in the unforced TRANS case, while the behavior in the FTRANS case is somewhat different. In FTRANS the wake spreads more uniformly in time and ultimately is not as wide as in the TRANS case at the same time.

Similarly, the evolution of the y -integrated turbulent kinetic energy shown in Fig. 8 shows little difference between the HTRANS and TRANS cases, but forcing early in the transition, as in FTRANS, results in sustained lower levels of turbulent kinetic energy

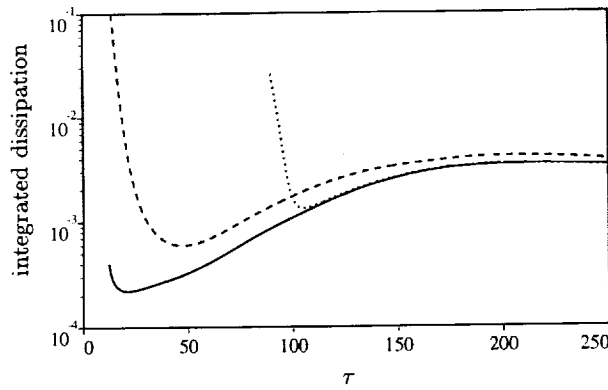


FIGURE 9. Time evolution of the cross-stream integrated turbulent kinetic energy dissipation. — TRANS, ---- FTRANS, and HTRANS.

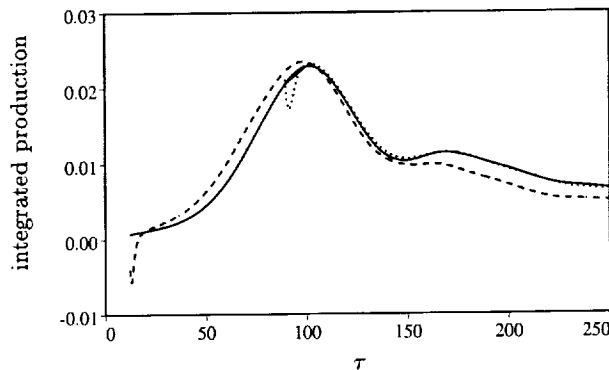


FIGURE 10. Time evolution of the cross-stream integrated turbulent kinetic energy production. — TRANS, ---- FTRANS, and HTRANS.

after $\tau \approx 150$. At $\tau = 250$ this reduction (FTRANS relative to TRANS) is 20.0%, whereas the reduction in wake width noted above is only 5.6%. The average turbulent kinetic energy density in the wake is thus reduced by 15%.

The sustained reduced turbulent kinetic energy levels in FTRANS are accompanied by sustained increased levels of turbulent kinetic energy dissipation. As seen in Fig. 9, the initial large increase in turbulent kinetic energy associated with the high-frequency forcing decays quickly, but in FTRANS there is still a 13% increase relative to TRANS at $\tau = 250$. In contrast, the differences between HTRANS and TRANS is virtually undetectable for $\tau > \tau_h + 20$.

Reductions in turbulent kinetic energy come about not only as a result of sustained increased dissipation levels, but also because of sustained decreased production levels. The time evolution of the y -integrated production of turbulent kinetic energy is shown in Fig. 10. In both FTRANS and HTRANS the high-frequency forcing results in a short term (for $\Delta\tau \approx 5$ to 7) reduction in production. In FTRANS the integrated production actually becomes negative; in HTRANS it is reduced by about 18%. As before, the evolution in HTRANS quickly relaxes to the unforced behavior, whereas FTRANS maintains a sustained reduction of 24% at $\tau = 250$. For $\tau < 100$ the main effect of the high-frequency forcing in FTRANS is to shift the integrated production and dissipation curves about $\Delta\tau = 6$ to earlier times. It is thus possible that the primary effect of the forcing is to

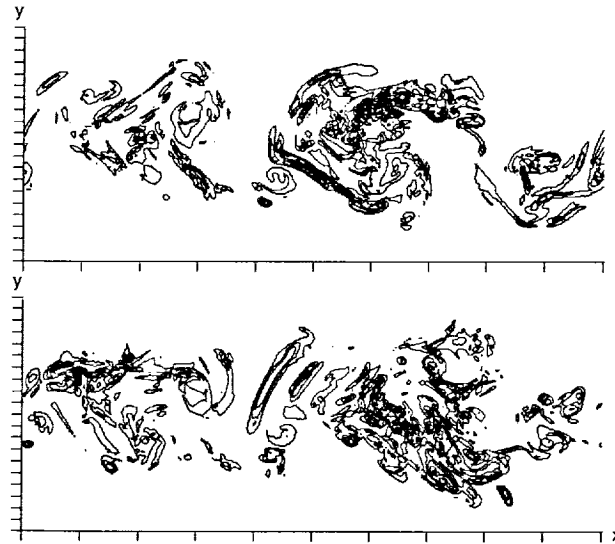


FIGURE 11. Contours of vorticity magnitude in the $z = 0$ plane at $\tau = 200$ for (top) TRANS and (bottom) FTRANS. Contour increment is U_0^0/b^0 .

initiate an earlier transition, which in turn results in a narrower wake with reduced levels of turbulent kinetic energy.

Given the reduced wake width and turbulent kinetic energy density in the FTRANS flow, it is of interest to examine the structure of the flow to determine what, if any, structural changes are associated with the changes in wake statistics. Early in the flow evolution the differences between the FTRANS and TRANS flows are minimal. Once the flow is developed, however, detectable differences are evident. Contours of vorticity magnitude are shown in Fig. 11 for both flows at $\tau = 200$. The forced flow FTRANS is less organized, with smaller, less coherent intrusions of irrotational flow into the layer from both freestreams. These differences are the same as those observed in Moser *et al.* (1998) for wakes of differing self-similar spreading rates that arise from large scale two-dimensional forcing. Also evident in the figure is the limited statistical sample of large-scale eddies (about 2.5) in the computational domain at $\tau = 200$, suggesting the need for some caution when drawing conclusions from these late-time results.

3. Conclusions and future work

In conclusion, simulations of fully turbulent wakes suggest that high-frequency forcing has a minimal impact on the evolution of this developed flow after a brief transient. On the other hand, transitional wakes appear to be more sensitive to high-amplitude, high-frequency forcing. Such forcing must be applied while the disturbance amplitudes are still small compared to their amplitudes in fully turbulent flow. In this case, the simulations suggest that sustained reductions in wake spreading and turbulent kinetic energy density may be possible. In particular, reductions in y -integrated turbulent kinetic energy of up to 20% were observed in the simulations, resulting from both increases in the dissipation-rate of turbulent kinetic energy and decreases in the turbulent kinetic energy production rate. Longer simulations might show even more significant effects but a much costlier, larger domain calculation would be required to confirm this.

The first author wishes to acknowledge the support of the Center for Turbulence Research during the initial and middle phases of this study and the support of the Air Force Office of Scientific Research (Dr. S. Walker, Program Manager) during the latter phase of this work. This work also benefited from discussions with Dr. V. Kibens, Dr. G. Raman, and Prof. A. Glezer regarding the related experimental work as well as from conversations with Prof. W. C. Reynolds.

REFERENCES

- CAIN, A. B. & THOMPSON, M. W. 1986 Linear and Weakly Nonlinear Aspects of Free Shear Layer Instability, Roll-Up, Subharmonic Interaction and Wall Influence. AIAA-86-1047, May, 1986.
- DAVIS, S. A. 2000 The manipulation of large and small flow structures in single and coaxial jets using synthetic jet actuators. *Ph.D. thesis*, Georgia Institute of Technology, May 2000.
- DRAZIN P.G. & REID, W.H. 1981 Hydrodynamic Stability. Cambridge University Press.
- HO, C. M., & HUERRE, P. 1984 Perturbed Free Shear layers. *Ann. Rev. Fluid Mech.* **16**, 365.
- MOSER, R. D., ROGERS, M. M. & EWING, D. W. 1998 Self-similarity of time-evolving plane wakes. *J. Fluid Mech.* **367**, 255-289.
- RAMAN, G., KIBENS, V., CAIN, A. & LEPICOVSKY, J. 2000 Advanced actuator concepts for active aeroacoustic control. AIAA 2000-1930, 6th AIAA/CEAS Aeroacoustics Conference, June 2000, Lahaina, Hawaii.
- ROGERS, M. M. & MOSER, R. D. 1994 Direct simulation of a self-similar turbulent mixing layer. *Phys. Fluids.* **6**, 903-923.
- ROGERS, M. M. 2001 The evolution of strained turbulent plane wakes. To appear in *J. Fluid Mech.*
- SPALART, P. R. 1988 Direct simulation of a turbulent boundary layer up to $Re_\theta = 1410$. *J. Fluid Mech.* **187**, 61-98.
- STANEK, M., RAMAN, G., KIBENS, V. AND ROSS, J. 2000 Cavity tone suppression using high frequency excitation. AIAA 2000-1905, 6th AIAA/CEAS Aeroacoustics Conference, June 2000, Lahaina, Hawaii.
- WILTSE, J.M. & GLEZER, A. 1998 Direct excitation of small-scale motions in free shear flows. *Phys. Fluids.* **10**, 2026-2036.

Low-dimensional dynamics of near-wall turbulence

By Javier Jiménez[†] AND Mark Simens[‡]

1. Introduction

Wall-bounded turbulent shear flows are perhaps the last area in ‘classical’ incompressible turbulence in which there still are open questions about basic physical mechanisms. There are two competing conceptual models. In the first one, wall turbulence is just a modification of ordinary shear turbulence occurring when the latter is a near wall, and is therefore dependent on the prior existence of an outside turbulent flow. In the second, it is an essentially different phenomenon which coexists with the outer flow and merges into it when the distance from the wall is large enough.

Jiménez (1999) took the latter view and argued that the dynamics of near-wall turbulence is essentially different from the Kolmogorov (1941) mechanism. While the latter is fundamentally isotropic and the energy is dissipated locally by cascading to smaller length scales, wall-bounded flows are intrinsically inhomogeneous and anisotropic, and a substantial part of their energy diffuses from the wall into the outer flow, increasing, rather than decreasing, its length scales in the process.

In this paper we examine the dynamics of the structures of the viscous and buffer layers in very simplified situations in which their interaction with the outer flow is severely restricted. Even natural flows scale in this region approximately in wall units, defined in terms of the kinematic viscosity ν and of the friction velocity $u_\tau = (\nu \partial_y U)^{1/2}$, where U is the mean velocity profile. In that approximation, and if we admit that near-wall turbulence is not a just a modification by the wall of the outside turbulent flow, only local quantities such as dimensionless distance to the wall, $y^+ = u_\tau y / \nu$, should matter, while global parameters such as the Reynolds number of the flow should be irrelevant.

In the reduced systems considered here, the outer flow is effectively removed, and the scaling in wall variables should be strict. No bulk Reynolds number may be relevant because no bulk turbulent flow exists. Since the local wall-normal Reynolds numbers are low, we may expect quasi-laminar structures whose behavior can be understood deterministically. In this sense this region corresponds to the Kolmogorov viscous range of isotropic turbulence, but we will see that, while the latter is a sink for the energy cascading from the larger scales, the structures studied here are not only self-sustaining, but actually export energy to the rest of the flow.

The organization of this paper is as follows. The energy balance is briefly examined in the next section. The wall region and the numerical experiments undertaken to isolated it are described next. The results are then discussed, with emphasis on the low-dimensional behavior of the structures in the simplified flows and on how they evolve into a fully turbulent flow once the constraints are removed.

[†] Also at U. Politécnica de Madrid

[‡] U. Politécnica de Madrid and U. Twente

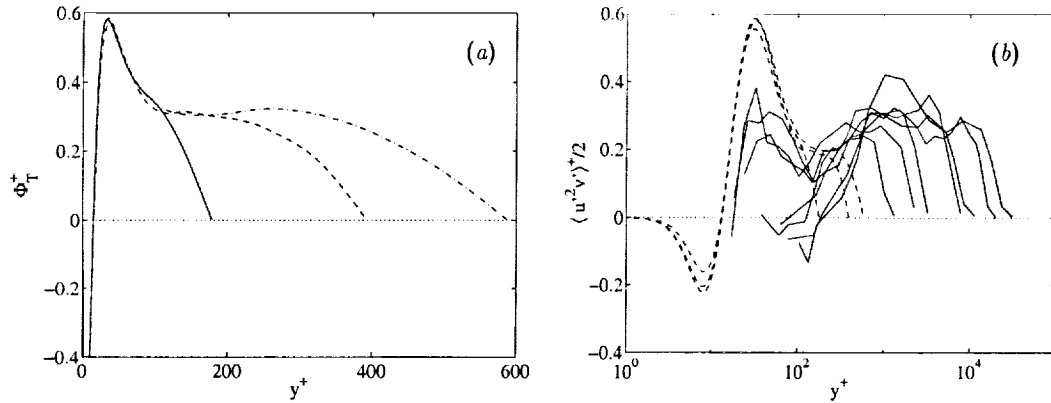


FIGURE 1. Spatial flux of turbulent energy in wall bounded flows, normalized by u_τ^3 . (a) Total flux computed from integrating Eq. (2.1) in numerical plane channels. —, $Re_\tau = 180$, from Kim, Moin & Moser (1987); ----, $Re_\tau = 395$; - · - ·, $Re_\tau = 590$, from Moser, Kim & Mansour (1999). (b) Flux of streamwise turbulent fluctuations. The dashed lines are the three channels in (a). The solid ones are boundary layers from Fernholz & Finley (1996). $Re_\tau \approx 1, 200 - 3 \times 10^4$.

2. The balance of turbulent energy

One of the reasons suggesting that the near-wall region is quasi-autonomous, independent of the outer flow, is the behavior of the kinetic energy fluxes as a function of the distance y to the wall. Consider a streamwise-homogeneous flow, such as a turbulent pipe, and separate the velocity into its mean value and fluctuations. We can write the evolution equation for the mean turbulent kinetic energy, $K = \langle u'^2 + v'^2 + w'^2 \rangle / 2$,

$$\partial_y \Phi_T = -\langle u'v' \rangle \partial_y U - \varepsilon + \nu \partial_{yy} K. \quad (2.1)$$

where u' , v' , and w' are the streamwise, wall-normal, and spanwise velocity fluctuations, and $\langle \rangle$ stands for averaging over time and over the two homogeneous coordinates parallel to the wall. The first term in the right-hand side is the production of turbulent energy by the interaction between the mean shear and the Reynolds stresses; the last one is the large-scale viscous diffusion of the kinetic energy, which can be neglected everywhere except in the viscous sublayer, and ε is the dissipation by the small scales $\nu \langle |\nabla \mathbf{u}|^2 \rangle$. The balance of these three terms is compensated in the left-hand side by the divergence of the spatial energy flux

$$\Phi_T = \frac{1}{2} \langle v'(u'^2 + v'^2 + w'^2) \rangle + \langle v'p' \rangle, \quad (2.2)$$

where p' are the pressure fluctuations.

It is generally agreed that production and dissipation are approximately in balance across the logarithmic layer (Townsend 1976), implying that the energy flux Φ_T should be approximately constant in that region. This is seen to be roughly true in Fig. 1(a), which contains data from three numerical channels at moderate Reynolds numbers. The flux is roughly constant and positive in an intermediate region, showing that energy flows away from the wall. Its positive slope near the wall, on the other hand, implies a local excess of energy production. Part of that extra energy diffuses into the wall, but the rest flows through the logarithmic layer into the outer flow where dissipation is dominant. In this sense, the wall provides the power needed to maintain turbulence in the outer region.

It is, unfortunately, difficult to measure all the terms of the energy equation in experimental flows, and there are no data equivalent to those in Fig. 1(a) for higher Reynolds numbers. Some parts of Φ_T have, however, been measured and can be used to check how representative are the numerical results. This is done in Fig. 1(b), which shows the triple product $\langle u'^2 v' \rangle / 2$, which is the main contribution to (2.2). The figure includes the numerical channels of Fig. 1(a) and experimental boundary layers at much higher Reynolds numbers. Notwithstanding the uncertainties in the experimental data, especially near the wall where the probe lengths are comparable to the wall distance, both sets of measurements coincide where they overlap, giving some confidence on the interpretation of the numerics.

The picture suggested is that there is an energy-producing region near the wall ($y^+ < 50$) which exports some of its turbulent energy across the logarithmic region into the outer flow.

Both the spatial and the Kolmogorov cascades are present in wall flows. It is difficult to compare their magnitude since Φ_T , which is an energy flux per unit area, has different units from ε , which is an energy flux per unit volume. We can, however, form a length from the two quantities, $\lambda_T = \Phi_T / \varepsilon$, which is the thickness of the layer over which the Kolmogorov cascade would be able to process all the energy provided by the spatial flux. It follows from Fig. 1(a), and from the logarithmic-layer estimate $\varepsilon \approx u_\tau^2 \partial_y U = u_\tau^3 / \kappa y$, where $\kappa \approx 0.4$ is the Kármán constant, that $\lambda_T \approx 0.15y$. The turbulent energy being exported across a plane parallel to the wall in the logarithmic region is equivalent to the dissipation in the top 15% of the layer bounded by the plane and the wall.

3. The near-wall region

Because of this influence on the global energy balance of the flow and, consequently, on the magnitude of the wall drag, the region below $y^+ \approx 100$ has been the subject of intensive study.

Its dominant structures are streamwise velocity streaks and quasi-streamwise vortices. The former are an irregular array of long ($x^+ \approx 1000$) sinuous alternating streamwise jets superimposed on the mean shear, with an average spanwise separation shown by Smith & Metzler (1983) to be $z^+ \approx 100$. At the spanwise locations where the jets point forward, the wall shear is higher than the average, while the opposite is true for the 'low velocity' streaks where the jets point backwards. The quasi-streamwise vortices are slightly tilted away from the wall, and each one stays in the near-wall region only for $x^+ \approx 200$ (Jeong *et al.*, 1997). Several vortices are associated with each streak, with a longitudinal spacing of the order of $x^+ \approx 400$ (Jiménez & Moin, 1991), and most of them merge into disorganized vorticity after leaving the immediate wall neighborhood (Robinson, 1991).

It was proposed by Kim, Kline & Reynolds (1971) that streaks and vortices are part of a cycle in which the vortices are the results of an instability of the streaks, while the vortices cause the streaks by advecting the mean velocity gradient (Swearingen & Blackwelder, 1987). While there is general agreement on the latter part of the cycle, the mechanism by which the vortices are generated is less clear. It was shown by Jiménez & Pinelli (1999) that disturbing the streaks inhibits the formation of the vortices, resulting in the eventual decay of the turbulence, and that the region in which the disturbances are effective is restricted to between $y^+ \approx 10$ and $y^+ \approx 60$. That paper contains a more

complete summary of the different models for the near-wall region in natural turbulent flows and should be consulted for additional references.

A slightly different point of view is that the cycle is organized around a nonlinear traveling wave, a fixed point in phase space, which would represent a permanently disturbed streak. This is actually not too different from the previous instability model, which essentially assumes that the undisturbed streak is a fixed point, and that the cycle is an approximation to a homoclinic orbit running through it. Candidate nonlinear waves have been computed by Waleffe (1998) and others, and identified as part of a particular path to turbulent transition by Toh & Itano (1999). Finally, reduced models based on this approach have been formulated by Waleffe (1997).

A difficulty with most of these studies, with the possible exception of the one by Toh & Itano (1999), is that there is no clear connection between the object being studied and full-scale turbulence. What we intend in this paper is to show that a turbulent flow can be continuously modified into one of those reduced objects while still remaining identifiably turbulent.

A way of doing this was proposed by Jiménez & Moin (1991), who substituted a full turbulent channel by an array of identical computational boxes, periodic in the streamwise and spanwise directions x and z , while retaining its full wall-normal extent. The idea was to substitute the complexity of all the mutually interacting turbulent units near the wall by a ‘crystal’ of identical structures executing synchronously the hypothetical turbulence regeneration cycle. The ‘unit cell’ of the crystal was adjusted to the smallest dimension that would maintain turbulence, which turned out to contain a single wavelength of a wavy low-velocity streak and a pair of quasi-streamwise vortices. These structures went through a complex cycle which was still difficult to analyze, while the statistics of the near-wall fluctuations were essentially identical to those of fully developed channels. This ‘minimal’ system has often been used as a surrogate for real wall turbulence, and most of the reduced models mentioned above actually refer to it.

The previous experiment eliminates the possibility that wall turbulence requires the interaction between neighboring wall structures, but says nothing about the importance of its interaction with the core flow. A step in clarifying that question was taken by Jiménez & Pinelli (1999), who eliminated the vorticity fluctuation in the outer flow of a numerical channel by using a numerical filter which acts as a variable viscosity which is low near the wall and increases away from it. They were able to show that the wall cycle was ‘autonomous’ in the sense that it could run independently of the outer flow as long as it was not disturbed below $y^+ \approx 60$. Again the statistics were similar, although no longer identical, to those of full turbulence.

In this paper we describe the results of simulations which are both ‘minimal’, in the sense that their wall-parallel size is small enough to contain a single copy of each structure, and autonomous in the sense that they have no turbulent external flow.

4. The numerical experiments

The numerical scheme used for the simulations is similar to the one described by Jiménez & Pinelli (1999). The Navier-Stokes equations are integrated in the form of evolution equations for the wall-normal vorticity ω_y and for $\phi = \nabla^2 v$, using a pseudospectral code with Fourier expansions in the two wall-parallel directions and Chebychev polynomials in y , as in Kim, Moin & Moser (1987). At each time step the right-hand sides of

the two evolution equations are multiplied by a damping filter

$$F(y) = 1 \quad \text{if } y \leq \delta_1, \quad F(y) = F_0 < 1 \quad \text{if } y \geq \delta_2, \quad (4.1)$$

with the two limits connected smoothly by a cubic spline. In all of our experiments $\delta_2 \approx 1.5 \delta_1$. Because the filter is applied at every time step, it is very effective in damping the vorticity fluctuations, and it was shown by Jiménez & Pinelli (1999) that the complete suppression of the fluctuations only requires that $1 - F \gg \Delta t^+$, where Δt is the computational time step. In practice we use $F_0 = 0.95$, and the damping is effective approximately midway between δ_1 and δ_2 . The evolution equations for the $(0, 0)$ Fourier modes of u and w , which cannot be expressed in terms of ω_y and ϕ , are not modified by the filter.

The flow is integrated at constant mass flux in a channel, periodic in x and z . No-slip impermeable boundary conditions are imposed at $y = 0$ and $y = 2$. The volumetric flux is adjusted so that the Reynolds number of an undamped turbulent channel would have been $Re_\tau \approx 200$. Because there are no Reynolds stresses in the region in which the filter is active, the mean velocity profile is there parabolic (see Fig. 2a), sequestering much of the total mass flux, and the final Reynolds number is usually closer to $Re_\tau \approx 120$. As previously mentioned, however, such Reynolds numbers are irrelevant because no turbulent flow extends to the far wall. The relevant turbulent Reynolds number is the height of the damping function $\delta_1^+ = u_\tau \delta_1 / \nu$, which determines the size of the largest turbulent scales.

It was stated by Jiménez & Pinelli (1999) that the damping function was approximately equivalent to a viscosity proportional to the velocity instead of to its Laplacian. This is only partly correct. While the effect of (4.1) is equivalent to a zeroth-order viscosity for the two evolution variables, the velocities are obtained from them using the definition of the vorticity and the continuity equation, and potential velocity fluctuations penetrate into the damped region. Even the vorticity fluctuations are not completely suppressed since only ω_y is directly damped while the other two vorticity components have to satisfy the solenoidality condition (i.e. the vortex lines have to close).

The flow below $y = \delta_1$ satisfies the unmodified Navier-Stokes equations. It was shown by Jiménez & Pinelli (1999) that the mean velocity and the fluctuations in that layer were very similar to those in regular channels even when $\delta_1^+ \approx 50$. Those results were obtained in a computational box whose length and width were much larger than the filter height and which was essentially turbulent. We will present here results for much smaller boxes, some of which contain very ordered flows in which there are no temporal chaotic fluctuations to smear the effect of the individual structures and whose mean profiles, therefore, differ substantially from those of natural turbulent channels. Some examples are given in Fig. 2.

The three boxes used for that figure contain respectively a fixed point in phase space, corresponding to a permanent traveling wave, a two-frequency torus, and a mildly chaotic flow. All of them are too short to sustain a strongly chaotic flow that could be interpreted as turbulence, and although they are wider than the mean distance between streaks in natural turbulence, each of them is shown by direct visualization to contain a single low-velocity streak (see Fig. 6 below).

The mean velocity profiles show a plateau which can be interpreted as an abortive logarithmic layer, although in this case the velocity decreases slightly before joining the parabolic profile of the irrotational region. The local maxima present in the vorticity profiles below the filter height are real, and correspond to individual features which,

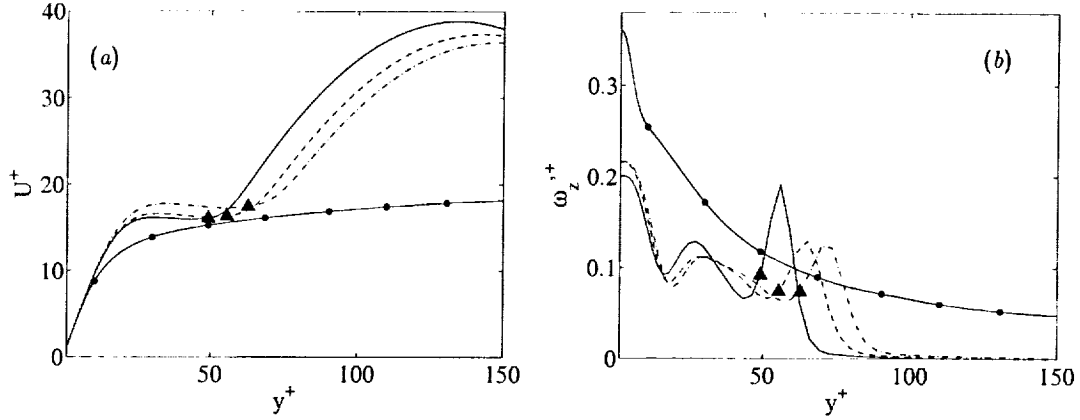


FIGURE 2. Mean profiles for three autonomous computational boxes. —, $L_x = 145$, $L_z = 180$, $\delta_1^+ = 49$, $\delta_2^+ = 71$; ----, $L_x = 150$, $L_z = 185$, $\delta_1^+ = 55$, $\delta_2^+ = 86$; - · - ·, $L_x = 155$, $L_z = 190$, $\delta_1^+ = 63$, $\delta_2^+ = 94$. The line with symbols is the full channel from Kim, Moin & Moser (1987), included for comparison. The solid triangle in each profile marks the lower limit of the damping function (4.1). (a) Mean velocity. (b) Fluctuation intensity of the spanwise vorticity.

in these relatively ordered flows, stay at a constant distance from the wall instead of wandering chaotically as in natural turbulence, but the strong peaks located just above δ_1 are artifacts of the damping filter. They mark the reconnection or the vortex lines after they are truncated by the damping, as described above.

Two types of numerical boxes were studied, both of which had widths $L_z^+ \approx 180$ when the filter height was set near its minimal value of $\delta_1^+ \approx 50$. The longer ones, which contain two streamwise copies of the basic structure, have $L_x^+ \approx 300$ and were run using $42 \times 97 \times 31$ spectral modes in the streamwise, wall-normal, and spanwise directions after dealiasing. The shorter boxes, which are only half as long in the streamwise direction, were run using 20 streamwise modes. The resolution, $\Delta x^+ \approx 7$, $\Delta z^+ \approx 6$, with the first collocation point at $y^+ \approx 0.07$, is therefore excellent.

As the filter height is raised, the effective Re_τ increases to values closer to 180, and the grid spacing increases by about 50% in wall units. The resolution of those simulations, which are essentially full minimal channels, is therefore correspondingly worse but still adequate.

5. Results

In a first series of numerical experiments, the vertical filter was set to $\delta_1^+ \approx 50$, and the wall-parallel box size was changed. The simulations were then run until they achieved statistically steady state. Each simulation was initialized from a statistically converged instantaneous field from another box of roughly similar dimensions. The transition from long to short boxes was made by zeroing all of the odd streamwise Fourier coefficients of one of the former, thus essentially averaging the two wavelengths contained in it. Because the basin of attraction of nontrivial solution in some of the tighter boxes is fairly small, this initialization procedure was essential for their survival.

The boxes discussed here are those which turn out to be small enough to contain recognizable simple flow structures and a single low-velocity streak in the spanwise direction. For two selected box lengths, the height of the filter was varied systematically. As the

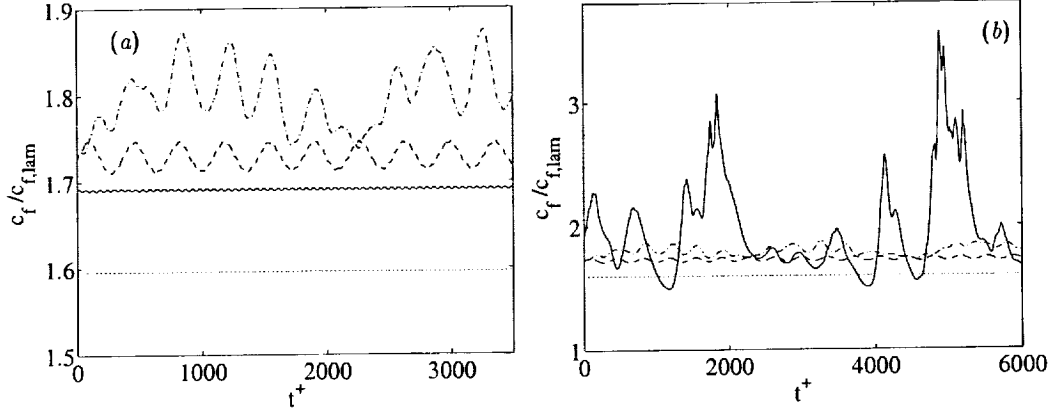


FIGURE 3. Time evolution of the instantaneous friction coefficient. (a) \cdots , $L_x^+ = 145$, $\delta_1^+ = 49$; --- , $L_x^+ = 150$, $\delta_1^+ = 52$; --- , $L_x^+ = 152$, $\delta_1^+ = 55$; --- , $L_x^+ = 154$, $\delta_1^+ = 63$. (b) Symbols are as in (a) except for, --- , $L_x^+ = 161$, $\delta_1^+ = 78$. Note the difference in scale between the two figures.

filter height increased, especially as it was made comparable to the channel half-height, the extent of the parabolic part of the profile decreased and the effective Re_τ increased. Although some efforts were made to compensate this effect by changing the length and width of the computational boxes, there is some systematic variation of both quantities with the filter height when expressed in wall units.

The time evolution of the flow was characterized in two different ways. The first one is the evolution of the instantaneous skin friction, defined as the gradient at the wall of the plane-averaged streamwise velocity. Because of the ambiguities regarding dimensional bulk variables, only the fluctuations relative to its own mean make sense

$$c_f^+ = \frac{\partial_y \bar{u}}{\partial_y U}, \quad (5.1)$$

where the overline stands for instantaneous averaging over wall-parallel planes and U is the long-time average of \bar{u} .

Some representative time histories are shown in Fig. 3. They have been normalized with the skin friction of a parabolic laminar profile with the same mass flux to separate them vertically for visual clarity, but we have seen that the different levels of the average wall friction have no physical significance. All of the simulations in Fig. 3 are ‘short’ boxes containing a single wavelength of the low-velocity streak. For the lowest filter height, the flow is a permanent wave which moves with a celerity $u_c^+ \approx 15$. This case corresponds to the solid line in the profiles in Fig. 2(a), and the advection velocity is very close to that of the plateau in the mean velocity profile. The next two filter heights result in two-frequency tori, with a short period $T^+ \approx 60$ and a long one $T^+ \approx 400$. The relative importance of both periods switches with the filter height. While for $\delta_1^+ = 52$ the long period is only a weak modulation of the short one, invisible at the scale of Fig. 3, the opposite is true when $\delta_1^+ = 55$.

As the filter is raised further, the flow becomes chaotic, with the longest period of the tori acting now as a dominant fast frequency. Finally, for $\delta_1^+ > 70$, intermittent bursts appear which are typical of fully developed turbulent flows and whose amplitude is substantially higher than in any of the three other cases (Fig. 3b). The shortest bursting

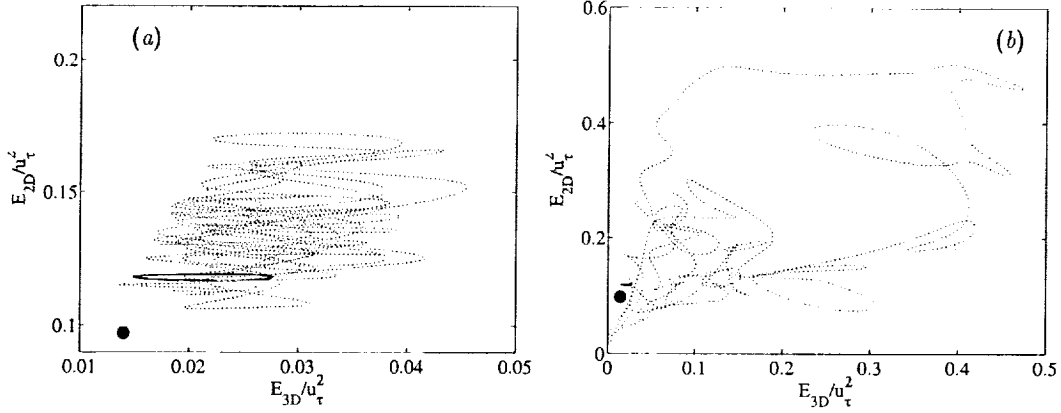


FIGURE 4. Time evolution of the fluctuating energies. (a) \bullet , $L_x^+ = 145$, $\delta_1^+ = 49$; —, $L_x^+ = 150$, $\delta_1^+ = 52$; \cdots , $L_x^+ = 154$, $\delta_1^+ = 63$. (b) Symbols are as in (a) except for, \cdots , $L_x^+ = 161$, $\delta_1^+ = 78$. Note the different scales of the two figures, which result in the weakly-modulated cycle in (a) being reduced to a short horizontal dash in (b).

events are roughly of the same length as the long period of the tori, while the longest ones are two or three times longer. These times are comparable to those identified for individual bursts in minimal channels by Jiménez & Moin (1991). The present boxes are actually too short to maintain bursting turbulence, which is metastable. The velocity fluctuations become very weak in the dips of the history of the skin friction until one of them fails to regenerate and the flow laminarizes completely.

Figure 4 shows the same data in a different representation introduced by Toh & Itano (1999). Orbits are drawn in terms of the two-dimensional and three-dimensional energy of the wall-normal velocity fluctuations. The two-dimensional energy is

$$E_{2D} = \frac{1}{H} \int_0^H \langle v_{2D}^2 \rangle dy, \quad (5.2)$$

where $v_{2D}(y, z, t)$ is the streamwise average of the fluctuation of v and therefore measures the intensity of objects which are long in the streamwise direction, essentially streaks. The three-dimensional energy is similarly defined for the remaining v fluctuations, $v_{3D} = v - v_{2D}$, and measures deviations from streamwise uniformity. In this representation the permanent wave is represented by a single point, while the weakly modulated torus of Fig. 3(a) appears almost as a limit cycle, wide in the sense of the three-dimensional energy but narrow in the two-dimensional one. The examination of this cycle as well as of the orbits corresponding to other cases shows that the skin friction correlates with the magnitude of the two-dimensional energy and, therefore, of the intensity of the streak, while the faster oscillations of the three-dimensional energy do not affect it strongly.

Figure 4(b) underscores the different range of amplitudes of the simple tori or chaotic flows, which are obtained for low filter heights, and of the bursts of the deeper channels, but it also suggests that the simplification process consists of damping the large bursting excursions, while the low-activity periods of the deeper flows share with the constrained systems the same region of the energy space.

Similar behaviors are found for the longer boxes, which contain at least two wavelength of the wavy streak. A summary of cases is found in Fig. 5(a), which classifies the different experiments in terms of their temporal behavior. Note the narrow range of filter heights

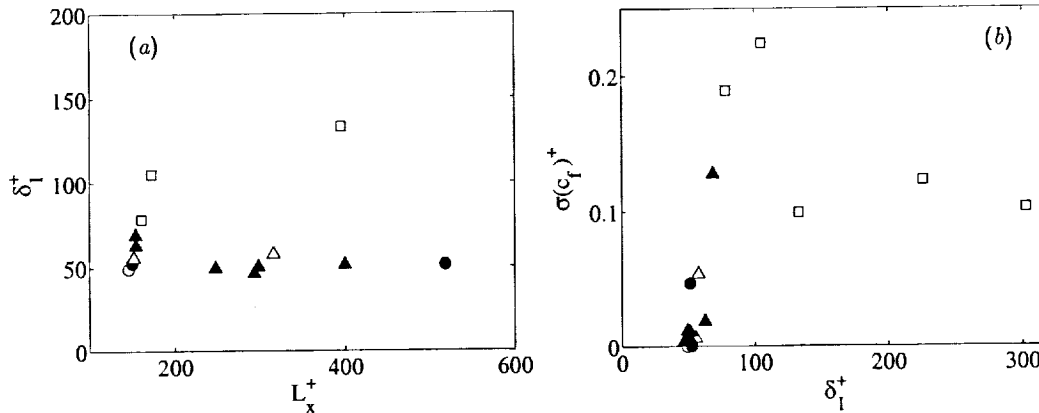


FIGURE 5. (a) Classification of the evolution of the different computational experiments, as a function of the box length L_x^+ , and of the filter height δ_1^+ . (b) Root mean squared temporal variation of the plane-averaged wall friction. \circ , permanent wave; \bullet , cycle or weak torus; Δ , simple torus; \blacktriangle , complex torus or chaos; \square , bursting turbulence.

which result in time evolutions which are not fully turbulent, but also that the bursting appears as a natural evolution of the weakly chaotic flows. In the longer boxes the bursting turbulence is self-sustaining and does not decay spontaneously.

The amplitude of the skin friction fluctuations, normalized as in (5.1), is given in Fig. 5(b). The bifurcation parameter that collapses the different experiments is δ_1^+ , and the fluctuations increase quickly above a minimum threshold $\delta_1^+ \approx 50$. There are two branches in this figure, representing respectively the long and the short boxes. The steeper branch consists of short boxes, and the lower fluctuation amplitude of the long ones reflects the fact that not all the structures burst simultaneously and that the amplitudes measured in the long boxes represent an average of bursting and quiescent structures.

A three-dimensional representation of the flow field in one of the longer boxes is shown in Fig. 6(a). It shows a low-velocity streak with two waves, associated to each of which there is a pair of quasi-streamwise vortices. During the turbulent cycle the amplitude of the lateral displacement of the streak grows and wanes, and so do the vortices, but the streak is never uniformly straight. Careful tracing of vortex lines, although generally complicated, proves that the streak and the vortices are not independent structures, but different aspects of the same one. The single permanent wave mentioned above when discussing the time histories is shown in Fig. 6(b). It should be emphasized that this wave is both permanent, moving at a constant velocity without change of shape, and autonomous, in the sense that there are no vorticity fluctuations in the numerical box except those seen in the figure and that it has been derived from a fully turbulent flow by a continuous set of transformations in which its statistical properties are either maintained or change smoothly. It is the best representation that we have up to now of the elemental 'engine' that powers near-wall turbulence.

Figures 6(a) and 6(b) are qualitatively very similar to the traveling waves obtained in Waleffe (1998) and to the structures deduced from larger channels by Jiménez & Moin (1991) and Jiménez & Pinelli (1999), as well as to the saddle point identified by Toh & Itano (1999).

Careful observation of the differences between computer animations of these and of deeper boxes suggests the root of the increased complexity of the latter. As the streak goes

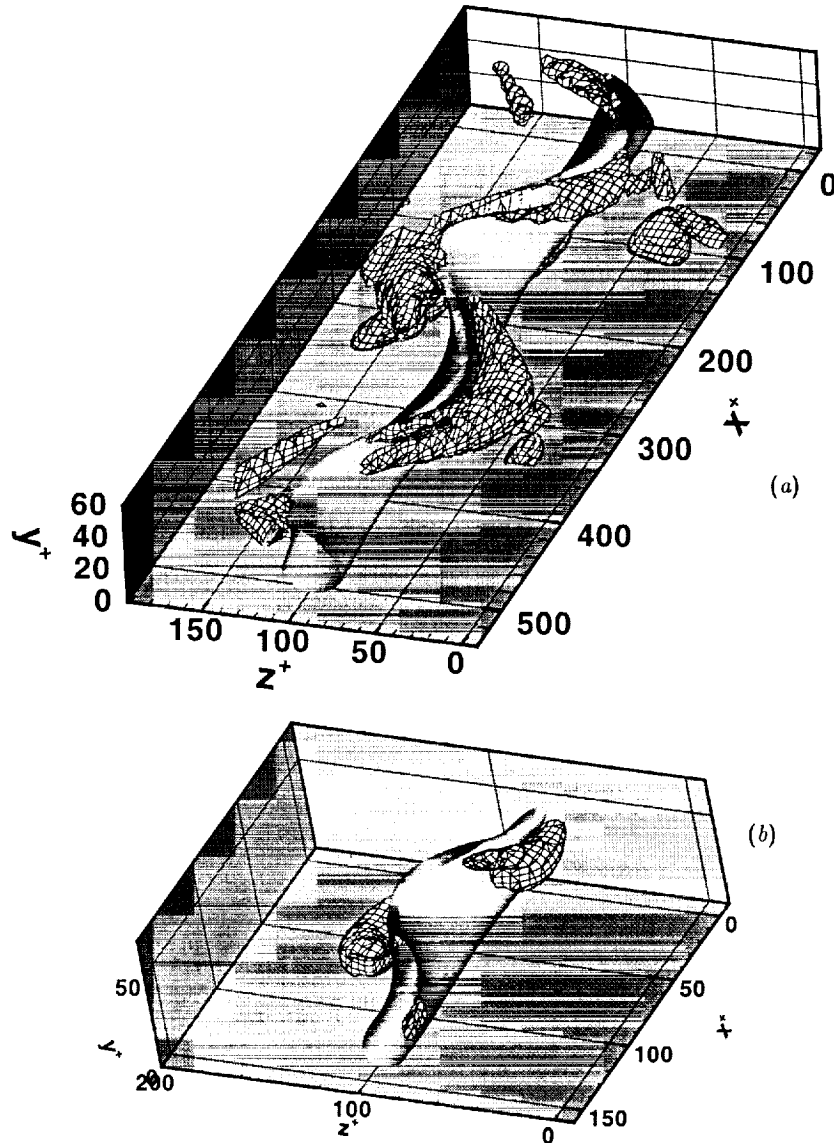


FIGURE 6. Three-dimensional representations of two of the flows discussed in the text. The shaded surface is in both cases $u^+ = -3.5$. The meshed objects are $\omega_x^+ = \pm 0.18$. The darker quasi-streamwise vortices are negative, so that the net effect of the vortex system is to induce a positive updraft along the low-velocity streak. The flow is from top-right to bottom-left. (a) is a regular cycle with $L_x^+ = 520$, $\delta_1^+ = 51$. (b) is the steady wave in Figs. 3 and 4.

through the cycle, it ejects some vorticity into the outer flow, essentially as a small vortex hairpin. In full-depth flows this vorticity evolves, becomes disorganized, and eventually modifies the next cycle of the streak. In autonomous flows the vorticity is damped by the filter as soon as it is ejected, and this randomizing mechanism is not present. The threshold filter height at which bursting first appears is that for which the vortices are

just allowed to move far enough from the wall to cross over the top of the streak and interact with one another.

6. Conclusions

We have shown that simple low-dimensional systems can be obtained from fully turbulent channels by a continuous set of transformations, the most important of which is the restriction of the distance from the wall at which the quasi-streamwise vortices are allowed to move.

The simplest solution identified in this way is a permanent traveling wave, similar to those found by other investigators in related flows. As the vertical constraints on the system are relaxed, this wave bifurcates into either a limit cycle or a two-frequency torus, depending on the parameters. The longest of the two periods of the torus evolves into the bursts of full-scale turbulence when the vertical restriction is further removed.

The critical bifurcation filter height is $\delta_1^+ \approx 50$, and the range of heights in which the bifurcation occurs is very narrow, with the flow becoming essentially turbulent for $\delta_1^+ \approx 70$. The bifurcation mechanism was identified visually as the interaction, across the top of the low-velocity streak, of the two counter-rotating vortices.

Even in the very short boxes used in these simulations, the only streamwise coherent structure is the low-velocity streak. The quasi-streamwise vortices, their associated wall-normal velocities, and the resulting high-shear regions near the wall are all discontinuous along the box length.

M. S. was supported in part by grant CT98-0175 of the TMR program.

REFERENCES

- FERNHOLZ, H. H., & FINLEY, P. J. 1996 The incompressible zero-pressure-gradient turbulent boundary layer: an assessment of the data. *Prog. Aerospace Sci.* **32**, 245-311.
- JEONG, J., HUSSAIN, F., SCHOPPA, W. & KIM, J. 1997 Coherent structures near the wall in a turbulent channel flow. *J. Fluid Mech.* **332**, 185-214.
- JIMÉNEZ, J. 1999 The physics of wall turbulence, *Physica A.* **263**, 252-262.
- JIMÉNEZ, J. & MOIN, P. 1991 The minimal flow unit in near wall turbulence. *J. Fluid Mech.* **225**, 221-240.
- JIMÉNEZ, J. & PINELLI, A. 1999 The autonomous cycle of near wall turbulence. *J. Fluid Mech.* **389**, 335-359.
- KIM, H. T., KLINE, S. J. & REYNOLDS, W. C. 1971 The production of turbulence near a smooth wall in a turbulent boundary layers. *J. Fluid Mech.* **50**, 133-160.
- KIM, J., MOIN, P. & MOSER, R. 1987 Turbulence statistics in fully developed channel flow at low Reynolds number. *J. Fluid Mech.* **177**, 133-166.
- KOLMOGOROV, A. N. 1941 The local structure of turbulence in incompressible viscous fluids at very large Reynolds numbers. *Dokl. Akad. Nauk. SSSR*, **30**, 301-305. Reprinted in *Proc. R. Soc. London A.* **434**, 9-13 (1991).
- MOSER, R., KIM, J. & MANSOUR, N. N. 1999 Direct numerical simulation of a turbulent channel flow up to $Re_\tau = 590$. *Phys. Fluids.* **11**, 943-945.
- ROBINSON, S. K. 1991 Coherent motions in the turbulent boundary layer. *Ann. Rev. Fluid Mech.* **23**, 601-639.

- SMITH, C. R. & METZLER, S. P. 1983 The characteristics of low speed streaks in the near wall region of a turbulent boundary layer. *J. Fluid Mech.* **129**, 27-54.
- SWEARINGEN, J. D. & BLACKWELDER, R. F. 1987 The growth and breakdown of streamwise vortices in the presence of a wall. *J. Fluid Mech.* **182**, 255-290.
- TOH, S. & ITANO, T. 1999 Low-dimensional dynamics embedded in a plane Poiseuille flow turbulence. Traveling-wave solution is a saddle point? Preprint *physics/9905012*.
- TOWNSEND, A. A. 1976 *The structure of turbulent shear flow*. Cambridge U. Press, second edition, pg. 135.
- WALEFFE, F. 1997 On a self-sustaining process in shear flows. *Phys. Fluids.* **9**, 883-900.
- WALEFFE, F. 1998 Three-dimensional coherent states in plane shear flows. *Phys. Rev. Letters.* **81**, 4140-4143.

Experimental results on the stabilization of lifted jet diffusion flames

By L. K. Su, D. Han AND M. G. Mungal

1. Motivation and objectives

Many researchers have studied the stabilization of lifted turbulent jet diffusion flames. Earlier work in this area was thoroughly reviewed by Pitts (1988). Recent advances in laser diagnostic methods have vastly increased the breadth of data available regarding this problem, while increased computational capacity has permitted the assessment of various models for flame stabilization. However, there remains no consensus regarding the stabilization mechanism.

Proposed models differ primarily on the role of premixing at the flame front. Given a jet of undiluted fuel issuing into air, it is undisputed that some degree of fuel-air premixing occurs upstream of the lifted flame. The stabilization theory of Vanquickenbourne & van Tiggelen (1966) assumed full premixedness of fuel and air at the stabilization point, with stabilization occurring through a balance of the local jet axial velocity and turbulent flame speed. Subsequently, Peters & Williams (1983) argued that, in axisymmetric turbulent jets, insufficient molecular mixing occurs upstream of the flame front to support the notion of premixed flame propagation. Instead, stabilization was proposed to be governed by the quenching of thin, laminar diffusion flamelets. Müller *et al.* (1994) later extended this work to consider partially premixed flamelets, concluding again that flamelet quenching was important to flame stabilization.

Recently, triple flame theories (Dold (1989), Veynante *et al.* (1994), Ruetsch *et al.* (1995)) have been applied to the stabilization problem. Essential to the formation of the triple flame structure is a gradient in the fuel mixture fraction profile normal to the flow direction, ranging from fuel-rich to fuel-lean conditions across the profile. On either side of the stoichiometric point, a premixed flame branch forms. The excess fuel and oxidizer from the rich and lean branches, respectively, then burn as a downstream diffusion flame. These three structures – the rich and lean premixed branches and the diffusion tail – motivate the 'triple flame' nomenclature. In the idealized case of a uniform incoming velocity profile, the premixed branches present a convex surface to the flow, with the fuel-rich and fuel-lean sides receding owing to the reduced flame speed with departure from stoichiometry. The addition of the diffusion tail downstream of this convex surface results in the characteristic triple flame shape, which resembles a boat anchor. In a lifted turbulent jet flame, however, the incoming velocity profile can be expected to be highly non-uniform. Veynante *et al.* (1994) computed triple flames with vortices superposed on the incoming velocity profiles. Under these conditions the flame branches are highly distorted from the idealized shape. For sufficiently high strain rates, one of the premixed branches may be extinguished while the other branches continue to burn. Because of these departures from the idealized triple flame structure, the term 'leading-edge flame'

or ‘edge flame’ is preferred when describing flame stabilization involving upstream partial premixing with a trailing diffusion flame branch.

Emergence of the edge flame theory of flame stabilization has been coincident with the extensive application of planar laser diagnostic methods to the problem. Measurements have been presented of mixture fraction, scalar dissipation rate, and temperature fields (Schefer *et al.* (1994), Kelman *et al.* (1998)), reaction zone locations (Maurey *et al.* (1998), Schefer & Goix (1998), Watson *et al.* (1999a), Watson *et al.* (1999b)), and fluid velocities in and around the reaction zones (Muñiz & Mungal (1997), Maurey *et al.* (1998), Schefer & Goix (1998), Watson *et al.* (1999a)). The mixture fraction and dissipation measurements of Schefer *et al.* (1994) show scalar dissipation rates well below quenching values at the flame stabilization points, indicating that scalar dissipation is not significant to the stabilization process for the lifted methane flames studied, in contradiction to the model of Peters & Williams (1983). The velocity measurements of Muñiz & Mungal, conditioned on flame location, show that the flame stabilizes in regions of low incoming fluid velocity (typically less than three times the laminar flame speed, S_L). This, together with velocity profiles normal to the flame base and streamline patterns in the upstream region, suggests triple flame behavior similar to that seen in the computations of Ruetsch *et al.* (1995). Using measurements of CH radical concentrations to locate reaction zones, Watson *et al.* (1999b) show evidence of both the lean premixed branch and diffusion tail of the idealized triple flame. It is hypothesized that the rich premixed branch is folded into the diffusion tail in the manner suggested by the simulations of Veynante *et al.* (1994).

The conclusions drawn from these experimental studies all have some degree of uncertainty, however, stemming from experimental limitations. Complete elucidation of the stabilization process in the context of the proposed models requires simultaneous knowledge of the reaction zone position, the local velocity field, and the local mixture fraction field; in the studies mentioned, at most two of these were measured. In particular, simultaneous measurements of mixture fraction and velocity have not been demonstrated. The current experiments address this by presenting simultaneous measurement of fuel concentration, using planar laser-induced fluorescence (PLIF) of acetone seeded into the fuel stream, and velocity, measured using particle image velocimetry (PIV), in the stabilization region of a lifted methane-air turbulent jet diffusion flame. The reaction zone can also be fairly well located by these measurements, as will be shown.

2. Results

Much of this work was presented earlier in Su, Han & Mungal (2000). More extensive experimental details can be found in that paper. That paper also contains several figures that have been omitted here for brevity.

2.1. *Experimental arrangement and image interpretation*

The experiments are performed in a vertical wind tunnel which provides a coflow velocity of 0.36 m/s. The methane fuel stream issues from a straight pipe (inner diameter 4.6 mm) placed in the center of the tunnel. Two cases are considered here. In the first, the jet exit speed is 15.3 m/s, giving a jet Reynolds number (based on jet excess velocity, nozzle diameter and methane kinematic viscosity) of roughly 4000. In the second case, the jet exit speed is 10.8 m/s, giving a Reynolds number of roughly 2800. A total of 103 and 88 velocity/scalar image pairs are available for the two cases, respectively.

To provide the Mie scattering signal for the PIV, the coflow air is seeded with a

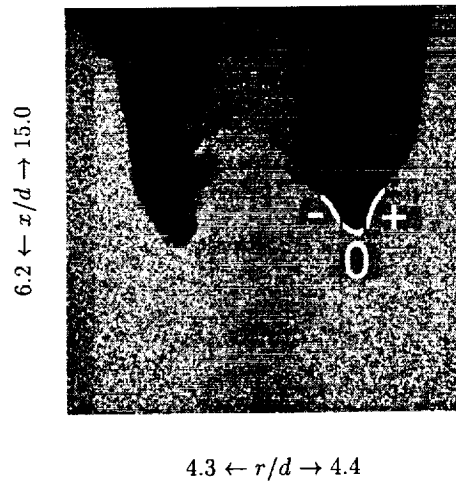


FIGURE 1. A sample Mie scattering field, showing the loss of signal in regions where the glycerol-water particles have evaporated at high temperatures.

glycerol-water fog. A dual cavity Nd:YAG laser, with 532 nm output, is used to produce two pulses with a temporal spacing of $30 \mu\text{s}$. The resulting scattering signal is collected by an interline transfer CCD camera (1008 x 1016 pixel resolution) which allows each of the two laser sheet pulses to be captured in a separate image. The cross-correlation PIV algorithm used (Hasselbrink (1999)), which incorporates iterative interrogation window offset (Westerweel *et al.* (1997)), offers high resolution and vector yield. The final processing step yields a 100×100 grid of velocity vectors.

For the PLIF, acetone is seeded into the methane fuel stream, to approximately 15% by volume. A XeCl excimer laser with 308 nm output excites the fluorescence. The resulting signal is captured by a low-noise, high-sensitivity CCD camera, with 515×650 pixel resolution. An optical filter isolates the fluorescence signal from ambient light and flame luminosity. The field of view of the PLIF measurements spans from the jet nozzle exit to a maximum of 18.2 jet diameters, d , downstream, and extends up to $7.3 d$ to either side of the centerline. It is necessary to include the potential core in the PLIF images in order to correlate signal levels with absolute fuel concentration. No such constraint exists with the PIV, so the PIV imaging windows were placed so as to capture only the flame base region. For case 1, the PIV window spanned from 9.5 to $17.3 d$ downstream of the nozzle, while for case 2 the PIV window spanned from 6.2 to $15.0 d$.

The use of glycerol-water fog particles in lifted flame experiments has previously been demonstrated (Hasselbrink & Mungal (1998)). A sample Mie scattering image, from case 2, is given in Fig. 1. The fog particles evaporate in the range 400-450 K, so the regions with no Mie scattering signal can be interpreted as having been heated by the flame. Because the reaction zone is known to be thin (Watson *et al.* (1999a) report CH regions with an average thickness of approximately 1 mm), the reaction zone can be assumed to follow closely the heated region outlined as in Fig. 1. Analogous to edge flame theories, previous researchers have assumed that the stabilization point of the lifted flame corresponds to the base (i.e. the most upstream position) of the region of elevated temperature. However, Watson *et al.* (1999a), through simultaneous measurements of OH and CH radical concentrations, cast some doubt on this assumption. The CH radical is a short-lived reaction intermediate and is believed to mark accurately the instantaneous

reaction zone, while the OH radical is removed by relatively slow three-body reactions and marks regions containing hot combustion products. Watson *et al.* observed that the thin CH zones tend to lie to the inside (toward the centerline) of the broader OH zones, and in fact presented some sample images in which the OH zones extend upstream of the CH zones. This implies that the base of the high temperature regions in Fig. 1 cannot be unambiguously interpreted as the flame base. In the present work we make use of the simultaneous information on fuel concentration provided by the acetone PLIF. As a necessary condition for any point on the temperature interface delineated in the Mie scattering signal to represent an instantaneous flame location, the fuel concentration immediately upstream of that point must be within the flammability limits.

The use of acetone PLIF as a fluid concentration diagnostic in combustion experiments proceeds with some caveats. One consideration is that acetone decomposes in the flame zones, confining information on fuel concentration to the flame upstream region. Another consideration is the variation in acetone fluorescence yield with temperature. Thurber (1999) found that, for constant pressure and constant laser excitation energy at 308 nm, the measured fluorescence per unit acetone mole fraction at 330 K is 0.938 (normalized by the value at 296 K), dropping to 0.875 at 374 K, and 0.806 at 424 K, which is roughly the temperature marked by the abrupt drop in the Mie scattering signal. Finally, differential diffusion effects may arise in attempting to use acetone to mark the methane fuel stream. In combustion, differential diffusion is thought to be significant because the diffusivity coefficients of hydrogen and heavier species can differ by up to an order of magnitude and because local laminarization by heat release increases the importance of molecular diffusion relative to turbulent transport (Bilger (1982)). Because we are concerned only with the non-burning region of the lifted flame and because the acetone-air and methane-air diffusion coefficients vary by only a factor of two (Reid *et al.* (1987)), we assume here that the effect of differential diffusion is negligible.

2.2. Data analysis

Figure 2 shows the measured scalar field corresponding to the Mie scattering field of Fig. 1. Overlaid on the scalar field are the temperature interface determined from the Mie scattering field as well as the boundary of that field. The scalar field shown is the fuel mole fraction, X_f , which corresponds directly to the measured fluorescence. In the unburned gases, the mixture fraction and fuel mass fraction are equivalent and relate to X_f as

$$Z = \frac{X_f M_f}{X_f M_f + (1 - X_f) M_{air}} \quad (2.1)$$

where the M are the molecular masses.

Because the jet-to-coflow velocity ratio is relatively high in these measurements (over 40:1 for case 1 and roughly 30:1 for case 2), the scalar field upstream of the flame should obey pure jet scalings. Figure 3 shows the evolution of flow width for the two cases, where $\delta(x)$ is defined as the full width of the mean radial profile between the 10% points. The width, δ , manifests the expected linear dependence on x for each case until a critical value of x is reached where this trend is broken, caused (as will be confirmed below) by the presence of the flame. Recall that in the flame zones, the acetone fluorescence no longer marks the fuel. The mean radial profiles themselves converge quickly to the Gaussian shape characteristic of jets (figure not shown). The downstream decay appears to attain the expected $1/x$ dependence, though this is not conclusive because of the limited downstream extent of the present measurements (Fig. 4). The decay curves in

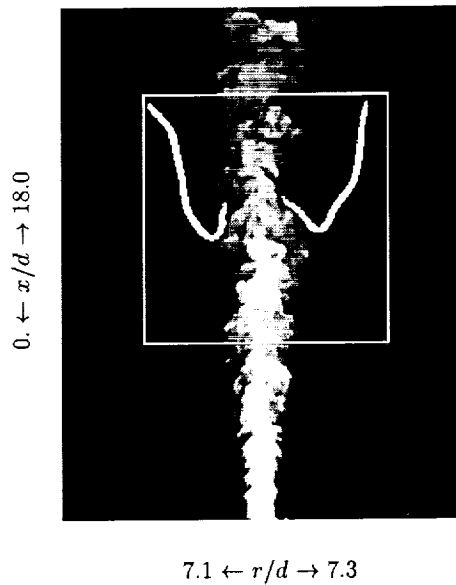


FIGURE 2. The fuel mole fraction field, X_f , (logarithmic grayscale) corresponding to the Mie scattering field of Fig. 1. The PIV imaging window is superimposed on the image, as is the high temperature interface determined from Fig. 1.

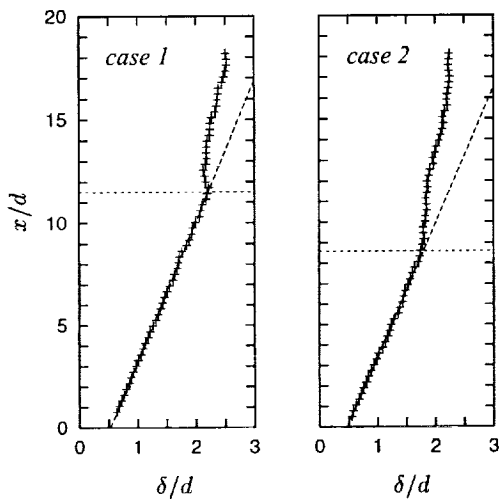


FIGURE 3. Evolution of the scalar flow width for the two cases.

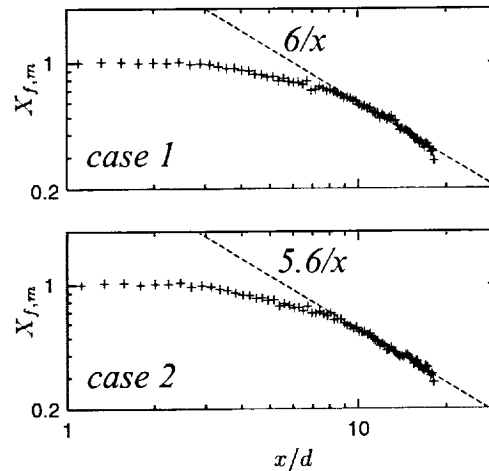


FIGURE 4. Evolution of the centerline scalar decay for the two cases.

Fig. 4 show no evidence of large drops in signal level which would be consistent with the presence of flame surfaces, indicating that the average flame position has not yet migrated to the centerline for the downstream positions shown.

As a first step in determining flame base locations, the temperature gradient interface is found from the Mie scattering images of the form shown in Fig. 1, and this interface is then mapped onto the scalar field image as demonstrated in Fig. 2. The most upstream points of these interfaces (in the following discussion, we will refer to these as the leading

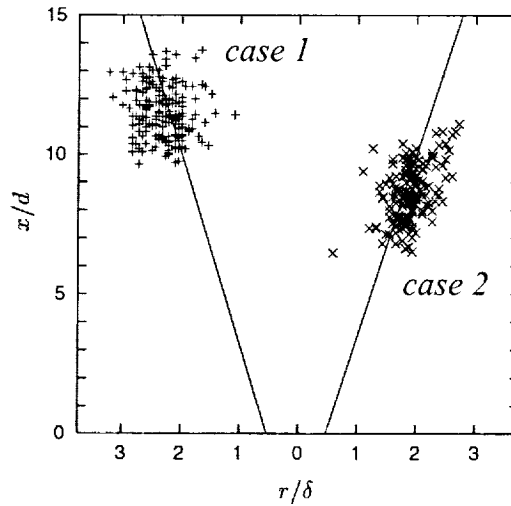


FIGURE 5. Scatterplot of the most upstream points of the high temperature interfaces (the leading points). Lines are the fits to the δ curves of Fig. 3.

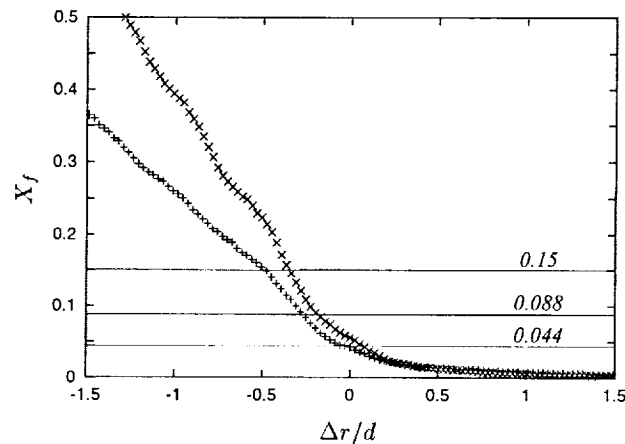


FIGURE 6. Averaged mixture fraction profiles immediately upstream of the instantaneous leading points. Δr measures the radial distance relative to the leading point. The stoichiometric value of X_f and the lean and rich flammability limits are indicated. +, case 1, \times , case 2.

points) for either side of the centerline are collected in Fig. 5. For case 1, the mean position of these points is found at $x = 11.5d$, $r = 2.3d$; for case 2, the mean position is $x = 8.6d$, $r = 1.9d$. As indicated in Fig. 3, these x values closely match the points at which the flow width, δ , deviates from its linear evolution.

As mentioned above, the structure of an edge flame is highly dependent on the incoming velocity and fuel concentration profiles. Figures 6 and 7 show the averaged fuel mole fraction and axial velocity profiles upstream of the instantaneous high temperature interfaces. The profiles are compiled along lines of fixed x , lying roughly 0.5 mm upstream of the leading points. In offsetting the profiles slightly from the high temperature interfaces, it is intended that the effect of varying temperatures on fluorescence signal be minimized. (At the profile locations, temperatures should be below approximately 400 K, so temperature effects will cause the measured mole fractions to deviate by no more than

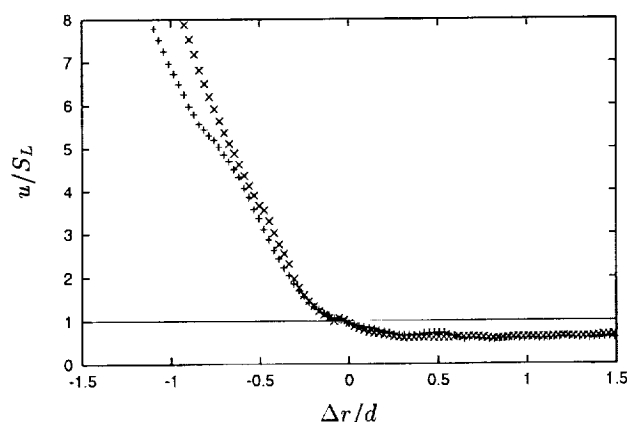


FIGURE 7. Averaged profiles of the axial velocity, normalized by the laminar flame speed, upstream of the instantaneous leading points. +, case 1, ×, case 2.

15% from the true mole fractions.) The horizontal axis of the profiles, Δr , is the radial position relative to the leading point. To interpret the fuel mole fraction profile, observe that the stoichiometric mole fraction for a methane-acetone mixture with respective mole fractions in the ratio 0.85:0.15 is 0.088. The lean flammability limit for methane (in air, at 298 K and 1 atm) lies at mole fraction 0.050, and for acetone lies at 0.026 (Glassman (1987)), so by Le Chatelier's principle, the lean flammability limit for the mixture is at mole fraction 0.044. The rich flammability limits are 0.15 mole fraction for methane and 0.13 for acetone. Immediately upstream of the leading point ($\Delta r = 0$), the fuel mole fraction is approximately the lean flammability limit for case 1, at a value of 0.042, and is slightly above the lean limit, at 0.056, for case 2. The fuel fraction quickly drops below the lean flammability limit towards the outside of the jet (positive Δr). Towards the inside of the jet, the fuel fraction gradient increases sharply. The stoichiometric point for case 1 is $\Delta r = -0.28$ and for case 2 is $\Delta r = -0.2$, and the fuel fraction exceeds 0.15 at $\Delta r = -0.42$ for case 1 and -0.36 for case 2. The profile for case 2 shows a higher gradient than that for case 1, owing to the smaller average jet width at the lower liftoff height for case 2.

The profiles of mean axial velocity, u , upstream of the instantaneous leading points for the two cases are shown in Fig. 7. Values are normalized by 0.43 m/s, the stoichiometric laminar burning velocity of both methane and acetone (Glassman (1987)). Immediately upstream of the leading point, the axial velocity is slightly below S_L . Towards the outside of the jet, the axial velocity profile drops below both S_L and the coflow velocity, indicating a deceleration of the flow upstream of the high temperature region. On the inside of the jet, the axial velocity rises steeply, with the higher gradient being seen for the case 2 profiles, as with the fuel fraction profiles shown above.

From probability distributions (not shown) of the axial velocity, u , at various positions on the high temperature interface determined from the Mie scattering images, statistics of the incoming fluid velocities can be compiled. We define the '0' position as on the interface, with Δr (relative to the leading point) between -1 and 1 mm. The '-' position is on the interface towards the jet centerline, $-3 \text{ mm} < \Delta r < -1 \text{ mm}$, and the '+' position is on the interface to the outside of the jet, $1 \text{ mm} < \Delta r < 3 \text{ mm}$. (These positions are indicated in Fig. 1.) Immediately around the leading point (the '0' position) the velocities average near S_L , with averages of $0.86 S_L$ for case 1 and $0.95 S_L$ for case 2. Towards the

centerline (the '-' position) the average axial velocity increases, to $2.02 S_L$ for case 1 and $2.51 S_L$ for case 2. Away from the centerline (the '+' position), the velocities average $0.51 S_L$ for case 1 and $0.58 S_L$ for case 2, indicating that the flow in that region has decelerated from the coflow speed of $0.84 S_L$.

2.3. Discussion

The profiles of fuel mole fraction and axial velocity immediately upstream of the high temperature regions (Figs. 6 and 7) are instructive in the context of theories of edge flames. The assumption that the leading point of these regions corresponds to a stoichiometric mixture with fuel-lean conditions to the outside and rich conditions to the inside is not supported here. Instead, the average fuel mole fraction at the leading point is near the lean flammability limit. The sample scalar field of Fig. 2 illustrates this point; the high temperature interface to the left of the centerline seems to show no fuel to the outside of the leading point, while the interface to the right of centerline shows low fuel concentrations to the outside. In general, the portion of the high temperature interface outside of the leading point will have insufficient fuel fraction to support combustion. Instead, it appears that flammable mixtures, and the flame zone position, are biased towards the inside of the high temperature regions.

This conclusion is in agreement with the simultaneous CH/OH PLIF measurements in lifted flames of Watson *et al.* (1999a), in which the CH zones were found to lie on the inner boundaries of the OH zones, and the more recent CH PLIF measurements by the same authors (Watson *et al.* (1999b)), which showed evidence of weak CH zones (thought to correspond to the lean premixed branch) curling outward from the bases of the primary CH zones (thought to correspond to the diffusion branch). These latter measurements were not performed simultaneously with OH PLIF, but it can be inferred that the weaker CH zones correspond to the region of the high temperature interface near and to the outside of the leading point. This lean premixed branch was only observed in roughly 30% of the images, which Watson *et al.* attributed to three-dimensional effects. The present measurements suggest that the absence of a lean premixed branch can be explained by the incoming fuel mixture fractions being below the flammability limit.

While the lean premixed branch of the idealized triple flame has been observed through CH imaging, the fuel-rich branch has not. Watson *et al.* (1999b) cite the simulations of Veynante *et al.* (1994), which demonstrate that incoming vortices can distort the edge flame in such a way that one or both of the premixed branches is obscured. This notion is supported by the axial velocity profiles upstream of the leading point (Fig. 7). The profiles show a strong velocity gradient consistent with a vortex which draws ambient fluid into the jet from below and moves jet fluid upward and away from the centerline. Such a vortex might possibly fold the rich premixed branch of an edge flame into the diffusion tail (Veynante *et al.* (1994)).

The axial velocity statistics discussed above indicate that velocities upstream of the high temperature interfaces are relatively low, consistent with previous observations (Muñiz & Mungal (1997), Schefer & Goix (1998), Watson *et al.* (1999a)). The actual values are, however, somewhat lower than those reported by Muñiz & Mungal or Watson *et al.* Schefer & Goix found that the incoming velocities diminished with lower jet Reynolds numbers. This was attributed to lower liftoff heights observed for the lower Re. At the lower positions, flammable layers are thinner, resulting in greater flame curvature and, it was concluded, less efficient preheating of reactants. The present Reynolds numbers are indeed lower than those of Muñiz & Mungal and Watson *et al.* However, the full set of current measurements encompasses a range of Reynolds numbers up to roughly 10000.

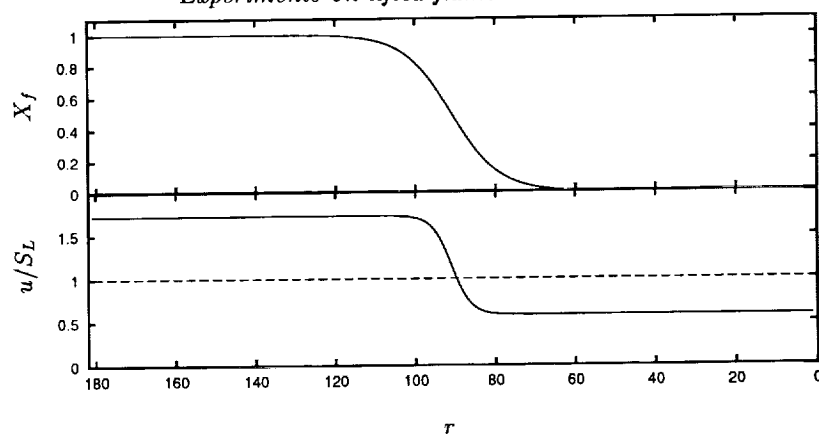


FIGURE 8. Inflow profiles of mixture fraction and axial velocity used in the edge flame simulation.

Analysis of this set in its entirety will permit an assessment of the effects of these issues of flammability layer thickness and flame curvature.

3. Future work

Preliminary work is underway to use the measured fuel mole fraction and axial velocity profiles from these experiments in the edge flame code of Ruetsch (Veynante *et al.* (1994), Ruetsch *et al.* (1995)). The resulting reaction rate fields can then be compared with those observed experimentally, for example by Watson *et al.* (1999b), using measurements of the CH radical. This comparison will shed some light on the ability of the simple edge flame formulation with laminar flow fields and simplified chemistry to describe the stabilization phenomenon in lifted, turbulent diffusion flames.

The code of Ruetsch computes the fully compressible, 2-D Navier-Stokes equations, and incorporates the single-step, irreversible reaction $F + O \rightarrow P$. The simulation is initialized with a premixed line flame of specified thickness δ_0 . The non-uniform mixture fraction and velocity profiles are introduced at the inflow boundary. An initial run has been performed using the experimental results presented in this paper as inputs to the simulation. For this run, we use hyperbolic tangent profiles for the velocity and mixture fraction profiles. We define δ_u and δ_X as the inverses of the slopes of the velocity and mixture fraction profiles, respectively, at the stoichiometric point. The ratios δ_u/δ_0 and δ_X/δ_0 are determined from the experimental profiles presented in Figs. 6 and 7.

The tanh inflow profiles used in the initial run are shown in Fig. 8. Contours of the reaction rate field at two later times are shown in Fig. 9. The incoming flow moves from bottom to top in the figures. Some tentative observations can be made. First, the flame migrates away from the initial stoichiometric location in fuel-lean regions, consistent with the present experiments. Secondly, for the later of the two times shown, the highest reaction rate on the flame leading edge (which corresponds to the local stoichiometric position) does not correspond to the leading point as defined in this paper, as has also been suggested by Chen *et al.* (2000). Finally, the configuration of the premixed flame branches begins to resemble the CH fields observed by Watson *et al.* (1999b). In particular, the fuel-rich branch for the later of the two times appears to

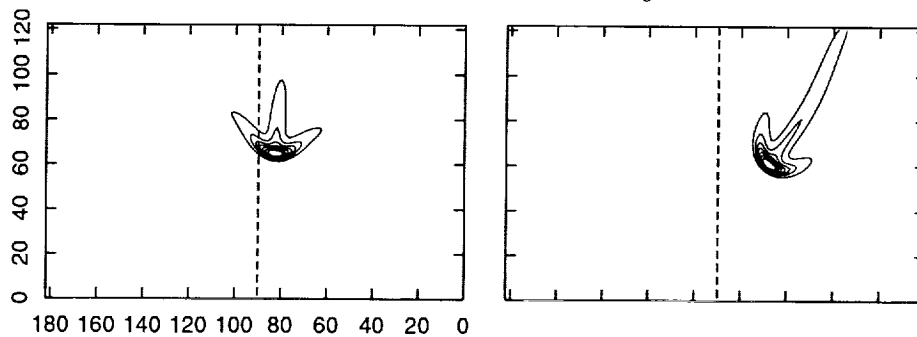


FIGURE 9. Reaction rate contours from the simulation at early (left) and later (right) times. The dashed line in each plot indicates the initial stoichiometric position. Axes represent simulation grid points.

be aligned roughly parallel to the incoming flow, while the fuel-lean branch is roughly normal to the incoming flow, curling up slightly at the extreme lean side.

These results, while far from conclusive, suggest that this laminar edge flame model with simple chemistry is well able to reproduce significant features seen in experimental lifted turbulent jet diffusion flames. Issues to be addressed in future work include carrying the simulation out to longer times, incorporating more realistic inflow profiles, and using inflow parameters from experimental results at different Reynolds numbers.

REFERENCES

- BILGER, R. W. 1982 Molecular transport effects in turbulent diffusion flames at moderate Reynolds numbers. *AIAA J.* **20**, 962-970.
- CHEN, M., HERRMANN, M. & PETERS, N. 2000 Flamelet modeling of lifted turbulent methane/air and propane/air turbulent jet diffusion flames. *Proc. Twenty-Eighth Symp. (Int'l) on Combustion, The Combustion Institute, Pittsburgh, PA.*
- DOLD, J. W. 1989 Flame propagation in a nonuniform mixture: analysis of a slowly varying triple flame. *Comb. Flame.* **76**, 71-88.
- GLASSMAN, I. 1987 *Combustion (2nd ed.)*, Academic Press, Orlando, FL, 1987.
- HASSELBRINK, E. F. 1999 *Transverse Jets and Jet Flames: Structure, Scaling, and Effects of Heat Release. Report No. TSD-121*, Thermosciences Division, Stanford University.
- HASSELBRINK, E. F. & MUNGAL, M. G. 1998 Characteristics of the velocity field near the instantaneous base of lifted non-premixed turbulent jet flames. *Proc. Twenty-Seventh Symp. (Int'l) on Combustion, The Combustion Institute, Pittsburgh, PA* 867-873.
- KELMAN, J. B., ELTOBAJI, A. J. & MASRI, A. R. 1998 Laser imaging in the stabilization region of turbulent lifted flames. *Comb. Sci. Tech.* **135**, 117-134.
- MAUREY, C., CESSOU, A. & STEPOWSKI, D. 1998 Simultaneous PIV and OH planar LIF in the stabilization region of a lifted turbulent jet flame. *Proc. 9th Int'l Symp. on Appl. of Laser Techniques to Fluid Mech., Lisbon*, 25.3.1-25.3.8.
- MÜLLER, C. M., BREITBACH, H. & PETERS, N. 1994 Partially premixed turbulent flame propagation in jet flames. *Proc. Twenty-Fifth Symp. (Int'l) on Combustion, The Combustion Institute, Pittsburgh, PA* 1099-1106.

- MUÑIZ, L. & MUNGAL, M. G. 1997 Instantaneous flame-stabilization velocities in lifted-jet diffusion flames. *Comb. Flame* **111**, 16-31.
- PETERS, N. & WILLIAMS, F. A. 1983 Liftoff characteristics of turbulent jet diffusion flames. *AIAA J.* **21**, 423-429.
- PITTS, W. M. 1988 Assessment of theories for the behavior and blowout of lifted, turbulent-jet flames. *Proc. Twenty-Second Symp. (Int'l) on Combustion, The Combustion Institute, Pittsburgh, PA.* 809-816.
- REID, R. C., PRAUSNITZ, J. M. & POLING, B. E. 1987 *The Properties of Gases and Liquids (4th ed.)*. McGraw-Hill, New York.
- RUETSCH, G. R., VERVISCH, L. & LIÑÁN, A. 1995 Effects of heat release on triple flames. *Phys. Fluids*. **7**, 1447-1454.
- SCHEFER, R. W., NAMAZIAN, M. & KELLY, J. 1994 Stabilization of lifted turbulent-jet flames. *Comb. Flame*. **99**, 75-86.
- SCHEFER, R. W. & GOIX, P. J. 1998 Mechanism of flame stabilization in lifted, turbulent-jet flames. *Comb. Flame*. **112**, 559-574.
- SU, L. K., HAN, D. & MUNGAL, M. G. 2000 Measurements of velocity and fuel concentration in the stabilization region of lifted jet diffusion flames. *Proc. Twenty-Eighth Symp. (Int'l) on Combustion, The Combustion Institute, Pittsburgh, PA.*
- THURBER, M. C. 1999 *Acetone Laser-Induced Fluorescence for Temperature and Multiparameter Imaging in Gaseous Flows. Report No. TSD-120*, Thermosciences Division, Stanford University, 1999.
- VANQUICKENBORNE, L. & VAN TIGGELEN, A. 1966 The stabilization mechanism of lifted turbulent diffusion flames. *Comb. Flame*. **10**, 59-69.
- VEYNANTE, D., VERVISCH, L., POINSOT, T., LIÑÁN, A. & RUETSCH, G. R. 1994 Triple flame structure and diffusion flame stabilization. *Summer Program Proceedings*, Center for Turbulence Research, NASA Ames/Stanford Univ. 55-73.
- WATSON, K. A., LYONS, K. M., DONBAR, J. M. & CARTER, C. D. 1999a Scalar and velocity field measurements in a lifted CH₄-air diffusion flame. *Comb. Flame*. **117**, 257-271.
- WATSON, K. A., LYONS, K. M., DONBAR, J. M. & CARTER, C. D. 1999b Observations on the leading edge in lifted flame stabilization. *Comb. Flame*. **119**, 199-202.
- WESTERWEEL, J., DABIRI, D. & GHARIB, M. 1997 The effect of a discrete window offset on the accuracy of cross-correlation analysis of PIV recordings. *Exp. Fluids*. **23**, 20-28.

Stochastic modeling of scalar dissipation rate fluctuations in non-premixed turbulent combustion

By Heinz Pitsch AND Sergei Fedotov†

1. Motivation and objectives

In non-premixed combustion chemical reactions take place when fuel and oxidizer mix on a molecular level. The rate of molecular mixing can be expressed by the scalar dissipation rate, which is for the mixture fraction Z defined as

$$\chi = 2D_Z (\nabla Z)^2, \quad (1.1)$$

where D_Z is the diffusion coefficient of the mixture fraction. The scalar dissipation rate appears in many models for turbulent non-premixed combustion as, for instance, the flamelet model (Peters (1984), Peters (1987)), the Conditional Moment Closure (CMC) model (Klimenko & Bilger (1999)), or the compositional pdf model (O'Brien (1980), Pope (1985)). In common technical applications, it has been found that if the scalar dissipation rates are much lower than the extinction limit, fluctuations of this quantity caused by the turbulence do not influence the combustion process (Kuznetsov & Sabel'nikov (1990), Pitsch & Steiner (2000)). However, it has been concluded from many experimental (Saitoh & Otsuka (1976)) and theoretical studies (Haworth *et al.* (1988), Mauss *et al.* (1990), Barlow & Chen (1992), Pitsch *et al.* (1995)) that there is a strong influence of these fluctuations if conditions close to extinction or auto-ignition are considered. For instance, in a system where the scalar dissipation rate is high enough to prohibit ignition, random fluctuations might lead to rare events with scalar dissipation rates lower than the ignition limit, which could cause the transition of the whole system to a burning state.

In this study, we investigate the influence of random scalar dissipation rate fluctuations in non-premixed combustion problems using the unsteady flamelet equations. These equations include the influence of the scalar dissipation rate and have also been shown to provide very reasonable predictions for non-premixed turbulent combustion in a variety of technical applications (Pitsch *et al.* (1996), Pitsch *et al.* (1998), Barths *et al.* (1998)). However, it is clear that these equations are actually not capable of describing all of the features which might occur in turbulent non-premixed flames. For instance, in jet diffusion flames, local extinction events might occur close to the nozzle because of high scalar dissipation rates. These extinguished spots might reignite downstream, not by auto-ignition, but by heat conduction and diffusive mass exchange with the still burning surroundings. It should be kept in mind that the motivation in this work is not to predict actual turbulent reacting flows, but to study the dynamical system defined by the equations described in the following section. The advantage of the present simplified approach allows a study of the extinction process isolated from auto-ignition and re-ignition events.

† UMIST, Manchester, England

The basic purpose of this paper is to analyze how random fluctuations of the scalar dissipation rate can affect extinction of non-premixed combustible systems. The approach, based on stochastic differential equations, allows us to take random extinction events into account. In this case the critical conditions must be different from those involving deterministic situations. Here, we look at these phenomena in terms of noise-induced transitions theory, where multiplicative noise of sufficient intensity can drastically change the behavior of a system (Horsthemke & Lefever (1984)). In the present case, the probability density function for the temperature in the reaction zone may undergo qualitative changes as the intensity of random fluctuations increases. It should be noted that a similar analysis has been done in a series of works on the stochastic analysis of thermal ignition of explosive systems in (Buyevich *et al.* (1993), Fedotov (1992), Fedotov (1993)).

Oberlack *et al.* (1999) have investigated the influence of Damköhler number fluctuations in a well-stirred reactor. The fundamental difference compared to the present study is that in a well stirred reactor the mixing process is assumed to be infinitely fast. The Damköhler number, therefore, represents the residence time rather than the mixing time and appears in the non-dimensional chemical source term. Hence, imposing stochastic variations of the Damköhler number corresponds to a fluctuating chemical source term. Here, however, the fluctuating quantity is the scalar dissipation rate, which appears as a diffusion coefficient. The response of the mixing field to this fluctuating diffusion coefficient and the interaction with the chemical source term are investigated. Moreover, in the present formulation we allow for temporal changes of the fluctuating quantity and also consider its pdf.

In this paper, we will first present the non-dimensional flamelet equations for a one-step global reaction. With this assumption the system can be reduced to a single equation for the temperature. We will then derive stochastic differential equations for the temperature and the scalar dissipation rate. These equations lead to a partial differential equation for the joint probability density function of the temperature and the scalar dissipation rate. This equation will be discussed and numerical solutions will be presented.

2. Governing equations

2.1. Flamelet equations

Assuming an irreversible one-step reaction of the form $\nu_F F + \nu_O O \rightarrow P$, where F, O, and P denote fuel, oxidizer, and reaction product, respectively, the flamelet equations for the mass fractions of fuel Y_F , oxidizer Y_O , reaction product Y_P , and the temperature T , can be written as

$$\frac{\partial Y_i}{\partial t} - \frac{\chi}{2} \frac{\partial^2 Y_i}{\partial Z^2} + \nu_i W_i w = 0, \quad i = F, O, P \quad (2.1)$$

$$\frac{\partial T}{\partial t} - \frac{\chi}{2} \frac{\partial^2 T}{\partial Z^2} - \frac{Q}{c_p} w = 0. \quad (2.2)$$

Here, ν_i are the stoichiometric coefficients, W_i the molecular weights, t is the time, ρ the density, c_p the specific heat capacity at constant pressure, and Q is the heat of reaction defined as $Q = -\sum_i \nu_i W_i h_i$, where h_i denotes the enthalpy of species i . The mixture fraction Z is defined as

$$Z = \frac{\hat{\nu} Y_F - Y_O + Y_{O,2}}{\hat{\nu} Y_{F,1} + Y_{O,2}} \quad \text{with} \quad \hat{\nu} = \frac{\nu_O W_O}{\nu_F W_F}, \quad (2.3)$$

where the subscripts 1 and 2 refer to the conditions in the fuel stream and the oxidizer stream, respectively.

The parameter χ appearing in Eqs. (2.1) and (2.2) is the scalar dissipation rate, which has already been defined by Eq. (1.1). The reaction rate per unit mass w is given by

$$w = \rho \frac{Y_F Y_O}{W_F W_O} A \exp\left(-\frac{E}{\mathcal{R}T}\right), \quad (2.4)$$

where A is the frequency factor and E the activation energy of the global reaction, respectively. \mathcal{R} is the universal gas constant.

2.2. Non-dimensionalization

In order to investigate the flamelet equations with respect to the relevant non-dimensional parameters, it is convenient to introduce the non-dimensional temperature θ and mass fractions of fuel y_F , oxidizer y_O , and reaction product y_P as

$$\theta = \frac{T - T_{st,u}}{T_{st,b} - T_{st,u}}, \quad y_F = \frac{Y_F}{Y_{F,st,u}}, \quad y_O = \frac{Y_O}{Y_{O,st,u}}, \quad y_P = (\nu + 1) \frac{\nu_F W_F}{\nu_P W_P} \frac{Y_P}{Y_{F,1}}, \quad (2.5)$$

where the index st refers to stoichiometric conditions and the unburnt values of temperature, fuel, and oxidizer at stoichiometric conditions are given by

$$T_{st,u} = T_2 + (T_1 - T_2) Z_{st}, \quad Y_{i,st,u} = Y_{i,2} + (Y_{i,1} - Y_{i,2}) Z_{st}, \quad i = F, O. \quad (2.6)$$

The adiabatic temperature for complete conversion of fuel to products is

$$T_{st,b} = T_{st,u} + \frac{L}{c_p}, \quad L = \frac{Y_{F,1} Q}{W_F \nu_F (\nu + 1)} \quad \nu = \hat{\nu} \frac{Y_{F,1}}{Y_{O,2}}. \quad (2.7)$$

With these definitions and Eq. (2.3), the mixture fraction can be expressed as

$$Z = \frac{\nu y_F - y_O + 1}{\nu + 1}, \quad (2.8)$$

from which the stoichiometric mixture fraction

$$Z_{st} = \frac{1}{\nu + 1} \quad (2.9)$$

follows.

The non-dimensional time τ is given by

$$\tau = \frac{\chi_{st,0}}{a} t \quad \text{with} \quad a = 2\Delta Z \cdot Z_{st}(1 - Z_{st}) = \frac{2\Delta Z \nu}{(1 + \nu)^2}, \quad (2.10)$$

where the reference value for the scalar dissipation rate $\chi_{st,0}$ and the parameter ΔZ will be introduced below.

The non-dimensional scalar dissipation rate x , the Damköhler number Da , and the Zeldovich number Ze are defined as

$$x = \frac{\chi}{\chi_{st,0}}, \quad Da = \frac{\nu \nu_F a \rho_{st,u} Y_{O,2}}{(\nu + 1) W_O} \frac{A}{\chi_{st,0}} \exp(-\beta_{ref}) \quad (2.11)$$

$$Ze = \alpha \beta, \quad \alpha = \frac{T_{st,b} - T_u}{T_{st,b}}, \quad \beta = \frac{E}{\mathcal{R}T_{st,b}}. \quad (2.12)$$

With the assumption of constant molecular weight of the mixture, the density ρ can

be expressed in terms of the non-dimensional temperature θ as

$$\rho = \frac{(1 - \alpha)}{1 - \alpha(1 - \theta)} \rho_{st,u}. \quad (2.13)$$

Introducing these definitions into the flamelet equations, Eqs. (2.1) and (2.2), yields

$$\frac{\partial y_F}{\partial \tau} - \frac{ax}{2} \frac{\partial^2 y_F}{\partial Z^2} + \frac{1}{\nu + 1} \omega = 0 \quad (2.14)$$

$$\frac{\partial y_O}{\partial \tau} - \frac{ax}{2} \frac{\partial^2 y_O}{\partial Z^2} + \frac{\nu}{\nu + 1} \omega = 0 \quad (2.15)$$

$$\frac{\partial y_P}{\partial \tau} - \frac{ax}{2} \frac{\partial^2 y_P}{\partial Z^2} - \omega = 0 \quad (2.16)$$

$$\frac{\partial \theta}{\partial \tau} - \frac{ax}{2} \frac{\partial^2 \theta}{\partial Z^2} - \omega = 0, \quad (2.17)$$

where the non-dimensional chemical source term is given by

$$\omega = \text{Da} \frac{(\nu + 1)^2 (1 - \alpha) \exp(\beta_{\text{ref}} - \beta)}{\nu (1 - \alpha(1 - \theta))} y_F y_O \exp\left(-Z e \frac{1 - \theta}{1 - \alpha(1 - \theta)}\right). \quad (2.18)$$

The boundary conditions for Eqs. (2.14) - (2.17) are

$$Z = 0 : \quad y_{F,2} = 0, \quad y_{O,2} = 1, \quad y_{P,2} = 0, \quad \theta_2 = 0 \quad (2.19)$$

$$Z = 1 : \quad y_{F,1} = 1, \quad y_{O,1} = 0, \quad y_{P,1} = 0, \quad \theta_1 = 0. \quad (2.20)$$

2.3. Coupling functions

Adding Eqs. (2.14), (2.15), and (2.17) yields a conservation equation for $y_F + y_O + \theta$ as

$$\frac{\partial}{\partial \tau} (y_F + y_O + \theta) - \frac{ax}{2} \frac{\partial^2}{\partial Z^2} (y_F + y_O + \theta) = 0. \quad (2.21)$$

The boundary conditions for the conserved scalar can be determined from Eqs. (2.19) and (2.20) to be unity at both sides. Then with the unburnt state as initial condition, the solution of Eq. (2.21) is given by

$$y_F + y_O + \theta = 1. \quad (2.22)$$

Note that this particular choice of the initial condition does not restrict the solution since it is a requirement of every possible physical initial condition that it has to be realizable from the unburnt state. Since the non-dimensional product mass fraction y_P and temperature θ are governed by a mathematically similar flamelet equation (Eqs. (2.16) and (2.17)) and have the same boundary and initial conditions, it follows that

$$y_P = \theta, \quad (2.23)$$

which shows that Eq. (2.22) represents the mass conservation condition.

With Eq. (2.22) and the definition of the mixture fraction, Eq. (2.8), the mass fractions of fuel and oxidizer can be expressed in terms of mixture fraction and temperature as

$$y_O = 1 - Z - \frac{\nu}{\nu + 1} \theta = 1 - Z - (1 - Z_{st}) \theta \quad (2.24)$$

$$y_F = Z - \frac{\theta}{\nu + 1} = Z - Z_{st} \theta \quad (2.25)$$

and the chemical reaction rate, defined in Eq. (2.18), as

$$\omega = \text{Da} \frac{(1 - \alpha) \exp(\beta_{\text{ref}} - \beta)}{1 - \alpha(1 - \theta)} \left(\frac{Z}{Z_{\text{st}}} - \theta \right) \left(\frac{1 - Z}{1 - Z_{\text{st}}} - \theta \right) \exp \left(-Z e \frac{1 - \theta}{1 - \alpha(1 - \theta)} \right). \quad (2.26)$$

With Eq. (2.26) the flamelet equation for the non-dimensional temperature given by Eq. (2.17) depends only on the temperature itself and can be integrated without solving the equations for the mass fractions of fuel, oxidizer, and product. If desired, these can be computed from Eqs. (2.23), (2.24), and (2.25).

2.4. Stochastic differential equations

In this section we want to derive an equation for the joint pdf of the temperature and the scalar dissipation rate. To complete Eq. (2.17) we need a stochastic differential equation (SDE) that governs the evolution of the scalar dissipation rate.

We consider a Stratonovich SDE given by Horsthemke & Lefever (1984)

$$d\chi_{\text{st}} = f(\chi_{\text{st}}) dt + \sigma \varphi(\chi_{\text{st}}) \circ dW(t), \quad (2.27)$$

where $W(t)$ denotes a Wiener process. In Eq. (2.27) the first term on the right-hand side is a drift term, the second a random term. The stationary probability density function corresponding to the Stratonovich SDE can be found to be

$$p_s(\chi_{\text{st}}) = \frac{N}{\sigma \varphi(\chi_{\text{st}})} \exp \left(\int_0^{\chi_{\text{st}}} \frac{2f(z)}{\sigma^2 \varphi^2(z)} dz \right). \quad (2.28)$$

It is well known that a good approximation for a stationary pdf of $\chi_{\text{st}}(t)$ is a lognormal distribution (Peters (1983)) given as

$$p_s(\chi_{\text{st}}) = \frac{1}{\chi_{\text{st}} \sqrt{2\pi\sigma^2}} \exp \left(-\frac{(\ln \chi_{\text{st}} - \ln \chi_{\text{st},0})^2}{2\sigma^2} \right), \quad (2.29)$$

from which it can easily be shown that the mean value of χ_{st} is

$$\bar{\chi}_{\text{st}} = \int_0^\infty \chi_{\text{st}} p_s(\chi_{\text{st}}) d\chi_{\text{st}} = \chi_{\text{st},0} \exp \left(\frac{\sigma^2}{2} \right). \quad (2.30)$$

To find $f(\chi_{\text{st}})$ and $\varphi(\chi_{\text{st}})$, one needs to equate Eqs. (2.29) and (2.28). From this we obtain

$$f(\chi_{\text{st}}) = -(\ln \chi_{\text{st}} - \ln \chi_{\text{st},0}) \frac{\chi_{\text{st}}}{t_\chi}, \quad \varphi(\chi_{\text{st}}) = \sqrt{\frac{2}{t_\chi}} \chi_{\text{st}}, \quad N = \frac{1}{\sqrt{\pi t_\chi}}. \quad (2.31)$$

For dimensional reasons a characteristic time scale t_χ has been introduced, which appears as a parameter of the problem. This time scale is associated with the time to reach a statistically stationary state. Therefore, it does not appear in the stationary pdf given by Eq. (2.29). The scalar dissipation rate $\chi(t)$ then obeys the following SDE

$$d\chi_{\text{st}} = -(\ln \chi_{\text{st}} - \ln \chi_{\text{st},0}) \frac{\chi_{\text{st}}}{t_\chi} dt + \sigma \sqrt{\frac{2}{t_\chi}} \chi_{\text{st}} \circ dW(t). \quad (2.32)$$

In non-dimensional form, this equation can be rewritten as

$$dx_{\text{st}} = -\frac{x_{\text{st}}}{\delta} \ln x_{\text{st}} d\tau + \sigma \sqrt{\frac{2}{\delta}} x_{\text{st}} \circ dW(\tau). \quad (2.33)$$

Here, $\delta = t_\chi \chi_{st,0}/a$ represents the ratio of the characteristic time scales of Eqs. (2.33) and (2.2). In a turbulent flow, the time scale t_χ would be modeled by the integral time scale of the turbulence or the scalar (Pope (2000)). Hence, t_χ can be expressed as

$$t_\chi = \frac{C_0 \overline{Z'^2}}{\chi_{st,0} \exp\left(\frac{\sigma^2}{2}\right)} \quad (2.34)$$

from which follows that

$$\delta = \frac{C_0 \overline{Z'^2}}{2\Delta Z \cdot Z_{st}(1 - Z_{st}) \exp\left(\frac{\sigma^2}{2}\right)}, \quad (2.35)$$

where C_0 is a constant and $\overline{Z'^2}$ is the mixture fraction variance. This shows that δ is independent of the mean scalar dissipation rate. Here, $\delta = 1$ will be assumed, which for $C_0 = 1$, $Z_{st} = 0.5$, and $\sigma = 1$ roughly corresponds to $Z' = 0.2$.

From a mathematical point of view, Eq. (2.17) with the source term Eq. (2.26) and the random scalar dissipation rate is a nonlinear stochastic partial differential equation, which can be solved but is very difficult to work with analytically. One way to analyze this equation is to derive the corresponding equation for the probability density functional for the temperature distribution $\theta(Z)$ (Fedotov (1992), Fedotov (1993)). However, since the random parameter $x(\tau, Z)$ appears in Eq. (2.17) as a multiplicative noise, it would be very difficult to obtain reasonable results. In order to simplify the problem, we will derive ordinary stochastic differential equations (SDE) for these quantities by modeling the diffusion term in Eq. (2.17).

It has been shown by Peters (1983) that these linear temperature profiles in the outer non-reactive structure can be found as the first order solution of an asymptotic analysis of the flamelet equations assuming one-step global chemistry. The assumption of linear temperature profiles in the outer structure will now be used for an approximation of the diffusion term appearing in Eq. (2.17).

The diffusion term evaluated at stoichiometric conditions can be written as a finite difference approximation over the reaction zone of width ΔZ as

$$\frac{\partial^2 T}{\partial Z^2} \Big|_{Z_{st}} \approx \frac{1}{\Delta Z} \left(\frac{\partial T}{\partial Z} \Big|^{+} - \frac{\partial T}{\partial Z} \Big|^{-} \right). \quad (2.36)$$

If the temperature gradients appearing in this expression are evaluated with the assumption of linear profiles in the non-reactive diffusion zones, the diffusion term can be approximated as

$$\frac{\partial^2 T}{\partial Z^2} \Big|_{Z_{st}} \approx -\frac{1}{\Delta Z} \left(\frac{T_{st} - T_1}{1 - Z_{st}} - \frac{T_2 - T_{st}}{Z_{st}} \right) = -\frac{T_{st} - T_{st,u}}{\Delta Z Z_{st} (1 - Z_{st})} = -\frac{(T_{st,b} - T_{st,u})}{\Delta Z Z_{st} (1 - Z_{st})} \theta_{st}. \quad (2.37)$$

Here, it has to be assumed that the reaction zone thickness ΔZ is independent of the scalar dissipation rate. Then, ΔZ is a constant which appears in the Damköhler number. The actual choice of ΔZ then only changes the value of the Damköhler number and is of no consequence for the conclusions of the paper. The validity of this assumption has been numerically evaluated by Cha (2000).

Introducing Eqs. (2.37) and (2.26) into Eq. (2.17) formulated at $Z = Z_{st}$ yields

$$\frac{d\theta_{st}}{d\tau} + x(\tau) \theta_{st} - \omega(\theta_{st}) = 0 \quad (2.38)$$

with

$$\omega = \text{Da} \frac{(1 - \alpha) \exp(\beta_{\text{ref}} - \beta)}{1 - \alpha(1 - \theta_{\text{st}})} (1 - \theta_{\text{st}})^2 \exp\left(-Z e \frac{1 - \theta_{\text{st}}}{1 - \alpha(1 - \theta_{\text{st}})}\right). \quad (2.39)$$

2.5. Joint probability density function

Now we are in a position to analyze how random fluctuations of the scalar dissipation rate can influence the non-premixed combustion process. It follows from Eqs. (2.38) and (2.33) that the pair process $(\theta_{\text{st}}(\tau), x_{\text{st}}(\tau))$ is Markovian, and therefore their probability density function $p = p(\tau, x_{\text{st}}, \theta_{\text{st}})$ is governed by the Fokker-Planck equation

$$\frac{\partial p}{\partial \tau} - \frac{1}{\delta} \frac{\partial}{\partial x_{\text{st}}} ((\ln x_{\text{st}} - \sigma^2) x_{\text{st}} p) + \frac{\partial}{\partial \theta_{\text{st}}} ((-x \theta_{\text{st}} + w(\theta_{\text{st}})) p) = \frac{\sigma^2}{\delta} \frac{\partial^2}{\partial x_{\text{st}}^2} (x_{\text{st}}^2 p) \quad (2.40)$$

with $0 < x_{\text{st}} < \infty$, $0 < \theta_{\text{st}} < 1$, and the boundary conditions

$$p(\tau, 0, \theta_{\text{st}}) = p(\tau, \infty, \theta_{\text{st}}) = p(\tau, x_{\text{st}}, 0) = p(\tau, x_{\text{st}}, 1) = 0. \quad (2.41)$$

It is convenient to introduce the natural logarithm of the stoichiometric scalar dissipation rate as a new independent variable

$$x_{\text{ln}} = \ln x_{\text{st}}. \quad (2.42)$$

The pdf of x_{ln} can then be obtained by the normalization condition

$$p(x_{\text{st}}) = \frac{p_{\text{ln}x}}{x_{\text{st}}} \quad (2.43)$$

and Eq. (2.40) can be written as

$$\frac{\partial p_{\text{ln}x}}{\partial \tau} - \frac{1}{\delta} \frac{\partial}{\partial x_{\text{ln}}} (x_{\text{ln}} p_{\text{ln}x}) + \frac{\partial}{\partial \theta_{\text{st}}} ((-e^{x_{\text{ln}}} \theta_{\text{st}} + \omega) p_{\text{ln}x}) - \frac{\sigma^2}{\delta} \frac{\partial^2 p_{\text{ln}x}}{\partial x_{\text{ln}}^2} = 0. \quad (2.44)$$

The boundary conditions are given by

$$p_{\text{ln}x}(\tau, -\infty, \theta_{\text{st}}) = p_{\text{ln}x}(\tau, \infty, \theta_{\text{st}}) = p_{\text{ln}x}(\tau, x_{\text{ln}}, 0) = p_{\text{ln}x}(\tau, x_{\text{ln}}, 1) = 0. \quad (2.45)$$

Note that, as shown by Eq. (2.43), the distribution $p_{\text{ln}x}$ is different from p and the maximum will in general be at a different value of the scalar dissipation rate. However, since both functions can easily be converted into each other, the conclusions do not depend on the choice of the formulation used for the analysis.

3. Numerical solution

Equation (2.44) has been solved numerically using a 4th order Runge-Kutta scheme with adaptive step-size control. The convection term in the x_{ln} -direction has been discretized using central differences, the convection term in the θ_{st} -direction by a robust, globally second order upwind scheme as given by Koren (1996). The equations are solved on a 300×300 equidistant grid. The numerical time-step is restricted by a CFL condition which is imposed by the high convection velocity in the θ_{st} -direction at high scalar dissipation rate. This can be observed in Fig. 2, which will be described below. The initialization is performed with a numerical δ -function at some point in the $x_{\text{ln}}-\theta_{\text{st}}$ -space.

4. Results and discussion

In this section we will first provide a general discussion of Eq. (2.44) and the parameters Da , Ze , and α appearing in this equation. Numerical solutions of Eq. (2.44) will then be presented for a variation of the scalar dissipation rate variance σ , and the results will be discussed.

Numerical solutions of Eq. (2.44) will then be presented. The results for different values of the scalar dissipation rate variance σ will be discussed.

4.1. General discussion

Equation (2.44) is a two-dimensional unsteady partial differential equation depending on x_{ln} and θ_{st} . In the direction of x_{ln} , the equation reveals a convective term and a diffusion term. The convective term describes the relaxation to the mean. The mean value is achieved when the convection velocity is zero. This implies that the mean value of the non-dimensional scalar dissipation rate is $x_{\text{ln}} = 0$, which follows trivially from the normalization of χ_{st} . However, it is interesting to note that only the scalar dissipation rate itself determines the speed at which it relaxes to its mean. The diffusion term describes the broadening of the pdf by fluctuations of the scalar dissipation rate with σ^2 appearing as the diffusion coefficient.

In the direction of θ_{st} , Eq. (2.44) only reveals a convection term. Setting the convection velocity $V_{\theta_{\text{st}}} = -e^{x_{\text{ln}}}\theta_{\text{st}} + \omega$ equal to zero yields the steady state relation between the temperature and the scalar dissipation rate in the absence of scalar dissipation rate fluctuations as

$$x(\theta_{\text{st}}) = Da \exp\left(\frac{Ze}{\alpha}\bigg|_{\text{ref}} - \frac{Ze}{\alpha}\right) \frac{(1-\alpha)(1-\theta_{\text{st}})^2}{\theta_{\text{st}}(1-\alpha(1-\theta_{\text{st}}))} \exp\left(-Ze\frac{1-\theta_{\text{st}}}{1-\alpha(1-\theta_{\text{st}})}\right). \quad (4.1)$$

This relation describes the so called S-shaped curve for non-premixed combustion (Peters (1984)), which depends on three parameters: the Damköhler number Da , the Zeldovich number Ze , and the heat release parameter α , where Ze and α only depend on the chemistry.

Figure 1 shows S-shaped curves from solutions of Eq. (4.1) for different values of these parameters†. It is well known and will be shown in the following discussion that stable solutions can only be achieved for the upper and the lower branch, whereas solutions given by the middle branch are unstable. Considering the fact that the S-shaped curves shown in Fig. 1 represent states with zero convection velocity in the direction of θ_{st} , it can be seen from Eq. (2.44) that the convection velocity $V_{\theta_{\text{st}}}$ is positive for scalar dissipation rates smaller than $x_{\text{ln}}(\theta_{\text{st}})$ as given from Eq. (4.1) and negative for larger values. The consequence is that the convection velocity in the θ -direction is always directed away from the intermediate branch, which shows that these solutions are unstable. It also shows that starting from an unburnt solution, the scalar dissipation rate has to be decreased below the value at the lower turning point of the curve to be able to auto-ignite. This value will, therefore, be referred to as ignition scalar dissipation rate x_{ig} . Correspondingly, starting from a burning solution, the flame can only be extinguished by increasing the scalar dissipation rate over the value at the upper turning point. This value will, therefore, be called extinction scalar dissipation rate x_{ex} .

For non-premixed methane flames, the activation energy of a one-step global reaction

† For constant scalar dissipation rate this relation would be plotted as function of the Damköhler number, which would be proportional to x_{ln}^{-1} . In the present paper these curves are plotted over x_{ln} and therefore mirrored. However, we still use the phrase S-shaped curve.

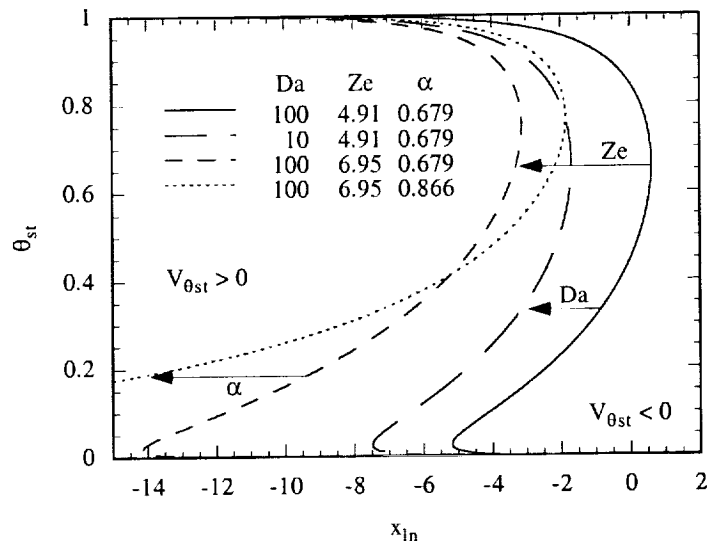


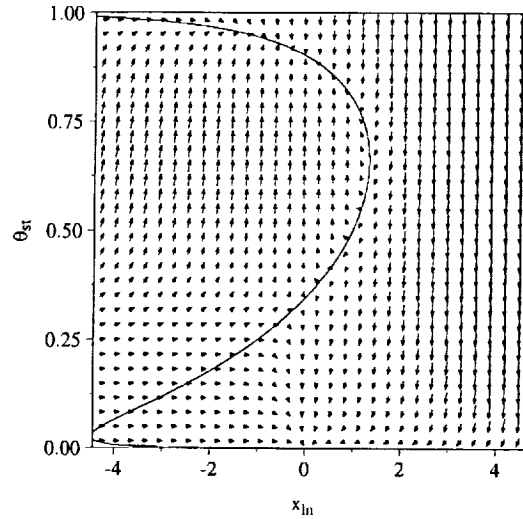
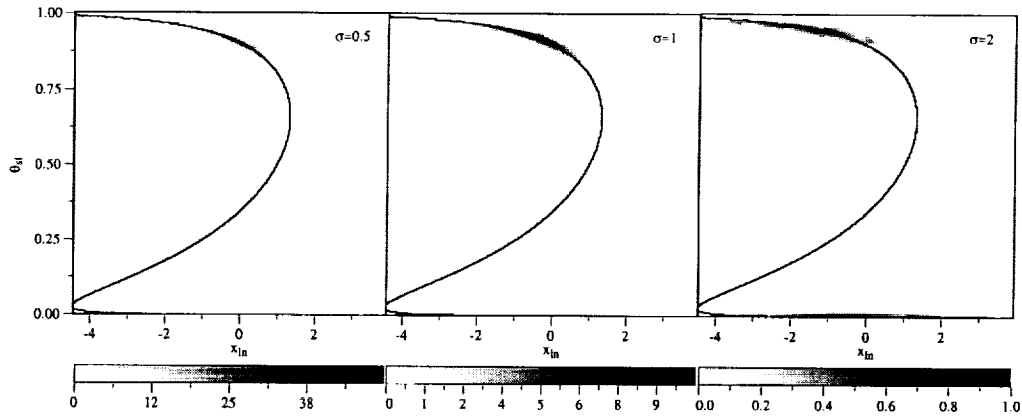
FIGURE 1. S-shaped curve determined from Eq. (4.1) for different parameter variations. Parameter changes are indicated by arrows.

can be assumed to be $E = 150 \text{ kJ/kg}$ (Seshadri (1999)). This implies a value of $\beta_{\text{ref}} = 8.03$ for a methane/air-system at ambient conditions. Then, the solid line in Fig. 1 corresponds to a case with preheated air at $T_2 = 800 \text{ K}$ and the dotted line to an air temperature of $T_2 = 300 \text{ K}$. For both cases the fuel temperature is assumed to be $T_1 = 300 \text{ K}$ and the pressure to be 1 bar. It is clear from Eq. (4.1) and it can be seen in Fig. 1 that a variation in the Damköhler number simply shifts the curve. In contrast, a variation of the Zeldovich number leads to moderately lower scalar dissipation rate for extinction and a strongly decreased ignition scalar dissipation rate.

The strongest influence however, can be seen by changing the heat release parameter. Although by increasing α the extinction scalar dissipation rate is only slightly increased, the ignition scalar dissipation rate is decreased very strongly to a value of approximately $x_{\text{ln,ig}} \approx -40$ corresponding to $x_{\text{ig}} \approx 10^{-17}$ for the example shown in Fig. 1. This merely shows that auto-ignition of methane at ambient conditions is almost impossible.

Figure 2 shows a two-dimensional vector representation of the velocities of particles in the $\theta_{\text{st}}-x_{\text{ln}}$ space, where the term particle is defined by a point and the associated velocity in this space. This figure again clearly shows that the pdf tends to move to $x_{\text{ln}} = 0$ and generally away from the unstable branch. However, at low temperature and low scalar dissipation rate on the left side of the S-shaped curve, for instance, the driving force in the direction of the mean scalar dissipation rate is so strong that particles might cross the unstable branch. Even though these particles were initially in a regime which would for constant x_{ln} lead to ignition, these particles will then be attracted by the lower branch.

In the present example this effect is not so obvious for particles originating from a burning state with a scalar dissipation rate higher than the extinction limit, which would be located in the upper right corner in Fig. 2. These particles can also change during the extinction process to lower scalar dissipation rates and might cross the S-shaped curve. This would lead to a recovery to the burning state. It has been discussed before and is indicated in Fig. 1 that, in the absence of scalar dissipation rate changes, all particles on the left side of the unstable branch of the S-shaped curve will change to the burning

FIGURE 2. Convection velocities in θ_{st} - x_{in} space.FIGURE 3. Calculated joint θ_{st} - x_{in} probability density function at $\tau = 5$.

state, whereas particles on the right will change to the non-burning state. However, it has clearly been demonstrated here that this is different in the case of a fluctuating scalar dissipation rate, where the unstable branch does not uniquely separate these two regimes.

4.2. Numerical results

For the numerical solution of the equation for the joint pdf of θ_{st} and x_{in} , Eq. (2.44), the parameters appearing in this equation have been set to $Da = 200$, $Ze = 4.91$, and $\alpha = 0.679$. As mentioned above, this corresponds to a methane/air-system, where the air is preheated to $T_2 = 800$ K. Results of the numerical simulations at time $\tau = 5$ are presented exemplarily for $\sigma = 1$ in Fig. 3. All calculations have been started with a δ -function at $\theta_{st} = 0.9$ and $x_{in} = 0$ as initial condition for the probability density function, which is then given by $p(\tau = 0, x_{in}, \theta_{st}) = \delta(x_{in}, \theta_{st} - 0.9)$.

The joint pdfs of θ_{st} and x_{in} are given in Fig. 3 for different values of the scalar dissipation rate variance σ . It can be observed that even for the low variance case $\sigma =$

0.5, the distribution of high probability density is already rather broad, extending from approximately $-1 < x_{\text{in}} < 1$ and mainly around the upper branch of the S-shaped curve. Even though this cannot be seen in Fig. 3, the numerical results show that there is already some probability to find the extinguished state around $x_{\text{in}} = 0$.

It follows from the above discussion that extinguished particles originate from burning particles, which, because of the fluctuations of the scalar dissipation rate, have experienced a scalar dissipation rate high enough to completely extinguish the particle without crossing the unstable branch of the S-shaped curve. This would result in re-ignition. The low probability of finding these high scalar dissipation rates then forces the extinguished particles to a state around $x_{\text{in}} = 0$. In a real turbulent diffusion flame, these extinguished areas could re-ignite by heat conduction from the surrounding, still burning gas. This effect, however, is not included in the current analysis. Therefore, re-ignition can only occur here if the scalar dissipation rate of an extinguished particle becomes smaller than the ignition limit. This, however, is prohibited in the present simulations by choosing the lower boundary for x_{in} larger than the ignition scalar dissipation rate. This allows study of the extinction process without the influence of auto-ignition.

It is important to recognize that because of this assumption the steady state solution is always completely non-burning. This means that, for this dynamic system scalar dissipation rate, fluctuations even of small amplitude lead to a phase transition from the burning to the non-burning state. This dynamical character would not be observed in the deterministic case.

For $\sigma = 1$ the distribution is even broader, revealing substantial probability for $-2 < x_{\text{in}} < 2$. Also, the probability of finding extinguished states is already of comparable magnitude as for the burning states. As for $\sigma = 0.5$ the region of high probability is still concentrated around the S-shaped curve, indicating that the chemistry is fast enough to compensate scalar dissipation rate fluctuations. It is also interesting to note that similar to the findings of Oberlack *et al.* (1999) there is only a very low probability of finding states between burning and extinguished. This shows that the extinction process is fast compared to other time scales of the system.

The solution for an even larger scalar dissipation rate variance of $\sigma = 2$ shows that the probability distribution is further broadened and the fraction of extinguished states is even higher. Most interesting here is the observation that, particularly at high scalar dissipation rates close to extinction, the high probability region clearly departs from the S-shaped curve. This can also be observed in Fig. 3 but to a smaller extent. The departure from the S-shaped curve indicates that the chemistry is not fast enough to relax the temperature in accordance with large scale scalar dissipation rate fluctuations to the steady solution. At low scalar dissipation rate, the high probability region is still very close to the S-shaped curve.

5. Conclusions and future work

In the present work the flamelet equations have been formulated for a one-step global reaction and used for the investigation of the influence of scalar dissipation rate fluctuations on non-premixed turbulent combustion. By modeling the diffusion term in the flamelet equation, ordinary stochastic differential equations were derived for the temperature and the scalar dissipation rate at stoichiometric mixture. From these, a Fokker-Planck equation for the joint probability density function of temperature and the scalar

dissipation rate has been derived. The equation has been discussed and numerical solutions for varying scalar dissipation rate variance provided.

The analysis shows that the S-shaped curve, which represents the steady-state solution for a given scalar dissipation rate in the absence of scalar dissipation rate fluctuations, separates the $\theta_{st}-x_{ln}$ space into two regimes, which will either lead to the burning or the extinguished state. It is also shown that scalar dissipation rate fluctuations even of small amplitude will under the present simplifications cause a phase transition from the burning to the completely extinguished state.

Numerical solutions show an increasing fraction of extinguished states for increasing scalar dissipation rate variance at a given time. It is also found that particles with a scalar dissipation rate higher than the extinction limit can recover to a burning solution during the extinction process. Therefore, for a fluctuating scalar dissipation rate, particles can cross the S-shaped curve, which thereby no longer separates regimes that uniquely lead to the extinguished or the burning state.

Furthermore, it is found that the low probability of finding high scalar dissipation rate forces particles which have been extinguished at high scalar dissipation rate to rapidly change to a state with lower scalar dissipation rate, where re-ignition could occur. For higher scalar dissipation rate variance it is observed that the high probability region clearly departs from the S-shaped curve. This indicates that the chemistry is not fast enough to relax large scale scalar dissipation rate fluctuations to the steady state solution. This has been shown to have an important implication in the application of flamelet type models in non-premixed turbulent combustion.

The presented method has been shown to provide a useful tool to study the effect of random scalar dissipation rate fluctuations. In future work, the model is to be corroborated with results from direct numerical simulations of turbulent reacting flows and the re-ignition process is to be included. The investigation of the influence of scalar dissipation rate fluctuations on auto-ignition delay times and pollutant formation could also be a worthwhile extension of the present work.

Acknowledgments

The authors gratefully acknowledge funding by the US Department of Energy in the frame of the ASCI program and the Center for Turbulence Research. We are indebted to Chong Cha for many inspiring discussions and for providing solutions of Monte Carlo simulations for the investigated problem.

REFERENCES

- BARLOW, R. S. & CHEN, J.-Y. 1992 On transient flamelets and their relationship to turbulent methane-air jet flames. *Proc. Combust. Inst.* **24**, 231-237.
- BARTHS, H., PETERS, N., BREHM, N., MACK, A., PFITZNER, M. & SMILJANOVSKI, V. 1998 Simulation of pollutant formation in a gas turbine combustor using unsteady flamelets. *Proc. Combust. Inst.* **27**, 1841-1847.
- BUYEVICH, Y. A., FEDOTOV, S. P. & TRET'YAKOV, M. V. 1993 Heterogeneous reaction affected by external noise. *Physica A*. **198**, 354-367.
- CHA, C. M. 2000 Private communication.
- FEDOTOV, S. P. 1992 Statistical model of the thermal ignition of a distributed system. *Comb. Flame*. **91**, 65-70.

- FEDOTOV, S. P. 1993 Stochastic analysis of the thermal ignition of a distributed explosive system. *Phys. Lett. A* **176**, 220-224.
- HAWORTH, D., C., DRAKE, M., C., POPE, S., B. & BLINT, R., J. 1988 The importance of time-dependent flame structures in stretched laminar flamelet models for turbulent jet diffusion flames. *Proc. Combust. Inst.* **22**, 589-597.
- HORSTHEMKE, W. & LEFEVER, R. 1984 *Noise-Induced Transitions*, Springer-Verlag.
- KLIMENKO, A. Y. & BILGER, R. W. 1999 Conditional moment closure for turbulent combustion. *Prog. Energy Combust. Sci.* **25**, 595-687.
- KOREN, B. 1996 A robust upwind discretization method for advection, diffusion and source terms. in C. B. Vreugdenhil & B. Koren (eds). *Numerical methods for advection-diffusion problems*, Vol. 45 of *Notes on Numerical Fluid Dynamics*, Vieweg Verlag, Braunschweig.
- KUZNETSOV, V. R. & SABEL'NIKOV, V. A. 1990 *Turbulence and Combustion*, Hemisphere Publishing Corp.
- MAUSS, F., KELLER, D. & PETERS, N. 1990 A lagrangian simulation of flamelet extinction and re-ignition in turbulent jet diffusion flames. *Proc. Combust. Inst.* **23**, 693-698.
- OBERLACK, M., ARLITT, R. & PETER, N. 1999 On stochastic Damköhler number variations in a homogeneous flow reactor. *Comb. Theory Modeling*, submitted.
- O'BRIEN, E. E. 1980 The probability density function (pdf) approach to reacting turbulent flows. in L. P. A. & F. A. Williams (eds). *Turbulent Reacting Flows*, Springer Verlag, pp. 185-218.
- PETERS, N. 1983 Local quenching due to flame stretch and non-premixed turbulent combustion. *Combust. Sci. Technol.* **30**, 1.
- PETERS, N. 1984 Laminar diffusion flamelet models in non-premixed turbulent combustion. *Prog. Energy Combust. Sci.* **10**, 319-339.
- PETERS, N. 1987 Laminar flamelet concepts in turbulent combustion. *Proc. Combust. Inst.* **21**, 1231-1250.
- PITSCH, H., BARTHS, H. & PETERS, N. 1996 Three-dimensional modeling of nox and soot formation in di-diesel engines using detailed chemistry based on the interactive flamelet approach. *SAE Paper 962057*.
- PITSCH, H., CHEN, M. & PETERS, N. 1998 Unsteady flamelet modeling of turbulent hydrogen/air diffusion flames. *Proc. Combust. Inst.* **27**, 1057-1064.
- PITSCH, H. & STEINER, H. 2000 Large-eddy simulation of a turbulent piloted methane/air diffusion flame (Sandia flame D). *Phys. Fluids*, submitted.
- PITSCH, H., WAN, Y. P. & PETERS, N. 1995 Numerical investigation of soot formation and oxidation under diesel engine conditions. *SAE Paper 952357*.
- POPE, S. B. 1985 Pdf methods for turbulent reactive flows. *Prog. Energy Combust. Sci.* **11**, 119.
- POPE, S. B. 2000 *Turbulent Flows*, Cambridge University Press, chapter 12.
- SAITOH, T. & OTSUKA, Y. 1976 Unsteady behavior of diffusion flames and premixed flames for count flow geometry. *Combust. Sci. Tech.* **12**, 135-146.
- SESHADRI, K. 1999 Rate-ratio asymptotics applied to flames. Paper presented at the Western States Section of the Combustion Institute, Fall 1999 Meeting, University of California at Irvine, Irvine, California.

A level-set approach to large eddy simulation of premixed turbulent combustion

By L. Duchamp de Lageneste AND H. Pitsch

1. Motivation and objectives

Large eddy simulation (LES) of premixed turbulent combustion is now considered to be a promising field. It has the potential to improve predictions of reacting flows over classical Reynolds-averaged Navier-Stokes (RANS) approaches.

Since the reaction zone thickness of premixed flames in technical devices is usually much smaller than the LES grid spacing, chemical reactions occur completely on the sub-grid scales and hence have to be modeled entirely. There are several ways to treat the problem.

One approach by Veynante *et al.* (1997) and Colin *et al.* (2000) is to thicken the flame by artificially increasing the diffusivity to be able to resolve the flame on the LES grid. In order to correct the effect on the flame propagation speed, the chemical source term has to be modified by the use of efficiency functions obtained from direct numerical simulations (DNS) (Angelberger *et al.* (2000)). The main drawback of this method is that it changes the principle underlying physical process from a transport controlled to a chemistry controlled combustion mode.

Chakravarthy *et al.* (2000) have suggested a method in which the scalar processes that can be resolved spatially and temporally are simulated on a 3D LES grid while small scales and faster subgrid combustion processes within each LES cell are simulated using the one dimensional Linear Eddy Model (LEM). This multiple scale approach, can lead to a significant increase in the complexity of the code due to the introduction of a Lagrangian volume-of-fluid (VOF) transport scheme used to track the flame in each cell and due to the definition of a grid-subgrid coupling procedure.

Another possible approach proposed by Peters in the context of RANS (Peters (1999)) is the use of a level-set approach to describe the turbulent flame front. In this methodology, the flame front is represented by an arbitrary iso-surface G_0 of a scalar field G whose evolution is described by the so-called G-equation. This equation is only valid at $G = G_0$ and is hence decoupled from other G levels. There have been various attempts to use this approach in LES of premixed turbulent combustion as well as in RANS. As the solution of the G-equation is not uniquely defined, different ways of defining the scalar G have been proposed. While Menon *et al.* (1991) and Chakravarthy *et al.* (2000) are considering G as a progress variable ($G=0$ in the fresh gases, unity in the burnt gases), Peters (1999), for instance, suggests defining G as a distance function which can be described by the condition $|\nabla G(\mathbf{x}, t)| = 1$, where the flame front is given by $G_0 = 0$.

The latter approach seems very suitable for the description of premixed flames propagation as it allows to precisely define some important geometrical quantities such as curvature or strain. Furthermore, the numerical treatment of the step profile, inherent for the progress variable formulation, is very difficult, often leading to the introduction of diffusive terms, which incorrectly broaden the flame (Kim *et al.* (2000), Menon *et al.* (1991)).

However, we will see below that the evolution equation for G does not conserve G as a distance function, and, consequently, this property has to be enforced at each time step by a so-called reinitialization procedure. Issues related to this important aspect of the level-set method will be addressed below.

Once the proper ansatz is chosen for the scalar G , one can apply the LES formalism to the evolution equation for G . We will explain the consequent modeling of the subgrid terms arising from this process in further detail in the next section. In particular, since we are interested in performing realistic 3D simulations of reactive flows, we will try to avoid introducing any artificial diffusion term in the model that would influence the accuracy of our computation.

The model is validated using data from a turbulent Bunsen burner experiment by Chen *et al.* (1996). Numerical results from the LES are compared with measured velocity and temperature data for the cold and the reactive flow.

2. Level-set approach for premixed turbulent combustion

2.1. The G -equation

The level-set approach for premixed turbulent combustion is based on the assumption that the reaction zone is much smaller than the LES grid.

The flame front can then be treated as being infinitely thin and represented by a particular iso-surface of a scalar field G . This iso-surface is then convected by the velocity field \mathbf{u} while it propagates normal to itself with the laminar burning velocity s_L . The G -field satisfies the following Hamilton-Jacobi equation known as the G -equation (Williams (1985)):

$$\rho \frac{\partial G}{\partial t} + \underbrace{\rho \mathbf{u} \cdot \nabla G}_{\text{Convection}} = \underbrace{\rho s_L |\nabla G|}_{\text{Propagation}}. \quad (2.1)$$

In this equation the balance of diffusion and chemical reactions within the flame is represented by the laminar burning velocity. Since this quantity is only defined for the flame front, Eq. 2.1 is valid only at the $G = G_0$ level.

There are two major issues concerning the numerical treatment of Eq. 2.1: The first is the necessity to avoid the formation of cusps that naturally arise from solving Eq. 2.1 and would result in numerical problems. The second is related to the fact that, if one initially defines G as the signed distance function from the flame front by setting $|\nabla G(x; t = 0)| = 1$, this property is not naturally conserved throughout the simulation, in particular when large velocity gradients are present (Sethian (1996)).

2.2. Regimes in premixed turbulent combustion

Premixed combustion can be classified in different regimes as illustrated in Fig. Fig. 1 (Peters (1999), Peters (2000)).

If l_F is the laminar flame thickness, $l_\delta = \delta l_F$ the inner layer thickness, where δ can be viewed as a measure for the reaction zone thickness (see Fig. 2), η the Kolmogorov length, l the integral turbulent lengthscale, and u' the turbulent velocity fluctuation, one can define the turbulent Reynolds number Re and two different Karlovitz numbers Ka and Ka_δ as

$$Re = \frac{u' l}{s_L l_F}, \quad Ka = \frac{l_F^2}{\eta^2}, \quad Ka_\delta = \frac{l_\delta^2}{\eta^2}. \quad (2.2)$$

The two regimes of particular practical interest are the corrugated flamelets regime

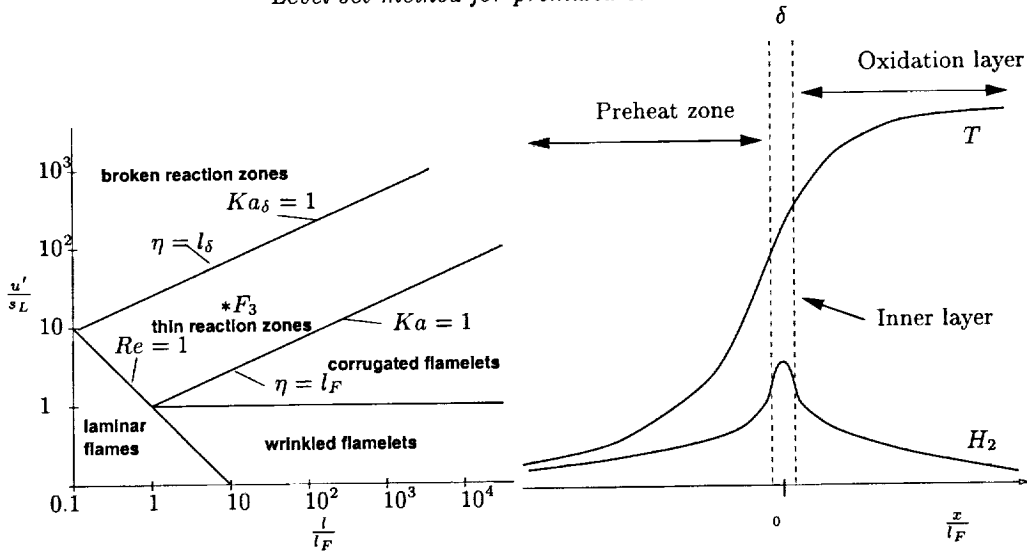


FIGURE 1. Combustion diagram.

FIGURE 2. Schematic flame structure of a laminar 1-D premixed flame.

and the thin reaction zones regime and are defined by $Re > 1$, $Ka < 1$ and $Re > 1$, $Ka > 1$, $Ka_\delta < 1$, respectively. In the corrugated flamelets regime, the entire flame structure including the preheat zone is smaller than the Kolmogorov scale ($l_F < \eta$). The interaction between flame and turbulence is, therefore, mainly kinematic, and the flame structure depicted in Fig. 2 remains quasi-steady. In the thin reaction zones regime, while the reaction zone is still smaller than the Kolmogorov scale, the smallest eddies can enter the pre-heat zone ($l_\delta < \eta < l_F$) and carry pre-heated fluid away to the unburnt side. This enhanced mixing is mainly responsible for the advancement of the front and a considerable thickening of the preheat zone.

In an LES framework, due to local variations in the turbulence intensity, combustion in both regimes might be present in a particular configuration. Hence, it is necessary to reflect the characteristics of both regimes in the governing equations.

A G-equation, valid in both regimes, has been derived by Peters (1999) as

$$\rho \frac{\partial G}{\partial t} + \rho \mathbf{u} \cdot \nabla G = \rho s_L |\nabla G| - \rho D \kappa |\nabla G|. \quad (2.3)$$

In this equation for both regimes, only the leading order terms which have been identified by an asymptotic analysis are included. These are the propagation term $s_L |\nabla G|$ in the corrugated flamelets regime and the curvature term $D \kappa |\nabla G|$ with D being the molecular diffusivity in the thin reaction zones regime.

2.3. LES modeling of the filtered G-equation

Following the classical LES filtering approach, we will decompose G and \mathbf{u} in their Favre-filtered values ($\tilde{G} = \overline{\rho G} / \bar{\rho}$, $\tilde{\mathbf{u}} = \overline{\rho \mathbf{u}} / \bar{\rho}$) and subgrid fluctuations (G' , \mathbf{u}').

Applying this formalism to Eq. 2.3 leads to:

$$\underbrace{\bar{\rho} \frac{\partial \tilde{G}}{\partial t}}_I + \underbrace{\bar{\rho} \tilde{\mathbf{u}} \cdot \nabla \tilde{G}}_{II} + \underbrace{\nabla \cdot (\bar{\rho} \mathbf{u}' G')}_III = \underbrace{(\bar{\rho} s_L) |\nabla \tilde{G}|}_{IV} - \underbrace{(\bar{\rho} D) \kappa |\nabla \tilde{G}|}_V \quad (2.4)$$

Terms I and II depend only on the filtered variables and do not require any modeling. Term V is proportional to the molecular diffusivity. This term can be expected to be small for the relatively large Reynolds numbers considered here and will therefore be neglected. As noted in Peters (1999) and Peters (2000), the turbulent transport term III cannot be modeled by a classical gradient transport approximation since this would result in an elliptic equation for \tilde{G} and contradict the mathematical nature of the original G -equation. Instead, according to Peters (1999), we will rewrite this term as the sum of a normal diffusion and a curvature term, where the normal diffusion term has to be included in the turbulent burning velocity and the curvature term is modeled as $\bar{\rho}D_t\tilde{\kappa}|\nabla\tilde{G}|$, where D_t is the turbulent eddy-diffusivity and $\tilde{\kappa}$ the filtered front curvature. Besides the fact that this model preserves the mathematical nature of the filtered G -equation, it also has the numerical advantage that the flame front will not develop any cusps since the propagation of the flame front is now a function of its own curvature (Sethian (1996)). The turbulent eddy-diffusivity D_t can be determined using the dynamic procedure (Moin *et al.* (1991)).

The remaining term to be modeled is the turbulent propagation term IV. This term can be modeled by introducing a turbulent burning velocity s_T and enforcing that the mass flow rate through the filtered and unfiltered fronts are the same, which leads to $(\rho s_L)|\nabla G| = \bar{\rho} s_T |\nabla \tilde{G}|$.

Introducing the modeled terms in the filtered G -equation reads

$$\bar{\rho} \frac{\partial \tilde{G}}{\partial t} + \bar{\rho} \tilde{\mathbf{u}} \cdot \nabla \tilde{G} = \underbrace{\bar{\rho} s_T |\nabla \tilde{G}|}_{\text{Propagation}} - \underbrace{\bar{\rho} D_t \tilde{\kappa} |\nabla \tilde{G}|}_{\text{Curvature}}. \quad (2.5)$$

To close the problem, an expression for the turbulent burning velocity s_T has still to be provided.

2.4. Modeling the turbulent burning velocity

There have been various attempts to model the turbulent burning velocity, and this problem remains one of the most important in premixed combustion.

Most models for this quantity are generally of the form:

$$\frac{s_T}{s_L} = 1 + C \left(\frac{u'}{s_L} \right)^n, \quad (2.6)$$

where n is a value that is found to depend on the combustion regime and C is a constant.

However, as pointed out by Peters (2000), in the thin reaction zones regime the turbulent burning velocity does not only depend on the ratio of the subgrid turbulent velocity to the laminar burning velocity u'/s_L , but also on the ratio of the subgrid length scale to the flame thickness Δ/l_F . An expression for s_T , valid in both the corrugated flamelets and thin reaction zone regime, has recently been proposed in the context of RANS by Peters (1999).

For LES it can be written as

$$\frac{s_T - s_L}{s_L} = -\frac{a_4 b_3^2}{2b_1} \frac{\Delta}{l_F} + \left[\left(\frac{a_4 b_3^2}{2b_1} \frac{\Delta}{l_F} \right)^2 + a_4 b_3^2 \frac{v' \Delta}{s_L l_F} \right]^{\frac{1}{2}}, \quad (2.7)$$

where Δ is the filter size and a_4 , b_1 , and b_3 are constants given in Peters (2000) for RANS. For LES, a_4 can be evaluated to be $a_4 = 1.37$. The other constants might also differ from the RANS case and can be determined by DNS.

3. Reinitialization procedure

The level set method is currently a popular method to study problems in which an interface separates regions of different physical properties (Sethian (1996)). It has been discussed above that it is often useful to define G as a distance function, and since this property is not conserved by the level set equation, this condition needs to be enforced in a different way, which is commonly called reinitialization. Several methods have been derived for the reinitialization of the level set function to a signed distance (Sethian (1996), Sussman *et al.* (1999), Russo *et al.* (2000)).

3.1. Problem formulation

Given the numerical context of our work, we decided to use the following method, first described in Sussman *et al.* (1994) and extended by Russo *et al.* (2000). It is based on solving the following p.d.e. to a steady state:

$$\begin{cases} \frac{\partial \tilde{G}}{\partial t} &= \text{sgn}(\tilde{G}^0)(1 - |\nabla \tilde{G}|) \\ \tilde{G}(\underline{x}, 0) &= \tilde{G}^0(\underline{x}) \end{cases}, \quad (3.1)$$

which can be also written as:

$$\frac{\partial \tilde{G}}{\partial t} + \text{sgn}(\tilde{G}^0) \underline{n} \cdot \nabla \tilde{G} = \text{sgn}(\tilde{G}^0), \quad (3.2)$$

where $\underline{n} = \nabla \tilde{G} / |\nabla \tilde{G}|$ is the unit normal to the level sets and $\text{sgn}(\tilde{G}^0)$ is the sign function defined by:

$$\text{sgn}(\tilde{G}^0) = \begin{cases} 1 & \text{if } \tilde{G}^0 > 0 \\ -1 & \text{if } \tilde{G}^0 < 0 \\ 0 & \text{otherwise} \end{cases} \quad (3.3)$$

Equation 3.2 clearly displays the hyperbolic nature of this equation, for which the characteristics are propagating away normally from the \tilde{G}^0 level. The steady solution \tilde{G} of Eq. 3.2 obviously satisfies $|\nabla \tilde{G}| = 1$ and has the same zero-level as \tilde{G}^0 . It is therefore the desired signed distance function.

3.2. Practical implementation

3.2.1. Narrow band method

Because the G -equation is only valid at the flame front, Eq. 3.1 does not need to be solved to a steady state in the entire domain, but only in a specified neighborhood of width L of the $\tilde{G} = 0$ surface (Sussman *et al.* (1999)). This so-called narrow-band strategy is used here to limit the impact of the reinitialization procedure on the overall computational efficiency.

3.2.2. Discretization

Due to the hyperbolic nature of Eq. 3.1, upwind methods can be used to compute the spatial derivatives. Since all of the information propagates outward from the $\tilde{G} = 0$ surface, boundary conditions do not have to be prescribed on the lateral boundaries of the domain. In the direct neighborhood of the front, a second order scheme is used to evaluate the signed distance function, and a first order scheme is used elsewhere.

A second order Runge-Kutta scheme is used for the time advancement. Furthermore,

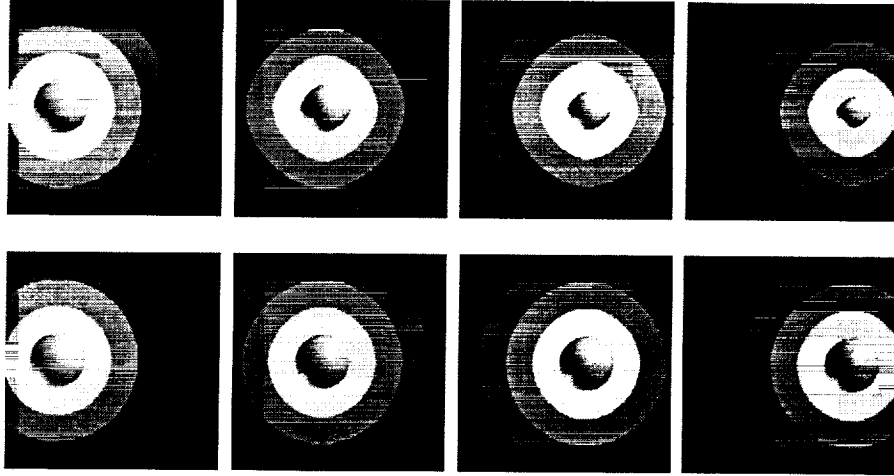


FIGURE 3. Uniform convection ($U_{conv} = 1$) of a sphere at different instants. Top: Eq. 3.1 is solved in the entire domain. Bottom: an exact method is used to determine the distance for the neighboring points of the front.

since the mesh can potentially be locally refined, we use a local time stepping strategy to alleviate the CFL condition and accelerate convergence to a steady state.

From a computational point of view, this method can easily and very efficiently be implemented in a parallel code.

3.2.3. Sub-cell accuracy

Some authors (Sethian (1996), Sussman *et al.* (1999), Russo *et al.* (2000)) have noticed that under certain conditions repeated reinitializations of the level set function could lead to a significant motion of the front. This is often attributed to the relative crudeness of the sign function involved in Eq. 3.1 and the fact that values of \tilde{G} at points on one side of the front are used to estimate spatial derivatives on the other side, which violates the upwind nature of the scheme (Russo *et al.* (2000)).

In a three-dimensional implementation, this can lead to a considerable loss of area of the \tilde{G}^0 surface. An example of this phenomenon will be given in the next section.

In a method described by Russo *et al.* (2000), a precise estimate of the distance to the \tilde{G}^0 level is computed for the points surrounding the \tilde{G}^0 surface. If this is used as a boundary condition for the upwind scheme described above, the surface of the \tilde{G}^0 level is essentially conserved.

We will also show that this method can initialize any given field to a signed distance function without any modifications, while preserving the shape of a prescribed interface. This is of practical importance when no *a-priori* initial location of the front can be proposed, as for instance during an ignition process.

3.3. Validation

3.3.1. Uniform convection of a sphere

In order to validate the reinitialization procedure described in the previous section, we compute the convection of a sphere in a uniform flow field.

The computational domain is a cylinder of radius $R = 1$ and length $L = 2$. It is

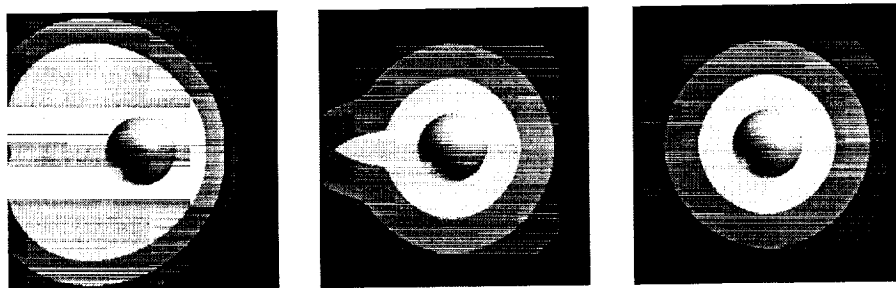


FIGURE 4. First-time initialization.

discretized using 32 points in the axial, radial, and azimuthal directions, respectively. The mesh is stretched in the radial direction towards the centerline to test the grid sensitivity of the algorithm.

The convection velocity of the sphere is prescribed by imposing a uniform inflow condition $U_{\text{conv}} = 1$ on the $x = 0$ boundary. All other boundaries are “free” (i.e. advective condition on $x = 2$ and $R = 1$). The \tilde{G} field is set to $\tilde{G}(x, r, \theta; t = 0) = \sqrt{x^2 + r^2} - 0.25$.

In a first calculation, Eq. 3.1 is solved in the whole domain. Results at different instants in time are displayed on the upper part of Fig. 3. Due to the multiple reinitialization iterations, the sphere loses area and shrinks rapidly as it is convected. Also, an influence of the mesh refinement near the centerline can be observed clearly.

In the second calculation, the upwind scheme is no longer used to reinitialize the points adjacent of the \tilde{G}^0 level. Instead, a direct estimate is used for the value of the signed distance function for these points. These values for \tilde{G} are then used as a boundary condition for the upwind scheme method. The resulting improvement of this method is demonstrated in the lower part of Fig. 3, where the sphere perfectly preserves its original form. Furthermore, the results do not reveal the grid sensitivity detected in the previous example.

3.3.2. First-time initialization

The ability of this method to initialize a given field to a signed distance function without altering the $\tilde{G} = 0$ level is demonstrated in Fig. 4. Here, a field initially defined by $\tilde{G}(x, r, \theta; t = 0) = f(x, r) \cdot \sqrt{x^2 + r^2} - 0.25$, where $f(x, r) = 0.1 + (x - 1)^2 + (r - 0.5)^2$ is a function designed to generate both large and small gradients near the \tilde{G}^0 sphere, is reinitialized to a distance function. The \tilde{G} field is progressively set to the signed distance from the \tilde{G}^0 level, while the shape of the $\tilde{G} = 0$ level is exactly preserved.

4. Numerical simulation

4.1. Experimental setup

The experimental setup studied by Chen *et al.* (1996) is a stoichiometric premixed methane-air flame, stabilized by a large pilot flame. Both incoming streams, the main jet and the pilot, have the same composition. The nozzle diameter D of the main stream is 12 mm. The pilot stream issues through a perforated plate (1175 holes of 1 mm in diameter) around the central nozzle, with an outer diameter of $5.67D$. The main stream



FIGURE 5. Instantaneous flame front location and axial velocity.

is turbulent with a Reynolds number of 23486, based on the inner nozzle diameter and a bulk velocity of $U_0 = 30$ m/s.

Experimental data is available for the cold and reactive flows at downstream stations located at $x/D = 2.5$, $x/D = 4.5$, $x/D = 6.5$, and $x/D = 8.5$, respectively.

Based on the estimated characteristic length and time scale given in Chen *et al.* (1996) ($u'/S_L = 11.9$, $l/l_f = 13.7$), flame F_3 can be identified in the combustion diagram shown in Fig. 1 to be located well within the thin reaction zones regime.

4.2. LES

We are using the code developed at the Center for Turbulence Research by Pierce (Pierce & Moin (1998)), in which the governing equations, here the filtered zero-Mach number approximation of the Navier-Stokes equations and the filtered G-equation, are solved in cylindrical coordinates. The mesh is structured and is refined in regions of high gradients around walls and in shear layers. The numerical method consists of a conservative, second-order finite-volume scheme on a staggered grid. A second-order semi-implicit time advancement is used, which alleviates the CFL restriction in regions where the grid is refined. Details about the method can be found in Akselvoll *et al.* (1996a). The code has been thoroughly validated in various studies (see Akselvoll *et al.* (1996b), Pierce & Moin (1998)).

The computational domain extends to $20D$ downstream of the nozzle and $4D$ in the radial direction. The LES grid is $256 \times 96 \times 64$, corresponding to approximately 1.6 M cells. At the inflow boundary, instantaneous velocities extracted from a separate LES of a fully developed pipe flow are prescribed. Convective conditions (Akselvoll *et al.* (1996a)) are prescribed at the outflow boundary while traction-free conditions (Boersma *et al.* (1998)) are imposed on the lateral boundary in order to allow entrainment of fluid into the domain.

5. Results and discussion

5.1. Instantaneous and mean flame front

A typical example of the instantaneous flame surface is shown in Fig. 5. The presence of small regions of high negative curvature (forming cusps toward the products side) and large regions of lower positive curvature is consistent with the fact that the flame propagation is accelerated in regions of negative curvature and slowed in regions of positive

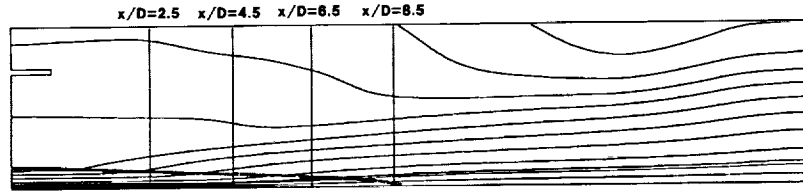


FIGURE 6. Mean flame front location and mean flow streamlines.

curvature. The acceleration of the burnt gases behind the flame front caused by the heat release is illustrated by the instantaneous field of the axial velocity given in the same figure.

This effect of dilatation induced by heat release is even more obvious in the mean quantities. The radial deflection of the mean streamlines around the time-averaged position of the turbulent flame front, which is given by a thick line, is illustrated in Fig. 6.

Due to the consumption of the unburnt mixture, the mean flame front position is converging toward the centerline. The computed time averaged axial position, where the fuel is completely consumed is at approximately $x/D = 8.6$, which is very close to the experimental value of $x/D = 8.5$ obtained by Chen *et al.* (1996). This result shows that the model for the turbulent flame speed s_T leads to a reasonable prediction of the averaged flame location.

The incoming streamlines through the upper boundary of Fig. 6 also illustrate the importance of imposing boundary conditions allowing for the entrainment of fluid into the computational domain.

5.2. Mean temperature and axial velocity

The mean radial profiles of temperature and axial velocity are shown in Fig. 7 for the different locations shown in Fig. 6 where $\langle \theta \rangle$ is the time-averaged non-dimensional temperature defined by $\langle \theta \rangle = (\langle T \rangle - T_u) / (T_b - T_u)$ and $\langle U \rangle$ is the time-averaged velocity normalized by the bulk velocity U_0 .

Significant differences can be observed between the cold and the reactive case. In the cold flow, the mean axial velocity at the centerline is decreasing much faster than in the reactive case, where the potential core with an almost constant mean axial velocity extends to an axial position where the fuel is almost consumed. Gas expansion in the reacting jet case causes the spreading rate to be higher than for the non-reactive case. Although this effect is slightly overestimated in the computation, the overall agreement between computational results and experimental data is very reasonable.

While the evolution of the mean temperature shows generally good agreement with the experimental data, the maximum temperature close to the nozzle is overestimated in the present computation. This can be attributed to heat losses to the burner surface, which are currently being neglected.

5.3. Turbulent kinetic energy

The radial profiles of the mean turbulent kinetic energy k are shown in Fig. 8 for different downstream locations. For the cold flow case, the predictions of the turbulent kinetic energy are in very good agreement with experimental data for all downstream locations. The evolution of k at the centerline is found to be very different in the cold and reactive

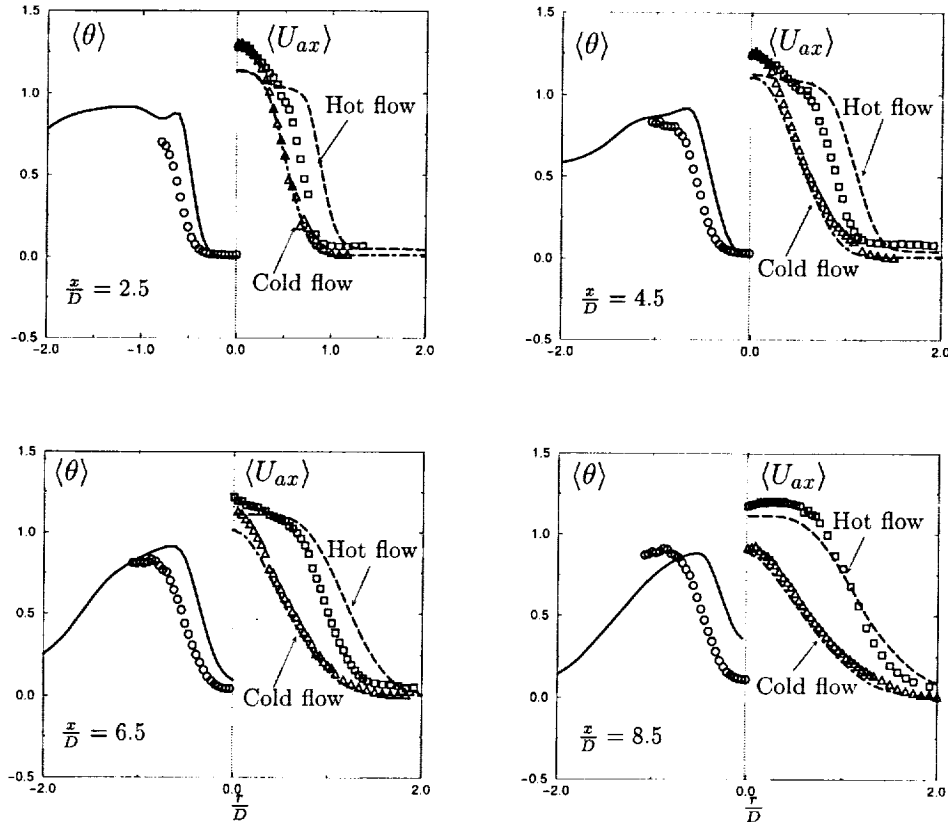


FIGURE 7. Radial profiles of the mean temperature and axial velocity at different axial positions. Symbols represent experimental data, lines are LES results.

cases. For the cold flow case, the turbulent kinetic energy is progressively increasing in downstream direction and reaches a maximum at $x/D = 8.5$, whereas it stays approximately constant for the reacting case. This result confirms that combustion strongly influences transport of turbulence toward the centerline by preventing radial mixing of turbulent kinetic energy produced within the shear layers. This important result (Chen *et al.* (1996)) is well reproduced in the simulation.

In the reactive case, the turbulent kinetic energy profile reveals two maxima, one on the burnt and one on the unburnt side of the mean flame position. At axial positions up to $x/D = 6.5$, the maximum in the unburnt is very well reproduced. Also the appearance of the second maximum on the burnt side can be observed in the predictions. However, the maximum value starts to be overpredicted at $x/D = 4.5$.

6. Conclusion and future plans

A level-set approach based on the G -equation has been formulated as a model for large-eddy simulation of turbulent premixed flames. Important issues concerning the proper implementation of this methodology in the context of LES, particularly the so called reinitialization procedure, have been discussed. To validate the model numerical

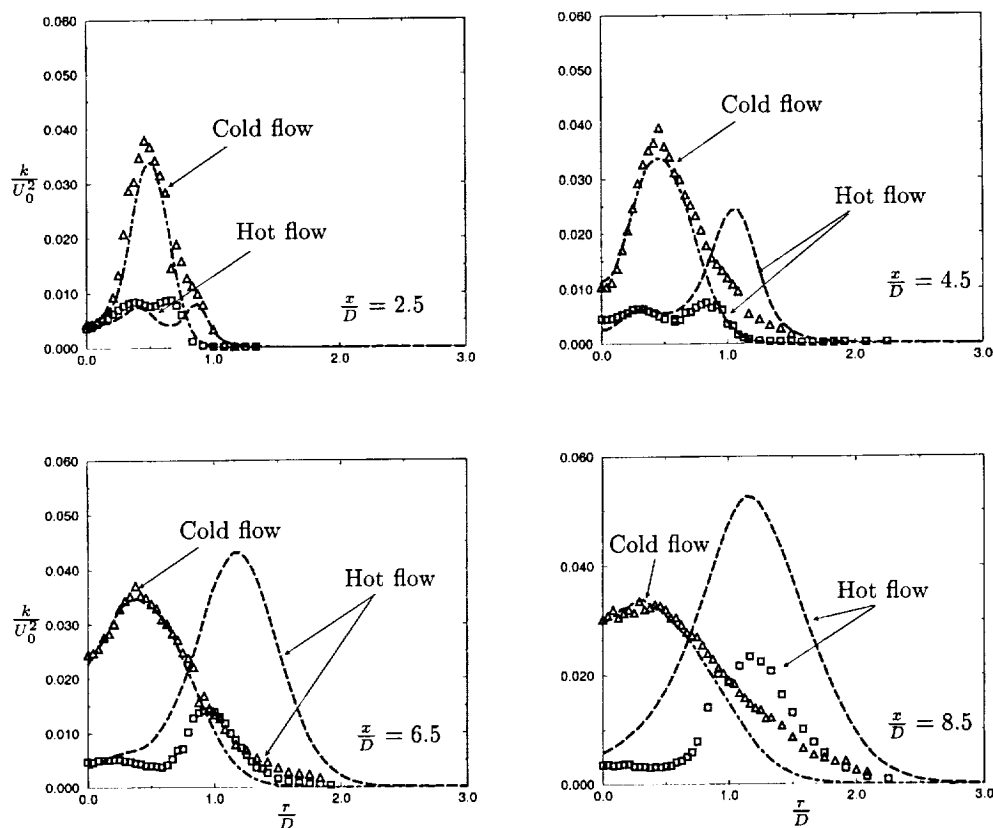


FIGURE 8. Radial profiles of the mean turbulent kinetic energy at different axial locations. Symbols represent experimental data, lines are LES results.

simulations have been performed for a turbulent methane/air Bunsen flame. The results are compared with experimental data, showing very good agreement for the mean axial velocity and turbulent kinetic energy for the cold flow case. For the reactive case mean temperature and axial velocity are essentially well predicted. However, the jet spreading rate is slightly overpredicted and the computed turbulent kinetic energy in the post-flame region is too high. In the future, a more elaborate model for the turbulent burning velocity will be applied. The resulting model will be used to study industrial-like combustor configurations.

Acknowledgments

This work was supported in part by SNECMA Motors.

REFERENCES

- AKSELVOLL, K. & MOIN, P. 1996a An efficient Method for Temporal Integration of the Navier-Stokes Equations in Confined Axisymmetric Geometries. *J. Comp. Phys.* **125**, 454-463.

- AKSELVOLL, K. & MOIN, P. 1996b Large-Eddy Simulation of Turbulent Confined Coannular Jets. *J. Fluid Mech.* **315**, 387-411.
- ANGELBERGER, C., VEYNANTE, D. & EFGELOPOULOS, F. 2000 LES of Chemical and Acoustic Effects on Combustion Instabilities. *Flow, Turb. and Comb.*, accepted for publication.
- BOERSMA, B., BRETHOUWER, G. & NIEUWSDAT, F. T. M. 1998 A Numerical Investigation on the Effect of the Inflow Conditions on the Self-Similar Region of a Round Jet. *Physics of Fluids*. **10**(4), 899-909.
- CHAKRAVARTHY, V. K. & MENON, S. 2000 Large Eddy Simulation of Turbulent Premixed Flames in the Flamelet Regime. *Comb. Sci. Tech.*, accepted for publication.
- CHEN, Y. C., PETERS N., SCHNEEMANN, G. A., WRUCK, N., RENZ, U. & MANSOUR, M. S. 1996 The Detailed Flame Structure of Highly Stretched Turbulent Premixed Methane-Air Flames. *Comb. and Flames*. **107**, 233-244.
- COLIN, O., DUCROS, F., VEYNANTE, D. & POINSOT, T. 2000 A Thickened Flame Model for Large Eddy Simulation of Turbulent Premixed Combustion. *Physics of Fluids*. **12**(7), 1843-1863.
- KERSTEIN, A. R., ASHURST, W. T. & WILLIAMS, F. A. 1988 Field Equation for Interface Propagation in an Unsteady Homogeneous Flow Field. *Phys. Rev.* **A37**, 2728-2731.
- KIM, W. W. & MENON, S. 2000 Numerical Modeling of Turbulent Premixed Flames in the Thin-Reaction-Zones Regimes. *Comb. Sci. Tech.* **00**, 1-32.
- MENON, S., JOU, W. H. 1991 Large Eddy Simulation of Combustion Instability in an Axisymmetric Ramjet Combustor. *Comb. Sci. Tech.* **75**, 53-72.
- MOIN, P., SQUIRES, K., CABOT, W. & LEE, S. 1991 A Dynamic Subgrid-Scale Model for Compressible Turbulence and Scalar Transport. *Phys. Fluids A*. **3**, 2746-2757.
- PETERS, J. A. 1999 The Turbulent Burning Velocity for Large-Scale and Small-Scale Turbulence. *J. Fluid Mech.* **384**, 107-132.
- PETERS, J. A. 2000 *Turbulent Combustion*. Cambridge University Press.
- PIERCE, C. D. & MOIN, P. 1998 Large Eddy Simulation of a Confined Jet with Swirl and Heat Release. *AIAA 98-2892*. 29th AIAA Fluid Dynamic Conference.
- POINSOT, T., VEYNANTE, D. & CANDEL, S. 1991 Quenching Process and Premixed Combustion Diagrams. *J. Fluid Mech.* **228**, 561-606.
- RUSSO, G. & SMEREKA, P. 2000 A Remark on Computing Distance Functions. *J. Comp. Phys.* **163**, 51-67.
- SETHIAN, J. A. 1996 *Level Set Methods: Evolving Interfaces in Geometry, Fluid Mechanics, Computer Vision and Material Science*. Cambridge University Press.
- SUSSMAN, M. SMEREKA, P. & OSHER, S. 1994 A Level Set Method for Computing Solutions to Incompressible Two Phase Flows. *J. Comp. Phys.* **119**, 146-63.
- SUSSMAN, M. & FATEMI, E. 1999 An Efficient, Interface-Preserving Level Set Redistancing Algorithm and Its Application to Interfacial Incompressible Fluid Flow. *SIAM J. Sci. Comp.* **20**(4), 1165-1191.
- VEYNANTE, D. & POINSOT, T. 1997 Large Eddy Simulation of Combustion Instabilities in Turbulent Premixed Burners. *Annual Research Briefs*, Center for Turbulence Research, NASA Ames/Stanford Univ. 253-274.
- WILLIAMS, F. A. 1985 Turbulent Combustion. *The Mathematics of Combustion*, J. Buckmaster, Ed. 97-131.

Local extinction-reignition in turbulent nonpremixed combustion

By Paiboon Sripakagorn[†], George Kosály[†] AND Heinz Pitsch

1. Introduction

Recent reports demonstrate progress in the modeling of burning diffusion flames in the absence of extinction (International Workshop on Measurement and Computation of Turbulent Nonpremixed Flame(2000)). However, the prediction of flames whose burning is frequently interrupted by local extinction-reignition events still presents a major modeling problem (Peters (2000)).

A recent report by Xu & Pope (1999) shows promising results in modeling of a combusting flame with considerable extinction. Xu & Pope use a PDF modeling approach that is known to be expensive computationally. There is incentive, therefore, to study possible generalizations of the mixture fraction based approaches (flamelet, CMC) that would account for local extinction-reignition events.

The present paper reports on direct numerical simulation (DNS) of initially non-premixed fields of fuel and oxidizer developing in a turbulent field. Initially, the scalar dissipation rate is increasing due to straining leading to localized extinction events. At later times molecular diffusion starts to decrease the scalar dissipation rate, resulting in gradual reignition.

Flame element tracking is utilized to show the fields as they would appear in local coordinate systems fixed to different points on the Z_{st} surface. The resulting data are used (a) to study the mechanism of extinction and especially reignition, (b) to elucidate the applicability of the flamelet model to describe these processes, and (c) to examine a possible extension of the model to account for lateral heat diffusion along the Z_{st} surface.

2. DNS of local extinction-reignition and flame element tracking

2.1. Direct numerical simulation

2.1.1. Velocity field

The simulated velocity field is incompressible decaying isotropic turbulence comparable to the turbulence downstream of a laboratory grid. The main parameters of the initial velocity and scalar fields are shown in Table 1.

As pointed out by Eswaran & Pope (1988), to resolve the small scales, the resolution condition $\eta_k k_{max} > 1$ must be met (see also Mell *et al.* (1994)). Here the parameter k_{max} is the wave number cutoff while η_k is the Kolmogorov scale of the velocity. To resolve quantities involving derivatives, $\eta_k k_{max} > 1.5$ is to be satisfied (Yeung & Pope (1989)).

The computational domain is a cube with the size of 2π using periodic boundary conditions at all sides. The integral length scale, l , must be kept adequately small so that the boundary conditions do not influence the results. The condition is $l\Delta k \leq O(1)$ where the smallest nonzero wavenumber is $\Delta k = 2\pi/L$ for the computational box of size L .

[†] University of Washington, Seattle, WA 98195-2600

$k_{\max}\eta_k$	l (cm)	u/l (1/s)	l/η_k	ν (cm/s ²)	Re_λ	N^3	l_Z/l	Sc
1.94	0.879	1.04	27.2	0.01	33	128 ³	0.968	0.7

TABLE 1. Initial conditions used in the DNS of the flow field and the mixture fraction field.

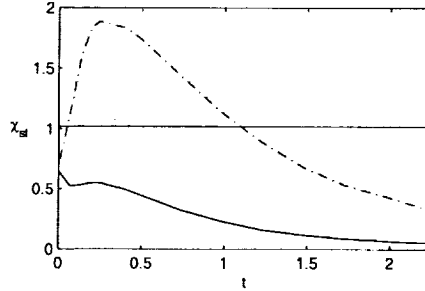


FIGURE 1. The time evolution of χ_{st} . Here χ_{st} is the scalar dissipation rate at $Z = Z_{st} = 0.5$. — : $\langle \chi_{st} \rangle$, ---- : 99% envelope of the fluctuations of χ_{st} . The horizontal line is drawn at $\chi_{st} = \chi_q = 1.02$. This is the largest possible value of χ_{st} where the steady flamelet equation has a burning solution. The numerical value refers to the chemistry parameters shown in Table 2.

2.1.2. Scalar fields

The initial mixture fraction is arranged in blobs of $Z=0$ and $Z=1$. The fuel blobs fill half of the computational domain; the average value of the mixture fraction ($\langle Z \rangle$) is close to 0.5. In the quasi-steady flamelet model (Peters (1983)), the mass fractions depend on space and time through the local, instantaneous values of Z and χ ($\chi = 2D|\nabla Z|^2$, the scalar dissipation rate). The fuel and oxidizer fields are initialized via the quasi-steady flamelet model.

The scalars are initialized when the characteristic length scales of the velocity field start to increase with time. This condition corresponds to a fully developed turbulent flow undergoing full spectrum decay. Once the scalars have been injected, turbulent strain creates large scalar gradients, and the magnitude of the scalar dissipation rate χ increases significantly. Due to the many different turbulent scales involved, the scalar dissipation rates induced by the straining fluctuate strongly (Fig. 1). It is only later that molecular mixing overcomes the influence of turbulent straining and leads to the decrease of the scalar gradients. This paper examines the extinction-reignition phenomena caused by the increase and subsequent decrease of the scalar dissipation rate shown in Fig. 1.

2.1.3. Simulations

The simulated velocity field evolves according to the incompressible Navier-Stokes equations,

$$\nabla \cdot \bar{\mathbf{u}} = 0 \quad (2.1)$$

$$\frac{\partial \bar{\mathbf{u}}}{\partial t} = \bar{\mathbf{u}} \times \bar{\boldsymbol{\omega}} - \nabla \left\{ p - \frac{|\bar{\mathbf{u}}|^2}{2} \right\} + \nu \nabla^2 \bar{\mathbf{u}}, \quad (2.2)$$

where \bar{w} denotes the vorticity vector and p is the hydrodynamic pressure. The kinematic viscosity, ν , is independent of the temperature.

The mixture fraction and species mass fractions satisfy the conservation equation

$$\frac{\partial Y_i}{\partial t} = -\mathbf{u} \cdot \nabla Y_i + D \nabla^2 Y_i - w_i. \quad (2.3)$$

Here D is the coefficient of molecular diffusion, $D = \nu / Sc$. In the Z -equation the reaction rate is zero.

The set of governing equations was solved using a pseudospectral code developed by Nilsen (1998). The spatial derivative fields were evaluated in Fourier space while nonlinear terms such as $\bar{\mathbf{u}} \times \bar{\mathbf{w}}$ or $\bar{\mathbf{u}} \cdot \nabla Y_i$ were computed in physical space. The time advancement was done by a second-order Adams-Bashforth scheme.

2.2. Flame element tracking

2.2.1. Flame elements

Unless the chemistry is slower than molecular mixing, the reaction zone is close to the instantaneous stoichiometric surface, defined as $Z(\bar{\mathbf{x}}, t) = Z_{st}$. The phrase ‘‘flame element’’ in this paper means a point on the instantaneous Z_{st} surface.

The Z_{st} surface moves relative to the laboratory reference frame. Gibson (1968) points out that the velocity of a point fixed on an isoscalar surface relative to the laboratory reference frame can be given as

$$\bar{\mathbf{u}}_Z = \bar{\mathbf{u}} - \frac{D \nabla^2 Z}{|\nabla Z|} \bar{\mathbf{i}}_Z = \bar{\mathbf{u}} - D \nabla^2 Z \frac{\nabla Z}{|\nabla Z|^2} \quad (2.4)$$

Here $\bar{\mathbf{u}}$ is the fluid velocity and $\bar{\mathbf{i}}_Z$ is the unit vector in the direction of local mixture fraction gradient. Since the Z_{st} surface is an isoscalar surface, the instantaneous velocity of a flame element can be calculated from Eq. (2.4).

Note that flame elements are not fluid particles. Fluid particles are convected by the velocity field. The second term on the RHS of Eq. (2.4) accounts for propagation due to molecular diffusion (Gibson (1968)). While several authors have used simulated and laboratory data to track fluid particles (Shlien & Corrsin (1974), Sato & Yamamoto (1987), Yeung & Pope (1989)), the technique of flame element tracking has been introduced by Mell *et al.* (1994). This paper uses flame element tracking to show the fields as they would appear in the frame of reference of an observer fixed to a point on the instantaneous Z_{st} surface.

2.2.2. Methodology

A number of selected points located on the Z_{st} surface were tagged in the initial scalar field. Since the velocity and mixture fraction fields are known from the DNS, the velocity of the points on the isoscalar surface is available from Eq. (2.4). Since the DNS fields are available on a 3-dimensional grid, an accurate interpolation scheme is needed to determine the velocity data between grid points. The updated positions of the flame elements can be obtained by integrating the equations of motion.

The accuracy of the interpolation scheme is crucial to the particle tracking routine. Yeung & Pope (1988) have compared results obtained from a 3rd-order, 13 points Taylor series (TS13) scheme and another scheme working with 4th order cubic splines. The approach via cubic splines was found to be our method of choice. The goal of this method is to get a formula that is smooth in the first derivative and continuous in the second derivative, both within an interval and at its boundaries. The resulting twice continuously

Z_{st}	r	α	β	K
0.5	1.0	0.87	4.0	100

TABLE 2. Numerical values used for the thermochemistry parameters defined in Section 3.1.

differentiable approximation of the interpolated variables leads to a low level of numerical noise in the time series obtained. Regarding the integration scheme, Yeung & Pope (1988) have shown that an explicit 2^{nd} -order Runge-Kutta scheme works well. This method has been also applied by Squires & Eaton (1991) and Elghobashi & Truesdell (1993).

In this study the 4^{th} -order accurate cubic spline interpolation has been implemented for the interpolation scheme. For the time stepping, the 2^{nd} -order Runge-Kutta scheme has been employed. The details of the interpolation method can be found in Yeung & Pope (1988). Note, however, that due to the possibility of large flame stretching and the highly three-dimensional structure of the isoscalar surface, the tagging location might start to wander away from the isoscalar surface by a small amount every timestep. A surface-searching module has been added to the tracking code to return the tagged flame element onto the the Z_{st} surface once every few timesteps.

3. Turbulent combustion model

3.1. Chemistry scheme

A single-step reversible reaction has been considered with an Arrhenius-type pre-exponential factor.



Considering identical equilibrium constants for the forward and backward reactions, the production rate of the product can be written (Lee & Pope (1995))

$$w_p = (r + 1)A_o \exp\left(\frac{-\beta}{\alpha}\right) \exp\left[\frac{-\beta(1 - Y_p)}{1 - \alpha(1 - Y_p)}\right] \left(Y_f Y_o - \frac{1}{K} Y_p^2\right). \quad (3.2)$$

Here r is the mass of oxidizer disappearing with unit mass of fluid; Y_f , Y_o , and Y_p stand for the mass fractions of fuel, oxidizer, and product in order.

Throughout the paper the fresh values of the fuel and oxidant mass fractions are considered unity; therefore, the stoichiometric value of the mixture fraction is given as $Z_{st} = 1/(1 + r)$. The present choice is $r = 1$, this means, $Z_{st} = 0.5$. The reaction kinetics is characterized by the following dimensionless quantities:

$$\text{Zel'dovich number, } \beta = \frac{T_a T_b - T_u}{T_b T_b} \quad (3.3)$$

$$\text{Heat-release parameter, } \alpha = \frac{T_b - T_u}{T_b} \quad (3.4)$$

$$\text{Reduced temperature, } \Theta = \frac{T - T_u}{T_b - T_u} \quad (3.5)$$

where T_a is the activation temperature, T_b is the adiabatic flame temperature, and T_u



FIGURE 2. The local coordinate system used in flamelet modeling. Point O is fixed on the stoichiometric surface.

is the (equal) temperature of the fuel and oxidizer streams. For this case, Θ is equal to Y_p . Table 2 shows the values of the thermochemistry parameters used in the simulations. The parameters were selected to lead to local extinction-reignition in a strongly burning flame (Overholt & Pope (1999)).

3.2. Flamelet modeling

Figure 2 shows a local coordinate system fixed to a point (point O) on the Z_{st} surface. Axes x_1 and x_2 are locally (close to point O) tangential to the Z_{st} surface, whereas the mixture fraction coordinate is locally perpendicular to the surface. Note that this coordinate system cannot be used to describe local burning unless the reaction zone is sufficiently thin in space, and, therefore, the mixture fraction changes monotonically along the direction that is locally perpendicular to the Z_{st} surface.

From the point of view of the observer located at point O (traveling with it) the mass fractions are dependent on the variables t, Z, x_1 , and x_2 . Straightforward calculations show (Peters (1983), (1984)) that in the local coordinate system the mass fraction $Y_i = Y_i(t, Z, x_1, x_2)$ satisfies the following equation:

$$\begin{aligned} \frac{\partial Y_i}{\partial t} - \frac{\chi}{2} \frac{\partial^2 Y_i}{\partial Z^2} \\ = - \left(v_2 \frac{\partial Y_i}{\partial Z_2} + v_3 \frac{\partial Y_i}{\partial Z_3} \right) + 2D \left(\frac{\partial Z}{\partial x_2} \frac{\partial^2 Y_i}{\partial Z \partial Z_2} + \frac{\partial Z}{\partial x_3} \frac{\partial^2 Y_i}{\partial Z \partial Z_3} \right) + D \left(\frac{\partial^2 Y_i}{\partial Z_2^2} + \frac{\partial^2 Y_i}{\partial Z_3^2} \right) + w_i \end{aligned} \quad (3.6)$$

where the scalar dissipation rate, χ is defined by $\chi = 2D(\nabla Z^2)$.

In the time dependent flamelet model (TFL) (Peters (1983), (1984)) the first three terms on the RHS are neglected compared to the term describing mixing across the Z_{st} surface (second term on the LHS). The model equation reads then (Peters (1983), (1984))

$$\frac{\partial Y_i}{\partial t} - \frac{\chi}{2} \frac{\partial^2 Y_i}{\partial Z^2} = w_i \quad (3.7)$$

Neglecting the time derivative in Eq. (3.7) the (quasi) steady flamelet model (SFL) follows (Peters (1983), (1984))

$$-\frac{\chi}{2} \frac{\partial^2 Y_i}{\partial Z^2} = w_i. \quad (3.8)$$

The three terms neglected on the RHS of Eq. (3.6) represent lateral convection, curvature, and lateral diffusion at O. The neglect of these terms in Eq. (3.7) and the neglect of the time derivative in Eq. (3.8) are related to the thinness of the reaction zone in mixture fraction space. Thin reaction zones are due to high values of the local Damköhler number.

Presently we assume that the scalar dissipation rate (χ) appearing in Eqs. (3.6-3.8)

can be modeled using

$$\chi(Z) = \chi_{\text{st}} F(Z), \quad (3.9)$$

where the form function, $F(Z) = \exp[-2(\text{erf}^{-1}(2Z - 1))^2]$ has been used. This modeling assumes that close to point O the mixing is “counterflow-like”. The simulations were designed such that this approximation shall be approximately valid.

3.3. Interacting flamelet model

According to Eqs. (3.7-3.8) the temperature at a point on the Z_{st} surface evolves under the influence of its own scalar dissipation rate; neighboring points have no influence on its temperature. Even the closest neighbors extinguish and reignite as isolated counterflows (auto-ignition). This behavior is due to the neglect of the first three terms on the RHS of Eq. (3.6) that represent lateral coupling (interaction) between neighboring points (cf. Fig. 2). We presently refer to Eq. (3.6) as the model equation of the interacting flamelet approach.

One of the goals of the present paper is to examine the role of the lateral interactions in extinction-reignition phenomena. To simplify the task let us write Eq. (3.6) at point O ($Z=0.5$, $Z_2 = Z_3 = 0$ in Fig. 2). The coordinate system shown in Fig. 2 propagates with the velocity of O, and at O the $Z_2 - Z_3$ plane is tangential to the Z_{st} surface. This means that at point O the first two interaction terms in Eq. (3.6) are zero; only the lateral diffusion term is left in the equation. We denote this lateral diffusion term by i_3 .

$$\frac{\partial Y_i}{\partial t} - \frac{\chi_{\text{st}}}{2} \left(\frac{\partial^2 Y_i}{\partial Z^2} \right)_{Z=0.5, Z_2=Z_3=0} - i_3 = w_i \quad (3.10)$$

$$i_3 \equiv D \left(\frac{\partial^2 Y_i}{\partial Z_2^2} + \frac{\partial^2 Y_i}{\partial Z_3^2} \right)_{Z=0.5, Z_2=Z_3=0}. \quad (3.11)$$

3.4. Implementation

The tracking procedure provides us with the entire temperature and scalar dissipation rate history of the flame elements we are tracking. Hence, it is possible to implement the time-dependent flamelet model (TFL), i.e. Eq. (3.7), for each tracked flame element. Since the DNS is initialized with the steady flamelet model, the TFL computations are initialized the same way.

The flamelet equation is solved by the flux-splitting technique. The diffusion term is advanced by the implicit Crank-Nicolson method while the source term is handled using the 2^{nd} -order Adam-Bashford approach. For simplicity a uniform grid of sufficient gridsize is used. The steady flamelet solution (SFL) is identified as the burning branch of the S-curve and is evaluated from Eq. (3.8) using the same set of codes. For the present chemistry parameters (Table 2), SFL gives $\chi_{\text{st}} = \chi_{\text{q}} = 1.02$ as the extinction limit. Above this limit Eq. (3.8) has no burning solution.

We remind the reader that Eq. (3.10) is valid only at point O indicated in Fig. 2. We will use information from the vicinity of this point to investigate the possibility of describing extinction-reignition via TFL and to look for possible correlation between the reignition process and the time evolution of the i_3 term. To obtain the value of the i_3 term, instead of evaluating the two 2^{nd} -derivative terms separately, the following relationship is used.

$$\frac{\partial^2 Y_i}{\partial Z_2^2} + \frac{\partial^2 Y_i}{\partial Z_3^2} = \nabla^2 Y_i - \frac{\partial^2 Y_i}{\partial x_1^2} \quad (3.12)$$

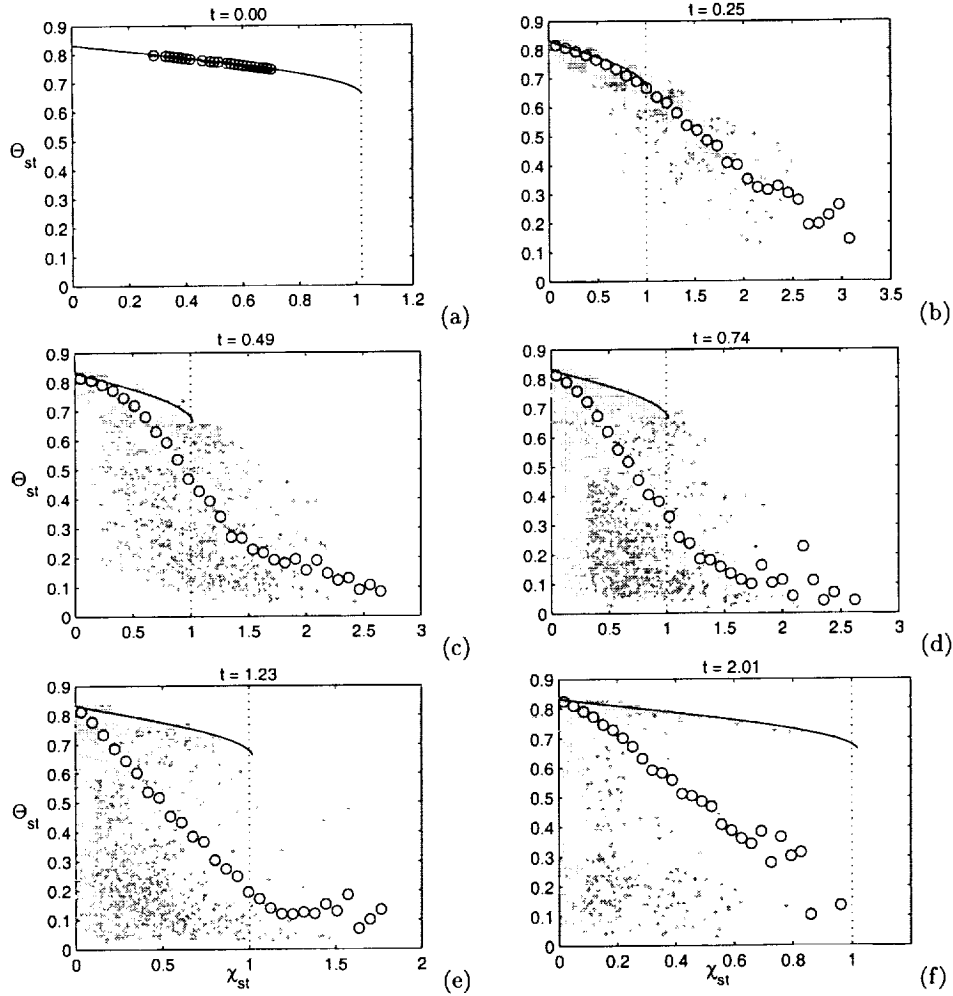


FIGURE 3. Extinction-reignition behavior on the Z_{st} surface. — : burning solution of the steady-flamelet equation. \circ : average temperature for chosen values of the scalar dissipation rate ($\langle \Theta | Z_{st}, \chi_{st} \rangle$). The grey dots represent the temperature of 5000 randomly selected flame elements. The vertical dotted line is at $\chi_{st} = \chi_q$.

The Laplacian of Y_i is easy and accurate to use to evaluate from the laboratory coordinate; the 2^{nd} -derivative in the Z -direction can be obtained from Eulerian data in the DNS. The 4^{th} -order central-difference formula was used to return the 2^{nd} -derivative on the right-hand side of Eq. 3.12.

4. Results and discussion

4.1. Extinction and reignition: DNS

Figure 3 exhibits the extinction and reignition behavior of the DNS field. The figure refers to $Z = Z_{st}$. The broken line indicates the burning branch of the steady-flamelet solution, the circles show the conditional average of the temperature for fixed value of $Z = Z_{st}$ and $\chi = \chi_{st}$ as computed from the data ($\langle \Theta | Z_{st}, \chi_{st} \rangle$). The vertical dotted line is at $\chi_{st} = \chi_q$. The reacting scalar field was initialized on the broken line (Fig. 3a). Very

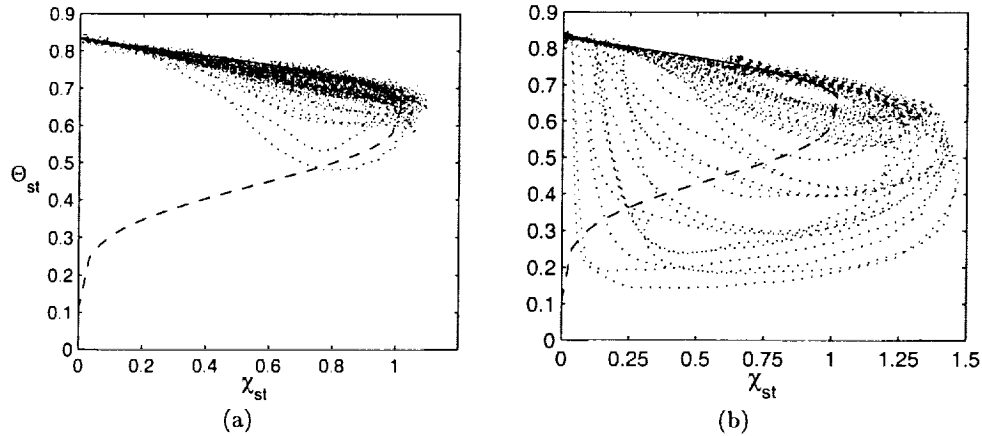


FIGURE 4. Particle paths in the $\Theta_{st} - \chi_{st}$ plane. (a) $0.95 < \chi_{max} < 1.1$. (b) $1.2 < \chi_{max} < 1.5$.

early in the simulation, the flame burns vigorously with little extinction and SFL predicts the conditional average well (Fig. 3b).

As more and more flame elements experience scalar dissipation rate values that are higher than χ_q (see Fig. 1), their temperature starts to decrease and the conditionally averaged temperature increasingly deviates from the SLFM prediction (Fig. 3c). At a later time, however, the local values of the scalar dissipation rate starts decreasing. Points whose temperature dropped down when their scalar dissipation rate was larger than χ_q are getting transported back into the $\chi < \chi_q$ region of the $\Theta_{st} - \chi_{st}$ plane. Figure 3d demonstrates a bimodal situation where steadily burning and nearly extinguished points exist at identical values of χ_{st} . Eventually, the temperature of the “extinguished” points starts increasing, the conditional average $\langle \Theta | Z_{st}, \chi_{st} \rangle$ starts rebounding, and gradual reignition takes place.

4.2. Extinction and reignition: flame element tracking

Figure 4 shows the paths of flame elements in the $\Theta - \chi$ space over a time interval of $t=0-0.50$. In the figure the burning branch of the steady flamelet solution is continued into the middle, unstable branch (broken line). Only a few of the flame elements shown in Fig. 4a are associated with χ values that exceed $\chi_q = 1.02$. Accordingly, the temperatures in this figure stay close to the steady burning branch at all times. Figure 4b refers to flame elements whose scalar dissipation rate gets higher than χ_q ; therefore, their temperatures drop below the unstable branch and get reignited from there.

Figure 4 demonstrates that, in the present simulations, the χ_q value derived from the flamelet model is a valid measure of the characteristic value of the scalar dissipation rate that leads to extinction. A similar conclusion has been reached recently by Overholt & Pope (1999).

According to the TFL approach for a fixed value of χ_{st} , any flame element that is above the unstable branch will reignite, while flame elements that are below this branch will extinguish. It follows that crossing the broken line contradicts flamelet modeling[†]. The reignition observed in Fig. 4b is certainly not the autoignition of isolated flamelets.

[†] If the flow “moves” the scalar dissipation rate of an element faster than the characteristic times of extinction or reignition, the flamelet can cross the broken line horizontally (Pitsch & Fedotov (2000)).

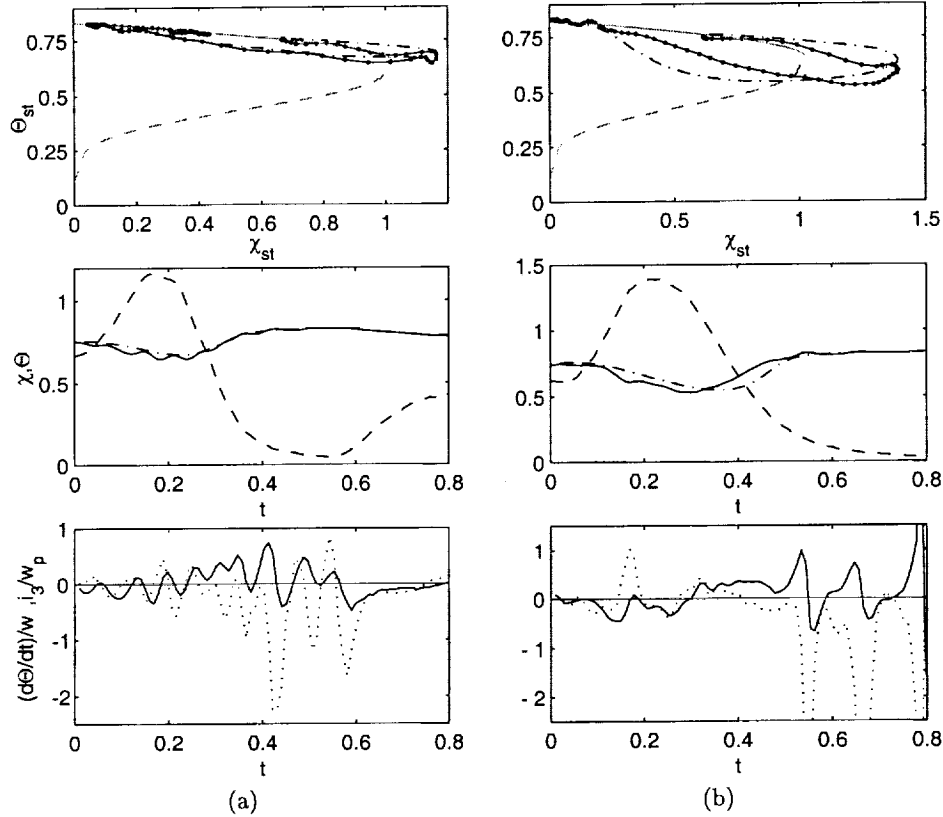


FIGURE 5. Various flame element histories with different patterns of extinction-reignition. Top two figures: — : temperature data; — · — : TFL model results; grey — and - - - : burning and unstable branches of the SFL solution; - - - : scalar dissipation rate. Bottom figure: — : $(d\Theta/dt)/w$ from DNS data; ····· : i_3/w term.

Almost all of the flame element temperatures plotted in Fig. 4b are already on the increase when they cross the unsteady branch. Since all the paths shown in Fig. 4b reignite through the broken line, the figure demonstrates that TFL is not consistent with the reignition of flame elements whose scalar dissipation rate at some point in time was well above χ_q .

It is also interesting to note that different flame elements exhibited quite different behavior. Some flame elements reignited fast; other elements did not reignite at all in the time interval considered. Some of these features are expected to be explained by the inclusion of the interaction term, i_3 .

A variety of extinction-reignition behavior is shown in Fig. 5-7. In the figures the full line indicates the DNS result, the dash-dot line the TFL calculations, while the respective grey full and broken lines depict the burning and unstable branches of the steady-flamelet (SFL) solution. The DNS and SFL results are denoted similarly in the lower figures, whereas the broken line shows the time evolution of χ_{st} . For the bottom figure, the full line is $(d\Theta/dt)/w$ from the DNS data while the dotted line is the i_3/w term.

In Fig. 5a, χ_{st} exceeds χ_q only slightly and for a short time; in Fig. 5b, χ_{st} exceeds χ_q by a larger margin but still for a relatively short time. TFL predicts the temperature

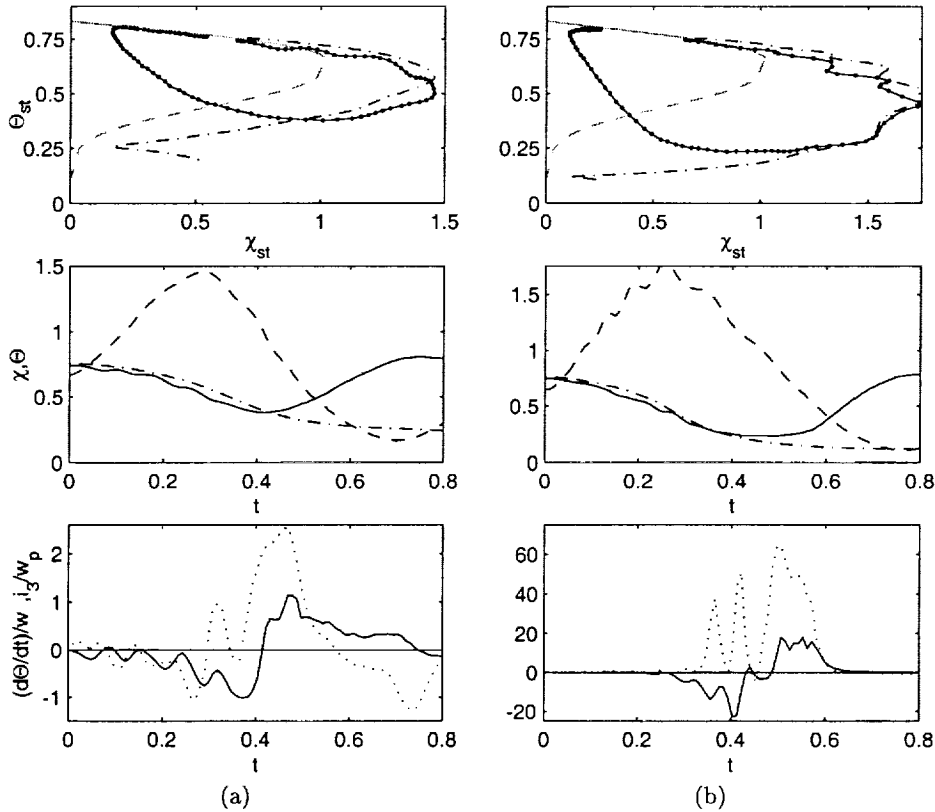


FIGURE 6. (See Fig. 5 for captions.)

correctly in both cases. It is interesting to notice, however, the difference between the data and the flamelet prediction in the uppermost part of Fig. 5b. The flamelet prediction crosses the unsteady branch horizontally (see footnote before), whereas the trace taken from the data shows slightly oblique crossing. This effect is obviously due to neighboring hot flame elements that are not considered in the flamelet approximation. In Fig. 5, the i_3 term is quite small and exerts no major influence on the results.

Figure 6-7 show flame elements undergoing major extinction followed by reignition. TFL predicts the initial extinction process quite well but fails to reignite the flame element except in Fig. 7b. In Figs. 6a,b and 7a, TFL predicts full extinction after the element gets below the unsteady branch. In Fig. 7b the flamelet model reignites due to crossing the broken line horizontally, but the data show very different behavior.

We believe that the reignition process in Figs. 6 and 7 is influenced by hot flame elements in the vicinity of the flame element we are following. Our expectation has been that i_3 would exhibit a positive peak at the time when the temperature of the extinguished element starts to increase. Physically speaking, the expectation is that it is a “bump” in i_3 that helps the flame element to cross the unsteady branch.

Close inspection of the $i_3(t)$ time evolution in Figs. 6 and 7 indeed shows behavior reminiscent of the expected behavior, but the effect seems to be influenced by resolution errors. We will investigate the matter further using better resolution.

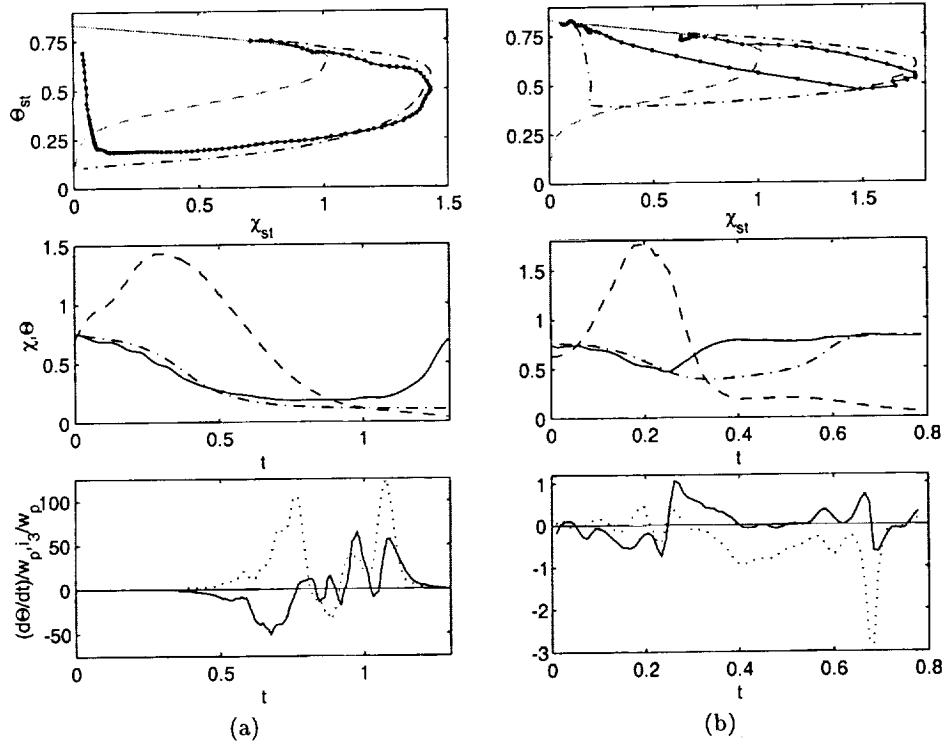


FIGURE 7. (See Fig. 5 for captions.)

5. Conclusions and future work

Direct numerical simulations have been performed to investigate the local extinction-reignition of initially nonpremixed fields of fuel and oxidant. The extinction-reignition process is due to the increase and decrease of the scalar dissipation rate caused by the initial strong straining followed by the dominance of molecular diffusion. To elucidate the applicability of the flamelet modeling, the entire time history of different fluid elements (points fixed on the Z_{st} surface) have been tracked. An extended flamelet model has been introduced that contains a term (i_3 in Eq. (3.10)) that accounts for lateral heat diffusion along the Z_{st} surface.

The results shows that the extinction criterion derived from flamelet modeling ($\chi_{st} > \chi_q$) works well. The data demonstrate, furthermore, that time dependent flamelet modeling correctly predicts the behavior of flame elements with little or no extinction. Even the extinction phase of the history of a flame element is captured by the model, approximately. Standard flamelet modeling was found to break down during reignition.

In flamelet modeling the flame elements extinguish and reignite as separated counterflows. We believe that this is the reason behind the failure of the model to describe reignition correctly. Our expectation is, therefore, that the $i_3(t)$ term in Eq. (3.10) has a decisive role in the reignition process. Due to our limited resolution, we could not confirm this behavior. Presently we are working on a better resolved simulation that will clarify this issue. We are also planning to use the new simulations to study the influence of (a) premixed pockets created by mixing in extinguished regions and (b) the interaction between extinguished and burning flame elements due to curvature.

Acknowledgments

Paiboon Sripakagorn's stay at CTR was supported by ASCI and CTR. George Kosály's sabbatical stay at Stanford is partially supported by CTR.

REFERENCES

- ELGHOBASHI, S. & TRUESDELL, G. C. 1993 Direct simulation of particle dispersion in a decaying isotropic turbulence. *J. Fluid Mech.* **242**, 655-700.
- ESWARAN, V. & POPE, S. B. 1988 Direct numerical simulations of the turbulent mixing of a passive scalar. *Phys. Fluids.* **31**, 506.
- GIBSON, C. H. 1968 Fine Structure of Scalar Fields Mixed by Turbulence. I. Zero-Gradient Points and Minimal Gradient Surfaces. *Phys. Fluids.* **11**, 2305.
- International Workshop on Measurement and Computation of Turbulent Nonpremixed Flames 2000. <http://www.ca.sandia.gov/tdf/Workshop.html>.
- LEE, Y. Y. & POPE, S. B. 1995 Nonpremixed Turbulent Reacting flow near Extinction. *Comb. Flame.* **101**, 501-528.
- MELL, W. E., NILSEN, V., KOSÁLY, G. & RILEY, J. J. 1994 Investigation of closure models for nonpremixed turbulent reacting flows. *Phys. Fluids A.* **6**, 1331.
- NILSEN, V. 1998 *PhD thesis*, Mechanical Engineering Department, University of Washington, Seattle, WA.
- OVERHOLT, M. R. & POPE, S. B. 1999 Direct numerical simulation of a statistically-stationary, turbulent reacting flow. *Combust. Theo. Modeling.* **3**(2), 371-408.
- PETERS, N. 1983 Local Quenching Due to Flame Stretch and Non-Premixed Turbulent Combustion. *Comb. Sci. Tech.* **30**, 1-17.
- PETERS, N. 1984 Laminar diffusion flamelet models in non-premixed turbulent combustion. *Prog. Energy Combust. Sci.* **10**, 319-339.
- PETERS, N. 2000 Turbulent combustion. *New York, Cambridge University Press.*
- PITSCH, H. & FEDOTOV, S. 2000 Investigation of Scalar Dissipation Rate Fluctuations in Non-premixed Turbulent Combustion Using a Stochastic Approach. *Comb. Theo. Modeling.* Submitted for publication.
- SATO, Y. & YAMAMOTO, K. 1987 Lagrangian measurement of fluid-particle motion in an isotropic turbulent field *J. Fluid Mech.* **175**, 183-199.
- SHLIEN, D. J. & CORRSIN, S. 1974 A measurement of Lagrangian velocity autocorrelation in approximately isotropic turbulence *J. Fluid Mech.* **62**, 255-271.
- SQUIRES, K. D. & EATON, J. K. 1991 Lagrangian and Eulerian statistics obtained from direct numerical simulations of homogeneous turbulence. *Phys. Fluids A.* **3**, 130-143.
- YEUNG, P. K. & POPE, S. B. 1988 An Algorithm for Tracking Fluid Particles in Numerical Simulations of Homogeneous Turbulence. *J. Comput. Phys.* **79**, 373-416.
- YEUNG, P. K. & POPE, S. B. 1989 Lagrangian statistics from direct numerical simulation of isotropic turbulence. *J. Fluid Mech.* **207**, 531.
- XU, J. & POPE, S. B. 1999 Assessment of numerical accuracy of PDF/Monte Carlo methods for turbulent reacting flows. *J. Comp. Phys.* **152**(1), 192-230.

Doubly-conditional moment closure modeling of turbulent nonpremixed combustion

By Chong M. Cha, George Kosály†, AND Heinz Pitsch

1. Motivation and objectives

The accurate treatment of extinction and reignition phenomena is thought to be an important factor in determining how flame stabilization occurs in practical, nonpremixed combustion systems (Peters (2000)). In the joint probability density function (PDF) approach (Pope (1985), Dopazo (1994)), extinction/reignition can be treated with improved mixing models (Xu & Pope (1999)). However, joint PDF methods employ a Monte-Carlo type solution procedure and thus become computationally expensive when many species increase the dimensionality of the modeled joint PDF evolution equation. Presumed PDF approaches such as flamelet modeling (Peters (1983), Peters (2000)) and conditional moment closure modeling (Klimenko (1990), Bilger (1993), Klimenko & Bilger (1999)) can be computationally tractable when many species are to be described, as is generally the case in problems of practical importance. First-order flamelet modeling and conditional moment closure modeling with singly-conditional, first-moment closure breaks down when extinction and/or reignition phenomena are present (Peters (2000), Klimenko & Bilger (1999)). The focus of the present paper concerns extensions of first-order conditional moment closure modeling to describe extinction/reignition.

Currently, a fundamental closure approximation in singly-conditional moment closure modeling is first-order closure of the average nonlinear chemical source terms, $\dot{\mathbf{w}}$, conditioned on the mixture fraction, $\xi(t, \mathbf{x}) = \eta$:

$$\langle \dot{\mathbf{w}}(\mathbf{Y}(t, \mathbf{x}), T(t, \mathbf{x}), \rho(t, \mathbf{x})) | \xi(t, \mathbf{x}) = \eta \rangle \approx \dot{\mathbf{w}}(\langle \mathbf{Y} | \eta \rangle, \langle T | \eta \rangle, \langle \rho | \eta \rangle),$$

where \mathbf{Y} are the vector of mass fractions of the reacting species, T and ρ are the temperature and density of the mixture, respectively, and η is the sample space variable of ξ . The first-order closure approximation is not valid when fluctuations about the conditional means become significant. Figure 1 shows local extinction/reignition events in (i) ξ space from experiments of a turbulent methane/air reacting jet (Barlow & Frank (1998)) and (ii) in scalar dissipation rate space at the stoichiometric value of ξ from a direct numerical simulation (DNS) of a single-step chemical reaction in grid turbulence (Sripakorn (2000)). The scalar dissipation rate is $\chi \equiv 2\mathcal{D}(\nabla\xi)^2$, where \mathcal{D} is the molecular diffusion coefficient. θ is the reduced temperature,

$$\theta \equiv \frac{T - T_\infty}{T_f - T_\infty},$$

with T_f the adiabatic flame temperature and T_∞ the reference temperature. The figure illustrates how extinction/reignition events appear as large fluctuations about $\langle \theta | \eta \rangle$.

Two strategies have been proposed to improve singly-conditional moment closure modeling (Klimenko & Bilger (1999)):

† University of Washington, Seattle, WA 98195-2600

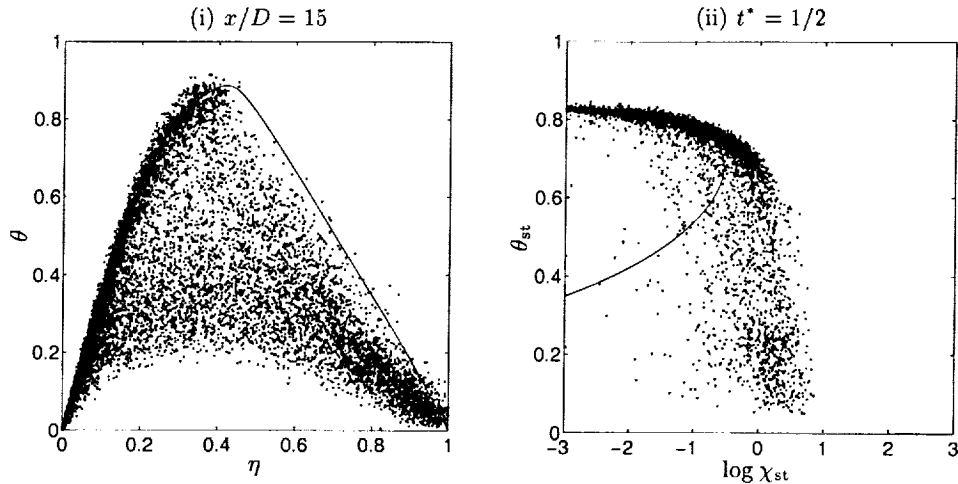


FIGURE 1. Motivation of the work: Scatter plots of the reduced temperature from (i) a planar cut at $x/D = 15$ of the piloted methane/air turbulent reacting jet F of Barlow & Frank (1998) and (ii) from a DNS of turbulence in a box of Sripakagorn (2000) at $t^* \equiv t/\tau_{\text{eddy}} = 1/2$ with a single-step, reversible reaction. D is the jet nozzle diameter, τ_{eddy} is the initial large-eddy turnover time. In (i), the stoichiometric value of the mixture fraction is $\xi_{\text{st}} = 0.351$; in (ii), values are at $\xi_{\text{st}} = 0.5$.

- (a) higher-order closures and/or
- (b) use of additional conditioning variables.

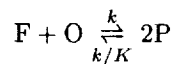
Testing of (a) have already begun (Swaminathan & Bilger (1998), Mastorakos & Bilger (1998)). This paper introduces the use of a second conditioning variable as a more promising alternative to a second-order closure strategy. The presumption is that the extinction/reignition events, seen in Fig. 1 for example, can be described in the space of χ (in addition to ξ and \mathbf{x}).

The paper is organized as follows: In the next section, an existing second-order closure remedy is reviewed. This extension is compared to a new conditional moment closure model where the scalar dissipation rate is introduced as a second conditioning variable. In Sec. 3, *a priori* modeling comparisons are made with DNS experiments of a single-step, second-order, reversible reaction in grid turbulence. Finally, the two conditional moment closure modeling extensions are assessed and future directions outlined.

2. Combustion model

2.1. DNS experiment

Presently, the *a priori* combustion modeling comparisons are made with DNS experiments performed by Sripakagorn (2000). Briefly, fuel (F), oxidizer (O), and product (P) involved in a one-step, second-order, reversible reaction,



($\xi_{\text{st}} = 0.5$) evolve in isotropic, homogeneous, and decaying turbulence. The flow is incompressible. The forward reaction rate, k , has an Arrhenius temperature dependence

with the equilibrium constant, K , held fixed. The reaction-rates are given by

$$\dot{w}(Y_F, Y_O, Y_P, \theta) = -A \exp\left(-\frac{Ze}{\alpha}\right) \exp\left[-\frac{Ze(1-\theta)}{1-\alpha(1-\theta)}\right] \left(Y_F Y_O - \frac{1}{K} Y_P^2\right),$$

$\dot{w}_F = \dot{w}$, $\dot{w}_O = \dot{w}$, and $\dot{w}_P = -2\dot{w}$. A is the frequency factor (multiplied by density and divided by molecular weight, assumed equal for all species), $\alpha \equiv (T_f - T_\infty)/T_f$ is the heat release parameter, $Ze \equiv \alpha T_a/T_f$ is the Zeldovich number, and T_a is the activation temperature. The Schmidt number is 0.7 and Lewis numbers unity. Figure 2 shows the level of extinction/reignition from the DNS experiment with $A = 8 \times 10^4/\text{sec}$, $\alpha = 0.87$, $Ze = 4$, and $K = 100$ (*cf.* Sripakagorn (2000) for details of the simulation).

2.2. Second-order closure

A strong nonlinearity of the chemical source terms is due to the exponential temperature dependence of the Arrhenius function, $k = A \exp(-T_a/T)$. A second-order closure strategy in singly-conditional moment closure results from conditionally averaging a series expansion of the Arrhenius function (Mastorakos & Bilger (1998)):

$$\langle k|\eta \rangle \approx -A \exp\left(-\frac{\beta}{\alpha}\right) \exp\left[-\frac{Ze(1-\langle \theta|\eta \rangle)}{1-\alpha(1-\langle \theta|\eta \rangle)}\right] (1+B) \quad (2.1a)$$

$$B = \frac{\alpha Ze \langle \theta'^2|\eta \rangle}{[1-\alpha(1-\langle \theta|\eta \rangle)]^3} \left[\frac{1}{2} \frac{\alpha/Ze}{[1-\alpha(1-\langle \theta|\eta \rangle)]} - 1 \right] \quad (2.1b)$$

valid for $\theta'/\langle \theta|\eta \rangle < 1$. For the present case of a single-step reaction, the conditional averages of all species and temperature can be obtained from the single equation for the singly-conditional average of Y_P :

$$\frac{d}{dt} Q_P = \frac{\langle \chi|\eta \rangle}{2} \frac{\partial^2}{\partial \eta^2} Q_P - 2\dot{w}(Q_F, Q_O, Q_P, \langle \theta|\eta \rangle)(1+B), \quad (2.2)$$

where $Q_F = \eta - Q_P/2$, $Q_O = 1 - \eta - Q_P/2$, and $\langle \theta|\eta \rangle = Q_P$. B is given by Eq. (2.1b), where $\langle \theta'^2|\eta \rangle$ is to be taken directly from the DNS experiment. Details of the derivation are found in Klimenko & Bilger (1999). Briefly,

(a) Terms representing the diffusion of the conditional averages in physical space in Eq. (2.2) have been ignored (e_Q closure).

(b) A closure hypothesis involving contributions to the balance of the conditional average by fluctuations about singly-conditional means has been invoked (e_Y closure), allowing the resulting terms to be ignored for the present fully-homogeneous case (Klimenko & Bilger (1999)).

Assumption (a) is strictly valid only at high Reynolds numbers in non-homogeneous (shear) flows (Klimenko & Bilger (1999)), has been shown to be valid at low Reynolds numbers for a semi-homogeneous flow (Bushe et al. (1999)), and is exact for the present spatially degenerate (homogeneous, isotropic) case. The closure hypothesis invoked in (b) has been validated against a DNS database of a temporal mixing layer (Bushe & Bilger (1999)). Thus, we offer both singly-conditional moment closure with and without a second-order closure of the chemical reaction-rate as baseline comparisons to the strategy of multiply-conditioning. We refer to Eq. (2.2) as the *cmc1* model throughout the remainder of the paper. Setting $B = 0$ gives the standard (singly-) conditional moment closure model and is referred to as model *cmc0*.

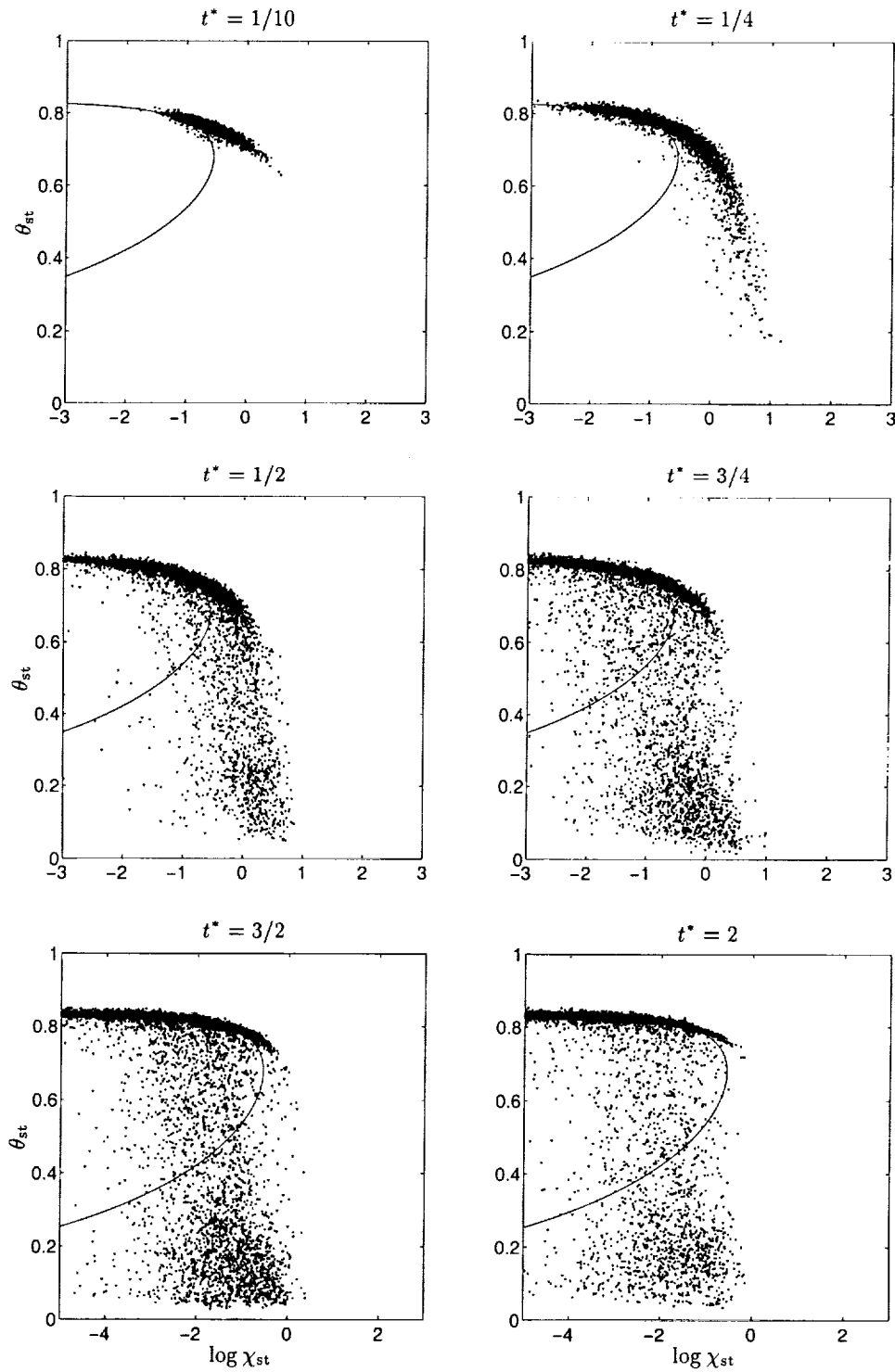


FIGURE 2. DNS experiment of spatially isotropic, homogeneous, and decaying turbulence performed by Sripakagorn (2000). The reduced temperature is shown at $\xi_{st} = 0.5$ as a function of the local scalar dissipation rate, $\chi \equiv 2\mathcal{D}(\nabla\xi)^2$.

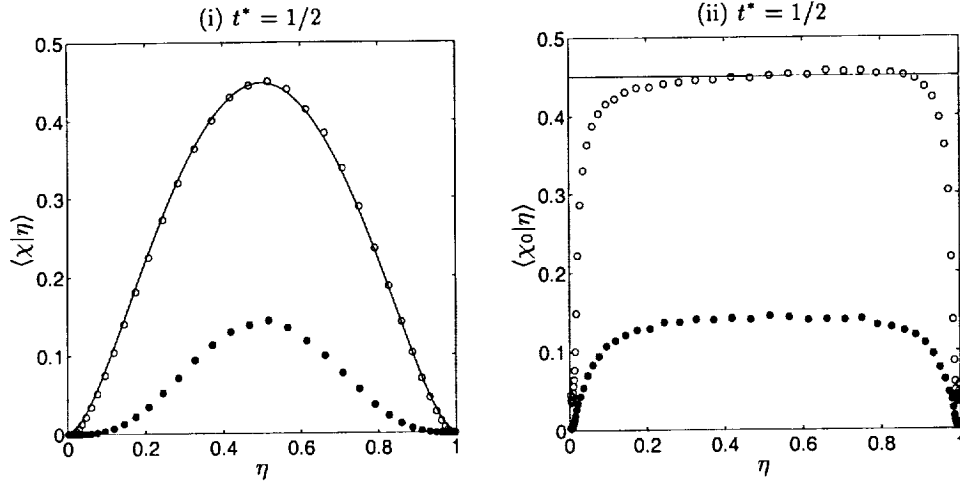


FIGURE 3. Illustration of (i) the $\langle \chi | \eta \rangle \equiv \langle \chi_0 \rangle F(\eta)$ dependence in the present DNS experiment with $F(\eta) \equiv \exp\{-2[\text{erf}^{-1}(2\eta - 1)]^2\}$ (counterflow function) and (ii) the approximate independence of $\chi_0 \equiv \chi/F$ with ξ . The variance is represented by the filled circles. Note, $\chi_0 = \chi$ at $\xi_{st} = 0.5$ for the present case.

2.3. Second conditioning variable

In Klimenko & Bilger (1999), the derivation of the multiply-conditional moment closure equations assumes a multi-stream mixing problem which is characterized by multiple conserved mixing variables. Two distinctions are to be made with the present formulation using a second conditioning variable:

(a) Only a two-stream mixing process is considered, where the advantage of multiply-conditioning expectations (in addition to the mixture fraction) is to account for additional fluctuations about the singly-conditional means.

(b) The scalar dissipation rate, used as the second conditioning variable presently, is not conserved. The source term for χ is (Ruetsch & Maxey (1992))

$$\frac{L(\chi)}{\rho} \equiv \left(\frac{\partial}{\partial t} + \mathbf{u} \cdot \nabla - \mathcal{D} \nabla^2 \right) \chi = -4\mathcal{D}(\nabla \xi \otimes \nabla \xi) : \nabla \mathbf{u} - 4\mathcal{D}^2(\nabla \xi \otimes \nabla \xi) : (\nabla \xi \otimes \nabla \xi) \quad (2.3)$$

for the present case of constant ρ and \mathcal{D} .

The choice of the scalar dissipation rate as the second conditioning variable follows, most recently, from the line of research pursued by Bushe & Steiner (1999). There, conditional source-term estimation is used to better approximate the chemical reaction-rates in physical space. In contrast, the present model performs combustion calculations in the space of χ (and ξ) and would convolve the conditionally-averaged solutions into physical space through the joint pdf of ξ and χ . Presently, we choose $\chi_0 \equiv \chi/F(\xi)$ (with $F(\xi) \equiv \exp\{-2[\text{erf}^{-1}(2\xi - 1)]^2\}$) as the second conditioning variable, further specializing the combustion modeling to the present DNS experiment where ξ and χ_0 have been found to be statistically independent (*cf.* Fig. 3).

Following the decomposition procedure (Klimenko & Bilger (1999)), the doubly-conditional moment closure equations with ξ and χ_0 as conditioning variables can be derived

using the differentiation rules:

$$\begin{aligned}\frac{\partial Y_P}{\partial t} &= \frac{\partial Q_P}{\partial t} + \frac{\partial Q_P}{\partial \eta} \frac{\partial \xi}{\partial t} + \frac{\partial Q_P}{\partial \chi_0} \frac{\partial \chi_0}{\partial t} + \frac{\partial Y_P'}{\partial t} \\ \nabla Y_P &= \nabla Q_P + \frac{\partial Q_P}{\partial \eta} \nabla \xi + \frac{\partial Q_P}{\partial \chi_0} \nabla \chi_0 + \nabla Y_P',\end{aligned}$$

where Y_P' represents fluctuations about the doubly-conditional mean $\langle Y_P | \eta, X \rangle = Q_P$ (with X the corresponding sample space variable for χ_0). Substitution into the local, instantaneous equation for Y_P and conditionally averaging yields

$$\begin{aligned}\left(\frac{d}{dt} + \alpha_0 \frac{\partial}{\partial X}\right) Q_P &= \left(\frac{XF}{2} \frac{\partial^2}{\partial \eta^2} + \beta_0 \frac{\partial^2}{\partial X^2} + \gamma_0 \frac{\partial^2}{\partial \eta \partial X}\right) Q_P \\ &\quad - 2\dot{w}(Q_F, Q_O, Q_P, \langle \theta | \eta, X \rangle)\end{aligned}\quad (2.4a)$$

$$\alpha_0 \equiv \frac{\langle \frac{L(X)}{\rho} | \eta, X \rangle}{F} + \frac{1}{F} \frac{dF}{d\eta} \gamma_0 + \frac{1}{2} X^2 \frac{\partial^2 F}{\partial \eta^2} \quad (2.4b)$$

$$\beta_0 \equiv \langle \mathcal{D}(\nabla \chi_0)^2 | \eta, X \rangle \quad (2.4c)$$

$$\gamma_0 \equiv \langle 2\mathcal{D}\nabla \xi \cdot \nabla \chi_0 | \eta, X \rangle \quad (2.4d)$$

where $F(\eta) \equiv \exp\{-2[\text{erf}^{-1}(2\eta - 1)]^2\}$. Again, for the present simplified chemistry case, $Q_F = \eta - Q_P/2$, $Q_O = 1 - \eta - Q_P/2$, and $\langle \theta | \eta, X \rangle = Q_P$. The relation $\chi \equiv \chi_0 F(\xi)$ has been used in Eq. (2.3) to obtain the source term of $L(\chi_0) \equiv \rho \alpha_0 \cdot Q_P$ in Eq. (2.4), henceforth termed model *cmc2*, is to be distinguished from the singly-conditional means of models *cmc0* and *cmc1*. With the exception of the convection term in X space (the second term on the left-hand side of Eq. (2.4a)), the same unclosed terms involving fluctuations about the conditional means result as detailed in the derivation in Klimenko & Bilger (1999). These terms are neglected following analogous arguments used in relation to Eq. (2.2). With doubly-conditioned moments, fluctuations are presumably reduced and their neglect a more accurate approximation. In particular, first-moment closure of the chemical reaction-rate in Eq. (2.4a) is expected to yield improved results over the analogous closure with singly-conditioned means (the *cmc0* model). It is to be shown that first-order doubly-conditional moment closure modeling yields further improvements to *cmc1* as well.

2.4. Implementation issues

All coefficients in Eq. (2.2) and (2.4) are calculated directly from the DNS experiment. Binning of the DNS experimental data is done with equal points per bin as opposed to using equally incremented bin sizes. Cubic interpolation is used in ξ and χ_0 space, and cubic splines are used to interpolate the one-dimensional profiles ($\langle \chi | \eta \rangle$ and $\langle Y_P'^2 | \eta \rangle$ for the *cmc0* and *cmc1* models) and the two-dimensional profiles (α_0 , β_0 , and γ_0 for the *cmc2* model) in time where the DNS data are not available.

Boundary conditions for the singly-conditional case (at $\eta = 0, 1$) are $Q_P(t, 0) = Q_P(t, 1) = 0$. For the doubly-conditional case, boundary conditions must be specified for $\eta \in [0, 1]$ at $X = X_{\min}, X_{\max}$ and for $X \in [X_{\min}, X_{\max}]$ at $\eta = 0, 1$. $Q_P(t, 0, X) = Q_P(t, 1, X) = 0$; at $X_{\min} \approx 0$, equilibrium solutions are used while pure mixing solutions are used at some $X_{\max} \gg \chi_q$. χ_q is the quenching value of the scalar dissipation rate. A value of $X_{\max} = \exp(3)$ was found to be large enough to not influence solutions. Cubic interpolation is also used to fit the DNS data at the initial time in (η, X) space for the initial conditions.

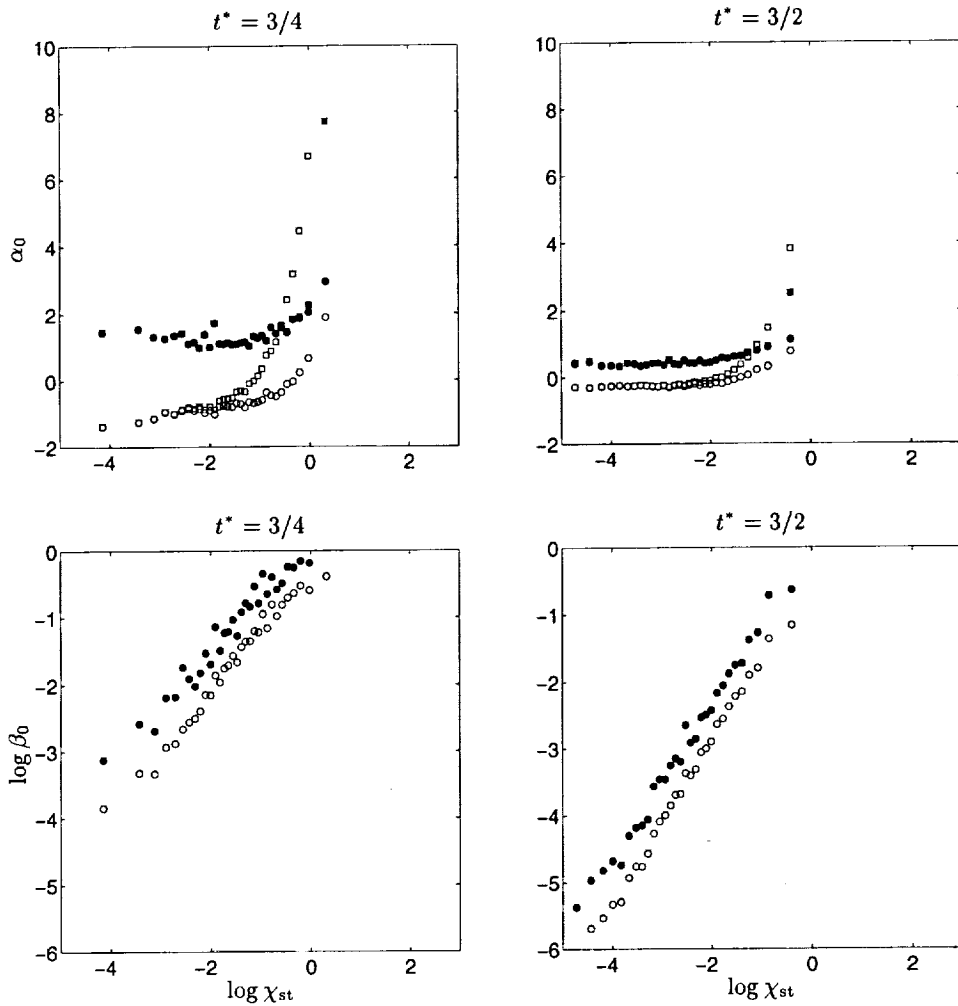


FIGURE 4. Scalar-dissipation rate dependence of the coefficients in doubly-conditional moment closure modeling. α_0 and β_0 (circles) and $\langle L(\chi)/\rho | \xi = \xi_{st}, \chi = X \rangle$ (note conditioning on χ , not χ_0) and $\langle \mathcal{D}(\nabla\chi)^2 | \xi = \xi_{st}, \chi = X \rangle$ (squares). Filled symbols are corresponding rms information.

Figure 3 (i) shows a typical profile illustrating the η dependence of $\langle \chi | \eta \rangle$ and $\langle \chi'^2 | \eta \rangle$. $\langle Y_P'^2 | \eta \rangle$ behaves similarly in η space: zero at the boundaries of η and maximum at $\eta = \xi_{st}$. Both $\langle \chi | \eta \rangle$ and $\langle Y_P'^2 | \eta \rangle$ are taken directly from the DNS for the singly-conditional moment modeling calculations. Singly-conditional moment modeling calculations show no appreciable effect on the solutions with $\langle \chi | \eta \rangle$ modeled as $\langle \chi_0 \rangle F(\eta)$ (cf. Fig. 3). This modeling has been used in all cmc0 and cmc1 results to follow.

Figures 4 and 5 show the ξ and χ_0 dependence of the coefficients α_0 , β_0 , and γ_0 (round symbols). Also shown are the analogous coefficients if χ were used as the second conditioning variable (square symbols): $\langle L(\chi)/\rho | \xi = \xi_{st}, \chi = X \rangle$ (analogous to α_0 , but with second conditioning on χ instead of χ_0), $\langle \mathcal{D}(\nabla\chi)^2 | \xi = \xi_{st}, \chi = X \rangle$ (analogous to β_0), and $\langle 2D\nabla\xi \cdot \nabla\chi | \xi = \eta, \chi = X \rangle$ (analogous to γ_0). With regard to Fig. 4, γ_0 and $\langle 2D\nabla\xi \cdot \nabla\chi | \xi = \eta, \chi = X \rangle$ are independent of X and are not shown. With regard to Fig. 5, α_0 , β_0 , and γ_0 are approximately independent of η , further corroborating the

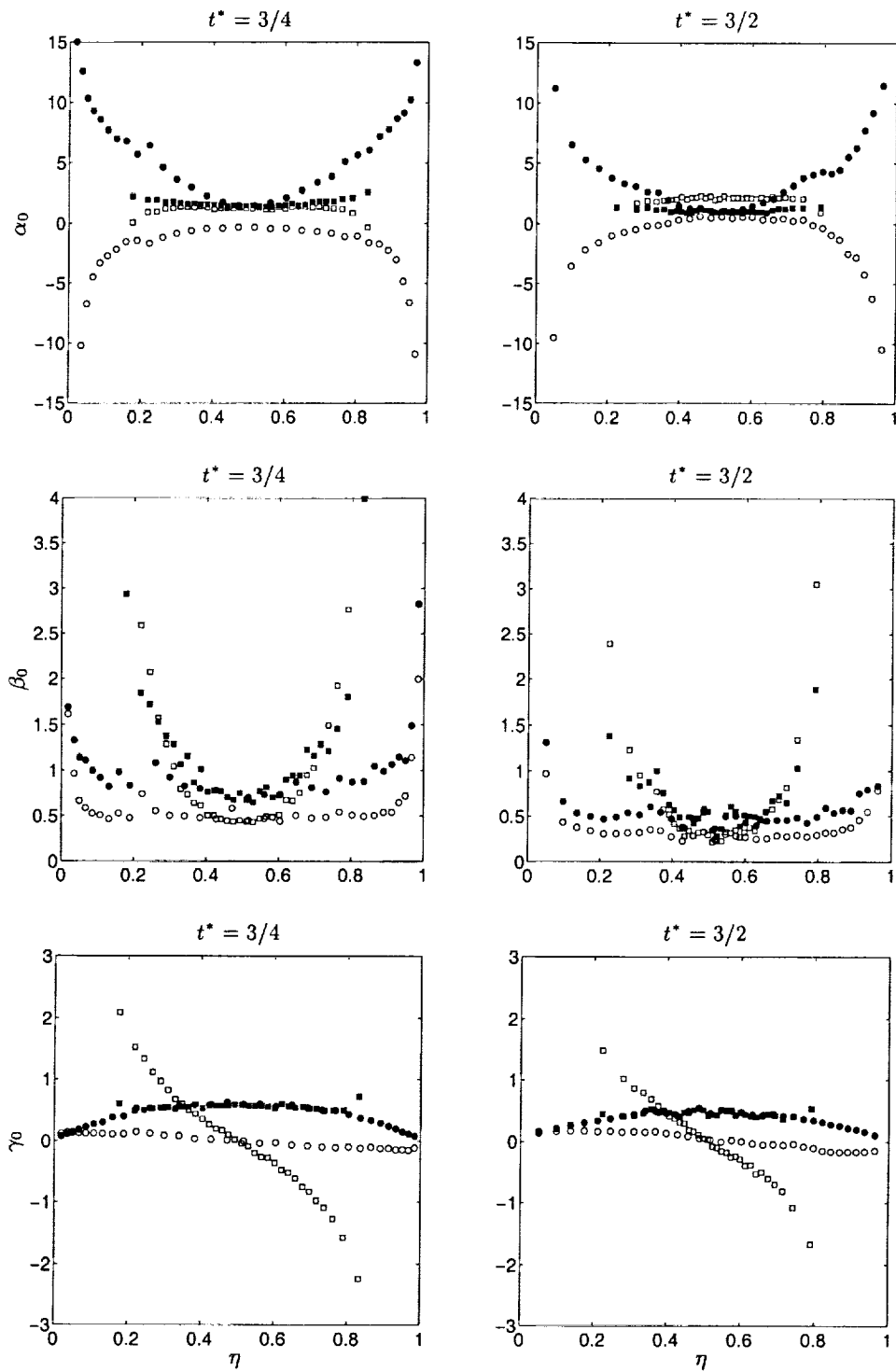


FIGURE 5. Mixture fraction dependence of the coefficients in doubly-conditional moment closure modeling: α_0 , β_0 , and γ_0 (circles) and $\langle L(\chi)/\rho | \xi = \eta, \chi = X_1 \rangle$ (note conditioning on χ , not χ_0), $\langle \mathcal{D}(\nabla\chi)^2 | \xi = \eta, \chi = X_1 \rangle$, and $\langle 2\mathcal{D}\nabla\xi \cdot \nabla\chi | \xi = \eta, \chi = X_1 \rangle$ (squares). Filled symbols are corresponding rms information.

independence of χ_0 and ξ . Doubly-conditional moment modeling calculations with and without the cross derivative term, $\partial^2 Q_p / \partial \eta \partial X$ (corresponding to the assumption of $\gamma_0 = 0$), shows no appreciable effect on the solutions. Hence, only values for α_0 and β_0 need to be specified on the X boundaries of the computational mesh. At X_{\min} , both are set to zero; at X_{\max} , $\alpha_0 = 0$ and a value for β_0 is extrapolated from a power law fit of the data (*cf.* Fig. 4).

3. Results and discussion

Figure 6 shows *cmc0* (— · —), *cmc1* (----), and *cmc2* (——) modeling results against the DNS data (symbols). Comparisons are made for increasing times from $t^* = 1/4$ (top row of subplots) to $t^* = 3/2$ (bottom row) and conditional on three representative values of the scalar dissipation rate: a relatively low value (left column of subplots), moderate (center column), and a relatively high value (right column). More precisely, the center column of subplots are conditioned on $X = \langle \chi_0 \rangle$, $X = \langle \chi_0 \rangle - \chi'_0$ in the left column (with $\chi'_0 \equiv \sqrt{\langle \chi_0'^2 \rangle}$), and $X = \langle \chi_0 \rangle + \chi'_0$ in the right column of subplots. Filled symbols are doubly-conditioned rms information of Y_p taken from the DNS experiment. As can also be seen from Fig. 2, the rms of Y_p (filled circles in Fig. 6) increases with time (moving from the top row down in Fig. 6) and higher scalar dissipation rates (moving from the left column to the right in Fig. 6).

Comparing overall modeling performance:

(a) The doubly-conditional moment approach (*cmc2*) yields the most significant improvement over both singly-conditional moment closure approaches (*cmc0* and *cmc1*) for times $t^* \lesssim 1/2$ and at relatively high scalar dissipation rate values (subplots (iii) and (vi) in Fig. 6). For all times, all three models are comparable at relatively low to moderate values of χ_0 , where the effects of extinction are not significant in the mean, and represent the data well.

(b) For increasing times, $t^* \gtrsim 3/4$, when reignition occurs in the mean (globally), the doubly-conditional model slowly converges to the *cmc0* and *cmc1* results and diverge from the data (witness subplots (ix) and (xii) in Fig. 6). This implies that the *cmc2* model predicts reignition too soon (or, alternatively, the level of extinction is underpredicted).

With regard to (a), the mean value of χ_0 never exceeds χ_q in the DNS experiment, hence the singly-conditional modeling results could never predict any extinction events. *cmc2* modeling accounts for the fluctuations of χ_0 , which can exceed χ_q by over a factor of 5 (*cf.* $t^* = 1/4$ in Fig. 2), and thus can yield the improved predictions seen in subplots (iii) and (vi) of Fig. 6 at the relatively large $X > \langle \chi_0 \rangle$. With regard to (b) ($t^* \gtrsim 3/4 =$ bottom half of Fig. 6), when extinction begins to occur at even moderate values of $X = \langle \chi_0 \rangle$, the required diffusion in X space is evidently insufficient to yield the reduction in the conditional means (seen in subplot (ix), for example). This may be due to the neglect of the influence of the fluctuations of the dissipation rate of the scalar dissipation rate, β_0 , the coefficient of the diffusion term in X space (*cf.* Eq. (2.4)). The present doubly-conditional moment closure model also neglects fluctuations about α_0 and γ_0 , which could also contribute to diffusion in scalar dissipation rate space.

Shortcomings of the *cmc2* model are due to the fluctuations (rms of Y_p) seen in Fig. 6 not accounted by the fluctuations of ξ and χ_0 . Accounting for fluctuations about α_0 , β_0 , and γ_0 may represent a fruitful course of action to improve results further. However, a second-order closure strategy (in conjunction with second-conditioning) cannot be used to improve the doubly-conditional moment closure modeling results where required. This

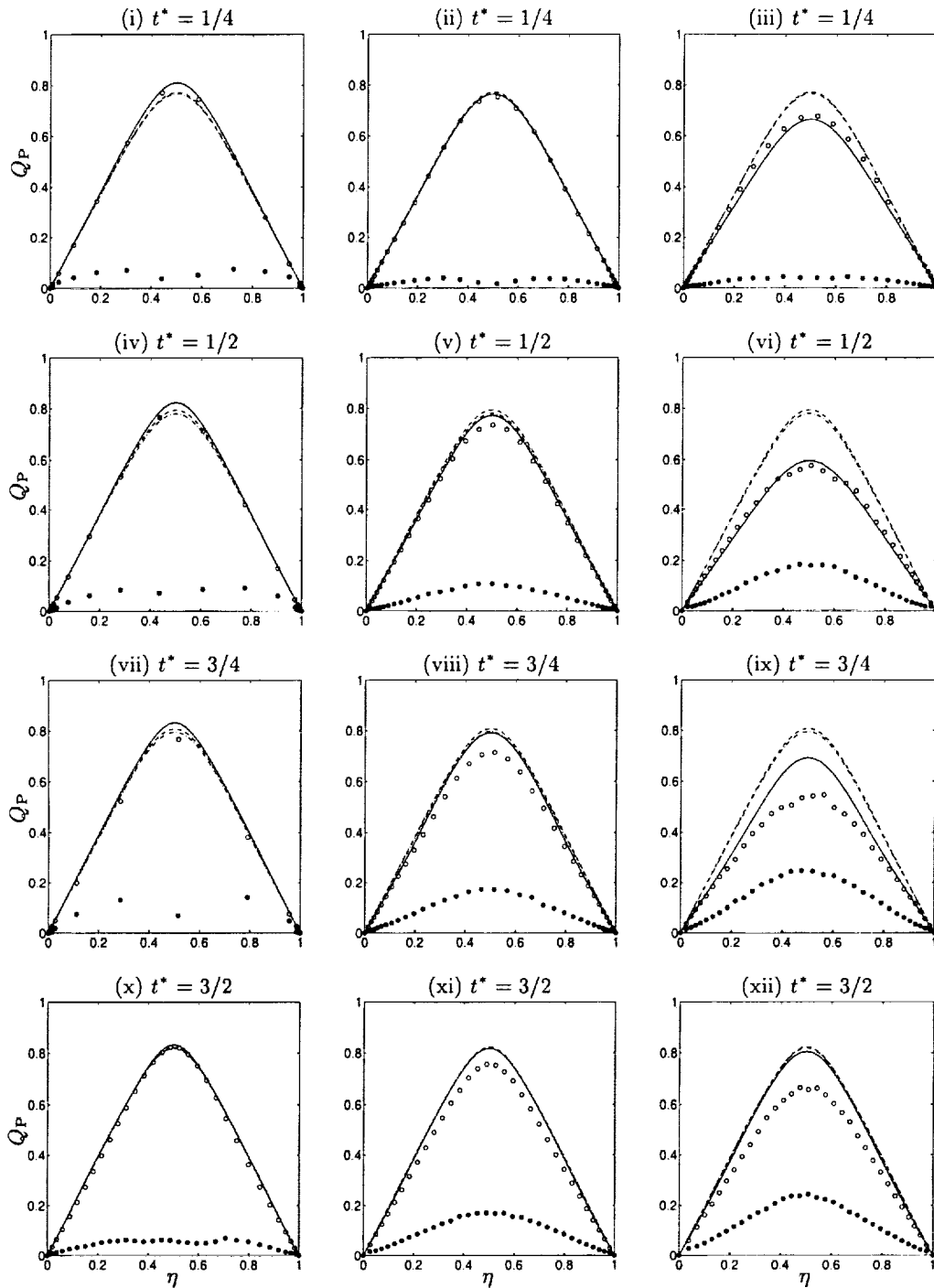


FIGURE 6. Modeling comparisons: Symbols, DNS data; ---, cmc0; - · - ·, cmc1; —, cmc2. Left column: conditioning on relatively low values of χ_0 ($X = \langle \chi_0 \rangle - \sqrt{\langle \chi_0'^2 \rangle}$), center column = conditioning at $X = \langle \chi_0 \rangle$, right column: conditioning on relatively high values of χ_0 ($X = \langle \chi_0 \rangle + \sqrt{\langle \chi_0'^2 \rangle}$). Filled symbols are corresponding rms information.

can readily be seen from comparisons between *cmc0* and *cmc1* modeling results, where the second-order closure strategy for \dot{w} (used in the *cmc1* model) yields larger Q_P predictions. The reason that the *cmc1* model gives larger conditional averages than *cmc0* can be seen from Eq. (2.2), where B for the present case is greater than zero. In fact, B will always be greater than zero at ξ_{st} if $Ze > \mathcal{O}(1)$, a realistic constraint on the Zeldovich number. Hence, the analogous strategy in doubly-conditional moment closure modeling will actually cause results to deviate more quickly from the data.

Within the framework of the current modeling then, this leaves e_Q and e_Y closure to be reexamined (in both the singly- and doubly-conditional approaches). These terms represent laminar (e_Q) and turbulent (e_Y) diffusion of the conditional averages in physical space (Klimenko & Bilger (1999)). These effects can only be incorporated into the present homogeneous, isotropic case if global averaging is abandoned. For example,

$$\langle D\nabla^2 Q_P | \eta \rangle - D\nabla^2 \langle Q_P | \eta \rangle \neq 0$$

under conditional spatial-filtering. Terms of this form appear in both the e_Q term and the closed form of e_Y (Klimenko & Bilger (1999)). This again means a more local treatment of the modeling may be required (even for the present homogeneous, isotropic case).

4. Conclusions and future work

Singly-conditional moment closure (with and without a second-order extension of the chemical source-term) is unable to describe the extinction and reignition seen on average in the current DNS experiment. A new conditional moment closure strategy using the scalar dissipation rate as a second conditioning variable describes extinction in the mean well, but predicts the onset of reignition too early. Shortcomings of the model are thought to be due to the neglect of “local effects” such as the influence of the fluctuations of the dissipation rate of the scalar dissipation rate and/or the neglect of the spatial diffusion of the conditional means due to the global averaging procedure.

Continued *a priori* studies to test these extensions are in progress. With regard to practical application, the doubly-conditional moment closure strategy in its present form may be able to account for a significant fraction of the extinction/reignition events seen in the jet-flame of Fig. 1 (a current benchmark data set for competing combustion models). A mapping of these events in scalar dissipation rate space would readily determine whether the present doubly-conditional moment closure strategy would yield good predictions. However, the necessary experimental data do not currently exist and so *a posteriori* doubly-conditional modeling studies are also underway to predict only the existing singly-conditioned data.

Acknowledgments

The authors express gratitude to Paiboon Sripakagorn for making available to us his DNS database before publication. George Kosály’s sabbatical stay at Stanford has been partially funded by CTR.

REFERENCES

- BARLOW, R. S. & FRANK, J. H. 1998 *Twenty-Seventh Symposium (International) on Combustion*, The Combustion Institute. 1087.

- BILGER, R. W. 1993 Conditional moment closure for turbulent reacting flow. *Phys. Fluids A* **5**(2), 436-444.
- BUSHE, W. K. & BILGER, R. W. 1999 Conditional moment closure modeling of turbulent non-premixed combustion with reduced chemistry. *Annual Research Briefs*, Center for Turbulence Research, NASA Ames/Stanford Univ. 139-154.
- BUSHE, W. K., BILGER, R. W. & RUETSCH, G. R. 1999 Direct numerical simulation of non-premixed combustion with realistic chemistry. *CTR manuscript 173*, Center for Turbulence Research, NASA Ames/Stanford Univ.
- BUSHE, W. K. & STEINER, H. 1999 Conditional moment closure for large eddy simulation of nonpremixed turbulent reacting flows. *Phys. Fluids* **11**(7), 1896-1906.
- DOPAZO, C. 1994 Recent developments in PDF methods. In *Turbulent Reacting Flows*, Academic Press, Chapter 7. 375-474.
- KLIMENKO, A. Y. 1990 Multicomponent diffusion of various admixtures in turbulent flow. *Fluid Dyn.* **25**, 327-334.
- KLIMENKO, A. Y. & BILGER, R. W. 1999 Conditional moment closure for turbulent combustion. *Prog. Energy Combust. Sci.* **25**, 595-687.
- MASTORAKOS, E. & BILGER, R. W. 1998 Second-order conditional moment closure for the autoignition of turbulent flows. *Phys. Fluids* **10**(6), 1246-1248.
- PETERS, N. 1983 Local quenching due to flame stretch in non-premixed turbulent combustion. *Combust. Sci. and Tech.* **30**, 1-17.
- PETERS, N. 2000 *Turbulent Combustion*, Cambridge.
- POPE, S. B. 1985 PDF methods for turbulent reacting flows. *Prog. Energy Combust. Sci.* **11**(2), 119-192.
- RUETSCH, G. R. & MAXEY, M. R. 1992 The evolution of small-scale structures in homogeneous isotropic turbulence. *Phys. Fluids A* **4**(12), 2747-2760.
- SRIPAKAGORN, P. 2000 *PhD thesis*, in progress, University of Washington.
- SWAMINATHAN, N. & BILGER, R. W. 1998 Conditional variance equation and its analysis. *Twenty-Seventh Symposium (International) on Combustion*, The Combustion Institute. 1191-1198.
- XU, J. & POPE, S. B. 1999 PDF calculations of piloted-jet turbulent flames of methane with local extinction, Cornell University. em Fluid Dynamics and Aerodynamics Report FDA-99-06.

Mapping closure approximation to conditional dissipation rate for turbulent scalar mixing

By Guowei He AND R. Rubinstein†

1. Motivation and objectives

The probability density function (PDF) approach has been shown to be a useful tool in turbulence research. The systematic approach for determining PDFs is by means of solving the transport equations for PDFs. In the PDF equations for turbulent scalar fields, conditional dissipation rate (CDR) appears as the only unclosed term (Pope (1985)). Recently developed large-eddy simulation schemes for turbulent reactive flow, such as the filtered PDF approach (Colucci, *et al.* (1998)), the conditional moment closure (Bushe & Steiner (1999)), and the Lagrangian flamelet model (Pitsch & Steiner (2000)), also require models for the CDR.

No satisfactory closure model for CDR had been constructed until the mapping closure approach (Kraichnan (1989), Chen, *et al.* (1989)) was formulated. Amplitude mapping closure suggests a CDR model (O'Brien & Jiang (1991)) whose form is separable in scalar and time variables. The model is in good agreement with direct numerical simulation (DNS) for initially symmetric binary mixing but fails in describing asymptotic behavior of the CDR for initially unsymmetric binary mixing (O'Brien & Sahay (1992)). Girimaji (1992) has developed a novel amplitude mapping closure approach in which the reference fields are time-dependent. The CDR model obtained from a time-evolving Gaussian reference field still fails to describe the asymptotic behavior, but the one from a time-evolving Beta reference field can successfully describe the asymptotic behavior. This strongly suggests that the amplitude mapping closure is inadequate to describe the asymptotic behavior by itself.

In the present research, we will develop a novel mapping closure approximation (MCA) to make successive approximations to statistics of a scalar in homogeneous turbulence. This technique will be used to construct a CDR model which accounts for the asymptotic behavior of the CDR. In Section 2.1, we will investigate the asymptotic behavior of the CDR model from amplitude mapping closure and explain the reason why it fails to describe the asymptotic behavior correctly. In Section 2.2, we will outline the MCA technique for successive approximation. In Section 2.3, we will use the MCA technique to formulate a novel CDR model and compare it with DNS results. We will conclude with a summary in Section 3.

2. Accomplishments

2.1. Asymptotic behaviors of amplitude mapping closure

In this section, we will show that the CDR model from amplitude mapping closure has incorrect asymptotic behavior for unsymmetric binary mixing. We consider the simple case of a single conserved scalar $Z(x, t)$ in incompressible homogeneous and isotropic

† ICASE, NASA Langley Research Center, Hampton, VA 23681-2199

turbulence. With $u(x, t)$ being the velocity field and κ the molecular diffusivity, the evolution equation for scalar Z is

$$\frac{\partial Z}{\partial t} + \mathbf{u} \cdot \nabla Z = \kappa \nabla^2 Z. \quad (2.1)$$

Here the boundary condition is periodic and the scalar is initially homogeneous and isotropic. Therefore, the scalar $Z(x, t)$ will remain homogeneous and isotropic for all time. We further assume that the scalar is binary (0 or 1) and its initial PDF is a double-delta distribution:

$$P(Z, 0) = \begin{cases} A & \text{if } Z = 0 \\ 1 - A & \text{if } Z = 1 \\ 0 & \text{if } Z \neq 0 \text{ or } 1, \end{cases} \quad (2.2)$$

where $0 \leq A \leq 1$. $A = 0.5$ implies that the binary scalar has the same weights and the corresponding PDF $P(Z, 0)$ is symmetric with respect to $Z = 0.5$, while $A \neq 0.5$ implies that the binary scalar has different weights and the corresponding PDF $P(Z, 0)$ is unsymmetric. DNS Eswaran & Pope (1988) has shown that the scalar PDF $P(Z, t)$ asymptotically approaches a Gaussian distribution whether the initial double-delta distribution is symmetric or unsymmetric. The mean $\langle Z \rangle = 1 - A$ remains unchanged in turbulent mixing. The CDR $\chi(Z, t) = \kappa \langle (\nabla Z)^2 | Z \rangle$ is nearly parabolic. At early stages, the CDR maximum is located at $Z = 0.5$, the mean of the initial interface of the binary scalar. The maximum then moves and finally approaches the mean $\langle Z \rangle$ of the scalar, accompanied by a distortion of the parabola. Therefore, for an initially symmetric binary scalar ($A = 0.5$), the maximum will remain fixed at $Z = 0.5$, where the mean of the scalar and the mean of the initial interface are coincident. For an initially unsymmetric binary scalar ($A \neq 0.5$), the maximum will shift to the mean $Z = 1 - A$ of the scalar from the mean $Z = 0.5$ of the initial interface.

Amplitude mapping closure assumes

$$Z = X(\phi_0, t), \quad (2.3)$$

where $\phi_0(\mathbf{x})$ is a homogeneous Gaussian random field. The governing equation for the mapping function X is

$$\frac{\partial X}{\partial t} = \kappa \langle \phi_{0x}^2 \rangle \left(-\frac{\phi_0}{\langle \phi_0^2 \rangle} \frac{\partial X}{\partial \phi_0} + \frac{\partial^2 X}{\partial \phi_0^2} \right), \quad (2.4)$$

where ϕ_{0x} is the spatial gradient of the scalar ϕ_0 . The initial mapping function corresponding to (2.2) is

$$X(\phi_0, 0) = \begin{cases} 0 & \text{if } \phi_0 \leq \gamma \\ 1 & \text{if } \phi_0 > \gamma, \end{cases} \quad (2.5)$$

where $\gamma = \sqrt{2} \operatorname{erf}^{-1}(2A - 1)$. The exact solution of Eq. (2.4) with the initial condition (2.5) is

$$X(\phi_0, t) = \frac{1}{2} \left[1 + \operatorname{erf} \left(\frac{\theta_0 - \gamma e^\tau}{\sqrt{2}\Sigma} \right) \right], \quad (2.6)$$

where

$$\begin{aligned} \theta_0 &= \frac{\phi_0}{\sqrt{\langle \phi_0^2 \rangle}}, \\ \tau &= \kappa \frac{\langle \phi_{0x}^2 \rangle}{\langle \phi_0^2 \rangle} t, \\ \Sigma &= \sqrt{\exp(2\tau) - 1}. \end{aligned} \quad (2.7)$$

We can calculate the CDR from the exact solution (2.6)

$$\begin{aligned} \chi(Z, t) &= \kappa \frac{\langle \phi_{0x}^2 \rangle}{\langle \phi_0^2 \rangle} \frac{1}{\sqrt{2\pi}\Sigma} \exp \left(-2 \left[\operatorname{erf}^{-1}(2Z - 1) \right]^2 \right) \\ &= \chi(0.5, t) \exp \left(-2 \left[\operatorname{erf}^{-1}(2Z - 1) \right]^2 \right). \end{aligned} \quad (2.8)$$

The most striking feature of the CDR model (2.8) is the separability of its form in Z and t . The separability suggests that the CDR's shape remains unchanged although its amplitude decays with time. The CDR maximum is located permanently at $Z = 0.5$ without any shift for either symmetric or unsymmetric initial conditions. The permanent location of the maximum for unsymmetric initial condition (Girimaji (1992), O'Brien & Jiang (1991), O'Brien & Sahay (1992)) is contrary to the known asymptotic behavior of the CDR. Therefore, the CDR model (2.8) from amplitude mapping closure is not able to describe the asymptotic behavior of the CDR. The amplitude mapping closure with a time-evolving Gaussian reference field gives a similar CDR model whose form is separable in t and Z and also fails to describe the shift of the maximum. Therefore, the separation in form is the main reason for the incorrect asymptotic behavior of the CDR model from amplitude mapping closure.

2.2. Mapping closure approximation

The basic idea of mapping closure is to represent an unknown random field by mapping of a known random reference field. The statistics of the unknown random field can be calculated from the mapping function and the known reference field. The governing equation for the mapping function can be obtained from the evolution equation of the unknown random field and the governing equation of its PDF.

Amplitude mapping closure assumes that the unknown random field can be mapped by a single known Gaussian reference field: $Z = X(\phi(x'), t)$ and a coordinate transformation $dx'/dx = J(d\phi(x')/dx', t)$ that accounts for turbulent stretching. The assumption Gotoh & Kraichnan (1993) holds if and only if the spatial level crossing frequency at which the unknown random field passes through a given value has a single maximum as a function of that value. Therefore, the existence of the mapping function as well as the coordinate transformation is not ensured for arbitrary unknown random fields. Physically, a turbulent field exhibits eddies of different length and time scales so that it cannot be mapped by a single reference Gaussian field with a compact spectrum. Therefore, it is necessary to introduce more reference fields accounting for different eddies of different time and length scales:

$$Z = X(\phi_0(x, t), \phi_1(x, t), \dots, \phi_n(x, t); x, t) \quad (2.9)$$

where ϕ_i , $i = 1, \dots, n$, are reference fields. So far, we have not imposed any constraints on the reference fields so that we have some freedom in choosing the reference fields. For example, ϕ_0 could be Gaussian but ϕ_1 could be a Beta random field.

A one-to-one mapping could be established artificially between $(Z, \phi_1, \dots, \phi_n)$ and $(\phi_0, \phi_1, \dots, \phi_n)$. Thus, we can calculate the PDF and the conditional dissipation rate of the scalar

$$P(Z; x, t) = \int P(\phi_0, \phi_1, \dots, \phi_n) \left(\frac{\partial X}{\partial \phi_0} \right)^{-1} d\phi_1 \dots d\phi_n, \quad (2.10)$$

$$\langle (\nabla Z)^2 | Z \rangle = \langle (\nabla X)^2 | Z \rangle. \quad (2.11)$$

Here the integration is taken over the entire subspace of the composition ϕ_1, \dots, ϕ_n . The ensemble average is taken over the level surface on which $(\phi_0, \phi_1, \dots, \phi_n)$ satisfies the constraint $X(\phi_0(x, t), \phi_1(x, t), \dots, \phi_n(x, t); x, t) = Z$ for a given Z .

Introduction of more reference fields is expected to improve the approximation accuracy of mapping closure. The reference fields might be chosen to be statistically orthogonal so that more information can be introduced at less expense. MCA provides a successive non-perturbative approximation approach which is different from the Wiener-Hermite expansion (Orszag & Bissonnette (1967)).

2.3. The model for conditional dissipation rate

Broad classes of mapping function are admissible to MCA approach. The form to be considered here is

$$Z = Y(\phi_0(x), \phi_1(t); t), \quad (2.12)$$

where $\phi_0(x)$ is a homogeneous random Gaussian field in space and $\phi_1(t)$ an inhomogeneous random Gaussian field in time. Amplitude mapping closure requires $\phi_1(t) = 0$, which fails in the asymptotic behavior of conditional dissipation rate due to lack of an independent time-evolving reference field.

Following the standard method (Gotoh & Kraichnan (1993), Kimura & Kraichnan (1993)), we can formulate the mapping equation:

$$\frac{\partial Y}{\partial t} + \frac{\partial Y}{\partial \phi_1} \left\langle \frac{d\phi_1}{dt} \middle| Z \right\rangle = -\langle u \nabla Y | Z \rangle + \kappa \langle \nabla^2 Y | Z \rangle. \quad (2.13)$$

The conditional averages in (2.13) can be evaluated by homogeneity of the velocity and scalar fields and Gaussianity of the reference fields

$$\begin{aligned} \langle u \nabla Y | Z \rangle &= 0, \\ \left\langle \frac{d\phi_1}{dt} \middle| Z \right\rangle &= \frac{\phi_1}{2\langle \phi_1^2 \rangle} \frac{d\langle \phi_1^2 \rangle}{dt}, \\ \langle \nabla^2 Y | Z \rangle &= -\phi_0 \frac{\langle \phi_{0x}^2 \rangle}{\langle \phi_0^2 \rangle} \frac{\partial Y}{\partial \phi_0} + \langle \phi_{0x}^2 \rangle \frac{\partial^2 Y}{\partial \phi_0^2} \end{aligned} \quad (2.14)$$

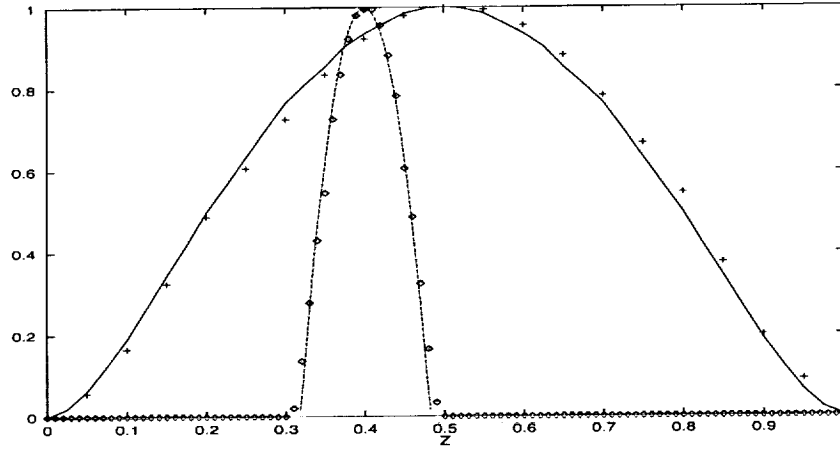


FIGURE 1. Normalized CDRs $\chi(Z, t)/F(t)$ for the initially unsymmetric double-delta distribution with $A = 0.6$. — (DNS) and + (model): initial CDRs; ---- (DNS) and \diamond (model): final CDRs.

An exact solution can be obtained from (2.13) with the evaluated conditional averages (2.14) and the initial condition (2.5) which requires $\phi_1(0) = 0$

$$Y = \frac{1}{2} \left[1 + \operatorname{erf} \left(\frac{\phi_0 - \gamma e^\tau}{\sqrt{2}\Sigma} \right) + \left(1 - \exp[\phi_1 - \langle \phi_1 \rangle + \int_0^t \langle \frac{d\phi_1}{dt} | Z \rangle dt] \right) (2\langle Z \rangle - 1) \right]. \quad (2.15)$$

We will calculate the CDR $\chi(Z, t) = \kappa \langle (\nabla Y)^2 | Z \rangle$, where ensemble average is taken over the level surface on which (ϕ_0, ϕ_1) satisfies $Y(\phi_0, \phi_1; t) = Z$. The expression obtained is then simplified by the first-order approximation of its Taylor expansion with respect to $\langle \phi_1(t) \rangle$. This leads to

$$\chi(Z, t) = F(t) \exp \left[-2 \left(\operatorname{erf}^{-1} [(2Z - 1) - (1 - \frac{1}{\sqrt{1 + f_{\phi_1} t}}) (2\langle Z \rangle - 1)] \right)^2 \right], \quad (2.16)$$

where

$$\begin{aligned} F(t) &= \frac{f_{\phi_0}}{\sqrt{2\pi\Sigma}}, \\ f_{\phi_0} &= \kappa \frac{\langle (\phi_{x0})^2 \rangle}{\langle \phi_0^2 \rangle}, \\ f_{\phi_1} &= \frac{d\langle \phi_1^2 \rangle}{dt} / \langle \phi_1^2 \rangle. \end{aligned} \quad (2.17)$$

The time scales f_{ϕ_0} and f_{ϕ_1} are parameters of the present closure which must be input externally. Usually, they are reset at each time using a dynamical scheme, such as $f_{\phi_0} = \kappa \langle (\nabla Z)^2 \rangle / \langle Z^2 \rangle$ and $f_{\phi_1} = f_{\phi_0}$, so as to give correct evolution of the CDR. The CDR

model (2.16) is compared with DNS of the diffusion equation with $\kappa = 1$. In the case of homogeneity, the use of the diffusion equation to validate the CDR model for turbulent mixing has a reasonable justification. Figure 1 shows the initial and final CDRs obtained by the DNS and the CDR model (2.16) for the initially unsymmetric binary scalar with mean $\langle Z \rangle = 0.4$. For exhibiting the shift of the maximum, the CDRs are normalized by their amplitudes $F(t)$ and (2.16) rescaled by the scalar's variances.

The CDR model (2.16) is no longer separable in Z and t . Its shape will shift while its amplitude decays with time. It is easy to verify that $\chi(0.5, 0)/F(t) = 1$ and that $\chi(\langle Z \rangle, \infty)/F(t) = 1$. Therefore, Eq. (2.16) correctly describes asymptotic behaviors of CDR: the CDR's maximum asymptotically approaches $Z = \langle Z \rangle$, while initially being at $Z = 0.5$.

It has been shown that the mapping (2.12) is an appropriate approximation for a scalar gradient field. However, it is not expected that the mapping (2.12) makes the same accurate approximation to the scalar field as it does to the scalar gradient field itself. The reason is that a homogeneous random field is statistically orthogonal to its gradient field. The amplitude mapping (2.3) is an appropriate approximation to scalar fields but fails to approximate its gradient field. Generally speaking, the mapping closure carried out at the level of single-point PDFs is not valid for two-point PDFs such as gradient fields. This is the motivation to develop mapping closure approximation of higher orders.

3. Conclusions and further plans

We have developed a novel model of the conditional dissipation rate for turbulent mixing. The model is able to describe the asymptotic behavior of the CDR for either symmetric or unsymmetric initial double-delta distributions. The amplitude mapping closure has unsatisfactory asymptotic properties for the shift of the CDR's maximum. The problem can be solved using the extended mapping closure approximation developed in this paper. Further research will involve extending the CDR model (2.16) to account for the evolution of scalar variance. MCA can incorporate the effect of multiple time and length scales of practical interest in its predictions using more than one reference field. It provides a useful approach to describe statistics of turbulent mixing.

Acknowledgment

The author (G. W. He) is grateful for the very valuable discussions on the subject with G. Kosaly and H. Pitsch. Special thanks are due to G. Kosaly for pointing out the exact solution (2.6).

REFERENCES

- BUSHE, W. K. & STEINER, H. 1999 Conditional moment closure for large eddy simulation of nonpremixed turbulent reacting flows. *Phys. Fluids*, **11**, 1896.
- CHEN, H., CHEN, S. & KRAICHNAN, R. H. 1989 Probability distribution of a stochastically advected scalar field. *Phys. Rev. Lett.* **63** 2657.
- COLUCCI, P. J., JABERI, F. A., GIVI, P. & POPE, S. B. 1998 Filtered density function for large eddy simulation of turbulent reacting flows. *Phys. Fluids*, **10**, 499.
- ESWARAN, V. & POPE, S. B. 1988 Direct numerical simulations of the turbulent mixing of a passive scalar. *Phys. Fluids* **31**, 506.

- GIRIMAJI, S. S. 1992 A mapping closure for turbulent scalar mixing using a time-evolving reference field. *Phys. Fluids A*. **4**, 2875.
- GOTOH, T. & KRAICHNAN, R. H. 1993 Statistics of decaying Burgers turbulence. *Phys. Fluids*. **5**, 445.
- KIMURA, Y. & KRAICHNAN, R. H. 1993 Statistics of an advected passive scalar. *Phys. Fluids*. **5**, 2264.
- KRAICHNAN, R. H. 1989 Closures for probability distribution. *Bull. Am. Phys. Soc.* **34** 2298.
- O'BRIEN, E. E. & JIANG, T. L. 1991 The conditional dissipation rate of an initial binary scalar in homogeneous turbulence *Phys. Fluids A*. **3**, 3121.
- O'BRIEN, E. E. & SAHAY, A. 1992 Asymptotic behavior of the amplitude mapping closure. *Phys. Fluids A*. **4**, 1773.
- ORSZAG, S. T. & BISSONNETTE, L. R. 1967 Dynamical properties of truncated Wiener-Hermite Expansions. *Phys. Fluids*. **10**, 2603.
- PITSCH, H. & STEINER, H. 2000 Large-eddy simulation of a turbulent piloted methane/air diffusion flame (Sandia flame D). *Phys. Fluids*. **12**, 2541.
- POPE, S. B. 1985 PDF methods for turbulent reactive flows. *Progr. Energy, Combust. Sci.* **11**, 119.

Extended flamelet model for LES of non-premixed combustion

By Heinz Pitsch

1. Motivation and objectives

In recent years large-eddy simulation (LES) of turbulent combustion has become a subject of intensive research and modeling efforts. The focus of most activities has been model development using *a priori* studies and LES of simplified flow configurations and chemistry for comparison with direct numerical simulations (DNS). The first application of LES for non-premixed combustion in a turbulent jet flame with detailed comparison with experimental data has recently been conducted by Pitsch & Steiner (1999, 2000). In this study the Lagrangian flamelet model (LFM), first introduced by Pitsch *et al.* (1998), has been used. In this model, rather than using steady state flamelets, unsteady flamelets are solved, which are introduced at the inlet nozzle and assumed to be transported downstream, essentially by convective transport. The time coordinate in the flamelet equations hence becomes a Lagrangian-like time. The scalar dissipation rate appearing as a parameter in the flamelet equations is modeled by its conditional average over cross-sectional planes perpendicular to the jet axis. The model has been applied to the so-called D-flame of the Sandia flame series, experimentally investigated by Barlow & Frank (1998a, 1998b). The results are compared to mean and conditionally averaged temperature and species mass fractions, showing in general very good agreement. However, in the rich part of the flame, mainly CO and H₂ are overpredicted. This has been attributed to the fact that in order to prevent formation of aromatic hydrocarbons, which would interfere with the experimental techniques, the fuel has been diluted with air and is hence partially premixed. This causes the occurrence of heat release in the rich premixed region in the predictions of the LES, which in turn leads to overpredictions of mass fractions of CO, H₂ and other species. Interestingly, similar trends appear in many other modeling studies using the steady flamelet model, the conditional moment closure model, the transported pdf model, and the linear eddy model (Barlow (1998, 1999)), which are mainly used in RANS simulations.

An obvious disadvantage of the LFM as it is applied in Pitsch & Steiner (2000) is that only an averaged scalar dissipation rate is used. This is also the case for most other models, particularly in the context of RANS, where only the time averaged scalar dissipation rate is known. It has been shown in Pitsch & Steiner (2000) that the filtered scalar dissipation rate including the resolved and the sub-grid part in a jet flame is a strongly fluctuating quantity appearing in large-scale organized structures. Figure 1 in Pitsch & Steiner (2000) shows the two-dimensional instantaneous distribution of this quantity from the LES of the Sandia flame D. It is obvious that regions of high scalar dissipation rate might be present on one side of the axis, while the scalar dissipation rate is very low on the other side. This spatial structure is being lost in the cross-sectional conditional averaging procedure applied in Pitsch & Steiner (2000). In recent work we have investigated the influence of fluctuations of the scalar dissipation rate in non-premixed combustion (Pitsch & Fedotov (2000) and Sripakagorn *et al.* (2000)),

showing that these can have a strong impact and can lead to local flame extinction, even if the conditional mean scalar dissipation rate is well below the extinction limit.

In the present work the LFM will be extended to account for local inhomogeneities of the scalar dissipation rate. In the following sections, first the governing equations will be derived and the relation to the flamelet equations derived in earlier work by Peters will be discussed. Following this, the numerical implementation of the resulting equations will be described, and finally, numerical results from the LES of a turbulent jet diffusion flame will be discussed and compared to the results obtained from the LFM and to experimental data.

2. Governing equations

In this section a new formulation of an unsteady flamelet model for LES of non-premixed combustion, the extended flamelet model (EFM), will be developed. The underlying ideas are similar to the LFM, but a different formulation allows for a more detailed consideration of local effects. We will first derive the flamelet equations as proposed by Peters (1983, 1994, 1987). This procedure is very well described, for instance, in Peters (1984), but will still be outlined in this section in order to clearly expose the underlying assumptions. The analysis here will only be discussed for the species mass fractions equations since the derivation for other scalar equations such as the temperature or enthalpy equation can be performed analogously.

We start with the governing equation for mixture fraction Z and species mass fractions Y_i , which can be written as

$$\rho \frac{\partial Z}{\partial t} + \rho \mathbf{v} \cdot \nabla Z + \nabla \cdot (\rho D \nabla Z) = 0 \quad (2.1)$$

$$\rho \frac{\partial Y_i}{\partial t} + \rho \mathbf{v} \cdot \nabla Y_i + \nabla \cdot (\rho D \nabla Y_i) - \dot{m}_i = 0. \quad (2.2)$$

Here, ρ is the density, t the time, \mathbf{v} the velocity vector, \dot{m}_i is the chemical source term of species i , and D the molecular diffusivity of the mixture fraction and all chemical species. For simplicity, all Lewis numbers are assumed to be unity for the following derivation of the flamelet equations. Non-constant Lewis numbers can be considered by applying the method of Pitsch & Peters (1998). In order to derive the flamelet equations, we consider the coordinate system introduced in Eqs. (2.1) and (2.2) such that one coordinate, say x_1 , at a given instant in time is normal to the surface of stoichiometric mixture. The origin of the coordinate system can be chosen to be traveling with the stoichiometric surface or to be independent of this surface without any implications on the results of the following procedure. According to Peters (1983, 1994, 1987) we then perform a Crocco type coordinate transformation, such that x_1 is replaced by the mixture fraction Z , where the other coordinates remain. The transformation is then given by

$$t, x_1, x_2, x_3 \longrightarrow \tau, Z, Z_2, Z_3. \quad (2.3)$$

For this transformation to be valid, x_1 has to be uniquely representable by the new coordinate Z , which is the case in many simplified laminar configurations but is not generally satisfied in a turbulent flow. We therefore have to assume that the reaction zone is smaller than the small scales of the turbulence and restrict the analysis to a small region around the reaction zone. This requirement will be used again in the subsequent derivation and can be called the *flamelet assumption*. Also the possible rotation of the new

coordinate Z with respect to the original coordinate x_1 during the temporal development of the flow field will be neglected. However, it has recently been pointed out by Klimenko (2000) that this error is small if the curvature radius is large compared to the reaction zone thickness, which is the case if the reaction zone is assumed to be thin compared to the turbulent scales.

After this formal transformation, an asymptotic approximation is performed. Again, we invoke the flamelet assumption of a thin reaction zone. Then, changes along mixture fraction iso-surfaces in the vicinity of stoichiometric mixture are small compared to the changes in the direction of the mixture fraction and can be neglected. The resulting equations are the so-called flamelet equations given by

$$\rho \frac{\partial Y_i}{\partial \tau} - \rho \frac{\chi}{2} \frac{\partial^2 Y_i}{\partial Z^2} - \dot{m}_i = 0, \quad (2.4)$$

where the scalar dissipation rate χ has been introduced as

$$\chi = 2D (\nabla Z)^2. \quad (2.5)$$

It should be noted that in this equation the newly introduced time τ is the time defined in the new coordinate system, which means that the time derivative $\partial/\partial\tau$ is to be evaluated at constant mixture fraction Z . Hence, τ is a Lagrangian-like time coordinate. With respect to a point in space which is independent of the stoichiometric surface, this new coordinate system moves with the velocity of a point on the stoichiometric surface. The unsteady flamelet model using Eq. (2.4) in a model for turbulent non-premixed combustion has, therefore, been called the Lagrangian Flamelet Model (Pitsch (2000) and Pitsch & Steiner (2000)).

We now want to derive an Eulerian form of the flamelet equations. For the Lagrangian-like time coordinate τ follows

$$\frac{\partial}{\partial \tau} = \frac{\partial}{\partial t} + \frac{\partial x_Z}{\partial t} \cdot \nabla, \quad (2.6)$$

where $\partial x_Z/\partial t$ is the velocity of a point on the mixture fraction iso-surface. The velocity of the scalar iso-contours has been discussed in connection with the LFM in Pitsch & Steiner (2000) and can, according to Gibson (1968), be given as

$$\frac{\partial x_Z}{\partial t} = \mathbf{v} - \frac{\nabla \cdot (\rho D \nabla Z)}{|\nabla Z|^2} \nabla Z, \quad (2.7)$$

where the first part is because of convection and the second part because of diffusion of the mixture fraction.

Introducing Eqs. (2.6) and (2.7) into Eq. (2.4) and for the reasons discussed in Pitsch & Steiner (2000) neglecting the diffusive part in Eq. (2.7) leads to the flamelet equations in an Eulerian system

$$\rho \frac{\partial Y_i}{\partial t} + \rho \mathbf{v} \cdot \nabla Y_i - \rho \frac{\chi}{2} \frac{\partial^2 Y_i}{\partial Z^2} - \dot{m}_i = 0. \quad (2.8)$$

The same equations could have been derived using a two-scale asymptotic analysis as recently suggested by Peters (2000). In this approach a short scale is defined in terms of the mixture fraction covering the range in the close vicinity of the flame surface. A second coordinate is assumed to describe variations on the long scales only and essentially replaces the spatial coordinates. Since the long scale coordinate is still Eulerian, the convection term remains during the derivation in the equation, and a transformation as given by Eq. (2.6) is not needed.

Equations 2.8 have been derived to be valid locally and instantaneously. To apply these flamelet equations as a sub-grid combustion model for LES, closure will be achieved as suggested by Pitsch *et al.* (1998). The scalar dissipation rate and the velocity in the flamelet equations will be replaced by the conditional means of the instantaneous local conditionally filtered values of the scalar dissipation rate and the velocity. Consequently, the species mass fractions obtained by solving the flamelet equations are also to be interpreted as conditional mean quantities. This implies that the influence of the sub-grid fluctuations of the scalar dissipation rate and the velocity is small, which excludes the validity of the current model for situations, where local extinction phenomena are important. Note, however, that the sub-grid part of the scalar dissipation rate certainly needs to be accounted for in the model for the filtered scalar dissipation rate.

The flamelet equations derived here show close resemblance to the first order conditional moment closure model (CMC) proposed by Klimenko (1990) and Bilger (1993). Only the turbulent transport term is missing here, which has been omitted because it is small in the present application. However, it could be included in the model by similar arguments as given in section 3.12 in Peters (2000).

The reason for the similarity of the flamelet equations given here and first order CMC is that both models assume the conditional fluctuations to be negligible. In flamelet modeling these fluctuations would be taken into account by averaging over ensembles of flamelets with different scalar dissipation rates and presuming a pdf of the scalar dissipation rate. In contrast to this, in CMC the conditional fluctuations appear as additional unclosed correlations in the CMC equations. These correlations then have to be modeled. Therefore, differences in both models only appear if conditional fluctuations are taken into consideration.

3. Numerical implementation

Unlike the application of steady state flamelet models, which is very straightforward, the numerical implementation of the present model needs some further consideration. The reason for this is that the flamelet equations derived here are time dependent, three-dimensional in space, and also depend on mixture fraction. Also, the intended use of complex chemistry requires solving Eq. (2.8) for a large number of chemical species. It seems, therefore, that the current approach is prohibitive in LES since this is known to be an expensive technique already for simulations of non-reactive flows.

However, an important aspect here is that in a spatially discretized form of Eq. (2.8) we solve in each computational cell not only for scalar values of Y_i , but for the function $Y_i(Z)$. Under the assumptions made earlier, this function is not likely to change rapidly in space. Strong changes of Y_i , however, are to be expected in the direction of Z . Therefore, the spatial discretization of Eq. (2.8) can be much coarser than the resolution of the remaining equations. The present simulations have been performed using a computational mesh in spherical coordinates with $192 \times 110 \times 48$ cells in the downstream (s), radial (θ), and circumferential (ϕ) direction, schematically shown in Fig. 1. The flamelet equations are spatially discretized in the downstream and circumferential direction only, using 48×8 cells. Since the mixture fraction varies mainly in θ -direction, changes of $Y_i(Z)$ with respect to θ are expected to be small. Therefore, for the solution of Eq. (2.8) the θ -direction is assumed to be homogeneous.

In the time discretization of Eq. (2.8), the unsteady term, the diffusion in Z , and the

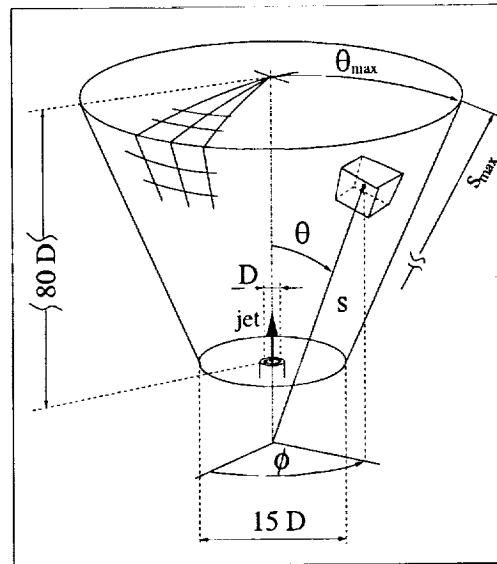


FIGURE 1. Schematic representation of the coordinate system.

chemical source term are solved implicitly. The convection term is explicit and treated as source term in the implicit solution of the remaining terms.

In order to further reduce the computational effort, a reduced 20-step mechanism has been derived for the present simulation. The reduced scheme is based on the GRI 2.11 mechanism by Bowman *et al.* (1998).

4. Results and discussion

In this section numerical results of the presented model will be presented and compared with earlier results obtained by the LFM (Pitsch & Steiner (2000)) and experimental data. Numerical simulations have been performed for a piloted methane/air jet diffusion flame (Sandia Flame D), experimentally investigated by Barlow & Frank (1998a, 1998b). As mentioned earlier, the fuel has been diluted by 75 vol. % of air in order to minimize the formation of polycyclic aromatic hydrocarbons and soot, which would interfere with the applied experimental techniques. The fuel nozzle is enclosed by a broad pilot nozzle and a co-flow of air. The Reynolds number based on the fuel stream is $Re = 22400$.

The time averaged mixture fraction development along the centerline predicted by the EFM and the LFM is given in Fig. 2 on the left. The overall agreement with the experimental data is very good. The differences between the two models are small and can, particularly in the far downstream part, be attributed to the statistical error, which should disappear for longer sampling time of both simulations. Also shown in Fig. 2 is the time averaged root mean square (RMS) along the centerline. Again the agreement with the experimental data is quite good, and the differences between the models are negligible. These trends were to be expected since the combustion model influences the conserved scalar field only through the density, which already seemed to be predicted quite well in the simulations using LFM and cannot be expected to change largely.

As an example for the main reaction products, centerline profiles of carbon dioxide and water mass fraction are also shown in Fig. 2 as function of the mean mixture fraction. The predictions of the EFM are in very good agreement with the experiments. For CO_2

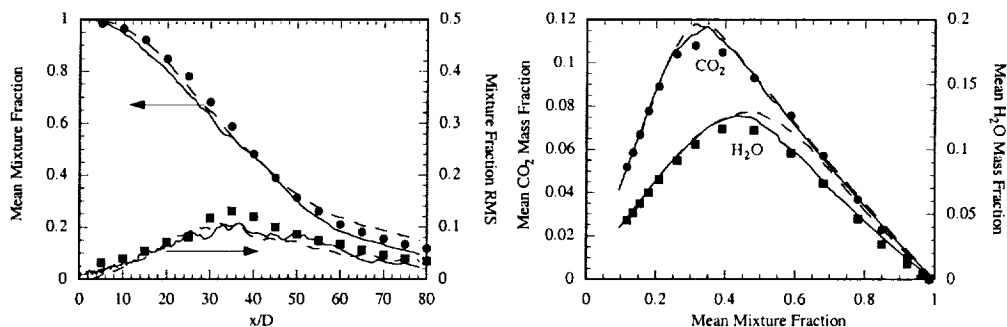


FIGURE 2. Left: Mean and root mean square (RMS) of the mixture fraction along the centerline. Right: Mean temperature and H_2O mass fraction as function of mean mixture fraction along centerline. — : EFM; - - - : LFM; ● : experimental data.

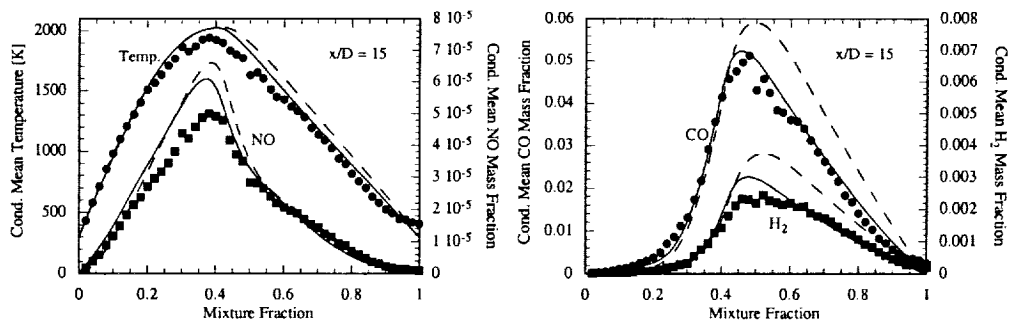


FIGURE 3. Conditional mean averages of temperature, NO, CO, and H_2 mass fractions at $x/D = 15$. — : EFM; - - - : LFM; ● : experimental data.

there are hardly any differences to the LFM. However, for H_2O the new model seems to give some improvement on the fuel rich side, where the mean mixture fraction is larger than 0.45. This corresponds to the region closer to the nozzle. The region with the largest discrepancies between the models is at $\tilde{Z} \approx 0.6$, which can from the left part of Fig. 2 be estimated to be at $x/D \approx 30$. The reason for these differences will be explained in the following discussion of the conditional averages.

Conditional mean quantities are given in Figs. 3, 4, and 5 at $x/D = 15$, 30, and 45, respectively. Temperature and NO mass fraction are given in the left-hand figures. As stable intermediates CO and H_2 mass fraction are shown in the respective right-hand figures. Again the results of the EFM are compared to the LFM and experimental data.

In the region close to the nozzle, at $x/D = 15$, the maximum temperature can be observed to be slightly overpredicted by both models. This has been discussed by Pitsch & Steiner (2000) in a comparison with the single shot data from the experiments. It has been found that the temperature is well predicted provided the flame is burning. The decreased conditionally averaged temperature found in the experiments is only caused by relatively few local extinction events, which are neglected in both the extended and the Lagrangian flamelet models. On the rich side the temperature is slightly overpredicted by the LFM, but well predicted by the EFM. Also for the NO profile given in Fig. 3 the new model leads to a significant improvement showing very good agreement with the experiments, whereas the predictions by the LFM overpredict the maximum NO concentration slightly. Since NO is well known to be strongly dependent on the temperature, it seems

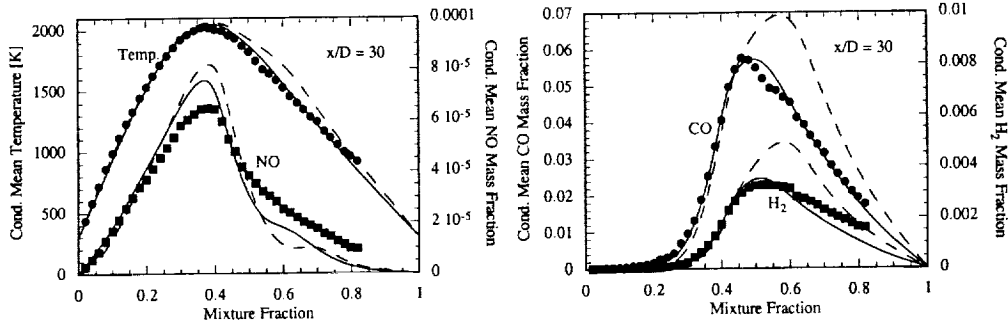


FIGURE 4. Conditional mean averages of temperature, NO, CO, and H₂ mass fractions at $x/D = 30$. — : EFM; - - - : LFM; ● ■ : experimental data.

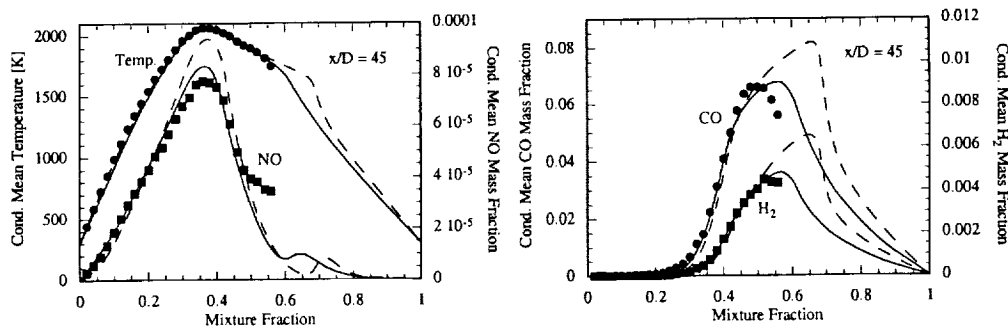


FIGURE 5. Conditional mean averages of temperature, NO, CO, and H₂ mass fractions at $x/D = 45$. — : EFM; - - - : LFM; ● ■ : experimental data.

at first surprising that NO agrees well even though the temperature is overpredicted. The reason is that the high activation temperature of the NO formation causes NO to be formed essentially at the highest temperatures. As explained earlier the local temperature seems to be well predicted and the overprediction of the temperature is only caused by a small volume fraction with significantly lower temperature, which in any case does not contribute to the formation of NO. Similarly to the temperature, but much more obvious, CO and H₂ mass fractions at $x/D = 15$ in the rich part of the flame are also overestimated by LFM. The predictions of the EFM again predict the experimental data very well. The reason for these differences will be explained in the following discussion.

At $x/D = 30$, shown in Fig. 4, the temperature profile predicted by the LFM shows a distinct heat release region approximately $Z = 0.6$. This heat release is caused by the high air content of the fuel stream mentioned earlier. The interaction with the main diffusion flame, located at approximately $Z = 0.35$, causes consumption of fuel and oxidizer, which essentially forms a rich premixed reaction zone. Within this region, because of the high local equivalence ratio, rich stable intermediates such as CO and H₂ are formed in large concentrations as shown in the same figure. However, the rich premixed heat release region cannot be observed in the experimental data. Hence, the temperature in this region is slightly overpredicted, and the CO and H₂ mass fractions are strongly overpredicted.

The main difference between both combustion models discussed here is that in the LFM the scalar dissipation rate is conditionally averaged over cross sections, whereas the EFM is able to take the local fluctuations of the scalar dissipation rate and the unsteady

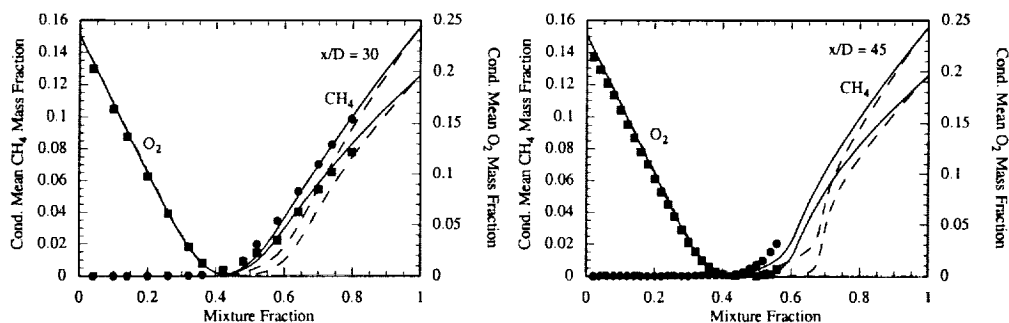


FIGURE 6. Conditional mean averages of temperature, CH_4 and O_2 mass fractions at $x/D = 30$ and $x/D = 45$. — : EFM; - - - : LFM; • ■ : experimental data.

response of the mixing process and the chemistry into account. The consideration of these fluctuations in the present simulations using the EFM obviously changes the turbulence-chemistry interaction in such a way that chemical reactions in the rich premixed part cannot occur, which is consistent with the experimental findings. Therefore, all quantities predicted by the EFM are in much better agreement with the experimental data. This is reflected in the temperature profile, which does not reveal the rich heat release region as well as in the conditionally averaged mass fractions of the stable intermediates. Both, CO and H_2 mass fraction show excellent agreement with the experiments. For NO this effect does not have a large influence since the mass fraction in the rich part is more governed by transport of NO from the formation region at the maximum temperature, which is only weakly influenced by the rich heat release region, even in the predictions by LFM. However, as shown in Fig. 4, at $Z \approx 0.6$ the LFM predictions reveal an NO consumption region caused by the heat release in this region. Even though NO seems underpredicted even by the results of the EFM, these do not show NO consumption, which is consistent with the experiments. A similar discrepancy as seen in the comparison of NO obtained from the EFM, and the experimental data has been found in a comparison of predictions of a laminar counterflow diffusion flame with experiments using the same fuel (Barlow (2000)), indicating that this underprediction might be caused by the chemical reaction scheme rather than the combustion model.

The observed trends continue for the farther downstream positions. In Fig. 5 the conditionally averaged quantities are given for $x/D = 45$. Here, the heat release in the rich region is even more pronounced in the temperature predictions by the LFM simulation. Interestingly, this can also be observed in a much weaker form in the predictions of the EFM and in the experimental data. This can be very clearly seen in the right-hand figure of Fig. 6, where the conditional averages of methane and molecular oxygen are shown for $x/D = 45$. Obviously the oxygen is depleted not only in the reaction zone of the diffusion flame at $Z = 0.35$, but over a much wider region, ranging from stoichiometric conditions to approximately $Z \approx 0.6$. Also the consumption of fuel starts at higher values of the mixture fraction as compared to $x/D = 30$, which is shown in the left-hand figure of Fig. 6.

The influence of the rich heat release on CO and H_2 at $x/D = 45$ is still quite strong. The results of the EFM again provide significantly improved predictions as compared to the LFM.

5. Conclusions

In the present paper an Eulerian formulation of the unsteady flamelet model for LES of non-premixed combustion is presented, which in contrast to the Lagrangian flamelet model, as formulated in an earlier study, accounts for local fluctuations of the scalar dissipation rate.

The model has been applied to the Sandia flame D and the predictions are compared to results obtained by the LFM and to experimental data. It is demonstrated that inaccuracies in the LFM predictions in the rich part of the flame are mainly because of wrongly predicted heat release in this region. It is shown that the results using the new model formulation provide a significant improvement over the LFM results, and are in excellent agreement with the experimental data.

The main conclusions of this study are that the most important reason for the improvement over the earlier model formulation is the consideration of the locally resolved fluctuations of the modeled scalar dissipation rate and the unsteady response of the interaction of molecular mixing and chemistry.

It seems noteworthy that these fluctuations of the scalar dissipation rate can only be observed in LES-type calculations, which implies that the level of accuracy obtained in the present study cannot be achieved using Reynolds averaged methods.

Acknowledgments

The authors gratefully acknowledge funding by the US Department of Energy in the frame of the ASCI program and by the Center for Turbulence Research.

REFERENCES

- BARLOW, R. S. (ED.) 1998 *Proc. of the Third International Workshop on Measurement and Computation of Turbulent Nonpremixed Flames*.
- BARLOW, R. S. (ED.) 1999 *Proc. of the Fourth International Workshop on Measurement and Computation of Turbulent Nonpremixed Flames*.
- BARLOW, R. S. (ED.) 2000 *Proc. of the Fifth International Workshop on Measurement and Computation of Turbulent Nonpremixed Flames*.
- BARLOW, R. S. & FRANK, J. H. 1998a Effect of Turbulence on Species Mass Fractions in Methane/Air Jet Flames. *Proc. Comb. Inst.* **27**, 1087-1095.
- BARLOW, R. S. & FRANK, J. H. 1998b www.ca.sandia.gov/tdf/Workshop.html.
- BILGER, R. W. 1993 Conditional moment closure for turbulent reacting flow). *Phys. Fluids A*, **5**, 436.
- BOWMAN, C. T., HANSON, R. K., DAVIDSON, D. F., GARDINER, JR., W. C., LISIANSKI, V., SMITH, G. P., GOLDEN, D. M., FRENKLACH, M., GOLDENBERG, M. 1998 GRI-Mech 2.11. http://www.me.berkeley.edu/gri_mech/.
- GIBSON, C. H. 1968 Fine structure of scalar fields mixed by turbulence. I. Zero-Gradient points and minimal gradient surfaces). *Phys. Fluids*, **11**, 2305.
- KLIMENKO, A. Y. 2000 Private communication.
- KLIMENKO, A. Y. 1990 Multicomponent diffusion of various scalars in turbulent flow. *Prog. Energy Combust. Sci.* **25**, 327-334.
- KLIMENKO, A. Y. & BILGER, R. W. 1999 Conditional moment closure for turbulent combustion. *Prog. Energy Combust. Sci.* **25**, 595-687.

- PETERS, N. 1983 Local quenching due to flame stretch and non-premixed turbulent combustion. *Combust. Sci. Tech.* **30**, 1.
- PETERS, N. 1984 Laminar diffusion flamelet models in non-premixed turbulent combustion. *Prog. Energy Combust. Sci.* **10**, 319-339.
- PETERS, N. 1987 Laminar flamelet concepts in turbulent combustion. *Proc. Combust. Inst.* **21**, 1231-1250.
- PETERS, N. 2000 *Turbulent Combustion*. Cambridge University Press.
- PITSCH, H., CHEN, M. & PETERS, N. 1998 Unsteady flamelet modeling of turbulent hydrogen/air diffusion flames. *Proc. Combust. Inst.* **27**, 1057-1064.
- PITSCH, H. & PETERS, N. 1998 A Consistent Flamelet Formulation for Non-Premixed Combustion Considering Differential Diffusion Effects. *Comb. Flame.* **114**, 26-40.
- PITSCH, H. & PETERS, N. 2000 Unsteady Flamelet Modeling of Differential Diffusion in Turbulent Jet Diffusion Flames. *Comb. Flame.* **123**, 358-374.
- PITSCH, H. & STEINER, H. 2000 Large-eddy simulation of a turbulent piloted methane/air diffusion flame (Sandia flame D). *Phys. Fluids*, **12**, 2541-2554.
- PITSCH, H. & STEINER, H. 2000 Scalar Mixing and Dissipation Rate in Large-Eddy Simulations of Non-Premixed Turbulent Combustion). *Proc. Comb. Inst.*, **28**, to appear.
- PITSCH, H. & STEINER, H. 1999 Large-eddy simulation of a turbulent piloted methane/air diffusion flame (Sandia flame D). *Annual Research Briefs*, Center for Turbulence Research, NASA Ames/Stanford Univ. 3-18.
- PITSCH, H. & FEDOTOV, S. 2000 Investigation of Scalar Dissipation Rate Fluctuations in Non-Premixed Turbulent Combustion Using a Stochastic Approach). *Comb. Theory Modeling*, submitted.
- SRIPAKAGORN, P., KOSÁLY, G. & PITSCH 2000 Local Extinction-Reignition in Turbulent Nonpremixed Combustion. *Annual Research Briefs*, Center for Turbulence Research, NASA Ames/Stanford Univ. This volume, 117-128.

A high-order approximate-mass spline collocation scheme for incompressible flow simulations

By Olivier Botella

1. Motivation and objectives

The development of numerical methods based on B-spline methodology is motivated by the substantial computational cost of large-eddy simulations (LES) of complex turbulent flows. Indeed, the large number of grid points needed in turbulent boundary layers remains one of the principle obstacles to a wider application of LES to flows of engineering interest. An active part of research in LES is devoted to reducing these resolution requirements by the formulation of approximate wall conditions (see *e.g.* Nicoud *et al.* (2001)) and by the development of highly accurate numerical methods for the precise representation of near-wall structures.

Several works (Shariff & Moser (1998); Kravchenko *et al.* (1999); Kravchenko & Moin (2000)) have been devoted to the development of B-spline methods on semi-structured embedded meshes. This technique allows a substantial reduction in the computational cost of a simulation by using fine grids in physically significant flow regions only. The use of B-splines is motivated by the development of robust and non-dissipative LES schemes on arbitrary meshes. The conservation of physical invariants such as kinetic energy is highly desirable for the simulation of turbulent flows (Kravchenko & Moin (1997)), and these requirements are difficultly reproduced by finite-difference schemes on non-uniform meshes (Vasilyev (2000)). Moreover, the resolution power of B-splines of maximum continuity allows the representation of a broad range of scales of a turbulent flow (Kravchenko *et al.* (1999)).

The work of Kravchenko *et al.* (1999) and Kravchenko & Moin (2000) has shown the high suitability of B-spline methods for the computation of complex turbulent flows. However, the Galerkin approximation that is employed is too CPU intensive. The method is burdened by the cost of evaluating nonlinear terms where, as observed in Kravchenko *et al.* (1999), 50% of the computational time is spent on their evaluation.

This report represents a follow-up to the work initiated in Botella (1999, 2001) for developing a cost-effective B-spline Navier-Stokes solver. The equations are discretized with the collocation method, which allows a drastic reduction of the cost of evaluating nonlinearities. A stable approximation of the pressure is obtained by constructing staggered bases for the velocity and pressure which are, in a sense, the B-spline equivalent to the popular staggered finite-difference discretization (Harlow & Welch (1965)). The time-discretization employs a fractional step scheme.

In association with “local” (or “explicit”) discretizations such as finite-difference or finite-volume approaches, fractional step techniques are widely considered as the most cost-effective method for solving the Navier-Stokes equations. Indeed, they provide a maximum decoupling of the velocity and the pressure so that only sparse elliptic problems need to be solved at each time-cycle. However, for “global” discretizations such as B-spline methods that yield a non-diagonal mass matrix, a straightforward application of these methods retains some coupling between the velocity and pressure: the pressure

operator associated with the projection step, which involves the dense inverse of the mass matrix, is dense and can only be constructed for modestly sized problems. As suggested in Botella (1999, 2001), the pressure equation can nonetheless be solved by means of a Uzawa algorithm, but the CPU cost of this iterative solution, even accelerated by modern Krylov subspace methods (Saad (1996)), is prohibitively high for large scale problems.

In order to make this B-spline method attractive with respect to CPU cost, we have made an effort to modify the fractional step scheme in order to obtain a simpler linear system for the pressure that would be sparse and to eliminate the need for Uzawa iterations. A modification of the mass matrix to get a sparse approximation of its inverse is a key element in this endeavor.

The modification of the “consistent approximation”, which generates the non-diagonal mass matrix, has always been a critical issue for finite-element type methods. A common *ad hoc* simplification consists in approximating the mass matrix by a diagonal matrix, usually by summing its rows and putting the result on the diagonal (the “lumped mass” approximation, see *e.g.* Gresho & Sani (1998)). For compressible flow simulations, this simplification is motivated by the use of explicit time-stepping such that, when the time-derivative term is lumped, the inversion of the consistent mass matrix is no longer needed at each time cycle. This mass lumping technique, however, diminishes the accuracy of the resulting scheme, most notably for unsteady flows dominated by convection effects (Gresho *et al.* (1978)), since this approximation is, in general, a first-order approximation of the consistent mass matrix.

So far, the most satisfying application of the lumping technique to incompressible flow computations is represented by the “projection 2” scheme of Gresho & Chan (1990). It uses a semi-consistent mass matrix approximation (SCM), *i.e.* the mass matrix is lumped in front of the pressure gradient only, while the continuity equation is unaltered. As a consequence, the pressure operator is sparse and can be efficiently inverted by standard elliptic solvers. Early applications of the SCM technique to the B-spline collocation method were reported in Botella (1999, 2001). For low-order spline approximations, this scheme performed accurate Navier-Stokes benchmark computations with only a fraction of the CPU time needed by the original consistent scheme. However, due to the crude approximation represented by the lumping of the mass matrix, the SCM scheme led to a loss of the accuracy that would be expected for high-order B-splines.

In order to preserve as far as possible the high accuracy of the B-spline method, it is thus necessary to build more accurate approximations of the consistent mass matrix than the lumped approximation. These considerations led us in this work to the development of approximate inverses of the mass matrix, *i.e.* highly-accurate sparse approximations of the inverse of the consistent mass matrix. This concept of approximate inverse is somewhat similar to the one developed for the iterative solution of linear systems, where the approximate inverse is an explicit preconditioner whose application in an iterative procedure requires a sparse matrix-vector multiplication only (see *e.g.* Saad (1996)). The main difference is that we are able to replace the solution of a mass matrix problem by a single sparse matrix-vector multiplication while keeping the order of accuracy of the B-splines.

For the B-spline collocation method, such sparse approximations are obtained by application of local interpolation schemes. These schemes of quasi-interpolation were developed in *e.g.* Lyche & Schumaker (1975); de Boor (1978) to build spline representation of a function from data values. The B-spline coefficients are not determined as the solution to a collocation system, as the consistent approximation would require, but rather as the

linear combination of the function values at a small number of data points. When these data points are chosen among the collocation points, this linear combination defines the entries of the approximate inverse of the mass matrix. The number of data points affects the order of accuracy of the approximate inverse. The case with a single data point corresponds to the low-order lumped approximation. The increase in the number of data points raises the order, and a sufficient number of points yields the order of accuracy of the consistent approximation. These approximate inverses thus represent a high-order generalization of the mass lumping technique.

The concepts of approximate inverse and local interpolation may have important application to numerical algorithms where a fast transformation from the physical (collocation) space to the B-spline coefficients space is required. Among others, we cite the development of restriction operators for spline multigrid methods (Christara & Smith (1997)) and the evaluation of nonlinearities in collocation space, as in the pseudospectral method. In this report, the use of an approximate inverse allows us to solve the pressure equation of the Navier-Stokes scheme with a fraction of the CPU time required by the consistent approximation, with the same order of accuracy. The slight loss of the resolving power of the semi-consistent schemes, caused by the replacement of the consistent mass matrix, is greatly counterbalanced by their computational efficiency. These issues are carefully addressed here by presenting numerical tests and Fourier analysis. The combination of these approximate inverses with the SCM fractional-step technique allows the construction of a highly-accurate cost-effective Navier-Stokes solver, as proved by the benchmark tests reported in this paper.

2. Background on B-spline numerical schemes

2.1. Construction of B-spline bases

A spline function is a piecewise polynomial of order k (the polynomial degree is $k - 1$ at most) defined on the interval $\Lambda =]a, b[$, whose derivatives at some order possess jump-discontinuities at breakpoints $\xi = \{\xi_i, i = 1, \dots, l + 1\}$ defined by

$$a = \xi_1 < \xi_2 < \dots < \xi_i < \dots < \xi_l < \xi_{l+1} = b. \quad (2.1)$$

In the following, we focus on the characterization of the so-called smoothest splines, which have jump discontinuities in their $k - 1$ derivative, since previous studies in Botella (1999, 2001) have assessed their superior resolving power in the collocation approach.

A spline function $\tilde{f}(x)$ is commonly described in its B-representation

$$\tilde{f}(x) = \sum_{i=1}^N \alpha_i B_i^k(x), \quad (2.2)$$

where $B_i^k(x)$ is a special spline function of order k called a B-spline which has, in particular, the property of having compact support (see *e.g.* de Boor (1978)), and the number of the B-splines is

$$N = l + k - 1. \quad (2.3)$$

The B-splines of order 1 are step functions defined by

$$B_i^1(x) = \begin{cases} 1 & \text{if } x \in [t_i, t_{i+1}[, \\ 0 & \text{otherwise,} \end{cases} \quad (2.4)$$

and an efficient construction of the B-splines of order $k \geq 2$ is given by the recurrence relation of Curry and Schoenberg (see *e.g.* de Boor (1978)):

$$B_i^k(x) = \frac{x - t_i}{t_{i+k-1} - t_i} B_i^{k-1}(x) + \frac{t_{i+k} - x}{t_{i+k} - t_{i+1}} B_{i+1}^{k-1}(x). \quad (2.5)$$

Formulae (2.4) and (2.5) introduce the knots $\{t_i, i = 1, \dots, N + k\}$, which enforce the regularity of the B-spline basis by requiring

$$t_{k+i-1} = \xi_i \quad \text{for } i = 2, \dots, l, \quad (2.6)$$

i.e. the knots coincide with the breakpoints in the interior of the domain. The construction of the basis given by Eqs. (2.4)-(2.6) leaves freedom in the first k and last k of the knots. A convenient choice for the approximation of boundary value problems is to set these end-knots as

$$t_1 = \dots = t_k = a, \quad t_{N+1} = \dots = t_{N+k} = b. \quad (2.7)$$

In that case, by using basic properties (de Boor (1978)) such as that of compact support,

$$B_i^k(x) = 0 \quad \text{for } x \notin [t_i, t_{i+k}], \quad (2.8)$$

and partition of unity,

$$\sum_{i=1}^N B_i^k(x) = 1 \quad \text{for } x \in [a, b], \quad (2.9)$$

the spline function (2) satisfies

$$\tilde{f}(a) = \alpha_1 \quad \text{and} \quad \tilde{f}(b) = \alpha_N, \quad (2.10)$$

so that Dirichlet boundary conditions are strongly imposed. A choice analogous to (2.7) for the first k and last k knots that is suitable for imposing periodic boundary conditions is discussed in de Boor (1978) and Kravchenko *et al.* (1999).

A useful property is that a B-spline basis of order k can represent elements of the space $\mathcal{P}_k(\Lambda)$, *i.e.* polynomials of degree $k-1$ at most. More precisely, Lyche & Schumaker (1975) established the identity

$$\sum_{i=1}^N \gamma_{im} B_i^k(x) = x^{m-1}, \quad m = 1, 2, \dots, k, \quad \text{where} \quad (2.11a)$$

$$\gamma_{im} = (-1)^{m-1} \frac{(m-1)!}{(k-1)!} \psi_i^{(k-m)}(0), \quad \text{with} \quad \psi_i(x) = \prod_{p=1}^{k-1} (x - t_{i+p}). \quad (2.11b)$$

In the following, the superscript referring to the order of the B-splines will be dropped for the sake of brevity.

2.2. Semi-consistent fractional step scheme

Numerical approximation of the Navier-Stokes equations for incompressible flows are obtained by approximating the velocity and the pressure as

$$\mathbf{v} = \sum_{i,j=1}^N \mathbf{v}_{i,j} B_i(x) B_j(y), \quad p = \sum_{i,j=1}^{N-2} p_{i,j} \tilde{B}_i(x) \tilde{B}_j(y), \quad (2.12)$$

where $\{B_i(x), i = 1, \dots, N\}$ and $\{\tilde{B}_i(x), i = 1, \dots, N - 2\}$ are the compatible B-spline bases of order k introduced in Botella (1999, 2001). The Navier-Stokes equations are discretized on the collocation grid $\{(x_i, y_j); i, j = 1, \dots, N\}$ that will be defined later. The time-integration is based on the following prototype fractional step scheme, where the nonlinear terms are discarded,

$$\mathcal{M} \frac{\bar{U} - U^n}{\Delta t} - \mathcal{K}\bar{U} + \mathcal{M}\mathcal{M}_A^{-1} \tilde{\mathcal{D}}P^n = F^{n+1}, \quad (2.13)$$

and

$$\mathcal{M} \frac{U^{n+1} - \bar{U}}{\Delta t} + \mathcal{M}\mathcal{M}_A^{-1} \tilde{\mathcal{D}}(P^{n+1} - P^n) = 0, \quad (2.14a)$$

$$\mathcal{D}U^{n+1} = 0. \quad (2.14b)$$

In these equations, Δt is the time step, U and P are vectors representing the unknown spline coefficients of the velocity and the pressure respectively, F is a source term, \mathcal{M} is the (non-diagonal) mass matrix, \mathcal{K} is the viscous diffusion matrix, and \mathcal{D} and $\tilde{\mathcal{D}}$ represent first derivatives of velocity and pressure respectively. In contrast to the standard B-spline discretization considered in Botella (1999, 2001), which will be referred to as the consistent method (CM), this scheme considers a modification of the pressure gradient in Eqs. (2.13) and (2.14a) by introducing the matrix \mathcal{M}_A^{-1} , which is the approximate inverse of the mass matrix \mathcal{M} in a sense to be defined later. The divergence equation (2.14b) is identical for both methods and expresses that the continuity condition be satisfied at the inner collocation points. Note that when $\mathcal{M}_A^{-1} = \mathcal{M}^{-1}$, the semi-consistent scheme (SCM) (2.13)-(2.14) reduces to the original CM scheme.

The main interest of the SCM scheme is that the projection step (2.14) yields the pressure equation

$$\mathcal{A}_A(P^{n+1} - P^n) = \mathcal{D}\bar{U}/\Delta t, \quad (2.15)$$

where the pressure operator

$$\mathcal{A}_A = \mathcal{D}\mathcal{M}_A^{-1} \tilde{\mathcal{D}}, \quad (2.16)$$

is sparse when \mathcal{M}_A^{-1} is sparse, resulting in a pressure equation that can be efficiently solved by standard iterative methods for elliptic problems.

The principle of scheme (2.13)-(2.14) was introduced by Gresho & Chan (1990) for the finite-element method with $\mathcal{M}_A^{-1} = \mathcal{M}_L^{-1}$, *i.e.* an approximate inverse generated by the lumped approximation which is, in general, a first-order approximation of the mass matrix. The use of a highly accurate approximate inverse is motivated by investigating the truncation error of the SCM scheme. When combining Eqs. (2.13) and (2.14a) to eliminate the provisional velocity \bar{U} , we get

$$\mathcal{M} \frac{U^{n+1} - U^n}{\Delta t} - \mathcal{K}U^{n+1} + \tilde{\mathcal{D}}P^{n+1} + \mathcal{E}_S + \mathcal{E}_A = F^{n+1}, \quad (2.17)$$

where, in addition to the $O(\Delta t^2)$ splitting error

$$\mathcal{E}_S = -\Delta t \mathcal{K}\mathcal{M}_A^{-1} \tilde{\mathcal{D}}(P^{n+1} - P^n), \quad (2.18)$$

common to fractional-step schemes, the approximation error

$$\mathcal{E}_A = (\mathcal{M} - \mathcal{M}_A)\mathcal{M}_A^{-1} \tilde{\mathcal{D}}P^{n+1}, \quad (2.19)$$

is a spatial error expressing the degree of accuracy to which \mathcal{M}_A approximates the consistent mass matrix \mathcal{M} . The use of an approximate inverse whose accuracy is consistent with the B-spline discretization is thus mandatory for preserving the accuracy of the SCM scheme.

3. Construction of approximate inverse of the mass matrix using local spline approximation

3.1. Consistent interpolation vs. local interpolation

The consistent interpolation of a function $f(x)$ consists in finding a spline function

$$\tilde{f}(x) = \sum_{i=1}^N \alpha_i(f) B_i(x), \quad (3.1)$$

that takes on the values of $f(x)$ at a given set of collocation points $\{x_j, j = 1, \dots, N\}$, *i.e.*

$$\sum_{i=1}^N \alpha_i(f) B_i(x_j) = f(x_j), \quad \text{for } j = 1, \dots, N. \quad (3.2)$$

This linear system takes the matrix form

$$\bar{\mathcal{M}}\alpha = \mathbf{f}, \quad (3.3)$$

where $\alpha = (\alpha_1(f), \dots, \alpha_N(f))$, $\mathbf{f} = (f(x_1), \dots, f(x_N))$ and $\bar{\mathcal{M}} = (B_i(x_j))_{i,j=1,\dots,N}$ is the consistent, non-diagonal mass matrix of bandwidth k . The solution of a linear system of equations is thus needed for determining the spline coefficients.

In contrast, local interpolation methods were developed in *e.g.* Lyche & Schumaker (1975); de Boor (1978) such that the determination of the coefficients does not require solving a collocation system. These methods are local in the sense that the evaluation of the coefficients depends on the value of the function and/or its derivatives at a small number of data points. In the following, we focus on local schemes involving function values, *i.e.* schemes such that the i^{th} spline coefficient is determined as

$$\alpha_i(f) = \sum_{j=1}^{k_1} \beta_{ij} f(\tau_{ij}), \quad (3.4)$$

where $\{\tau_{ij}, j = 1, \dots, k_1\}$ is a given set of distinct data locations in Λ , $k_1 \leq k$ is the number of data points used for the evaluation of each spline coefficient and will be referred to as the order of the local scheme, and $\{\beta_{ij}, j = 1, \dots, k_1\}$ are coefficients to be determined.

In the case where the data points are chosen from the set of collocation points, scheme (3.4) can be written in matrix form as

$$\alpha = \bar{\mathcal{M}}_A^{-1} \mathbf{f}, \quad (3.5)$$

where the coefficients $\{\beta_{ij}\}$ in (3.4) define the entries of the square matrix $\bar{\mathcal{M}}_A^{-1}$ that is precisely the approximate inverse of the consistent mass matrix $\bar{\mathcal{M}}$ we are seeking. The matrix $\bar{\mathcal{M}}_A^{-1}$ is sparse, each of its row possessing k_1 non-zero entries at most. Thus, the linear system solution required by the consistent approximation is now replaced by a sparse matrix-vector multiplication involving the same right-hand side.

3.2. Derivation of the local interpolant

The local interpolation scheme we use for the determination of the entries of \mathcal{M}_A^{-1} is the scheme based on point evaluations considered in Example 3.4 of Lyche & Schumaker (1975). This construction is valid for B-spline bases of any order k and an arbitrary distribution of knots.

Given $k_1 \leq k$ and some data points $\{\tau_{ij}; i = 1, \dots, N, j = 1, \dots, k_1\}$ such that $\{\tau_{i1}, \dots, \tau_{ik_1}\}$ are distinct for all i , the coefficients $\{\beta_{ij}; i = 1, \dots, N, j = 1, \dots, k_1\}$ in (3.4) are determined so that the local scheme reproduces polynomial of order k_1 , i.e.

$$\tilde{f} = f, \quad \forall f \in \mathcal{P}_{k_1}(\Lambda), \quad k_1 \leq k. \tag{3.6}$$

For this purpose, it is convenient to write Eq. (3.4) as

$$\alpha_i(f) = \sum_{j=1}^{k_1} \mu_{ij} [\tau_{i1}, \dots, \tau_{ij}] f, \tag{3.7}$$

where $[\cdot, \cdot]f$ represents the divided difference of $f(x)$ (see e.g. de Boor (1978)). Condition (3.6) amounts to representing each monomial x^{m-1} , $m = 1, \dots, k_1$, as

$$\sum_{i=1}^N \left(\sum_{j=1}^{k_1} \mu_{ij} [\tau_{i1}, \dots, \tau_{ij}] x^{m-1} \right) B_i(x) = x^{m-1}. \tag{3.8}$$

By using (2.11), the coefficients μ_{ij} are obtained as the solution of the lower triangular linear system, for each $i = 1, \dots, N$

$$\sum_{j=1}^{k_1} \mu_{ij} [\tau_{i1}, \dots, \tau_{ij}] x^{m-1} = \gamma_{im}, \quad \text{for } m = 1, \dots, k_1, \tag{3.9}$$

from which the μ_{ij} can be obtained by back-solution. The values of μ_{ij} for $j = 1, \dots, 4$ are given in Lyche & Schumaker (1975) and are listed hereafter for completeness:

$$\mu_{i1} = 1, \tag{3.10a}$$

$$\mu_{i2} = \gamma_{i2} - \tau_{i1}, \tag{3.10b}$$

$$\mu_{i3} = \gamma_{i3} - (\tau_{i1} + \tau_{i2}) \mu_{i2} - \tau_{i1}^2, \tag{3.10c}$$

$$\mu_{i4} = \gamma_{i4} - (\tau_{i1} + \tau_{i2} + \tau_{i3}) \mu_{i3} - (\tau_{i1}^2 + \tau_{i1} \tau_{i2} + \tau_{i2}^2) \mu_{i2} - \tau_{i1}^3. \tag{3.10d}$$

Due to the structure of system (3.9), the values of the $\{\mu_{ij}\}$ do not depend on k_1 . Thus, the coefficients of a scheme of order $k_1 \leq 4$ are given by the first k_1 lines in Eq. (3.10). The extra effort to determine the coefficients of a scheme of order 5 would only be to calculate μ_{i5} from (3.9). Once the μ_{ij} are determined, the β_{ij} can be obtained by equating (3.7) to (3.4).

Lyche & Schumaker (1975) have shown that this local scheme yields an accuracy of order k_1 in the maximum norm. In particular, for the case $k_1 = k$, it is thus possible to obtain a local interpolant that preserves the order of accuracy of the consistent approximation.

Another important case occurs for $k_1 = 2$: if, to obtain the i^{th} B-spline coefficient, the first data point τ_{i1} is chosen to be equal to x_i^* defined as

$$x_i^* = \gamma_{i2}, \quad \text{where from (2.11b)} \quad \gamma_{i2} = \sum_{p=1}^{k-1} t_{i+p} / (k-1), \tag{3.11}$$

then $\mu_{i2} = 0$ in Eq. (3.10b) for any choice of the second data point τ_{i2} . Thus, the spline function

$$\tilde{f}(x) = \sum_{i=1}^N f(x_i^*) B_i(x), \quad (3.12)$$

is a second-order approximation to $f(x)$. This scheme is precisely the variation-diminishing approximation of Marsden & Schoenberg (see *e.g.* de Boor (1978)), and the collocation points (3.11) will subsequently be referred to as the Marsden-Schoenberg points.

A last important remark concerns the accuracy of the imposition of Dirichlet boundary conditions with the local scheme in the case where the end-knots are set using Eq. (2.7). From Eqs. (2.10) and (3.7), the value of the spline at the end-point $x = a$ is

$$\tilde{f}(a) = \alpha_1(f), \quad \text{with } \alpha_1(f) = \sum_{j=1}^{k_1} \mu_{1j} [\tau_{11}, \dots, \tau_{1j}] f, \quad (3.13)$$

where the coefficients $\{\mu_{1j}, \dots, \mu_{1k_1}\}$ are solution to

$$\sum_{j=1}^{k_1} \mu_{1j} [\tau_{11}, \dots, \tau_{1j}] x^{m-1} = a^{m-1}, \quad m = 1, \dots, k_1. \quad (3.14)$$

If τ_{11} is chosen to be equal to a , the unique solution is then $\mu_{11} = 1, \mu_{12} = \dots = \mu_{1k_1} = 0$. From Eq. (3.13) we get $\tilde{f}(a) = f(a)$ and, correspondingly, $\tilde{f}(b) = f(b)$ at the other end-point, showing that Dirichlet boundary conditions are satisfied exactly just as in the consistent approximation (Eq. (2.10)).

3.3. Approximate inverse of the mass matrix

The local interpolant allows us to build an approximate inverse $\bar{\mathcal{M}}_A^{-1}$ of the mass matrix when the data points $\{\tau_{i,j}\}$ are chosen from the set of collocation points $\{x_i, i = 1, \dots, N\}$. For the imposition of Dirichlet conditions with the end-knots (2.7), an additional constraint would be to set $\tau_{11} = a$ and $\tau_{N1} = b$, the choice of the remaining data points $\{\tau_{1j}, j = 2, \dots, k_1\}$ and $\{\tau_{Nj}, j = 2, \dots, k_1\}$ having no consequence.

A case of special interest arises when the approximate inverse reduces to $\bar{\mathcal{M}}_A^{-1} = \mathcal{I}$. This approximate inverse corresponds to the lumped mass matrix widely used in the finite-element community (see *e.g.* Gresho & Sani (1998)), obtained by summing the rows of the consistent mass matrix $\bar{\mathcal{M}}$ and putting the result on the diagonal. For the spline-collocation method, the local interpolant of order $k_1 = 1$ with $\tau_{i1} = x_i$ generates such a matrix, and thus yields first-order accuracy in general. However, as shown by the variation-diminishing scheme (3.12), the lumped mass matrix is second-order accurate when the Marsden-Schoenberg collocation points (3.11) are used.

The latter case identifies the Marsden-Schoenberg points as an alternative to the usual choice of the collocation points, *i.e.* the location of the maximum of the B-splines. These two definitions are equivalent in particular cases only, such as a periodic domain with uniform knots. They nonetheless yield the same characterization of the first and last collocation points when the end-knots (2.7) are used, namely $x_1 = a$ and $x_N = b$. In the following, the Marsden-Schoenberg points will be used as much as possible even though no advantages have yet been observed when local interpolants of order higher than 2 are employed.

As sketched in Fig. 1, the approximate inverse generated by a local scheme of order $k_1 \geq 3$ can be viewed as a high-order generalization of the mass lumping technique.

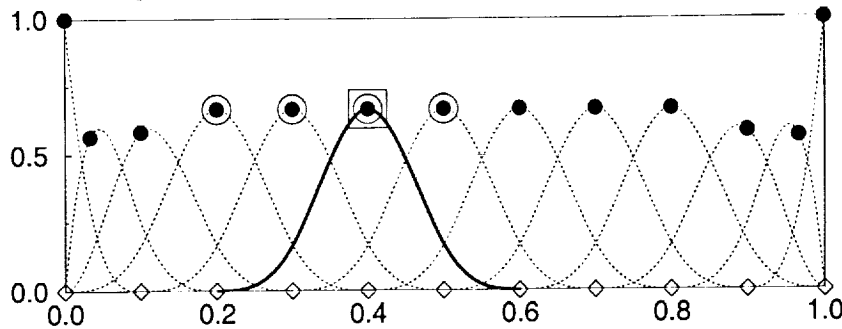


FIGURE 1. Sketch to illustrate the approximation of a function $f(x)$ with a B-spline basis of order $k = 4$, on $l + 1 = 10$ equidistant breakpoints (\diamond) with end-knots (2.7). The coefficient associated to the 6th B-spline (—) is evaluated with the values of $f(x)$ at: all Marsden-Schoenberg collocation points (\bullet) with the consistent approximation; a unique collocation point (framed) with the mass lumping approximation; and 4 collocation points (circled) when a local scheme of order $k_1 = 4$ is used.

Since $\bar{\mathcal{M}}^{-1}$ is dense, the evaluation of the spline coefficient $\alpha_i(f)$ by the consistent approximation involves values of $f(x)$ at all collocation points. In contrast, the mass lumping technique consists in identifying $\alpha_i(f)$ to the value of $f(x)$ at the collocation point associated with the i^{th} B-spline. More generally, the local approximation of $\alpha_i(f)$ involves values of $f(x)$ at several collocation points, which are located in Fig. 1 in the support of $B_i(x)$. This approximation has the consequence of expanding the bandwidth of $\bar{\mathcal{M}}_A^{-1}$ while raising the accuracy of the evaluation of $\alpha_i(f)$.

Several issues have to be addressed for generating approximate inverse of practical interest. A loss in the spatial resolution power of the spline-collocation method would predictably result from the replacement of the consistent mass by the local mass approximation. Furthermore, while a $O(N^{-k_1})$ asymptotical accuracy is assured when k_1 data points per coefficient are used, the definition of the local interpolant leaves freedom in their positioning. The influence of the location of the data points on the accuracy of the resulting local scheme is investigated in the next section.

4. Numerical results

4.1. Local approximation in a one-dimensional periodic domain

It is convenient to analyze the resolution properties of the local approximation for B-spline bases on a uniform distribution of breakpoints, with periodic boundary conditions. The investigation of the influence of the position of the data points used for generating $\bar{\mathcal{M}}_A^{-1}$ is then greatly simplified since, in this configuration, the bases are generated by translation of the same cardinal B-spline (de Boor (1978)). As a result, the i^{th} Marsden-Schoenberg point is characterized as the maximum of the spline $B_i(x)$, *i.e.* for k even

$$x_i^* = t_{i+k/2}, \quad i = 1, \dots, N. \quad (4.1)$$

Moreover, this configuration allows to perform the modified wavenumber analysis of the semi-consistent schemes.

The influence of the choice of the data points on the accuracy of the resulting schemes is performed for local interpolant of order $k_1 = 4$. For completeness, results are also provide for the popular variation-diminishing scheme (*i.e.* mass lumping approximation, $k_1 = 2$). Table 1 displays the various sets of data points that we consider. Those sets

Set of data points	Index of data points used for local interpolation	Offset of nonzero diagonals of \mathcal{M}_A^{-1} with respect to the main diagonal
Set <i>I</i>	$\{i\}$	0,
Set <i>II</i>	$\{i-2, i-1, i, i+1\}$	-1, 0, 1,
Set <i>II'</i>	$\{i-1, i, i+1, i+2\}$	-1, 0, 1,
Set <i>III</i>	$\{i, i+1, i+2, i+3\}$	0, 1, 2, 3,
Set <i>III'</i>	$\{i-3, i-2, i-1, i\}$	-3, -2, -1, 0,
Set <i>IV</i>	$\{i-2, i-1, i+1, i+2\}$	-2, -1, 1, 2,

TABLE 1. Description of the sets of data points used for local interpolation. The index i refers to the collocation point associated with the i^{th} B-spline.

of points are located as close as possible to the support $[t_i, t_{i+k}]$ of $B_i(x)$ in order to minimize the bandwidth of $\tilde{\mathcal{M}}_A^{-1}$.

Set *I* corresponds to the variation-diminishing scheme, while the five other sets use the local interpolant of order 4.

Sets *II* and *II'* represent the two possible choices of data points that yield approximate inverses with the shortest bandwidth. For the particular case of equidistant knots with periodicity conditions considered in this section, these two sets happen to generate the same symmetric tridiagonal matrix $\tilde{\mathcal{M}}_A^{-1}$. In general, this property is lost when the knots are not distinct and equally spaced. As an example, for a B-spline basis on a uniform distribution of breakpoints with Dirichlet boundary conditions, the tridiagonality of $\tilde{\mathcal{M}}_A^{-1}$ is lost at its first and last $k-1$ lines due to the fact that the end-knots are identical (see Eq. (2.7)).

Sets *III* and *III'* correspond respectively to a left and right biasing of the data points with respect to x_i^* . It should be noted that even though these sets generate distinct approximate inverses, they yield identical results on the accuracy tests and the modified wavenumber analysis presented below. This phenomenon is understood by observing that these numerical examples do not reflect the influence of the biasing direction on the behavior of the resulting schemes.

Finally, set *IV* is designed to generate an approximate inverse, with a sparsity pattern that is symmetric on arbitrary grids, by not considering the datum at point x_i^* .

The first numerical test concerns the interpolation of the periodic function

$$f(x) = \sin(10\pi x) + \cos(2\pi x + 2), \quad \text{in } \Lambda =]0, 1[. \quad (4.2)$$

We recall that the consistent approximation requires a linear system solution while the semi-consistent schemes require a single sparse matrix-vector multiplication. The maximal value of the error, sampled on a fine grid of 1001 equidistant points, is displayed in Fig. 2 for splines of order $k=4$. The poor accuracy of the lumping approximation is obvious, yielding second order accuracy. The order of accuracy of the consistent approximation is recovered for all the local schemes of order 4. These results show the importance of data point positions. Not surprisingly, the lowest error of the local schemes is obtained with set *II*. Note also that for a moderate spatial resolution ($N \leq 25$), sets *III* and *IV* yield results inferior to those obtained with the lumping approximation.

For completeness, Fig. 3 displays analogous results obtained with splines of order 6. As in the previous case, fourth-order accuracy is obtained with local schemes of order 4 and, again, set *II* displays the lowest magnitude error. The results obtained with these local

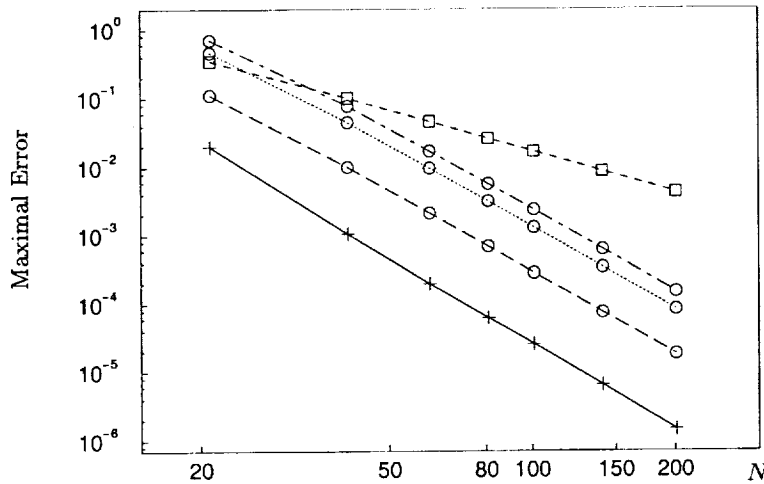


FIGURE 2. Maximal error vs. N , number of B-splines of order $k = 4$, for the various approximation methods. Local scheme with $k_1 = 2$ (\square): set I ---- ; local schemes with $k_1 = 4$ (\circ): set II ---- , set III , set IV -.-.- ; consistent approximation ——— .

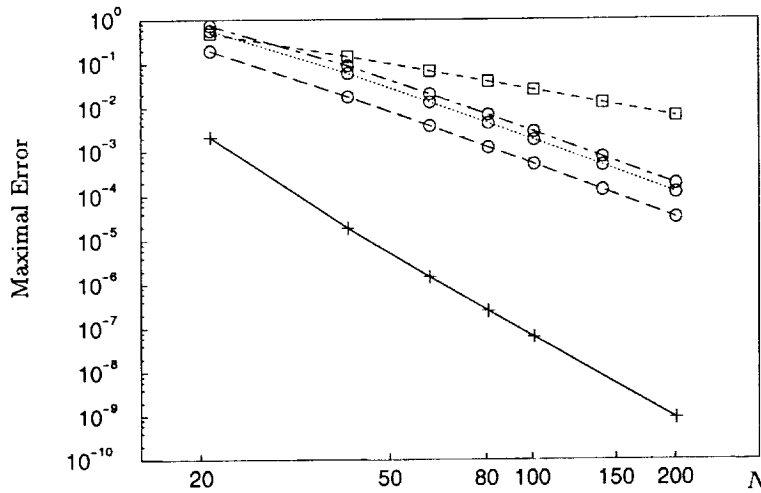


FIGURE 3. Maximal error vs. the number of points N with splines of order $k = 6$. See the caption of Fig. 2 for the labeling.

schemes are, of course, far from the 6th-order accuracy of the consistent approximation. This rate of convergence would nonetheless be obtained with local schemes of order 6.

A classical evaluation of the resolving power of a scheme is given by the modified wavenumber analysis of the first derivative (*e.g.* Lele (1992)). For this purpose, the eigenvalue problem

$$u' = \lambda u \quad \text{in } \Lambda =] - \pi, \pi[, \tag{4.3}$$

is solved numerically with periodic boundary conditions. The complex eigenvalues with real imaginary part are denoted $\{i \lambda_n, n = 0, \dots, N/2\}$, the remaining ones being their

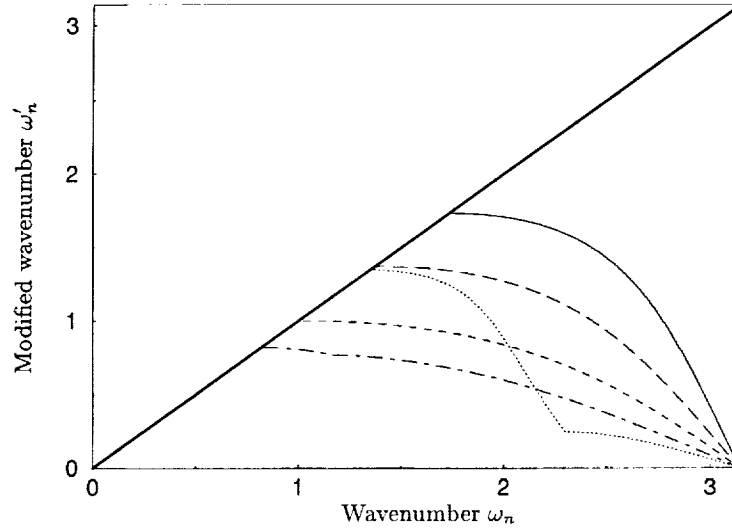


FIGURE 4. Modified wavenumber of the first derivative yielded by the different methods for splines of order $k = 4$. Local scheme with $k_l = 2$: set I - - - - ; local schemes with $k_l = 4$: set II - · - · - , set III · · · · · , set IV - - - - ; consistent scheme ——— ; exact ——— .

conjugates. The discretization of (4.3) by the consistent approximation is

$$\bar{\mathcal{M}}\alpha = \lambda \bar{\mathcal{D}}\alpha, \quad (4.4)$$

where $\bar{\mathcal{D}} = (B'_i(x_j^*))$ is the first derivative collocation operator. Correspondingly, the spectrum of the local schemes is obtained by solving

$$\alpha = \lambda \bar{\mathcal{M}}_A^{-1} \bar{\mathcal{D}}\alpha. \quad (4.5)$$

For splines of order $k = 4$ and 6 respectively, Figs. 4 and 5 sketch the modified wavenumber spectrum $\tilde{\omega}_n = 2\pi\lambda_n/N$ versus the wavenumber $\omega_n = 2\pi n/N$ given by the different approximations. As expected, the local scheme I degrades the resolving power compared to the consistent approximation. For the local schemes of order 4, the location of the data points has a great influence on their resolving ability, yielding very disparate wavenumber plots. It is particularly striking that set IV gives lower resolving power than even the lumped mass approximation.

A more quantitative measurement of the resolving ability of a scheme is given by the resolving efficiency r_ϵ , i.e. the fraction of wavenumbers accurately represented within a relative tolerance of ϵ . This quantity is defined as $r_\epsilon = 2M_\epsilon/N$, where M_ϵ is the number of the modified wavenumber $\tilde{\omega}_n$ that satisfies the error tolerance

$$\frac{|\tilde{\omega}_n - \omega_n|}{\omega_n} \leq \epsilon, \quad n = 0, \dots, N/2. \quad (4.6)$$

The resolving efficiency r_ϵ of the various schemes are given in Table 2 for characteristic values of ϵ . We observe that this measurement gives, once more, set II as the most accurate of the local schemes. In particular, for splines of order $k = 4$, set II recovers up to 80%, 79% and 75% of the resolved fraction r_ϵ of the consistent approximation for $\epsilon = 10^{-1}$, 10^{-2} and 10^{-3} respectively. In comparison, the lumping approximation recovers only 57%, 57% and 32% of this resolved fraction.

In summary, accurate approximate inverses that preserve the order of accuracy of the

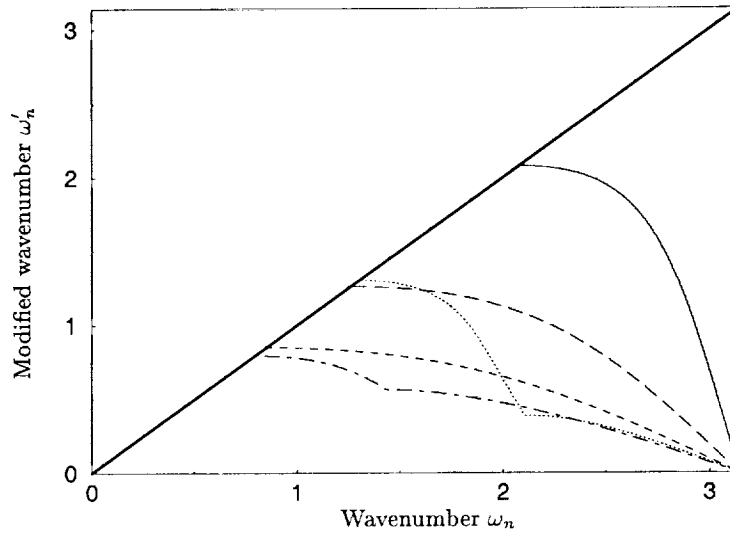


FIGURE 5. Modified wavenumber of the first derivative for splines of order $k = 6$. See the caption of Fig. 4 for the labeling.

Schemes	Order $k = 4$			Order $k = 6$		
	$\epsilon = 0.1$	$\epsilon = 0.01$	$\epsilon = 0.001$	$\epsilon = 0.1$	$\epsilon = 0.01$	$\epsilon = 0.001$
Consistent	0.61	0.56	0.44	0.73	0.67	0.61
Set I	0.36	0.32	0.14	0.30	0.27	0.16
Set II	0.49	0.44	0.33	0.45	0.41	0.30
Set III	0.48	0.43	0.28	0.46	0.42	0.26
Set IV	0.29	0.27	0.20	0.28	0.26	0.19

TABLE 2. Resolving efficiency τ_ϵ of the first derivative for the various approximations with $N/2 = 750$.

consistent approximation can be generated when a sufficient number of data points is used. The location of these data points is nonetheless of crucial importance. These numerical tests have found the best position of these data points on a periodic uniform grid to be set II. The resolution properties of the consistent approximation are, nonetheless, not fully recovered by the local schemes. The marginal loss in accuracy is greatly counterbalanced by their much lower computational cost, as it will be illustrated in the next section.

In the case of Dirichlet boundary conditions, set II is used as a template for building approximate inverses of order $k_1 = 4$ on a uniform distribution of breakpoints. The local approximation of coefficients with indices $i = k, \dots, N - k + 1$ is performed with this set, generating a centered tridiagonal approximation as in the periodic case. A modification has to be performed for the first and last $k - 1$ deficient B-splines, *i.e.* which display multiple knots in their support. The first and last coefficients use the datum at the endpoint a and b respectively, leading to the exact imposition of the Dirichlet conditions. For the remaining B-spline coefficients with indices $i = 2, \dots, k - 1$ and $i = N - k, \dots, N - 1$, we use the collocation points with indices $\{i - 1, i, i + 1, i + 2\}$ and $\{i - 2, i - 1, i, i + 1\}$ respectively.

4.2. Semi-consistent approximation of the Div-Grad problem

We are now ready to describe the semi-consistent approximation (SCM) of the projection step (2.14) by considering as model equations the Div-Grad problem:

$$\sigma \mathbf{v} + \nabla p = \mathbf{f} \quad \text{in } \Omega =]0, 1[^2, \quad (4.7a)$$

$$\nabla \cdot \mathbf{v} = 0 \quad \text{in } \Omega =]0, 1[^2, \quad (4.7b)$$

$$\mathbf{v} = \mathbf{g} \quad \text{on } \partial\Omega. \quad (4.7c)$$

This new discretization follows essentially along the lines of the consistent method (CM) introduced in Botella (1999, 2001). Eqs. (4.7a) and (4.7b) are evaluated on the $(N-2) \times (N-2)$ inner collocation points, while the remaining boundary points are used for the determination of the boundary conditions (4.7c). The discretization of the divergence equation (4.7b) is identical for both methods and reads in matrix form:

$$DU = G, \quad (4.8)$$

where the velocity coefficients determined from the boundary conditions are put in the right-hand side (RHS).

The SCM approximation of Eq. (4.7a) is now described with some details related to the imposition of non-homogeneous boundary conditions. For this purpose, we denote by \mathcal{I}_I the set of indices of collocation points in the interior of domain, and, correspondingly, \mathcal{I}_B refers to the indices of the boundary nodes. The discretization of Eq. (4.7a) at the interior collocation point (x_i, y_k) is

$$\sigma \sum_{(j,l) \in \mathcal{I}_I} \mathcal{M}_{i,k,j,l}^A U_{j,l} + \sum_{(j,l) \in \mathcal{I}_I} \tilde{d}_{i,k,j,l} P_{j,l} = F_{i,k}, \quad (4.9a)$$

where $\{\tilde{d}_{i,k,j,l}\}$ are the gradient coefficients of the pressure spline, and

$$F_{i,k} = \mathbf{f}(x_i, y_k) - \sigma \sum_{(j,l) \in \mathcal{I}_B} \mathcal{M}_{i,k,j,l}^A U_{j,l}, \quad (4.9b)$$

corresponds to a RHS augmented with boundary velocity coefficients. The matrix form of (4.9a) reads

$$\sigma U + \mathcal{M}_A^{-1} \tilde{D} P = \mathcal{M}_A^{-1} F, \quad (4.10)$$

where \mathcal{M}_A^{-1} is constructed from the tensor product of one-dimensional matrices $\bar{\mathcal{M}}_A^{-1}$ in each spatial direction, which use the distribution of data points for Dirichlet conditions described in the previous section.

On the other hand, the entries $\{\mathcal{M}_{i,k,j,l}^A\}$ in Eq. (4.9b) need to be determined for the imposition of the boundary conditions. For this purpose, the sum in (4.9b) is expanded as

$$\sum_{(j,l) \in \mathcal{I}_B} \mathcal{M}_{i,k,j,l}^A U_{j,l} = \sum_{(j,l) \in \mathcal{I}_B} \bar{\mathcal{M}}_{i,j}^A \bar{\mathcal{M}}_{k,l}^A U_{j,l}, \quad (4.11)$$

by using tensor product properties. For $j = 1, \dots, N$, the coefficients $\{\bar{\mathcal{M}}_{i,j}^A; i = 2, \dots, N-1\}$ in the x -direction are then obtained by solving the one-dimensional problems

$$\bar{\mathcal{M}}_A^{-1} \mathbf{x}^j = \boldsymbol{\delta}^j, \quad \text{with } \boldsymbol{\delta}^j = (\delta_{j,m}; m = 1, \dots, N), \quad (4.12)$$

giving as solution $\mathbf{x}^j = (\bar{\mathcal{M}}_{i,j}^A; i = 1, \dots, N)$. An analogous procedure is performed for determining the coefficients in the y -direction.

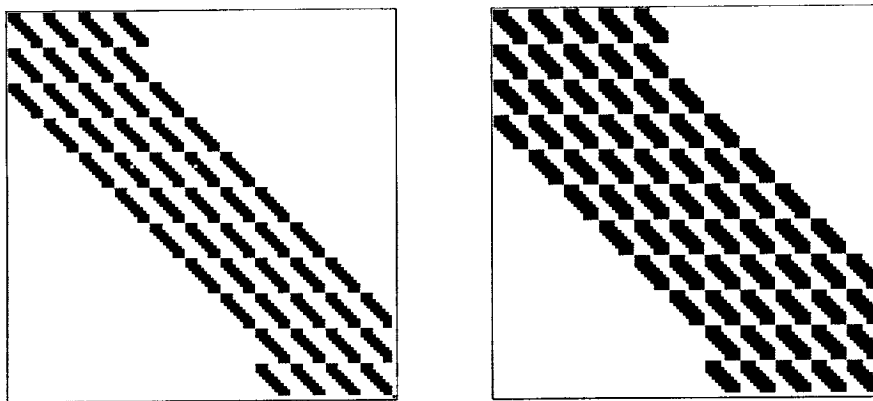


FIGURE 6. Sparsity pattern of \mathcal{A}_A on a 13×13 uniform grid for splines of order $k = 4$, generated with the mass lumping approximation (left) and the approximate inverse of order 4 (right).

Equations (4.8) and (4.10) yield the pressure equation

$$\frac{1}{\sigma} \mathcal{A}_A P = \frac{1}{\sigma} \mathcal{D} \mathcal{M}_A^{-1} F - G, \tag{4.13a}$$

where the pressure operator

$$\mathcal{A}_A = \mathcal{D} \mathcal{M}_A^{-1} \tilde{\mathcal{D}}, \tag{4.13b}$$

is constructed by multiplication of sparse matrices. These operations are performed with the SPARSKIT package (Saad (1990)).

Raising the order of the approximate inverse increases the number of non-zero entries of \mathcal{A}_A . In two dimensions, when a natural ordering of the unknowns is used, a modification of the block structure of \mathcal{A}_A is observed. As an illustration, Fig. 6 compares the structure of pressure operators generated by the lumping approximation and the approximate inverse of order 4. These operators have a similar block-structured pattern where the 11×11 blocks are more or less filled according to the order of the approximate inverse. For splines of order 4, we observe that an approximate inverse of order 4 doubles the number of non-zero entries of the pressure operator compared to the lumped mass approximation. Correspondingly, an increase of 70% of the entries is observed for splines of order 6.

The semi-consistent method is now evaluated against the consistent method by numerically solving problem (4.7) with $\sigma = 1$, for the solution

$$\mathbf{v} = \mathbf{rot} \sin 4\pi x \sin 4\pi y, \quad p = \cos 4\pi x \cos 4\pi y,$$

on a uniform distribution of knots. For comparison with results obtained in Botella (1999, 2001), the collocation points are set as the location of the maximum of the velocity B-splines. The maximum error on the first-component of the velocity u and the pressure, sampled on a 300×300 uniform grid, is reported in Fig. 7. For splines of order 4 (Fig. 7(a)), the use of an approximate inverse of order 4 maintains the order of accuracy of the consistent approximation, namely $O(N^{-4})$ for u and $O(N^{-2})$ for p . It is striking to observe that the magnitude of the error on p is almost identical for both schemes, while the velocity errors of the SCM scheme are only marginally higher. The latter is certainly the consequence of the inferior resolving power of the semi-consistent approximation that we observed in Section 4.1. As it would be expected, the 6th-order accuracy on u displayed in Fig. 7(b) by the CM scheme with splines of order 6 is not recovered by the

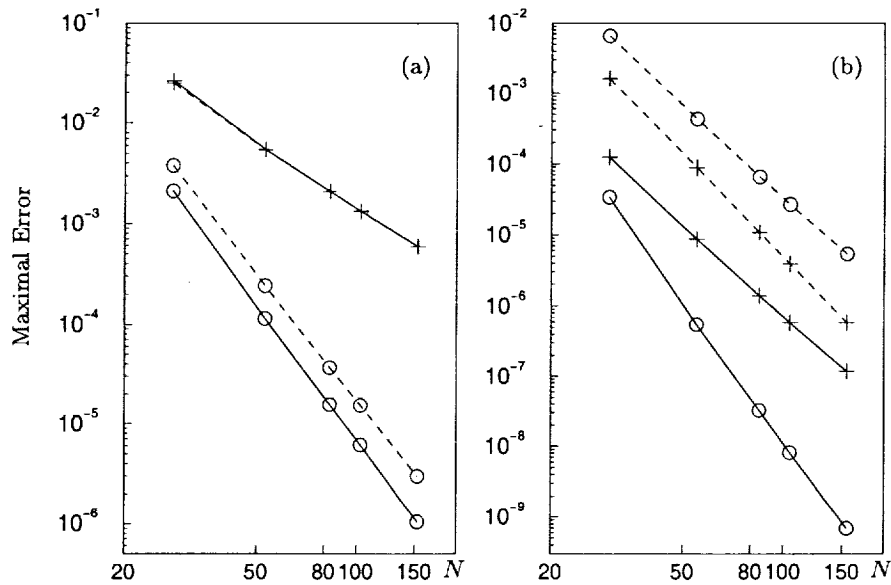


FIGURE 7. Solution of the Div-Grad problem with (a) splines of order 4, and (b) splines of order 6. Maximum error on u \circ — \circ , p +—+ , CM approximation; maximum error on u \circ --- \circ , p +---+ , SCM approximation with approximate inverse of order 4.

approximate inverse of order 4, and a fourth-order convergence rate is observed in this case.

It is valuable to compare the CPU cost required by the iterative solution of the CM and SCM equations. To give a fair evaluation, both systems are solved by similar iterative techniques with the error tolerance (*i.e.* the l^2 norm of the discrete divergence (4.8)) set to $\epsilon = 10^{-8}$.

Since the pressure operator of the CM discretization is dense and thus cannot be stored, the equations are solved by the Uzawa algorithm developed in Botella (1999, 2001), which is accelerated by the Bi-CGSTAB method (see *e.g.* Saad (1996)). The preconditioner of this system is $\mathcal{A}_L = \mathcal{D}\mathcal{M}_L^{-1}\tilde{\mathcal{D}}$, *i.e.* an SCM pressure operator where the lumping approximation is used. The use of this preconditioner has the effect of making the number of Uzawa iterations independent from the mesh size. Each step of the Uzawa algorithm requires inversions of the consistent mass matrix and the preconditioner. These problems are respectively solved by a direct method and the Bi-CGSTAB algorithm with ILU(m) preconditioning. The value $m = 0$ is used for splines of order 4 and $m = 2$ for splines of order 6, and the error tolerance is set to 10^{-10} .

The SCM system precludes the use of Uzawa iterations, resulting in a far less cumbersome solution procedure. The pressure equation (4.13) is solved with the same Bi-CGSTAB algorithm used for inverting the preconditioner \mathcal{A}_L of the CM system. The velocity is then recovered by using Eq. (4.10).

Table 3 reports the CPU time observed for solving these systems on a sequence of increasingly fine grids. The savings in CPU time yielded by the SCM method are tremendous: for splines of order $k = 4$ the CPU cost is divided by 30, while this ratio reaches 100 for $k = 6$. Intuitively, these savings can be understood when observing that the computational cost of the solution of the SCM pressure equation is roughly equivalent to a single inversion of the preconditioner of the CM solution procedure. The ratio of savings

Splines of order $k = 4$				Splines of order $k = 6$			
N	SCM	CM	Ratio	N	SCM	CM	Ratio
28	0.06	2.57	42.8	30	0.05	5.53	110.6
53	0.46	14.76	32.1	55	0.29	26.52	91.4
83	1.88	60.80	32.3	85	1.11	131.63	118.6
153	12.32	399.34	32.4	105	1.98	211.71	106.9

TABLE 3. Comparison of CPU time (in seconds) observed for the solution various approximation of the Div-Grad problem.

is thus proportional to the number of Uzawa iterations required for convergence. Since the number of Uzawa iterations is independent of the grid size but increases with the order of the B-splines, the SCM solution method becomes more attractive as the order of the discretization is raised.

5. Conclusion and future plans

Preliminary results on the application of the SCM scheme to the solution of the Navier-Stokes equations have been obtained. These important tests assess (a) the high spatial accuracy of the Navier-Stokes solver and (b) its robustness for unsteady computations. The time-integration is based on scheme (2.13)-(2.14), with second-order backward-differentiation of the time-derivative and Adams-Bashforth discretization of the nonlinear term. This fractional step scheme yields second-order time accuracy for both velocity and pressure (Botella (1999, 2001)). In order to obtain a fourth-order spatially accurate method, B-splines of order $k = 6$ are used in each direction, with the approximate inverse of order $k_1 = 4$.

The first test concerns the validation of the spatial accuracy of the SCM scheme on a uniform grid. For this purpose, we consider the steady solution

$$\mathbf{v} = \mathbf{rot} \sin \pi x \sin \pi y, \quad p = \frac{1}{4}(\cos 2\pi x \cos 2\pi y) + 10(x + y),$$

in the domain $\Omega =]-1, 1[^2$. Fig. 8 displays the normalized l^2 errors obtained when the steady-state is reached. This figure confirms that the method is indeed fourth-order accurate for both velocity and pressure.

The second test illustrates the accuracy and stability of the method for computing unsteady solutions. We consider the computation of the periodic flow in the regularized driven cavity flow at $Re = 12,000$, taking as a reference the spectral computation of Shen (1991) performed with 65 Chebyshev polynomials in each direction and the time step $\Delta t = 5 \times 10^{-3}$. For comparison purpose, the SCM computation uses the same discretization parameters with a similar grid refined near the boundary by a Chebyshev distribution of knots. The initial condition is defined as the steady flow at $Re = 10,000$. Fig. 9 displays the time-evolution of the kinetic energy on nearly half a million time-steps. The periodic state is asymptotically reached with the same period $T = 3.085 \pm \Delta t$ measured by Shen (1991). This result shows the ability of the SCM method to conserve kinetic energy on a long time integration and to reproduce spectral results with a similar coarse spatial resolution.

The use of highly accurate approximate inverse in association to the SCM scheme led to the development of a Navier-Stokes solver that preserves the accuracy of the B-spline

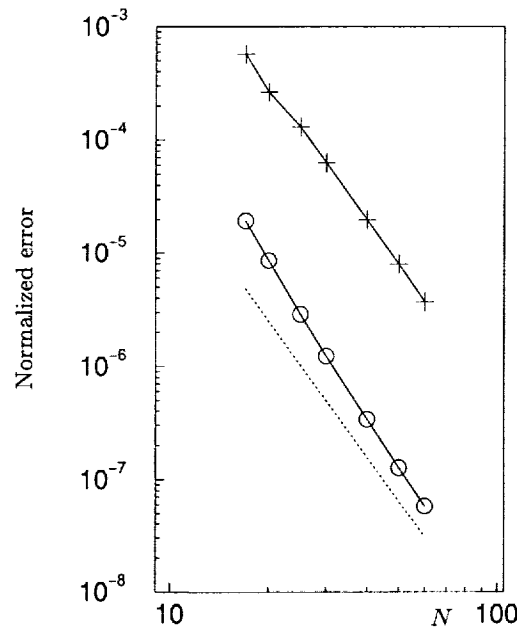


FIGURE 8. Spatial error on u (\circ — \circ) and p ($+$ — $+$) obtained on the steady state solution of the Navier-Stokes equations; \cdots : reference line of slope -4.

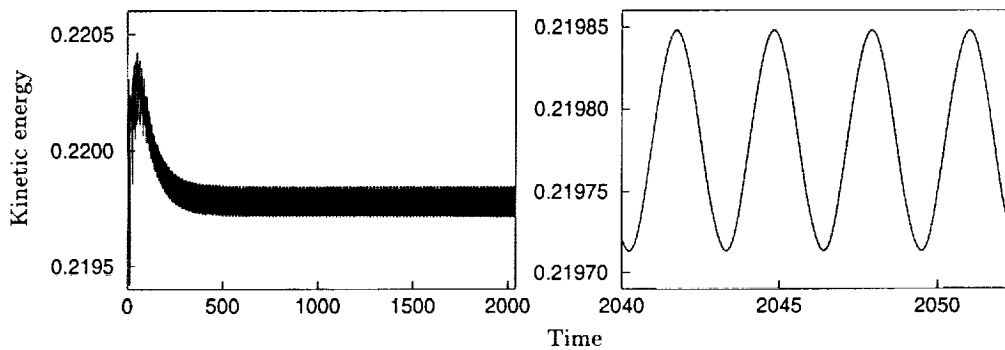


FIGURE 9. Time evolution of the kinetic energy in the driven cavity at $Re = 12000$ computed by the SCM fractional-step scheme on a 65×65 grid with $\Delta t = 5 \times 10^{-3}$.

in a cost-effective way. The high computational interest of the fractional step method is indeed recovered: the full decoupling of the velocity and pressure allows the solution to sparse elliptic problems only at each time-cycle.

This solver would serve as the building block for performing highly-accurate LES simulations of complex flow on semi-structured meshes. The solver is currently updated for the handling of more general geometries, the flow past a circular cylinder being considered as a first application. The semi-structured multidimensional approximations will be constructed by using the mesh embedding algorithm of Shariff & Moser (1998). Several issues related to the extension of the tensor product B-spline approximation have to be addressed. The algorithm should be modified to generate in a compatible fashion the semi-structured staggered bases of the velocity and pressure. In addition, the construction of approximate inverse has to be extended to the case of these multidimensional B-splines.

Acknowledgments

The author is grateful to Dr. K. Shariff for valuable discussions during the course of this work.

REFERENCES

- DE BOOR, C. 1978 *A Practical Guide to Splines*. Springer.
- BOTELLA, O. 1999 A velocity-pressure Navier-Stokes solver using a B-spline collocation method. *Annual Research Briefs*, Center for Turbulence Research, NASA Ames/Stanford Univ. 403-421.
- BOTELLA, O. 2001 On a collocation B-spline method for the solution of the Navier-Stokes equations. *Computers & Fluids*, to be published.
- CHRISTARA, C. C. & SMITH, B. 1997 Multigrid and multilevel methods for quadratic spline collocation. *BIT*. **37**(4), 781-803.
- GRESHO, P. M. & CHAN, S. T. 1990 On the theory of semi-implicit projection methods for viscous incompressible flow and its implementation via a finite element method that also introduces a nearly consistent mass matrix. Part 1: Theory & Part 2: Implementation. *Int. J. Numer. Methods Fluids*. **11**, 587-620 & 621-659.
- GRESHO, P. M., LEE, R. L. & SANI, R. L. 1978 Advection-dominated flows, with emphasis on the consequence of mass lumping. *Finite Elements in Fluids*, J. Wiley & Sons. **3**, 335-350.
- GRESHO, P. M. & SANI, R. L. 1998 *Incompressible Flow and the Finite Element Method*. J. Wiley & Sons.
- HARLOW, F. H. & WELCH, J. 1965 Numerical calculation of time-dependent viscous incompressible flow of fluid with free surfaces. *Phys. Fluids*. **8**, 2181-2189.
- KRAVCHENKO, A. G. & MOIN, P. 1997 On the effect of numerical errors in large eddy simulations of turbulent flows. *J. Comput. Phys.* **131**, 310-322.
- KRAVCHENKO, A. G. & MOIN, P. 2000 Numerical studies of flow over a circular cylinder at $Re_D > 3900$. *Physics Fluids*. **12**, 403-417.
- KRAVCHENKO, A. G., MOIN, P. & SHARIFF, K. R. 1999 B-spline method and zonal grids for simulation of complex turbulent flows. *J. Comput. Phys.* **151**, 757-789.
- LELE, S. K. 1992 Compact finite difference schemes with spectral-like resolution. *J. Comput. Phys.* **103**, 16-42.
- LYCHE, T. & SCHUMAKER, L. L. 1975 Local spline approximation methods. *J. Approx. Theory*. **15**, 294-325.
- NICOUD, F., BAGGETT, J. S., MOIN, P. & CABOT, W. 2001 LES wall modeling based on optimal control theory. *Phys. Fluids*, to be published.
- SAAD, Y. 1990 SPARSKIT: A basic tool kit for sparse matrix computations. *Tech. Rep. 90-20*. Research Institute for Advanced Computer Science, NASA Ames Research Center, Moffett Field, CA.
- SAAD, Y. 1996 *Iterative Methods for Sparse Linear Systems*. PWS.
- SHARIFF, K. & MOSER, R. D. 1998 Two-dimensional mesh embedding for B-spline methods. *J. Comput. Phys.* **145**, 471-488.
- SHEN, J. 1991 Hopf bifurcation of the unsteady regularized driven cavity flow. *J. Comput. Phys.* **95**, 228-245.
- VASILYEV, O. V. 2000 High order finite difference schemes on non-uniform meshes with good conservation properties. *J. Comput. Phys.* **157**, 746-761.

Construction of commutative filters for LES on unstructured meshes

By Alison L. Marsden, Oleg V. Vasilyev† AND Parviz Moin

1. Motivation and objectives

Application of large eddy simulation (LES) to flows with increasingly complex geometry necessitates the extension of LES to unstructured meshes. A desirable feature for LES on unstructured meshes is that the filtering operation used to remove small scale motions from the flow commutes with the differentiation operator. If this commutation requirement is satisfied, the LES equations have the same structure as the unfiltered Navier Stokes equations. Commutation is generally satisfied if the filter has a constant width. However, in inhomogeneous turbulent flows, the minimum size of eddies that need to be resolved varies throughout the flow. Thus, the filter width should also vary accordingly. Given these challenges, the objective of this work is to develop a general theory for constructing discrete variable width commutative filters for LES on unstructured meshes.

Variable width filters and their commuting properties have been the focus of several recent works. Van der Ven (1995) constructed a family of continuous filters which commute with differentiation up to arbitrary order in the filter width. However, this set of filters applies only to an infinite domain without addressing the practical issue of boundary conditions in a finite domain. More recently, a class of discrete commutative filters was developed by Vasilyev *et al.* (1998) for use on nonuniform structured meshes. Their formulation uses a mapping function to perform the filtering in the computational domain. Although this type of mapping is impossible for the unstructured case, the theory developed in Vasilyev *et al.* (1998) was used as a starting point for the present work.

In this paper we present a theory for constructing discrete commutative filters for unstructured meshes in two and three dimensions. In addition to commutation, other issues such as control of filter width and shape in wavenumber space are also considered. In particular, we wish to specify a desired filter width at each point in space and obtain a discrete filter which satisfies this requirement regardless of the choice of the computational mesh.

2. Commutation error of filtering and differentiation operations in physical space

Recently Vasilyev *et al.* (1998) developed a general theory of discrete filtering in arbitrarily complex geometries. With the use of a mapping function, the filtering is done in the computational domain. Here, we extend the theory of commutative filters developed in Vasilyev *et al.* (1998) to the physical domain. We begin by discussing filtering in one-dimensional space and then extend it to three spatial dimensions.

† Dept. of Mechanical & Aerospace Engr., University of Missouri, Columbia, MO 65211

2.1. Commutation error in one spatial dimension

Following Vasilyev *et al.* (1998), an operator to measure commutation error is defined as follows. Given a function $\phi(x)$, the commutation error is

$$\left[\frac{d\phi}{dx} \right] = \overline{\frac{d\phi}{dx}} - \frac{d\bar{\phi}}{dx}. \quad (2.1)$$

where over-bar denotes the filtered quantity. The continuous filtering operation is defined by

$$\bar{\phi}(x) = \frac{1}{\Delta(x)} \int_a^b G\left(\frac{x-y}{\Delta(x)}, x\right) \phi(y) dy, \quad (2.2)$$

where $\Delta(x)$ is the filter width and $G(\eta, x)$ is the location dependent filter function. With the change of variables $\eta = \frac{x-y}{\Delta(x)}$, Eq. (2.2) can be written as

$$\bar{\phi}(x) = \int_{\frac{x-b}{\Delta(x)}}^{\frac{x-a}{\Delta(x)}} G(\eta, x) \phi(x - \Delta(x)\eta) d\eta. \quad (2.3)$$

Taking the Taylor series expansion of $\phi(x - \Delta(x)\eta)$ in powers of Δ gives

$$\phi(x - \Delta(x)\eta) = \sum_{l=0}^{+\infty} \frac{(-1)^l}{l!} \Delta^l(x) \eta^l \mathcal{D}_x^l \phi(x), \quad (2.4)$$

where $\mathcal{D}_x = d/dx$ is the derivative operator. This series was proven to be convergent in Vasilyev *et al.* (1998) for the case of uniform Δ by assuming that the spectrum did not include wavenumbers higher than some finite cutoff wavenumber k_{max} . The proof is analogous for the case of varying Δ and with the same assumptions the radius of convergence in this case is considered to be infinite. Substituting (2.4) into (2.3) and changing the order of summation and integration, we have

$$\bar{\phi}(x) = \sum_{l=0}^{+\infty} \frac{(-1)^l}{l!} \Delta^l(x) \phi^{(l)}(x) \int_{\frac{x-b}{\Delta(x)}}^{\frac{x-a}{\Delta(x)}} \eta^l G(\eta, x) d\eta. \quad (2.5)$$

Defining the filter moment as

$$M^l(x) = \int_{\frac{x-b}{\Delta(x)}}^{\frac{x-a}{\Delta(x)}} \eta^l G(\eta, x) d\eta \quad (2.6)$$

and substituting (2.6) into (2.5), we obtain

$$\bar{\phi}(x) = \sum_{l=0}^{+\infty} \frac{(-1)^l}{l!} \Delta^l(x) M^l(x) \mathcal{D}_x^l \phi(x). \quad (2.7)$$

In the same manner as in Vasilyev *et al.* (1998) we let

$$M^l(x) = \begin{cases} 1 & l = 0 \\ 0 & l = 1, \dots, n-1. \end{cases} \quad (2.8)$$

With this definition we have

$$\bar{\phi} = \phi(x) + \sum_{l=n}^{\infty} \frac{(-1)^l}{l!} \Delta^l(x) M^l(x) \mathcal{D}_x^l \phi(x). \quad (2.9)$$

The filter of the derivative of the function is

$$\overline{\frac{d\phi}{dx}}(x) = \frac{d\phi}{dx} + \sum_{l=n}^{+\infty} \frac{(-1)^l}{l!} \Delta^l(x) M^l(x) \mathcal{D}_x^{l+1} \phi(x). \quad (2.10)$$

The derivative of the filtered quantity is

$$\frac{d\overline{\phi}}{dx}(x) = \frac{d\phi}{dx} + \sum_{l=n}^{+\infty} \frac{(-1)^l}{l!} \frac{d}{dx} (\Delta^l(x) M^l(x) \mathcal{D}_x^l \phi(x)). \quad (2.11)$$

Applying the chain rule to (2.11) and subtracting (2.11) from (2.10), we obtain an expression for the commutation error:

$$\left[\frac{d\phi}{dx} \right] = \sum_{l=n}^{+\infty} \frac{(-1)^l}{l!} \left\{ \frac{d}{dx} (\Delta^l(x) M^l(x)) \right\} \mathcal{D}_x^l \phi(x). \quad (2.12)$$

Using the properties in (2.8) it follows that

$$\frac{dM^l}{dx}(x) = 0 \quad \text{for } l = 1, \dots, n-1. \quad (2.13)$$

As a result, the local commutation error is

$$\left[\frac{d\phi}{dx} \right] = O(\Delta^n(x)), \quad (2.14)$$

provided that $d\Delta/dx = O(\Delta)$, which is true for most of the smoothly varying grids. For highly stretched grids $d\Delta/dx$ is $O(\Delta^\gamma)$, $\gamma < 1$, which results in lowering the order of the commutation error to $O(\Delta^{n+\gamma-1})$. The extension to three dimensions is quite straightforward, and has been presented in Marsden (1999).

3. Construction of discrete commutative filters

The filters developed by Vasilyev *et al.* (1998) were constructed by applying the necessary number of constraints to the filter weights to achieve both commutation and an acceptable filter shape. The following constraints were imposed in finding the filter weights. The zeroth moment should be one, a specified number (order of commutation error) of higher moments should be zero, and other constraints were added for defining the filter shape.

These ideas were used as a starting point for developing filters for the unstructured case. However, in the unstructured mesh formulation it is impossible to use the same discrete filter at all points on the mesh as was possible in Vasilyev *et al.* (1998). Instead, filter weights must be computed at each mesh point and stored in a table. This restriction means that the algorithm must have a way to assess the filter shape at each point since the user cannot adjust the filter constraints by hand at each mesh point.

An initial formulation for filter construction on an unstructured mesh used the ideas presented in Vasilyev *et al.* (1998) generalized to physical space. Given a mesh point to filter about, a set of neighboring points was chosen to make up the filter. Then, constraints were applied directly on the filter moments and shape in order to determine the filter weights. This procedure followed directly from Vasilyev *et al.* (1998). Two problems arose in implementing this method. First, it was found that in the case of a non-uniform point distribution such as an unstructured mesh, the shapes of the resulting filters were highly

unpredictable. In order to overcome this problem, the filter construction algorithm would have to choose the most appropriate constraints to apply based on some filter shape criterion. Second, the nature of unstructured meshes is such that a point may have any number of neighboring points. The algorithm would, therefore, have to decide which points to include and possibly apply different constraints at each mesh point, leading to inconsistencies in the filters from one part of the mesh to another.

Greater predictability and ease of implementation can be gained by using interpolation based filters to achieve commutation rather than directly implementing constraints as discussed above. The construction of discrete filters on unstructured meshes is motivated by work on interpolating wavelets Donoho (1992) and the theory of second generation wavelets Sweldens (1996), Sweldens (1997), Daubechies & Sweldens (1998). To illustrate the idea of construction of discrete filters based on polynomial interpolation, let us consider a one-dimensional example. Suppose we have a set of N unevenly spaced grid points x_i and the values of the function f_i are known at these points. We can uniquely define the $N - 1$ order polynomial $P_{N-1}(x)$ that passes through the data. Polynomial coefficients are uniquely determined by locations x_i and values f_i . Evaluating this polynomial at the point x_0 and substituting the values of the polynomial coefficients expressed in terms of the values f_i , we easily find that $P_{N-1}(x_0) = \sum_{k=1}^N w_k f_k$. If we treat these weights as the weights of the corresponding discrete filter, then this filter will have the unique property that when it is applied to the polynomial of degree less than $N - 1$ it does not change this polynomial. Then the discrete filter moments defined by

$$M^l = \sum_{k=1}^N w_k (x_k - x_0)^l \quad (3.1)$$

automatically satisfy the conditions (2.8) since $(x - x_0)^l$ is exactly zero at $x = x_0$ for $l = 1, \dots, N - 1$ and 1 for $l = 0$. Consequently, the discrete filters based on polynomial construction automatically guarantee an N^{th} order commutation error. To control the shape and other properties of the discrete filters, we can construct a filter as a linear combination of as many polynomial based filters as we like while preserving the commutation properties of the filter. The same idea can be easily extended to n dimensions using an n -dimensional polynomial. This simple idea gives us all the flexibility we need to construct filters with the desired shape and properties in any dimension, yet it is very straightforward to implement.

In general, with an N^{th} order numerical scheme, the filtering operation must commute to order N . Reducing error further has no significant impact on overall accuracy because the discretization error is also of order N . As in the case for a structured mesh, the filters developed here must have $N - 1$ zero moments to commute to order N . In developing filters for an unstructured mesh, we will begin by assuming a second order finite difference scheme. However, as discussed above, the extension to a higher order method is straightforward. With this second order scheme in mind, we proceed with the goal of developing filters which ensure a second order commutation error. A two-dimensional discrete filter based on first order polynomial interpolation can be constructed using a triangle where (x_0, y_0) is the point where we want the filtered value. A triangle is chosen because in two dimensions three points are needed for exact reconstruction of a first order polynomial. Weights are calculated by fitting a polynomial to the vertices of the triangle, and they are then used to find a weighted average at the central point (x_0, y_0) . The shape of the resulting filter in wavenumber space is very well defined, and the number of points used can be the same at each mesh point because any three close points can be chosen to

make up a triangle. The method for finding the filter weights using a triangle in two dimensions is presented here, but is extended to three dimensions in Marsden (1999). Details on choosing which points to use in the filter are discussed in Sections 4.1 and Marsden (1999).

The vector of interpolating weights, \mathbf{w} is calculated as follows. Let (x_1, y_1) , (x_2, y_2) , and (x_3, y_3) be coordinates of the points where the function is given and (x_0, y_0) be the coordinates of the point to interpolate to. Let

$$P(x, y) = a_{00} + a_{10}(x - x_0) + a_{01}(y - y_0) \quad (3.2)$$

be a first order polynomial interpolant. Requiring that interpolant (3.2) goes through the data points f_i ($i = 1, \dots, 3$), we obtain the following set of linear equations

$$\begin{aligned} f_1 &= a_{00} + a_{10}(x_1 - x_0) + a_{01}(y_1 - y_0), \\ f_2 &= a_{00} + a_{10}(x_2 - x_0) + a_{01}(y_2 - y_0), \\ f_3 &= a_{00} + a_{10}(x_3 - x_0) + a_{01}(y_3 - y_0). \end{aligned} \quad (3.3)$$

Note that interpolant (3.2) is chosen such that a_{00} is the value of interpolant at point (x_0, y_0) . This value is also the weighted sum of the functional values given by

$$P(x_0, y_0) = w_1 f_1 + w_2 f_2 + w_3 f_3, \quad (3.4)$$

where, w_i are the filter weights.

Some manipulation shows that the weights can be simply calculated with a single matrix inversion. If

$$\mathbf{A} = \begin{pmatrix} 1 & x_1 - x_0 & y_1 - y_0 \\ 1 & x_2 - x_0 & y_2 - y_0 \\ 1 & x_3 - x_0 & y_3 - y_0 \end{pmatrix} \quad (3.5)$$

and

$$\mathbf{b} = (1 \ 0 \ 0) \quad (3.6)$$

the vector of weights, \mathbf{w} , is given by

$$\mathbf{w} = \mathbf{b} \cdot \mathbf{A}^{-1}. \quad (3.7)$$

We now have weights which make up a two-dimensional discrete filter which satisfies commutation to second order. The three-dimensional equivalent is straightforward and requires four points instead of three to satisfy commutation. The extension to three dimensions is discussed in Marsden (1999).

4. Implementation of commutative filters

4.1. Two-dimensional filters

In Section 3 we demonstrated construction of discrete two-dimensional filters with second order commutation error using polynomial interpolation. The result was a set of discrete triangular filters with weights assigned to each vertex and the central point. Using these triangular filters as a basis, the topic of this section is the construction of commutative filters which combine multiple triangles into one filter and allow for a variable filter width.

Although one triangular filter satisfies the properties of commutation, it is undesirable because it offers no flexibility in filter width or shape. Also, an ideal filter would

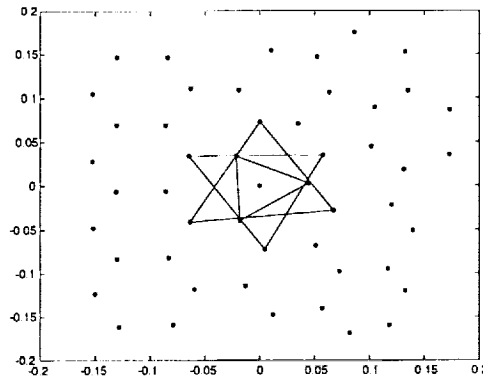


FIGURE 1. Example of filter constructed with triangles on an unstructured grid.

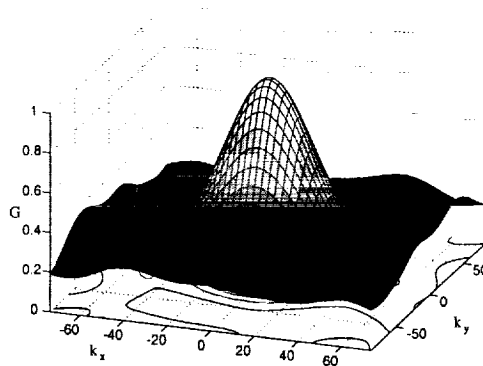


FIGURE 2. Transfer function corresponding to filter in Fig. 1.

include more neighboring points to obtain a nice distribution. To take advantage of the predictability of simple triangle based filters while adding flexibility in filter width, it is possible to use a linear combination of multiple triangular filters. This method offers the advantage of a predictable and well defined transfer function shape while ensuring that the resulting filter will satisfy commutation to the same order as the basis triangles.

Figure 1 shows an example of a 2-D filter constructed from three triangles. The corresponding transfer function, which has very nice characteristics, is shown in Fig. 2. To achieve flexibility in filter width, each triangle as well as the central point is assigned a weight which applies equally to all vertices of the triangle. We will refer to the weights on triangles as β_i whereas the filter weights on individual vertices calculated in section 3 are w_i . The value of β_i can be varied from 0 to 1 as long as the sum total is 1. The optimum value of β for the central point is $1/2$ because this results in the most desirable filter shape.

4.2. Implementation in two dimensions

We are now ready to discuss details of filter construction in two dimensions. The first task for the filter construction algorithm is to choose the set of points to include in the filter. Each included point is part of a triangle which will later be linearly combined with other triangles to form the total filter as discussed in section 4.1. The number of triangles included in each filter may be specified by the user; however, the filters presented in this paper consist of three triangles because this provides a nice distribution of points on a

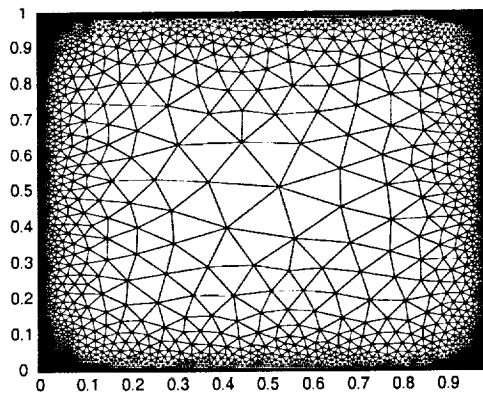


FIGURE 3. Example of mesh used for filter development.

regular unstructured mesh in two dimensions. After the set of points is chosen, the next step is to calculate the weights associated with each mesh point included in the filter. From these, we calculate the transfer function G and apply the filter to the discrete data. Figure 3 shows an example mesh which was used in testing the algorithm which chooses filter points.

Points to include in the filter are selected based on chosen criterion for the triangles which make up the filter. Given a point to filter about, surrounding points are searched in groups of three until a set of triangles to use in the filter is settled on. It is obviously undesirable to search points on the entire mesh because of computational cost. Because of this, the first step in the algorithm is to come up with a set of neighboring points to include in the search. This is done by using the tree structure of the mesh connectivity to obtain a set of surrounding points. In two dimensions, three levels of the tree are sufficient for obtaining a large enough group of points.

Having found a group of surrounding mesh points, the next step is to calculate the distance to each point in the group as well as the angle from the x axis. The points are then sorted according to angle into three zones of 120° each. The zones are created to ensure that the chosen points have a nice distribution of angles about the central point. Figure 4 shows these three zones. Within each zone, the points are sorted by distance from the central point.

Triangles are systematically formed by taking a point from each zone, starting with the closest point in each, and then seeing if the chosen triangle meets the criterion for being included in the filter. For each triangle formed, we must determine whether to use it in the filter or continue the search by trying the next combination of three points. When three triangles have been found, the choice of points for the filter is complete.

Triangles must satisfy two criterion to be selected for use in the filter. First, the central point must be inside the triangle and second, the central point must be as close to the centroid of the triangle as possible. Both criterion involve drawing lines from the central point to each vertex of the triangles to form three sub-triangles. If the summed area of the sub-triangles exceeds that of the larger triangle, the central point is outside. If the area of any of the sub triangles is a large percentage of the total area of the triangle, the central point is too close to the side of the triangle. The allowable percentage is a user specified parameter. If one of these checks is true, the triangle is rejected and we advance to the next row of the table, continuing until the desired number of triangles has been found.

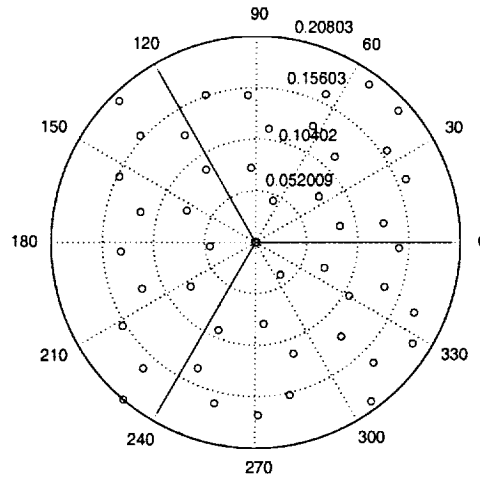


FIGURE 4. Mesh nodes sorted by angle.

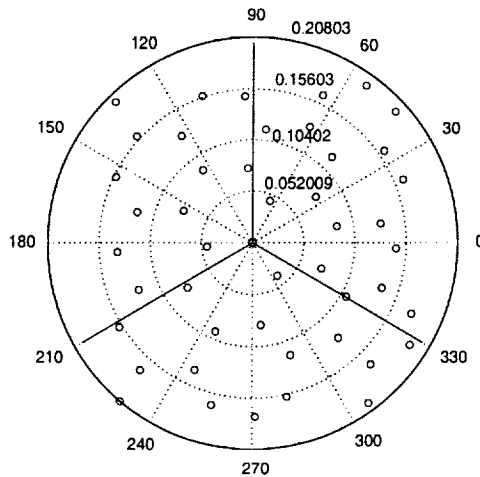


FIGURE 5. Mesh nodes sorted by angle, rotated from Fig. 4.

This procedure has one drawback. When the best choice of triangle has two points in the same region, usually very close to the region boundaries, it is never tried as a possibility for the filter. As a solution to this problem, the next step in the algorithm is to rotate the zone boundaries as shown in Fig. 5, and the procedure of choosing triangles is performed again, returning a new set of triangles. The set of triangles whose collective weights are closest to one third is then chosen to make up the final filter.

We now have a set of three triangles to make up the filter which can be linearly combined to create the complete filter as described in Section 4.1. Flexibility is gained by applying the same filter over again with different triangle weights, β_i , to capture low and high wavenumbers and achieve a nice transfer function shape. In addition, by applying the same filter more than once, it is possible to increase the filter width until the desired value is reached. With this method it also becomes possible to exactly specify the filter ratio for use in the dynamic model.

5. Prescribing the filter width

The main advantage of the filtering method presented is that the filter width can be prescribed by the user *a priori*. For example, in a boundary layer it is typical to use an exponential form of the filter width function since the scale of eddies increases with distance away from the wall. The filter width can be defined as the radius Δ of an equivalent circular top hat filter. The corresponding second moment, M_2 , can be defined by the following integral.

$$M_2 = \int_0^{2\pi} \int_0^\Delta r^2 \cos^2 \theta \frac{1}{\pi \Delta^2} r dr d\theta. \quad (5.1)$$

Evaluating this integral we have a relation between the second moment and the filter width.

$$\Delta = \sqrt{4M_2} \quad (5.2)$$

Given a target value for the filter width, which is specified by the user, the above relation can be used to prescribe target values for the second moment. This second moment target value can be used to find the values of β which will result in the closest value to the desired value of Δ . The values of β are chosen by solving the following set of equations using least squares method with constraints on the values of β as follows, where β_0 is the value assigned to the central point and $\beta_1, \beta_2, \beta_3$ are assigned to the three triangles in the filter.

$$\beta_0 = 1/2 \quad (5.3)$$

$$\beta_1 + \beta_2 + \beta_3 = 1 \quad (5.4)$$

The target second moment values in x , y , and xy are M^{02} , M^{20} , and M^{11} respectively and m_i^{02} , m_i^{20} , and m_i^{11} are the moments of the individual triangles.

$$\begin{aligned} M^{02} &= m_1^{02} \beta_1 + m_2^{02} \beta_2 + m_3^{02} \beta_3 \\ M^{20} &= m_1^{20} \beta_1 + m_2^{20} \beta_2 + m_3^{20} \beta_3 \\ M^{11} &= m_1^{11} \beta_1 + m_2^{11} \beta_2 + m_3^{11} \beta_3 \end{aligned} \quad (5.5)$$

6. Demonstrating commutation

In order to validate that the filters developed commute to the desired order, a series of numerical tests were performed. Measuring the commutation properties of the directional derivatives was found not to be a good test, since the accuracy of derivative calculations strongly depends on the orientation of the mesh element, and as a consequence the resulting truncation error is very nonuniform. As it was demonstrated in Perot (2000), a more natural operation to perform on an unstructured mesh is to calculate the curl at each mesh point. It is relatively straightforward to demonstrate that commutative properties of filtering and the curl operators are the same as discussed in Section 2.

Using the curl operator and the notation of Section 2.1, the commutation error is defined by

$$[\nabla \times f] = \nabla \times \bar{f} - \overline{\nabla \times f} \quad (6.1)$$

where f is the value of the prescribed function at each mesh point. The trivial case of the linear function $f = ax + by + c$ was used to verify that the resulting error was within machine zero range. With this check complete, the commutation and truncation errors were calculated on a series of consecutively finer meshes, using the equations describing

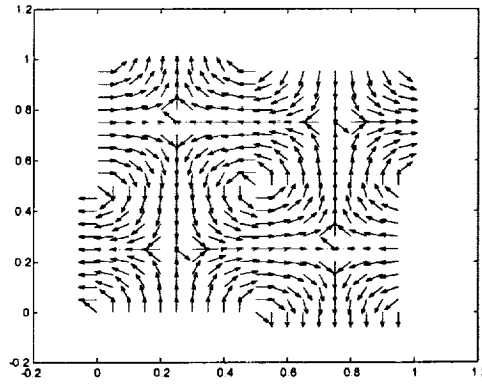


FIGURE 6. Streamlines of vortices in a box.

a vortex in a box.

$$u = -\cos(\beta_1 x + \phi_1) \sin(\beta_2 y + \phi_2) \quad (6.2)$$

$$v = \sin(\beta_1 x + \phi_1) \cos(\beta_2 y + \phi_2) \quad (6.3)$$

A plot of streamlines of these equations for the case $\beta_1 = \beta_2 = 2\pi$, $\phi_1 = \phi_2 = 0$ is shown in Fig. 6. The truncation error for the above function is the difference between the exact value of the curl

$$C_{exact} = (\beta_1 + \beta_2)[\cos(\beta_1 x + \phi_1) \cos(\beta_2 y + \phi_2)] \quad (6.4)$$

and the numerically calculated value.

The procedure for calculating the commutation error at each mesh element center using the curl operator is as follows. First, the functional values are calculated at the cell centers. These values are filtered discretely at the cell centers using the method described in Section 4.2, and then the curl of the filtered value is found numerically using surrounding filtered values. This gives the first term in Eq. 6.1. The second term in Eq. 6.1 is found by first taking the curl of the functional values at all cell centers and then filtering these values using the values of the curl which were found at adjacent mesh elements. The commutation error can then be compared to the truncation error at each mesh element center.

Both high and low order integration schemes were used to calculate the curl. For simplicity, only filters with with one triangle, or three filter points, were used. Using the low order integration method, the circulation is computed by interpolating values from the cell centers to the midpoints of the edges to find the velocity tangent to the side of the element and then integrating over the three triangle edges. The curl is then obtained by dividing by the cell area. Overall this is a first order operation. Using this method, it was found that the resulting commutation and truncation errors had first order convergence. Thus, the second order accuracy of the filtering method had been reduced when integration was performed. A plot of the commutation and truncation errors using the curl operation is shown in Fig. 7. All error plots are the L_∞ error vs. square root of the number of mesh points, and all use the same series of increasingly finer meshes to demonstrate convergence. Plotted in this way, the slope of the error is equal to the order of accuracy. All errors have been normalized with the maximum value of the curl.

The high order integration method was developed for a uniform symmetric unstruc-

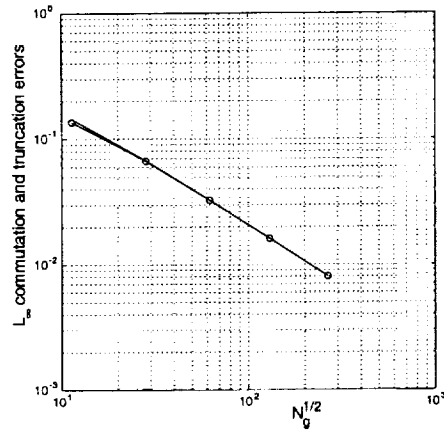


FIGURE 7. Normalized L_∞ commutation and truncation errors of curl, low order method. —, truncation error; -o-, commutation error.

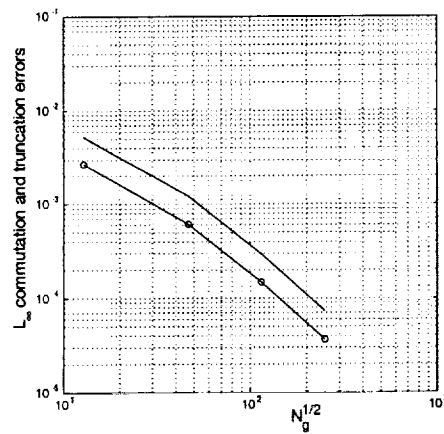


FIGURE 8. Normalized L_∞ commutation and truncation errors of curl, high order method. —, truncation error; -o-, commutation error.

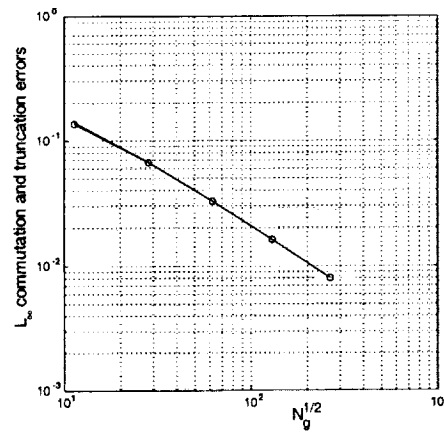


FIGURE 9. Normalized L_∞ commutation and truncation errors of circulation, low order method. —, truncation error; -o-, commutation error.

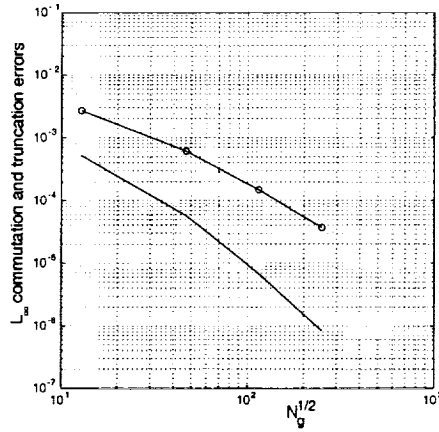


FIGURE 10. Normalized L_∞ commutation and truncation errors of circulation, high order method. —, truncation error; —○—, commutation error.

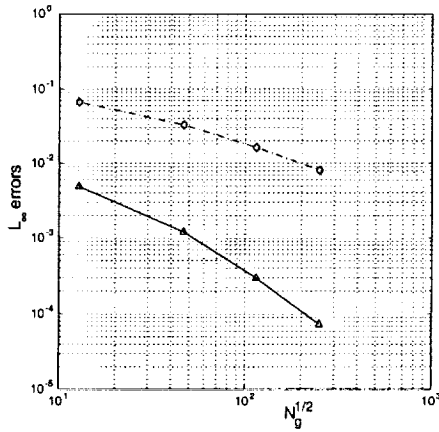


FIGURE 11. Comparison of filtered and unfiltered normalized L_∞ truncation errors. ○: $\Gamma_{low}(V) - \Gamma_{high}(V)$; ○: $\Gamma_{low}(\bar{V}) - \Gamma_{high}(\bar{V})$; -△-: $\bar{\Gamma}_{low}(V) - \bar{\Gamma}_{high}(V)$; -△- : $\bar{\Gamma}_{low}\bar{V} - \bar{\Gamma}_{low}(V)$.

tured mesh. While use of a “structured” unstructured mesh is ludicrous for any practical application, it serves the purpose of demonstrating commutation of the filtering method. As discussed earlier, the filtering method presented here can be applied to any unstructured mesh. The integration method first requires interpolating to the vertices from twelve surrounding cell centers, using weights $2/9$ for the nearest six cells and $-1/18$ for neighboring cells. The routine then interpolates to the edges using the two vertices and two cell centers which lie on the line connecting the edge midpoint and the vertices of the neighboring points using the weights $(-1/16, 9/16, 9/16, -1/16)$. Finally, integration can be carried out along each edge of the cell using the value at the edge midpoint and the values at the two vertices using the weights $(1/6, 2/3, 1/6)$. A plot of the high order method using the curl operator is shown in Fig. 8. Due to the division by area, the curl operator is second order regardless of integration scheme. So, we see second order convergence of both commutation and truncation error as expected. However, it is important to

note that the magnitude of the commutation error is consistently less than the truncation error.

The results using the curl operator show that the truncation error is associated with division by area even for the higher order scheme. In order to eliminate this difficulty, we can introduce the discrete values of circulation that correspond to each mesh element. We can therefore compute the commutation error using values of circulation. In this way, we can clearly demonstrate that the truncation error will be higher order, and the commutation properties of the filter will become apparent. The exact value of circulation must be found for each mesh element to compute the truncation error. This is done by integrating the function exactly along the sides of each mesh element.

The commutation error using the circulation was analyzed using the low order method, and results are shown in Fig. 9. These plots also show a first order convergence in which the commutation error was contaminated due to the truncation error.

We are able to show that with this low order integration scheme, using both the curl and circulation, the commutation error is contaminated by the truncation error due to high frequency components. Figure 11 shows the truncation error and the filtered truncation error and proves that, without these high frequency components, the truncation error is a full order of magnitude decreased. Therefore, the commutation error is contaminated and the values of the commutation error and truncation error are nearly identical.

The high order method applied with the circulation shows a third order convergence in the truncation error and a second order convergence in the commutation error. This time, the order of integration was high enough that the commutation error was not affected, and we can confirm that it has second order convergence. The results for this case are shown in Fig. 10. The convergence of the truncation error for the cases using circulation, compared with the cases using the curl, confirms that dividing by the area reduced the order of magnitude by two. These tests confirm that the filtering method has a second order commutation error, which was predicted in section 3. Although filters consisting of one triangle were used, it is fully expected that filters with multiple triangles will have similar convergence properties, thus giving the user control over the filter width. In addition, even though it was necessary to use a uniform mesh for the numerical tests, it is fully expected that the filtering method used will have similar convergence properties for any unstructured mesh.

7. Conclusions

A method of constructing commutative filters for unstructured LES has been developed and validated. The method is intended for use in the ASCI unstructured solver at the Center for Turbulence Research for use in a wide variety of applications. The convergence tests performed confirm that the filtering method leads to a second order commutation error and can therefore be used in conjunction with a second order accurate numerical scheme.

One important feature of the method of filter construction presented here is that it has no requirements on the type of mesh used. Because the filter can be constructed simply from a set of points in two- or three-dimensional space, there are no constraints on the shape of mesh elements or the connectivity. It is possible to use connectivity to improve the efficiency of the algorithm, but the method remains general to any mesh. In addition, the filters presented have a consistent filter shape and flexible filter width. This allows the filter width ratio to be exactly specified for use in the dynamic model.

It would be relatively straightforward to extend the filter construction procedure developed here to higher order accuracy. For example, if one desired to use a third order finite difference scheme, the polynomial interpolant would have to be second order, requiring six neighboring points in two dimensions.

REFERENCES

- CARATI, D. & EIJNDEN, E. V. 1997 On the self-similarity assumption in dynamic models for large eddy simulations. *Phys. Fluids*. **9**(7), 2165-2167.
- DAUBECHIES, I. & SWELDENS, W. 1998 Factoring Wavelet Transforms into Lifting Steps. *J. Fourier Anal. Appl.* **4**(3), 245-267.
- DONOHO, D. L. 1992 Interpolating Wavelet Transforms. *Technical Report 408*, Department of Statistics, Stanford University.
- GERMANO, M., PIOMELLI, U., MOIN, P. & CABOT, W. H. 1991 A dynamic subgrid-scale eddy viscosity model. *Phys. Fluids A*. **3**(7), 1760-1765.
- Ghosal, S. & Moin, P. 1995 The basic equations of the large eddy simulation of turbulent flows in complex geometry. *J. Comp. Phys.* **118**, 24-37.
- GHOSAL, S. 1993 On the large eddy simulation of turbulent flows in complex geometry. *Annual Research Briefs*, Center for Turbulence Research, NASA Ames/Stanford Univ. 111-128.
- GHOSAL, S. 1999 Mathematical and Physical Constraints on Large-Eddy Simulation of Turbulence. *AIAA J.* **37**(4), 425-433.
- LUND, T. S. 1997 On the use of discrete filters for large eddy simulation. *Annual Research Briefs*, Center for Turbulence Research, NASA Ames/Stanford Univ. 83-95.
- MARSDEN, A. L., VASILYEV, O. V. 1999 Commutative filters for LES on unstructured meshes. *Annual Research Briefs*. Center for Turbulence Research, NASA Ames/Stanford Univ. 389-402.
- PEROT, P. 2000 Conservation Properties of Unstructured Staggered Mesh Schemes. *J. Comp. Phys.* **159**, 58-89.
- SWELDENS, W. 1996 The lifting scheme: A custom-design construction of biorthogonal wavelets. *Appl. Comput. Harmon. Anal.* **3**(2), 186-200.
- SWELDENS, W. 1997 The lifting scheme: A construction of second generation wavelets. *SIAM J. Math. Anal.* **29**(2), 511-546.
- VAN DER VEN, H. 1995 A family of large eddy simulation (LES) filters with nonuniform filter widths. *Phys. Fluids*. **7**(5), 1171-1172.
- VASILYEV, O. V., LUND, T. S. & MOIN, P. 1998 A General Class of Commutative Filters for LES in complex Geometries. *J. Comp. Phys.* **146**, 82-104.

Shock-capturing in LES of high-speed flows

By M. P. Martín

1. Motivation and objectives

The bursting events that are present in a turbulent boundary layer bring low-momentum fluid from the near wall region into the boundary layer edge. In high-speed boundary layers, shocks form where the low-momentum fluid meets the incoming free-stream. Thus, to perform accurate large-eddy simulations (LES) of these flows, shock-capturing techniques are necessary.

There are two types of shock-capturing techniques: total variation diminishing (TVD) and essentially nonoscillatory (ENO) schemes. TVD shock-capturing techniques reduce to first-order accuracy near shocks and damp the small-scale flow features. Thus, this type of technique is not desired for turbulent flows. ENO schemes are designed to maintain high-accuracy but not high-bandwidth, which is necessary for performing accurate numerical simulations of turbulent flows. Also, ENO schemes are inherently dissipative due to the upwinded, optimal difference stencils and the smoothness measurement. Recently, Weirs and Candler (1997) designed an optimized ENO scheme for simulating compressible turbulent flows based on the weighted essentially nonoscillatory (WENO) scheme of Jiang and Shu (1996). Weirs and Candler used bandwidth optimization techniques and developed symmetric optimal stencils with reduced dissipation and greater resolving efficiency than those provided by typical ENO schemes. Martín and Candler (2000) show that this WENO scheme gives good results for the direct numerical simulation (DNS) of supersonic turbulent boundary layers.

In the present work, the presence of shock waves in high-speed boundary layers is illustrated and the results from the LES of a supersonic boundary layer using the WENO scheme are assessed.

2. Flow conditions

In the present work we use the perfect gas boundary layer database from the DNS of Martín and Candler (2000) and the LES of Martín *et al.* (2000a). The boundary layer edge conditions are $Re_\theta = 7000$, $M_\infty = 4$, $T_\infty = 5000$ K, and $\rho_\infty = 0.5$ kg/m³. These conditions represent the boundary layer on a 26 degree wedge at Mach number of 20 and 20 km altitude and are illustrated in Fig. 1.

The numerical method combines a WENO scheme for the inviscid fluxes with an implicit time advancement technique. The third-order accurate, high-bandwidth, WENO scheme was designed for low dissipation (Weirs and Candler, 1997) and provides shock-capturing. The time advancement technique is based on the Data-Parallel Lower-Upper (DPLU) relaxation method of Candler *et al.* (1994), which was extended to second-order accuracy by Olejniczak & Candler (1997). The derivatives required for the viscous terms are evaluated using 4th-order central differences. The subgrid-scale terms appearing in the conservative form of the momentum and total energy equations are described in Martín *et al.* (2000b).

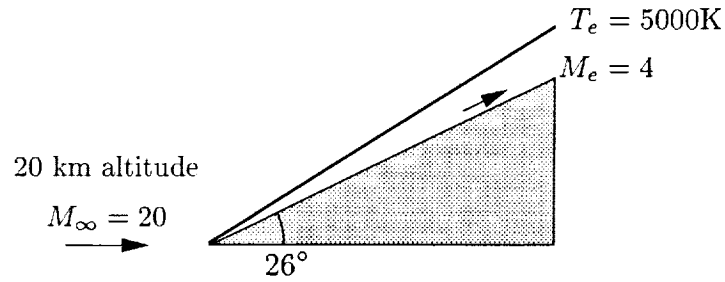


FIGURE 1. Flow conditions.

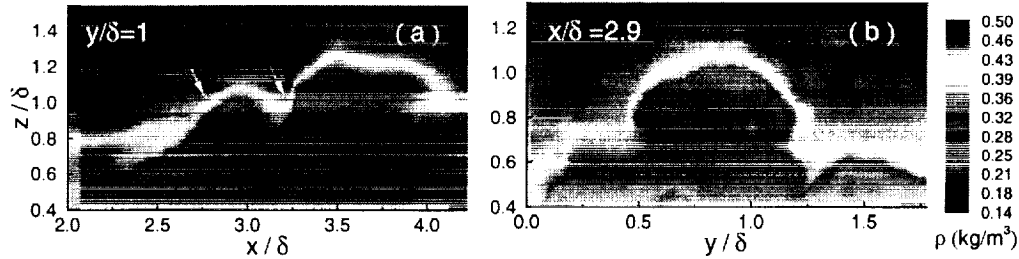


FIGURE 2. Density contours in (a) streamwise-wall-normal plane and (b) spanwise-wall-normal plane.

3. Results

3.1. High-speed boundary layer flow physics from DNS

In this section, the presence of shock waves in high-speed boundary layers is illustrated. Figure 2 shows density contours in streamwise-wall-normal and spanwise-wall-normal planes, respectively. The large-scale bursting events cause strong density gradients near the boundary layer edge. Figure 2b illustrates the three-dimensional character of the strong compression regions. To determine the presence of shock waves, the entropy and pressure changes along a streamline that cross the strong density gradients are considered. The non-isentropic flow condition and a pressure jump are necessary conditions for a shock to occur. Thus, the isentropic and constant pressure relations given by

$$\frac{\rho'}{\langle \rho \rangle_v} = (\gamma - 1) \frac{T'}{\langle T \rangle_v}, \quad (3.1)$$

$$\frac{\rho'}{\langle \rho \rangle_v} = - \frac{T'}{\langle T \rangle_v}, \quad (3.2)$$

must not be met across the shock, where $\langle \rho \rangle_v$ and $\langle T \rangle_v$ are the average density and temperature in the volume that encloses the streamline. Figure 3 shows a scatter plot of the normalized density and temperature fluctuations along the streamline crossing the strong gradients shown in Fig. 2a. The solid line represents the isentropic flow relation. The dashed line represents the constant pressure condition. A turbulence field is non-conservative, thus we do not expect that the data will line up along the solid line. As it can be seen in Fig. 3, the flow is not isentropic. For the most part, the fluid particle follows a constant pressure path. However, the red symbols show that somewhere along the streamline the flow undergoes a pressure change. Jumps in the density, temperature,

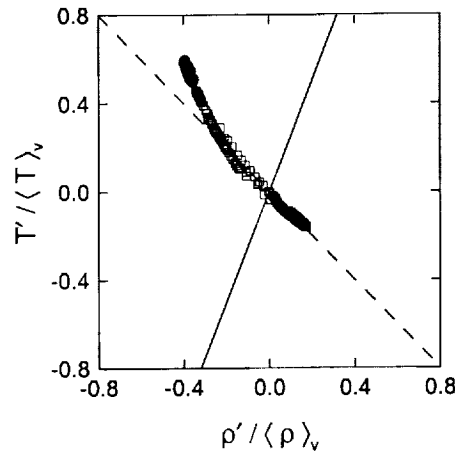


FIGURE 3. Scatter plot of the normalized temperature and density fluctuations along the flow-particle path across the density gradients shown in Fig. 2. Symbols, DNS data; —, isentropic relation; ---, constant pressure relation.

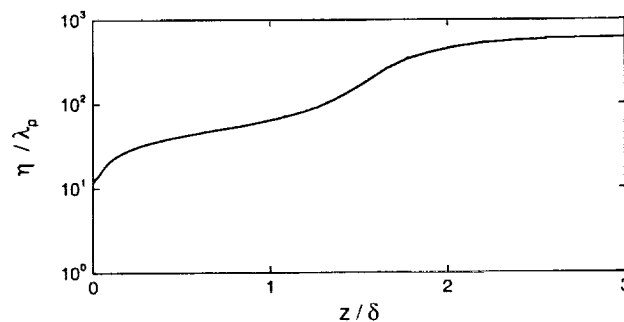


FIGURE 4. Ratio of the Kolmogorov scale to the molecular mean free path.

and dilatation are also associated with the red symbols. The pressure increases by 2 and 5% across the two weak shocks that are shown in Fig. 2. Also the entropy changes by 6% and the Mach number is reduced by a factor of 1.3 along the streamline. These shocks have also been observed experimentally in a Mach 6 boundary layer (Huntley, 2000).

The thickness of a shock is of the order of magnitude of the molecular mean free path λ_p . Figure 4 shows the ratio of the Kolmogorov scale η to λ_p . For the conditions chosen, λ_p is one to two orders of magnitude smaller than η . Today, the type of resolution required to resolve such a small length scale is not practical.

Figure 5 shows the instantaneous density contours in a streamwise-wall-normal plane given using a shock-capturing technique (Weirs & Candler, 1997) (a) and using a hybrid scheme (Olejniczak *et al.*, 1996) combining finite-difference and upwinding techniques (b). For the solution given by the hybrid scheme, the lack of shock-capturing capabilities generates noise near the boundary layer edge. As the simulation progresses in time, the numerical noise penetrates the boundary layer and the solution is no longer physical. Thus, a shock capturing technique is necessary for performing DNS and LES of hypersonic and supersonic boundary layers.

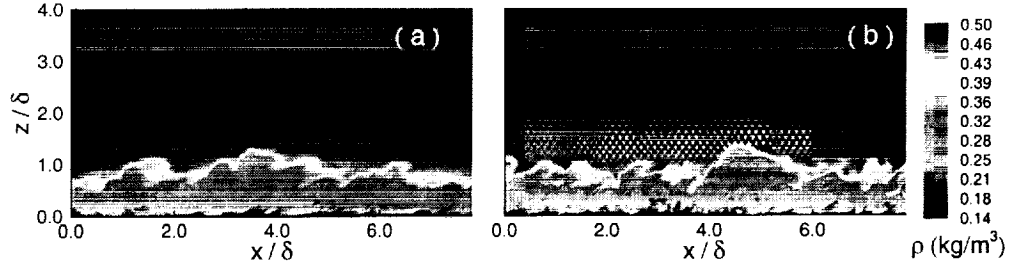


FIGURE 5. Density contours along a streamwise-wall-normal plane using an (a) shock-capturing technique and (b) no shock-capturing technique.

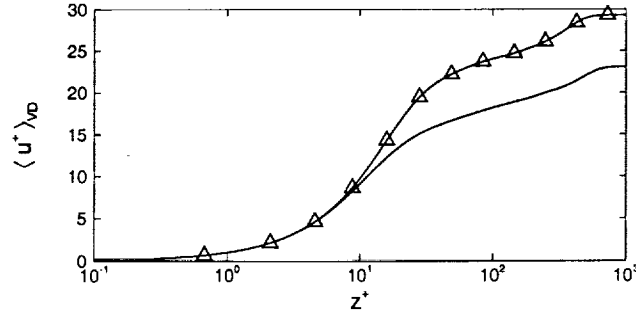


FIGURE 6. Van-Driest transformed velocity profile scaled on inner variables. —, DNS; — Δ —, LES using WENO.

3.2. Shock capturing and LES

The weighted ENO scheme (Weirs & Candler, 1997) was designed for low dissipation. In smooth regions, the convective fluxes are represented using a symmetric, six-point stencil which provides third-order accuracy, high bandwidth, and low dissipation. In calculating the flux, a smoothness measurement allows the stencil to adapt in regions where the data is not smooth. The adaption mechanism selects a more dissipative, upwinded stencil to approximate steep gradients without introducing spurious oscillations.

Figure 6 shows the performance of the WENO scheme when it is used for DNS and LES. Whereas the DNS result is acceptable, the LES result is not good. The adaption mechanism does not distinguish shock waves from turbulence fluctuations on coarse grids. Thus, the WENO scheme provides too much dissipation when used in a LES.

If we could better predict the shock location on coarse grids, we could use no adaption in smooth regions and full adaption near shocks. In the following, the compressibility ratio is used to predict the shock location. Shock waves are a result of a compression. Thus, the increased dissipation across a shock wave must be associated with the compressible dissipation only. An index of the compressibility is given by

$$\chi = \frac{\langle |\nabla \cdot \mathbf{u}'|^2 \rangle}{\langle |\nabla \times \mathbf{u}'|^2 \rangle} \quad (3.3)$$

Thus, a jump in the compressibility ratio represents a jump in the dilatation and, therefore, the location of a shock. Figure 7 shows that near the boundary layer edge the compressibility ratio increases suddenly near $z/\delta = 1.25$.

Using the compressibility ratio to find the shock location and control the adaption

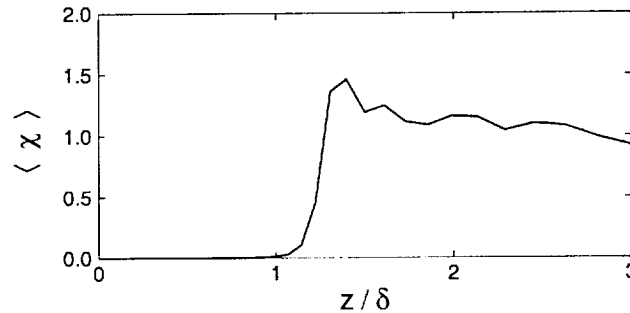
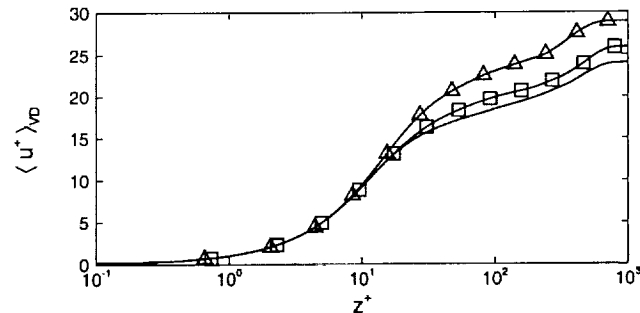


FIGURE 7. Relative compressible to incompressible energy ratio.

FIGURE 8. Van-Driest transformed velocity profile scaled on inner variables. —, DNS; \triangle , WENO (25% error); \square , LWENO (7% error).

mechanism decreases the dissipation significantly and gives more accurate predictions. Figure 8 plots the Van-Driest velocity versus the distance from the wall for the DNS, the WENO and the WENO using local shock-capturing, LWENO. The more sophisticated shock prediction mechanism decreases the error in the solution from 25% to 7%.

3.3. Conclusions and future work

The presence of shock waves in supersonic boundary layers has been illustrated. Since the required resolution to resolve shock waves is impractical, shock-capturing techniques are necessary for the DNS and LES of supersonic or hypersonic turbulent boundary layers. It is found that the information provided by the smoothness measurement is not enough to determine the shock location on coarse, LES grids. A new shock-location prediction is obtained using the compressibility ratio. The local WENO shock-capturing mechanism based on the compressibility ratio gives good predictions when performing LES of supersonic boundary layers. Ongoing work includes the application of this new shock-capturing technique to the LES of hypersonic flow configurations.

REFERENCES

- CANDLER, G. V., WRIGHT, W. J. & McDONALD, J. D. 1994 *Data-Parallel Lower-Upper Relaxation method for reacting flows*. *AIAA J.* **32**, 2380-2386.
- HUNTLEY, M. B. 2000 *Transition on elliptic cones at Mach 8*, PhD thesis, Princeton University.

- JIANG, G.-S. & SHU, C.-W. 1996 Efficient implementation of weighted ENO schemes. *J. Comp. Phys.* **126**, 202-228.
- MARTÍN, M. P. & CANDLER, G. V. 2000 DNS of a Mach 4 Boundary Layer with Chemical Reactions. *AIAA Paper No. 00-0399*. Also *AIAA Paper No. 98-2817*.
- MARTÍN, M. P., WEIRS, V. W., CANDLER, G. V., PIOMELLI, U., JOHNSON, H., & NOMPELIS, I. 2000a Toward the large-eddy simulation over a hypersonic elliptical cross-section cone. *AIAA Paper No. 00-2311*.
- MARTÍN, M. P., CANDLER, G. V., PIOMELLI, U. 2000b Subgrid-scale models for compressible large-eddy simulations. *Theor. and Comp. Fluid Dyn.* **13**, 361-376.
- OLEJNICZAK, D. J., WEIRS, V. G., LIU, J., & CANDLER, G. V. 1996 Hybrid finite-difference methods for DNS of compressible turbulent boundary layers. *AIAA Paper No. 96-2086*.
- WEIRS, V. G. & CANDLER, G. V. 1997 Optimization of weighted ENO schemes for DNS of compressible turbulence. *AIAA Paper No. 97-1940*.

A new method for accurate treatment of flow equations in cylindrical coordinates using series expansions

By G. S. Constantinescu AND S. K. Lele

1. Motivation and objectives

The motivation of this work is the ongoing effort at CTR to use large eddy simulation (LES) techniques to calculate the noise radiated by jet engines. The focus on engine exhaust noise reduction is motivated by the fact that a significant reduction has been achieved over the last decade on the other main sources of acoustic emissions of jet engines, such as the fan and turbomachinery noise, which gives increased priority to jet noise. To be able to propose methods to reduce the jet noise based on results of numerical simulations, one first has to be able to accurately predict the spatio-temporal distribution of the noise sources in the jet. Though a great deal of understanding of the fundamental turbulence mechanisms in high-speed jets was obtained from direct numerical simulations (DNS) at low Reynolds numbers (Freund *et al.*, 1997), LES seems to be the only realistic available tool to obtain the necessary near-field information that is required to estimate the acoustic radiation of the turbulent compressible engine exhaust jets. The quality of jet-noise predictions is determined by the accuracy of the numerical method that has to capture the wide range of pressure fluctuations associated with the turbulence in the jet and with the resulting radiated noise, and by the boundary condition treatment and the quality of the mesh. Higher Reynolds numbers and coarser grids put in turn a higher burden on the robustness and accuracy of the numerical method used in this kind of jet LES simulations.

As these calculations are often done in cylindrical coordinates, one of the most important requirements for the numerical method is to provide a flow solution that is not contaminated by numerical artifacts. The coordinate singularity is known to be a source of such artifacts (Freund *et al.*, 1997, Mohseni and Colonius, 2000). In the present work we use 6th order Pade schemes in the non-periodic directions to discretize the full compressible flow equations. It turns out that the quality of jet-noise predictions using these schemes is especially sensitive to the type of equation treatment at the singularity axis.

The objective of this work is to develop a generally applicable numerical method for treating the singularities present at the polar axis, which is particularly suitable for highly accurate finite-differences schemes (e.g., Pade schemes) on non-staggered grids. The main idea is to reinterpret the regularity conditions developed in the context of pseudo-spectral methods. A set of exact equations at the singularity axis is derived using the appropriate series expansions for the variables in the original set of equations. The present treatment of the equations preserves the same level of accuracy as for the interior scheme. We also want to point out the wider utility of the method, proposed here in the context of compressible flow equations, as its extension for incompressible flows or for any other set of equations that are solved on a non-staggered mesh in cylindrical coordinates with

finite-differences schemes of various level of accuracy is straightforward. The robustness and accuracy of the proposed technique is assessed by comparing results from simulations of laminar forced-jets and turbulent compressible jets using LES with similar calculations in which the equations are solved in Cartesian coordinates at the polar axis, or in which the singularity is removed by employing a staggered mesh in the radial direction without a mesh point at $r = 0$.

2. Accomplishments

2.1. Background

The singularities at the centerline of a cylindrical coordinate system are due to the presence of terms containing the factor $1/r$, where r is the radial distance, in the equations governing the flow. The flow field itself does not have any singularity at the polar axis, but as the computational domain is defined as $(0, 2\pi) \times (0, R)$, one has to specify numerical boundary conditions at $r = 0$ even if physically there is no boundary at the polar axis.

Several numerical methods have been proposed to address the singularity of the flow equations in cylindrical or spherical coordinates. At first sight they seem to vary greatly depending on whether a pseudo-spectral, finite-volume or finite-differences framework is adopted, but in fact there are many similarities among them. This is especially true for the new finite-difference method on non-staggered grids proposed here and the treatment used with pseudo-spectral methods. There are also common elements with methods that use l'Hopital's rule (Griffin *et al.*, 1979) or use a 'shifted' distribution of points in the radial direction (Mohseni and Colonius, 2000) to eliminate the points on the polar axis.

The main idea behind using spectral methods in cylindrical coordinates is to seek an approximation using polynomial expansions in the radial direction that satisfy some regularity conditions which insure a well-behaved solution near the polar axis. There seems to be great latitude in choosing the basis functions for the radial expansions. For example, Patera and Orszag (1981) employed Chebyshev polynomials, Zhang *et al.* (1994) used Jacobi polynomials as the expansion basis in the radial direction close to the polar axis and Legendre-Lagrangian interpolants away from the axis, while Loulou (1996) used B-splines polynomials expansions. The regularity conditions in spectral methods are formulated in terms of having a certain behavior in r near the origin in the polynomial expansions of the Fourier modes and are imposed as constraints on the coefficients of the polynomials expansions. The conditions are essentially the same ones we are going to use in our method, but in the present work everything is formulated in the physical (r, θ, z) space as opposed to wavenumber space (r, k_θ, k_z) . In the spectral methods the essential information is the order of the leading term in the polynomial expansions in r for each mode of the Fourier expansion in θ . No explicit equations at the polar axis are derived, and there is no need to calculate the values of the coefficients in these expansions.

Finite-volume and finite-differences methods are less accurate than spectral methods, but they can handle complex geometrical configurations more easily. Finite-volume methods for flows in cylindrical geometries were employed by Eggels *et al.* (1994), Akselvoll and Moin (1996), and Boersma *et al.* (1998) among others. The main difficulty here is related to the fact that the azimuthal and streamwise fluxes are not defined at the centerline. Due to the definition of velocity components at the center of the volume cells, the singularity for the azimuthal and streamwise fluxes is removed. However, if the control volume closest to the centerline is not wedge shaped, the flux at the first control-volume surface off the polar axis whose normal is oriented in the radial direction must be eval-

uated. Verzicco and Orlandi (1996) developed a second-order finite-differences scheme in cylindrical coordinates for staggered grids. The main feature of their method was the introduction of a radial flux (ru_r) on a staggered grid. As for finite-volume methods, this is the only flux to be calculated right at $r = 0$, and its value there is obviously equal to zero. These methods seem to be very appealing in the context of second-order schemes, but extension to higher-order schemes is not straightforward.

Griffin *et al.* (1979) used finite differences and L'Hopital's rule to recast the governing equations at the origin. For all the singular terms they calculated the radial derivatives using one-sided second-order-accurate finite differences, while the azimuthal derivatives for the variables that are multi-valued at the origin were formally evaluated using the values at neighboring azimuthal locations and $\Delta\theta = 2\pi/N_\theta$, where N_θ is the number of cells in the azimuthal direction. This resulted in a set of new equations at the origin that do not contain any singularities. Formally this treatment is not very rigorous as all these values are physically located at the same point, but the second-order method seemed to produce smooth solutions near the polar axis at least in the framework of the inviscid calculation of an I.C. engine that they considered. However, its use for DNS or LES simulations using higher-order schemes is doubtful, and in the next section we will discuss in a more rigorous way using series expansions the errors introduced by the use of L'Hopital's rule to remove the singularities at the polar axis.

Finally, Freund (1999) and Boersma and Lele (1999) used compact finite differences on non-staggered meshes in cylindrical coordinates to compute the radiated jet noise of compressible jets. They solved the equations at the polar axis using a Cartesian coordinate system. The directions of the Cartesian system were arbitrarily chosen, and the multi-valued variables (u_r, u_θ) for the other directions were obtained by rotation of the system at $r = 0$ where only modes $m = 1$ and $m = -1$ may exist. As the present numerical scheme is very similar to the ones used in these studies, more details can be found in the validation section. Another option to remove the singularities at the polar axis is to eliminate the points at $r = 0$ by distributing the points in the radial direction starting with $\Delta r/2$ (for a uniform grid spacing in r) and mapping the domain $(0, 2\pi) \times (0, R)$ into $(0, \pi) \times (-R, R)$ when radial derivatives must be computed. In this scheme no numerical boundary conditions need to be specified at the polar axis. The radial derivative stencils will span the centerline without evaluation at $r = 0$. This is essentially the method of Mohseni and Colonius (2000). We will use their idea but recast it for the case in which we have points at the polar axis. As we will derive a set of exact equations which are well defined on the polar axis, we will not have to avoid the presence of such points at the centerline.

2.2. Numerical method

Let's suppose that the system of governing equations may be written as:

$$\frac{\partial Q}{\partial t} = RHS(Q) \quad (2.1)$$

where, for instance, in the case of compressible flows $Q = (\rho u_x, \rho u_r, \rho u_\theta, \rho, e)$, and the right-hand side term (RHS) contains the usual operators in cylindrical coordinates associated with the continuity or the transport equations of momentum and energy, including the terms associated with the sub-grid scale contributions in the case of LES simulations.

The numerical method we developed here is general enough so that the particular form of the operators in the RHS is not really important. A detailed description of the present method is given in Constantinescu and Lele, 2000. Here, we are just going to highlight its

main points. The only important difference between the equations in (2.1) is determined by whether the variable in the left-hand side of (2.1) is single valued or multi-valued at the polar axis. Following Boyd (1989), the most general series expansion of a single valued quantity (S) at the polar axis can be written as:

$$S(r, \theta) = \sum_{m=0}^{\infty} r^m \left(\sum_{n=0}^{\infty} \alpha_{mn} r^{2n} \right) \cos(m\theta) + \sum_{m=0}^{\infty} r^m \left(\sum_{n=0}^{\infty} \beta_{mn} r^{2n} \right) \sin(m\theta) \quad (2.2)$$

while the expressions for multi-valued quantities (e.g., u_r and u_θ) assume the following form:

$$M(r, \theta) = \sum_{n=1}^{\infty} A_{0n} r^{2n-1} + \sum_{m=1}^{\infty} r^{m-1} \left(\sum_{n=0}^{\infty} A_{mn} r^{2n} \right) \cos(m\theta) + \sum_{m=1}^{\infty} r^{m-1} \left(\sum_{n=0}^{\infty} B_{mn} r^{2n} \right) \sin(m\theta) \quad (2.3)$$

The form of the series expansions for multi-valued quantities (e.g., for u_r) can be deduced by observing that u_r can be written in terms of the Cartesian velocity components u_y and u_z as:

$$u_r = u_y \cos(\theta) + u_z \sin(\theta) \quad (2.4)$$

where the form of u_y and u_z 's expansions is given by (2.2). By regrouping the terms and using algebraic identities of the form $2 \cos(\theta) \cos(m\theta) = \cos((m-1)\theta) + \cos((m+1)\theta)$, one can easily recover (2.3). As we previously mentioned any scalar or Cartesian velocity component is uniquely defined at the origin, so one can write:

$$\left. \frac{\partial S}{\partial \theta} \right|_{r=0} = 0 \quad (2.5)$$

This relation holds in particular for $u_z = u_\theta \cos(\theta) + u_r \sin(\theta)$, so by taking the derivatives with respect to θ and requiring that the relation holds for any θ , one obtains:

$$\frac{\partial u_r}{\partial \theta} = u_\theta \quad \text{and} \quad \frac{\partial u_\theta}{\partial \theta} = -u_r \quad \text{at } r = 0 \quad (2.6)$$

There is another important constraint on the general form of the series expansions for u_r and u_θ . If $A_{ij}^{(r)}$, $B_{ij}^{(r)}$, $A_{ij}^{(\theta)}$, and $B_{ij}^{(\theta)}$ are the coefficients of the series expansions for u_r and u_θ in (2.3), the following relation holds for all $i \geq 1$:

$$A_{i0}^{(\theta)} = B_{i0}^{(r)} \quad \text{and} \quad B_{i0}^{(\theta)} = -A_{i0}^{(r)} \quad (2.7)$$

This relation can be obtained by using the corresponding series expansions given by (2.2) for u_y and by (2.3) for u_r and u_θ , respectively. These series expansions are plugged into:

$$u_y = u_r \cos(\theta) - u_\theta \sin(\theta) \quad (2.8)$$

and using algebraic identities similar to the ones used to deduce the general form of the series expansions for multi-valued variables at the polar axis (2.3), one can see that the polynomial multiplying $\cos(2\theta)$ in the RHS of (2.8) has the form:

$$\frac{1}{2} \left(B_{10}^{(\theta)} + A_{10}^{(r)} + r^2(\dots) + \dots \right) \quad (2.9)$$

As this polynomial should have a double zero at the origin, one should require $B_{10}^{(\theta)} =$

$-A_{10}^{(r)}$. The other relations in (2.7) follow similarly from analysis of the form of polynomials multiplying the other modes in the RHS of (2.8).

By calculating the derivatives with respect to θ and r of the series expansions given by (2.2) and (2.3) for all operators present in the RHS of (2.1) and taking the limit $r \rightarrow 0$, a new form of the governing equations that is valid at $r = 0$ is obtained. These are a set of exact equations at the polar axis, provided that we can calculate exactly the coefficients of terms present in the RHS of (2.1). For a system of PDE's with second-order radial derivatives, it is sufficient to calculate at most the coefficients (A_{mn} , etc.) whose indices m and n vary between 0 and 2, as we show next. The final expressions in the RHS of (2.1) are dependent on the particular set of equations that is solved (inviscid, laminar, turbulent, compressible, incompressible, etc.). For a complete description of the form of the RHS expressions corresponding to the fully compressible equations, including the treatment of the LES terms, the reader is referred to Constantinescu and Lele, 2000. However, in the following discussion we will focus our attention on pointing out some general features, regardless of the particular system of equations that is solved.

At this point it is relevant to look at the expressions for the series expansions of a single-valued variable at the origin, let's say u_x (coefficients are labeled $\alpha_{mn}^{(x)}$ and $\beta_{mn}^{(x)}$), and for a multi-valued one, u_r , as well as their first and second order radial derivatives:

$$u_x = \alpha_{00}^{(x)} \quad (2.10)$$

$$\frac{\partial u_x}{\partial r} = \alpha_{10}^{(x)} \cos(\theta) + \beta_{10}^{(x)} \sin(\theta) \quad (2.11)$$

$$\frac{\partial^2 u_x}{\partial r^2} = 2\alpha_{01}^{(x)} + 2\alpha_{20}^{(x)} \cos(2\theta) + 2\beta_{20}^{(x)} \sin(2\theta) \quad (2.12)$$

$$u_r = A_{10}^{(r)} \cos(\theta) + B_{10}^{(r)} \sin(\theta) \quad (2.13)$$

$$\frac{\partial u_r}{\partial r} = A_{01}^{(r)} + A_{20}^{(r)} \cos(2\theta) + B_{20}^{(r)} \sin(2\theta) \quad (2.14)$$

$$\frac{\partial^2 u_r}{\partial r^2} = 2A_{11}^{(r)} \cos(\theta) + 2B_{11}^{(r)} \sin(\theta) + 2A_{30}^{(r)} \cos(3\theta) + 2B_{30}^{(r)} \sin(3\theta) \quad (2.15)$$

As expected, the series expansions of scalar quantities (e.g., u_x) contain only the $m=0$ mode, while those of u_r and u_θ contain only the $m=1$ ($\cos(\theta)$) and $m=-1$ ($\sin(\theta)$) modes. Meanwhile, the first derivative of a scalar quantity is multivalued as it contains the $m=1$ and -1 modes, while the second derivative contains the $m=0, 2$ and -2 modes. In particular, this applies to the pressure, p , which is a single-valued scalar, but $\partial p / \partial r$ is multi-valued at $r = 0$. If we go back to equation (2.1) for the u_x variable and take the limit as $r \rightarrow 0$, we obtain:

$$\frac{\partial u_x}{\partial t} = \frac{\partial \alpha_{00}^{(x)}}{\partial t} = RHS_{u_x} \quad (2.16)$$

where RHS_{u_x} contains terms corresponding to the convective and viscous operators that would obviously involve modes $m=0, 1, -1, 2, -2, 3$, and -3 . For (2.16) to be valid, the coefficients resulting from the series expansions of the different variables and their derivatives should be such that the coefficients multiplying all but the $m=0$ mode in RHS_{u_x} must be equal to zero. Indeed, this is what happens when we sum the contributions coming from all the terms contained in RHS_{u_x} and use (2.7). However, individual terms may contain non-zero coefficients multiplying the $m \neq 0$ modes. In fact, it can be proven that this property holds not only for the RHS of the equations describing the transport of a

single-valued variable at the polar axis as a whole, but also for independent operators such as convective, viscous, dilatation, viscous dissipation in the energy equation, etc. For instance, the dilatation operator, which is a scalar quantity and thus should contain only the $m=0$ mode, can be expressed as:

$$\frac{\partial u_x}{\partial x} + \frac{\partial u_r}{\partial r} + \frac{1}{r} \left(u_r + \frac{\partial u_\theta}{\partial \theta} \right) = \frac{\partial \alpha_{00}^{(x)}}{\partial x} + 2A_{01}^{(r)} \quad (2.17)$$

where the streamwise derivative can be calculated with exactly the same method used (6^{th} order compact differences in the present work) for points situated away from the polar axis. Another example is the Laplacian operator (e.g., the viscous term in the u_x -momentum equation):

$$\frac{\partial^2 u_x}{\partial x^2} + \frac{\partial^2 u_x}{\partial r^2} + \frac{1}{r} \frac{\partial u_x}{\partial r} + \frac{1}{r^2} \frac{\partial^2 u_x}{\partial \theta^2} = \frac{\partial^2 \alpha_{00}^{(x)}}{\partial x^2} + 4\alpha_{01}^{(x)} \quad (2.18)$$

For the u_r and u_θ -momentum equations, the RHS will contain only the $m=-1$ and $m=1$ modes once contributions from all the terms are added. These two equations are identical in the limit $r \rightarrow 0$, thus it is sufficient to calculate the limit for only one of the equations, e.g.:

$$\frac{\partial u_r}{\partial t} = \frac{\partial (A_{10}^{(r)} \cos(\theta) + B_{10}^{(r)} \sin(\theta))}{\partial t} = RHS^{m=1} \cos(\theta) + RHS^{m=-1} \sin(\theta) \quad (2.19)$$

In fact, we will end up with two scalar equations corresponding to the $m=1$ and -1 modes, respectively, as one can see from the previous relation because as $r \rightarrow 0$, u_r can be obtained from u_θ by a counterclockwise rotation of $\pi/2$. Relation (2.18) can also be used to show an inherent problem with methods in which l'Hopital's rule is applied numerically to remove singularities at the polar axis (e.g., see Griffin *et al.*, 1979). In these methods the Laplacian will be calculated by numerically evaluating the following:

$$\frac{\partial^2 u_x}{\partial x^2} + 2 \frac{\partial^2 u_x}{\partial r^2} + \frac{\partial^2}{\partial r^2} \left(\frac{\partial^2 u_x}{\partial \theta^2} \right) = \frac{\partial^2 \alpha_{00}^{(x)}}{\partial x^2} + 4\alpha_{01}^{(x)} - 4\alpha_{20}^{(x)} \cos(2\theta) - 4\beta_{20}^{(x)} \sin(2\theta) \quad (2.20)$$

which introduces a finite error as the coefficients of modes $m=2$ and -2 are now present.

The last step is to describe how the series coefficients that are needed to evaluate the RHS in (2.1) are computed. We will show that all that is required to calculate these coefficients accurately is to be able to estimate numerically the first and second order radial derivatives of all the variables in the RHS with the same order of accuracy as at points away from the polar axis. In particular, in our compressible flow solver we are using Pade schemes to calculate the radial derivatives. To do this, the following algorithm, similar to the one used by Mohseni and Colonius (2000), is adopted. The computational domain is mapped at every $x = constant$ such as there is no need to specify numerical boundary conditions at $r = 0$. The mapping function $(r, \theta) \rightarrow (\hat{r}, \hat{\theta})$ is:

$$\begin{cases} \hat{r} = r & 0 < \theta < \pi \\ \hat{\theta} = \theta & 0 < r < R \end{cases} \quad \text{and} \quad \begin{cases} \hat{r} = -r & \pi < \theta < 2\pi \\ \hat{\theta} = \theta - \pi & 0 < r < R \end{cases} \quad (2.21)$$

All the signs of scalar quantities, streamwise velocities, and azimuthal derivatives are left unchanged by the mapping, while u_r , u_θ and the radial derivatives change sign for $\pi < \theta < 2\pi$. The radial derivatives are now taken from $-R$ to R with $r = 0$ being a regular interior point instead of a 'numerical' boundary point.

Next, we will expand on the calculation of the required coefficients in the asymptotic

expansions for u_r and its radial derivatives. All other variables are treated in a similar fashion using the appropriate series expansions. Suppose that $N_\theta + 1$ is the number of points in the azimuthal direction (with modes $0, \pm 1, \pm 2, \dots, \pm N_\theta/2$). According to (2.13) only the $m=1$ and -1 modes should be present in a series formed by these N_θ values. We will formally associate the N_θ values with θ going from 0 ($n = 1$) to 2π ($n = N_\theta + 1$). Supposing that N_θ is divisible by 8, meaning that for every element in the series there is another situated exactly $\pi/4$ away, one can take advantage of the properties of $\sin(\theta)$ and $\cos(\theta)$ functions to evaluate the coefficients in (2.13), (2.14), and (2.15). For instance, using (2.13) for θ and $\theta + \pi/2$, a system of two linear equations with two unknowns ($A_{10}^{(r)}$ and $B_{10}^{(r)}$) is obtained:

$$u_r(\theta) = A_{10}^{(r)} \cos(\theta) + B_{10}^{(r)} \sin(\theta) \quad u_r(\theta + \pi/2) = -A_{10}^{(r)} \sin(\theta) + B_{10}^{(r)} \cos(\theta) \quad (2.22)$$

To eliminate the bias toward a certain direction, one can solve the above system for every $\theta = (2\pi/N_\theta)(n - 1)$ with $n=1, N_\theta$, and average the results to get final values for $A_{10}^{(r)}$ and $B_{10}^{(r)}$. Same kind of treatment can be applied to determine $A_{01}^{(r)}$, $A_{20}^{(r)}$, $B_{20}^{(r)}$ by first getting $A_{01}^{(r)}$ and then using (2.14) for θ and $\theta + \pi/4$ to calculate the remaining two coefficients. In a similar way, the coefficients involved in the expressions for the second radial derivatives of u_r and u_θ require solving three systems of two linear equations.

2.3. Validation of proposed numerical algorithm

The general numerical method is described in detail in Freund *et al.* (1997), while Boersma and Lele(1999) give the details of the implementation of the dynamic LES model in the original DNS code. It employs compact six-order Pade schemes for the spatial derivatives in the non-homogeneous directions and Fourier spectral methods in the homogeneous (azimuthal) direction. The number of modes is dropped near the polar axis so that the CFL constraint will be determined by the radial (or axial) spacing. The solution is advanced in time using a four-step Runge-Kutta method. The Reynolds number is $Re = U(2R_0)/\nu = 36,000$ and the Mach number $Ma = U/c_\infty = 0.9$, where R_0 is the initial radius of the jet in the inlet section. In all of the calculations discussed here, the computational grid consists of $192 \times 128 \times 64$ points in the (x, r, θ) directions, which is about an order of magnitude coarser than the grid used by Freund (1999) to calculate a similar jet at $Re = 3,600$ using DNS. The mean flow distribution at the inlet plane is assumed to be a rounded top-hat profile.

In a first test case no randomized forcing is applied and the LES model is turned off. A sinusoidal perturbation at a Strouhal number $St = 0.5$ is applied at the inlet. The forced-jet solution is quasi-axisymmetrical and laminar as seen from the total vorticity contours in Fig. 1a. The effects of the different treatments at the polar axis are investigated in Fig. 2, where snapshots of the dilatation fields in the region $x > 20R_0$ are shown for different treatments at the polar axis. We choose the dilatation because this quantity is very sensitive to the centerline treatment and also provides relevant information for the jet acoustics in the near field. Case L1 corresponds to the method where the equations are solved in Cartesian coordinates, case L2 corresponds to the a grid with no points placed at the polar axis, while case L3 corresponds to the treatment using series expansions at the centerline. In the second test case randomized azimuthal forcing is applied in the input plane to trigger the three-dimensional instabilities for the LES calculation. All other parameters of the simulations as well as the computational mesh are kept the same as those used in the first test case. As seen in Fig. 1b the jet undergoes transition to turbulence at the end of the potential core situated around $x = 15R_0$. Results are shown

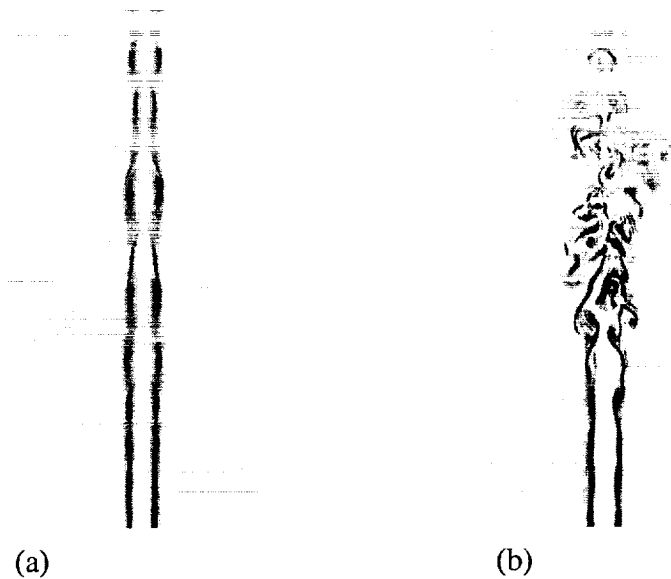


FIGURE 1. Total vorticity contours. Vorticity shown using 18 equally spaced contours between 0 and $2\omega R_0/U$. (a) Laminar forced jet; (b) Turbulent jet.

in Fig. 3 for two simulations; the first (T1) uses the method of Mohseni and Colonius (2000) while the second (T2) used the series expansion treatment.

As we are interested in simulating jets at very high Reynolds numbers (2 to 3 orders of magnitude higher than the ones at which DNS is presently possible), the robustness of the method on coarser meshes is an obvious requirement. Our simulation showed that even for a laminar forced jet (case L1) strong oscillations in the dilatation field developed near the centerline in the form of two-delta waves. They are evident in Fig. 2a in the region near the polar axis starting with the streamwise ($x \sim 15R_0$) location where ring vortices begin to be shed from the jet. These point-to-point oscillations in dilatation are of the order of $1.5R_0/U$, which is more than one order of magnitude higher than the values of $0.1R_0/U$ associated with the maximum dilatation inside the coherent structures of the jet. For case L1 the simulation did not diverge, but obviously the quality of the solution, especially the sound information that can be collected from these fields, is poor. When used to calculate a turbulent jet, we were not able to get a well-behaved solution on the relatively coarse mesh used in these simulations without substantial filtering of the solution to remove the two-delta waves (every couple of time steps), and the quality of the solution was poor. This shows that the robustness of this polar axis treatment deteriorates rapidly on coarse meshes and for high Reynolds numbers when strong non-linear interactions are present in the flow. Several features of this method are suspected to be responsible for the above-mentioned problems. First, the derivatives in the directions corresponding to the Cartesian coordinates are evaluated using six-order explicit central-differences instead of 6th order Pade schemes while in the evaluation of the radial derivatives with compact differences numerical boundary conditions using one-sided differences of lower order have to be formulated. Another source of errors may be associated with the bias introduced

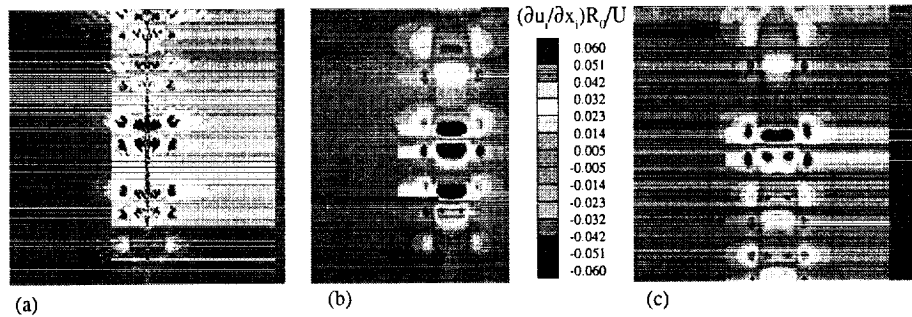


FIGURE 2. Dilatation contours in the laminar forced jet. (a) Cartesian coordinates; (b) Method of Mohseni and Colonius; (c) Series expansions treatment.

in the solution by the arbitrary choice ($N_\theta/2$ possibilities) of the two perpendicular directions after which the flow equations are solved at the centerline. Both of these approximations are automatically removed when a staggered mesh in the radial direction is employed in simulation L2. However, our results using the technique proposed by Mohseni and Colonius showed that in the absence of filtering the solution would diverge after approximately 1000 time steps. That was due to a very local instability situated at the first point off the polar axis at a certain streamwise location. The dilatation field remained fairly smooth at all other streamwise locations close to the polar axis in contrast to the results seen in case L1. However, when a 6th order accurate explicit filter was applied every 300 time steps to smooth the velocity field, the dilatation contours shown in Fig. 2b remained smooth and no unphysical oscillations were observed near the polar axis.

Finally, in case L3 where the new treatment using asymptotic series expansion was used at the polar axis, the dilatation fields are smooth (Fig. 3c) and the flow features are very similar to the results obtained with the method of Mohseni and Colonius, but no filtering was necessary to avoid numerical instabilities near the polar axis.

Based on the results from the first test case, we focus our attention for turbulent calculations on the method proposed by Mohseni and Colonius and the method based on series expansions. Filtering of the solution every 30 time steps, while sufficient in keeping the solution from diverging, does not remove the unphysical spurious oscillations in the dilatation field that are observed very close to the polar axis at all streamwise locations for $x > 15R_0$ (Fig. 3a). In fact, the maximum values of the dilatation in these elongated structures very close to the polar axis are around $1.2R_0/U$, which is significantly higher than the levels of dilatation recorded in the rest of the computational domain. That is true even if the filter is applied more often. One should point out that this amount of filtering was found to have non-negligible effects if sound sources were calculated from these fields. Thus, even though their method gives comparable results with the series-expansions based technique for laminar forced jets, in turbulent simulations the robustness and accuracy of their method seems to be inferior. The turbulent case is much more difficult to handle because the level of non-linear flow interactions is much higher and jet structures are passing through the centerline. Convergence of the solution on relatively coarse meshes can be obtained only by filtering the solution when the method of Mohseni and Colonius is used.

In simulation T2, patches of high dilatation are observed in a region of about $10R_0$

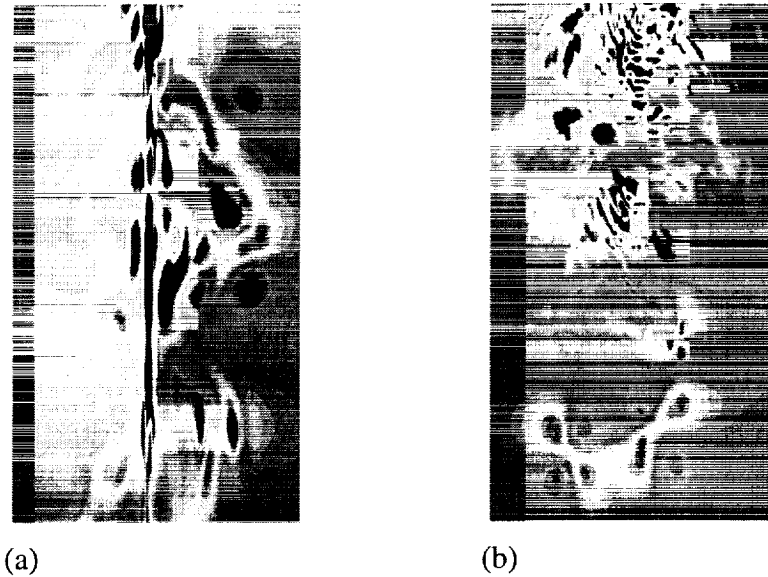


FIGURE 3. Dilatation contours in an area situated after the end of the potential core for the turbulent jet. Dilatation fields are shown with 18 equally spaced contours between $-0.08R_0/U$ and $0.08R_0/U$. (a) Method of Mohseni and Colonius; (b) Series expansions treatment.

in the streamwise direction starting at the end of the inviscid core. The position of these patches is not very close to the polar axis (Fig. 3b, except at times when they are convected by the mean jet motion through the polar axis. The maximum absolute value of the dilatation field in the turbulent region is at all times around $0.2R_0/U$, including at the polar axis. The short waves that are seen at the top of Fig. 3b are, rather, related to the high aspect ratio $\Delta x/\Delta r$ of the present grid and are not a consequence of centerline instabilities. Spurious waves or unrealistically high values of the dilatation (Fig. 3a - case T1) or vorticity at the first 2-3 points off the centerline are not observed. The level of the unphysical spurious dilatation oscillations present in the domain close to the polar axis is greatly reduced compared to the case in which the method of Mohseni and Colonius was used, while filtering was practically eliminated. The 6th order filter was applied every 500 time steps to eliminate the high-frequency waves that form because of the high grid stretching ratio. As we are primarily interested in extracting sound information from the near fields, elimination of filtering that may compromise substantially the quality of the sound data is a key factor in assessing the different methods.

3. Summary and future plans

In this paper a general method for handling the singularities arising at the polar axis of the governing flow equations in cylindrical coordinates based on power series expansions in the radial direction and Fourier series in the azimuthal direction was presented. Using the most general form of these series expansions, a new set of equations at the polar axis was derived by calculating the limit of the various operators appearing in the governing

system of equations (2.1). The new method is computationally easy to implement and is less expensive than solving the equations in Cartesian coordinates at the centerline.

The present algorithm avoids the loss in accuracy at the centerline where most of the finite-volume and finite-differences methods use some kind of one-sided differences to approximate the operators at the centerline. This is because in the context of the present method we were able to calculate the radial derivatives at the origin with the same order of accuracy as in the rest of the domain (6th order compact differences) by using a domain mapping so that the points on the polar axis become regular interior points. As this is the only information needed to calculate the coefficients of the newly derived polar equations, there is no loss in the overall accuracy of the method. The coefficients in the asymptotic expansions are unique, so we do not have to choose any arbitrary directions as is the case when the equations are solved in Cartesian coordinates at origin. One of the advantages is that the first point off the axis, where the various terms with singular behavior have to be evaluated, will be situated at Δr as opposed to $\Delta r/2$ (as is the case in the method of Mohseni and Colonius, 2000). This may avoid an important source of errors or instabilities (e.g., due to the nonlinear interactions of eddies near the polar axis in a DNS or LES simulation).

The robustness of the proposed approach was tested successfully by comparing results for a deterministically forced jet with similar calculations using same numerical method but with the equations solved at the centerline in Cartesian coordinates, or without any points at $r = 0$ using the method proposed by Mohseni and Colonius. Finally, the present technique was shown to give improved results compared to the method of Mohseni and Colonius for the simulation of a compressible jet using LES on relatively coarse meshes, in which the flow interactions taking place near the polar axis are very important and where a flow solution that is not contaminated by numerical artifacts originating at the singularity axis is required to accurately calculate the jet noise sources.

The algorithm presented here to deal with the polar-axis singularities is not restricted to the use of the present numerical method that uses sixth-order Pade schemes to evaluate the derivatives in the radial and streamwise directions, or to solving the compressible flow equations. As spherical coordinates are locally cylindrical coordinates near the two singularity axes, the application of the method in spherical coordinates is straightforward.

Acknowledgments

This work was supported in part by Grant No. NAG2-1373 from the NASA Ames Research Center. The authors gratefully acknowledge valuable discussions with Prof. J. Freund and Prof. B. Boersma.

REFERENCES

- AKSELVOLL K. & MOIN, P. 1996 An efficient method for temporal integration of the Navier-Stokes equations in confined axisymmetric geometries. *J. Comp. Phys.* **125**, 454-462.
- BOERSMA, B. J., BRETHOUWER, G. & NIEUWSTADT, F. T. M. 1998 A numerical investigation on the effect of the flow conditions on the self-similar region of a round jet. *J. Comp. Phys.* **10(4)**, 899-909.
- BOERSMA, B. J. & LELE, S. K. 1999 Large eddy simulation of compressible turbu-

- lent jets. *Annual Research Briefs-1999*, Center for Turbulence Research, NASA Ames/Stanford Univ. 365-377.
- BOYD, J. P. 1989 *Chebyshev and Fourier Spectral methods*. Springer-Verlag. Berlin/Heidelberg, 1989.
- CONSTANTINESCU, G. S. & LELE, S. K. 2000 A highly accurate technique for the treatment of flow equations at the polar axis in cylindrical coordinates using series expansions. Submitted to *J. Comp. Phys.*
- GRIFFIN, M. D., JONES, E. & ANDERSON, J. D. 1979 A computational fluid dynamic technique valid at the centerline for non-axisymmetric problems in cylindrical coordinates. *J. Comp. Phys.* **30**, 352-360.
- EGGELS, J. G. M., UNGER, F., WEISS, M. H., WESTERVEEL, J., ADRIAN, R. J., FRIEDRICH, R. & NIEUWSTADT, F.T.M. 1994 Fully developed turbulent flow: A comparison between direct numerical simulation and experiment. *J. Fluid Mech.* **268**, 175-209.
- FREUND, J. B., MOIN, P. & LELE, S. K. 1997 Compressibility effects in a turbulent annular mixing layer. *Report No. TF-72*, Dept. of Mech. Engr., Stanford University.
- FREUND, J. B. 1999 Acoustic sources in a turbulent jet: A Direct Numerical Simulation study. *AIAA Paper 99-1858*, 5th AIAA/CEAS Aeroacoustics Conference, 10-12 May 1999, Seattle, WA.
- LOULOU, P. 1996 Direct numerical simulation of incompressible flow using a B-spline spectral method. *Ph. D. Thesis*, Department of Aeronautics and Astronautics, Stanford University.
- MOHSENI, K. & COLONIUS, T. 2000 Numerical treatment of polar coordinate singularities. *J. Comp. Phys.* **157**, 787-795.
- PATERA, A. T. & ORSZAG, S. A. 1981 Finite amplitude stability of axisymmetric pipe flow. *J. Fluid Mech.* **128**, 347-361.
- VERZICCO R. & ORLANDI, P. 1996 A finite-difference scheme for three-dimensional incompressible flows in cylindrical coordinates. *J. Comp. Phys.* **123**, 402-414.
- ZHANG, Y., GANDGI, A., TOMBOULIDES, A. G. & ORSZAG, S. A. 1994 Simulation of pipe flow. *AGARD-Volume CP-551*, Symposium on application of direct and large eddy simulation to transition and turbulence, 17.1-17.9.

An evaluation of a conservative fourth order DNS code in turbulent channel flow

By Jessica Gullbrand

1. Motivation and objectives

Direct numerical simulation (DNS) and large eddy simulation (LES) of turbulent flows require a numerical method that is able to capture a wide range of turbulent length scales. In DNS, all the turbulent length and time scales are resolved. In LES, the large energy carrying length scales of turbulence are resolved and the small structures are modeled. The separation of large and small scales is done using a filtering procedure that is applied to the Navier-Stokes equations. The effect of the small scale turbulence on the resolved scales is modeled using a subgrid scale (SGS) model.

Widely used SGS models are the scale similarity models by Bardina *et al.* (1980) and Liu *et al.* (1994) and the eddy viscosity based dynamic Smagorinsky model proposed by Germano *et al.* (1991). In general, scale similarity models do not dissipate enough energy, and eddy viscosity models do not carry enough stress (Baggett *et al.* (1997) and Jiménez (1998)). SGS models tend to over- and underpredict velocity fluctuations (Kravchenko & Moin (1997), Domaradzki & Loh (1999), Sarghini *et al.* (1999)).

SGS models typically use information from the smallest resolved length scales to model the stresses of the unresolved scales. Therefore, it is of great importance that these resolved length scales are captured accurately. This requires that the numerical error of the scheme is sufficiently small. One approach is to use high order finite difference schemes. However, high order schemes require that the differentiation and filtering operations commute. This is generally not the case in inhomogeneous flow fields where the required smallest resolved length scales vary throughout the flow field. For this situation, the filter width varies introducing commutation errors of $O(\Delta^2)$ where Δ represents the filter width (Ghosal & Moin (1995) and Ghosal (1996)).

High order finite difference schemes with good conservation properties and three-dimensional commutative filters have been developed by Morinishi *et al.* (1998), Vasilyev *et al.* (1998) and Vasilyev (2000). These discretization schemes can conserve energy, which ensures a stable simulation free of numerical dissipation. The proposed commutative filters are discrete and can be constructed to commute up to any desired order.

The objective of this work is to investigate the SGS shear stresses predicted by different SGS models and investigate the influence of numerical errors and filtering in three dimensions. This is done using a fourth order finite difference channel flow code. The code was developed by Morinishi *et al.* (1998), Vasilyev *et al.* (1998) and Vasilyev (2000). It conserves kinetic energy and uses commutative filters. Most channel flow simulations have been made using either spectral codes or second order finite differences using filtering in the homogeneous directions only.

To validate the fourth order algorithm, both DNS and LES have been performed of a turbulent channel flow for different Reynolds numbers. Mean velocity profiles, fluctuation velocities and energy spectra are compared to results from a second order finite difference code and to DNS data computed with a spectral code.

2. Numerical method

2.1. Governing equations

The governing equations for incompressible flow are the continuity equation and the Navier-Stokes equations

$$\frac{\partial u_i}{\partial x_i} = 0 \quad (2.1)$$

$$\frac{\partial u_i}{\partial t} + \frac{\partial u_i u_j}{\partial x_j} = -\frac{\partial p}{\partial x_i} + \frac{1}{Re_\tau} \frac{\partial^2 u_i}{\partial x_j^2}. \quad (2.2)$$

Here, u_i is the velocity component in the x_i direction, t denotes time, and p denotes pressure. All terms are normalized with the friction velocity, u_τ , and channel half width, h . $Re_\tau = u_\tau h / \nu$ is defined as the Reynolds number.

In LES, a filter function is applied to the flow variable f

$$\bar{f}(x, \Delta, t) = \int_{-\infty}^{\infty} G(x, x', \Delta) f(x', t) dx' \quad (2.3)$$

where G is a filter function and Δ the filter width. Filtering Eqs. 2.1 and 2.2 in space yields

$$\frac{\partial \bar{u}_i}{\partial x_i} = 0 \quad (2.4)$$

$$\frac{\partial \bar{u}_i}{\partial t} + \frac{\partial \bar{u}_i \bar{u}_j}{\partial x_j} = -\frac{\partial \bar{p}}{\partial x_i} + \frac{1}{Re_\tau} \frac{\partial^2 \bar{u}_i}{\partial x_j^2} - \frac{\partial \tau_{ij}}{\partial x_j}. \quad (2.5)$$

where τ_{ij} is the SGS stress tensor defined as $\tau_{ij} = \bar{u}_i \bar{u}_j - \bar{u}_i \bar{u}_j$. This stress tensor describes the interaction between the large resolved grid scale (GS) and the small unresolved SGS. The SGS stress tensor contains the unknown velocity correlation $\bar{u}_i \bar{u}_j$, which cannot be expressed in the resolved flow quantities. This term has to be modeled.

2.2. Subgrid scale models

The goal of SGS modeling is to account for the SGS stresses using resolved flow field variables. The most important requirement of a SGS model is that it has to be dissipative.

The most widely used SGS models are the scale similarity models by Bardina *et al.* (1980) and Liu *et al.* (1994) and the Smagorinsky model (Smagorinsky (1963)) with the dynamic approach proposed by Germano *et al.* (1991) to calculate the model coefficient. The scale similarity models and the dynamic procedure uses the assumption that similar behavior exists between the resolved and unresolved stresses. When the filter function can be expressed as a polynomial of differentials, there exist an explicit relation between unfiltered and filtered flow variables (Fuchs (1996)). This approach results in an explicit expression of the SGS stress in terms of the resolved flow variables, *i.e.*, an exact differential SGS model.

2.3. Solution algorithm

In the code used, the continuity and Navier-Stokes equations are discretized using a fourth order finite difference scheme on a staggered grid. The convective term is discretized in

a skew-symmetric form

$$\frac{\partial u_i u_j}{\partial x_j} = \frac{1}{2} \frac{\partial u_i u_j}{\partial x_j} + \frac{1}{2} u_j \frac{\partial u_i}{\partial x_j}.$$

This ensures conservation of kinetic energy (Morinishi *et al.* (1998) and Vasilyev (2000)). The no slip boundary condition is applied at the walls and the flow is assumed to be periodic in the streamwise and spanwise directions. A semi-implicit time marching algorithm is used in which the diffusion terms in the wall normal direction are treated implicitly with a Crank-Nicolson scheme. All other terms use a third order Runge-Kutta scheme described by Spalart *et al.* (1991). The splitting method of Dukowicz & Dvinsky (1992) is used to enforce the solenoidal condition. The resulting discrete Poisson's equation of pressure is solved using a penta diagonal direct matrix solver in the wall normal direction and a discrete Fourier transform in the periodic directions. A fixed mean pressure gradient is used in the streamwise direction.

The initial flow field is set to a parabolic profile in the streamwise direction with randomly generated fluctuations. The initial flow field in the wall normal direction and in the spanwise direction consist of these random fluctuations. The initial guess of the flow field is advanced in time to a statistically stationary solution before statistics are sampled.

To obtain a commutative system, a general class of discrete filters applied to nonuniform filter widths was proposed by Vasilyev *et al.* (1998). The procedure applies mapping of the nonuniform grid onto a uniform one in computational space in which the filtering is applied. The filters are constructed by applying a number of constraints to the filter weights to achieve both commutation and an acceptable filter shape. The filter weights are calculated by forcing the zeroth moment to be one and a number of higher moments to be zero. This determines the order of the commutation error. Other constraints are added to adjust the filter shape.

3. Turbulent channel flow simulations

In order to validate the fourth order finite difference (FD) scheme, numerical simulations of turbulent channel flow were performed using both DNS and LES. The same simulations were made with a second order FD code by Morinishi (1995) to compare the influence of the numerical scheme on the results. The FD results are compared to DNS data obtained using a spectral code (Kim *et al.* (1987) and Moser *et al.* (1999)).

The DNS and LES were carried out for Reynolds numbers $Re_\tau=180$ and $Re_\tau=395$, respectively. In both computations, the grid is stretched in the direction normal to the wall according to the following hyperbolic-tangent function,

$$x_j = -\frac{\tanh(\gamma(1 - \frac{2j}{N_2}))}{\tanh(\gamma)} \quad j = 0, \dots, N_2 \quad (3.1)$$

Here, N_2 is the number of grid points in the j direction and γ is the stretching parameter.

3.1. DNS results

DNS was performed for $Re_\tau=180$. The grid resolution is 128^3 and the computational domain is $(4\pi h, 2h, 4/3\pi h)$, which is the same as in the spectral simulations. The stretching parameter is $\gamma = 2.8$.

The mean velocity profile normalized with the friction velocity as a function of the

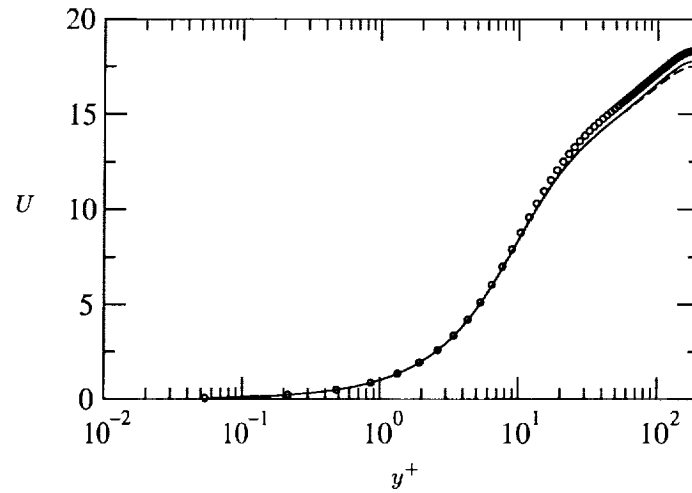


FIGURE 1. Mean velocity profile U as a function of the distance to the wall y^+ . $Re_\tau=180$. DNS \circ : spectral code, — : 4th order FD code and - - - : 2nd order FD code.

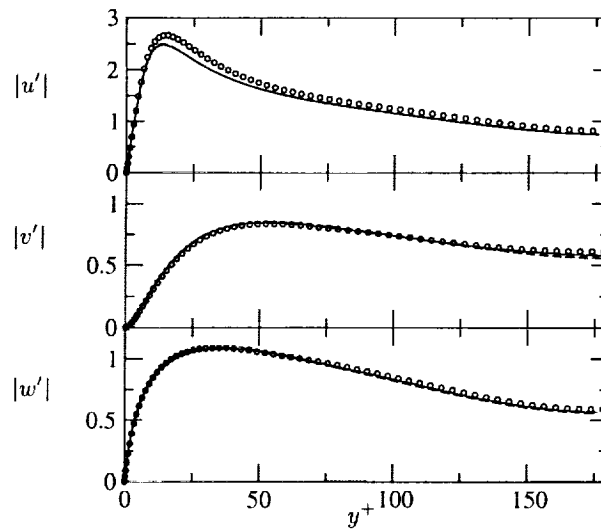


FIGURE 2. Velocity fluctuations in streamwise $|u'|$, wall normal $|v'|$ and spanwise $|w'|$ direction as a function of the distance to the wall y^+ . $Re_\tau=180$. DNS \circ : spectral code, — : 4th order FD code and - - - : 2nd order FD code.

dimensionless distance to the wall is shown in Fig. 1. The comparison with the spectral code shows an underprediction of the mean velocity profiles by the FD codes.

Velocity fluctuations are plotted in Fig. 2. Again, the difference between the second and fourth order codes is negligible. Note that the streamwise velocity fluctuation is underpredicted by the FD codes, which is to be expected due to the drop in the modified wavenumber (Kravchenko & Moin (1997)).

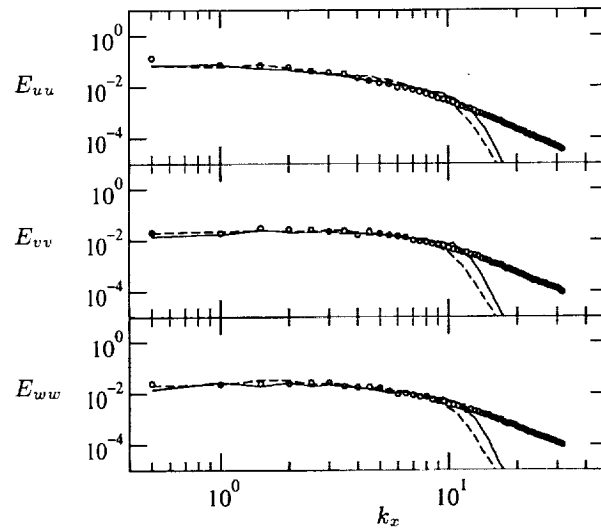


FIGURE 3. Energy spectrum of the streamwise E_{uu} , wall normal E_{vv} and spanwise E_{ww} velocity correlation as a function of the streamwise wavenumber k_x . $Re_\tau=180$ at $y^+ \approx 180$. DNS \circ : spectral code, — : 4th order FD code and - - - : 2nd order FD code.

The energy spectra as a function of the wavenumber in the streamwise direction are shown in Fig. 3. The second order code deviates from the energy spectra from the spectral code for smaller wavenumbers than compared with the fourth order code. Both FD results show a steep slope of the energy spectra in the high wavenumber part of the spectra.

3.2. LES results

LES was performed for $Re_\tau=395$ using the dynamic Smagorinsky model proposed by Germano *et al.* (1991) to model the SGS stresses. To calculate the model coefficient dynamically in the Smagorinsky model, the least square approximation by Lilly (1992) and averaging in the homogeneous directions as in Germano *et al.* (1991) are used. The grid resolution is (64,49,48), which is a quarter of the grid points in each direction compared to the DNS grid. The domain is $(2\pi h, 2h, \pi h)$. The mesh is stretched normal to the wall with $\gamma = 2.75$.

The mean velocity profiles are shown in Fig. 4. The fourth order code predicts the mean velocity profile closer to the DNS data. The second order code predicts a larger mass flow.

Velocity fluctuations are plotted in Fig. 5. The streamwise components are overpredicted using LES, while the wall normal and spanwise fluctuations are underpredicted when compared to the DNS results. Note that the overprediction of the streamwise velocity fluctuation is larger with the second order FD code than with the fourth order code. Kravchenko & Moin (1997) reported that this is due to the truncation error of the second order scheme.

The energy spectra in the streamwise direction are shown in Fig. 6. As for $Re_\tau=180$, the second order code deviates for smaller wavenumbers from the spectral results compared to the fourth order code. The slopes of the energy spectra in the high wavenumber part of the spectra are steep for the FD codes. This is of concern because most SGS models use

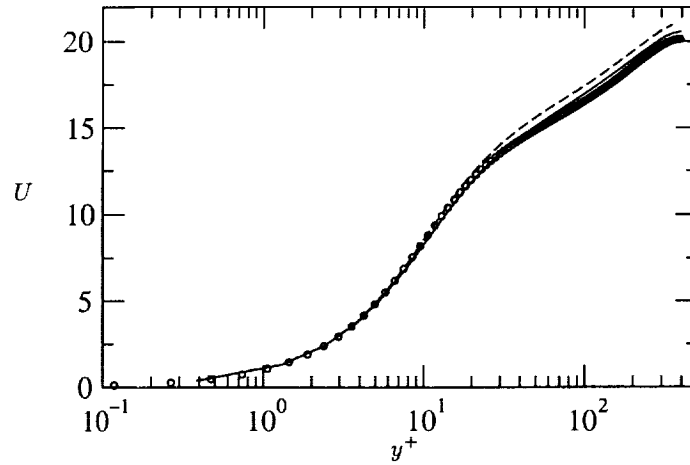


FIGURE 4. Mean velocity profile U as a function of the distance to the wall y^+ . $Re_\tau=395$. \circ : DNS spectral code, — : LES 4th order FD code and - - - : LES 2nd order FD code.

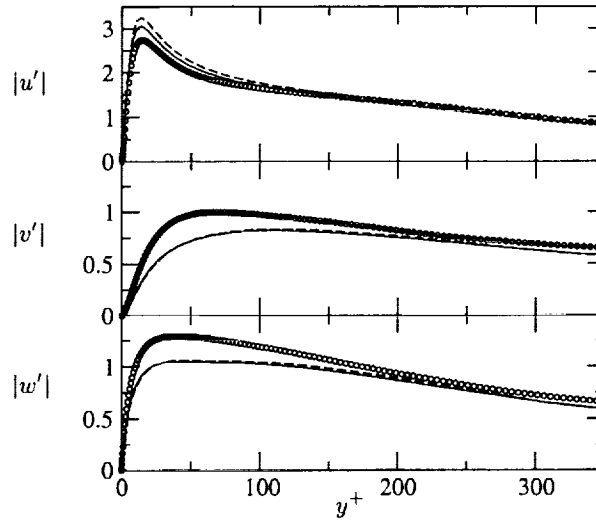


FIGURE 5. Velocity fluctuations in streamwise $|u'|$, wall normal $|v'|$ and spanwise direction $|w'|$ as a function of the distance to the wall y^+ . $Re_\tau=395$. \circ : DNS spectral code, — : LES 4th order FD code and - - - : LES 2nd order FD code.

information from the smallest resolved length scales (highest wavenumbers) to model the SGS stresses. Fig. 6 clearly shows that even when a high order scheme such as the fourth order FD scheme is used, the high wavenumber part of the spectra is contaminated with numerical errors.

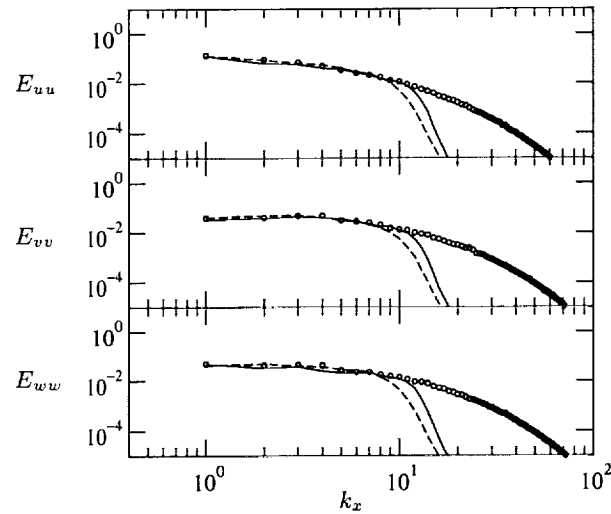


FIGURE 6. Energy spectrum of the streamwise E_{uu} , wall normal E_{vv} and spanwise E_{ww} velocity correlation as a function of the streamwise wavenumber k_x . $Re_\tau=395$ at $y^+ \approx 395$. \circ : DNS spectral code, — : LES 4th order FD code and - - - : LES 2nd order FD code.

4. Current work

The fourth order finite difference scheme requires further evaluation with the use of the three-dimensional commutative filters in order to perform a “true” LES, defined as a solution that converges to an LES solution and not to a DNS solution as the computational grid is refined. This can be made by separating the filter width from the computational grid size. By keeping the filter width constant while the computational grid is refined, the solution should converge to the “true” LES solution.

Different SGS models will also be investigated as well as the influence of numerical errors. The influence of the finite difference schemes on the high wavenumber part of the energy spectra and its influence on the predicted SGS stresses need to be determined. An approach to reduce the influence from the numerical error might be to use information from the length scales (or wavenumbers) that are not contaminated with large numerical errors and still is in the inertial subrange of the energy spectrum.

The cause of the over- and underprediction of the velocity fluctuations needs to be determined. The problem depends upon the SGS model, the grid resolution and the numerical method.

Acknowledgments

The author wishes to thank Prof. Oleg V. Vasilyev for providing the channel flow codes. The financial support from the Swedish Research Council for Engineering Science (TFR) and Center for Turbulence Research are gratefully acknowledged.

REFERENCES

- BAGGETT, J. S., JIMÉNEZ, J. & KRAVCHENKO, A. G. 1997 Resolution requirements in large-eddy simulations of shear flows. *Center for Turbulence Research, Annual Research Briefs 1997*, 51-66.
- BARDINA, J., FERZIGER, J. H. & REYNOLDS, W. C. 1980 Improved subgrid scale models for large eddy simulation. *AIAA-80-1357*, 1-9.
- DOMARADZKI, J. A. & LOH, K. C. 1999 The subgrid-scale estimation model in the physical space representation. *Phys. Fluids*, **11**, 2330-2342.
- DUKOWICZ, J. K. & DVINSKY, A. S. 1992 Approximation as a higher order splitting for the implicit incompressible flow equations. *J. Comp. Phys.*, **102**, 336-347.
- FUCHS, L. 1996 An exact SGS-model for LES. *Advances in Turbulence IV, Kluwer Academic Publishers*, 23-26.
- GERMANO, M., PIOMELLI, U., MOIN, P. & CABOT, W. H. 1991 A dynamic subgrid-scale eddy viscosity model. *Phys. Fluids A*, **3**, 1760-1765.
- GHOSAL, S. 1995 An analysis of numerical errors in large-eddy simulations of turbulence. *J. Comp. Phys.* **125**, 187-206.
- GHOSAL, S. & MOIN, P. 1995 The basic equations of the large eddy simulation of turbulent flows in complex geometry. *J. Comp. Phys.* **118**, 24-37.
- JIMÉNEZ, J. 1998 LES: where are we and what we can expect. *AIAA-98-2891*. 1-11.
- KIM, J., MOIN, P. & MOSER, R. D. 1987 Turbulence statistics in fully developed channel flow at low Reynolds number. *J. Fluid Mech.* **177**, 133-166.
- KRAVCHENKO, A. G. & MOIN, P. 1997 On the effect of numerical errors in large eddy simulations of turbulent flows. *J. Comp. Phys.* **131**, 310-322.
- LILLY, D. K. 1992 A proposed modification of the Germano subgrid-scale closure method. *Phys. Fluids A*, **4**, 633-635.
- LIU, K. C., MENEVEAU, C. & KATZ, J. 1994 On the properties of similarity subgrid-scale models as deduced from measurements in a turbulent jet. *J. Fluid Mech.* **275**, 83-119.
- MORINISHI, Y. 1995 Conservative properties of finite difference schemes for incompressible flow. *Annual Research Briefs, Center for Turbulence Research, NASA Ames/Stanford Univ.* 121-132.
- MORINISHI, Y., LUND, T. S., VASILYEV, O. V. & MOIN, P. 1998 Fully conservative higher order finite difference schemes for incompressible flow. *J. Comp. Phys.* **143**, 90-124.
- MOSER, R. D., KIM, J. & MANSOUR, N. N. 1999 Direct numerical simulation of turbulent channel flow up to $Re_\tau=590$. *Phys. Fluids*, **11**, 943-945.
- SARGHINI, F., PIOMELLI, U. & BALARAS, E. 1999 Scale-similar models for large-eddy simulations. *Phys. Fluids*, **11**, 1596-1607.
- SMAGORINSKY, J. 1963 General circulation experiments with the primitive equations. *Mon. Weather Rev.* **91**, 99-152.
- SPALART, P., MOSER, R. & ROGERS, M. 1991 Spectral methods for the Navier-Stokes equations with one infinite and two periodic directions. *J. Comp. Phys.* **96**, 297-324.
- VASILYEV, O. V. 2000 High order finite difference schemes on non-uniform meshes with good conservation properties. *J. Comp. Phys.* **157**, 746-761.
- VASILYEV, O. V., LUND, T. S. & MOIN, P. 1998 A general class of commutative filters for LES in complex geometries. *J. Comp. Phys.* **146**, 82-104.

Large-eddy simulation of gas turbine combustors

By Krishnan Mahesh, George Constantinescu AND Parviz Moin

1. Motivation and objectives

The objective of this study is to develop tools to perform large-eddy simulation (LES) of turbulent flows in realistic engineering configurations. Of particular interest is the flow inside gas-turbine combustors. LES is an attractive approach for these flows, which are at relatively lower Reynolds numbers than external flows, and involve scalar mixing as a central component. This report discusses our progress towards developing a numerical algorithm and solver for this purpose. As outlined in last year's report (Mahesh *et al.* Annual Research Briefs 1999), we have developed a conservative numerical algorithm that staggers the dependent variables to simulate incompressible flow on unstructured grids. Our report last year outlined the algorithm as well as some details of its implementation on parallel platforms. It was noted that the algorithm was applicable to hybrid elements, the data structures used compressed storage formats to reduce memory use, a grid reordering technique was developed, and validation simulations were just being initiated.

2. Accomplishments

Our progress in the last year is as follows:

- A more efficient version of the constant density algorithm was derived for hybrid grids.
- Severe memory bottlenecks in the pre-processor part of the solver were removed. The pre-processor was rewritten to store data out of core; as a result, memory requirements of the order of gigabytes were reduced to the order of megabytes.
- The solver was validated for a variety of steady and unsteady flows.
- Simulations in a combustor geometry provided by Pratt & Whitney geometry were initiated; the unsteady flow in a subset of the overall geometry was simulated; the simulations retained the geometrical complexities of the full configuration.
- The dynamic Smagorinsky model for LES was extended to unstructured grids and implemented.
- The algorithm was extended to low Mach number, variable density flows; validation is in progress.

2.1. Algorithm improvements

2.1.1. Base algorithm

Recall that the constant density algorithm stores pressure at the centroids of the elements and velocity at their faces. As shown in Fig. 1, only one component of velocity is stored and advanced in time; the other two components are reconstructed. The velocity component v_n satisfies

$$\frac{\partial v_n}{\partial t} - (\vec{u} \times \vec{\omega}) \cdot \vec{n} + \frac{\partial}{\partial n} \left(\frac{\vec{u} \cdot \vec{u}}{2} \right) = -\frac{1}{\rho} \frac{\partial p}{\partial n} + \nu (\nabla^2 \vec{u}) \cdot \vec{n}. \quad (2.1)$$

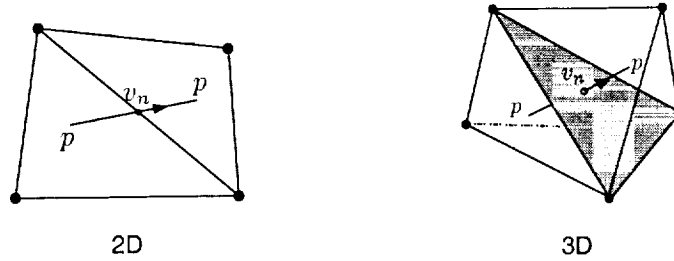


FIGURE 1. Positioning of variables in staggered algorithm.

Note that the convection term is written in terms of velocity and vorticity. The pressure-projection approach is used to ensure that the velocity field is discretely divergence-free; the resulting Poisson equation is solved using the conjugate gradient method with diagonal preconditioning. As shown in Fig. 1, v_n is not necessarily aligned with the face normal. As a result, the projection step involves the tangential velocities, which have to be reconstructed at every iteration. A more efficient formulation was therefore derived — the face normal velocity is now stored at the face centroid. Storing the normal component makes the projection step cheaper, while storing velocities at the centroid makes flux calculations more accurate.

2.1.2. The dynamic model

The dynamic Smagorinsky model (Germano *et al.* 1991) was extended to unstructured grids. Recall that the LES equations are

$$\frac{\partial \bar{u}_i}{\partial t} + \frac{\partial \bar{u}_i \bar{u}_j}{\partial x_j} = -\frac{\partial \phi}{\partial x_i} + \frac{1}{Re} \frac{\partial^2 \bar{u}_i}{\partial x_j \partial x_j} - \frac{\partial q_{ij}}{\partial x_j} \quad (2.2)$$

where q_{ij} denotes the anisotropic part of the subgrid-scale stress, $\bar{u}_i \bar{u}_j - \bar{u}_i \bar{u}_j$, and the overbar indicates filtered variables. Note that the above equation can equivalently be written with the convection term in rotational form.

The details of the dynamic modeling procedure may be found elsewhere and are not repeated here. We only note that the Smagorinsky model assumes that

$$q_{ij} = -2C\bar{\Delta}^2 |\bar{S}| \bar{S}_{ij} \quad (2.3)$$

where \bar{S}_{ij} denotes the filtered strain-rate tensor. Application of the dynamic procedure using the least-squares approach (Lilly 1992) yields the following expression for C :

$$C\bar{\Delta}^2 = -\frac{1}{2} \frac{L_{ij} M_{ij}}{M_{kl} M_{kl}} \quad (2.4)$$

where

$$L_{ij} = \widehat{\bar{u}_i \bar{u}_j} - \widehat{\bar{u}_i} \widehat{\bar{u}_j} \quad (2.5)$$

and

$$M_{ij} = \left(\widehat{\bar{\Delta}} / \bar{\Delta} \right)^2 |\widehat{\bar{S}}| \widehat{\bar{S}}_{ij} - |\bar{S}| \bar{S}_{ij} \quad (2.6)$$

The dynamic procedure requires definition of a test-filter and the ratio of test to grid filter widths. The ratio of filter widths is commonly assumed to be 2; we do the same. We define the filter width at the faces of the grid as $V^{1/3}$ where V denotes the average of the volumes of the elements that straddle the face. This yields a filter width of $(\Delta_x \Delta_y \Delta_z)^{1/3}$ for a Cartesian grid. The test filter is assumed to be a top-hat filter

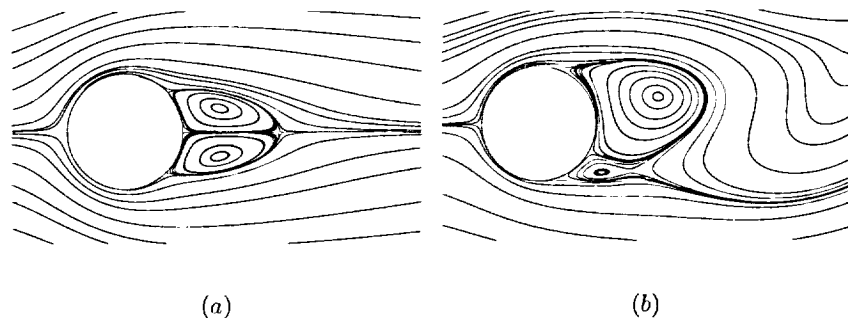


FIGURE 2. Streamlines in the immediate vicinity of the cylinder. (a) : $Re = 20$, (b) : $Re = 100$.

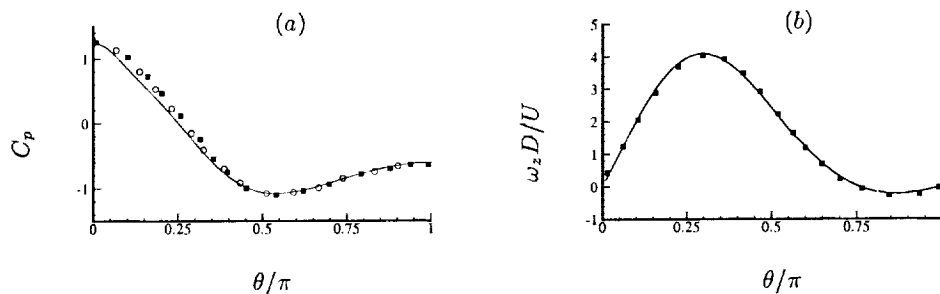


FIGURE 3. The vorticity and pressure coefficient (C_p) on the cylinder surface at $Re = 20$ are compared to experimental data. The solid lines are from the calculations, while the symbols are experimental data from Nieuwstadt & Keller (1973). (a): C_p , (b): vorticity.

and uses information from the neighboring volumes to obtain test-filtered values of the velocity at the faces. In practice, the dynamic model constant C is usually averaged over homogeneous directions, should such directions be present. Other approaches have been proposed for flows without homogeneous directions; e.g. Ghosal *et al.* (1994), Meneveau *et al.* (1996). Ghosal's approach requires solution of a variational problem and was successfully applied to flow over a backstep by Akselvoll & Moin (1995). The Lagrangian averaging proposed by Meneveau *et al.* (1996) has been successfully applied to channel flow but can exhibit sensitivity to the Lagrangian averaging time (D. You, private communication). In this report, we have chosen to filter the dynamic model coefficient in space instead of Lagrangian averaging. This implementation of the dynamic model is considered preliminary; the rationale for test-filtering the coefficients is that spatial filtering is consistent with the assumption in the dynamic procedure that the model coefficient does not vary over the test filter width.

2.1.3. Variable density flow

The constant density algorithm has been extended to variable density flow in the low Mach number limit. The dependent variable is now ρv_n instead of v_n , and the convection term is rewritten in terms of $\rho \vec{u}$ and its curl. Again, a pressure-projection approach is used to enforce the continuity equation. The energy equation may either be solved for, or temperature may be obtained by mapping from the scalars. Validation is in progress and is composed of two parts—evolving the scalars for constant density flow and evolving the variable density equations while specifying the density, and combining the two. The first two validations have been completed; similar computations in other simple laminar flows were performed.

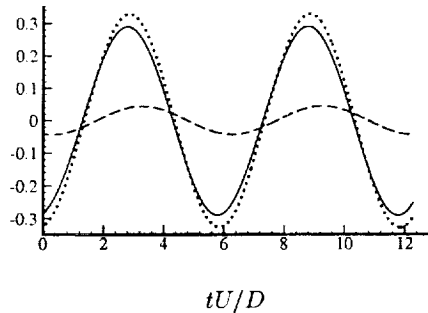


FIGURE 4. Lift coefficients at $Re = 100$. — (C_{lp}), ---- (C_{lv}), (C_l). The subscripts p and v stand for contributions from pressure and viscosity respectively.

2.2. Results

Several computations were carried out to validate the numerical method. Some of these are discussed below.

2.2.1. Flow over a cylinder

The flow over a cylinder has been studied extensively by both experiments and computations. The flow is sensitive to Reynolds number, has attached and separated regions, and exhibits steady and unsteady regimes. It was therefore used for validation. Four simulations are planned: direct numerical simulation at $Re = 20$, $Re = 100$, $Re = 300$, and LES at $Re = 3900$. The first two calculations are completed and are reported here, while the latter two are in progress. Note that the flow at $Re = 20$ is two-dimensional and steady, that at $Re = 100$ it is two-dimensional and unsteady, while those at $Re = 300$ and 3900 are three-dimensional and unsteady. Regardless of the regime and dimensionality of the flow, all simulations reported solve the three-dimensional unsteady equations.

Figure 2 shows streamlines in the immediate vicinity of the cylinder at $Re = 20$ and 100 . The asymmetry in the presence of shedding is apparent. Quantitative validation is provided in Figs. 3 and 4 and tables 1 and 2, where good agreement with experiment and other computations is found.

2.2.2. Flow over a sphere

The flow over a sphere was chosen as a validation case since it exhibits Reynolds number sensitivity while being three-dimensional even in the laminar regime. Currently a computation at $Re = 50$ has been completed, and the results are reported here. Although not a complex geometry, the use of unstructured grids allows the problem of polar singularity to be side stepped; the surface of the sphere is paved with quadrilateral elements which are then extruded normal to the sphere surface to generate the volume grid. As shown in Fig. 5, good agreement is obtained with structured-grid computations by Johnson & Patel (1999).

2.2.3. Flow in a coaxial combustor

The flow in a coaxial dump combustor geometry has been extensively studied experimentally (Roback & Johnston 1983, Sommerfeld & Qiu 1991) as well as computationally using LES (Pierce & Moin 1998). Data for both cold and reacting flow are available. It is therefore used for validation purposes. Figure 6 shows a cross-section of the geometry. Two cases were considered. Prior to inclusion of the LES model in the code, laminar

	Present results	Computations	Experiments
Drag coefficient	2.01	1.99	2.05
Pressure drag	1.18	—	1.22
Viscous drag	0.83	—	0.83
Separation angle	42.5°	43.8°	41.6°
Min. vel. in bubble	-0.032U	-0.031U	-0.040U
Position of min. vel.	0.42D	0.42D	0.36D

TABLE 1. Comparison to experiments (Taneda 1956, Coutanceau & Bouard 1977, Nieuwstadt & Keller 1973), and computation (Beaudan & Moin 1994) for $Re = 20$.

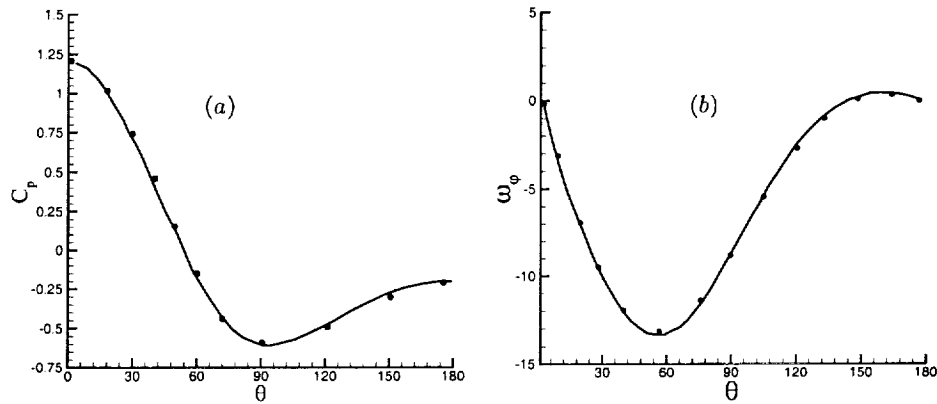


FIGURE 5. The vorticity and pressure coefficient (C_p) on the sphere surface at $Re = 50$ are compared to experimental data. The solid lines are from the calculations, while the symbols are experimental data from Johnson & Patel (1999). (a): C_p , (b): vorticity.

flow in the same geometry was computed. The objective of the laminar calculations was to validate the code by comparing to computations by Pierce (personal communication) using a structured solver in cylindrical coordinates. The three components of the coaxial geometry—core inlet, annular inlet, and test section—were independently considered. The solutions in the inlets are trivial and are not shown here. Figure 7 compares the solution in the test section to results from Pierce, and good agreement is observed.

Currently LES in the same geometry is in progress at conditions corresponding to those of Roback and Johnston, 1983.

2.3. Flow in a Pratt & Whitney combustor

Our goal is to perform LES in an industrial gas turbine combustor as part of the overall integrated simulation. A step in that direction is to simulate cold and then reacting flow in an industrial combustor. Pratt & Whitney has provided us with a combustor

	Present results	Computations	Experiments
Drag coeff. (max)	1.329	1.314 - 1.365	1.35
Pressure drag (max)	0.989	1.021	1.01
Viscous drag (max)	0.340	0.344	0.34
Lift. coef. (max)	0.328	0.314 - 0.328	-
Lift coef. (amp)	0.684	0.657	-
Pressure lift (max)	0.290	0.297	-
Viscous lift (max)	0.043	0.045	-
Strouhal no.	0.166	0.164 - 0.166	0.164
$-C_{p_{base}}$	0.77	0.73 - 0.74	0.72
$-C_{p_{stag}}$	1.08	1.11	-
Sep. angle	116.1°	117.4°	117.0°

TABLE 2. Flow over a cylinder at $Re = 100$. Comparison to experiments (Williamson 1991, Henderson 1995) and computation (Beaudan & Moin 1994, Mittal (private communication), Kravchenko & Moin 1998).

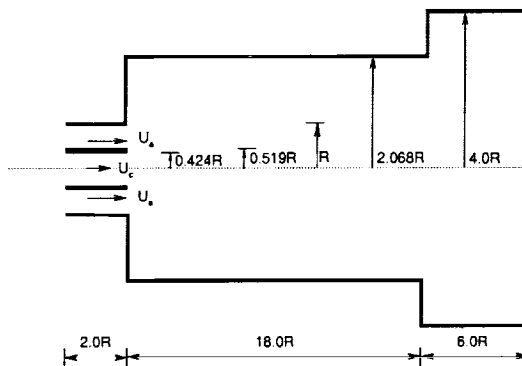


FIGURE 6. Cross-section of coaxial combustor.

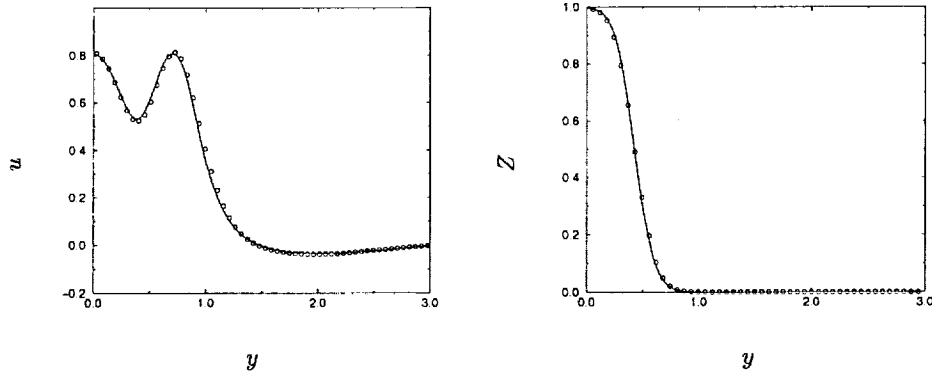


FIGURE 7. Laminar validation in the coaxial combustor geometry. The profiles at $x = 2$ are compared to results from Pierce (private communication) using a structured grid solver. (a): u , (b): Scalar — (Pierce), \circ (present results).

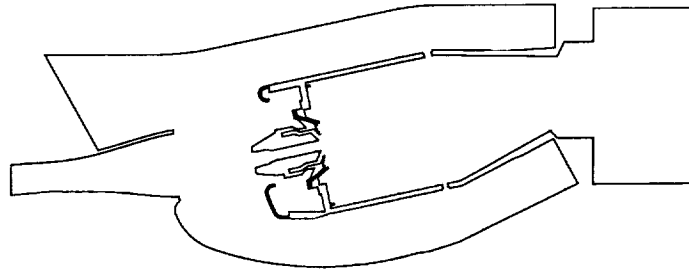


FIGURE 8. Cross-section of combustor.

geometry for which they have data. Simulating flow in the real combustor geometry tests the algorithm and the code as well as our grid generating capability.

Our first step has been to assess our ability to handle the intricate internal details of the combustor geometry and to assess the resolution requirements in the different regions of the flow. Towards that end we have extracted from the original three-dimensional geometry a plane containing important features such as the pre-diffuser, outer diffuser, fuel and air nozzle, and injection holes (Fig. 8). The midplane was extruded in the spanwise direction, and a completely hexahedral grid of about half a million elements was generated. Figure 9 illustrates a portion of the grid.

Plug flow at a Reynolds number of around 3000 was specified at the inlet; the calculations were started from rest and monitored for qualitative accuracy. Figures 10 and 11 show instantaneous streamlines in the pre-diffuser, nozzle, and dilution hole regions respectively. The computation is seen to capture separation, reattachment, and recirculation regions at both large scales (such as in the diffuser and downstream of the nozzle) and small scales (e.g. small corners around the nozzle). Also, the evolution of the flow was tracked, and unsteady details such as starting vortices and separation at sharp edges were seen to be captured. Animation shows a flow that appears periodic and is driven by periodic shedding in the pre-diffuser. This is consistent with the presence of sharp edges and the absence of three-dimensional features.

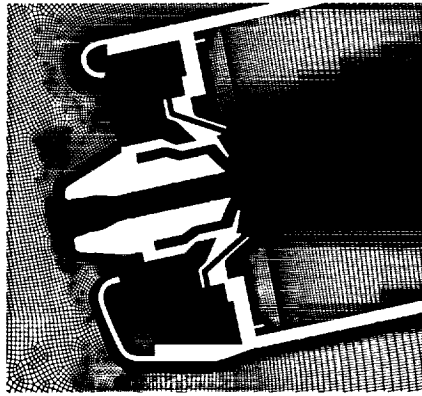


FIGURE 9. A closer view of the grid used in the nozzle.

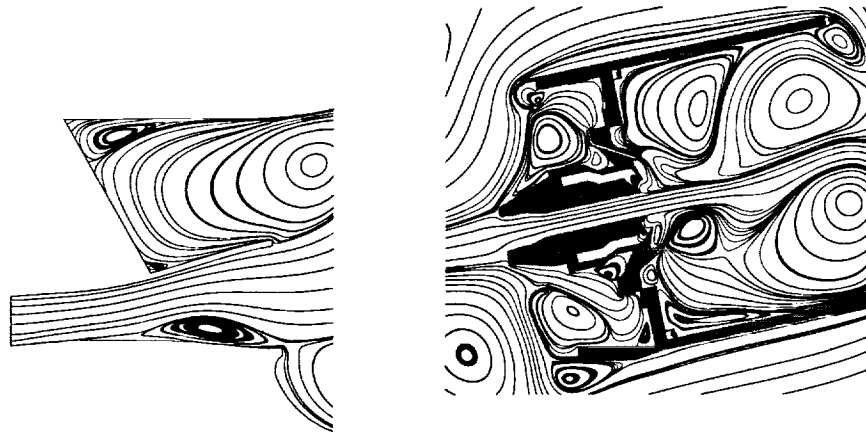


FIGURE 10. Streamlines in the prediffuser and nozzle regions respectively.

Our next step is to generate a suitable grid for the three-dimensional geometry and then simulate scalar mixing in the full configuration.

2.4. *Parallel performance*

The constant density solver was tested on the SGI Origin 2000 and found to scale quite well with the number of processors. Figure 12 shows results from calculations on two different grid sizes, 64000 and 216000 nodes. Note that these grids are quite small as compared to the grids commonly used for turbulence simulations. The computations with 64000 nodes scales linearly almost up to 32 processors, at which point there are only 2000 nodes per processor. The simulations with 216000 nodes is seen to scale linearly far beyond. An empirical rule of thumb used in our calculations is to partition the grid into as few as 5000 elements per processor, should that many processors be available.

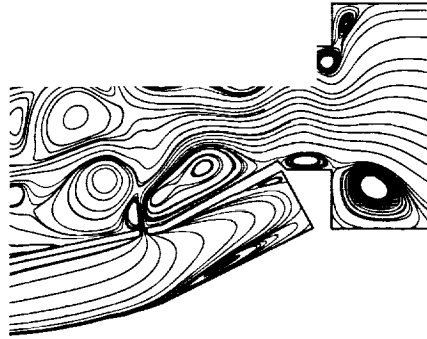


FIGURE 11. Streamlines illustrating flow around the dilution holes.

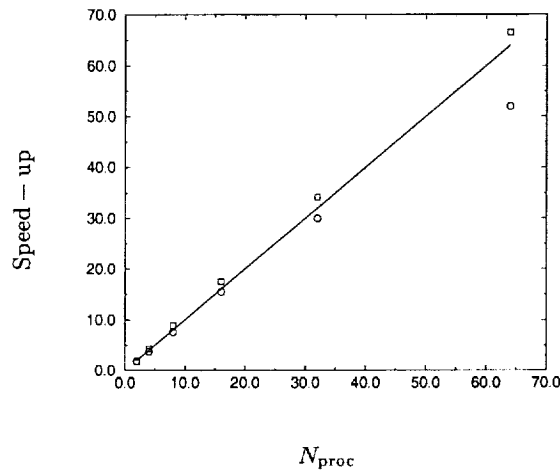


FIGURE 12. Results of a scaling study on the Origin 2000. Two different grid sizes were considered: 64000 nodes (\circ), and 216000 nodes (\square).

3. Summary

This report describes our progress in the last year towards large-eddy simulation of gas turbine combustors. Our progress in the last year is as follows:

- A more efficient version of the constant density algorithm was derived for hybrid grids.
- The constant density algorithm was implemented for hybrid grids, and validated for a variety of steady and unsteady flows.
- Simulations in the Pratt & Whitney geometry have been initiated; the unsteady flow in a subset of the overall geometry was simulated.
- The dynamic Smagorinsky model was extended to unstructured grids, and implemented in the code.

- The algorithm was extended to low Mach number, variable density flows; validation is in progress.
- The spray module is being incorporated.

Acknowledgments

We would like to acknowledge Mr. Gianluca Iaccarino for his expertise and generous help in generating the grids used in our simulations. Financial support for this work is provided by the Department of Energy's ASCI program.

REFERENCES

- AKSELVOLL, K. & MOIN, P. 1995 Large-eddy simulation of turbulent confined coannular jets and turbulent flow over a backward facing step. *Report TF-63*, Mechanical Engineering Dept., Stanford University, Stanford, California.
- BEAUDAN, P. & MOIN, P. 1994 Numerical investigations on the flow past a circular cylinder at sub-critical Reynolds number. *Report TF-62*, Mechanical Engineering Dept., Stanford University, Stanford, California.
- COUTANCEAU, M. & BOUARD, R. 1977 Experimental determination of the main features of the viscous flow in the wake of a cylinder in uniform translation. Part 1. Steady flow. *J. Fluid Mech.* **79**, 231-256.
- GERMANO, M., PIOMELLI, U., MOIN, P. & CABOT, W. H. 1991 A dynamic subgrid-scale eddy viscosity model. *Phys. Fluids A.* **3**(7), 1760-1765.
- GHOSAL, S., LUND, T. S., MOIN, P. & AKSELVOLL, K. 1994 A dynamic localization model for large-eddy simulation of turbulent flows. *J. Fluid Mech.* **282**, 1-27.
- HENDERSON, R. D. 1995 Details of the drag curve near the onset of vortex shedding. *Phys. Fluids.* (i)7(9), 2102-2104.
- KRAVCHENKO, A. G. & MOIN, P. 1998 B-spline methods and zonal grids for numerical simulations of turbulent flows. *Report TF-73*, Mechanical Engineering Dept., Stanford University, Stanford, California.
- LILLY, D. K. 1992 A proposed modification of the Germano subgrid-scale closure method. *Phys. Fluids A.* **4**(3), 633-635.
- MENEVEAU, C., LUND, T. S., & CABOT, W. H. 1996, A Lagrangian dynamic subgrid-scale model of turbulence. *J. Fluid Mech.* **319**, 353-385.
- NIEUWSTADT, F. & KELLER, H. B. 1973 Viscous flow past circular cylinders. *Computers & Fluids.* **1**, 59-71.
- PIERCE, C. D. & MOIN, P. 1998 Large eddy simulation of a confined coaxial jet with swirl and heat release. *AIAA Paper 98-2892*.
- ROBACK, R. & JOHNSTON, B. V. 1983 Mass and momentum turbulent transport experiments with confined swirling coaxial jets. *NASA CR 168252*.
- SOMMERFELD, M. & QIU, H. H. 1991 Detailed measurements in a swirling particulate two-phase flow by a phase-doppler anemometer. *Int. J. of Heat and Fluid Flow.* **12**(1), 20-28.
- TANEDA, S. 1956, Experimental investigation of the wakes behind cylinders and plates at low Reynolds numbers. *J. Phys. Soc. Japan.* **11**, 302.
- WILLIAMSON, C. H. K. 1996 Vortex dynamics in the cylinder wake. *Ann. Rev. Fluid Mech.* **28**, 477-539.

Towards LES models of jets and plumes

By A. T. Webb† AND N. N. Mansour‡

1. Motivation and objectives

As pointed out by Rodi (1982) standard integral solutions for jets and plumes developed for discharge into infinite, quiescent ambient are difficult to extend to complex situations - particularly in the presence of boundaries such as the sea floor or ocean surface. In such cases the assumption of similarity breaks down and it is impossible to find a suitable entrainment coefficient. The models are also incapable of describing any but the most slowly varying unsteady motions.

There is therefore a need for full time-dependent modeling of the flow field for which there are three main approaches - Reynolds averaged numerical simulation (RANS), large eddy simulation (LES) and direct numerical simulation (DNS). Rodi (1982) applied RANS modeling to both jets and plumes with considerable success, the test being a match with experimental data for time-averaged velocity and temperature profiles as well as turbulent kinetic energy and rms axial turbulent velocity fluctuations. This model still relies on empirical constants, some eleven in the case of the buoyant jet, and so would not be applicable to a partly laminar plume, may have limited use in the presence of boundaries, and would also be unsuitable if one is after details of the unsteady component of the flow (the turbulent eddies). At the other end of the scale DNS modeling includes all motions down to the viscous scales. Boersma *et al.* (1998) have built such a model for the non-buoyant case which also compares well with measured data for mean and turbulent velocity components. The model demonstrates its versatility by application to a laminar flow case. As its name implies, DNS directly models the Navier-Stokes equations without recourse to subgrid modeling so for flows with a broad spectrum of motions (high Re) the cost can be prohibitive - the number of required grid points scaling with $Re^{9/4}$ and the number of time steps with $Re^{3/4}$ (Piomelli and Chasnov, 1996).

The middle road is provided by LES whereby the Navier-Stokes equations are formally filtered with the filter chosen to only exclude the smallest turbulent motions. If successful, LES should provide much of the detail available to DNS but at more bearable cost. Fatica *et al.* (1994) in comparing LES with DNS for a low Reynolds number jet showed that the LES could simulate the temporally evolving behavior including growth of the jet thickness.

It is the intention of this report to explore the application of an LES model to jets and plumes. As always, before tackling complex situations, the model must be tested for the simplest of cases and so we address only two, a non-buoyant axisymmetric jet issuing steadily from an orifice into a semi-infinite stationary environment and a buoyant jet in the same environment. The work is a continuation of Basu and Mansour (1999).

† University of New South Wales, Australian Defence Force Academy
‡ NASA Ames Research Center, Moffett Field, CA

2. Numerical method

2.1. Governing equations

In the present study, we aim to compute the evolution of a circular jet and plume in uniform surroundings. Since the density differences away from the source of a plume are typically small compared to ambient density, we take advantage of the Boussinesq approximation, whereby the effects of density variations are neglected, except in that they are modeled by a source or buoyancy term in the momentum equations. The equations to be solved are the modified incompressible Navier-Stokes equations under the Boussinesq approximation together with the continuity equation and a scalar transport equation where for the buoyant case the scalar represents buoyancy or temperature deficit.

The non-dimensional governing parameters for this flow are:

$$\begin{aligned} \text{Reynolds number} &= Re = U_o D_o / \nu, \\ \text{Prandtl number} &= Pr = \nu / \kappa, \\ \text{Grashof number} &= Gr = g'_0 / D_o^3 / \nu^2, \end{aligned}$$

where U_o is the mean vertical velocity of the fluid leaving the source (used to non-dimensionalize all velocities), D_o is the diameter of the orifice (used to non-dimensionalize lengths), ν is the kinematic viscosity of the fluid, κ the scalar diffusivity, and g'_0 the initial buoyancy. For the non-buoyant case, Gr is set to zero.

In the following we use T to represent the dimensionless scalar concentration (eg. pollutant, buoyancy, temperature deficit etc).

2.2. Large eddy simulation

To create a computational model, the LES approach is to spatially filter the Navier-Stokes/continuity/tracer equations with the filter cutoff chosen to retain the energy-containing wavenumbers. In the present study, the SGS stresses and fluxes are modeled using the dynamic approach (Germano *et al.*, 1991, Lilly, 1992, and Cabot and Moin, 1996), which automatically determines, using different filter widths, the spatial distribution of the magnitude of eddy viscosity as required by the subgrid-scale Smagorinsky model; this procedure obviates the need for any empirical determination of the Smagorinsky constant. A major attraction of this method is that it is much more likely to be successful for inhomogeneous flows, particularly in cases where part of the domain is laminar as we have in jets and plumes. This issue was explored by Liu *et al.* (1994) who compared the Smagorinsky and the dynamic models with particle image velocimetry laboratory measurements in the far field of a turbulent round jet. The Smagorinsky model was found to correlate poorly with the real turbulent stress, while the dynamic model yielded appropriate coefficients. The inadequacy of the Smagorinsky model was also demonstrated by Bastiaans *et al.* (1994) in an LES model of transient buoyant plumes in an enclosure where they found they could only get a match of the evolving plume by tuning the Smagorinsky constant. Such tuning reduces the generality of a model.

2.3. Numerical scheme

The numerical scheme for the Navier-Stokes/continuity equations is a fractional step method similar to that of Kim & Moin (1985) who extended the method of Chorin (1968). At the start of each step the subgrid model results are converted to a viscosity to be added to the molecular value and the corresponding diffusivity is estimated from the viscosity with a constant Prandtl number.

We use the LES code of Boersma, an adaptation of DNS code used in a study of pure jets (Boersma *et al.*, 1998). A spherical polar coordinate system (R, θ, ϕ ; along the

radial vector, lateral and azimuthal directions respectively) is used here because, for the present flow with its conical mean growth, a spherical coordinate system allows for a well-balanced resolution of the flow field without excessive grid points. For presentation purposes, however, and for comparison to laboratory data, the results are converted to the axisymmetric cylindrical coordinate system (z axial and r radial). The symbols U and V are used for velocities in the z and r directions respectively. Further details of the computational scheme can be found in the above references.

2.4. Boundary conditions and test parameters

For the chosen staggered grid only velocities normal to the boundary need be specified - i.e. six components. The equation for the tracer (T) is second order in each spatial direction and so we need six boundary conditions for temperature as well.

For the bottom boundary outside the orifice, the velocity is set to zero (i.e. a solid wall). Inside the orifice the vertical velocity profile is specified as a log profile matching smoothwall pipe flow (although the wall boundary layer is not resolved). Other profiles were also tested (tophat and parabolic) with little difference in the substantive results. In addition to the prescribed inlet velocity profile we impose a random white noise perturbation of peak magnitude 2% on the axial velocity component at the inlet; this roughly corresponds to the reported fluctuation level near the inlet in the experiments of Shabbir & George (1994). Similar conditions are applied to temperature, viz tophat profile of zero outside and unity inside.

At the lateral boundary of the computational domain we apply a stress-free condition (Boersma *et al.*, 1998, Gresho, 1991) which in spherical coordinates reads:

$$-P + 2\nu \left(\frac{1}{r} \frac{\partial u_\theta}{\partial \theta} + \frac{u_R}{R} \right) = 0.$$

As adopted by Boersma *et al.* (1998) the value of P at this boundary is set to a constant value (assumed zero) representing its value at infinity. We will revisit this choice at the end of the Report.

At the outflow boundary or the top end of the current computational domain, we use the so-called advective boundary condition, which has been applied successfully by many for similar flows (e.g. Boersma *et al.*, 1998). Negative values of u_R at the outflow boundary are set to zero in order to ensure that no flow enters the computational domain from the outflow region at the top. Corresponding values of T are likewise set to zero at these points.

Periodic boundary conditions are used along the azimuthal ϕ direction boundaries and lateral velocity (u_θ) is set to mean value at $\theta = 0$.

The test conditions were originally chosen to match the particular conditions of round turbulent buoyant plume reported in Shabbir & George (1994) although we subsequently compare with a broader range of experiments. Together with the boundary conditions the following parameters completely determine the flow:

$$Re = 3500, \quad Pr = 0.7, \quad Gr = 9.25 \times 10^6 \text{ for plume, } Gr = 0 \text{ for jet.}$$

There are two points to made about these values - viz whether we would expect the flow to be turbulent and secondly for the buoyant case, at what point we would expect the buoyancy effects to dominate the initial momentum effects.

On the first issue, although there are no critical values of these parameters to guarantee turbulent flow, the value of Re is within the range of experimental data for which the plume is turbulent at or near the nozzle (see Chen and Rodi, 1980, for a discussion

on this issue). Note that for the buoyant case, the value of Gr , would not in itself be high enough to guarantee a turbulent plume. However the concomitant high Re and our random perturbation at the source do yield turbulent flow from the nozzle.

From the experiments of Ricou & Spalding (1961) transition from jet-like to plume-like behavior occurs at a dimensionless height scaled by the so-called Morton length. In our terms the scaling length is $.557/.254\sqrt{2}/\pi^{.25}D_0Re/\sqrt{Gr} \approx 2D_0Re/\sqrt{Gr}$, and so in our buoyant case the transition to plume occurs within about 2.5 diameters of the source.

A third issue that cannot be related quantitatively to the test parameters is the distance over which a core region characterized by the flow profile at the source persists. From experimental data this distance is of order $6D_0$ (Chen and Rodi, 1980) although fully developed jet flow may take some additional distance.

The computations are carried out in a domain that extends to 50 diameters downstream of the source. The domain encompasses a conical volume of lateral angle $\pi/12$, with a virtual origin that is 15 diameters upstream of the orifice. For the purpose of LES, this volume is discretized using a grid of size $(N_r = 128, N_\theta = 40, N_\phi = 32)$, where N_r, N_θ, N_ϕ are the number of finite-volume cells along the (r, θ, ϕ) directions respectively. The grid spacing along r increases linearly from 0.1 near the source to 0.7 near the outflow boundary. Grid spacing is maintained constant along θ and ϕ . Time stepping was chosen to satisfy CFL conditions Boersma *et al.* (1998) and for the jet model a typical time step in dimensionless time units (D_0/U_0) was 0.01 while for the plume it was 0.003. Spatially the grid is an order of magnitude smaller than the expected large scale (typically $0.4z$, although there is an arbitrariness about the definition of the plume edge) and an order of magnitude larger than the Kolmogorov length scale (see Papantoniou and List, 1989) as appropriate for LES modeling. Temporally the sampling is much smaller than the Kolmogorov time scale - i.e. instantaneous.

The computations are carried out for over 100,000 time-steps (a non-dimensional time of about $t = 300$). Averaging for statistical quantities was done towards the end of the simulations when we were convinced the flow was statistically stationary. The throughput on a 195 MHz 8-processor SGI Origin 2000 is about 0.7 seconds per time step.

3. Results

3.1. Jet imaging

A meridional section of tracer concentration simulates a Schlieren photograph that might be captured in the laboratory and enables visualization of several features. Figure 1 is a sequence of three such sections at time steps of 7.4 dimensionless time units.

From any one of these one can see, for example, the zone of flow establishment (zfe) between $z = 0$ and $z \approx 7$. The dark central region with concentration of unity represents source fluid, the edge of which is being eroded by vortices whose dimensions are quite large compared to the nozzle diameter. These vortices grow until they encompass the full radius of the source fluid core. Moreover, there is a regularity in these vortices that results in pulses of higher than locally averaged concentration that advect away from the zfe.

The arrow in the three images follows an eddy apparently in the process of engulfing a patch of ambient fluid. This large scale process is distinctly different from an image implied by integral models of a smooth diffusion process whereby there would be a gradual increase in concentration from the jet edge to the center. Engulfing eddies can be seen

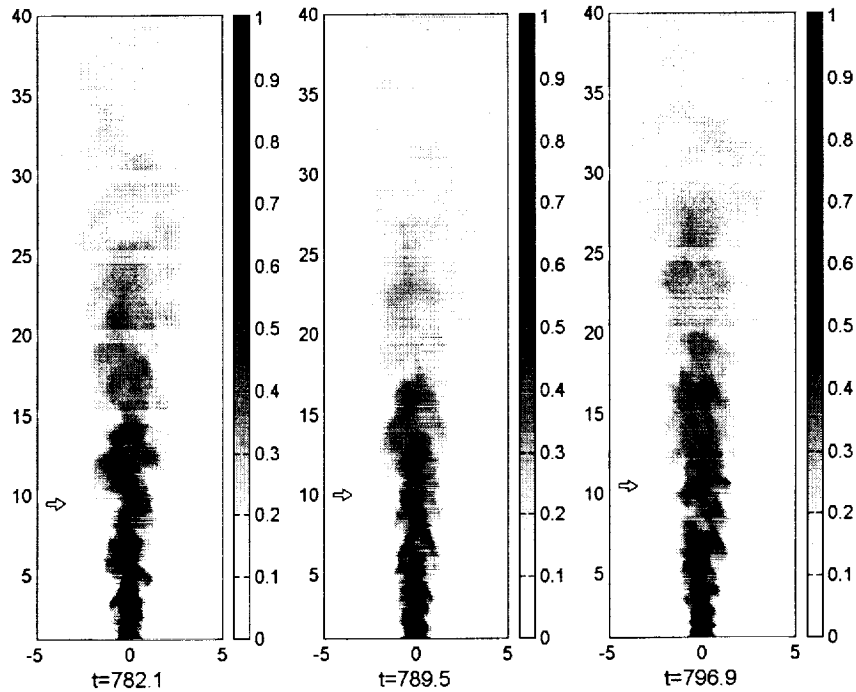


FIGURE 1. A sequence of meridional tracer slices. The arrows track a particular eddy as it engulfs ambient fluid.

throughout the images with speed decreasing and size increasing with distance (z) from the origin.

3.2. Quantifying scale

The apparent underlying regularity in the image sequence suggests that we can seek a reliable way of defining time and space scales for the dominant eddies. For time, the obvious method is to look for a spectral peak computed from a time series and indeed when that is done one finds a clear peak somewhat higher than the expected large scale frequency but much lower than the Kolmogorov frequency.

One could invoke the Taylor frozen-field assumption to deduce a spatial scale but an impediment to computing such a scale is the obvious inhomogeneity. However we can make use of the scaling determined from the mean and variance to transform an axial sample of the tracer to a homogeneous equivalent. Subtracting the mean centerline temperature and then dividing by the mean removes these two trends but still leaves a z -dependent wavelength. However if we transform the z -axis by the antiderivative of the expected inverse growth rate the z -dependence is removed. In this case the growth is expected to be linear and hence the transformation is simply logarithmic. A sample centerline record and its transformed homogeneous equivalent are shown in Fig. 2. The spectra of 100 such records were averaged to yield the spectrum shown in Fig. 3. The interpretation of the peak at 5 transformed wave number units is that the centerline eddy length is equal to $0.2z$. This provides a definitive measure of the large scale motions and may be a better representation than the plume width with its uncertainty in definition.

The small peaks to the right of the peak are not due to uncertainty in the spectral estimates. Rather they arise because of the asymmetry of the shape of the puffs. This

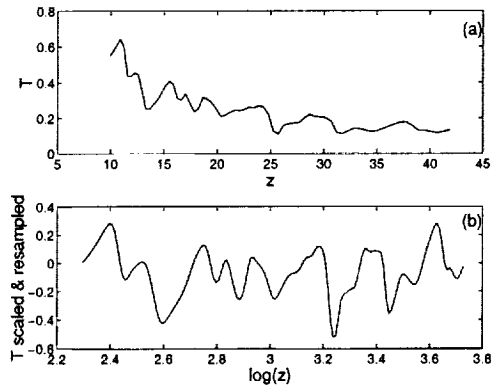


FIGURE 2. A sample centerline temperature trace (a) and its equivalent (b) after transforming to homogeneous form

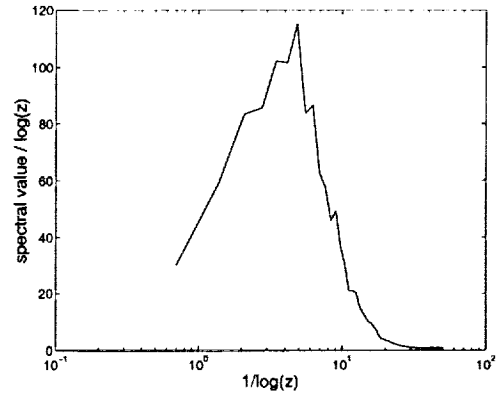


FIGURE 3. Spectrum of centerline scalar in homogeneous transformed space

feature can be clearly seen in the transformed centerline trace (Fig. 3b) where the front of an advancing eddy is typically steeper than the back. The manifestation of this feature in the spurious spectral peaks was confirmed by finding the spectrum of an artificial asymmetrical wave shape (results not shown here).

3.3. Comparisons with laboratory data

To have confidence in the exploration of scale we must be assured that the model is producing reliable results and one way of doing that is by comparing with laboratory data. There is a wealth of such data and we use a selection reviewed by List (1982). The data represent air in air and water in water. Despite the range of fluids and laboratory conditions there is a surprising consistency between the results and hence we would expect our model to be able to match them well.

To produce the model results for comparison we have averaged first moment and second moment statistics (third moment statistics were also computed but are not shown here) over many snapshots. For the results shown here a total of 324 snapshots spaced at 100 timesteps were used. The data were also averaged azimuthally so we have a total of about 10000 samples and if they were independent, the uncertainty for a mean quantity (such as the centerline axial velocity) would be about 0.3%. Now the samples are far from uncorrelated (particularly the azimuthal values) but even discounting the azimuthal averaging gives an uncertainty estimate of 2%.

3.3.1. Mean flow statistics

Here we examine two statistics, the mean z -direction velocity (U) and the tracer concentration (T). The procedure for reducing the data was to fit Gaussian curves (using Matlab's routine `nlinfit` with emphasis on the inner radius) to the r -direction profiles. The fitted e-folding radius (r_e) and the fitted maximum value were used to scale the data. A typical collapse of the data is given in Fig. 4 along with the fitted Gaussian. There are two checks we can perform on this data - that the centerline value of U or T decays as z^{-1} and that the jet e-folding width grows linearly at $0.107z$ for U and $0.126z$ for T . The uncertainty for the growth rates is 3% for both U and T (List, 1982).

The model centerline averages (Fig. 5) show an initial region of approximate length 4 where there is little change from the source value. The decay profile then steepens until

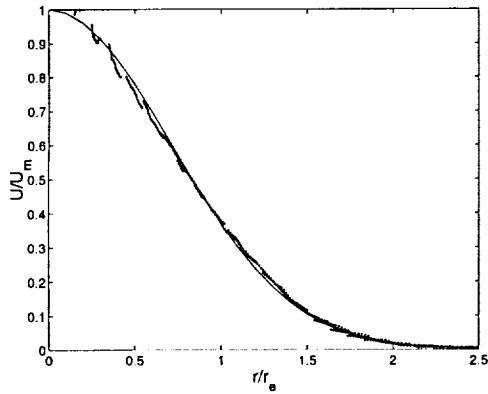


FIGURE 4. Collapse of average axial velocity. The points represent scaled axial velocities at a range of z -positions. The solid line is the common fitted Gaussian profile.

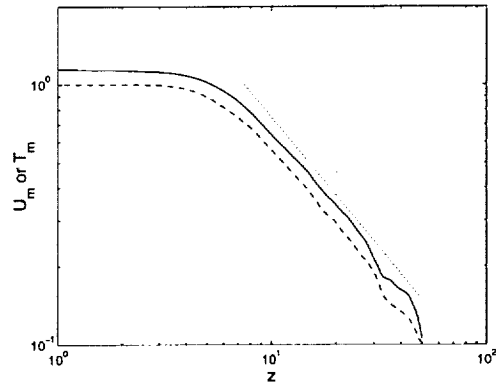


FIGURE 5. Centerline mean velocity (solid) and scalar (dashed). The dotted line is a slope of z^{-1} as found from laboratory data for both U_m and T_m .

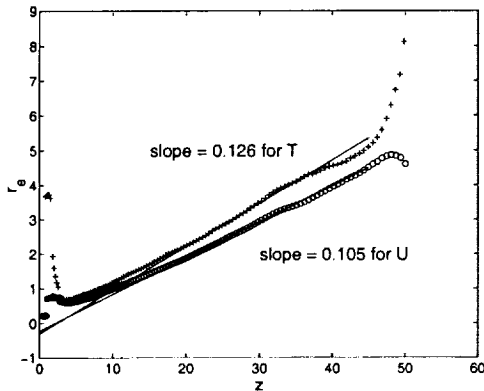


FIGURE 6. Growth of plume width in terms of the e-folding width for z -direction velocity (circles) and tracer (crosses).

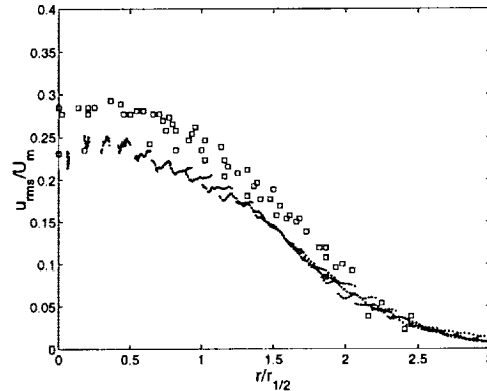


FIGURE 7. z -direction velocity rms fluctuations scaled by centerline mean velocity. The model results are the points, while laboratory results from a variety of sources reviewed by List (1982) are represented by the open boxes.

it approaches something like a constant slope. The effect of an imperfect downstream boundary condition is evident in the region beyond about 30. For both U and T the slope approaches z^{-1} as expected from the laboratory results.

We choose the segment between $z = 20$ and $z = 30$ where the centerline most closely matches the expected value to check for the width growth rate (Fig. 6). The matches are remarkably close to the laboratory data and well within the data uncertainty. The poor Gaussian fit in the z fe and the influence of the downstream boundary are also evident in these plots.

3.3.2. Turbulent statistics

If we were only interested in mean flow information, there would be no point in using anything but the asymptotic models. But we are also interested in the variability as given by the second moment statistics. Of the many such statistics that were computed we

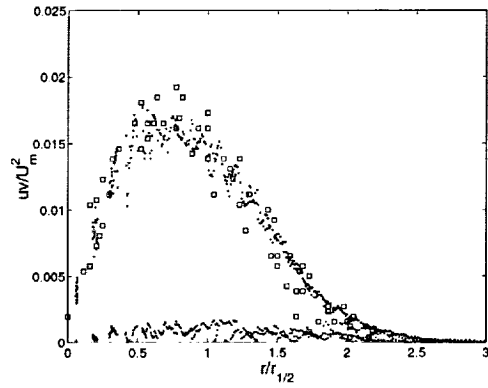


FIGURE 8. Turbulent flux scaled by square of centerline mean velocity. The symbols match Fig. 7. The additional points (small open circles) near the bottom are the subgrid contribution.

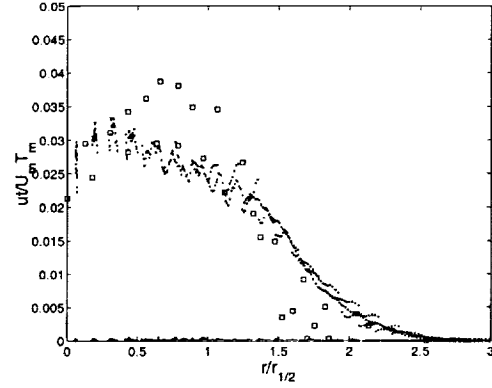


FIGURE 9. Turbulent scalar transport scaled by centerline mean velocity and scalar concentration. The symbols match Fig. 8.

present only three – the z -velocity fluctuations, $u_{rms} = \sqrt{u'^2}$, the turbulent momentum transport, $uv = \overline{u'v'}$ (v is the r -direction velocity) and the turbulent scalar transport $uT = \overline{u'T'}$.

For an LES model we would expect the resolved field to provide most of the variance information and we can check that by computing subgrid scale estimates at least for the two transport statistics using $uv_{sg} = \nu_{sg}(\frac{\partial U}{\partial r} + \frac{\partial V}{\partial z})$ and $uT_{sg} = \nu_{sg}(\frac{\partial T}{\partial z})/Pr$.

As for the mean statistics we scale these data using centerline velocities and scalars as appropriate. The radius is also scaled, although to match the data quoted by List (1982) we use $r_{1/2}$, the point at which the velocity is half maximum rather than the e -folding radius. (They are related by $r_{1/2} = \sqrt{-\log(1/2)}r_e$.)

The z -direction turbulent velocity is plotted in Fig. 7. The model results can be seen to lie at the lower end of the laboratory data, appropriately because this data corresponds to $z = 15$ and $z = 20$, while the higher data corresponds to $z > 50$, outside our model domain. The implication here is that we have not truly reached the self-similar region despite the match for the mean statistics. It is unlikely that subgrid scale would contribute significantly to these values.

Turbulent momentum transport (Fig. 8) is an even closer match – well within the spread of both model and data. The subgrid contribution has been computed here and can be seen to have little bearing on the total turbulent transport. An observation worth making is that the maximum subgrid transport appears to be near $r/r_{1/2} = 1.2$ which corresponds to $r/r_e = 1$, the point of maximum mean $\frac{\partial U}{\partial r}$.

The turbulent tracer transport (Fig. 9) is perhaps the least satisfactory comparison. The model results do sit in the region of one of two data sets – notably not the higher one which includes some co-flow. However the spread appears a little wide and the peak appears too close to the axis.

Two other comparisons were made but are not shown here. They were u_{rms}/u_{rms-m} and T_{rms}/T_{rms-m} , where the subscript m signifies a centerline value. In both cases the match to data was excellent (better than that shown Figs. 7 and 9) and it leaves open the question as to why Fig. 9 did not show a better match.

3.4. Plume modeling

The model was then run with the same boundary conditions and with buoyancy switched on ($Gr \neq 0$). The mean z-direction velocity and temperature show the same sort of excellent collapse by fitting Gaussian profiles and the centerline decay matches the slopes of $z^{-1/3}$ for U_m and $z^{-4/3}$ for T_m as expected from laboratory data of many sources. However the growth of the plume width is about 25% lower than expected and recent effort has been targeting the reason for this mismatch. Three candidates have come to mind - (i) failure of the Boussinesq assumption, (ii) misapplication of the stress-free lateral boundary condition, and (iii) an error in the model for the (now active) tracer.

3.4.1. The Boussinesq assumption

Of the several requirements for this assumption to hold (see Tritton, 1988) one is that the relative density difference $\delta\rho/\rho$ should be much lower than unity. However our numerical model was set up to match a particular data set of Shabbir & George (1994) who induced buoyancy by heating air to about 300°C. Near the source $\delta\rho/\rho$ is about one, well outside the range for which Boussinesq should apply.

To check whether this could cause the narrowing of the numerical plume we lowered Gr from 9.25×10^6 to 2×10^5 , a value well within the Boussinesq range and furthermore, one which should result in an initially momentum-dominated jet transitioning to a buoyancy plume within the model domain.

However the jet width remains too narrow, particularly towards higher z where buoyancy would be taking over from momentum as the dominant driving mechanism. While the density differences in the original model are high near the source, the Boussinesq assumption would be applicable over most of the domain and hence this would not significantly affect the results.

3.4.2. The stress-free lateral boundary condition

Given that our problem is apparently related to entrainment it is natural to examine the lateral boundary condition and the uniform pressure assumption. From the laboratory data and integral models we know that whereas entrainment for a jet is constant, for a plume it increases with z . We explore this issue by developing simple irrotational flow models for the entrainment fields. The assumptions are: velocity and pressure are zero at $r = \infty$, there is a reflection at $z = 0$, along the axis ($r = 0$) there is a line sink with strength matching that found from integral models. The zone of flow establishment is ignored. The solutions are found by superposition of point sinks (Batchelor, 1970).

For the jet, the sink strength is given by $m = -0.25W_0\sqrt{A}$ where A is the area of the inlet (Fischer *et al.*, 1979), and the entrainment velocities are $U = 0$ for the z-component and $V = m/(2\pi r)$ for the r-component.

For the plume, the sink strength is $m = -0.155/3B^{1/3}z^{2/3} = -az^{2/3}$ (Fischer *et al.*, 1979), where $B = \delta\rho/\rho g U_0 A$ is the initial buoyancy flux. The entrainment velocities are found by numerically integrating the following expressions (the singularities in these integrals at $z = 0$ and $z = \infty$ are managed by appropriate transformations.):

$$U = \frac{a}{4\pi} \int_{-\infty}^{\infty} \frac{(z-z')z'^{2/3}}{(r^2 + (z-z')^2)^{3/2}} dz'$$

$$V = \frac{a}{4\pi} r \int_{-\infty}^{\infty} \frac{z'^{2/3}}{(r^2 + (z-z')^2)^{3/2}} dz'$$

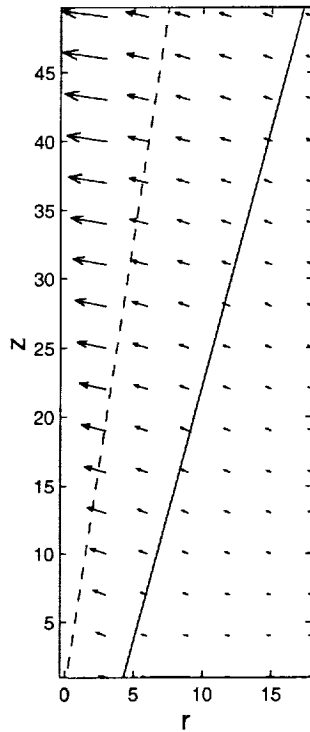


FIGURE 10. Entrainment flowfield predicted by a linesink model for a pure plume. The dashed line is the approximated edge of a plume (2σ). The solid line is the model boundary.

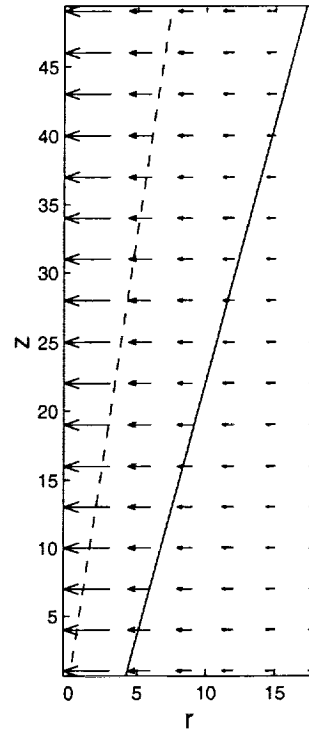


FIGURE 11. Entrainment flowfield predicted by a linesink model for a pure jet. The linestyles match Fig. 10

The solutions have been checked for consistency with the entrainment velocities for integral jet and plume models (i.e. the radial velocities at the e-folding radius match) and hence we can be confident of the applicability of these line sink solutions for the whole of the entrainment region including at the model boundary.

An examination of the velocities at the lateral boundary shows (Fig. 10) that there is a tangential component. With little curvature in the streamlines that means that there is indeed a pressure gradient along the boundary and hence the stress-free assumption is not strictly correct. However this true for the jet model as well (Fig. 11) and if the inaccuracy of the boundary condition were to cause the too-narrow plume then it should do so for both models. Therefore it appears that this is not a factor in the plume width problem and it may be that the generous volume of the entrainment region in the model allows circulation to adjust for the slight error at the boundary.

In fact the jet model does produce θ -direction boundary velocities consistent with those predicted by the line sink model (Fig. 12).

4. Future plans

Elimination of the Boussinesq approximation and the stress-free boundary conditions as culprits in the erroneous plume result leaves us with the third candidate - the subgrid

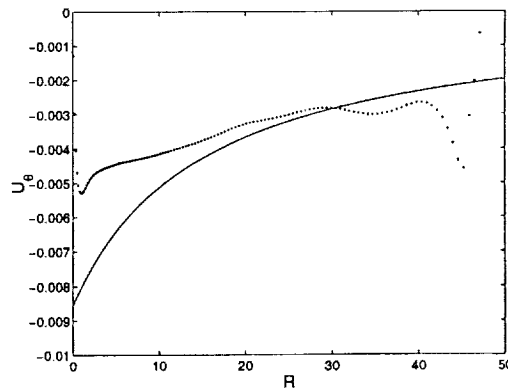


FIGURE 12. Normal velocity at lateral boundary. The points are the average model velocities, while the solid line has been obtained from a line-sink model.

scalar model. We have assumed that the subgrid diffusivity can be scaled from the subgrid viscosity using a constant Prandtl number of 0.7. Other experiments with LES models have found that lower Prandtl numbers, about 0.4, are consistently obtained for a range of molecular Prandtl numbers (Moin *et al.*, 1991). We will experiment with a range of Prandtl numbers. We can go further, however, and build in an explicit model for the subgrid diffusivity. In a way this would be more satisfying in that it would remove the imposition of what could be viewed as a tuning parameter which may be dependent on such things as the dimension of the LES filter.

Acknowledgment

Tony Webb's sabbatical stay at Stanford/NASA AMES is supported in part by CTR.

REFERENCES

- BASTIAANS, R. J. M., RINDT, C. C. M., VAN STEENHOVEN, A. A. & NIEUWSTADT, F. T. M. 1994 Direct and large-eddy simulations of transient buoyant plumes: a comparison with an experiment, in P.R. Voke *et al.*(eds), *Direct and Large-Eddy Simulation I*, Kluwer Academic Publishers. 399-410
- BASU, A. J. & MANSOUR, N. N. 1999 Large eddy simulation of a forced round turbulent buoyant plume in neutral surroundings. *Annual Research Briefs*, Center for Turbulence Research, NASA Ames/Stanford Univ. 239-248.
- BATCHELOR, G. K. 1970 *An Introduction to Fluid Mechanics*. Cambridge U Press.
- BOERSMA, B. J., BRETHOUWER, G. & NIEUWSTADT, F. T. M. 1998 A numerical investigation on the effect of the inflow conditions on the self-similar region of a round jet. *Phys. Fluids*. **10**, 899-909.
- CABOT, W. & MOIN, P. 1996 Large eddy simulation of scalar transport with the dynamic subgrid-scale model. In *Simulation and modelling of turbulent flows*, (ed. Gatski T. B., M. Y. Hussaini, J. L. Lumley), Oxford University Press.
- CHEN, C. J. & RODI, W. 1980 *Vertical turbulent buoyant jets, a review of experimental data*. HMT, the science and applications of heat and mass transfer, vol. 4, Pergamon Press.

- CHORIN, A. J. 1968 Numerical solution of the Navier-Stokes equation. *Math. Comput.* **22**, 745-.
- FATICA, M., ORLANDI, P. & VERZICCO, R. 1994 Direct and large eddy simulations of round jets. In P. R. Voke *et al.*(eds), *Direct and Large-Eddy Simulation I*, Kluwer Academic Publishers. 49-60.
- FISCHER, H. B., LIST, E. J., KOH, R. C. Y., IMBERGER, J. & BROOKS, N. H. 1979 *Mixing in inland and coastal waters*. Academic Press.
- GERMANO, M., PIOMELLI, U., MOIN, P. & CABOT, W. H. 1991 A dynamic subgrid-scale eddy viscosity model. *Phys. Fluids*. **A3**, 1760-1765.
- GRESHO, P. M. 1991 Incompressible fluid dynamics: some fundamental formulation issues. *Ann. Rev. Fluid Mech.* **23**, 413-454.
- KIM, J. & MOIN, P. 1985 Application of a fractional-step method to incompressible Navier-Stokes equations. *J. Comp. Phys.* **59**, 308-323.
- LILLY, D. K. 1992 A proposed modification of the Germano subgrid-scale closure method. *Phys. Fluids*. **A4**, 633-635.
- LIST, E. J. 1982 Mechanics of turbulent buoyant jets and plumes. In W. Rodi (ed) *Turbulent buoyant jets and plumes*, HMT, the science and applications of heat and mass transfer, vol. 6, Pergamon Press. 1-68.
- LIU S., C. MENEVEAU AND J. KATZ 1994 Experimental study of similarity subgrid-scale models of turbulence in the far-field of a jet. In P.R. Voke *et al.* (eds), *Direct and Large-Eddy Simulation I*, Kluwer Academic Publishers. 37-48.
- MOIN, P., SQUIRES, K., CABOT, W. & LEE, S. 1991 A dynamic subgrid-scale model for compressible turbulence and scalar transport. *Phys. Fluids A*. **3**, 2746.
- PAPANTONIOU, D. & LIST, E. J. 1989 Large scale structure in the far field buoyant jets. *J. Fluid Mech.* **209**, 151-190.
- PIOMELLI, U. & CHASNOV, J. R. 1996 Large-eddy simulations: theory and applications. M. Hallbäck *et al.* (eds), *Turbulence and transition modelling*, Kluwer Academic Publishers. 269-336.
- RICOU, F. P. & SPALDING, D. B. 1961 Measurements of entrainment by axisymmetric turbulent jets. *J. Fluid Mech.* **11**, 21-32, (1961)
- RODI, W.(ED) 1982 *Turbulent buoyant jets and plumes*. HMT, the science and applications of heat and mass transfer, **6**, Pergamon Press.
- SHABIR, A. & GEORGE, W. 1994 Experiments on a turbulent buoyant plume. *J. Fluid Mech.* **275**, 1-32.
- TRITTON, D. J. 1988 *Phys. Fluid Dyn.* Clarendon Press.

Dynamic wall modeling for LES of complex turbulent flows

By Meng Wang

1. Motivation and objectives

Large-eddy simulation (LES) of wall-bounded flows becomes prohibitively expensive at high Reynolds numbers if one attempts to resolve the small but dynamically important vortical structures (streaks) in the near-wall region. The number of grid points required scales as the square of the friction Reynolds number (Baggett, Jiménez & Kravchenko 1997), which is nearly the same as for direct numerical simulation (DNS). To circumvent the severe near-wall resolution requirement, LES can be combined with a wall-layer model. In this approach, LES is conducted on a relatively coarse grid designed to resolve the desired outer flow scales. The dynamic effects of the energy-containing eddies in the wall layer (viscous and buffer regions) are determined from a wall model calculation, which provides to the outer flow LES a set of approximate boundary conditions, often in the form of wall shear-stresses. Wall models which supply wall stresses to the LES are also called wall stress models.

The simplest wall stress models are analogous to the wall functions commonly used in Reynolds-averaged Navier-Stokes (RANS) approaches except that they are applied in an instantaneous sense in time-accurate calculations. The wall function provides an algebraic relationship between the local wall stresses and the tangential velocities at the first off-wall velocity nodes. This approach was first employed in a channel flow simulation by Schumann (1975), who assumed that the streamwise and spanwise velocity fluctuations are in phase with the respective surface shear stress components. A number of modifications to Schumann's model have been made by, for example, Grötzbach (1987) and Werner & Wengle (1991) to eliminate the need for *a priori* prescription of the mean wall shear stress and to simplify computations, and by Piomelli *et al.* (1989) to empirically account for the phase shift between the wall stress and near-wall tangential velocity due to the tilting of near-wall eddies. See Cabot & Moin (2000) and Nicoud *et al.* (2000) and the references therein for a review of the various wall stress models.

The algebraic wall stress models mentioned above all imply the logarithmic (power) law of the wall for the mean velocity, which is not valid in many complex flows. To incorporate more physics into the model, wall stress models based on boundary layer approximations have been proposed in recent years (Balaras, Benocci & Piomelli 1996; Cabot 1995; Cabot & Moin 2000). In this method, turbulent boundary-layer equations are solved numerically on an embedded near-wall mesh to compute the wall stress. These equations are forced at the outer boundary by the tangential velocities from LES, while no-slip conditions are applied at the wall. The turbulent eddy viscosity is modeled by a RANS type model, such as the mixing-length model with wall damping. Reasonable success has been achieved in predicting attached flows and flows with fixed separation points, such as the backward facing step flow. Cabot & Moin (2000) found that, in the case of the backward facing step, improved solutions were obtained when the mixing-length eddy viscosity was lowered from the standard RANS value. A dynamic procedure was suggested to determine the suitable model coefficient.

The present work is concerned with the use of wall models in the LES of complex turbulent flows with strong favorable/adverse pressure gradients and incipient separation. The wall model based on turbulent boundary layer equations (Cabot & Moin 2000) is employed and extended to carry out LES of boundary layer flows past an asymmetric trailing-edge shown in Fig. 1. The results are compared with those from the full LES with resolved wall-layers (Wang & Moin 2000) and the experimental measurements of Blake (1975). In particular, we are interested in determining the predictive capabilities of this hybrid LES/wall-modeling approach for flow separation, surface pressure fluctuations, and aerodynamic noise.

It will be shown that the LES with wall modeling procedure can result in drastic savings in computational cost with minimal degradation of flow statistics compared with the fully resolved LES. The wall model based on boundary layer equations and dynamically adjusted eddy viscosity is considerably more superior to its simpler variants based on the instantaneous log law. A main objective of this article is to highlight the need for reducing the value of RANS eddy viscosity when it is used in the LES context, which has not been emphasized enough by Cabot & Moin (2000). We will show that this is important for all flows, particularly attached flows. A modified dynamic procedure is used to determine the mixing-length model coefficient, and the simulation results are found to be in very good agreement with those from the full LES.

2. Results

2.1. The trailing-edge flow

The flow configuration is shown in Fig. 1, which depicts contours of the mean streamwise velocity of turbulent boundary layer flows past an asymmetric trailing-edge as computed by Wang & Moin (2000) using standard LES with wall resolution. This trailing-edge flow was originally studied experimentally by Blake (1975). The chord Reynolds number is 2.15×10^6 , and the trailing-edge tip-angle is 25 degrees. In the numerical simulation, only the aft section (approximately 38% chord) of the model airfoil and the near wake are included in the computational domain, and the inlet Reynolds numbers based on the local momentum thickness and boundary-layer edge velocity are 2760 on the lower side and 3380 on the upper side. These values, obtained from an auxiliary RANS calculation, are used to duplicate the experimental conditions at the LES inflow station, although some questions remain concerning their fidelity. Details of the trailing-edge LES can be found in Wang & Moin (2000).

The complexity of the flow is best illustrated in Fig. 2, which plots the distributions of the mean pressure coefficient C_p (solid line) and skin-friction coefficient C_f ($\times 100$, dashed line) along the upper surface of the trailing-edge. Distributions along the lower surface, which is flat, resemble those of a flat plate boundary-layer and are thus not plotted. As the flow approaches the trailing-edge, it first experiences favorable pressure gradient, causing flow acceleration and increased skin friction. A region of adverse pressure gradient ensues, leading to flow deceleration and eventually unsteady separation. The skin friction decreases and becomes negative in the separated zone near the tip of the trailing-edge. It is worth noting that the discontinuous slope at the skin friction peak corresponds to the intersection of the flat surface with a circular arc (hence a discontinuity in surface curvature). Given the presence of strong favorable/adverse pressure gradients and flow separation, and the complex response of the skin friction, this flow provides a challenging test case to evaluate the predictive capabilities of wall models.

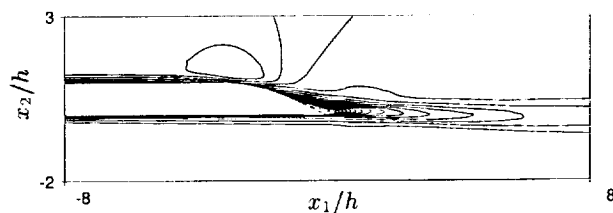


FIGURE 1. Boundary-layer flow past a trailing-edge. The contours (-0.081 to 1.207 with increment 0.068) represent the mean streamwise velocity normalized by the free-stream value (from Wang & Moin 2000).

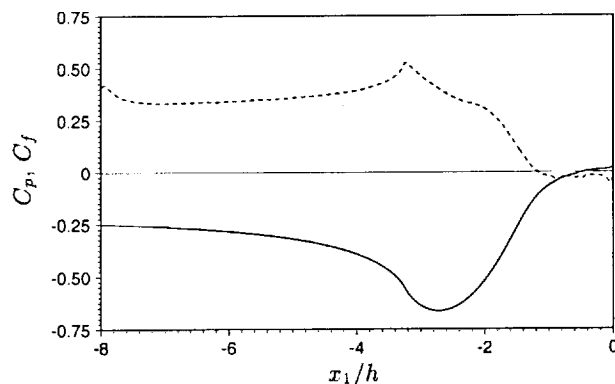


FIGURE 2. Distributions of the mean pressure and skin-friction coefficients along the upper surface: — C_p ; ---- $C_f \times 10^2$.

2.2. Simulation method

The same energy-conserving finite difference scheme with dynamic subgrid-scale (SGS) stress model used for the wall-resolved LES (Wang & Moin 2000) is employed. The computational domain is also identical to that of the full LES. It is of size $16.5h$, $41h$, and $0.5h$, where h denotes the airfoil thickness in the streamwise (x_1), wall-normal (x_2 or y), and spanwise (x_3) directions, respectively. The grid is coarsened to $768 \times 64 \times 24$, $1/6$ of the original number of points. The first off-wall velocity nodes (on staggered mesh) are located at the lower edge of the logarithmic layer ($x_2^+ \approx 60$ for u_2 and $x_2^+ \approx 30$ for u_1 and u_3) near the computational inlet. The new grid is chosen to resolve the desired flow scales in the outer layer and is thus not strongly dependent on the Reynolds number. The total reduction in CPU time, due to both the smaller number of grid points and larger time steps, is over 90% compared to the full LES.

Since the simulation does not resolve the viscous sublayer, approximate wall boundary conditions are needed. They are imposed in terms of wall shear stress components τ_{wi} ($i = 1, 3$) determined from wall models of the form (Balaras *et al.* 1996; Cabot & Moin 2000)

$$\frac{\partial}{\partial x_2} (\nu + \nu_t) \frac{\partial u_i}{\partial x_2} = F_i, \quad i = 1, 3, \quad (2.1)$$

where

$$F_i = \frac{1}{\rho} \frac{\partial p}{\partial x_i} + \frac{\partial u_i}{\partial t} + \frac{\partial}{\partial x_j} u_i u_j. \quad (2.2)$$

The eddy viscosity ν_t is obtained from a RANS type mixing-length eddy viscosity model

with near-wall damping (Cabot & Moin 2000):

$$\frac{\nu_t}{\nu} = \kappa y_w^+ \left(1 - e^{-y_w^+/A}\right)^2, \quad (2.3)$$

where $y_w^+ = y_w u_\tau / \nu$ is the distance to the wall in wall units (based on the local instantaneous friction velocity u_τ), κ is the model coefficient, and $A = 19$. The pressure in (2.2) is assumed x_2 -independent, equal to the value from the outer-flow LES solution. Eqs. (2.1) and (2.2) are required to satisfy no-slip conditions on the wall and match the outer layer solutions at the first off-wall LES velocity nodes: $u_i = u_{\delta i}$ at $x_2 = \delta$.

Two simpler variants of the above wall model, with $F_i = 0$ and $F_i = \frac{1}{\rho} \frac{\partial p}{\partial x_i}$, have been considered previously (Wang 1999). These two cases, called equilibrium stress balance models (without and with pressure gradient), are particularly easy to implement since (2.1) can be integrated to give a closed-form expression for τ_{wi} .

In the general case, however, the boundary layer equations (2.1)–(2.3) have to be solved numerically to obtain u_1 and u_3 , and hence τ_{w1} and τ_{w3} . They are integrated in time along with the outer flow LES equations, using the same numerical scheme (fractional step in combination with the Crank-Nicolson method for the diffusion term and third order Runge-Kutta scheme for convective terms). The wall-normal velocity component u_2 is determined from the divergence-free constraint. Note that no pressure Poisson equation is required since pressure is assumed constant in the wall-normal direction. The grid for wall layer computation coincides with the LES grid in the wall-parallel directions. In the direction normal to the wall, 32 points are distributed uniformly between the airfoil surface and the first off-wall velocity nodes for LES, with resolution of $\Delta x_2^+ \approx 1$ near the inlet. The computational cost for solving the boundary layer equations is insignificant compared with that for the outer layer LES because (1) there is no need to solve the x_2 -momentum equation and the pressure Poisson equation, and (2), more importantly, the equations are solved in locally orthogonal coordinates instead of the general curvilinear coordinates used for the LES.

2.3. The effect of model coefficient

A good indicator of wall model performance is the prediction of the mean skin friction coefficient, which is shown in Fig. 3. The simple stress balance models, with $F_i = 0$ and $F_i = \frac{1}{\rho} \frac{\partial p}{\partial x_i}$ (dashed and chain-dashed lines respectively) and $\kappa = 0.4$ (the von Kármán constant), predict well the skin friction coefficient C_f on the flat surfaces, but deviate significantly from the full LES solution (dotted line) downstream of the C_f peak, where the flow undergoes a favorable-to-adverse pressure gradient transition. This suggests that terms not included in the model, such as the convective terms, are important.

The skin friction coefficient computed using the full boundary layer equations (2.1)–(2.3) and the standard von Kármán constant $\kappa = 0.4$ shows improved qualitative trend (chain-dotted lines). However, the magnitude is overpredicted in most regions, particularly on the flat surface, by up to 20%. This overprediction can be explained as follows: If the streamwise component of (2.1) and (2.2) are integrated from the wall to $y = \delta$ and then time-averaged, one obtains

$$\bar{\tau}_{w1} = \mu \frac{\partial U_1}{\partial x_2} \Big|_{x_2=0} = \frac{\rho}{\int_0^\delta \frac{dy}{\nu + \nu_t}} \left\{ U_{\delta 1} - \frac{1}{\rho} \frac{\partial P}{\partial x_1} \int_0^\delta \frac{y dy}{\nu + \nu_t} - \int_0^\delta \frac{\int_0^y \frac{\partial}{\partial x_j} \bar{u}_1 \bar{u}_j dy'}{\nu + \nu_t} dy \right\}. \quad (2.4)$$

Note that to facilitate the analysis, ν_t has been treated as constant in the time-averaging as a first approximation. The first term in the curly brackets, which is always posi-

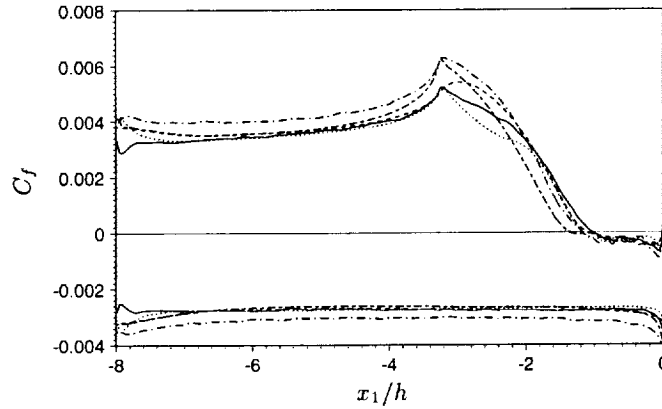


FIGURE 3. Distribution of the mean skin friction coefficient computed using LES with wall models given by (2.1). ---- $F_i = 0$; - - - $F_i = \frac{1}{\rho} \frac{\partial p}{\partial x_i}$; - · - $F_i = \frac{1}{\rho} \frac{\partial p}{\partial x_i} + \frac{\partial u_i}{\partial t} + \frac{\partial}{\partial x_j} u_i u_j$ and $\kappa = 0.4$; — $F_i = \frac{1}{\rho} \frac{\partial p}{\partial x_i} + \frac{\partial u_i}{\partial t} + \frac{\partial}{\partial x_j} u_i u_j$ and dynamic κ ; ····· full LES (no wall model).

tive, represents the wall shear stress from an equilibrium stress balance model without pressure gradient. The second term accounts for the mean pressure gradient effect, which contributes positively (negatively) to the wall shear stress under favorable (adverse) pressure gradient. The contribution from the nonlinear convective terms is represented by the last term in the brackets. This part, denoted by $\bar{\tau}_{w1}^c$, can be expanded to give

$$\bar{\tau}_{w1}^c = -\frac{\rho}{\int_0^\delta \frac{dy}{\nu + \nu_t}} \left\{ \int_0^\delta \frac{1}{\nu + \nu_t} \frac{\partial}{\partial x_1} \int_0^y \overline{u_1^2} dy' dy + \int_0^\delta \frac{\overline{u_1 u_2}}{\nu + \nu_t} dy \right\}. \quad (2.5)$$

The first term in (2.5) vanishes if the flow is homogeneous in the streamwise direction, such as in a turbulent channel flow. In the case of a flat-plate boundary layer with zero pressure gradient, it makes a positive, albeit small, contribution to the wall shear stress due to the thickening of the boundary layer. The dominant contribution to $\bar{\tau}_{w1}^c$ comes from the second term, which is positive for a flat plate boundary layer.

Thus we have shown mathematically that, at least on the flat section of the airfoil, the inclusion of the nonlinear terms in the wall model equation increases the wall stress, causing the overprediction shown in Fig. 3 if contributions from other terms in (2.4) are not altered. To offset this increase, the only option is to reduce the turbulent eddy viscosity ν_t and hence the multiplication factor before the curly brackets in (2.4). This mainly affects the equilibrium part of the wall stress (first term inside the brackets). The pressure-gradient and nonlinear parts of the wall stress are insensitive to ν_t because it appears both inside and outside the brackets with opposite effects.

The physical explanation for requiring lower ν_t , as pointed out by Cabot & Moin (2000), is the fact that the Reynolds stress carried by the nonlinear terms in the boundary layer equations is significant. Hence, instead of modeling the total stress as in typical RANS calculations, the eddy-viscosity model is expected to account for only the unresolved part of the Reynolds stress. Cabot & Moin (2000) suggested to compute the model coefficient dynamically by matching the stresses between the inner layer (wall model) and outer layer (LES) solutions. In the present case, since the horizontal grid is the same for both the LES and wall model calculations, and because the velocities are matched at the edge of the wall layer, the resolved portions of the nonlinear stresses from the

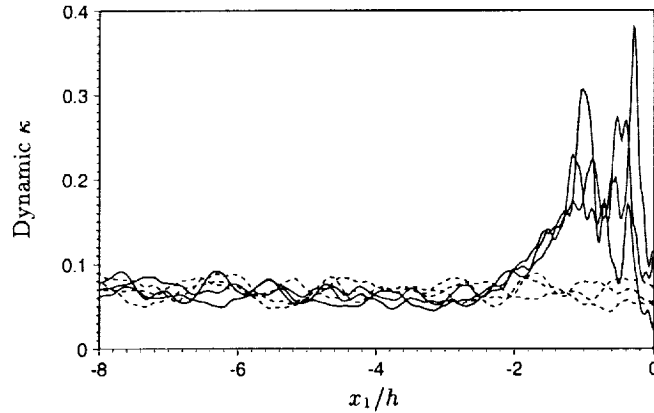


FIGURE 4. Dynamic κ for the mixing-length eddy viscosity model at three time instants. — upper side; ---- lower side.

inner and outer layer calculations are the same. To match the unresolved portions of the stresses approximately, we equate the mixing-length eddy viscosity to the SGS eddy viscosity at the matching points, $\langle \nu_t \rangle = \langle \nu_{sgs} \rangle$, from which the model coefficient κ is extracted using (2.3). The averaging denoted by the angular brackets is performed in the spanwise direction as well as over the previous 150 time steps to obtain reasonably smooth data. One difficulty with this method is that ν_{sgs} is poorly behaved at the first off-wall velocity nodes because the velocities at the wall are not well defined (we used slip velocities extrapolated from the interior nodes to compute the strain rate tensor and ν_{sgs}). As a practical matter, the matching points for eddy viscosities are moved to the second layer of velocity nodes from the wall instead.

The dynamically computed κ at three time instants are exemplified in Fig. 4, where the solid lines represent those on the upper side and dashed lines on the lower side. They are found to be only a small fraction of the standard value of 0.4. This figure indicates that on average, on the flat surfaces, only less than 20% of the Reynolds stress is modeled by the mixing-length eddy viscosity. The rest is directly accounted for by the nonlinear terms in the wall layer equations. By using the reduced, variable model coefficient κ , the computed skin friction coefficient is much improved, as demonstrated by the solid line in Fig. 3. This modeling approach gives the best overall agreement with the results of the resolved LES compared with other wall models tested.

2.4. Comparisons with full LES solutions

Comparisons of the velocity predictions using the wall modeling approach described above and those from the full LES (Wang & Moin 2000) show very good agreement. In Fig. 5 the velocity magnitude, defined as $U = (U_1^2 + U_2^2)^{1/2}$ and normalized by its value U_e at the boundary-layer edge, is plotted as a function of the vertical distance to the upper surface, at (from left to right) $x_1/h = -3.125, -2.125, -1.625, -1.125, -0.625$, and 0 (trailing-edge). With the exception of the trailing-edge point, these locations correspond to the measurement stations in Blake's (1975) experiment. The mean velocity profiles obtained with wall modeling (solid lines) agree extremely well with the full LES profiles (dashed lines) at all stations, including those in the separated region which starts at $x_1/h = -1.125$. The agreement between both computational solutions and the experimental data

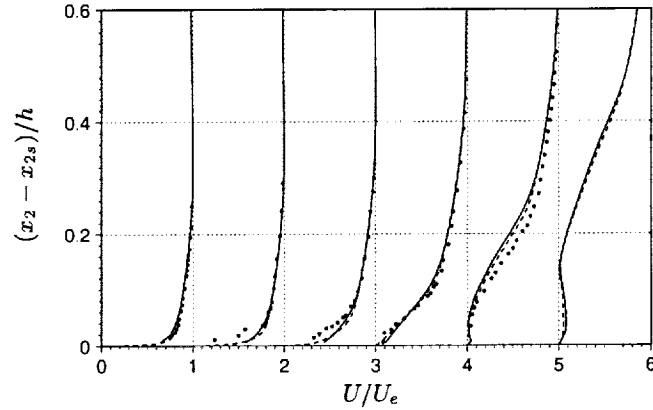


FIGURE 5. Profiles of the normalized mean velocity magnitude as a function of vertical distance to the upper surface, at (from left to right) $x_1/h = -3.125, -2.125, -1.625, -1.125, -0.625,$ and 0 (trailing-edge). — LES with wall model; ---- full LES; • Blake's experiment.

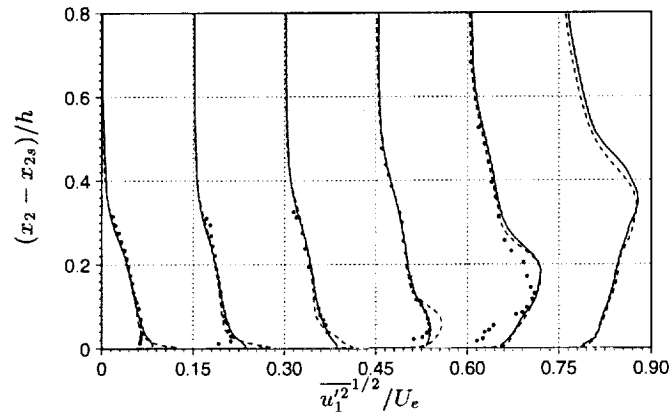


FIGURE 6. Profiles of the rms streamwise velocity fluctuations as a function of vertical distance from the upper surface, at (from left to right) $x_1/h = -4.625, -2.125, -1.625, -1.125, -0.625,$ and 0 (trailing-edge). — LES with wall model; ---- full LES; • Blake's experiment.

is also reasonable, and the potential reasons for the observed discrepancies have been discussed by Wang & Moin (2000).

Fig. 6 depicts the profiles of the rms streamwise velocity fluctuations at (from left to right) $x_1/h = -4.625, -2.125, -1.625, -1.125, -0.625,$ and 0. Again, excellent agreement between the present solutions and those of the full LES is observed, with the notable exception at $x_1/h = -1.125$, where the wall model solution agrees (perhaps fortuitously) better with the experiment. It should be pointed out that the LES/wall-modeling predictions shown in Figs. 5 and 6 are significantly more accurate, judging from comparisons with the full LES data, than those reported by Wang (1999) using the simpler equilibrium stress balance models.

In Fig. 7 the mean streamwise velocity profiles (normalized by free-stream velocity U_∞) are compared at select near-wake stations $x_1/h = 0, 0.5, 1.0, 2.0,$ and 4.0. The solid lines are obtained from the present simulation, and the dashed lines are from the full LES. The corresponding rms streamwise velocity fluctuations are depicted in Fig. 8. The

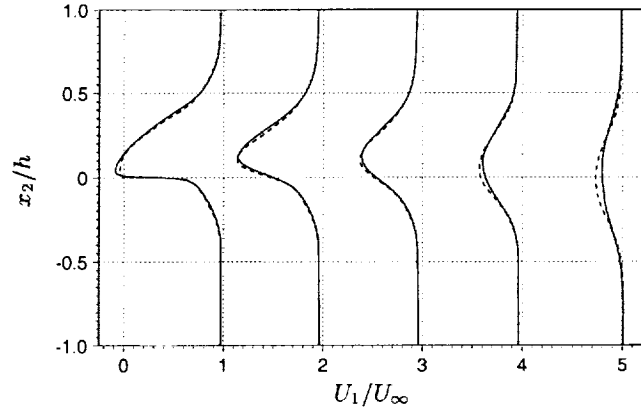


FIGURE 7. Profiles of the normalized mean streamwise velocity in the wake, at (from left to right) $x_1/h = 0, 0.5, 1.0, 1.5, 2.0,$ and 4.0 . — LES with wall model; ---- full LES.

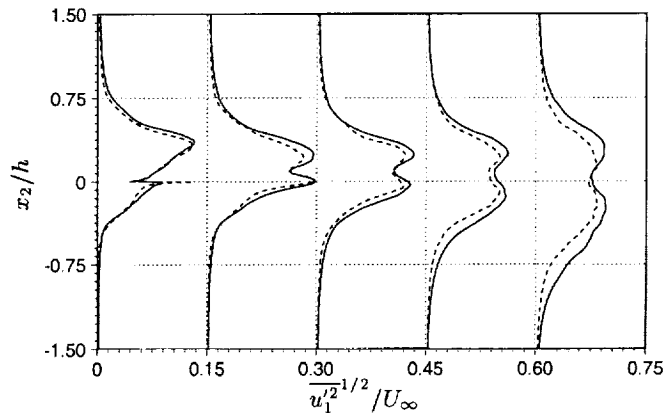


FIGURE 8. Profiles of the rms streamwise velocity fluctuations in the wake, at (from left to right) $x_1/h = 0, 0.5, 1.0, 1.5, 2.0,$ and 4.0 . — LES with wall model; ---- full LES.

agreements between the LES solutions with and without wall modeling are good near the trailing-edge and deteriorate gradually in the downstream direction. This is caused by the much reduced grid resolution in the case of LES with wall modeling. The grid has been coarsened by the same factor in the wake as in the wall bounded region, even though the wall model does not play a role there. Apparently, this has caused insufficient grid resolution, particularly in the streamwise and spanwise directions.

Finally, Fig. 9 depicts the frequency spectra of surface pressure fluctuations obtained from LES in conjunction with the wall model and compares them with those from the full LES and Blake's experiment. The variable q_∞ used in the normalization is the dynamic pressure, defined as $\rho U_\infty^2/2$. Relative to the experimental data, the pressure spectra from the simulation employing the wall model are of comparable accuracy as those from the full LES, although the resolvable frequency ranges are narrower due to the coarser grid. However, relative to the full LES spectra, the spectral levels are somewhat overpredicted, particularly in the attached flow region (parts (a)–(c) of the figure). This phenomenon has also been observed previously in channel flow LES with wall models. The discrepancies, as pointed out by Wang (1999), may be attributable to the approximation of wall pressure

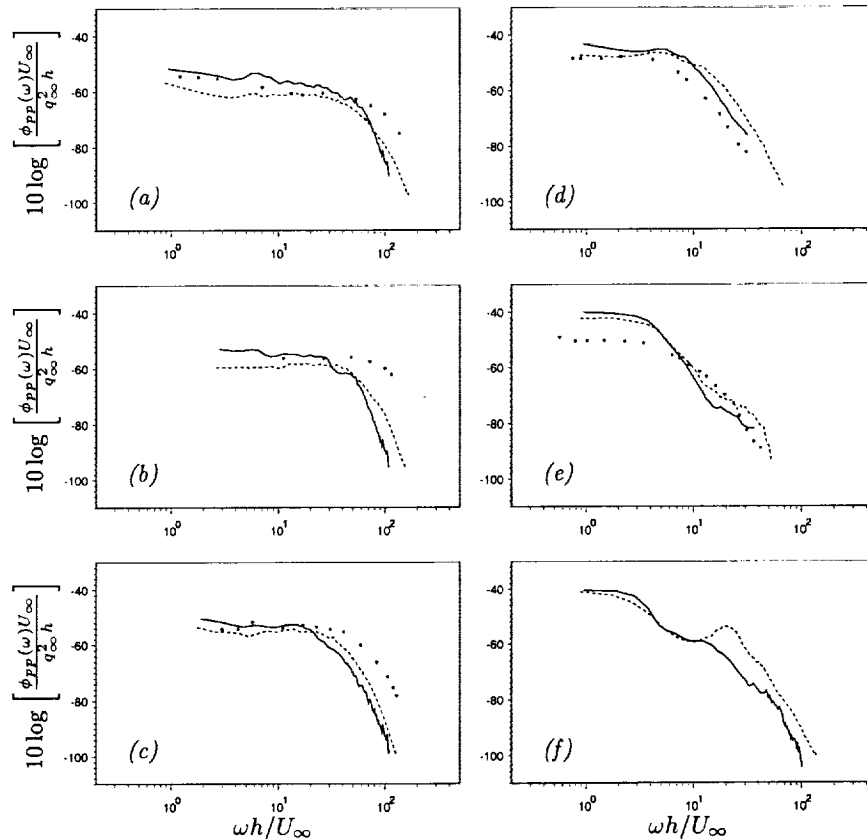


FIGURE 9. Frequency spectra of pressure fluctuations on the upper surface at $x_1/h =$ (a) -3.125 , (b) -2.125 , (c) -1.625 , (d) -1.125 , (e) -0.625 , and (f) 0 (trailing-edge). — LES with wall model; ---- full LES; • Blake's experiment.

by the cell-centered values adjacent to the wall and the fact that in the present LES formulation the “pressure” actually contains the subgrid-scale kinetic energy. The latter is negligibly small at the first off-wall pressure node if the wall layer is resolved but may not be negligible in the present case because of the coarse mesh. This issue needs to be examined in future investigations.

3. Conclusions and future work

In summary, we have developed a numerical procedure using a combination of LES with wall modeling for simulating complex wall-bounded flows. It is demonstrated that when a RANS type eddy viscosity is used in wall-layer equations that contain nonlinear convective terms, its value must be reduced to account for only the unresolved part of the Reynolds stress. A dynamically adjusted wall-model eddy viscosity is employed in the LES of turbulent boundary layer flows past an asymmetric trailing-edge. The method is shown to predict low-order velocity statistics in very good agreement with those from the full LES and at less than 10% of the original computational cost. In particular, the unsteady separation near the trailing-edge is predicted correctly. This cost-effective approach will be very useful for simulating the high Reynolds number trailing-edge ex-

periment currently underway in the Navy's large cavitation channel (Bourgoyne, Ceccio & Dowling 2000) and for shape optimization in order to achieve passive noise control. The latter two items are among the planned activities as an extension of the present trailing-edge aeroacoustics project. In addition, we will continue to develop improved approximate wall boundary conditions for LES applications and critically evaluate their impact on the predictions of unsteady surface pressure and radiated noise.

Acknowledgments

This research was supported by ONR Grant N00014-95-1-0221. We would like to thank P. Bradshaw, W. Cabot, and J. Jiménez for valuable discussions during the course of this work.

REFERENCES

- BAGGETT, J. S., JIMÉNEZ, J. & KRAVCHENKO, A. G. 1997 Resolution requirements in large-eddy simulations of shear flows. *Annual Research Briefs*, Center for Turbulence Research, NASA Ames/Stanford Univ. 51-66.
- BALARAS, E., BENOCCHI, C. & PIOMELLI, U. 1996 Two-layer approximate boundary conditions for large-eddy simulation. *AIAA J.* **34**, 1111-1119.
- BLAKE, W. K. 1975 *A Statistical Description of Pressure and Velocity Fields at the Trailing Edge of a Flat Strut*. DTNSRDC Report 4241, David Taylor Naval Ship R & D Center, Bethesda, Maryland.
- CABOT, W. 1995 Large-eddy simulations with wall-models. *Annual Research Briefs*, Center for Turbulence Research, NASA Ames/Stanford Univ. 41-50.
- CABOT, W. & MOIN, P. 2000 Approximate wall boundary conditions in the large-eddy simulation of high Reynolds number flow. *Flow Turb. Combust.* **63**, 269-291.
- BOURGOYNE, D., CECCIO, S. & DOWLING, D. 2000 Hydrofoil trailing-edge hydrodynamics at high Reynolds numbers. *ONR Turbulence and Wake Review 2000*, Tucson, Arizona.
- GRÖTZBACH, G. 1987 Direct numerical and large eddy simulation of turbulent channel flows. In *Encyclopedia of Fluid Mechanics*, Cheremisinoff, N. P. ed., Gulf Pub. Co., Chap. 34. 1337-1391.
- NICOUD, F., BAGGETT, J. S., MOIN, P. & CABOT, W. 2000 LES wall modeling based on suboptimal control theory. To appear in *Phys. Fluids*.
- PIOMELLI, U., FERZIGER, J., MOIN, P. & KIM, J. 1989 New approximate boundary conditions for large eddy simulations of wall-bounded flows. *Phys. Fluids*. **1**, 1061-1068.
- SCHUMANN, U. 1975 Subgrid scale model for finite difference simulations of turbulent flows in plane channels and annuli. *J. Comp. Phys.* **18**, 376-404.
- WANG, M. 1999 LES with wall models for trailing-edge aeroacoustics. *Annual Research Briefs*, Center for Turbulence Research, NASA Ames/Stanford Univ. 355-364.
- WANG, M. & MOIN, P. 2000 Computation of trailing-edge flow and noise using large-eddy simulation. *AIAA J.* **38**, 2201-2209.
- WERNER, H. & WENGLE, H. 1991 Large eddy simulation of turbulent flow over and around a cube in a plane channel. In *Proc. Eighth Symp. Turb. Shear Flows*. 1941-1946.

Flow in an impeller stirred tank using an immersed boundary method

By R. Verzicco[†], G. Iaccarino, M. Fatica AND P. Orlandi[‡]

1. Motivation and objectives

The present study is concerned with the flow induced by an impeller in a cylindrical tank. Although this is a model problem, it is relevant to many chemical and food-industry technological processes. In the last decade significant effort has been devoted to simulate and predict such flows since full-scale testing is very expensive and considerable savings could be achieved if reliable numerical models could predict the performance of prototypes.

Despite the relatively simple geometries and the low Reynolds numbers involved, the simulation of these turbulent flows is considerably challenging. Some of the difficulties encountered are the strongly inhomogeneous nature of the turbulence, the small surface of the impeller blades, and the large disparity in time and length of flow scales. In particular, given the short blade lengths, the boundary layers developing on their surfaces will not be fully developed; therefore, all turbulence models based on wall functions would give inaccurate results. In addition, RANS models, even when implemented in the unsteady form, are unlikely to capture all of the time scales ranging from that of the vortex shedding at the blade tips to the large scale meridional circulation induced in the tank.

DNS and LES approaches, in contrast, do not suffer from the abovementioned problems although they are more computationally expensive, especially when applied to complex geometry flows. However, in a recent paper by Verzicco *et al.*, (2000), it has been shown that the combination of the “immersed boundary” (IB) procedure with DNS and LES simulations can efficiently be used for the accurate prediction and analysis of many technologically relevant flows. In particular, since the presence of complex boundaries is mimicked by body forces, the simulations are, in fact, carried out on “simple grids”, thus taking advantage of the efficiency and accuracy of optimized solution procedures. IB/DNS simulations of complex-geometry turbulent-flows can be carried out with 1-2 million gridpoints on a PC with CPU times ranging between a few hours and a few days.

In this paper we will show some examples of these simulations for an impeller-stirred cylindrical tank, and the results will be compared with experiments and RANS simulations.

2. Physical problem and numerical set-up

The flow investigated in this study is intended to reproduce one of the experiments by Dong *et al.*, (1994). It consists of a cylindrical unbaffled tank stirred by an impeller rotating at constant velocity Ω at mid-height of the tank. The impeller has 8 blades equispaced over the whole azimuthal span. A sketch of the device is given in Fig. 1 where all the lengths have been scaled with the blade radius, which is $R = 1.25\text{cm}$. The

[†] DIMeG, Politecnico di Bari, Via Re David, 200, 70125, Bari, Italy.

[‡] DMA, Università di Roma, “La Sapienza”, Via Eudossiana, 18, 00184, Roma, Italy

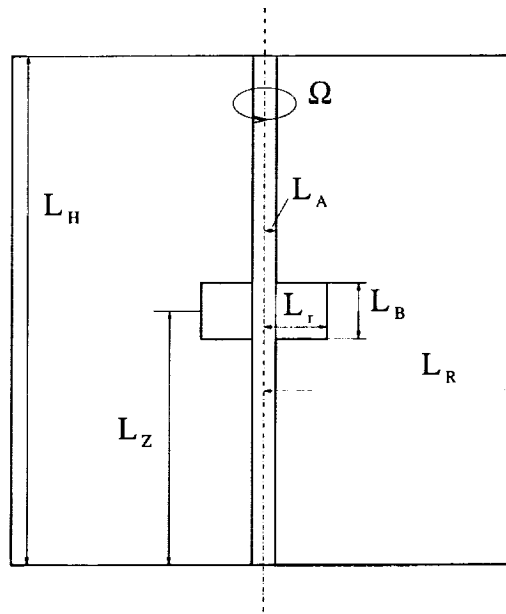


FIGURE 1. Sketch of the mixer geometry: $L_r = 1$, $L_B = 0.8$, $L_A = 0.32$, $L_R = 4$, $L_Z = 4$ and $L_H = 8$.

impeller rotation speed is $\Omega = 100\text{rpm}$, and the working fluid is water ($\nu = 10^{-6}\text{m}^2/\text{s}$), thus yielding a Reynolds number $Re = \Omega R^2/\nu = 1636$.

For the numerical solution of the flow, the Navier-Stokes equations are solved in a frame of reference fixed with the impeller and therefore rotating with constant angular velocity Ω . When scaled with the velocity $U = \Omega R$ and the length $L = R$, the equations in the rotating frame read:

$$\frac{D\mathbf{u}}{Dt} = -\nabla p - \frac{1}{Ro} \hat{\Omega} \times \mathbf{u} + \frac{1}{Re} \nabla^2 \mathbf{u} + \mathbf{f}, \quad \nabla \cdot \mathbf{u} = 0, \quad (2.1)$$

with $Ro = 1/2$, $\hat{\Omega}$ the unit vector directed as the impeller rotation vector, and \mathbf{f} a body force to be described later. In this frame of reference the lateral cylindrical wall of the tank has an azimuthal velocity $V_\theta(L_R) = -\Omega L_R$ while the lower horizontal no-slip surface moves according to $V_\theta(r) = -\Omega r$ with r the radial coordinate.

The computational domain is discretized by a mesh which is nonuniform in the radial and axial directions in such a way as to cluster the gridpoints in the blade region and close to the no-slip surfaces (Fig. 2). The mesh is uniform in the azimuthal direction.

An important aspect of this study was the initialization of the simulation. In the experiments, in fact, it has been observed that starting from rest, the flow needs from 5 to 10 minutes to attain a statistically stationary configuration which corresponds to 500 to 1000 impeller revolutions. In the present DNS simulation each revolution is discretized by about 300 time steps, thus requiring $3 \cdot 10^5$ time steps for the initial transient to be exhausted. This computational overhead is clearly unacceptable since it would require, on the finest grid, more CPU hours than the useful part of the simulation. Several strategies have been followed in order to reduce the computation of the transient, and they were only partially successful. The most straightforward approach consisted of several simulations starting from a very coarse grid with a progressive refinement via succes-

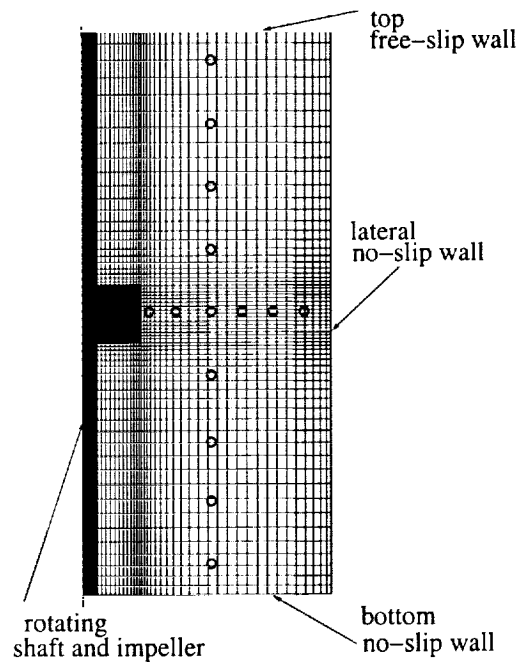


FIGURE 2. Example of grid in a meridional plane and boundary conditions (only one every 6 grid-points are shown). Open circles indicate the position of numerical probes used for the flow analysis.

sive interpolations. The initial flow evolution was obtained by simulating only $1/8^{\text{th}}$ of azimuthal domain and, therefore, only one impeller blade; the field was then replicated in such a way to reproduce the whole impeller. Unfortunately, the adjustments of the solutions from one grid to another introduced additional transients that turned out to be also time consuming. As an alternative we tried to start from a low-Reynolds coarse-grid flow and to increase grid and Reynolds number together. However, in this case the flow adjustment was very slow as well, and almost a total of 500 impeller revolutions were necessary to attain a developed flow field. Most of the transient, however, was simulated over coarse grids; therefore, the total CPU time was equivalent to 40 impeller revolutions on the finest grid.

The boundary body force \mathbf{f} of Eq. (2.1) is prescribed at each time step to establish the desired velocity \mathbf{V}_b on an arbitrary surface that need not coincide with the grid. The time-discretized version of Eq. (2.1a) can be written as,

$$\mathbf{u}^{n+1} - \mathbf{u}^n = \Delta t(RHS + \mathbf{f}), \quad (2.2)$$

where Δt is the computational time step, RHS contains the nonlinear, pressure, and viscous terms, and the superscript denotes the time-step level. To impose $\mathbf{u}^{n+1} = \mathbf{V}_b$, the body force \mathbf{f} must be,

$$\mathbf{f} = -RHS + \frac{\mathbf{V}_b - \mathbf{u}^n}{\Delta t}, \quad (2.3)$$

in the flow region where we wish to mimic the solid body and zero elsewhere. In general, the surface of the region where $\mathbf{u}^{n+1} = \mathbf{V}_b$ does not coincide with a coordinate line. In that case, the value of \mathbf{f} at the node closest to the surface but outside the solid body is linearly interpolated between the value that yields \mathbf{V}_b inside the solid body and the

value in the interior of the flow domain. This interpolation procedure is consistent with the centered second-order finite-difference approximation, and the overall accuracy of the scheme remains second-order (Fadlun *et al.*, (2000)).

Equations (1) have been spatially discretized in a cylindrical coordinate system using staggered central second-order finite-difference approximations. Details of the numerical method are given in Verzicco & Orlandi, (1996); only the main features are summarized here. In a three-dimensional inviscid flow without immersed boundaries and free-slip condition, kinetic energy is conserved, and this feature is retained in the spatially discretized equations.

The discretized system is integrated in time using a fractional-step method where the viscous terms are computed implicitly and the convective terms explicitly. The large sparse matrix resulting from the implicit treatment is inverted by an approximate factorization technique. At each time step the momentum equations are provisionally advanced using the pressure at the previous time step, giving an intermediate non-solenoidal velocity field. A scalar quantity Φ then is introduced to project the non-solenoidal field onto a solenoidal one. The large-band matrix associated with the elliptic equation for Φ is reduced to a penta-diagonal matrix using trigonometric expansions (FFT's) in the azimuthal direction; this matrix is inverted using the FISHPACK package (Swartzrauber, (1974)). A hybrid low-storage third-order Runge-Kutta scheme is used to advance the equations in time, and the body-forces are enforced at each stage of the Runge-Kutta scheme. It is worth noting that application of \mathbf{f} , in fact, does not require the computation of extra terms, but rather the cancellation of pre-existing ones. As a matter of fact, the integration of the equations with the body forces only takes 5% more CPU time than in absence of the forcing.

The simulation of the flow inside mixing devices is usually performed using RANS modeling owing to their reduced computational cost. Since one aim of the present paper is to compare the performance of DNS/LES *vs* RANS models, we have also performed a couple of RANS simulations of the flow previously described. Steady RANS equations in a frame rotating with the impeller are solved on a $1/8^{\text{th}}$ sector of the tank using a commercial CFD code. Periodicity conditions are imposed in the azimuthal direction. Low-Reynolds number turbulence models have been used, namely the $k - \epsilon$ by Launder & Sharma (1974) and the V2F model by Durbin, (1995).

3. Results

Several preliminary simulations were performed to investigate the mesh distribution and grid resolution, the necessity for a turbulence model, possible effects of the upper free-surface deformation, and how many blades of the impeller had to be simulated. Concerning the first point, grids ranging from 5×10^5 to 1.9×10^6 gridpoints have been used in order to assess the reliability and grid independence of the results.

The need for turbulence modeling has been verified by running an identical case with and without sub-grid-scale model. Given the operational conditions of the test, the Reynolds number is quite small ($Re = 1636$) and direct numerical simulation (DNS) is possible. Consistently, a simulation with the dynamic subgrid scale large eddy simulation (LES) model yielded results almost coincident with those of the DNS with a turbulent viscosity close to zero. It must be noted, however, that DNS is possible only for the present "simplified" model problem in which geometrical dimensions and rota-

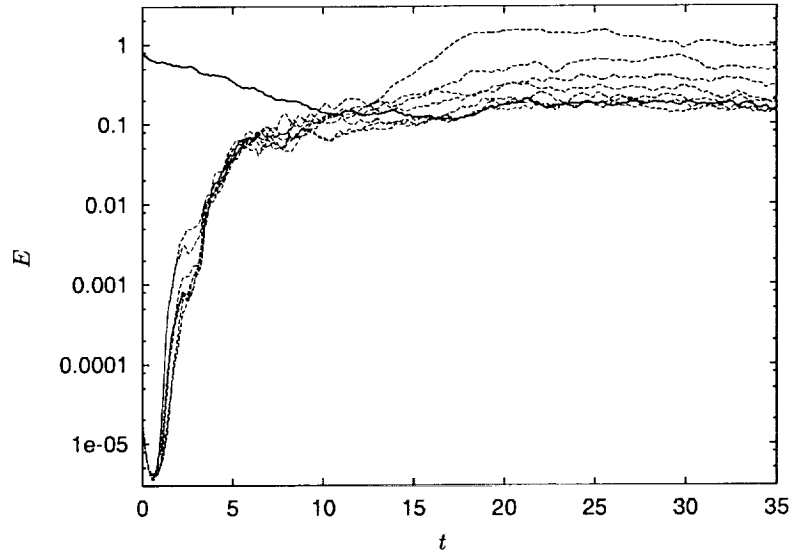


FIGURE 3. Time evolution of the kinetic energy of azimuthal modes starting from a simulation on $1/8^{\text{th}}$ of the domain and 1 impeller blade: — $n = 8$ mode, ---- all modes from $n = 1$ to $n = 7$. Note that time has been rescaled so that each time unit corresponds to one rotation period of the impeller.

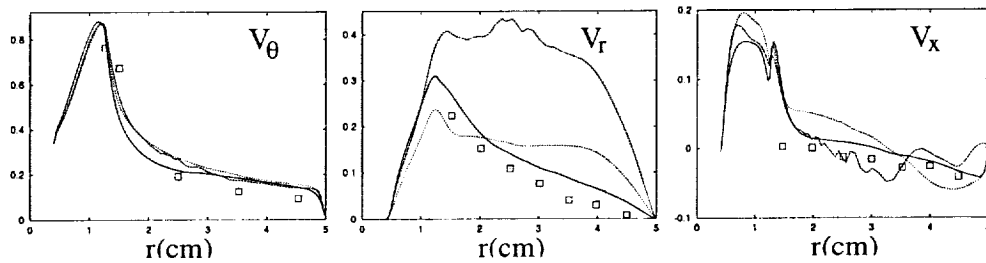


FIGURE 4. Averaged radial velocity profiles in a section crossing the impeller ($x = 4$). *Left* azimuthal velocity, *Center* radial velocity, *Right* axial velocity: ---- simulation on $1/8^{\text{th}}$ of the domain (1 blade), $1/4^{\text{th}}$ of the domain (2 blades), — whole domain, symbols are experimental data of Dong *et al.*, (1994).

tion speed are both small. In contrast, for the simulation of practical cases, operational conditions are more severe and the use of a turbulence model would be mandatory.

Free-surface deformation is induced by the azimuthal rotation and the resulting hydrostatic and centrifugal forces at the interface between fluid and air. This deformation is often disregarded in numerical simulations, and the upper boundary of the tank is modeled by a flat free-slip wall. This strategy was also followed in the main case presented in this report. However, a few remarks about the free-surface effects are in order. Assuming that the bulk of the flow is in solid body rotation, the shape of the free-surface would be given by $z = \Omega^2 r^2 / (2g)$, which for the present flow conditions yields a maximum deformation $\Delta z \simeq 1.4 \text{ cm}$. This displacement is larger than the blade radius; therefore, it is in principle possible that the results would be changed by this additional effect. In one case the free-surface deformation has been modeled by the same body forces used for

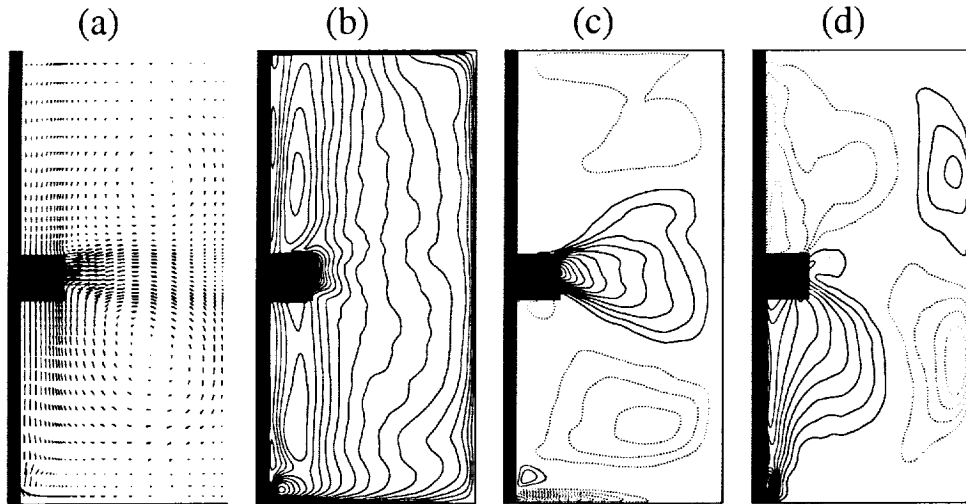


FIGURE 5. Averaged velocity fields: (a) velocity vector field, contours of: (b) azimuthal, (c) radial, (d) axial velocity components ($\Delta u = \pm 0.025$).

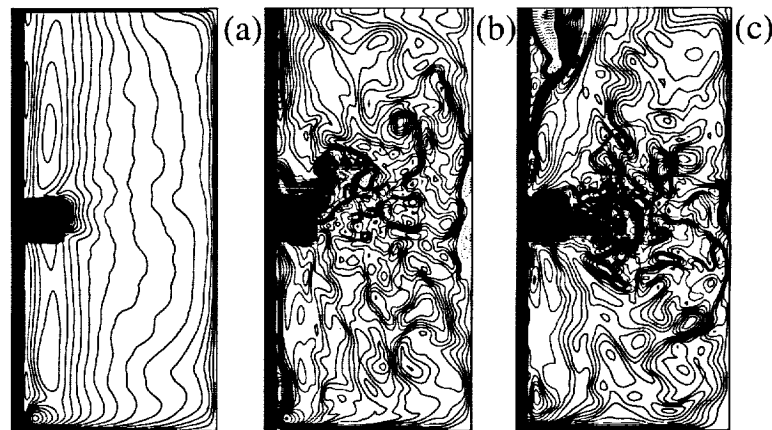


FIGURE 6. Comparison between averaged (a) and instantaneous (b), (c) velocity fields: velocity magnitudes are shown, (section passing through the blade), ($\Delta u = 0.05$)

the rotating impeller (and therefore rotating with the same angular velocity) with the results being only slightly modified by this new effect (and only in the region close to the upper surface). We will see that, in fact, the flow rotates much slower than a solid-body rotation; therefore, the free-surface deformation would be smaller than previously estimated. This implies that the approximation of the upper surface as a flat, stress-free boundary is indeed appropriate.

Since the impeller consists of 8 equispaced blades, it is tempting, for computational purposes, to reduce the domain to $1/8^{\text{th}}$ of the tank and only one blade; this assumption yields a considerable reduction of computational effort. Nevertheless, it must be noted that on a domain reduced to $1/8^{\text{th}}$ of the azimuthal span, only structures with 8-fold symmetry and multiples can be supported. This prevents the development of modes smaller than 8 and of all the modes which are not multiples of 8. We have verified by

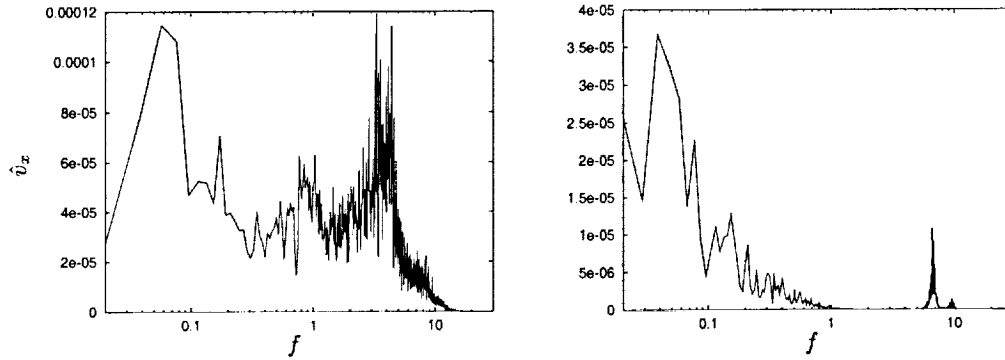


FIGURE 7. Frequency spectra of the axial velocity component for the probes at $(r = 2, x = 4)$ (Left) and $(r = 2, x = 2)$ (Right). The probes are, respectively, in the radial jet emanating from the impeller and in the center of the lower meridional recirculation. Note that the frequencies in the abscissa have been rescaled so that $f = 1$ corresponds to the rotation period of the impeller.

simulations which included one or two impeller blades, and therefore on $1/8^{\text{th}}$ and $1/4^{\text{th}}$ of the domain, respectively, that this assumption is not appropriate for the present problem and that the results were significantly different from the experiments. The inadequacy of the simulation on $1/8^{\text{th}}$ of the domain is confirmed also by Fig. 3 showing the time evolution of the azimuthal energy modes for a simulation over the whole domain but initiated from a simulation performed over a $1/8^{\text{th}}$ sector. We can see that the energy in the $n = 8$ mode slowly decreases in time while the lower modes experience an exponential growth and after saturation attain an energy comparable or bigger than the original mode. This shows that the 8-fold symmetry was only an artifact of the computational domain while the system would tend to distribute the energy also among odd and low-order modes. This point is further stressed by the velocity profiles shown in Fig. 4 where it is shown that the radial velocity is severely overpredicted in the simulation over $1/8^{\text{th}}$ of the domain. This overprediction is less evident when the simulation is extended over two impeller blades while the best results are obtained for the whole domain. It is worth mentioning that the prediction of the azimuthal velocity profiles is as accurate as in Fig. 4 for all the radial sections, and it is independent of whether a section or the whole domain is simulated. Radial and axial velocity profiles, in contrast, are much more sensitive to the azimuthal extension of the domain, and this point will be further discussed when comparing the DNS with RANS results. From the above results it is concluded that, in order to get accurate simulations, it is not possible to reduce the domain using impeller symmetries, but the whole problem must be solved.

We shall now describe the results of the DNS simulation simulation and compare it with the available experimental and RANS data. In Fig. 5 we report the computed mean field, averages being performed in the azimuthal direction and in time.

It is evident that the meridional plane is roughly divided into two halves by the radial jet emanating from the impeller. It can be noted, however, that the two recirculations are not symmetric owing to the different boundary conditions on the upper and lower horizontal surfaces. An important effect of the lower no-slip wall is the strongly positive vertical velocity in the lower half of the domain in the region close to the shaft (Fig. 5d). This effect is characteristic of wall-bounded rotating flows and is known as ‘Eckman-pumping’; it causes the fluid to be pushed radially inward at the plate (Fig. 5c) and

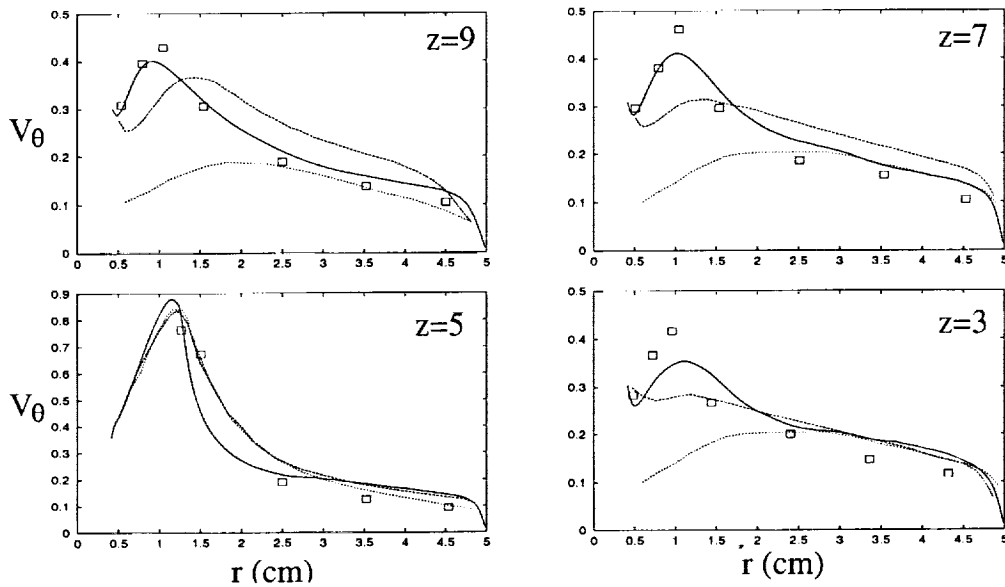


FIGURE 8. Radial profiles of averaged azimuthal velocity at different heights in the tank: — present DNS results, ---- RANS simulation with the V2F model, RANS simulation with $k - \epsilon$ model, Symbols are experiment by Dong *et al.* (1994). The radial coordinate is in centimeters and the azimuthal velocity is scaled by the blade tip velocity. (The values of z are in tenth of the tank height).

axially upward at the axis of rotation (Fig. 5d). Because of mass conservation, a vertical ascending fluid column at the axis induces a descending current at the external radial wall, thus reinforcing the lower-half recirculation with respect to the upper one. This is also well evidenced by the radial jet that does not point exactly in the radial direction, but rather has a positive vertical velocity close to the blade region and then a weakly negative vertical velocity.

In Fig. 6 instantaneous snapshots analogous to those of Fig. 5 are reported and compared with an averaged field, thus confirming the strongly unsteady nature of the flow. This point is further stressed by the analysis of the velocity signals taken from the numerical probes whose positions are reported in Fig. 2. Spectra are computed from the temporal series and are plotted in semi-log axes in order to separate the frequency peaks due to coherent motion from the background turbulence (Fig. 7). It can be noticed that many widely separated frequencies are present, and these range from the slow dynamics due to the precession and meridional oscillation of the large-scale recirculation to the fast vortex shedding at the blade tips[†]. Given the different time-scales of the described flow phenomena, it is very difficult for the RANS models to correctly parameterize all of the flow fluctuations, and this is confirmed by the velocity profile results.

Radial profiles of azimuthal, radial, and vertical velocity components are compared with experimental data and RANS simulations in Figs. 8, 9, and 10. The DNS prediction for the azimuthal velocity component is quite accurate, in particular in the region near the shaft above and below the impeller where a peak is observed. This is due to the large

[†] Note that in the spectra, the peak corresponding to the period of revolution of the impeller is missing because the equations are solved in a frame of reference rotating with the blade.

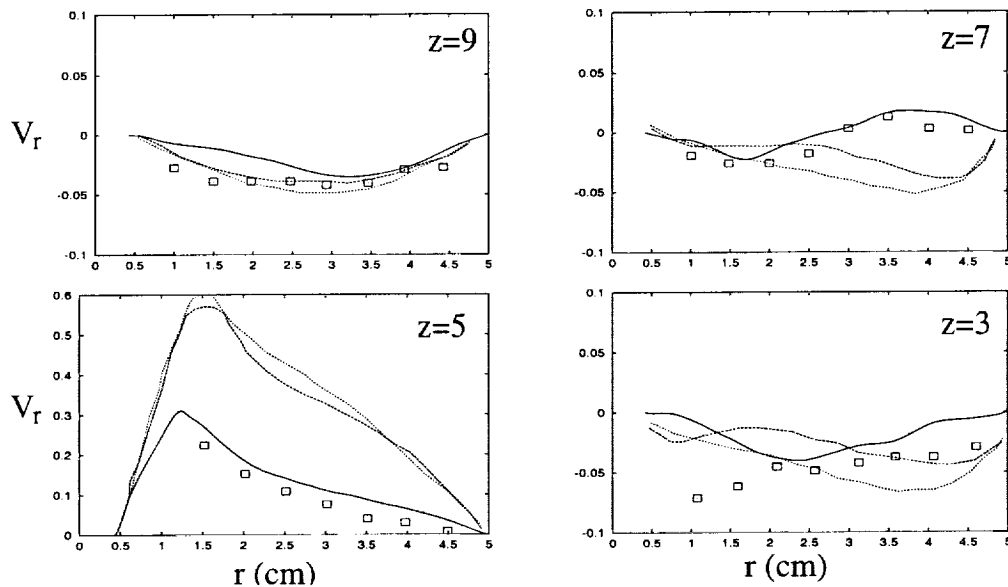


FIGURE 9. The same as Fig. 8 for averaged radial velocity.

scale recirculation that drives the fluid from the external radial region towards the axis, thus increasing the azimuthal velocity owing to the conservation of angular momentum. Except for the section crossing the impeller, RANS simulations severely underpredict the peak velocity, thus confirming the findings of Jones, *et al.*, (2000). As already mentioned, the accurate DNS prediction of the azimuthal velocity profiles is independent of the computational domain extension; therefore, the RANS velocity underprediction must be attributed to the inadequacy of the modeling for this flow and not to the restriction of the computational domain to $1/8^{\text{th}}$ of the full size.

Radial and vertical velocity components are also accurately predicted by the DNS simulation with results that are generally better than RANS. This is especially true for the radial velocity profile in the section crossing the blade where RANS results overpredicted the velocity by more than a factor of two. This mismatch, however, can only partially be attributed to RANS modeling since a major effect is induced by the limitation of the computational domain to only one blade as shown in Fig. 4.

4. Conclusions

In this paper we have performed a DNS of flow in an impeller stirred unbaffled cylindrical tank with an immersed boundary procedure to deal with the complex geometry. The main motivation comes from the literature showing that, although the geometry is relatively simple and the Reynolds number quite low, standard RANS simulations yield a very poor flow prediction.

It is found that the flow is strongly unsteady and inhomogeneous even if the Reynolds number is low enough to make the DNS affordable. Accordingly, an LES simulation with a dynamic subgrid-scale model yielded the same results as the DNS with a turbulent viscosity close to zero. RANS models, in contrast, can not automatically switch off when the

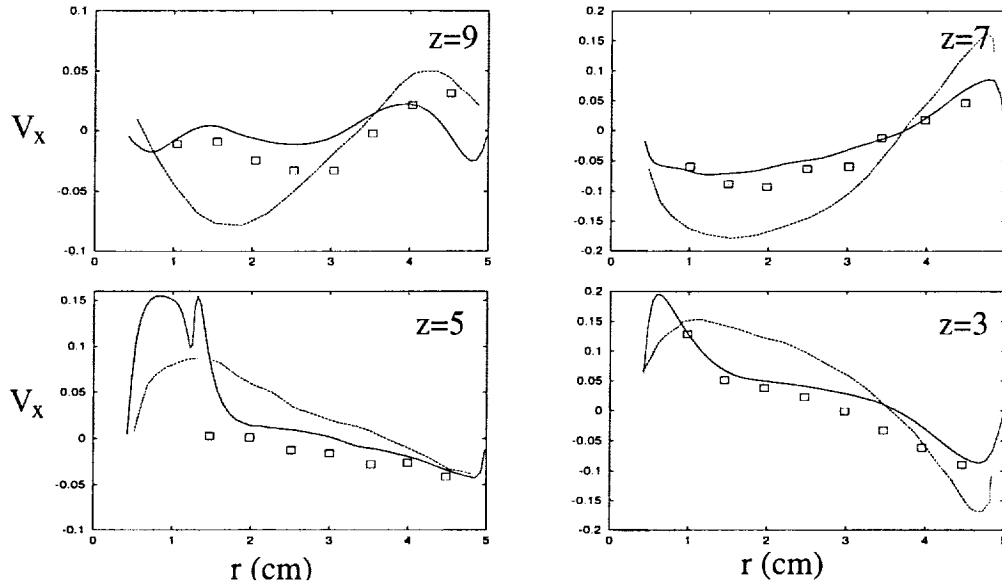


FIGURE 10. The same as Fig. 8 for averaged axial velocity. ($k - \epsilon$ RANS data are missing).

resolution is fine enough, and they parameterize all the velocity oscillations as turbulent fluctuations.

Since the impeller has 8 azimuthally equispaced blades, simulations in the literature have always been performed over a sector of the domain spanning $1/8^{\text{th}}$ of the domain. Although this assumption reduces the computational cost by a factor of 8, the results do not agree with the experiments since the flow is forced to maintain a symmetry that is not physical. A posteriori this result is not surprising since, looking at Fig. 1, it is unlikely that blades whose area is less than $1/50^{\text{th}}$ of the meridional section could enforce any symmetry on the large-scale flow.

Some remarks of the computational costs of these DNS simulations are in order. In contrast to RANS where a steady solution is forced, for unsteady simulations mean quantities are obtained by averaging the solution in time. In the present case, the intense velocity fluctuations required long-term averages (typically 15-20 impeller revolutions) to obtain smooth converged statistics. This must be added to the initial transient that consisted of an equivalent time of about 40 impeller revolutions on the finest grid. The computation of this flow evolution is highly expensive compared to RANS simulations where the mean field is directly obtained. Fortunately, the use of the immersed boundary procedure makes the simulation of complex-geometry three-dimensional unsteady flows quite affordable. As an example, in the present case on a grid of 1.9×10^6 points, the code uses 85Mb of RAM and requires 32s for each 3^{rd} Runge-Kutta time step (consisting of three complete substeps) on a single 900MHz Athlon processor; the entire simulation required slightly less than 5 days.

REFERENCES

- DONG, L., JOHANSEN, S. T. & ENGH, T. A. 1994 Flow Induced by an Impeller in an Unbaffled Tank-I. Experimental. *Chem. Engng. Sci.* **49**(4), 549.

- DURBIN, P. A. 1995 Separated Flow Computations with the $k - \epsilon - v^2$ Model. *AIAA J.* **33**, 659.
- FADLUN, E. A., VERZICCO, R., ORLANDI, P. & MOHD-YUSOF, J. 2000 Combined immersed-boundary/finite-difference methods for three-dimensional complex flow simulations. *J. of Comp. Phys.* **161**, 35.
- JONES, R. M., HARVEY III, A. D. & ACHARYA, S. Two-Equation Turbulence Modeling for Impeller Stirred Tanks. *Private communication*.
- LAUNDER, B. E., & SHARMA, A. 1974 Application of the Energy-Dissipation Model of Turbulence to the Calculation of Flow Near a Spinning Disk. *Letters in Heat and Mass Transfer.* **1**, 131.
- SWARTZRAUBER, P. N. 1974 Direct Method for the Discrete Solution of Separable Elliptic Equations. *SIAM J. Num. Anal.* **11**, 1136.
- VERZICCO, R. & ORLANDI, P. 1996 A finite-difference scheme for three-dimensional incompressible flows in cylindrical coordinates. *J. of Comp. Phys.* **123**, 402.
- VERZICCO, R., MOHD-YUSOF, J., ORLANDI, P. & HAWORTH, D. 2000 Large Eddy Simulation in Complex Geometric Configurations Using Boundary Body Forces. *AIAA J.* **38**(3), 427.

Unsteady 3D RANS simulations using the v^2-f model

By Gianluca Iaccarino AND Paul Durbin

1. Motivation & background

Recent increased computational power has led to interest in the simulation of time-dependent flows for problems ranging from noise prediction to fluid/structure interactions. The computational cost and the resolution requirements are mainly related to the inviscid flow structures induced by geometry and wall layers; nevertheless, turbulence plays a crucial role in establishing such flow structures.

Several approaches can be used to numerically simulate the behavior of unsteady flows: in the simplest, the Navier-Stokes equations are ensemble-averaged, converting turbulent fluctuations into Reynolds stresses (Reynolds-Averaged Navier-Stokes equations, RANS), while leaving the large scale, rotational motions to be resolved as unsteady phenomena. The large eddy simulation (LES) approach, on the other hand, employs a spatial averaging over a scale sufficient to remove scales not resolved by the particular grid being used. The subgrid scale turbulence is then modeled.

A practical difference is in the degree of mesh resolution required: LES resolves the larger eddies of the turbulence itself, whereas the unsteady RANS approach models the turbulence and resolves only unsteady, mean flow structures – primarily larger than the turbulent eddies. Consequently, LES typically requires much higher grid resolution, at least locally, and is therefore more costly. On the other hand, LES only models the subgrid turbulence structures and is universally applicable to the extent that a universal grid-independent subgrid model can be established.

In addition, LES resolves the complete range of scales of random motion, up to the cut-off frequency, while unsteady RANS aims to capture a single frequency (e.g. corresponding to coherent shedding) and to model the random motions using standard turbulence closures. Therefore, LES requires very long integration time to build a statistically-averaged solution; on the other hand, a few shedding periods are usually enough to obtain accurate phase-averaged solution with RANS, thus limiting its overall computational cost.

The objective of this work is to apply the RANS approach with the $\overline{v^2} - f$ turbulence model (Durbin, 1995) to the solution of the flow around a surface mounted cube. A complete and reliable experimental database is available (Hussein & Martinuzzi, 1996) and, in addition, LES simulations have been carried out with considerable success (Shah, 1998 and Krajnovic, 2000). This problem was one of the test case presented at the “Workshop on Large Eddy Simulation of Flows Past Bluff Bodies”; several LES calculations were compared, showing a high degree of accuracy (Rodi, 1997). RANS results were also included for comparison; they were obtained using simple turbulence models derived from $k-\epsilon$ and, generally, gave worse agreement with the measurements than did LES.

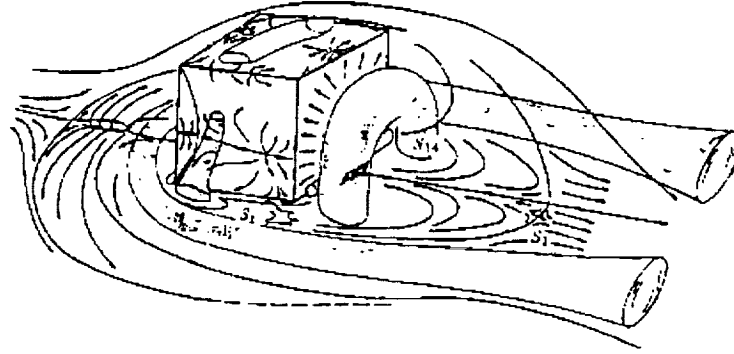


FIGURE 1. Schematic representation of the main flow features (Hussein & Martinuzzi, 1996).

2. Results

The flow around a cube exhibits characteristics common to other flows past three-dimensional obstacles: strong three-dimensionality of the mean flow, separation, and large scale unsteadiness. A schematic representation of the flow features (due to Hussein & Martinuzzi, 1996) is reported in Fig. 1: a strong horseshoe vortex and an arc-shaped vortex in the near wake are inferred from the analysis of the oil-flow patterns on the wind tunnel floor.

The (steady/unsteady) RANS equations are solved on a structured grid made up of 500,000 grid cells with clustering close to the walls to capture the near-wall turbulent regions (y^+ is less than one everywhere). The Reynolds number is 40,000 (based on the inlet bulk velocity, $u_b = 32\text{m/s}$ and the height of the cube, $h = 1\text{m}$). The domain size is the same as used by Shah (1998): $10h$, $2h$, and $3h$ in the streamwise, normal, and spanwise directions, respectively. The cube is located at $x = 3h$ from the inlet. A fully developed channel flow solution is used at the inlet, and solid walls are considered in the spanwise direction (this is the main difference with respect to the LES simulation by Shah (1998) where periodic conditions were employed).

The eddy viscosity is computed according to the $\overline{v^2} - f$ turbulence model (Durbin, 1995); the model requires the solution of three transport equations for turbulent quantities plus the solution of an elliptic equation. The model has a built-in realizability limiter (Durbin, 1996) and does not require any damping or wall function to correctly capture the near-wall turbulence (Durbin, 1991).

A second order discretization scheme (both in time and space) is used. Initially, a very large time step is employed leading to a steady solution; later the time step is decreased (to $\Delta t = 0.00156$ seconds) and a time accurate simulation is carried out. A coherent vortex shedding is obtained after ≈ 3 seconds, corresponding to ≈ 10 flow through times. Then, an averaged solution is computed on a period of ≈ 3 seconds, and in what follows it is referred to as unsteady solution.

Comparisons of the available experimental data and the steady and the unsteady solutions are presented; the LES results by Shah (1998) are also reported.

In Fig. 2 (left column) the streamwise velocity component (u/u_b) on the symmetry plane is reported. The experimental data (confirmed by the LES results) indicate a separation length of $\approx 1.6h$ downstream of the block; the steady solution overpredicts

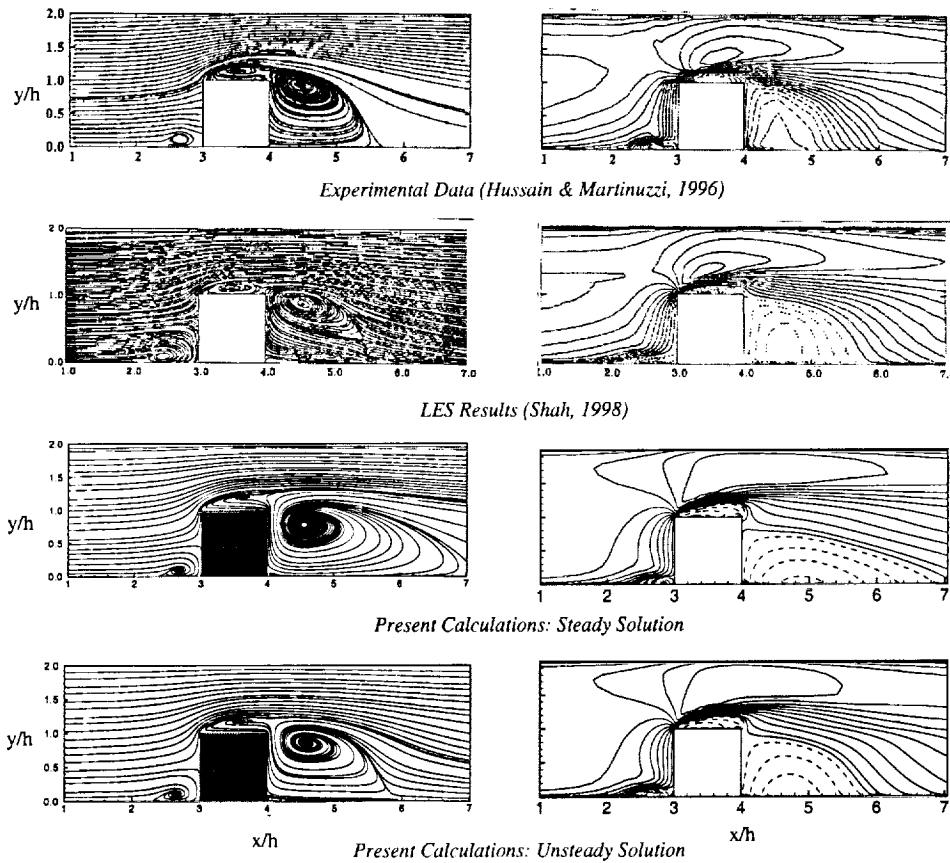


FIGURE 2. Streamlines (left) and streamwise velocity (right) on the symmetry plane. Dashed lines indicate negative velocity.

the extent by more than 100% ($3.3h$). On the other hand, the unsteady solution predicts a reattachment length of $\approx 1.9h$ in reasonable agreement with the measurements.

An analysis of the streamlines (Fig. 2, right column) suggests that the vortex cores are in the same locations, and the reattachment lengths (both upstream and downstream of the cube) are in remarkable agreement. The steady solution yields a too large recirculation area in the wake of the cube but a fairly good agreement elsewhere.

In Table I a summary of the length of the downstream and upstream recirculation bubbles is reported together with the experimental data and the numerical results presented in Rodi (1997), Shah (1998), and Krajnovic (2000).

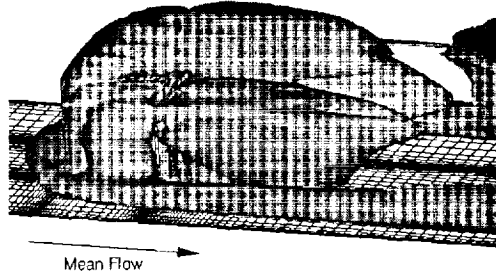


FIGURE 3. Visualization of the Horseshoe Vortex Using λ_2 (Jeong & Hussain, 1994)

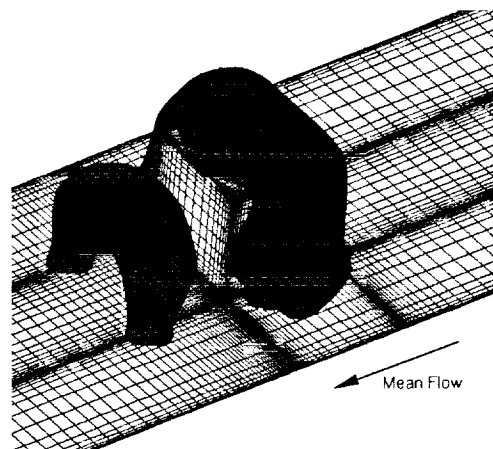


FIGURE 4. Visualization of the arch-vortex in the wake using an isobar surface.

Contribution	Model	x_F/h	x_{R_1}/h	x_{R_2}/h
Martinuzzi & Tropea, 1993	Experiments	1.040	1.612	-
Rodi <i>et al.</i> , 1997	LES	0.998	1.432	0.134
	RANS	0.950	2.731	0.252
Shah, 1998	LES	1.080	1.690	0.160
Krajnovic & Davidson, 1999	LES	1.060	1.380	-
Present Calculations	RANS Steady	0.640	3.315	0.310
	RANS Unsteady	0.732	1.876	0.204

x_F/h : upstream separation;
 x_{R_1}/h and x_{R_2}/h : downstream primary and secondary recirculation.
 Table I. Recirculation bubble lengths.

The LES calculations reported in Rodi (1997) used either the wall function approach in conjunction with the Smagorinsky sub-grid scale (SGS) model, or the dynamic SGS model; the latter gave better results, as reported in Table I. The calculations showed a very good overall agreement with the measurements. The steady RANS computations, on the other hand, were not accurate in capturing the length of the wake bubble; even the best results (reported in Table I under Rodi, *et al.*), obtained using a two-layer approach for the near-wall turbulence, severely overestimate the recirculation region. The LES results of Shah (1998) and of Krajnovic (1999), both obtained with the dynamic SGS model, confirms the reliability of LES in reproducing the mean flow behavior. The

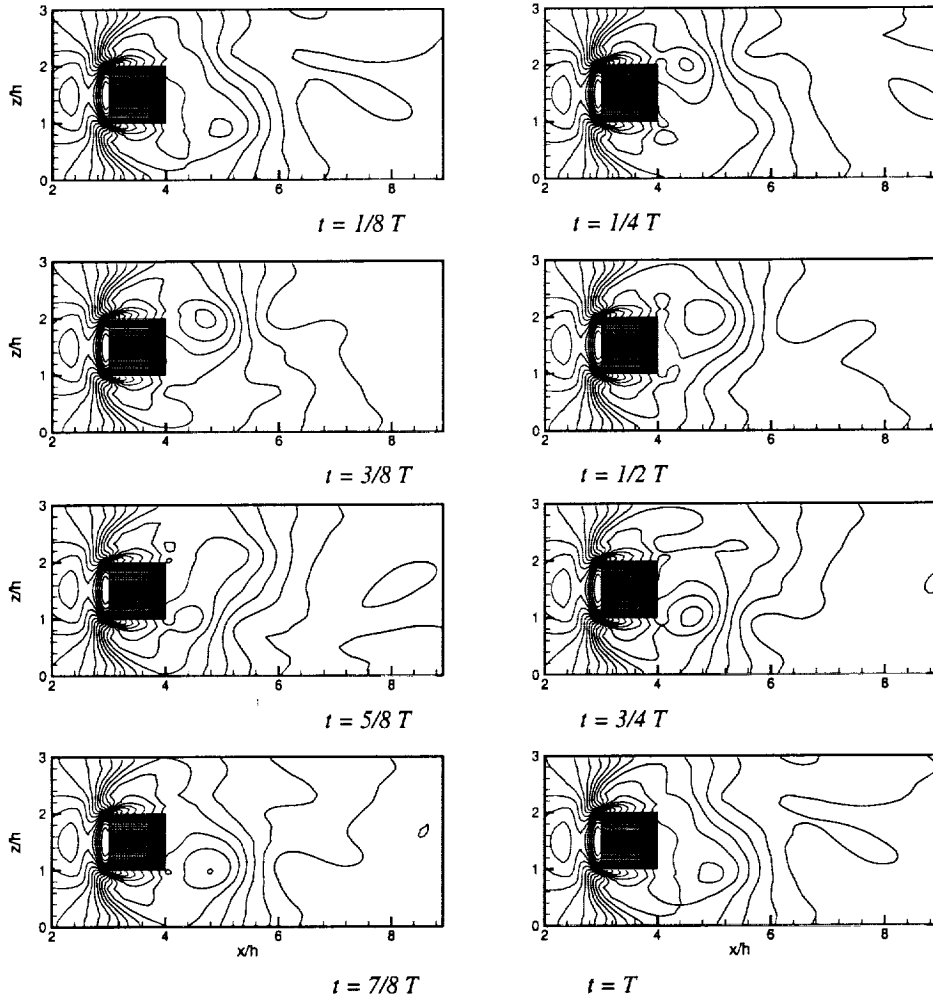


FIGURE 5. Time-history of the pressure distribution on the floor.

present time-averaged, unsteady computations are also in very good agreement with the experimental data, with only a slight overprediction of the wake reattachment length (x_{R_1}).

Two flow visualizations of the unsteady solution are reported. In the first (Fig. 3), the horseshoe vortex is represented by using the vortex-detection criterion of Jeong and Hussain (1995). The visualization of the arch vortex in the wake is performed using an isosurface of the pressure (Fig. 4).

In addition, the time evolution (during a period) of the pressure distribution on the wind tunnel floor is reported in Fig. 5. The flow is indeed periodic. The vortex shedding from the side of the cube induces an oscillation (yaw) of the arch vortex. One leg becomes stronger because of the vorticity contribution coming from the detached boundary layer on the cube side; it moves downward while a new vortex is shed from the opposite side. The shedding period is $T = 0.184$ seconds, corresponding to a Strouhal number of 0.17

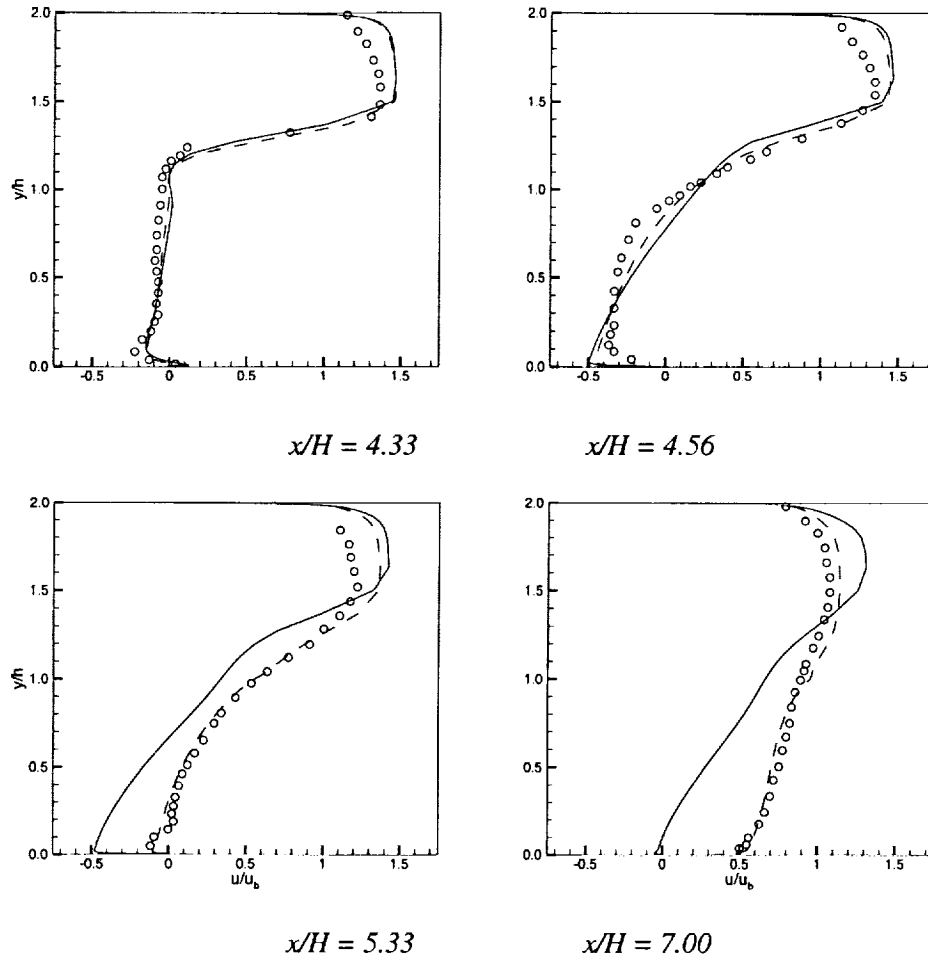


FIGURE 6. Streamwise velocity profiles in the symmetry plane. Symbols: — : steady solution; ---- : unsteady solution; o: experiments.

(experimental value 0.145). No vortex shedding is observed for the boundary on the roof of the cube, and no unsteadiness related to the horseshoe vortex is seen.

The quantitative comparison between the computed results and the experimental data is reported in Fig. 6. The streamwise velocity profiles at four stations on the symmetry plane are shown. The agreement between the experimental data and the unsteady solution is satisfactory. The main discrepancy is due to the inadequate prediction of the high-speed flow between the cube and the wind tunnel roof. The underprediction of the velocity in that region may be due to incorrect capturing of the separated boundary layer on the cube roof (in conjunction with an unsteadiness not detected by the simulation). As expected, the steady solution significantly overpredicts the strength of the recirculation velocity in the wake.

In conclusion, good quantitative and qualitative agreement with the experimental results shows the ability of the present approach (unsteady RANS with the $\overline{v^2} - f$ turbulence

model) to correctly reproduce the essential physics associated with massively separated flows.

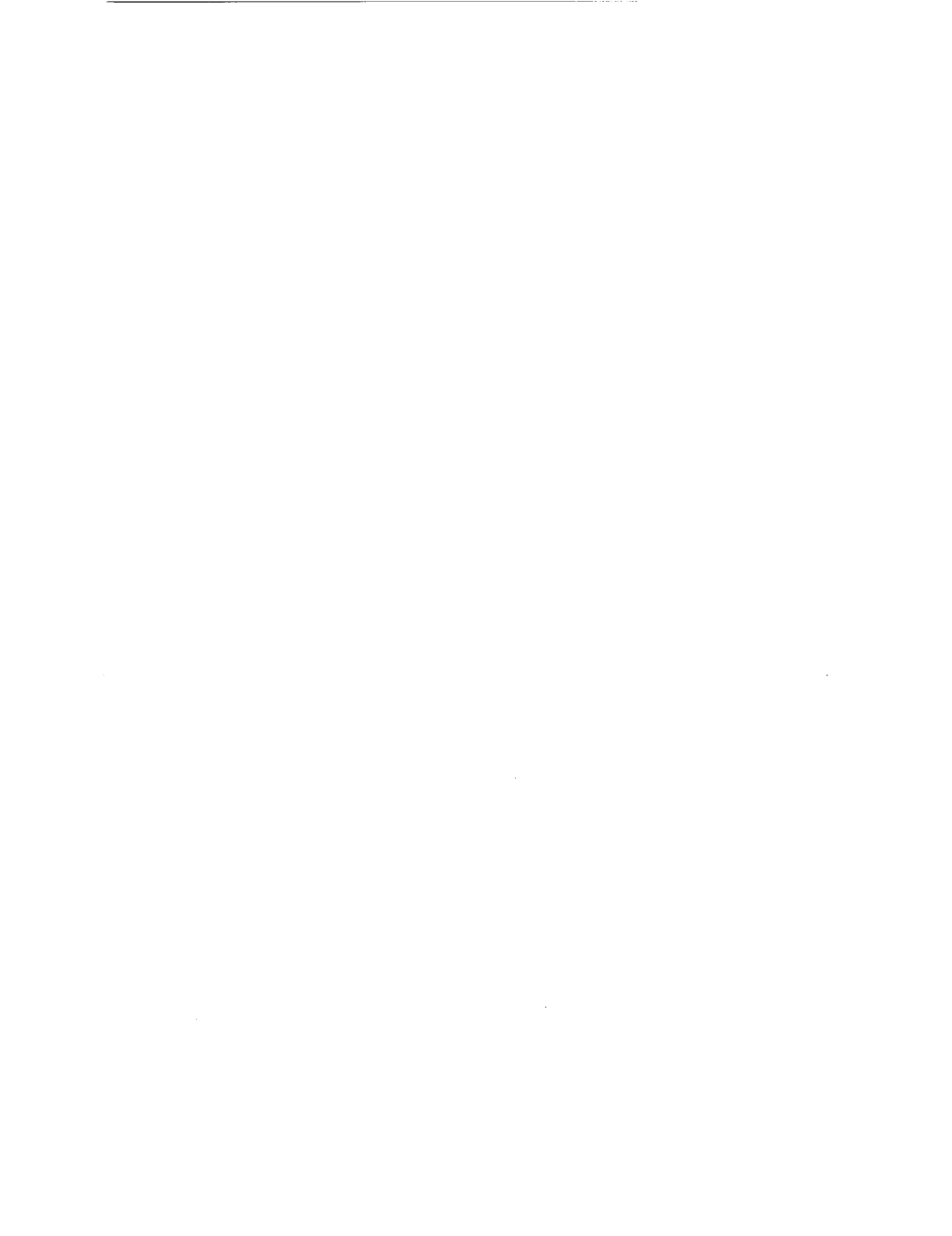
The presence of the horseshoe vortex and the arch-shaped vortex in the near wake, inferred by the analysis of the experimental oil-flow patterns on the wind tunnel floor, has been demonstrated by means of two vortex-detection criteria. In addition, the inadequacy of steady RANS calculations for flows over bluff bodies has been confirmed by the present results.

3. Future work

The results presented in this report show that the simulation of three-dimensional unsteady flows can be carried out accurately using RANS; this confirms the results obtained by Durbin (1995) for two-dimensional flows. The configurations analyzed, however, are characterized by flow separation fixed at sharp edges (the cube herein, and a triangular cylinder in Durbin, 1995). It remains to verify the ability of the model to accurately predict the unsteady wake development for separation occurring on a smooth surface. Future work will be focusing on the simulation of the flow around a sphere; in this case, to eliminate uncertainties associated with the prediction of the laminar/turbulent transition, high Reynolds number will be considered.

REFERENCES

- DURBIN, P. A. 1991 Near-Wall Turbulence Closure Modeling without 'Damping Functions'. *Theoret. Comput. Fluid Dyn.* **3**, 1-13.
- DURBIN, P. A. 1995 Separated Flow Computations with the $k - \epsilon - v^2$ Model. *AIAA J.* **33**, 659-664.
- DURBIN, P. A. 1996 On the $k - \epsilon$ Stagnation Point Anomaly. *Int. J. Heat and Fluid Flow.* **17**, 89-90.
- HUSSEIN, H. J. & MARTINUZZI, R. J. 1996, Energy Balance for the Turbulent Flow Around a Surface Mounted Cube Placed in a Channel. *Phys. Fluids.* **8**, 764-780.
- JEONG, J. & HUSSAIN, F. 1995 On the Identification of a Vortex. *J. Fluid Mech.* **285** 69-94.
- KRAJNOVIC, S. & DAVIDSON, L. 1999 Large Eddy Simulation of the Flow Around a Surface Mounted Cube Using a Dynamic One-Equation Subgrid Model. *The First Symp. on Turbulence and Shear Flow Phenomena.*
- RODI, W., FERZIGER, J. H., BREUER, M. & POURQUIE, M. 1997 Status of Large Eddy Simulation: Result of a Workshop. *J. Fluids Eng.* **119**, 248-262.
- SHAH, K. B. 1998 Large Eddy Simulation of the Flow Past a Cubic Obstacle. *PhD. Thesis*, Stanford University.



Prediction of the turbulent flow in a diffuser with commercial CFD codes

By Gianluca Iaccarino

1. Motivation & background

There have been a few attempts in the literature to compare the performance of commercial CFD codes; for instance, laminar and turbulent test cases have been proposed to several CFD code vendors by the Coordinating Group for Computational Fluid Dynamics of the Fluids Engineering Division of ASME (Freitas, 1995). A series of five benchmark problems were calculated, with all the mesh generation and simulations performed by the vendors themselves; only two of the problems required turbulent simulations. The first of these benchmarks is the flow around a square cylinder: the flow is unsteady and all of the codes predicted the measured Strouhal number reasonably well. However, poor accuracy was obtained in the details of the wake flow field. It was also noted that, depending on the code used (and assuming grid-converged results), the *same* $k-\epsilon$ model predicted very different results (from 2% to 16% accuracy in the Strouhal number, for example). The reasons for this difference include different grids, non-demonstrated grid convergence, different implementation of the models, and different boundary conditions. It must be pointed out that the predictions for this problem are strongly affected by the treatment of the stagnation point region: as reported in Durbin (1996), the $k-\epsilon$ models predict a *spurious* high level of turbulent kinetic energy near the stagnation point.

The other turbulent problem reported in Freitas (1995) was the three-dimensional, developing flow in a 180-degree bend. In this case all of the solutions reported were unsuccessful in predicting the measured data in the bend region. The resolved structure of the flow field was significantly affected by the choice of the turbulence model.

The uncertainties associated with different computational grids (*i*), boundary conditions definition (*ii*), convergence (*iii*), and numerical schemes (*iv*) do not allow specific conclusions to be drawn from the comparison other than that *further research into more advanced turbulence models for use in commercial CFD codes is required* (Freitas, 1995).

In order to complete a fair comparison between different CFD codes and to establish concrete conclusion on the state-of-the-art of commercial CFD codes, all of the differences (*i-iv*) must be fully addressed and, if possible, eliminated. In the present work an effort has been made to control all of these parameters. The codes available to us for comparison are CFX, Fluent, and Star-CD. The objective is to compare their predictive capabilities for the simulation of a turbulent separated flow. Several turbulent closures are available in these codes, ranging from $k-\epsilon$ -type models to full Reynolds stress closures. In addition, various near-wall treatment are available in the codes. Two models are selected: the $k-\epsilon$ Low-Reynolds model by Launder & Sharma (1974) and the $\overline{v^2} - f$ by Durbin (1995).

The test case is two-dimensional, turbulent flow in a diffuser. Due to the adverse pressure gradient, the flow is separated and a long recirculation bubble exists. This problem has been selected because a very reliable experimental database is available. In addition to laboratory data, a detailed large eddy simulation (LES) study was carried

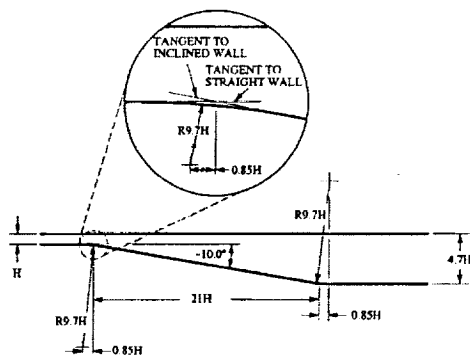


FIGURE 1. Asymmetric diffuser geometry.



FIGURE 2. Computational grid.

out at the Center for Turbulence Research, and the resulting numerical database is also available for comparison.

2. Numerical method

The incompressible Navier-Stokes (NS) equations are solved, together with additional equations for turbulent quantities as are needed to compute an eddy viscosity. The discretized equations are solved in a segregated manner with the SIMPLE (Semi-Implicit Method for Pressure-Linked Equations) algorithm or its "consistent" variant, SIMPLEC (Vandoormaal, 1984), used for stability to achieve the pressure-velocity coupling. In the SIMPLE algorithm, the continuity equation is converted into a discrete Poisson equation for the pressure.

The solution procedure can be described as follows: the differential equations are linearized and solved implicitly in sequence, starting with the pressure equation, followed by the momentum equations, by the pressure correction equation, and finally by the equations for the scalars (turbulence variables). Within this loop, the linearized equations for each variable are integrated using a linear system solver.

Three codes have been used in this work: CFX, Fluent, and Star-CD. All of the codes allow the user to implement customized models through user defined subroutines.

In all of the simulations SIMPLEC has been used (SIMPLE for Star-CD) with QUICK (Leonard, 1979) space discretization for the mean flow and first order upwinding for the turbulence equations. The same under-relaxation factors were used in all the calculations.

Several turbulence models are available in these codes; most of them are derived from the standard $k-\epsilon$ model with different treatment of the wall region.

The Low-Reynolds model of Launder & Sharma (1974) and the $\overline{v^2} - f$ model (Durbin, 1995) are used in this work. The first model is available as a standard option in all the codes (even if slightly different damping function are employed in Star-CD); the $\overline{v^2} - f$ model has been implemented using the user defined subroutines in each of the codes. Such implementation ensures that exactly the same model is used in each of the codes.

3. Results

The two-dimensional diffuser considered here was a test-case for the 8th ERCOFTAC/IAHR/COST Workshop on Refined Turbulence modeling in Espoo, Finland, 17-18

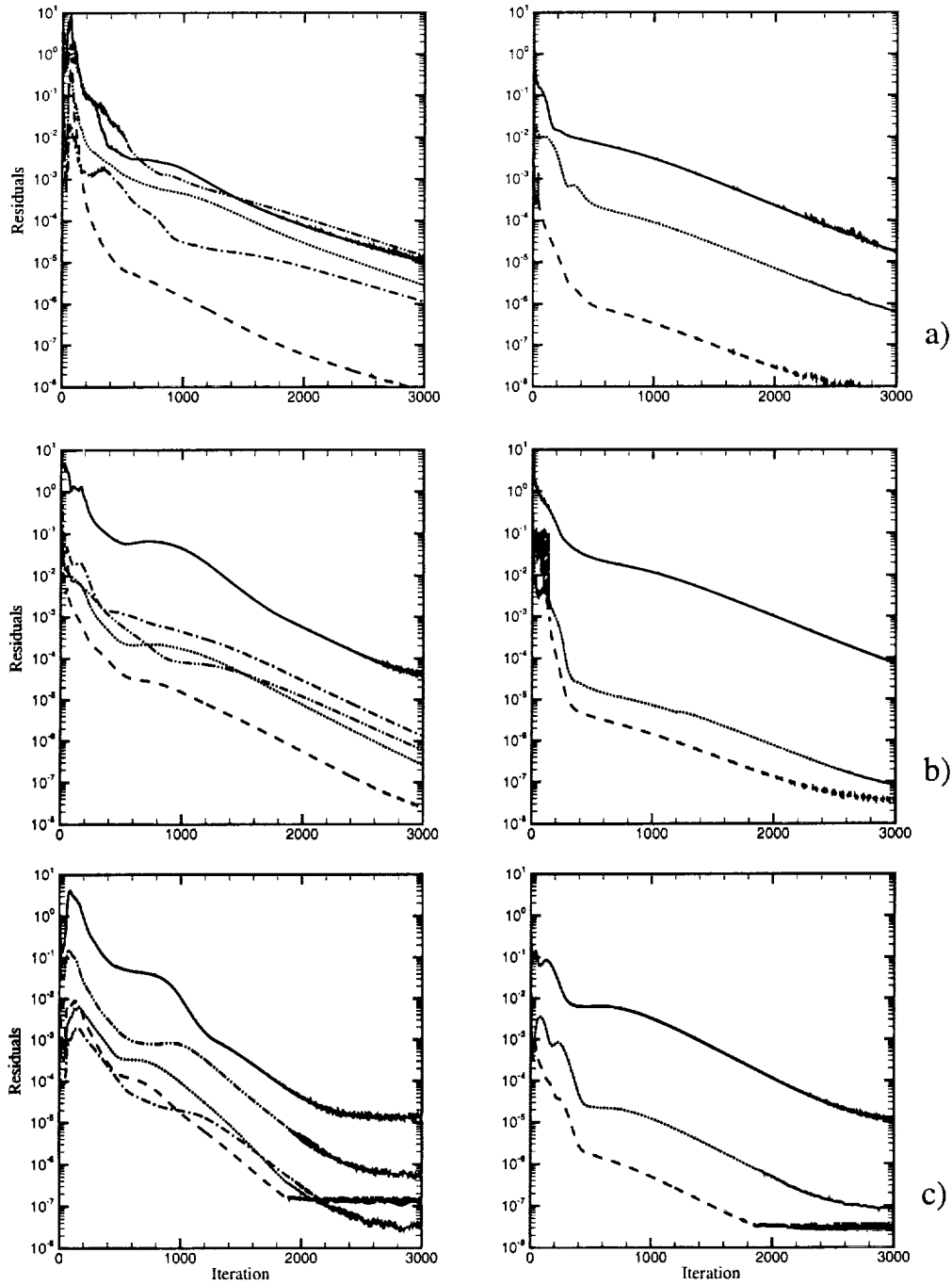


FIGURE 3. Convergence history (L_∞ Norm). Left column: $\overline{v^2} - f$ model; right column: Low-Reynolds $k-\epsilon$ model. a) CFX v4.3; b) Fluent v5.3; c) Star-CD v3.1. - Symbols: — x-momentum, k , - - - ϵ , - · - v^2 , - - - f

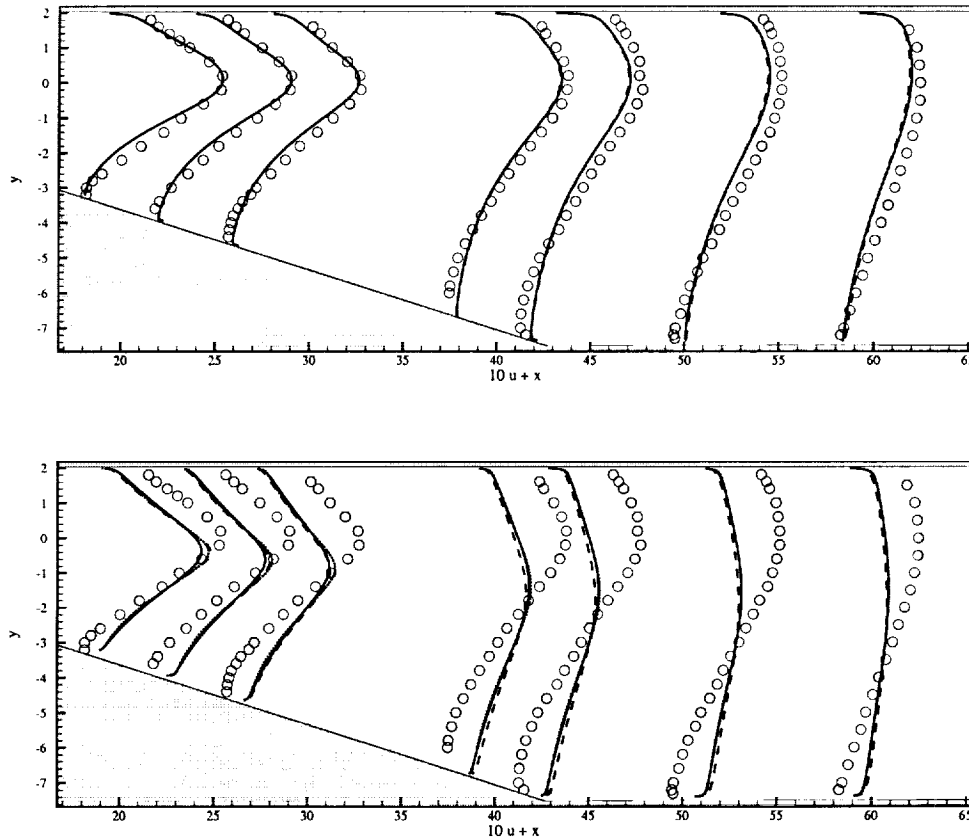


FIGURE 4. Streamwise velocity profiles. Top: $\overline{v^2} - f$ model; bottom: Low-Reynolds $k-\epsilon$ model - Symbols: \circ Experiments, — CFX, ---- Fluent, Star-CD

June 1999. The geometry is presented in Fig. 1 and the inlet conditions are specified as fully-developed channel flow at $Re=20,000$, based on the centerline velocity and the channel height. Separate channel flow computations were carried out using each code and each turbulence model, and the resulting profiles were used as inlet conditions for the simulation of the diffuser.

An experimental database is available from Obi (1993) and Buice & Eaton (1997); the data include mean and fluctuating velocities at various stations in the diffuser and skin friction on both walls. The data can be obtained directly from the following Website (www.aero.hut.fi/Ercoftac/ws8/case8.2).

A structured grid made up of 124×65 points in the streamwise and wall normal direction, respectively, was used. A detail of the computational grid in the region close to the connection between the channel and the diffuser is included in Fig. 2.

The same grid was also used in the LES study by Kaltenback *et al.* (1999). In this study a very detailed comparison between numerical and experimental data was carried out, and the agreement was very good. The simulations provided insights into the physics of the separation process and provided a verification of the suitability of this problem as a CFD test case.

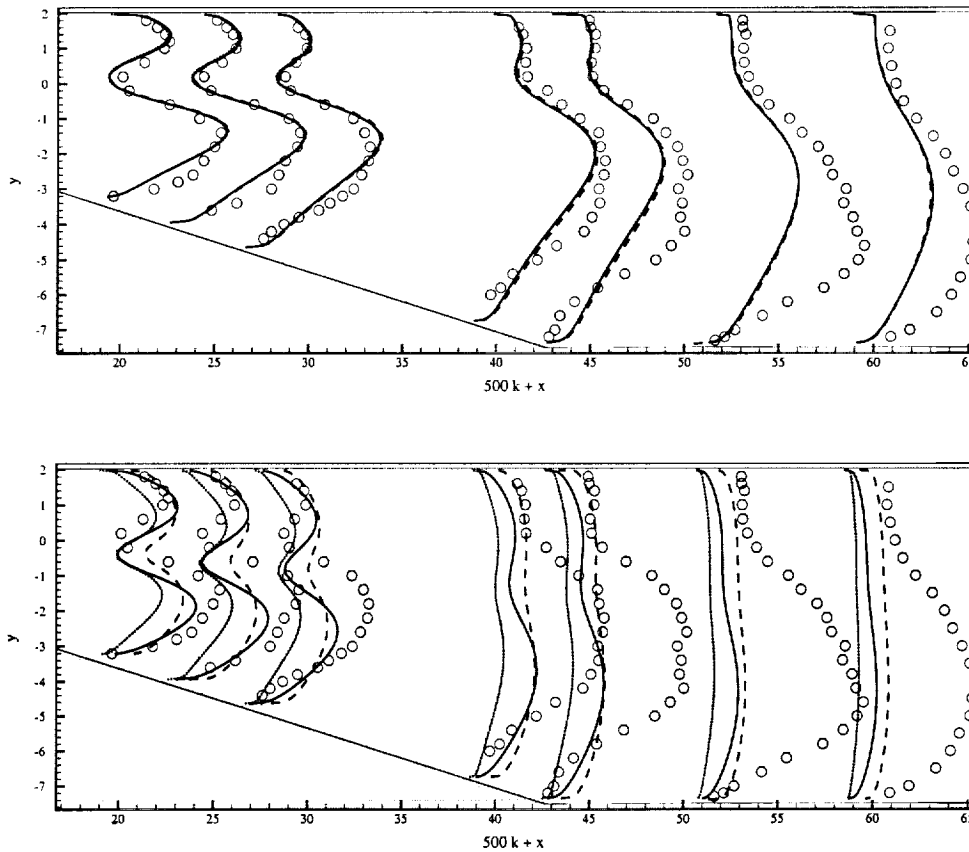


FIGURE 5. Turbulent kinetic energy profiles. Top: $\overline{v^2} - f$ model; bottom: Low-Reynolds $k-\epsilon$ model - Symbols: \circ Experiments, — CFX, ---- Fluent, Star-CD

In Fig. 3, convergence histories for the all simulations are presented. The residuals have been normalized by their values at the first iteration. The convergence level reached after 3,000 iterations is comparable in all the cases, although slightly lower residuals are obtained using the $\overline{v^2} - f$ in both Fluent and CFX, and vice-versa in Star-CD.

A comparison between the computations and the experimental data on mean velocity is reported in Fig. 4 at several stations in the diffuser. The $\overline{v^2} - f$ results are consistently in very good agreement with the measurements for the mean velocity; in particular, the separation zone is captured (even if the maximum intensity of the recirculating velocity is underestimated). The predictions using the $k-\epsilon$ model are in poor agreement with the data because the model fails to respond correctly to the adverse pressure gradient and misses the separation completely. The comparisons reported in Fig. 5 confirm the quality of the $\overline{v^2} - f$ predictions as compared to the $k-\epsilon$; in this plot the turbulent kinetic energy is presented.

The peak of the turbulent intensity is very well predicted by the $\overline{v^2} - f$ model in the diffuser, but in the recovery region (after the reattachment), the model underestimates the level of kinetic energy. This is consistent with the $\overline{v^2} - f$ calculations shown in Durbin (1995), the LES results reported in Kaltenback *et al.* (1999), and with the recent

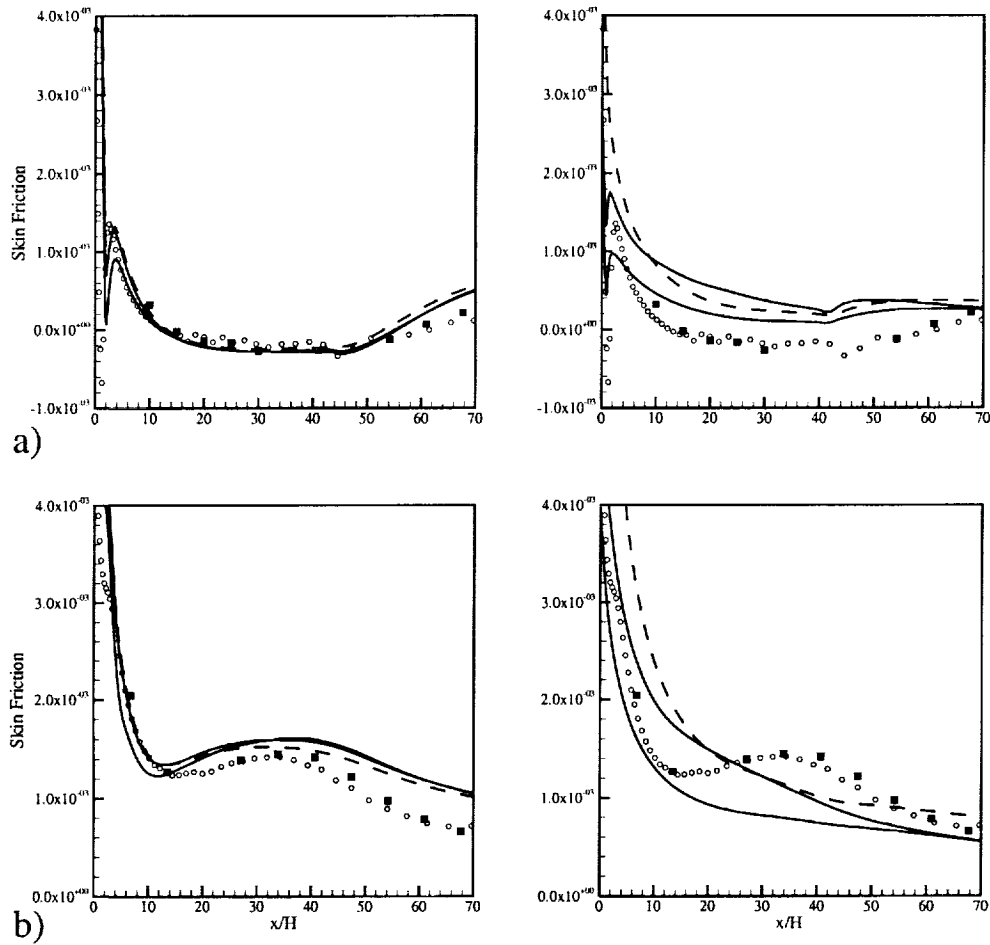


FIGURE 6. Skin friction distribution. Left column: $\overline{v^2} - f$ model; right column: Low-Reynolds $k-\epsilon$ model. a) Lower wall; b) Upper wall - Symbols: \circ LES, \blacksquare Experiments, — CFX, ---- Fluent, Star-CD

computations presented in Apsley & Leshziner (2000) using quadratic and cubic nonlinear $k-\epsilon$ models. One possible reason for this disagreement is the presence of strong three-dimensional effects after the flow reattachment.

The results using the $k-\epsilon$ model fail to capture the asymmetric development of the turbulent kinetic energy and underestimate its magnitude in the diffuser. In addition, the three codes show some differences when nominally the same $k-\epsilon$ model is invoked. The disparities are in the mean velocity and especially in the turbulence intensity. The very good agreement obtained by using the $\overline{v^2} - f$ suggests that the differences are not related to the numerical technique used, but to the implementation of the turbulence model itself. For example, different discretization or approximation of the source terms in the $k-\epsilon$ equations could lead to the mentioned differences.

Finally, in Fig. 8 the skin friction coefficients on the lower and upper wall are reported. The separation bubble on the curved wall is indicated by a negative friction from $x/H \approx 7$

to $x/H \approx 30$. The $\overline{v^2} - f$ model predicts a bubble in very close agreement with the experiments. The $k-\epsilon$ model fails to predict any separation (as already noted); in addition, the three codes predict quite different friction levels when the $k-\epsilon$ closure is employed.

4. Conclusions

A comparison between three CFD commercial codes has been reported for the turbulent flow in a planar asymmetric diffuser. Two turbulence models have been used: the first is the Low-Reynolds $k-\epsilon$ model (with Launder and Sharma damping functions) which is available as a standard feature in the codes; the second is the $\overline{v^2} - f$ model, which has been implemented through user defined routines.

The same grid and the same spatial discretization have been used for all the simulations. In addition, a similar iterative procedure based on the SIMPLE technique has been used. In terms of convergence behavior, all of the codes reach the steady state approximately in the same number of iterations, regardless of the turbulence model used. The accuracy of the calculations as compared to the experimental and LES data is very good using the $\overline{v^2} - f$ model. The length of the recirculation region is captured within 6% and the friction levels on both walls agree reasonably well with the data. The negative velocity in the separation bubble is slightly underestimated. The results using the $k-\epsilon$ model do not show any recirculation. The flow is fully attached, and this leads to a severe underprediction of the maximum velocity in the diffuser.

An effort has been made to control all of the aspects of the simulations so that exactly the same results were expected using different codes; in particular, the implementation of the $\overline{v^2} - f$ turbulence model has been carried out consistently. $\overline{v^2} - f$ results do indeed show an almost perfect agreement: CFX and Star-CD predict almost exactly the same results, with Fluent being slightly more dissipative. The results using the $k-\epsilon$ model, on the other hand, show a strong sensitivity to the code used. The damping functions used in CFX and Fluent are exactly the ones proposed by Launder and Sharma, but the results are different, especially in terms of turbulent quantities and friction coefficients. This may be due to differences in implementation details which are not specified in the user manuals. In general, the differences between the $k-\epsilon$ results are much larger than those obtained using $\overline{v^2} - f$, suggesting that they are less due to details of the numerical procedure used in the code than to the definition of the turbulence model itself.

Today, one of the challenges in using commercial CFD codes is to choose between several physical/numerical models available. The cross comparison presented in this work proves that the basic numerical techniques are reliable and deliver the expected performance in terms of accuracy and convergence. On the other hand, the selection of the correct physical model is crucial for the success of the simulations. Using one of the available turbulence models, the results were not accurate and, in addition, are not reproducible between the codes.

REFERENCES

- APSLEY, D. D. & LESHZINER, M. A. 2000 Advanced Turbulence Modeling of Separated Flow in a Diffuser. *Flow, Turbulence and Combustion*. **63**, 81-112.
- BUICE, C. U. & EATON, J. K. 1997 Experimental investigation of flow through an asymmetric plane diffuser. *Report No. TSD-107*, Thermosciences Division, Department of Mechanical Engineering, Stanford University, Stanford, CA, USA.

- CFX 4 1999 *User Guide*. AEA Technologies Engineering Software.
- DURBIN, P. A. 1995 Separated Flow Computations with the $k - \epsilon - v^2$ Model. *AIAA J.* **33**, 659-664.
- DURBIN, P. A. 1996 On the $k-\epsilon$ Stagnation Point Anomaly. *Int. J. Heat and Fluid Flow.* **17**, 89-90.
- Fluent 5 1998 *User Guide*. Fluent Inc..
- FREITAS, C. J. 1995 Perspective: Selected Benchmarks From Commercial CFD Codes. *J. Fluids Eng.* **117**, 210-218.
- KALTENBACK, H. J., FATICA, M., MITTAL, R., LUND, T. S. & MOIN P. 1999 Study of the Flow in a Planar Asymmetric Diffuser Using Large Eddy Simulations. *J. Fluid Mech.* **390**, 151-185.
- LAUNDER, B. E. & SHARMA, A. 1974 Application of the Energy-Dissipation Model of Turbulence to the Calculation of Flow Near a Spinning Disk. *Letters in Heat and Mass Transfer.* **1**, 131-138.
- LEONARD, B. P. 1979 A Stable and Accurate Convective Modeling Procedure Based on Quadratic Upstream Interpolation. *Computer Methods in Applied Mechanics and Engineering.* **19**, 59-98.
- OBI, S., AOKI, K. & MASUDA, S. 1993 Experimental and Computational Study of Turbulent Separating Flow in an Asymmetric Plane Diffuser. *Ninth Symp. on Turbulent Shear Flows*, Kyoto, Japan, August 16-19, p. 305.
- SPEZIALE, C. G., ABID, R., ANDERSON, E. C. 1990 A critical evaluation of two-equation models for near wall turbulence. *AIAA Paper 90-1481*.
- Star-CD 1998 Manuals Version 3.1. *Computational Dynamics, LTD.*
- VANDOORMAAL, J. P., & RAITBY, G. D. 1984 Enhancements of the SIMPLE Method for Predicting Incompressible Fluid Flows. *Numer. Heat Transfer.* **7**, 147-163.

Computation of turbulent flow in a rotating pipe using the structure-based model

By S. V. Poroseva, S. C. Kassinos, C. A. Langer AND W. C. Reynolds

1. Motivation and objectives

Mean rotation induces dynamical effects on turbulence that enter the transport equations through the non-local pressure-strain-rate correlation. It was shown in Kassinos & Reynolds (1994) and Reynolds & Kassinos (1995) that, to describe this effect accurately using one-point turbulence statistics, a turbulence model should include the transport equations not only for Reynolds stresses, but also for additional tensors providing information on turbulence structure missing from the Reynolds stresses. Two second-rank tensors, *dimensionality* D_{ij} and *circulicity* F_{ij} , as well as the third-rank *stropholysis* tensor Q_{ijk}^* along with the Reynolds stresses R_{ij} , form a minimal set of independent tensors necessary for a one-point closure in the case of inhomogeneous turbulence. Relying on these ideas, the structure-based model has been developed in Kassinos & Reynolds (1994-1998) and tested successfully for a wide range of deformations of homogeneous turbulence as well as for some simple wall-bounded flows (Kassinos *et al.*, 2000).

Currently, the structure-based model is being used for the computation of complex inhomogeneous turbulent flows with imposed system rotation. Here we report on the case of a turbulent flow in an axially rotating pipe. Despite the simple geometry, the structure of the turbulence in a rotating pipe flow changes substantially both as the flow develops with downstream distance from the pipe entrance and with increasing rotation rate, and as a result this flow serves as a severe benchmark for any turbulence closure. From a practical point of view, the modeling of a turbulent pipe flow is of interest because it relates to phenomena encountered in various engineering systems involving boundary layers on rotating surfaces, *e.g.*, heat exchangers and rotor cooling systems.

2. Model outline

Information carried by the turbulence structure tensors and the Reynolds stresses can be obtained from a single third-rank tensor \mathbf{Q} (Kassinos & Reynolds, 1994; Reynolds & Kassinos, 1995), which relates to the other structure tensors as:

$$Q_{ijk}^* = \frac{1}{6} [Q_{ijk} + Q_{jki} + Q_{kij} + Q_{ikj} + Q_{jik} + Q_{kji}],$$

$$R_{ij} = \epsilon_{imp} Q_{mjp}, \quad D_{ij} = \epsilon_{imp} Q_{pmj}, \quad F_{ij} = \epsilon_{imp} Q_{jpm}. \quad (2.1)$$

Therefore, the structure-based model considered in this work includes a model transport equation for the one-point third-rank tensor \mathbf{Q} as well as the standard transport equations for the mean velocity components

$$U_{i,i} = 0, \quad \frac{\bar{D}U_i}{Dt} = \nu U_{i,jj} - \langle u_i u_j \rangle_{,j} - \bar{P}_{,i} / \rho, \quad (2.2)$$

and the standard model equation for the dissipation rate ε with a rotation modification (last term) to account for the suppression of ε due to mean rotation (Kassinos *et al.*, 2000):

$$\frac{\bar{D}\varepsilon}{Dt} = \left[\left(\nu\delta_{jk} + \frac{C_\nu}{\sigma_\varepsilon} T \langle u_j u_k \rangle \right) \varepsilon_{,j} \right]_{,k} - \frac{1}{T} (C_o\varepsilon - C_s P) - C_\Omega \varepsilon \sqrt{\Omega_j \Omega_k d_{jk}}, \quad (2.3)$$

where

$$\frac{\bar{D}}{Dt} = U_j \frac{\partial}{\partial x_j} + \frac{\partial}{\partial t}.$$

The equations were derived in the generalized coordinates, but for the sake of simplicity of presentation, the Cartesian tensor notation is used in (2.2)-(2.3) and in what follows. U_i and u_i are components of the mean and fluctuating velocities, \bar{P} is the mean pressure, ρ is the flow density, ν is the kinematic viscosity, δ_{ij} is the Kronecker delta tensor, ϵ_{ijk} is the Levi-Civita alternating tensor, $q^2 = 2k = \langle u_i u_i \rangle$ is the turbulent kinetic energy, $\langle u_i u_j \rangle = R_{ij}$, $P = -R_{ij} U_{i,j}$, $d_{ij} = D_{ij}/q^2$, $\Omega_i = \epsilon_{ijk} U_{k,j}$ is the mean vorticity vector, C_α and σ_β are model coefficients. Time scale T is modeled as $T = \sqrt{(k/\varepsilon)^2 + 36 \cdot \nu/\varepsilon}$ (Durbin, 1993).

Now, let us consider the transport equation for **Q**-tensor. In homogeneous turbulence, the transport equation for the **Q**-tensor is (Kassinos *et al.*, 2000):

$$\begin{aligned} \frac{\bar{D}Q_{ijk}}{Dt} = & -G_{jm}^{(v)} Q_{imk} - G_{mk}^{(n)} Q_{ijm} - G_{sm}^{(v)} \epsilon_{its} M_{jmtk} - G_{mt}^{(n)} \epsilon_{its} M_{jismk} + \quad (2.4) \\ & (G_{ms}^{(v)} + G_{ms}^{(n)}) Q_{ismjk} + 2G_{ms}^{(n)} Q_{ijkms} - \frac{C_1}{\tau^*} \Omega^* f_{ms} (Q_{ijkms} + Q_{jikms}) \\ & - \sqrt{\frac{S_{pq} S_{qp} \Omega_m \Omega_s d_{ms}}{S_{pq} S_{qp} + \Omega_m \Omega_s d_{ms}}} (C_2 \epsilon_{ijm} (R_{mk} - D_{mk}) + C_3 \epsilon_{ikm} (F_{mj} - D_{mj})) \\ & - C_4 \sqrt{\Omega_m \Omega_s d_{ms}} Q_{ijk}^{(R)}, \end{aligned}$$

$$Q_{ijk}^{(R)} = Q_{ijk} - \frac{1}{6} (-\epsilon_{ijk} q^2 - \epsilon_{ikm} D_{mj} + 2\epsilon_{jim} D_{mk} - \epsilon_{kjm} D_{mi}), \quad G_{ij} = U_{i,j}.$$

C_1, C_2, C_3 , and C_4 are model coefficients, which are chosen to be equal to 8.5, 0.2, 0.1, and 0.5 respectively. The detailed explanation of Eq. (2.4) is given in Kassinos & Reynolds (1998) and Kassinos *et al.* (2000). Here, we just note that the fourth-rank tensor **M** can be obtained from Q_{ijkmn} by contracting with ϵ_{ijk} , and for weak anisotropies Q_{ijkmn} can be modeled as a linear function of Q_{ijk} (Kassinos *et al.*, 2000).

To take into account inhomogeneous effects such as turbulent transport and the influence of the wall on the turbulence structure, some modifications to (2.4) have been suggested by Kassinos *et al.* (2000). Turbulent and molecular transport is incorporated in Eq. (2.4) through the additional model term:

$$\Gamma_{ijk} = \left[\left(\nu\delta_{mn} + \frac{C_\nu}{\sigma_Q} T \langle u_m u_n \rangle \right) Q_{ijk,m} \right]_{,n}. \quad (2.5)$$

Model (2.5) is derived in such a way that after contraction with ϵ_{tik} it gives the known model presentation of the turbulent diffusion term (Daly & Harlow, 1970) in the transport

equation for R_{lj} :

$$\Gamma_{lj} = \epsilon_{tik} \Gamma_{ijk} = \left[\left(\nu \delta_{mn} + \frac{C_\nu}{\sigma_Q} T \langle u_m u_n \rangle \right) R_{lj,m} \right]_{,n}.$$

Near-wall effects are incorporated in the \mathbf{Q} -equation through an elliptic relaxation scheme based on ideas of Durbin (1993). If \wp_{ijk} denotes the right-hand side of (2.4), then, all terms in \wp_{ijk} that are not associated with either production or dissipation of the turbulent kinetic energy are lumped in a term named Π_{ijk} . The simplest model for Π_{ijk} is

$$\Pi_{ijk} = \wp_{ijk} - H_{ijk}, \quad (2.6)$$

where

$$H_{ijk} = -G_{jm} Q_{imk} - \frac{1}{2} G_{tm} \epsilon_{tik} R_{mj} + \frac{1}{2} (Q_{imk} + Q_{kmi}) - \frac{1}{T} Q_{ijk}$$

(Kassinos *et al.*, 2000).

Expression (2.6) is a model for redistributive processes that is valid for homogeneous turbulence. Now, we use $k f_{ijk}$ to denote an augmented version of this model that is valid in inhomogeneous turbulence. The components of the tensorial function f_{ijk} are found from the elliptic relaxation equation:

$$L^2 \nabla^2 f_{ijk} - f_{ijk} = -\frac{\Pi_{ijk}}{k}. \quad (2.7)$$

With models (2.5) - (2.7), governing Eq. (2.4) for Q_{ijk} in an inhomogeneous flow takes the form:

$$\frac{DQ_{ijk}}{Dt} = \left[\left(\nu \delta_{mn} + \frac{C_\nu}{\sigma_Q} T \langle u_m u_n \rangle \right) Q_{ijk,m} \right]_{,n} + k f_{ijk} + H_{ijk}.$$

3. Numerical procedure

To compute a pipe flow, all equations were written using the boundary layer approximation in the axisymmetric cylindrical frame of reference $x^i = (x, r, \varphi)$, where x , r , and φ are axial, radial, and angular coordinates respectively. In such coordinates, the covariant and contravariant components of the velocity are $U_i = (U, V, rW)$, $U^i = (U, V, W/r)$. The control volume technique (Spalding, 1977) was used to solve the transport equations.

In the computation we used the same conditions as those in the experiments of Zaets, Safarov & Safarov (1985), where a swirling flow was obtained by conveying a fully-developed turbulent flow ($U_o = 10^3$ cm/sec, $\nu = 0.149$ cm²/sec, friction velocity $u_{*o} = 43.5$ cm/sec) from a stationary straight cylindrical pipe of 100-diameter length into a rotating cylindrical section of the same diameter ($D = 6$ cm).

On the pipe axis the boundary conditions are:

$$\frac{\partial U}{\partial r} = \frac{\partial \epsilon}{\partial r} = W = 0, \quad U = U_o, \quad \frac{\partial Q_{ijk}}{\partial r} = 0 \quad \text{if } i = j, \quad \text{or } j = k, \quad \text{or } i = k,$$

$$\text{and } Q_{ijk} = 0, \quad \text{if } i \neq j \neq k.$$

At the wall,

$$U = Q_{ijk} = 0, \quad W = W_o, \quad \epsilon_w = \frac{2\nu k_w}{y_w^2},$$

where k_w is the value of the turbulent kinetic energy at the last grid node next to the

wall and y_w is the distance between the wall and that node. This last condition ensures that $k_w = O(y_w^2)$.

The correct behavior of the different components of the \mathbf{Q} -tensor was obtained by applying appropriate boundary conditions on f_{ijk} . The limiting behavior for each Q_{ijk} -component was derived by Kassinos (private communication). In particular, he showed that the correct behavior of Q_{ijk} components should give the correct behavior of the corresponding Reynolds stresses (Eq. (2.1)). Following these principles, the boundary conditions for f_{ijk} were derived and verified by comparison with DNS data (Moser, Kim & Mansour, 1988) by Langer (private communication) for a channel flow. Comparison of the DNS data for a channel (Moser, Kim & Mansour, 1988) and for a pipe (Eggels *et al.*, 1994) shows that in the near-wall area turbulent statistics behave in the same way in both flows. Therefore, in the present work, similar boundary conditions were applied to f_{ijk} at the pipe wall:

$$\begin{aligned} f_{xx\varphi}^{(w)} &= -\frac{20\nu^2 Q_{xx\varphi}}{\varepsilon_w y_w^4}, & f_{\varphi\varphi x}^{(w)} &= -\frac{20\nu^2 Q_{\varphi\varphi x}}{\varepsilon_w y_w^4}, & f_{x\varphi\varphi}^{(w)} &= -\frac{20\nu^2 Q_{x\varphi\varphi}}{\varepsilon_w y_w^4}, \\ f_{\varphi xx}^{(w)} &= -\frac{20\nu^2 Q_{\varphi xx}}{\varepsilon_w y_w^4}, & f_{\varphi rx}^{(w)} &= -\frac{20\nu^2 Q_{\varphi rx}}{\varepsilon_w y_w^4}, & f_{xr\varphi}^{(w)} &= -\frac{20\nu^2 Q_{xr\varphi}}{\varepsilon_w y_w^4}, \\ f_{xii}^{(w)} &= 0, & f_{iix}^{(w)} &= 0, & f_{\varphi ii}^{(w)} &= 0, & f_{i i \varphi}^{(w)} &= 0, \\ f_{\alpha\alpha\alpha}^{(w)} &= 0 \quad (\text{no summation over } \alpha); \\ f_{r\phi x}^{(w)} &= -0.2 f_{xr\varphi}^{(w)} = 0, & f_{\phi xr}^{(w)} &= -0.8 f_{xr\varphi}^{(w)} = 0, \\ f_{x\phi r}^{(w)} &= -0.2 f_{\varphi rx}^{(w)} = 0, & f_{rx\phi r}^{(w)} &= -0.8 f_{\varphi rx}^{(w)} = 0. \end{aligned}$$

The rest of the components are equal to zero at the wall. On the pipe axis, the boundary conditions for f_{ijk} are the same as for Q_{ijk} .

Equation (2.7) was solved using a standard finite-difference scheme. The grid was non-uniform in r , with the total number of N nodes being 64 for $Re_o = U_o D/\nu = 4 \cdot 10^4$ and 81 for $Re_o = 7 \cdot 10^3$ (D is the pipe diameter, $R = D/2$). The streamwise grid spacing δx was $0.0001R$.

For the length scale L in (2.7), various functional forms, including the ones suggested in Durbin (1993) and Pettersson, Andersson & Brunvoll (1998), have been tested. However, it was found that the best results were obtained by using a simple function like $L^2 = 1$, at $y_+ \leq 60$, and $L^2 = 0$, at $y_+ \geq 60$. Despite its simplicity this form seems somewhat unphysical, and even though here we are reporting results based on this form of L , we are currently pursuing a more fundamental basis for the length scale profile. It is also worth noting that in the initial section of the rotating pipe, where strong suppression of turbulence statistics occurs in the whole flow area including the near-wall one, the influence of this length scale is rather weak. At a rotation number of $N = W_o/U_o = 0.6$, both the peak value as well as the extent of the profile of L from the pipe wall seem to have practically no influence on the results of the calculations.

4. Results

As experiments demonstrate, it is possible to distinguish two regions in a rotating pipe flow with different turbulence structure: the initial section of a pipe with the length of

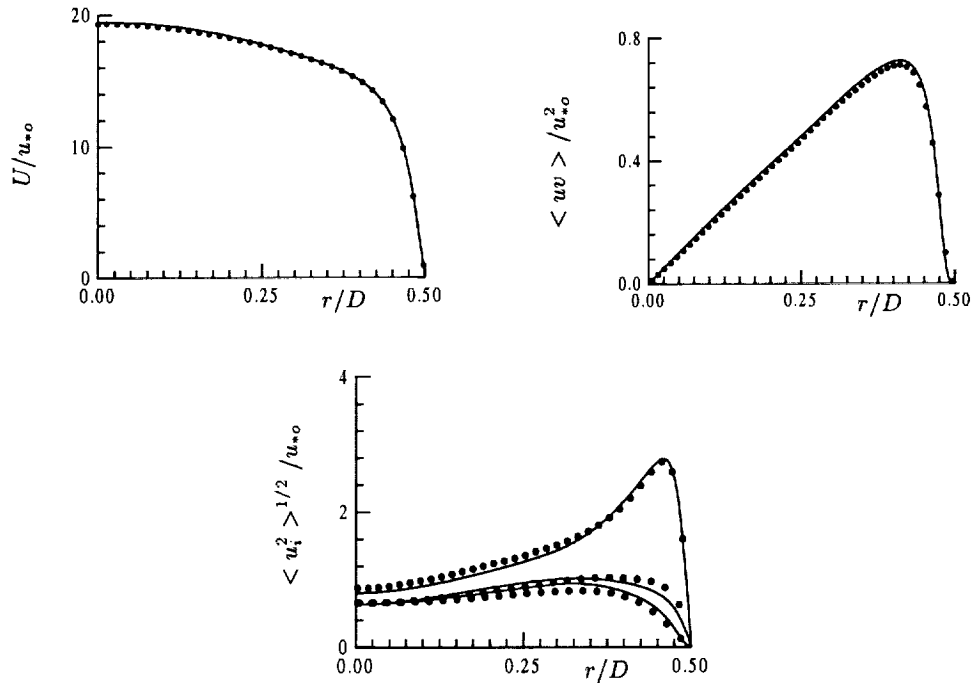


FIGURE 1. Stationary pipe flow: (—) Q-model, (●) DNS data.

about $30D$ and the fully developed turbulent flow which is observed at about $170D$. In the former region, strong turbulence suppression is observed (Zaets, Safarov & Safarov, 1985). In the latter one, profiles of statistical variables reach their limit shapes (Kikuyama *et al.*, 1983; Nishibori, Kikuyama & Murakami, 1987; Imao, Itoh & Harada, 1996, in particular).

The components of the mean velocity behave monotonically along the pipe axis and under rotation. The profile of the axial component tends to be parabolic as the one in a laminar flow, but does not reach this shape. The profile of the angular component has nearly parabolic limit shape ($W/W_o = (r/R)^2$, R is the pipe radius) instead of the expected linear one as it would be in the case of a forced rotational flow.

In contrast to the mean velocity components, the velocity moments of second and higher orders behave non-monotonically with increase of one of the parameters: downstream distance from the pipe entrance or rotation number. In the initial pipe section, indeed, strong suppression of turbulence characteristics is observed (Zaets, Safarov & Safarov, 1985). After suppression, however, they increase in the value and are stabilized on the high level enough (Nishibori, Kikuyama & Murakami, 1987).

In the following subsections, the results of computations using the Q-model are presented for the various regimes of a turbulent pipe flow.

4.1. Stationary pipe

Calculations have been done for a turbulent flow in a stationary pipe at two Reynolds numbers, $Re_o = 7 \cdot 10^3$ and $Re_o = 4 \cdot 10^4$, to verify an ability of the Q-model to give reasonable results in both low and high Reynolds number regimes. The results were

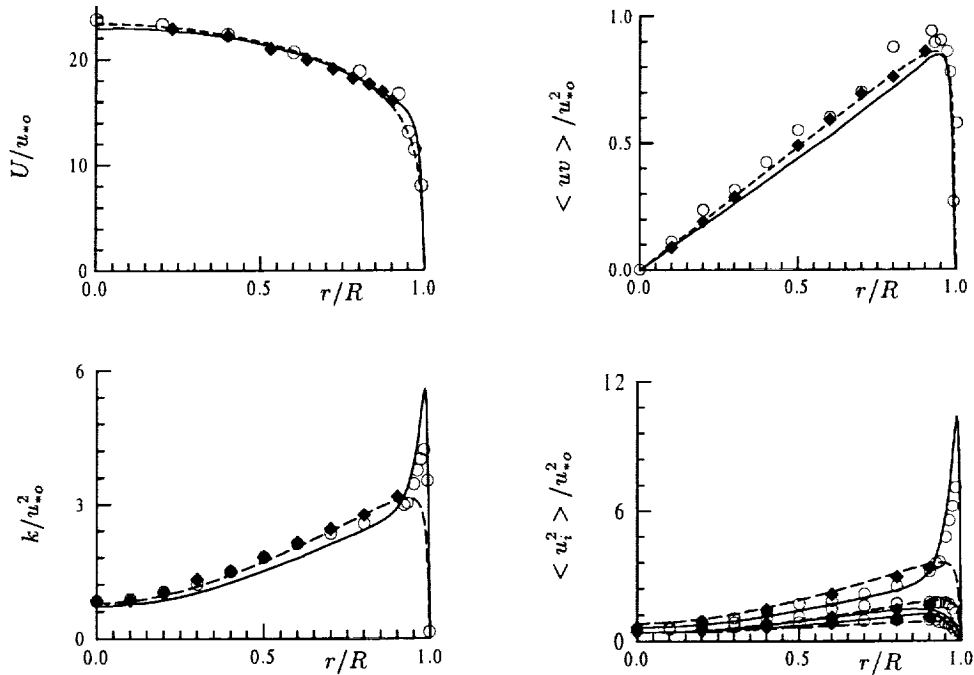


FIGURE 2. Calculations: (—) Q-model, (---) RSTM; experiments: (◆) Zaets, Safarov & Safarov (1985), (○) Laufer (1954).

compared for $Re_o = 4 \cdot 10^4$ (Fig. 2) with the experimental data of Zaets, Safarov & Safarov (1985) and Laufer (1954). The latter were obtained at $Re_o = 5 \cdot 10^4$. For $Re_o = 7 \cdot 10^3$ (Fig. 1), the DNS data (Eggels *et al.*, 1994) were used for comparison. As shown in Figs. 1 and 2, the model gives quite good results.

In Fig. 2, profiles are also shown from the calculations of Kurbatskii, Poroseva & Yakovenko (1995) that used the linear Reynolds stress transport (RST) model (IP model (Launder, Reece & Rodi, 1975) with the damping functions similar to ones suggested in Gibson & Launder (1978) to describe wall effects). Though this model reproduces turbulent characteristics and mean velocity well enough at the high Reynolds number, it describes only qualitatively the features of the low Reynolds number flow.

To describe flows at different Reynolds numbers, the coefficient C_s in Eq. (2.3) varies from 1.58 at $Re_o = 4 \cdot 10^4$ to 1.65 at $Re_o = 7 \cdot 10^3$. In both cases this value differs from the value found optimal for a homogeneous flow; that is, $C_s = 1.5$. The similar situation is observed when the RST models are used. The other model coefficients are found to be $\sigma_Q = 1$, $\sigma_\varepsilon = 1.1$, $C_\nu = 0.22$.

4.2. Initial section of a rotating pipe

It was found that to describe the strong suppression of the turbulence observed in this part of the flow, one has to modify the equation for the dissipation rate by including the additional term with the Richardson number (Kurbatskii, Poroseva & Yakovenko, 1995). The Richardson number characterizes the influence of streamline curvature on turbulence like that of medium stratification on turbulent transport (Bradshaw, 1969). The same modification was introduced in ε -equation (2.3) used with the Q-model; that

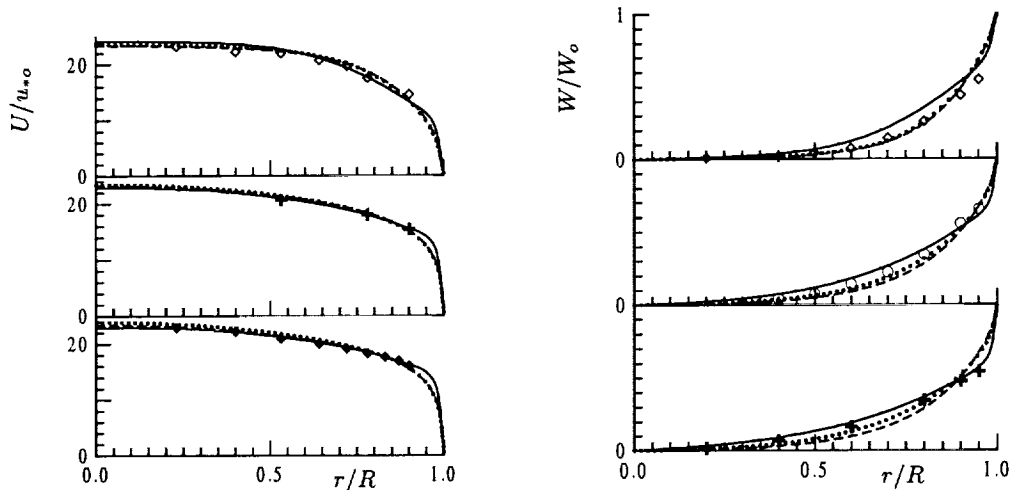


FIGURE 3. Mean velocity components. Calculations: (—) **Q**-model, (---) IP, (.....) SSG1; (◆) $N = 0.$, (+) $N = 0.15,$ (○) $N = 0.3,$ (◇) $N = 0.6.$

is, the coefficient C_o was changed by C_o^* , where

$$C_o^* = \max(1.4, C_o(1 - C_R Ri)), \quad C_R = 2, \quad C_o = 11/6, \quad Ri = \frac{\frac{\partial W}{\partial r} \cdot \frac{W}{r}}{(\frac{\partial W}{\partial r})^2 + (\frac{\partial U}{\partial r})^2}$$

The condition on C_o^* is applied to avoid excessive values of the dissipation rate close to a wall, which can occur under rotation.

The turbulent flow in the initial pipe section ($x/D \leq 25$) was computed at $Re_o = 4 \cdot 10^4$. In Figs. 3-6 the calculated profiles are compared with the experimental data (Zaets, Safarov & Safarov, 1985) and with the results of calculation by RST models: linear (IP) and non-linear (SSG1) (Speziale, Younis & Berger, 2000). In both RST models, damping functions similar to the ones suggested in Gibson & Launder (1978) were applied to describe wall effects. Profiles in Figs. 3-5 correspond to the section $x/D = 25$. As shown, the **Q**-model describes quite well the axial velocity profiles in the whole flow area: from the wall to the pipe axis at different rotation numbers. Moreover, the **Q**-model catches correctly dynamics of the axial velocity with increasing rotation. That is, at the low rotation number $N = 0.15$, the axis value of U slightly decreases, but with further increasing of N , it begins to grow. The behavior of the angular component of the mean flow velocity also is well reproduced.

The behavior of turbulent statistics is reproduced very well, especially near the pipe axis (Figs. 4-6). This is an important result because turbulent transport at the core of a pipe flow at moderate swirl is similar to turbulent transport in concentrated vortex formations in the atmosphere. The damping coefficient Ku_i on Figs. 5-6 is determined as $Ku_i = \langle u_i^2 \rangle (N > 0) / \langle u_i^2 \rangle (N = 0)$.

In experiments it has been observed that near the pipe entrance there exists a conical core in which the developing turbulence is only weakly influenced by the rotation. The streamwise extent of this conical core decreases with increasing rotation. The **Q**-model is more sensitive to the influence of rotation on this initial pipe section and describes

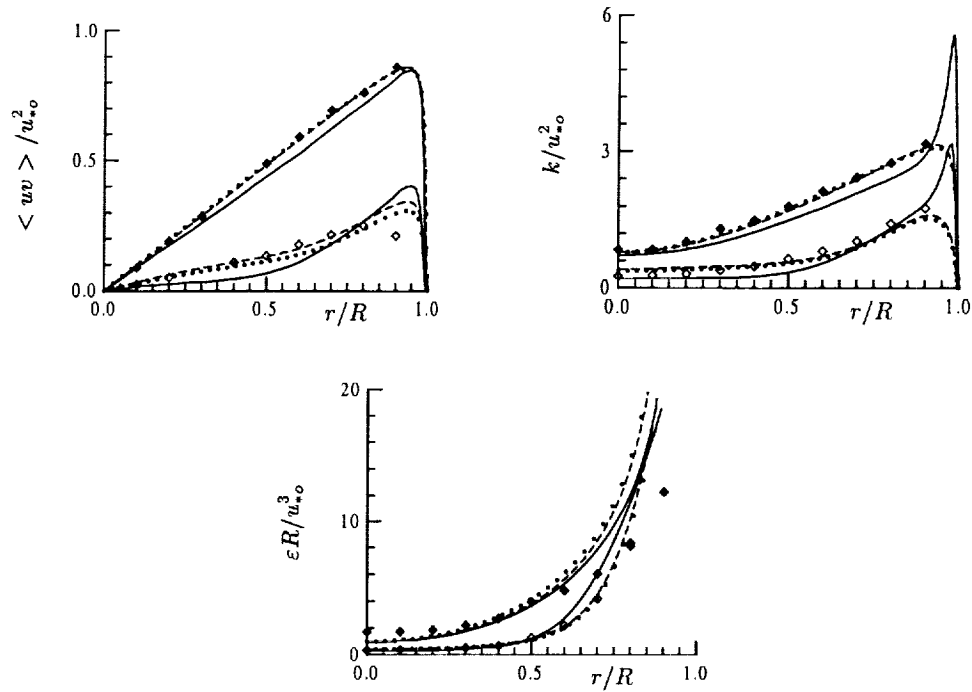


FIGURE 4. (See denotations on Fig. 3).

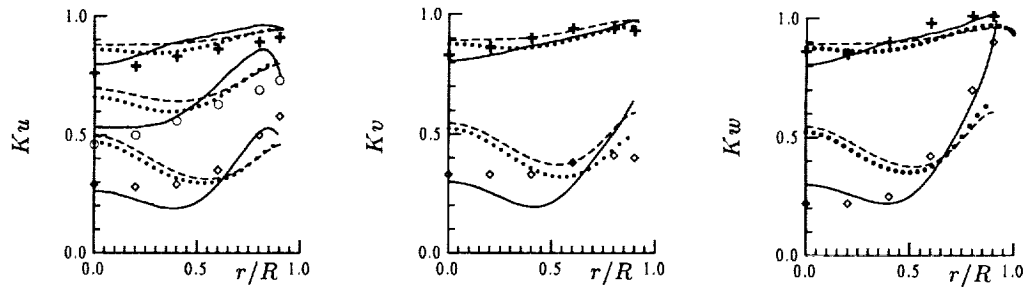


FIGURE 5. (See denotations on Fig. 3).

correctly the shortening of the conical core. In contrast, the RST model is less sensitive to rotational effects in this section and tends to overpredict the extent of the conical core (especially near the centerline) as the rotation is increased. This effect is shown in Fig. 6 where the streamwise evolution of Ku is shown along the initial pipe section.

Finally, it is worth noting that in the initial pipe section, the performance of linear and non-linear RST models are comparable.

4.3. Fully developed flow

With increasing rotation and distance from the pipe entrance, the \mathbf{Q} -model with ε -equation (2.3) using the modified C_o^* predicts full suppression of the turbulence, like the RST models do, in contradiction with the experimental data. Therefore, a fully de-

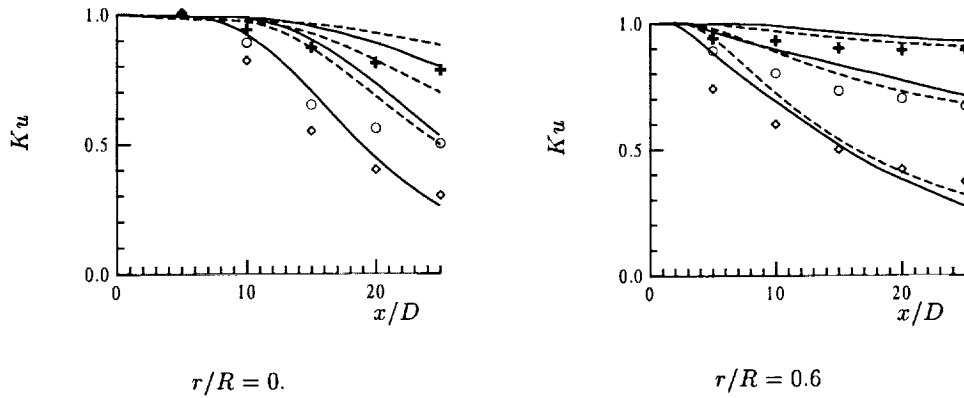


FIGURE 6. Evolution of Ku along the pipe axis. (See denotations on Fig. 3.)

veloped turbulent flow in a rotating pipe was computed by the **Q**-model with ε -equation (2.3) without modification by C_o^* . Some results obtained at $Re_o = 2 \cdot 10^4$ are shown on Fig. 7 in comparison with the experimental data of Imao, Itoh & Harada (1996) and the data obtained with the non-linear RST model (SSG2) (Speziale, Younis & Berger, 2000) with a near-wall model developed in Durbin (1993).

The flow simulated by the **Q**-model reaches the fully developed state at the distance close to the experimental value (Kikuyama *et al.*, 1983; Nishibori, Kikuyama & Murakami, 1987). The model reproduces the evolution of the axial component of the mean velocity better than the RST models do. For the angular velocity, the computational results obtained with the **Q**-model are close to the profiles obtained with the linear RST models (Pettersson, Andersson & Brunvoll, 1998; Speziale, Younis & Berger, 2000; Kurbatkii & Poroseva, 1999). The non-linear RST model provides better agreement for W with the experimental data.

The shear stresses are reproduced well with the **Q**-model. However, in this part of the flow, like other turbulence models, the **Q**-model significantly overpredicts the turbulent kinetic energy level in comparison with experimental data.

Most importantly, the **Q**-model is able to reproduce the correct behavior of turbulence characteristics at relatively high rotation rates, *e.g.*, $N = 1$, whereas RST models predict relaminarization of the flow (Pettersson, Andersson & Brunvoll, 1998) already at this N in contrast to the experiments of Kikuyama *et al.* (1983), which show no sign of turbulence disappearance even at considerably higher N .

5. Conclusions and future plans

The main goal of the present work was to test the **Q**-model in a complex rotated turbulent flow and compare its performance with that of RST models, using in all models similar equations for the dissipation rate.

The **Q**-model is able to predict the flow accurately at various Reynolds numbers and under stronger rotation than possible with a good RST model. In the fully developed pipe flow at moderate rotation numbers, the **Q**-model slightly improves the profiles obtained with the non-linear RST model, which gives the best results among RST models for this part of flow. Most importantly, the **Q**-model is able to reproduce the correct behavior of turbulence characteristics at relatively high rotation rates, *e.g.*, $N = 1$, whereas the RST models predict relaminarization of the flow in contrast to experiments. Also, under

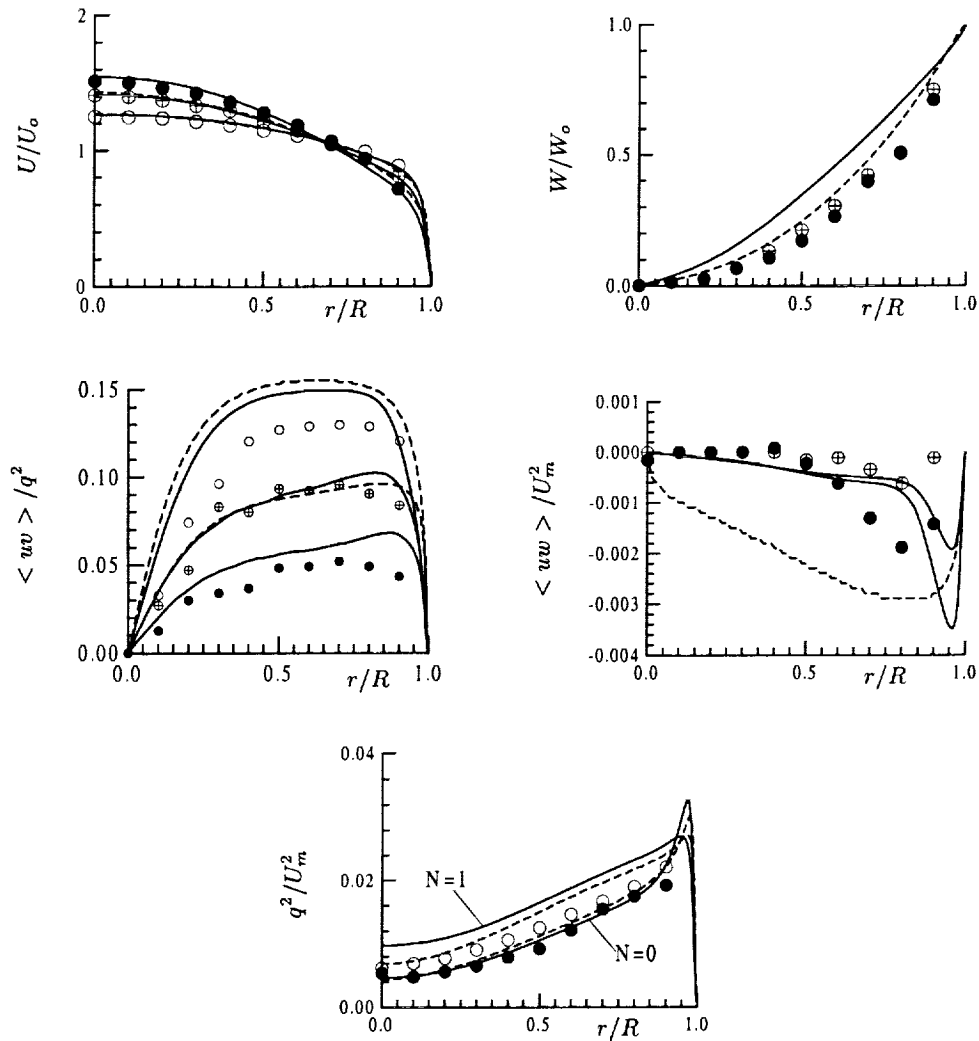


FIGURE 7. Fully developed pipe flow. Calculations: (—) **Q**-model, (----) SSG2; experiments: (○) $N = 0$, (⊕) $N = 0.5$, (●) $N = 1$.

some parameter combinations (N , Re) computations using RST models fail to converge (Pettersson, Andersson & Brunvoll, 1998; Kurbatskii & Poroseva, 1999), whereas such difficulties have not been encountered with the **Q**-model.

However, the **Q**-model as tested in this work, does not solve all problems. One of the possible reasons for this is that, in order to be consistent, a one-point turbulence closure based on the transport equation for Q should also include structure information in the equation for the dissipation rate ε . We are currently working in this direction and hope to be able to report on our progress soon. In the RST models, such modifications would not be possible since they do not carry the necessary information. We are also working on improving the length scale model used in the elliptic relaxation of Q . Finally, we

are currently using these ideas as the basis for the development of a simplified algebraic two-equation structure-based model.

Acknowledgments

We would like to thank Dr. B. A. Petterson-Reif for providing the simulation data obtained with the non-linear SSG2 model in the fully developed pipe flow (Figs. 7).

REFERENCES

- BRADSHAW, P. 1969 The analogy between streamline curvature and buoyancy in turbulent shear flow. *J. Fluid Mech.* **36**, 177-191.
- DALY, B. J. & HARLOW, F. H. 1970 Transport equations in turbulence. *Phys. Fluids*. **13**(11), 2634-2649.
- DURBIN, P. 1993 A Reynolds-stress model for near-wall turbulence. *J. Fluid Mech.* **249**, 465-498.
- EGGELS, J. G. M., UNGER, F., WEISS, M. H., WESTERWEEEL, J., ADRIAN, R. J., FRIEDRICH, R. & NIEUWSTADT, F. T. M. 1994 Fully developed turbulent pipe flow: a comparison between direct numerical simulation and experiment. *J. Fluid Mech.* **268**, 175-209.
- GIBSON, M. M. & LAUNDER, B. E. 1978 Ground effects on pressure fluctuations in the atmospheric boundary layer. *J. Fluid Mech.* **86**, 491-511.
- IMAO, S., ITOH, M. & HARADA, T. 1996 Turbulent characteristics of the flow in an axially rotating pipe. *Int. J. Heat and Fluid Flow* **17**(5), 444-451.
- KASSINOS, S. C. & REYNOLDS, W. C. 1994 A structure - based model for the rapid distortion of homogeneous turbulence. *Report TF - 61*, Thermosciences Division, Department of Mechanical Engineering, Stanford University.
- KASSINOS, S. C. & REYNOLDS, W. C. 1995 An extended structure - based model based on a stochastic eddy - axis evolution equation. *Annual Research Briefs*, Center for Turbulence Research, NASA Ames/Stanford University. 133-148.
- KASSINOS, S. C. & REYNOLDS, W. C. 1996 An interacting particle representation model for the deformation of homogeneous turbulence. *Annual Research Briefs*, Center for Turbulence Research, NASA Ames/Stanford University. 31-53.
- KASSINOS, S. C. & REYNOLDS, W. C. 1997 Advances in structure - based modeling. *Annual Research Briefs*, Center for Turbulence Research, NASA Ames/Stanford University. 179-193.
- KASSINOS, S. C. & REYNOLDS, W. C. 1998 A structure - based model with stropholysis effects. *Annual Research Briefs*, Center for Turbulence Research, NASA Ames/Stanford University. 197-209.
- KASSINOS, S. C., LANGER, C. A., HAIRE, S. L. & REYNOLDS, W. C. 2000 Structure - based turbulence modeling for wall-bounded flows. *Int. J. Heat and Fluid Flow*. **21**, 599-605.
- KIKUYAMA, K. *et al.* 1983 Flow in an axially rotating pipe (a calculation of flow in the saturated region). *Bull. JSME*. **26**(214), 506-513.
- KURBATSKII, A. F., POROSEVA, S. V. & YAKOVENKO, S. N. 1995 Calculation of statistical characteristics of a turbulent flow in a rotated cylindrical pipe. *High Temperature*. **133** (5), 738-748.

- KURBATSKII, A. F. & POROSEVA, S. V. 1999 Modelling turbulent diffusion in a rotating cylindrical pipe flow. *Int. J. Heat and Fluid Flow*. **20**(3), 341-348.
- LAUFER, J. 1954 The structure of turbulence in fully developed pipe flow. *NASA Report N 1174*.
- LAUNDER, B. E., REECE, G. J. & RODI, W. 1975 Progress in development of a Reynolds-stress turbulent closure. *J. Fluid Mech.* **68**, 537-566.
- MOSER, R. D., KIM, J. & MANSOUR, N. N. 1988 Direct numerical simulation of turbulent channel flow up to $Re_\tau = 590$. *Phys. Fluids*. **11**(4), 943-945.
- NISHIBORI, K., KIKUYAMA, K., & MURAKAMI M. 1987 Laminarization of turbulent flow in the inlet region of an axially rotating pipe. *Bull. JSME*. **30**(260), 255-262.
- PETTERSSON, B. A., ANDERSSON, H. I. & BRUNVOLL, A. S. 1998 Modeling near - wall effects in axially rotating pipe flow by elliptic relaxation. *AIAA J.* **36**(7), 1164-1170.
- REYNOLDS, W. C. & KASSINOS, S. C. 1995 A one - point model for the evolution of the Reynolds stress and structure tensors in rapidly deformed homogeneous turbulence. *Proceed. Roy. Soc. London A*. **451** (1941), 87-104.
- SPALDING, D. B. 1977 *GENMIX: a General Computer Program for Two - Dimensional Parabolic Phenomena*. Pergamon Press.
- SPEZIALE, C.G., YOUNIS, B. A. & BERGER, S. A. 2000 Analysis and modeling of turbulent flow in an axially rotating pipe. *J. Fluid Mech.* **407**, 1-26.
- ZAETS, P. G., SAFAROV, N. A., & SAFAROV R.A. 1985 Experimental study of the behavior of turbulence characteristics in a pipe rotating around its axis (in Russian). *Modern problems of continuous medium mechanics*, Moscow Physics and Technics Institute. 136-142.

Towards a robust and efficient v^2 - f implementation with application to transonic bump flow

By Georgi Kalitzin

1. Motivation and objectives

In the last few years, Durbin's v^2 - f turbulence model has been extensively tested for subsonic and transonic flows using different numerics for the discretization of the equations and for their solution. Three versions of the model have been successively developed. The original model, Durbin (1995), includes a non-trivial wall boundary condition for the quantity f , which represents the pressure-strain term and is obtained from an elliptic relaxation equation. It also requires the distance to no-slip walls, albeit for the determination of the coefficient $C_{\epsilon 1}$ which regulates the production of dissipation of turbulent kinetic energy in the ϵ equation. The version developed by Parneix & Durbin (1997) defines a new expression for the coefficient $C_{\epsilon 1}$ substituting the distance to the wall with the ratio $\overline{v^2}/k$. Lien & Durbin (1996) developed another version of the model with a trivial wall boundary condition for f to improve the numerical robustness of the model, in particular for codes which solve equation by equation in a segregated manner.

An extensive, systematic comparison of each version has been conducted in Kalitzin (1999a) and Lien & Kalitzin (2000) for external flow around airfoils, wings, and over a bump. The conclusion of these studies was that all three versions predict in general very similar results for the potential flow region and most of the boundary layer. However, the $C_{\epsilon 1}(\overline{v^2}/k)$ definition causes an overprediction of the boundary layer growth rate in high Reynolds number flows with strong adverse pressure gradients. Forcing f to zero at no-slip walls has been found to delay transition. This is often desirable in transitional flow predictions, as RANS models generally trigger transition too far upstream. However, it has also been found responsible for a significant overprediction of skin friction in flow recovery regions, for example downstream of shock induced separation.

The present report is a continuation of this validation effort. It also describes the current implementation of Durbin's v^2 - f turbulence model in the turbomachinery code TFLO, CITS (2000). This RANS code will be used in the framework of the Accelerated Strategic Computing Initiative (ASCI) at the Center for Integrated Turbulence Simulations (CITS) for large scale computations of flow through the compressor and turbine of an aircraft engine. This requires a robust and efficient implementation of the model. A three-factored scheme which is able to handle the wall boundary conditions of the original model has been developed for this purpose, and its description is included in the report.

2. v^2 - f turbulence model

The v^2 - f turbulence model is an advanced eddy-viscosity model. It can be regarded as an abbreviated Reynolds stress model consisting of three transport equations: for the

turbulent kinetic energy k , the dissipation of the turbulent kinetic energy ϵ , and for the scalar quantity $\overline{v^2}$. Close to solid walls the latter represents the energy of the fluctuations normal to the wall. The production term in the $\overline{v^2}$ transport equation is a pressure strain term. Its nonlocal dependency on the flow, in particular in the presence of solid walls, is modeled with an elliptic relaxation equation for a quantity f . The equations of the original model and of the modified version considered in the present study can be found in Durbin (1995) and Lien & Durbin (1996), respectively. These model versions will be referred to in this report as version A and B, respectively. The main differences between version A and B are the wall boundary conditions for f , which are: $f_w = -20\nu^2\overline{v_1^2}/\epsilon_w y_1^4$ and $f_w = 0$, respectively. Index w and 1 denotes the value at the wall and in the first cell above the wall, respectively. To enforce, in version B, the trivial condition for f at the wall, the term $5\epsilon\frac{\overline{v^2}}{k}$ has been subtracted from the $\overline{v^2}$ transport equation and added to the f equation. This modification preserves the correct asymptotic behavior of the quantity $\overline{v^2}$. The coefficients of version A and B are slightly different, most notable is the coefficient $C_{\epsilon 1}$, which regulates the production of dissipation of turbulent kinetic energy. In version A the coefficient $C_{\epsilon 1}$ is a function of the distance to the wall, and in version B it is a function of the ratio of $\overline{v^2}/k$.

3. Implementation of v^2 - f in TFLO

The v^2 - f model is solved in TFLO in a separate set of subroutines segregated from the mean flow. Multigrid is used for the mean flow, and at each multigrid cycle on the finest grid the model's subroutines are called. They return an updated value for the eddy viscosity and the turbulent kinetic energy. Only these two quantities are passed to the mean flow solver for the determination of the Reynolds stresses.

Different solution algorithms have been employed for each model version. In both versions, the k and ϵ equations are solved first in an implicit, pairwise coupled manner with a cell centered finite difference scheme. The f and $\overline{v^2}$ equations of version A are solved similarly coupled, allowing an implicit treatment of the f -wall boundary condition. The solution follows the description in Kalitzin (1999). The f equation in version B is solved separately with an elliptic solver. Its solution subsequently enters the production term in the $\overline{v^2}$ equation. The zero wall boundary condition for f basically decouples the f from the $\overline{v^2}$ equation. The net source term in the f equation is invariably non-negative, ensuring a non-negative solution f in the entire computational domain.

In both versions, the diffusion terms are discretized with second order central differences. First order upwind differences are used for the discretization of the convective terms. At the current stage, the model is implemented to provide a steady state solution by marching in time from an initial guess. The time derivative term is discretized with a first order forward difference. Local timesteps are used to accelerate convergence. These timesteps are determined by the spectral radius analysis from mean flow quantities, the eddy viscosity and the input CFL number. Multigrid is not used for the turbulence equations. The timesteps for the advancement of the turbulence variables have been weighted with a constant factor. Except for the f -equation in version B, the algebraic system of equations resulting from the implicit operators are solved with a three-factored, approximate factorization scheme. The f -equation in version B is solved with a conjugate gradient method.

Next, a factorization scheme is described which has been developed to handle the wall boundary conditions in the v^2 - f model, version A. The f wall boundary condition is a

critical issue in the implementation. The value of f_w at the wall depends strongly on the value of $\overline{v^2}$ in the first cell above the wall (see also the profiles of the scalars $\overline{v^2}$ and f in Fig. 1 for flow over a flat plate). A small change of $\overline{v_1^2}$ in the first cell above the wall changes the value f_w at the wall, which affects in an elliptic manner the f distribution across the entire boundary layer. This requires an accurate solution of the model's equations close to solid walls.

The $\overline{v^2}$ - f equations can be written in matrix form notation as:

$$(I + S + L_\eta + L_\xi + L_\zeta)\Delta\phi = RHS \quad (3.1)$$

whereby L_γ , with $\gamma = \xi, \eta, \zeta$, contains the convection and diffusion terms in a grid oriented (ξ, η, ζ) coordinate system. S and $\Delta\phi$ contain the implicitly treated source terms and the solution update, respectively. I is the identity matrix. RHS is the right-hand side.

A computer memory and CPU time efficient algorithm for the solution of Eq. (3.1) is critical in large three-dimensional computations. Ordinary ADI algorithms developed for structured grids often converge better if certain directions of the computational coordinate system are normal to walls. Only one direction may be normal to a solid wall for turbulence models with stiff wall boundary conditions as in the case of the v^2 - f model. Even in a multi-block concept, this directionality of the factorization algorithm may lead to severe constraints for the grid generation process for complex geometries, especially in wall corners of cavities or wing-body junctions of an aircraft.

An ADI algorithm requires an approximation for Eq. (3.1), which allows a split into a set of one-dimensional equations. As proposed in Kalitzin *et al.* (2000) the approximation of Eq. (3.1) with

$$(I + S + L_\eta)(I + S)^{-1}(I + S + L_\xi)(I + S)^{-1}(I + S + L_\zeta)\Delta\phi = RHS \quad (3.2)$$

allows a split into the three one-dimensional equations

$$(I + S + L_\eta)\Delta\phi' = P \quad (3.3)$$

along η grid lines,

$$(I + S + L_\xi)\Delta\phi'' = (I + S)\Delta\phi' \quad (3.4)$$

along ξ grid lines, and

$$(I + S + L_\zeta)\Delta\phi''' = (I + S)\Delta\phi'' \quad (3.5)$$

along ζ grid lines. In contrast to earlier formulations in Krist (1998), the source terms are treated implicitly in each computational direction. This leads to a consistent implicit operator on the left-hand side in each computational direction and allows in the case of the v^2 - f model different computational directions to be normal to solid walls.

The scheme described follows Klopfer *et al.* (1998). However, they derive a diagonally dominant scheme for the solution of the Navier-Stokes equations which does not include source terms. The efficiency of the scheme described is of the same order as of an ordinary factorization scheme.

4. Flow over flat plate

The current implementation of the v^2 - f model in TFLO has been tested for subsonic flow over a flat plate. The flow is computed for a Reynolds number of $6 \cdot 10^6$ and a Mach

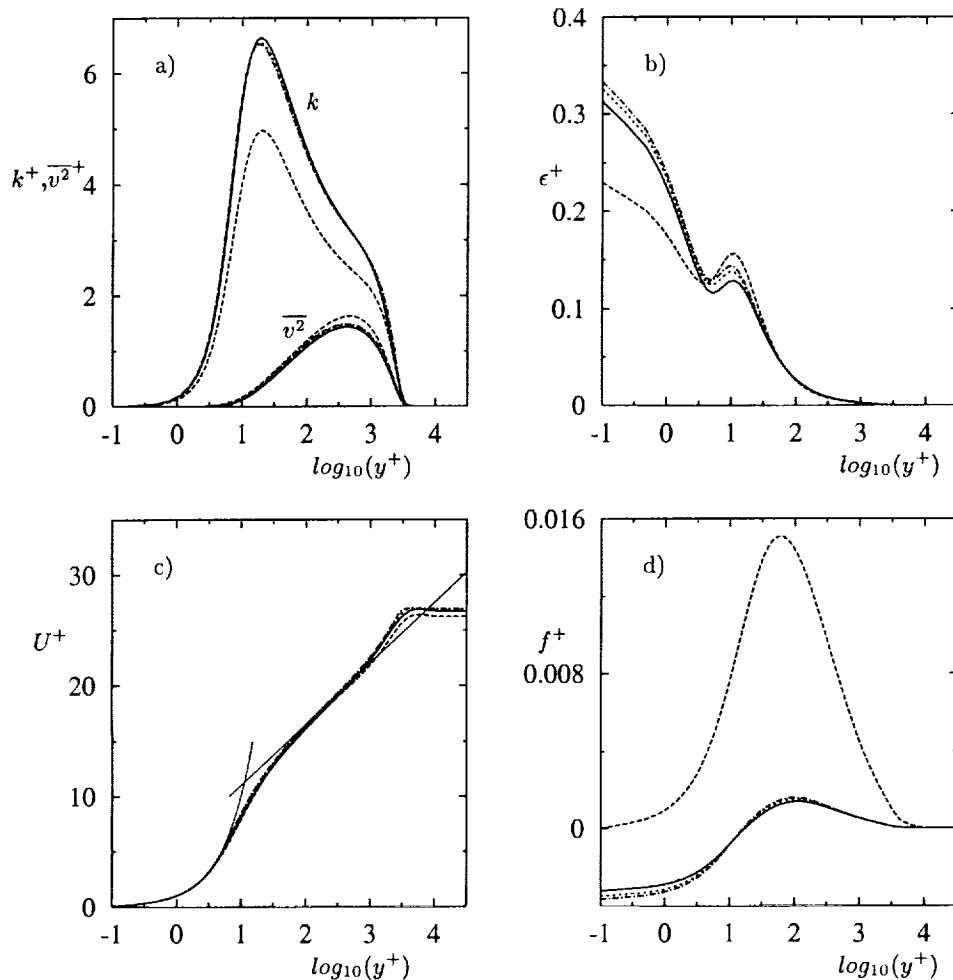


FIGURE 1. Profiles of a) k and $\overline{v^2}$ b) ϵ , c) U^+ and d) f for flow over a flat plate; v^2 - f : --- : version A, CFL3D; : version A, TFLO, VIS4=0.3; — : version A, TFLO, VIS4=1.0 ——— : version B, TFLO, VIS4=1.0).

number of 0.2. The mesh of 64×96 cells is provided with version 5 of CFL3D (Krist (1998)). An average of 40 grid points lie within the boundary layer.

A comparison of v^2 - f results is shown in Fig. 1. The log law and profiles of the normalized turbulent quantities are shown for $x/c = 0.9$. The discrepancy in the results obtained with version A in TFLO and CFL3D (the latter code has been previously extensively validated against several applications) is particularly large for the ϵ and f distribution. It could be traced back to the numerical dissipation of the mean flow solver. While the turbulence transport equations are solved with a first order upwind scheme in both codes, the mean flow is solved in TFLO with a dissipation scheme of Jameson, Schmidt & Turkel (1981) and in CFL3D with an upwind flux difference splitting of Roe (1986). The discrepancy reduces by setting VIS4 in TFLO from the default value of 1 to 0.3, reducing the artificial fourth order background dissipation.

The same plots include the solution of version B. As shown in Fig. 1d, f is larger zero over the entire boundary layer, and its maximum value is significant larger than for version A. At the wall f is zero. As shown in Fig. 1a, $\overline{v^2}$ has the same asymptotic behavior approaching the wall as for version A. The peak value of the turbulent kinetic energy, k^+ , is about 5, and this is significantly lower than for version A. While it corresponds to predictions with other models, this value might be too low. Turbulent kinetic energy profiles obtained with version A for the Bachalo-Johnson bump described next agree significantly better with the experiments.

The solution converged for both versions to a five orders of magnitude in the L_2 norm of the density, turbulent kinetic energy, and $\overline{v^2}$ residual in about 2000 iterations. This is usually required for this type of computation and comparable to other turbulence models. Version B converges more robustly and for a wider range of various numerical parameters.

5. Flow over Bachalo-Johnson bump

Transonic flow over the Bachalo-Johnson bump (Bachalo (1986)) has been chosen to study the performance of TFLO/ v^2 - f in predicting shock-boundary layer interaction. This test case is an axisymmetric configuration, and the flow is not dependent on the circumferential direction and is thus two-dimensional even in the case with massive separation. The flow is computed for an inflow Mach number of 0.873 and a Reynolds number of $Re_c = 2.66 \cdot 10^6$. The computational mesh consists of $192 \times 100 \times 8$ cells. The two-dimensional mesh, shown in Fig. 3, is the same as used in Kalitzin (1999) with some additional cells at the exit in order to split the mesh in several multigridable blocks. Cells are clustered in the region of the shock. The flow is computed fully turbulent, neglecting the influence of wind tunnel walls.

The pressure and skin friction distribution on the wall of the cylinder and bump are shown in Fig. 5. The bump geometry is shown in the background with the symmetry axis coinciding with the frame line. The x -coordinate is chosen such that the bump is located between 0 and 1. Note that the C_p -axis in the pressure plot is reversed. Versions A and B predict roughly the same pressure distribution with the correct shock location and a slightly higher pressure in the separation region. The latter indicates that the separation bubble is underpredicted. The separation region is clearly visible in the negative skin friction in Fig. 5b. There is no experimental data for skin friction available. However, the plot shows that the flow computed with version B recovers faster with a significantly larger skin friction downstream of the separation region. This is consistent with the results obtained for the RAE 2822 airfoil in Lien & Kalitzin (2000).

In Figs. 2 and 4 velocity, shear stress, and turbulent kinetic energy profiles are shown for 6 stations, the location of which is indicated in Fig. 3. The Reynolds shear stress is consistently underpredicted for both versions, in particular in the separation region. Note that, as described in Johnson (1987), the comparison of shear stresses in a shear layer aligned coordinate system will result in better agreement of the computational and experimental data. The computed turbulent kinetic energy profiles differ significantly for both versions. As for the flat plate, Fig. 1a, the turbulent kinetic energy profiles obtained with version A are significantly larger and agree well with the experimental data.

Results for the same test case using the v^2 - f model, version Parneix & Durbin (1997), the Spalart-Almaras, and Menter SST are given in Kalitzin (1999).

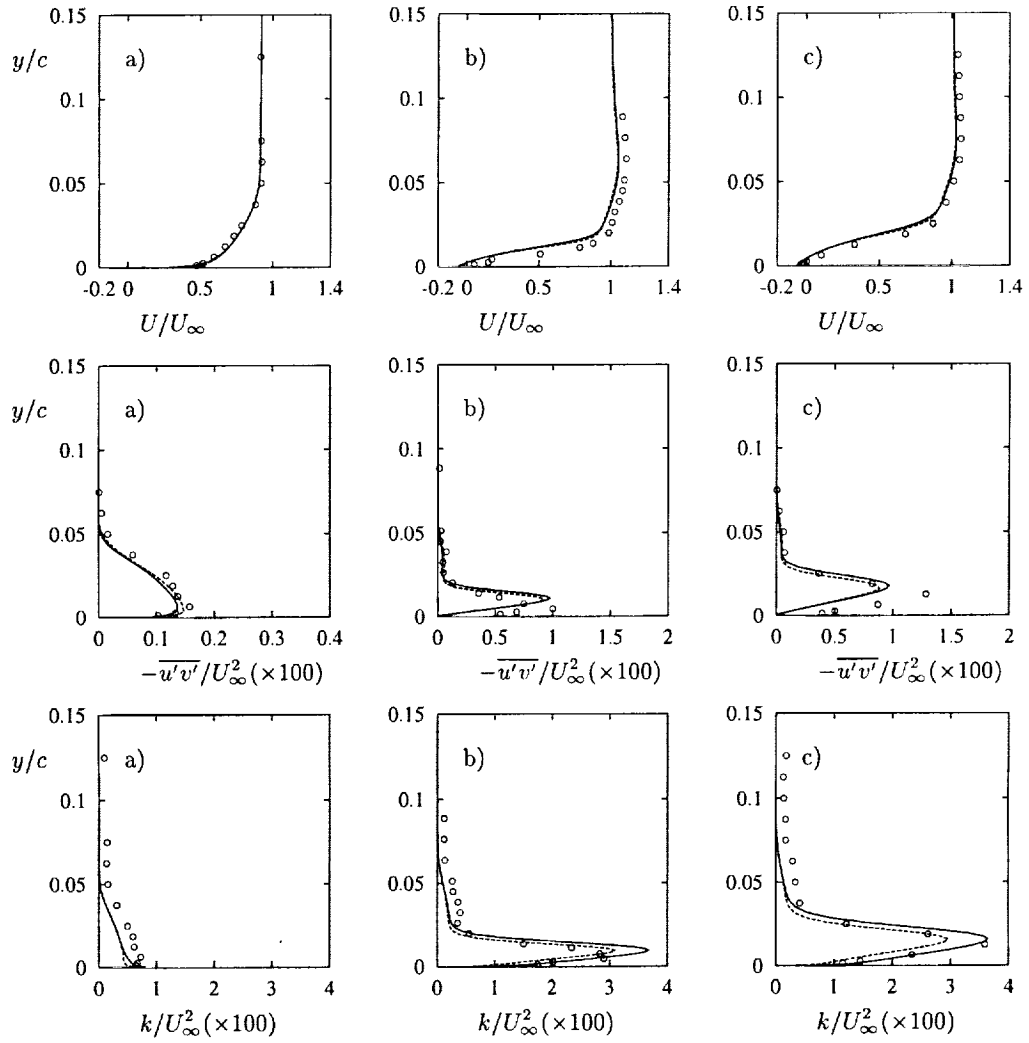


FIGURE 2. Bachalo-Johnson bump: velocity, shear-stress and turbulent kinetic energy; v^2 - f :
 — : version A, - - - : version B, \circ : expt.

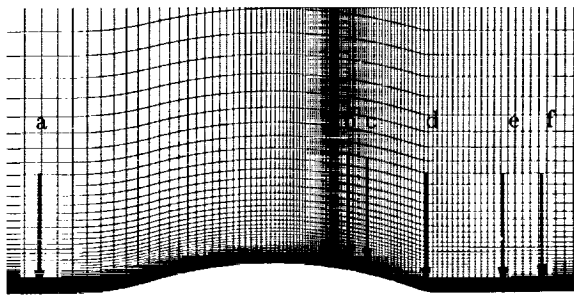


FIGURE 3. Bachalo-Johnson bump: computational mesh. $x/c = -0.250$ (a), 0.750 (b), 0.813 (c), 1.000 (d), 1.250 (e), 1.375 (f).

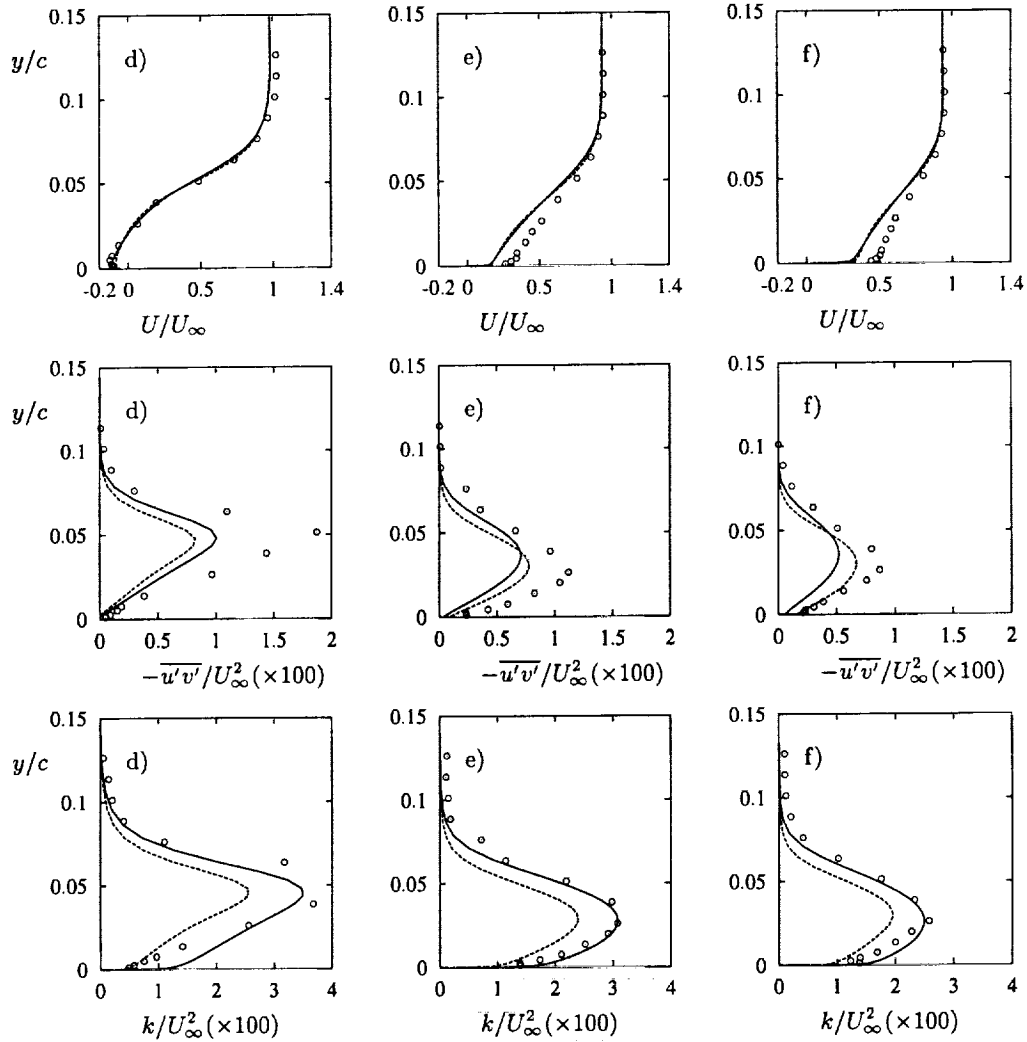


FIGURE 4. Bachalo-Johnson bump: velocity, shear-stress, and turbulent kinetic energy; (continuation); v^2 - f : — : version A, - - - : version B, \circ : expt.

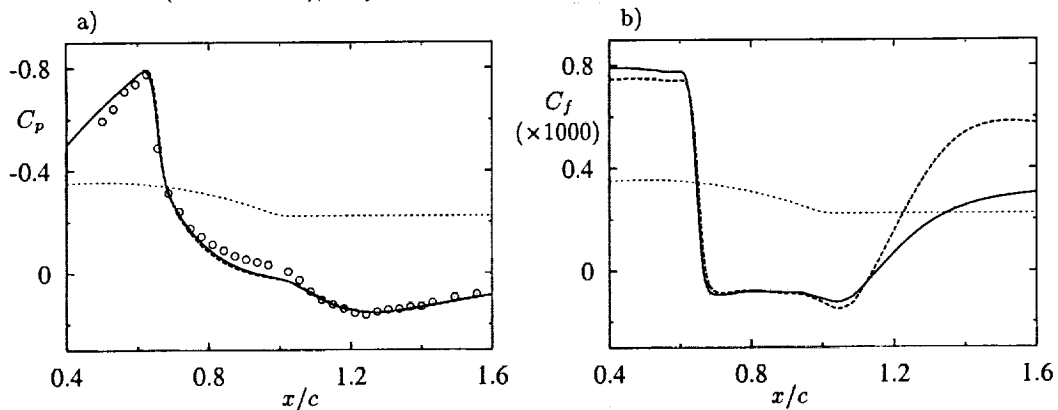


FIGURE 5. Bachalo-Johnson bump: a) pressure and b) skin friction dist.; v^2 - f : — : version A, - - - : version B, \circ : expt.

6. Conclusions and future work

Two versions of the v^2 - f model, version A and B, have been implemented in TFLO and successfully tested for 2 two-dimensional test cases. In both cases, subsonic flow over a flat plate and transonic flow over a axisymmetric bump, the TFLO/ v^2 - f code performs similarly in terms of accuracy and computational costs to previous v^2 - f implementations.

The results for the Bachalo - Johnson bump support the conclusions from previous computations. Version A and B predict main differences in skin friction and turbulent kinetic energy profiles. The understanding of the cause of these differences is important for further development of the v^2 - f model.

Version B is due to the zero f wall boundary condition being significantly more robust. In addition to the test cases presented, its implementation in TFLO has also been successfully tested for three-dimensional transonic flow at a turbine blade-endwall. The results for this test case will be described in a future report. Version B is currently being implemented in TFLO as the default version, and it is used for the initial iterations with the v^2 - f model.

A three-factored approximate factorization scheme has been developed to handle the wall boundary conditions of version A. In contrast to earlier schemes, it allows any computational direction to be normal to solid walls. It is currently being tested for the turbine blade-endwall test case.

Future work includes the implementation in TFLO/ v^2 - f of a higher order time integration scheme which is required for unsteady computations. It is planned to implement a dual time stepping scheme in which a pseudo timestep is used for the inner iteration to a pseudo steady state. For rotational flows, modifications to the Boussinesq approximation proposed by Pettersson-Reif *et al.* (1999) will be investigated. These modifications were designed to sensitize the v^2 - f model to mimic rotational effects on turbulence.

REFERENCES

- BACHALO, W. D. & JOHNSON, D. A. 1986 Transonic turbulent boundary layer separation generated on an axisymmetric flow model. *AIAA J.* **24**, 437-443.
- CITS 2000 *CITS - Center for Integrated Turbulence Simulations - Annual Technical Report.*
- DURBIN, P. A. 1995 Separated flow computations with the k - ϵ - v^2 model. *AIAA J.* **33**, 659-664.
- JAMESON, A., SCHMIDT, W. & TURKEL, E. 1981 Solutions of the Euler Equations by Finite Volume Methods Using Runge-Kutta Time-Stepping Schemes. *AIAA 81-1259.*
- JOHNSON, D. A. 1987 Transonic separated flow predictions with an eddy-viscosity/Reynolds-stress closure model. *AIAA J.* **25**, 252-259.
- KALITZIN, G. 1999a Application of the v^2 - f model to aerospace configurations. *Annual Research Briefs*, Center for Turbulence Research, NASA Ames/Stanford Univ. 289-300.
- KALITZIN, G., KALITZIN, N., & WILDE, A. 2000 A Factorization Scheme for RANS Turbulence Models and SNGR Predictions of Trailing Edge Noise. *AIAA 2000-1982.*
- KALITZIN, G. 1999 Application of v^2 - f turbulence model to transonic flows. *AIAA 99-3780.*
- KLOPFER, G. H., HUNG, C. M., VAN DER WIJNGAART, R. F. & ONUFER, J. T. 1998

- A Diagonalized Diagonal Dominant Alternating Direction Implicit (D3ADI) Scheme and subiteration correction. *AIAA 98-2824*.
- KRIST, S., BIEDRON, R. & RUMSEY, C. 1998 CFL3D User's Manual (Version 5.0). *NASA/TM-208444*.
- LIEN, F. S. & DURBIN, P. A. 1996 Non-linear $k - \epsilon - \overline{v^2}$ modeling with application to high lift. *Proc. of the Summer Program*, Center for Turbulence Research, NASA Ames/Stanford Univ. 5-22.
- LIEN, F. S. & KALITZIN, G. 2000 Computations of transonic flow with the v^2 - f turbulence model. *Int. J. of Heat and Fluid Flow*. **6238**, 1-9.
- PARNEIX, S. & DURBIN, P. A. 1997 Numerical simulation of 3D turbulent boundary layers using the V2F model. *Annual Research Briefs*, Center for Turbulence Research, NASA Ames/Stanford Univ. 135-148.
- PETTERSSON-REIF, B. A., DURBIN, P. A. & OOI, A. 1999 Modeling rotation effects in eddy-viscosity closures. *Int. J. of Heat and Fluid Flow*. **20**, 563-573.
- ROE, P. L. 1986 Characteristic Based Schemes for the Euler Equations *A Numerical Review of Fluid Mech.* 337-365.

APPENDIX Roster

NAME/TERM		AREA OF RESEARCH
POSTDOCTORAL FELLOWS		
BOTELLA, Dr. Olivier 9/98-present	(Ph.D. Engineering, 1997 University of Nice Sophia Antipolis, France)	Numerical methods
CHA, Dr. Chong 4/00-present	(Ph.D. Mechanical Engr., 2000 University of Washington)	Turbulent combustion
CONSTANTINESCU, Dr. George 10/99-5/00	(Ph.D. Engineering, 1998 University of Iowa)	Computational acoustics
DARVE, Dr. Eric 9/99-present	(Ph.D. Mathematics, 1999 Pierre et Marie Curie Univ. Paris, France)	Computational biology
DUCHAMP de LAGEN- ESTE, Dr. Laurent 2/00-present	(Ph.D. Mechanics, 1999 Ecole Centrale de Lyon France)	Turbulent combustion
FAVIER, Dr. Valerie 10/00-present	(Ph.D. Fluid Physics, 2000 INSA Rouen, France)	Cardiovascular mechanics
GULLBRAND, Dr. Jessica 12/99-present	(Ph.D. Fluid Mech., 1999 Lund Institute of Technology Sweden)	Large eddy simulation
HILGERS, Dr. Angela 12/98-4/00	(Ph.D. Theoretical Phys., 1998 RWTH-Aachen/QMW London)	Optimization and control
IDOWU, Dr. Olusola 10/00-present	(Ph.D. Applied Math., 2000 University of Newcastle, U.K.)	Protoplanetary accretion disks

NAME/TERM		AREA OF RESEARCH
KALITZIN, Dr. Georgi 1/97-12/99	(Ph.D. Mechanical Engr. 1991 Technical University, Magdeburg, Germany)	Turbulence modeling
LOUCH, Dr. Derek S. 9/98-6/00	(Ph.D. Engineering, 1998 University of Cambridge, U.K.)	Turbulent combustion
PECK, Dr. Bill 6/99-8/00	(Ph.D. Mechanical Eng., 1998 Univ. of Alberta, Canada)	Two-phase flow
POROSEVA, Dr. Svetlana 8/99-present	(Ph.D. Fluid/Plasma Mech. 1996 Novosibirsk State University Russia)	Structure based modeling
SCHLUTER, Dr. Jörg 10/00-present	(Ph.D. Fluid Mech., 2000 ENS/CERFACS, France)	Large eddy simulation
SU, Dr. Lester 10/98-8/00	(Ph.D. Aerospace Engr. 1995 University of Michigan)	Turbulent combustion
UMURHAN, Dr. Matt 9/98-present	(Ph.D. Astronomy, 1998 Columbia Univ.)	Protoplanetary disks
SR. RESEARCH ASSOCIATES		
CABOT, Dr. William H. 3/88-12/99	(Ph.D. Physics, 1983 Univ. of Rochester)	Large eddy simulation and convection
WANG, Dr. Meng 9/92-present	(Ph.D. Mechanical Engr., 1989 University of Colorado)	Aerodynamic noise
RESEARCH STAFF		
FATICA, Dr. Massimiliano 10/95-present	(Ph.D. Fluid Mech., 1995 Univ. of Rome, Italy)	Parallel computing
IACCARINO, Gianluca 4/98-present	(University of Naples, Italy)	Turbulence modeling

NAME/TERM		AREA OF RESEARCH
KASSINOS, Dr. Stavros 1/95-present	(Ph.D. Mechanical Engr., 1994 Stanford University)	Turbulence modeling
MAHESH, Dr. Krishnan 6/96-10/00	(Ph.D., Mechanical Engr., 1996 Stanford University)	Numerical methods
MARTIN, Dr. M. Pino 8/00-present	(Ph.D. Mechanical Engr., 1999 University of Minnesota)	Hypersonics
PITSCH, Dr. Heinz 5/99-present	(Ph.D. Mechanical Eng., 1998 RWTH-Aachen, Germany)	Turbulent combustion
RUETSCH, Dr. Gregory 9/93-6/00	(Ph.D. Applied Math., 1991 Brown University)	Turbulent combustion Parallel computing
SR. VISITING FELLOWS		
CAIN, Dr. Alan Spring/Summer 2000	Innovative Technology Applications Co.	Flow Control
FEDOTOV, Dr. Sergei 8/00-9/00	University of Manchester, UMIST, U.K.	Turbulent combustion
HE, Dr. Guowei 5/00-6/00	Los Alamos Natl. Lab. Chinese Academy of Sciences	Turbulent combustion
KOSALY, Prof. George 1/00-3/00, 9/00-12/00	University of Washington	Turbulent combustion
MOHAMMADI, Prof. Bijan 11/00	University of Montpellier France	Large eddy simulation
NICOLLEAU, Dr. Franck 8/00	University of Sheffield, U.K.	Large eddy simulation
WEBB, Dr. Anthony 8/00-12/00	Univ. of New South Wales Australia	Stratified flows

NAME/TERM		AREA OF RESEARCH
SR. RESEARCH FELLOWS		
JIMENEZ, Prof. Javier 1987-present		Wall turbulence
KOUMOUTSAKOS, Dr. Petros 8/94-present		Turbulence physics Control and optimization
GRADUATE STUDENTS		
HAN, Donghee 10/00-present	(Stanford University)	Turbulent combustion
MARSDEN, Alison 10/98-present	(Stanford University)	Large eddy simulation
SBALZARINI, Ivo 7/00-9/00	(Swiss Federal Institute of Technology)	Evolution strategies
SRIPAKAGORN, Paiboon 4/00-6/00	(University of Washington)	Turbulent combustion

2000 ADVISORY COMMITTEE

Dr. Ron F. Blackwelder
University of Southern California

Prof. Norbert Peters
RWTH - Aachen

Dr. David E. Crow
United Technologies Pratt & Whitney

Prof. A. Richard Seebass (Chairman)
University of Colorado at Boulder

Prof. Steven Crow
Starcar Development Company

Dr. Julian Tishkoff
Air Force Office of Scientific Research

Mr. Robert H. Kelly-Wickemeyer
Boeing Commercial Airplane Group

Dr. Dennis M. Bushnell (Ex-officio)
NASA Langley Research Center

Prof. Brian Launder
University of Manchester

Dr. Marvin E. Goldstein (Ex-officio)
NASA Glenn Resesarch Center

Dr. Spiro Lekoudis
Office of Naval Research

Dr. Jack Hansen (Ex-officio)
NASA Ames Research Center

2000 STEERING COMMITTEE

Prof. Paul A. Durbin
Mechanical Engineering, Stanford

Prof. Parviz Moin
Director, Center for Turbulence Research
Professor, Mechanical Engineering,
Stanford, and
Sr. Staff Scientist, NASA Ames Research
Center

Prof. Javier Jiménez
Senior Research Fellow,
Center for Turbulence Research, and
Professor, University of Madrid

Prof. William C. Reynolds
Professor, Mechanical Engineering,
Stanford, and
Sr. Staff Scientist, NASA Ames Research
Center

Prof. Sanjiva K. Lele
Aeronautics & Astronautics and
and Mechanical Engineering, Stanford

Dr. Nagi N. Mansour
Sr. Staff Scientist
NASA Ames Research Center

